

minerals

Special Issue Reprint

Structure and Origin of Gold Mineralization

From Primary to Placer Gold Deposits

Edited by
Javier Fernández-Lozano, Erik Melchiorre and Pablo Caldevilla Domínguez

mdpi.com/journal/minerals

MDPI

Structure and Origin of Gold Mineralization: From Primary to Placer Gold Deposits

Structure and Origin of Gold Mineralization: From Primary to Placer Gold Deposits

Guest Editors

Javier Fernández-Lozano
Erik Melchiorre
Pablo Caldevilla Domínguez

MDPI

Basel • Beijing • Wuhan • Barcelona • Belgrade • Novi Sad • Cluj • Manchester

Guest Editors

Javier Fernández-Lozano
Departamento de Tecnología Minera, Topografía y Estructuras
Universidad de León
León
Spain

Erik Melchiorre
Department of Geological Sciences
California State University
San Bernardino, CA
USA

Pablo Caldevilla Domínguez
Departamento de Tecnología Minera, Topografía y Estructuras
Universidad de León
León
Spain

Editorial Office
MDPI AG
Grosspeteranlage 5
4052 Basel, Switzerland

This is a reprint of the Special Issue, published open access by the journal *Minerals* (ISSN 2075-163X), freely accessible at: https://www.mdpi.com/journal/minerals/special_issues/F5121FX741.

For citation purposes, cite each article independently as indicated on the article page online and as indicated below:

Lastname, A.A.; Lastname, B.B. Article Title. *Journal Name* **Year**, *Volume Number*, Page Range.

ISBN 978-3-7258-8713-2 (Hbk)
ISBN 978-3-7258-8714-9 (PDF)
https://doi.org/10.3390/books978-3-7258-8714-9

Cover image courtesy of Erik Melchiorre

© 2026 by the authors. Articles in this reprint are Open Access and distributed under the Creative Commons Attribution (CC BY) license. The reprint as a whole is distributed by MDPI under the terms and conditions of the Creative Commons Attribution-NonCommercial-NoDerivs (CC BY-NC-ND) license (https://creativecommons.org/licenses/by-nc-nd/4.0/).

Contents

About the Editors . . . . . **vii**

Preface . . . . . **ix**

Javier Fernández-Lozano, Erik Melchiorre and Pablo Caldevilla Domínguez
Editorial for Special Issue "Structure and Origin of Gold Mineralization: From Primary to Placer Gold Deposits"
Reprinted from: *Minerals* **2026**, *16*, 556, https://doi.org/10.3390/min16050556 . . . . . **1**

Kamal Abdelrahman, Reda Abdu Yousef El-Qassas, Mohammed S. Fnais, Peter Andráš and Ahmed M. Eldosouky
Geological Structures Controlling Au/Ba Mineralization from Aeromagnetic Data: Harrat ad Danun Area, Saudi Arabia
Reprinted from: *Minerals* **2023**, *13*, 866, https://doi.org/10.3390/min13070866 . . . . . **5**

Amr Abd El-Raouf, Fikret Doğru, Islam Azab, Lincheng Jiang, Kamal Abdelrahman, Mohammed S. Fnais and Omar Amer
Utilizing Remote Sensing and Satellite-Based Bouguer Gravity data to Predict Potential Sites of Hydrothermal Minerals and Gold Deposits in Central Saudi Arabia
Reprinted from: *Minerals* **2023**, *13*, 1092, https://doi.org/10.3390/min13081092 . . . . . **18**

Dave Craw, Neil Phillips and Julian Vearncombe
Unconformities and Gold in New Zealand: Potential Analogues for the Archean Witwatersrand of South Africa
Reprinted from: *Minerals* **2023**, *13*, 1041, https://doi.org/10.3390/min13081041 . . . . . **39**

Oliver P. Kreuzer, Bijan Roshanravan, Amanda J. Buckingham, Daniel P. Core, Brian A. Konecke, Daniel McDwyer and Roger Mustard
Controls, Expressions, and Discovery Potential of Gold Mineralization in the Central-Eastern Yilgarn Craton, Western Australia: New Insights from an Integrated Targeting Study
Reprinted from: *Minerals* **2025**, *15*, 1255, https://doi.org/10.3390/min15121255 . . . . . **70**

Erik B. Melchiorre, Ryan Mathur, George Kamenov and Jorge Paredes
Geochemical Overprinting and Secondary Placer Crystal Formation in the La Cholla District, Quartzsite, Arizona, USA: Evidence from Copper Isotopes, Morphology, and Trace Elements
Reprinted from: *Minerals* **2023**, *13*, 1444, https://doi.org/10.3390/min13111444 . . . . . **125**

Akumbom Vishiti, Cheo Emmanuel Suh, Ralain Bryan Ngatcha, Erik B. Melchiorre, Elisha Mutum Shemang, Benjamin Odey Omang, et al.
Soil Geochemistry Combined with Particulate Gold Microchemistry Provides Evidence of Eluvial Gold Genesis and Anthropogenic Hg Use in Eastern Cameroon Goldfields
Reprinted from: *Minerals* **2024**, *14*, 567, https://doi.org/10.3390/min14060567 . . . . . **147**

Guo Li, Shanshan Ru, Chuandong Xue and Wei Wang
Evolution of the Ore-Bearing Fluid of Alin Sb–Au Orebodies in Shuixie Cu–Co Orefield, SW China: Constraints on the Rare Earth Element and Trace Element Components of Auriferous Pyrite and Host Rock
Reprinted from: *Minerals* **2025**, *15*, 491, https://doi.org/10.3390/min15050491 . . . . . **171**

Sergei Shevyrev and Natalia Boriskina
Analysis of Structural Position of Carlin-Type Gold Deposits with Lineament Analysis of Remote Sensing Data Using pyLEFA Software
Reprinted from: *Minerals* **2025**, *15*, 219, https://doi.org/10.3390/min15030219 . . . . . **188**

Arkadii A. Kalinin, Nickolay M. Kudryashov and Yevgeny E. Savchenko
Timing and Evolution of Gold Mineralization in the Maljavr Occurrence (NW Russia), NE Part of the Fennoscandian Shield
Reprinted from: *Minerals* **2024**, *14*, 535, https://doi.org/10.3390/min14060535 . . . . . **206**

Dmitry L. Konopelko, Valeriia S. Zhdanova, Sergei Y. Stepanov, Ekaterina S. Sidorova, Sergei V. Petrov, Aleksandr K. Kozin, et al.
Mineralization Styles in the Orogenic (Quartz Vein) Gold Deposits of the Eastern Kazakhstan Gold Belt: Implications for Regional Prospecting
Reprinted from: *Minerals* **2025**, *15*, 885, https://doi.org/10.3390/min15080885 . . . . . **230**

About the Editors

Javier Fernández-Lozano

Javier Fernández-Lozano is a geologist whose interest in earth sciences began at an early age, inspired by his father's passion for nature. He holds a degree in Geology from the Complutense University of Madrid and completed a PhD in Geosciences at Utrecht University in the Netherlands. During his postdoctoral career at several Spanish universities, he worked across various fields of geology, including tectonic and structural geology, geomorphology, and mining. His research has also focused on the use of emerging technologies, particularly drones equipped with different sensors, and their application to the study of mineral deposits. He is a certified drone pilot and operator accredited by the Spanish Aviation Safety and Security Agency. Throughout his scientific career, he has received several international early-career researcher awards, and the Spanish Ministry of Education has formally recognised his postdoctoral trajectory as outstanding following the completion of prestigious research programmes. He is currently an Associate Professor at the Higher and Technical School of Mining Engineering of the University of León, where he conducts teaching and research on gold mining and critical raw materials through several research projects.

Erik Melchiorre

Erik Melchiorre was introduced to gold panning at scout camp on the banks of the Stanislaus River, and around Angels Camp, California. Erik received his Bachelor of Science degree in Geology from the University of Southern California, his Master of Science degree in Geology from Arizona State University, and his Ph.D. in Earth and Planetary Sciences from Washington University in St. Louis, Missouri. He previously worked at the Cyprus-Bagdad Copper Mine, the Phelps Dodge Morenci Copper Mine, and mines in Idaho and South Dakota. For the past twenty-four years, Erik has worked as Professor of Geology at California State University, San Bernardino, where he was named the 2022 Research Professor of the Year. Erik and his students work on the geochemistry of ore deposits around the world, having visited over 160 mines across five continents.

Pablo Caldevilla Domínguez

Pablo Caldevilla Domínguez is an Assistant Lecturer and researcher at the University of León, where he teaches in the area of Mining Prospecting and Research, including subjects such as Geology, Mineralogy and Petrography, and Mineral Deposits. His research focuses on the geology, petrology, geochemistry, and metallogeny of ore deposits, with particular emphasis on orogenic gold deposits and critical raw materials such as tungsten and tin. He completed his Ph.D. researching the W-Sn and Au deposits in NW Iberia, and has published studies on mineral deposit characterization, ore-forming processes, and the geological controls of gold and strategic mineralization. He has authored or co-authored more than 25 research publications, presented his work at national and international conferences, and participated in projects on metallic mining resources, geoconservation, geological heritage, and responsible resource development.

Preface

Gold has been coveted for thousands of years due to its rarity in nature, beauty and physical properties such as durability and ductility. From the early Egyptian civilization to the California gold rush, the prospection and exploitation of gold ores have aroused considerable interest. Gold represents a reserve asset material, as a safe haven for capital in times of crisis. Since the stock market crash in October 1987, gold has acquired notable interest from economies worldwide. Recent advances in the study of gold mineralization require a multidisciplinary approach based on geological, geochemical, and geophysical data. The integration of remote sensing techniques and hyperspectral imagery with soil, water, and biogeochemical data has led to the recognition of potential economic deposits across a variety of tectonic settings. The development of aeromagnetic surveying has also enabled large-scale prospecting in remote or difficult-to-access areas of the planet, improving the geological characterization of near-surface deposits. Studies range from the analysis of macro- and micro-scales based on traditional geological prospection and metallogenetic relations observed in new and different types of gold deposits to the advanced analysis of isotope geochemistry and fluid inclusions using the latest techniques to gain insight into the genesis and evolution of mineralization. This Special Issue aims to contribute to understanding the origin and structure of gold mineralization using different methods and techniques. The main goal is to provide readers with a comprehensive and updated overview via studying primary and secondary gold occurrences.

Javier Fernández-Lozano, Erik Melchiorre, and Pablo Caldevilla Domínguez
Guest Editors

minerals

MDPI

Editorial

Editorial for Special Issue "Structure and Origin of Gold Mineralization: From Primary to Placer Gold Deposits"

Javier Fernández-Lozano [1,*], Erik Melchiorre [2] and Pablo Caldevilla [1]

[1] Área de Prospección e Investigación Minería, Escuela Superior y Técnica de Ingenieros de Minas, Universidad de León, 24071 León, Spain; pcald@unileon.es
[2] Department of Geological Sciences, California State University, San Bernardino, CA 92405, USA; emelch@csusb.edu
* Correspondence: jferl@unileon.es

The high price of gold reached in recent years—exceeding USD 5000/oz in 2026 and expected to continue rising—has generated renewed interest in this precious metal.

The study of the structure and origin of gold deposits is a dynamic area of economic geology, not only because of the strategic importance of gold but also because of the complexity of the processes involved in its formation, redistribution, and concentration.

The main objective of this Special Issue is to adopt a multidisciplinary approach that offers new perspectives by integrating field observations, mineralogical and geochemical analyses, and remote-sensing data for prospective modelling and deposit assessment.

The studies presented in this volume demonstrate that gold research is advancing toward increasingly integrative models, in which structural controls, geochemical fingerprints, geophysical signals, and supergene processes are analysed as parts of a single mineral system.

To achieve this goal, this collection brings together ten contributions, organised in by geographic location and main thematic focus. Some studies focus on geophysical and remote-sensing methods for gold exploration, as well as integrated lithostructural and mineral-potential modelling. Other contributions examine sedimentological and placer-related processes, together with the geochemical and mineralogical characterisation of gold systems. In addition, several studies apply machine learning-based techniques to prospectivity analysis and target modelling. Together, these contributions provide a broad overview of current research on the structure, genesis, redistribution, and exploration of gold deposits in different geological contexts.

Abdelrahman et al. (Contribution 1) explore the use of geophysical methods—specifically magnetic surveying, widely used in the exploration and mapping of precious metals, as well as in the detection of structures capable of hosting mineral deposits—in the Harrat ad-Danun area of Saudi Arabia. This area is characterised by metamorphic and plutonic rocks that form part of the western Arabian Shield and demonstrate the value of aeromagnetic data in delineating structures favourable to Au/Ba mineralisation. The authors identify several favourable aeromagnetic trends and magnetic anomalies associated with faults, shear zones, and subsurface dykes, and conclude that these structural elements directly control the location of mineralisation. The main contribution of this paper is showing that regional tectonic architecture can be accurately reconstructed from potential-field geophysics and, therefore, used as a first-order tool for the exploration of gold deposits.

Modern gold exploration integrates surface and subsurface signals to reduce uncertainty and prioritise exploration targets, as demonstrated by El-Raouf et al. (Contribution 2). They present a methodological workflow for identifying hydrothermal zones and deep

structures with potential for gold. The combination of Landsat imagery, topographic data, and the processing of gravity lineaments—on which an oriented principal component analysis (PCA) was performed—allowed for the delineation of alteration areas and the establishment of their relationship with regional structural corridors.

The research of Craw et al. (Contribution 3) utilises the role of unconformities on an extensive regional scale in New Zealand. Based on the analysis of extensive marine unconformities in the South Island of New Zealand, the authors draw analogies to the famous Archean gold-bearing succession of the Witwatersrand Supergroup and examine the importance of transgressive sedimentary settings in concentrating gold in placer-type deposits. This article offers a valuable conceptual reflection on the need to establish analogues among certain gold deposits through sedimentological studies, basin-evolution analyses, and metallogeny, particularly in discussing the origin of paleoplacers and stratabound gold systems.

Australia is a major producer of gold. The integrated study of the central-eastern Yilgarn Craton in Western Australia by Kreuzer et al. (Contribution 4) provides a new lithostructural interpretation using geophysical and remote-sensing tools specifically tailored to the area. The mineral potential modelling workflow used five complementary techniques. Kreuzer et al. (Contribution 4) identified significant spatial relationships between gold mineralisation, gravity ridges and edges, K/Th radiometric anomalies, and certain spectral signatures linked to goethite, clays, and iron. The authors' integrated strategy can drastically reduce the search space and highlight underexplored areas with high gold potential.

Melchiorre et al. (Contribution 5) incorporate geochemical studies into the investigation of the La Cholla placer gold deposits in Arizona and document how late geothermal fluids can modify pre-existing placers, generating apparently contradictory features. The authors demonstrate that placers should not be interpreted solely as products of mechanical concentration, but also as open systems in which post-depositional chemical processes may operate, reconfiguring the mineralogy and texture of gold.

The Batouri goldfields in eastern Cameroon, South Africa, were studied by Vishiti et al. (Contribution 6). Their research stands out for its combination of soil geochemistry and the microchemistry of particulate gold, and they use both approaches to locate possible source lithologies. The morphological and compositional variability of the gold particles suggests a proximal source in quartz veins hosted by the granitic basement. This article broadens the scope of the Special Issue by connecting gold genesis, regolith exploration, and the impact of artisanal mining activity on the surface geochemical signal.

Li et al. (Contribution 7) analyse the geochemical dimension of the mineralising fluids in the Alin Sb-Au orebodies of the Shuixie metallogenic field in southwestern China. They examined the use of trace and rare-earth elements in auriferous pyrite and the host rock, enabling reconstruction of fluid evolution, and combine an integrated study of mineral microgeochemistry, fluid evolution, and ore formation to provide new insights into this polymetallic gold-bearing deposit.

Shevyrev and Boriskina (Contribution 8) present a k-means machine learning model for Carlin-type gold deposits that enables unsupervised classification of areas of interest using only predictor variables. Their study of such deposits through the analysis of lineaments extracted from remote imagery and digital terrain models, using the pyLEFA software, provides deeper insight into the role of crustal fracture fields in controlling gold concentrations detectable by remote sensing. They demonstrated how combining tectonic information and remote sensing can be used to map the prospectivity of Carlin-type deposits, even in the absence of direct evidence of magmatic sources.

https://doi.org/10.3390/min16050556

The occurrence of significant gold deposits in Archean conglomerates at Maljavr, in northwestern Russia, adds a particularly relevant temporal and metallogenic dimension. The research by Kalinin et al. (Contribution 9) proposes a complex evolution of gold mineralisation, including an initial stage of metasomatism and a subsequent redistribution of gold associated with the intrusion of a tourmaline-bearing pegmatite. The authors highlight its significance as one of the first recognised examples of gold mineralisation in Archean conglomerates in the Fennoscandian Shield. This study contributes to the volume's objective by showing that the history of a gold system may be polyphase and that the mineralisation observed today may result from superimposed events of different ages and origins.

Finally, the auriferous quartz-vein deposits of the Eastern Kazakhstan Gold Belt, an important black-shale-hosted gold province, are also noteworthy. Konopelko et al. (Contribution 10) differentiate mineralisation styles and document associations with auriferous sulphides and veins containing visible gold. They demonstrate the value of alteration zones and Au–As–Pb–Sb geochemical associations for regional prospecting.

Overall, the contributions brought together in this Special Issue show that the study of gold mineralisation can no longer be approached from a single perspective and that geological structure continues to play a fundamental role in controlling gold mineralisation. The interpretation of the structural setting becomes more powerful when integrated with other techniques, such as geochemistry, geophysics, remote sensing, spatial modelling, and advanced mineralogical characterisation. This volume confirms that gold deposits result from complex histories of formation, reworking, overprinting, redistribution, and more, and its contributions are at the intersection between origin, structure, exploration, and mineral behaviour.

Thus, this collection may contribute to the detection of new deposits in deep-crustal domains by integrating geological knowledge accumulated in recent years through scientific research applied to mineral exploration. The context of exploration today is one in which a large proportion of the resources cropping out near the Earth's surface are already known, and thus, future exploration must be directed toward concealed targets hosted in deeper levels of the crust. Exploration will likely be supported by predictive geological models, robust metallogenic criteria, and geophysical, geochemical, and remote-sensing tools, combined with advances in artificial intelligence, to successfully explore deep-crustal levels that are not directly accessible.

Author Contributions: J.F.-L.: conceptualisation, writing—original draft, and writing—review and editing; E.M.: writing—review and editing; P.C.: writing—review and editing. All authors have read and agreed to the published version of the manuscript.

Conflicts of Interest: The authors declare no conflicts of interest.

List of Contributions:

1. Abdelrahman, K.; El-Qassas, R.A.Y.; Fnais, M.S.; Andráš, P.; Eldosouky, A.M. Geological structures controlling Au/Ba mineralization from aeromagnetic data: Harrat ad danun area, Saudi Arabia. *Minerals* **2023**, *13*, 866. https://doi.org/10.3390/min13070866.
2. El-Raouf, A.A.; Doğru, F.; Azab, I.; Jiang, L.; Abdelrahman, K.; Fnais, M.S.; Amer, O. Utilizing remote sensing and satellite-based Bouguer gravity data to predict potential sites of hydrothermal minerals and gold deposits in Central Saudi Arabia. *Minerals* **2023**, *13*, 1092. https://doi.org/10.3390/min13081092.
3. Craw, D.; Phillips, N.; Vearncombe, J. Unconformities and Gold in New Zealand: Potential Analogues for the Archean Witwatersrand of South Africa. *Minerals* **2023**, *13*, 1041. https://doi.org/10.3390/min13081041.

https://doi.org/10.3390/min16050556

4. Kreuzer, O.P.; Roshanravan, B.; Buckingham, A.J.; Core, D.P.; Konecke, B.A.; McDwyer, D.; Mustard, R. Controls, Expressions, and Discovery Potential of Gold Mineralization in the Central-Eastern Yilgarn Craton, Western Australia: New Insights from an Integrated Targeting Study. *Minerals* **2025**, *15*, 1255. https://doi.org/10.3390/min15121255.
5. Melchiorre, E.B.; Mathur, R.; Kamenov, G.; Paredes, J. Geochemical overprinting and secondary placer crystal formation in the La Cholla District, Quartzsite, Arizona, USA: evidence from copper isotopes, morphology, and trace elements. *Minerals* **2023**, *13*, 1444. https://doi.org/10.3390/min13111444.
6. Vishiti, A.; Suh, C.E.; Ngatcha, R.B.; Melchiorre, E.B.; Shemang, E.M.; Omang, B.O.; Cho Ngang, T.; Castro Valdez, F.; Sekem, S.G. Soil Geochemistry Combined with Particulate Gold Microchemistry Provides Evidence of Eluvial Gold Genesis and Anthropogenic Hg Use in Eastern Cameroon Goldfields. *Minerals* **2024**, *14*, 567. https://doi.org/10.3390/min14060567.
7. Li, G.; Ru, S.; Xue, C.; Wang, W. Evolution of the Ore-Bearing Fluid of Alin Sb–Au Orebodies in Shuixie Cu–Co Orefield, SW China: Constraints on the Rare Earth Element and Trace Element Components of Auriferous Pyrite and Host Rock. *Minerals* **2025**, *15*, 491. https://doi.org/10.3390/min15050491.
8. Shevyrev, S.; Boriskina, N. Analysis of Structural Position of Carlin-Type Gold Deposits with Lineament Analysis of Remote Sensing Data Using pyLEFA Software. *Minerals* **2025**, *15*, 219. https://doi.org/10.3390/min15030219.
9. Kalinin, A.A.; Kudryashov, N.M.; Savchenko, Y.E. Timing and Evolution of Gold Mineralization in the Maljavr Occurrence (NW Russia), NE Part of the Fennoscandian Shield. *Minerals* **2024**, *14*, 535. https://doi.org/10.3390/min14060535.
10. Konopelko, D.L.; Zhdanova, V.S.; Stepanov, S.Y.; Sidorova, E.S.; Petrov, S.V.; Kozin, A.K.; Seltmann, R. Mineralization Styles in the Orogenic (Quartz Vein) Gold Deposits of the Eastern Kazakhstan Gold Belt: Implications for Regional Prospecting. *Minerals* **2025**, *15*, 885. https://doi.org/10.3390/min15080885.

Disclaimer/Publisher's Note: The statements, opinions and data contained in all publications are solely those of the individual author(s) and contributor(s) and not of MDPI and/or the editor(s). MDPI and/or the editor(s) disclaim responsibility for any injury to people or property resulting from any ideas, methods, instructions or products referred to in the content.

minerals

MDPI

Article

Geological Structures Controlling Au/Ba Mineralization from Aeromagnetic Data: Harrat ad Danun Area, Saudi Arabia

Kamal Abdelrahman [1], Reda Abdu Yousef El-Qassas [2], Mohammed S. Fnais [1], Peter Andráš [3] and Ahmed M. Eldosouky [4,*]

[1] Department of Geology & Geophysics, College of Science, King Saud University, P.O. Box 2455, Riyadh 11451, Saudi Arabia; khassanein@ksu.edu.sa (K.A.); mfnais@ksu.edu.sa (M.S.F.)
[2] Exploration Division, Nuclear Materials Authority (NMA), Cairo P.O. Box 530, Egypt; redaelqassas@yahoo.com or redaelqassas@nma.org.eg
[3] Faculty of Natural Sciences, Matej Bel University in Banska Bystrica, Tajovského 40, 974 01 Banska Bystrica, Slovakia; peter.andras@umb.sk
[4] Department of Geology, Suez University, Suez 43518, Egypt
* Correspondence: dr_a.eldosoky@yahoo.com or ahmed.eldosouky@sci.suezuni.edu.eg

Abstract: Positive and negative magnetic anomalies occupied the total aeromagnetic (TM) map of the Harrat ad Danun area, Saudi Arabia. Reduction to the pole (RTP) maps display the range of magnetic values (−312.4 to 209.4 nT) that vary in shape, size, and magnitude. These anomalies generally follow the NNW–SSE (Red Sea axis trend), NE–SW, and NNE–SSW trends. The NNW-SSE linear negative and positive magnetic anomalies could be brought on by buried faults, shear zones, or subsurface dikes. In the central part, the position of *Au* and *Ba* mineralization was connected to this trend. It is concluded that the principal structures are represented by the NNW–SSE, NE–SW, and NNE–SSW tendencies. Based on gridded RTP magnetic data, the 2-D power spectrum was computed and revealed the frequency of the near-surface and deep magnetic components. It is believed that the depths of the shallow and deep magnetic sources are typically 80 m and 570 m, respectively. Additional negative and positive magnetic anomalies with varied amplitudes and frequencies, trending in the NNW–SSE, ENE–WSW, and NE–SW directions, are seen when the high-pass and low-pass maps are closely examined. Many faults in various directions cut into these anomalies. The occurrence of negative linear magnetic anomalies (−36.6 nT to −137.3 nT) at this depth (80 m) is also confirmed by this map. The TDR filter and the Euler deconvolution method were used to identify the horizontal variations in magnetic susceptibility as well as the source position and depth of magnetic sources. The linear clustering rings are thought to be caused by contacts or faults with depths between 1 m to 474 m that are oriented WNW–ESE, NNE–SSW, and NNW–SSE. These faults or contacts are thought to be particularly prominent in the western, eastern, southern, northern, and central zones. The majority of felsic and mafic dikes are found to be connected to subsurface structures, showing that three structural trends—WNW–ESE, NNE–SSW, and NNW–SSE—affect the studied area. This demonstrates that important features and shear zones control the majority of Saudi Arabia's gold deposits. A negative magnetic anomaly that is centered in the area, trending NNW–SSE and crossing the NNE–SSW fault, is connected to the plotted gold and barite mineralization in the study area. This may imply that these two tendencies are responsible for mineralization. This result raises the possibility of mineralization in the NNW negative magnetic feature located in the western part of the area. The occurrence of gold and barite was significantly impacted by the NNW–SSE and NNE–SSW structural lineaments.

Keywords: gold mineralization; aeromagnetic map; shear zones; Harrat ad Danun; Saudi Arabia

1. Introduction

Saudi Arabia has not historically been known for its mining industry. Nonetheless, significant mining production has been observed at least three different times over

the past three thousand years [1]. The Abbasid Caliphate (750–1258 A.D.), the reign of King Solomon (961–922 B.C.), and the era of the Saudi Arabian Mining Syndicate (1939–1954) were the last three periods when gold was mined at Mahd ad Dahab, a mine that had produced gold intermittently since King Solomon's time and has been reopened since 1984 [2]. The former mining history of this nation is not reported in any other notable ways. Since 1947, Saudi Arabia has expressed interest in the use of its natural resources, but it was not until the 1950s and 1960s that infrastructure geology and exploration began in earnest. The massive entry of mineral raw materials into the post-World War II reconstruction of Europe at this time led to a boom in the global mining sector [3]. The Saudi Arabian government formed a separate ministry for petroleum and mineral resources in 1967 and provided it with a sizable budget, laying the groundwork for a well-organized program of mineral exploration. Since then, Saudi Arabia has pursued an aggressive exploration agenda with the help and assistance of some foreign agencies, resulting in the discovery of a diverse range of minerals, including precious and base metals, energy minerals (other than petroleum), industrial minerals, construction minerals, and ornamental stones. While some of these discoveries have already been turned into working mines, others are still being researched and investigated [4,5].

Saudi Arabia is acutely conscious of the need to diversify its economy and attain self-sufficiency in its many industrial sectors despite having 25% of the world's known oil reserves and deriving a fairly consistent income from them. Everything in their country's thinking and planning is based on this fundamental idea. Furthermore, it is believed that mineral resources and their exploitation are crucial to a nation's efforts to develop [2]. The development of mineral resources has also taken on a unique significance in Saudi Arabia given this context. Mineral development, on the other hand, will unleash a variety of benefits and multiplying effects into the process of national economic and social development. This will open up new doors for investment and the growth of other industries with the specific goal of extending their economic and industrial base. Saudi Arabia thus keeps up concerted efforts to look for, assess, and exploit its mineral resources.

There are two main geological settings in Saudi Arabia, each having a clear age and lithological difference. The Precambrian metamorphosed rocks from the Arabian Shield, the main source of mineral occurrences and discoveries, make up the western region of Saudi Arabia. The country's western region has exposed Shield rocks, which make up nearly one fourth of Saudi Arabia [6]. The alternative setting consists of more recent sediments from the Paleozoic, Mesozoic, and Tertiary eras that have not been altered or significantly disturbed. These cover rocks are dispersed across the north, east, and south of the Shield region and sit atop the stable Precambrian basement. Moreover, from the Tertiary to the present, there have been sporadic volcanic eruptions with some alkaline basaltic outflows, primarily in the Shield region. However, in Saudi Arabia, the most impressive Quaternary deposits are sands and gravels that cover rocks to create massive sand deposits [7–9].

The Shield area, which comprises stratiform deposits, veins, contact metamorphic deposits along the borders of igneous rocks, and magmatic and late magmatic deposits in igneous rocks, is the region with the best potential for finding metallic minerals. In contrast, non-metallic resources are dispersed across the entire nation, including the Shield, and are not limited to any particular region. Also abundant are several evaporites. The coastal region between the Red Sea and the Shield yields several minerals [6,10]. Investigation of the Red Sea's mineral deposits on the seabed has also produced promising results. In conclusion, Saudi Arabia offers a potential host environment that is rich in a range of metallic and non-metallic minerals, where numerous gold (Au) occurrences and other deposits have been found in the AS (more than 800); some of them, such Mahd ad Dahab, Al-Sukhaibarat, and Bulghah, are currently in production [10,11]. In addition, the base metals (copper, zinc, and lead) are demarcated in select AS areas, such as Al-Nuqrah, Al-Amar, and Jabal Sayid [10].

The authors of [12] concluded that mining is crucial to the process of development because it transforms mineral resources into a form of capital that boosts a country's

output. Additionally, according to the conventional perspective, mining, like other economic activities, plays a vital role in the development process and may turn a mineral resource into sustained improvements in people's lives [13]. Together with the size of mineral resources over time, environmental costs, such as large amounts of solid waste, diminishing ore grades, energy, chemical, and water inputs, as well as pollution outputs, particularly greenhouse gases, are crucial components in determining how sustainable mining can proceed [8]. In order to properly control and encourage the sector's sustainable development, the Saudi government must increase the sectoral institutions' capabilities. A new mining code will also simplify the licensing processes and increase predictability and transparency by removing the administrative and legal barriers that prevent private sector participation in the minerals sector [14]. Recently, some research was conducted to assess Saudi Arabia's mineralization activities and structures [15–22]. Several areas in Saudi Arabia are promising because they hold great reserves of mineralization and have yet to be investigated in detail.

The magnetic survey was widely used in different applications such as mineral exploration, geological mapping, engineering, detect magnetic sources and their boundaries. Additionally, it was utilized to detect geologic structures (faults, contacts, folds, and shear zones) that might be relevant to the search for minerals [23–36].

2. Geological Setting

The study area is situated in Saudi Arabia's Western province, 158 km northeast of Jeddah. It covers the area between 21°50′ and 21°56′ north and 39°48′ to 39°56′ east (Figure 1a,b). The study area is situated in the Arabian Shield's western region. A simple geological map of the area under study (Figure 1c), which is a portion of the Makkah Quadrangle map created in [37], is shown in Figure 1c. A combination of metamorphic and plutonic rocks makes up the Western Arabian Shield, which includes the investigation area. The tertiary-layered rocks of the Rahat group make up the Harrat Rahat area, which serves as the region's southern boundary. Shaw Hit, Amah Basalt, and some alluvial debris make up this collection. Sedimentary rocks from the Tertiary period make up the lowest portion of the study area, which is covered in flows of basaltic lava. Precambrian–Cambrian complexes, Tertiary–Quaternary–Recent alluvial deposits, and Cretaceous–Tertiary sedimentary successions make up the area. Gabbro rocks in the east eventually ascend into Precambrian intrusions of biotite granodiorite and monzogranite from the north to the southeast [38]. The study area contains the following types of rocks:

1. Precambrian rocks: the Fayiadah Formation, which includes felsic volcaniclastic rocks, andesitic rhyolitic and basaltic lavas, as well as andesitic volcaniclastic rocks, is attributed to this group.
2. Precambrian intrusive rocks: belong to the Hishash Complex (igd), which is composed of granodiorite, and the Shiwan Complex (Kwtn), which is composed of hornblende tonalite.
3. Tertiary rocks: these rocks primarily come from the Haddat ash Sham (Tsh) and Hammah Basalt formations (Tmhb). Whereas the latter is made up of alkalic olivine basalt, the former is composed of pebbly sandstone and siltstone and is exposed in the study area's north and south.
4. Quaternary deposits: these make up a significant component of the study area and are mostly the result of weathering of the existing rocks. The alluvium's thickness varies from place to place, rarely exceeding 4 m in the study area's higher terrain while rising in the lower terrain and increasing to 29 m [37]. The Wadi Hishash soils are highly rich in quartz sand. In this region, the elevation decreases from 425 m to roughly 200 m. Pebbly sandstone and siltstone, which are composed of sand and gravel, surround the alluvial deposits.

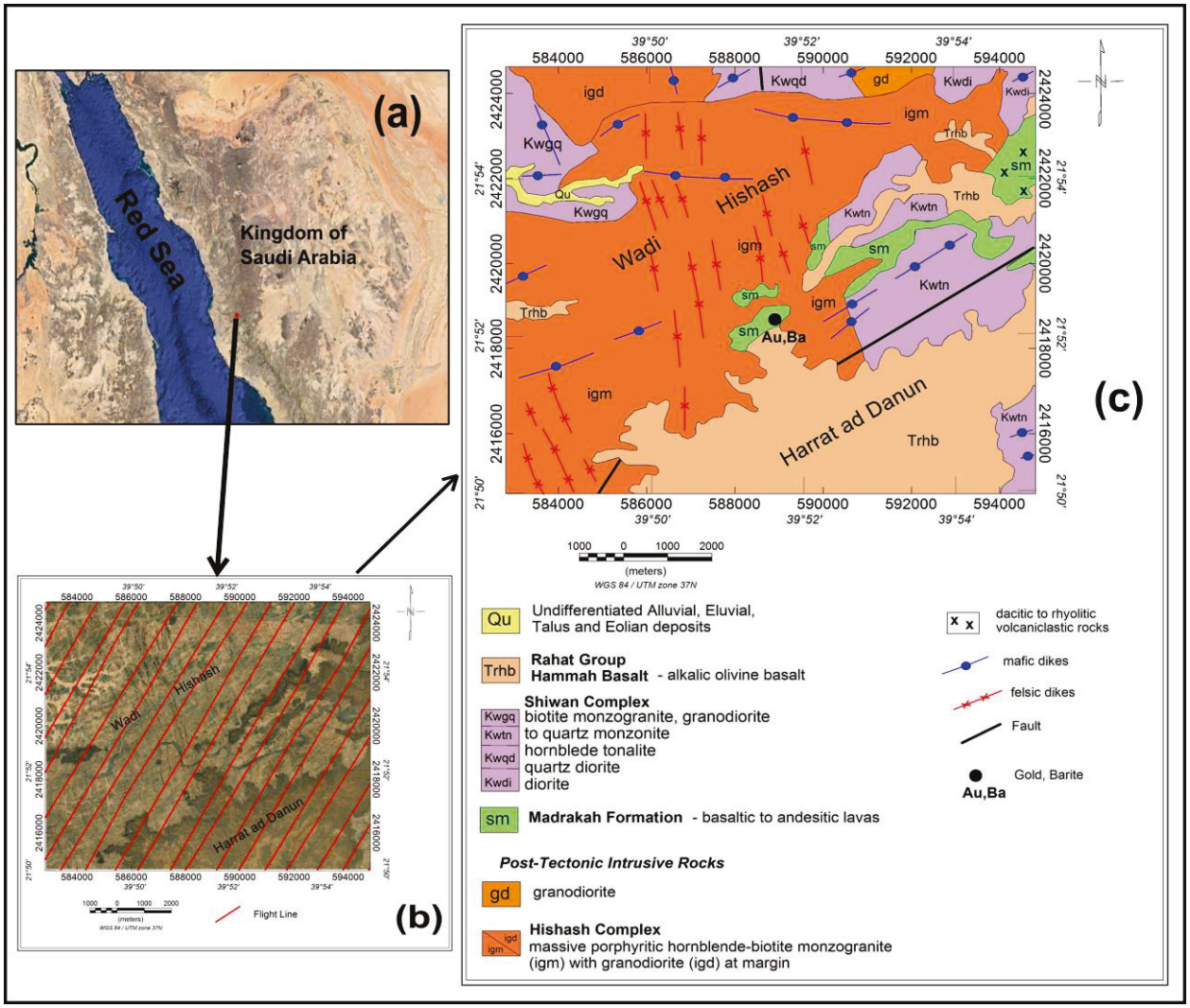


Figure 1. (**a**) Location map of Harrat ad Danun area, (**b**) Google Earth image, and (**c**) Geologic map of Harrat ad Danun area (after Moore and Al-Rehaili, 1989), Kingdom of Saudi Arabia.

3. Materials and Methods

The study area was flown by a consortium of Aero Service Corporation, Hunting Geology and Geophysics Limited, and Lockwood Survey Corporation Limited under the supervision of the Bureau de Recherches Géologiques et Minières for the Ministry of Petroleum and Mineral Resources of the Kingdom of Saudi Arabia between 1965 and 1966. This survey was carried out by the Fluxgate Gulf Mark III magnetometer with analog recording. The aeromagnetic survey flight lines were flown along parallel traverse lines oriented in a NE–SW direction, with an azimuth of 30° from true north and 800 m spacing. The tie lines were flown in an NW–SE direction, at a right angle to the flight line direction, with an azimuth of 150° from true north [39]. The tie line spacing was chosen as 16 km intervals. The total magnetic intensity (TMI) was conducted at a nominal sensor altitude of 300 m of terrain clearance [39].

The TMI grid was reduced to the pole (RTP) grid map in order to properly locate the magnetic anomalies across the magnetic source bodies. In the current experiment, residual and regional magnetic component maps were generated from the RTP aeromagnetic data using Fast Fourier transformation (FFT). The RTP aeromagnetic map was further subjected to Tilt Derivative (TDR) and Euler Deconvolution in order to find the characteristics that might be important in mineral prospecting.

The ratio of the potential field's first vertical derivative to its horizontal gradient serves as a proxy for the tilt angle [40]. When employing the zero-contour line to locate the margins of sources at shallow and deep depths, tilt angle derivative (TDR) offers an advantage [40,41]; the tilt derivative (TDR) method is expressed as the following:

$$\mathrm{TDR} = tan^{-1}\left(\frac{VDR}{HGM}\right) \quad (1)$$

where VDR is the vertical derivative of the magnetic field, and HGM is its horizontal gradient magnitude.

Reid et al. (1990) employed gridded data and generalized the Euler deconvolution to show the position and depth of the magnetic sources. This technique has successfully been utilized for regional interpretation and has proven its effectiveness in identifying lineaments and geological structures (contacts and faults). The authors of [42] suggested modifications to Euler deconvolution for application to magnetic data.

$$\frac{\partial \mathrm{T}}{\partial \mathrm{x}}\left(\mathrm{x}-\mathrm{x}_0\right)+\frac{\partial \mathrm{T}}{\partial \mathrm{y}}\left(\mathrm{y}-\mathrm{y}_0\right)+\frac{\partial \mathrm{T}}{\partial \mathrm{z}}\left(\mathrm{z}-\mathrm{z}_0\right)=\mathrm{N}(\mathrm{B}-\mathrm{T}) \quad (2)$$

where T is the total field detected at (x, y, z) by the magnetic source at position (x_0, y_0, z_0), B is the background value of the total field, and N is the degree of homogeneity or geophysics related to the structural index (SI).

In the current study, aeromagnetic data were gridded, processed, and mapped using the Geosoft Oasis Montaj program. Furthermore, the results obtained from structural lineaments were presented as rose diagrams using the RockWorks program.

4. Results and Discussion

The total aeromagnetic (TM) map (Figure 2) shows positive and negative magnetic anomalies. The positive anomalies vary from 2.6 nT to 220.9 nT with orange, red, and magenta colors. The highest positive magnetic anomalies (more than 47.7 nT to 220.9 nT) occupy the central, southeast–central, western, eastern, and northern parts. The negative magnetic anomalies (−7.8 nT to −288.3 nT) are characterized by yellow, green, and light-to-deep-blue colors (Figure 2). The western region is home to the highest negative magnetic anomalies, which extend from −288.3 nT to −95.9 nT (Figure 2).

The RTP map (Figure 3) displays the range of magnetic values, which range in size, shape, and magnitude from −312.4 to 209.6 nT. These anomalies generally follow the NNW–SSE (Red Sea axis trend), NE–SW, and NNE–SSW trends. It is possible that hidden faults, shear zones, or subsurface dikes are the cause of the NNW–SSE negative and positive magnetic anomalies (Figure 3). In the center of the research region, the position of Au and Ba mineralization was connected to this trend. According to [43], the NNW–SSE linear magnetic anomalies in the Kingdom of Saudi Arabia are related to mineralization.

Gridded RTP magnetic data were used to determine the 2D power spectrum (Figure 4). An examination of the power spectrum curve reveals the frequency of the near-surface and deep magnetic components. The shallow and deep magnetic sources are thought to have typical depths of 80 m and 570 m, respectively (Figure 4).

When looking at the high-pass (residual) map (Figure 5) of RTP data, it is possible to see a number of different negative and positive magnetic anomalies with varying amplitudes and frequencies, trending in the NNW–SSE, ENE–WSW, and NE–SW directions. These anomalies are dissected by many faults in different directions. In addition, this map confirms the existence of negative linear magnetic anomalies (−36.6 nT to −137.3 nT) at this depth (80 m). The negative and positive magnetic anomalies are depicted on the low-pass (regional) map of RTP data with varying amplitudes and frequencies (Figure 6). They are trending in the NNW–SSE and NE–SW directions.

The TDR filter was applied to the RTP grid to highlight structures such as faults and contacts to help in the mineral exploration research, to find magnetic sources' edges. The

zero-contour line, which shows the location of changes in magnetic susceptibility on the TDR map (Figure 7), is highlighted.

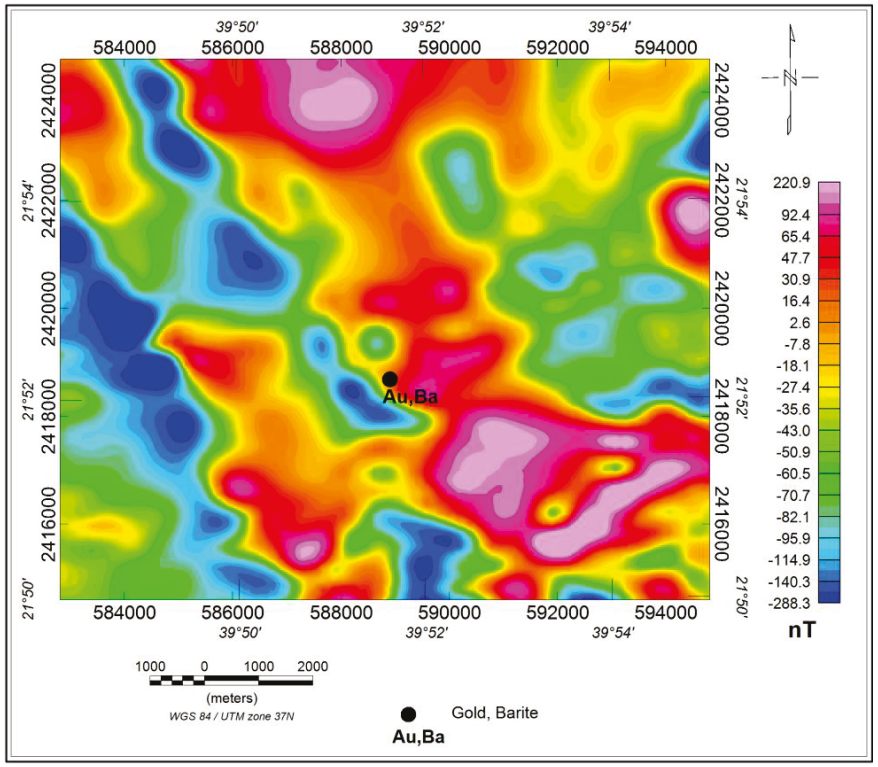


Figure 2. Total intensity aeromagnetic map, Harrat ad Danun area, Kingdom of Saudi Arabia (Aero Service, 1966).

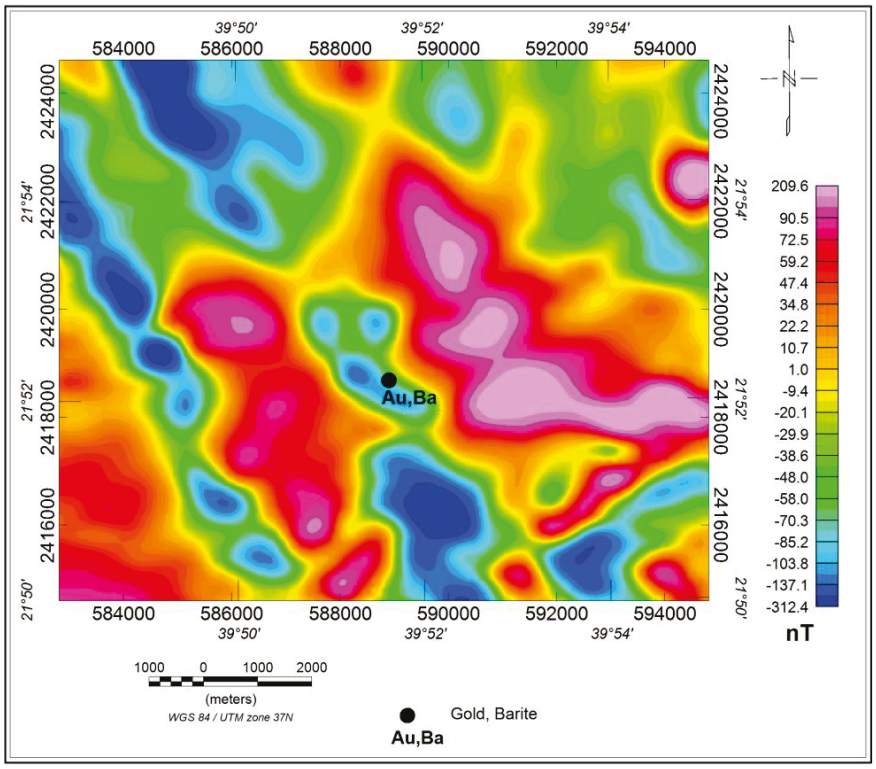


Figure 3. Reduction to the pole (RTP) aeromagnetic map, Harrat ad Danun area, Kingdom of Saudi Arabia (Aero Service, 1966).

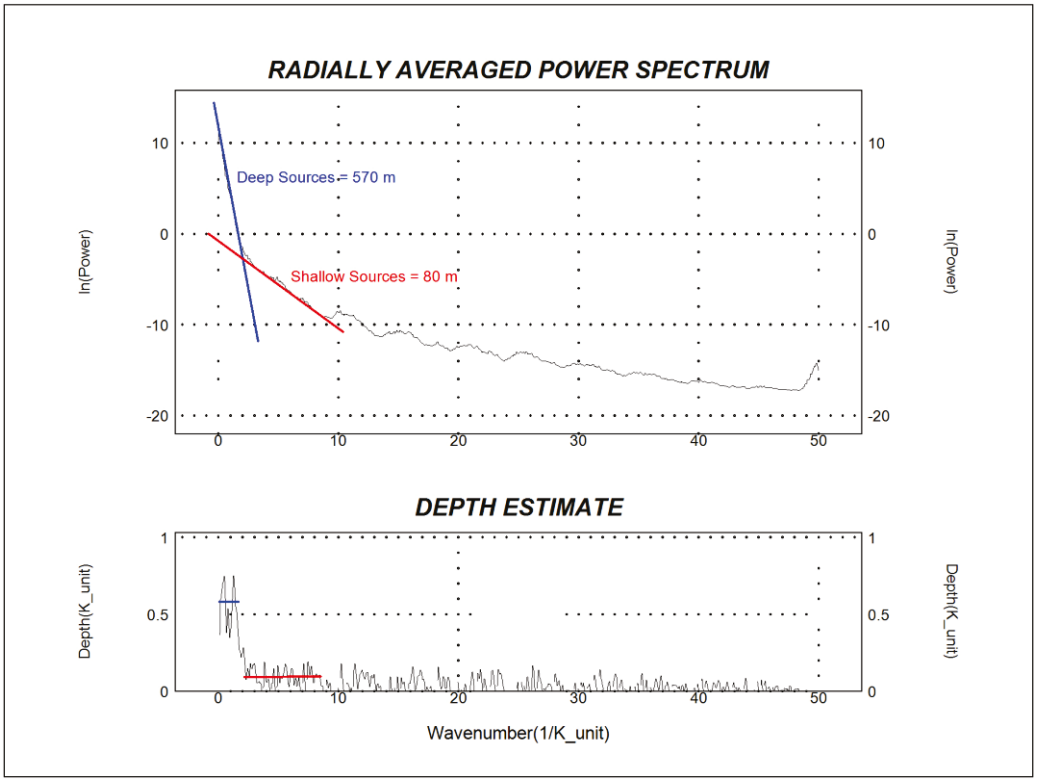


Figure 4. Radially averaged power spectrum and depth estimate from RTP aeromagnetic map, Harrat ad Danun area, Kingdom of Saudi Arabia.

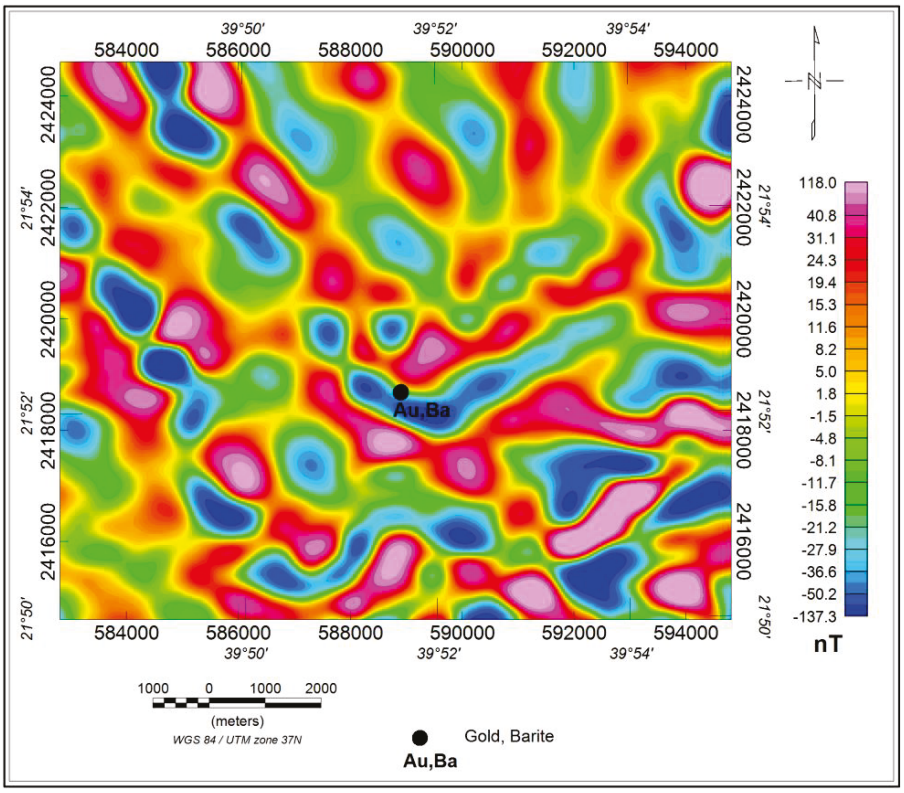


Figure 5. High-pass filtered (residual) aeromagnetic map at 80 m depth, Harrat ad Danun area, Kingdom of Saudi Arabia.

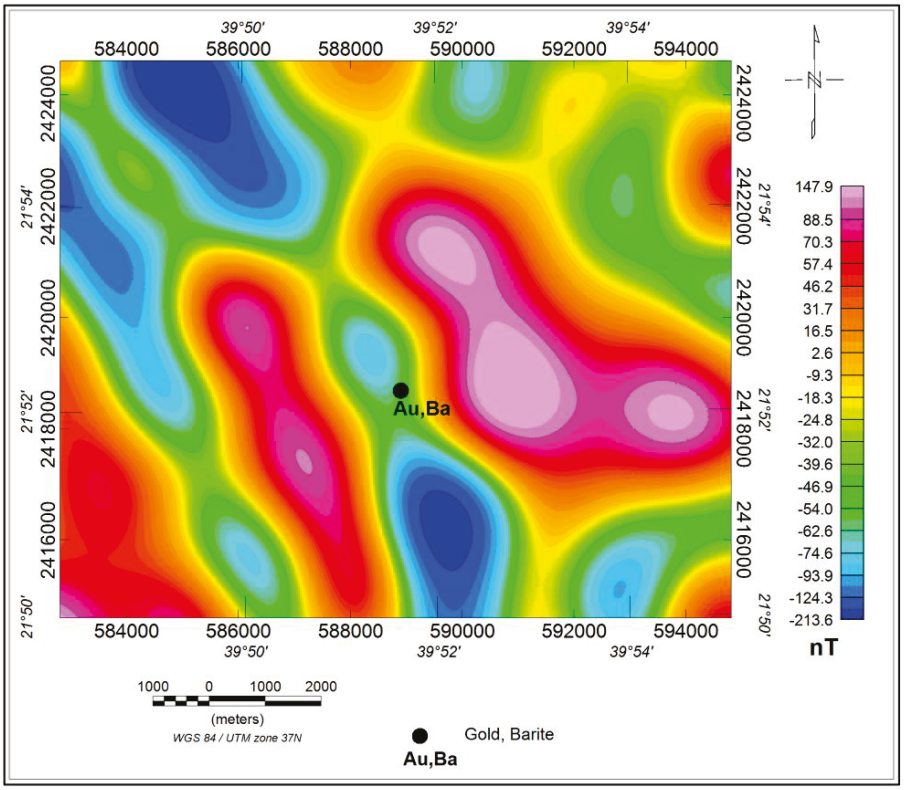


Figure 6. Low-pass filtered (regional) aeromagnetic map at 570 m depth, Harrat ad Danun area, Kingdom of Saudi Arabia.

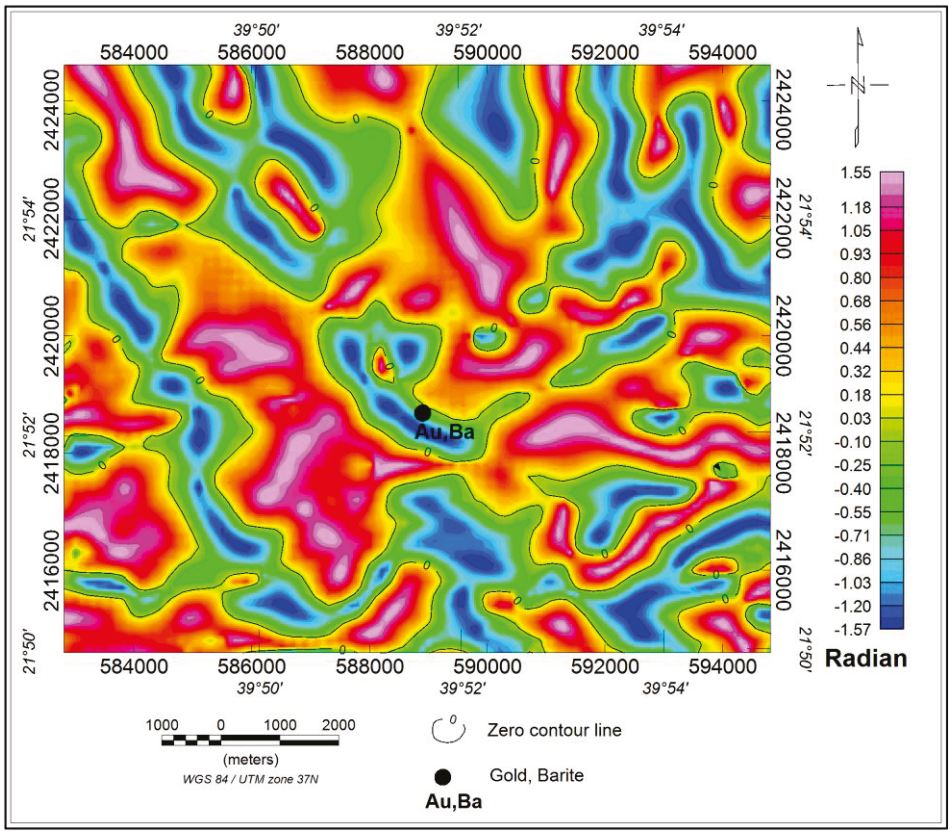


Figure 7. Tilt Derivative (TDR) aeromagnetic map, Harrat ad Danun area, Kingdom of Saudi Arabia.

The research area's RTP aeromagnetic data grid was subjected to the Euler deconvolution algorithm. The lower structural indices from 0 to 1 are superior depth estimators, as [44] showed. In order to characterize connections and faults in the regional interpretation of the study area, one structural indicator (SI) with a value of 0.0 has been chosen. The Euler deconvolution technique's produced findings are shown as colored circles placed on maps to show the source position and depth.

The Euler map (Figure 8) was created by applying Euler deconvolution with SI = 0.0, which displays clusters of circles in linear and curved shapes to represent the nature of probable contacts between the rock units. It is believed that faults or contacts with depths between 1 and 474 m are what caused the linear clustering rings.

In the studied area, the linear solutions of depths (1 m–208 m) are widely dispersed (Figure 8). The main trends of these solutions are NNW–SSE, NW–SE, NE–SW, and NNE–SSW. These solutions relate to contacts and faults (Figures 3 and 8). While this examination was being carried out, it was discovered that several areas of the negative and positive magnetic anomalies, particularly in the western, eastern, southern, northern, and central areas (Figures 3 and 8), were associated with solutions that have depths between 208 m and 474 m (Figures 3 and 8).

The subsurface features (faults) that impacted the research area are depicted in Figure 9 by converting the zero-contour lines of the TDR map to lineaments. It is concluded that the primary structures in the study region are represented by the NNW–SSE, NE–SW, and NNE–SSW tendencies (Figure 9). It is notable that it was found that the majority of felsic and mafic dikes are connected to subterranean structures by comparing the geological map (Figure 1) with the TDR map and its lineaments (Figures 7 and 9). According to Figure 10's analysis of lineament structures using Euler deconvolution, the research area is impacted by three structural trends: WNW–ESE, NNE–SSW, and NNW–SSE [30].

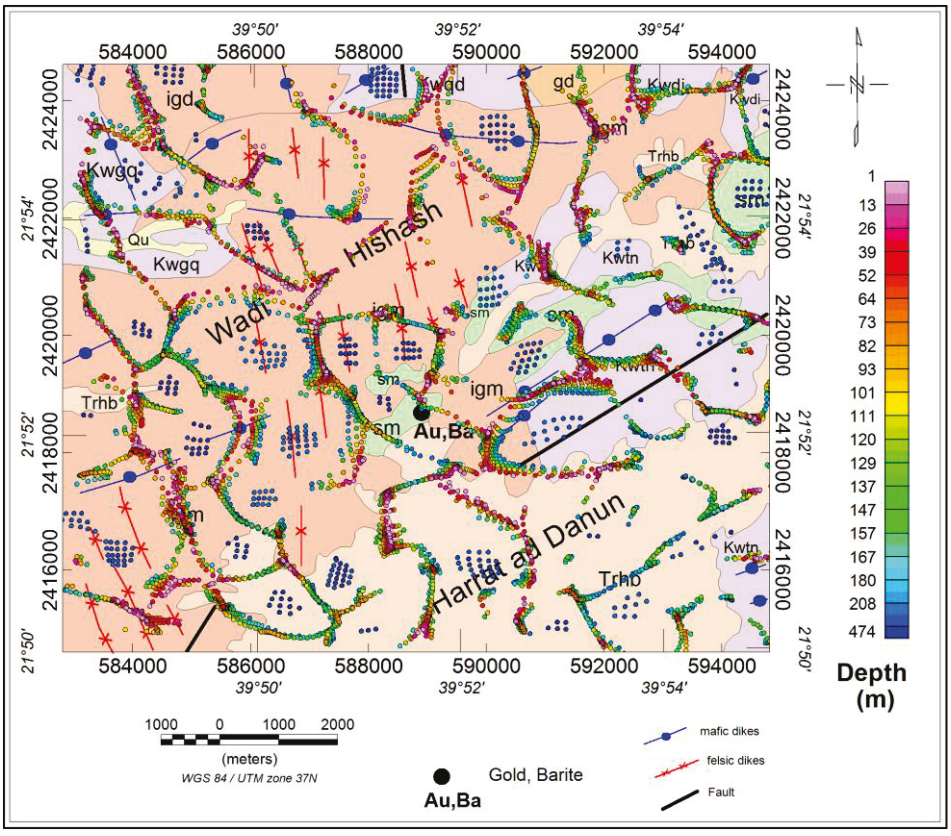


Figure 8. Euler deconvolution solutions with structural index 0.0 (SI = 0.0) of the RTP aeromagnetic map, Harrat ad Danun area, Kingdom of Saudi Arabia. Geologic map as background.

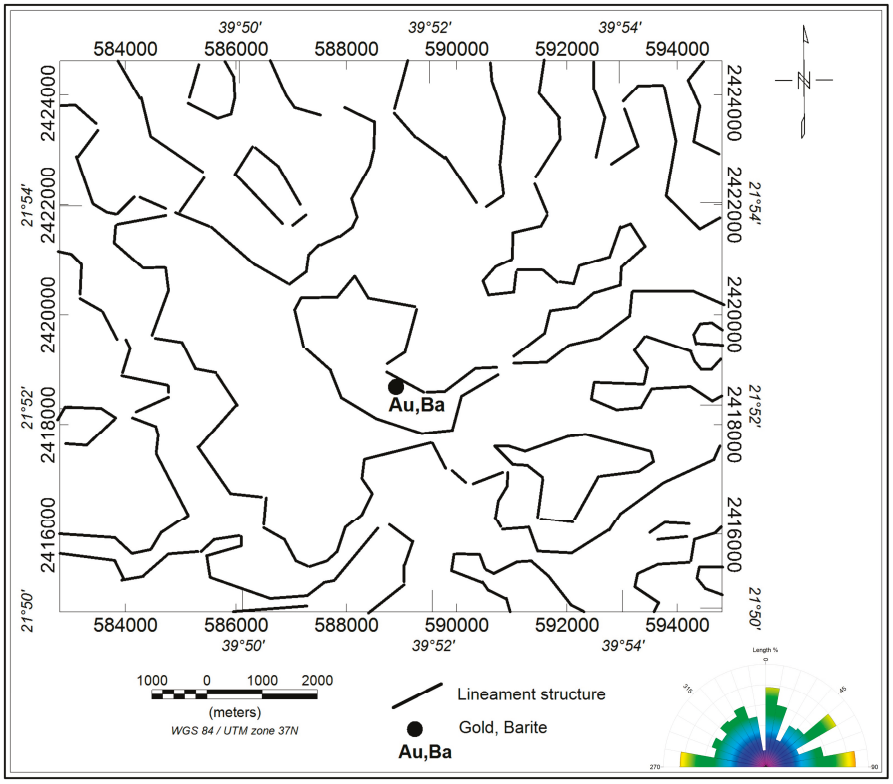


Figure 9. The lineament structures as traced from the TDR aeromagnetic map (Figure 7) and rose diagram (inset), Harrat ad Danun area, Kingdom of Saudi Arabia.

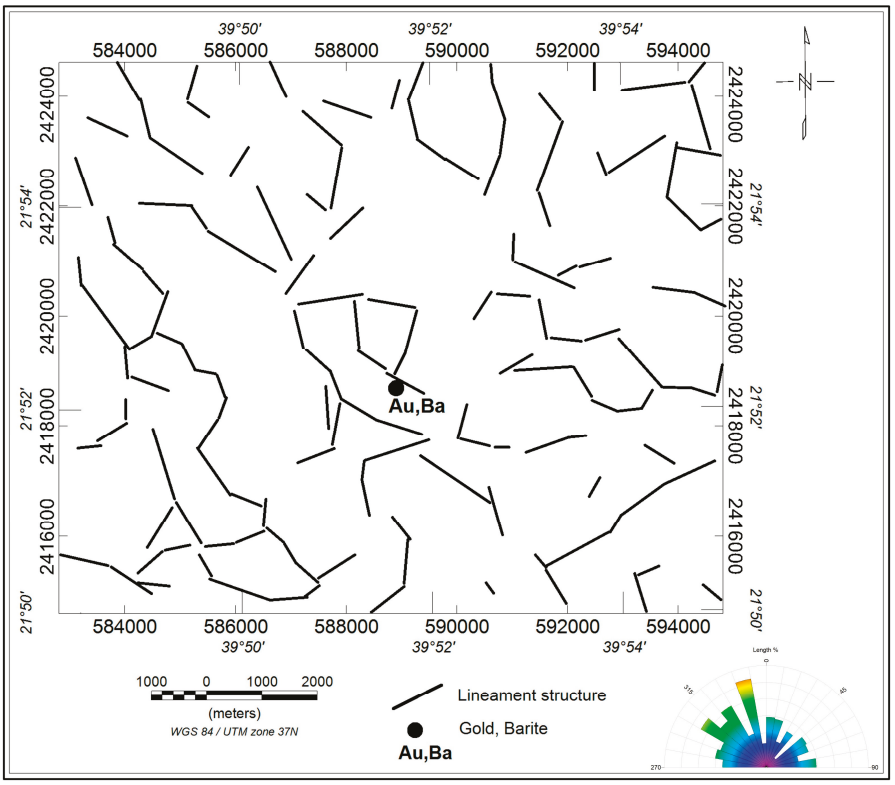


Figure 10. The lineament structures as traced from Euler deconvolution solutions with structural index 0.0 (SI = 0.0) (Figure 8) and rose diagram (inset), Harrat ad Danun area, Kingdom of Saudi Arabia.

Most Au deposits in Saudi Arabia are controlled by major structures and shear zones [29,30,45,46]. The study area's mapped gold and barite mineralization corresponds to a negative magnetic anomaly that is centered there and trends in the Red Sea fault system's NNW–SSE direction, intersecting with the NNE–SSW fault (Figures 3 and 5–7). This may suggest that mineralization is controlled by these two trends. Based on this finding, the NNW negative magnetic feature in the western portion of the area (Figures 3, 5 and 7) may likely contain mineralization. It is clear that mineralization is connected with both source depths of 80 m and 570 m for the residual and regional findings. Moreover, the mineralized zones are connected to the NNW–SSE direction. This is in agreement with the results of [22,43].

5. Conclusions

On the total aeromagnetic (TM) map, alternately distributed positive and negative magnetic anomalies are shown. The reduced to the pole (RTP) map exhibits a range of magnetic values (−312.4 to 209.6 nT) that differ in shape, size, and magnitude. These anomalies' general patterns include NNW–SSE (Red Sea axis trend), NE–SW, and NNE–SSW. Subsurface buried dikes, faults, or shear zones could explain the NNW–SSE linear negative and positive magnetic anomalies. This trend was linked to the presence of Au and Ba mineralization in the research area's center. It is concluded that the principal structures in the studied area are the NNW–SSE, NE–SW, and NNE–SSW tendencies. The gridded RTP magnetic data were used to estimate the 2D power spectrum. The power spectrum curve analysis reveals the frequency of the deep-seated and near-surface magnetic components. The estimated average depths of the shallow and deep magnetic sources are 80 m and 570 m, respectively. A variety of other negative and positive magnetic anomalies with differing amplitudes and frequencies are also visible when comparing the high-pass and low-pass maps, with the majority of them trending in the NNW–SSE, ENE–WSW, and NE–SW directions. Many faults cut through these anomalies in different directions. This map also shows the presence of negative linear magnetic anomalies at this depth (80 m) (−36.6 nT to −137.3 nT). The TDR filter and Euler deconvolution technique were utilized to identify horizontal variations in magnetic susceptibility as well as the source position and depth of magnetic sources. With depths ranging from 1 m to 474 m and orientations in the NNW–SSE, NW–SE, NE–SW, and NNE–SSW directions, the linear clustering rings are thought to be the result of contacts or faults. They exhibit both positive and negative magnetic anomalies, especially in the western, eastern, southern, northern, and central zones.

The majority of felsic and mafic dikes have been discovered to be connected to subsurface structures, demonstrating that three structural trends influence the study area: WNW–ESE, NNE–SSW, and NNW–SSE. This indicates that significant structural and shear zones regulate the majority of the Au deposits in Saudi Arabia. The plotted gold and barite mineralization in the study region corresponds to an area-centered negative magnetic anomaly with an NNW–SSE trend that crosses the NNE-SSW fault. This could imply that these two trends are responsible for mineralization. The NNW negative magnetic feature in the western part of the area is anticipated to have mineralization based on this detection.

A detailed ground magnetic survey should be conducted around possible Au and Ba locations to identify the subsurface structures framework that affected the area. Furthermore, electromagnetic (EM) and induced polarization (IP) surveys should be applied to the existing mineralization (Au, Ba) to explore any subsurface extensions. In addition, geochemical studies should be carried out at the known mineralization (Au, Ba) locations and similar areas to determine the grade of mineralization.

Author Contributions: Conceptualization, A.M.E. and R.A.Y.E.-Q.; methodology, R.A.Y.E.-Q. and K.A.; software, R.A.Y.E.-Q.; validation, A.M.E., P.A. and M.S.F.; formal analysis, K.A.; investigation, A.M.E., R.A.Y.E.-Q. and P.A.; resources, M.S.F.; data curation, R.A.Y.E.-Q.; writing—original draft preparation, R.A.Y.E.-Q., A.M.E., P.A. and K.A.; it writing—review and editing, A.M.E.; visualization,

M.S.F.; supervision, A.M.E.; project administration, A.M.E.; funding acquisition, K.A. and M.S.F. All authors have read and agreed to the published version of the manuscript.

Funding: Deputyship for Research and Innovation, "Ministry of Education" in Saudi Arabia, project no. (IFKSUOR3-192-3).

Data Availability Statement: Not applicable.

Acknowledgments: The authors extend their appreciation to the Deputyship for Research and Innovation, "Ministry of Education" in Saudi Arabia for funding this research through the project no. (IFKSUOR3-192-3).

Conflicts of Interest: The authors declare no conflict of interest.

References

1. DMMR. *Saudi Arabian Directorate General of Mineral Resources. Mineral Resources Activities*; Ministry of Petroleum and Mineral Resources: Riyadh, Saudi Arabia, 1970; pp. 46–70.
2. Darwish, M.A.; Dar Ikram, H.; Abdulaziz, M.I. *Saudi Arabia Starts Up a New Gold Mine at Mahd-Adh-Dahab, E&M/J*; Macgraw-Hill: New York, NY, USA, 1988; pp. 34–38.
3. Darwish, M.A.; Hanif, M. Minerals potential of Saudi Arabia. In Proceedings of the 1st Conference on Indigenous Materials and Their Utilization in the Gulf Region, Kuwait, 1 November 1986.
4. Ibrahim, M. *Big Plans for Mineral Investment in the Kingdom of Saudi Arabia*; The Arab News Daily: Jeddah, Saudi Arabia, 1992.
5. Babhair, A. *Kingdom of Saudi Arabia, A Country Report*; Saudi Geological Survey: Jeddah, Saudi Arabia, 2002.
6. DMMR. *Saudi Arabian Deputy Ministry for Mineral Resources Activities and Achievements 1990–1994*; Ministry of Petroleum and Mineral Resources: Jeddah, Saudi Arabia, 1995.
7. DMMR. *Ministry of Petroleum and Mineral Resources, Saudi Arabian Mineral Resources Annual Report*; Ministry of Petroleum and Mineral Resources: Jeddah, Saudi Arabia, 1984; pp. 13–14.
8. Mudd, G. *The Sustainability of Mining in Australia: Key Production Trends and Their Environmental Implications for the Future*; Research Report No RR5; Department of Civil Engineering, Monash University and Mineral Policy Institute: Melbourne, Australia, 2007.
9. Mudd, G.; Ward, J. Will Sustainability Constraints Cause 'Peak Minerals'? In Proceedings of the 3rd International Conference on Sustainability Engineering and Science: Blueprints for Sustainable Infrastructure, Auckland, New Zealand, 9–12 December 2008.
10. Darwish, M.A.; Butt, N.A. Mineral Resource Potential and Its Development in Saudi Arabia. *JKAU Eng. Sci.* **1996**, *8*, 107–120. [CrossRef]
11. *Fourth Development Plan (1985–1990)*; Ministry of Planning KSA: Riyadh, Saudi Arabia, 1985; pp. 167–184.
12. Davis, G.; Tilton, J. Should Developing Countries Renounce Mining? A Perspective on the Debate, Colorado School of Mines. 2002. Available online: https://www.icmm.com/uploads/62TiltonDavisfinalversion.pdf (accessed on 1 April 2023).
13. Togolo, M. Mining and sustainability—Placer Niugini Limited. In Proceedings of the PACRIM'99, International Conference on Earth Science, Exploration and Mining around the Pacific Rim, Bali, Indonesia, 10–13 October 1999.
14. Aldagheiri, M. The minerals sector and sustainable development in Saudi Arabia. In Proceedings of the Sustainable Development Indicators in the Minerals Industry (SDIMI) 2009 Conference, Gold Coast, Australia, 6–8 July 2009. 28p.
15. Alharbi, O.; Amjad, M.; Alabdulaaly, A.; Khater, G.; Alsari, A. Industrial utilization of white silica sandstone in Riyadh area, Saudi Arabia. *Arab. Gulf J. Scient. Res.* **1997**, *15*, 29–39.
16. Al Jahdli, N.S. Geology of Jabal Ghadarah Area, Bi'r Tawilah District with Special Emphasis on Listvinite as a Potential Source for Gold in the Kingdom of Saudi Arabia. Master's Thesis, King Abdulaziz University, Jeddah, Saudi Arabia, 2004.
17. Harbi, H.A.; Eldougdoug, A.A.; Al Jahdali, N.S. Evolution of the Arabian Shield and associated mineralization. In Proceedings of the 9th Arab Conference of Mineral Resources, Jeddah, Saudi Arabia, 30 October–1 November 2006; pp. 1–11.
18. Gabr, S.; Ghulam, A.; Kusky, T. Detecting areas of high-potential gold mineralization using ASTER data. *Ore Geol. Rev.* **2010**, *38*, 59–69. [CrossRef]
19. Al-Garni, M.A.; Hassanein, H.I.E. Aeromagnetic data analysis to enhance the demonstration of the subsurface mineralized zone occurrences, As-Safra prospect area, Saudi Arabia. *Arab. J. Geosci.* **2010**, *5*, 313–326. [CrossRef]
20. Surour, A.A.; Harbi, H.M.; Ahmed, A.H. The Bi'r Tawilah deposit, central western Saudi Arabia: Supergene enrichment of a Pan-African epithermal gold mineralization. *J. Afr. Earth Sci.* **2014**, *89*, 149–163. [CrossRef]
21. Torres, J.E.A. The Potential for CO_2 Disposal in Western Saudi Arabia: The Jizan Group Basalts. Master's Thesis, King Abdullah University of Science and Technology, Thuwal, Saudi Arabia, 2020.
22. Eldosouky, A.M.; El-Qassas, R.A.Y.; Pham, L.T.; Abdelrahman, K.; Alhumimidi, M.S.; El Bahrawy, A.; Mickus, K.; Sehsah, H. Mapping Main Structures and Related Mineralization of the Arabian Shield (Saudi Arabia) Using Sharp Edge Detector of Transformed Gravity Data. *Minerals* **2022**, *12*, 71. [CrossRef]
23. Alsaud, M.M. Structural mapping from high resolution aeromagnetic data in west central Arabian Shield, Saudi Arabia using normalized derivatives. *Arab. J. Geosci.* **2008**, *1*, 129–136. [CrossRef]
24. Elawadi, E.; Mogren, S.; Ibrahim, E.; Batayneh, A.; Al-Bassam, A. Utilizing potential field data to support delineation of groundwater aquifers in the southern Red Sea coast, Saudi Arabia. *J. Geophys. Eng.* **2012**, *9*, 327–335. [CrossRef]

25. Alandoonisi, N.; Harbi, H.M.; Atef, A.; Aboualnaga, H.; Rashed, M. Geophysical Assessment of the Environmental Pollution at Downstream of Wadi Uranah, Southwest of Makkah, Saudi Arabia. *Nat. Environ. Pollut. Technol.* **2018**, *17*, 391–398.
26. Abuelnaga, H.S.; Aboulela, H.A.; El-Sawy, E.-S.K.; El Qassas, R.A. Detection of structural setting that controlling Hammam Faroun area, using aeromagnetic and seismicity data, Gulf of Suez, Egypt. *J. Afr. Earth Sci.* **2019**, *158*, 103560. [CrossRef]
27. Assran, A.; El Qassas, R.; Yousef, M. Detection of prospective areas for mineralization deposits using image analysis technique of aeromagnetic data around Marsa Alam-Idfu road, Eastern Desert, Egypt. *Egypt. J. Pet.* **2019**, *28*, 61–69. [CrossRef]
28. Eldosouky, A.M.; Pham, L.T.; Hassan, P.; Pradhan, M.B. A comparative study of THG, AS, TA, Theta, TDX, and LTHG techniques for improving source boundaries detection of magnetic data using synthetic models: A case study from G. Um Monqul, North Eastern Desert, Egypt. *J. Afr. Earth Sci.* **2020**, *170*, 103940. [CrossRef]
29. Eldosouky, A.M.; El-Qassas, R.A.; Pour, A.B.; Mohamed, H.; Sekandari, M. Integration of ASTER satellite imagery and 3D inversion of aeromagnetic data for deep mineral exploration. *Adv. Space Res.* **2021**, *68*, 3641–3662. [CrossRef]
30. Eldosouky, A.M.; Pham, L.T.; El-Qassas, R.A.Y.; Hamimi, Z.; Oksum, E. Lithospheric Structure of the Arabian-Nubian Shield Using Satellite Potential Field Data. In *The Geology of the Arabian-Nubian Shield*; Regional Geology Reviews; Hamimi, Z., Fowler, A.R., Liégeois, J.P., Collins, A., Abdelsalam, M.G., Abd EI-Wahed, M., Eds.; Springer: Cham, Switzerland, 2021.
31. El-Qassas, R.A.Y.; Ahmed, S.B.; Abd-ElSalam, H.F.; Abu-Donia, A.M. Integrating of Remote Sensing and Airborne Magnetic Data to Outline the Geologic Structural Lineaments That Controlled Mineralization Deposits for the Area around Gabal El-Niteishat, Central Eastern Desert, Egypt. *Geomaterials* **2021**, *11*, 1–21. [CrossRef]
32. El-Qassas, R.A.Y.; Abu-Donia, A.M.; Omar, A.E.A. Delineation of hydrothermal alteration zones associated with mineral deposits, using remote sensing and airborne geophysics data. A case study: El-Bakriya area, Central Eastern Desert, Egypt. *Acta Geod. Geophys.* **2023**, *58*, 71–107. [CrossRef]
33. Elkhateeb, S.O.; Eldosouky, A.M.; Khalifa, M.O.; Aboalhassan, M. Probability of mineral occurrence in the Southeast of Aswan area, Egypt, from the analysis of aeromagnetic data. *Arab. J. Geosci.* **2021**, *14*, 1514. [CrossRef]
34. Kharbish, S.; Eldosouky, A.M.; Amer, O. Integrating mineralogy, geochemistry and aeromagnetic data for detecting Fe–Ti ore deposits bearing layered mafic intrusion, Akab El-Negum, Eastern Desert, Egypt. *Sci. Rep.* **2022**, *12*, 15474. [CrossRef]
35. Ekwok, S.E.; Akpan, A.E.; Achadu, O.-I.M.; Thompson, C.E.; Eldosouky, A.M.; Abdelrahman, K.; Andráš, P. Towards Understanding the Source of Brine Mineralization in Southeast Nigeria: Evidence from High-Resolution Airborne Magnetic and Gravity Data. *Minerals* **2022**, *12*, 146. [CrossRef]
36. Mahdi, A.M.; Eldosouky, A.M.; El Khateeb, S.O.; Youssef, A.M.; Saad, A.A. Integration of remote sensing and geophysical data for the extraction of hydrothermal alteration zones and lineaments; Gabal Shilman basement area, Southeastern Desert, Egypt. *J. Afr. Earth Sci.* **2022**, *194*, 104640. [CrossRef]
37. Moore, T.A.; Al-Rehaili, M.H. Explanatory Notes to the Geologic Map of the Makkah Quadrangle, Sheet21d, Kingdom of Saudi Arabia: Saudi Arabian Dir. Gen. Min. Res. Geoscience Map GM-107C, 1:250,000 Scale. 1989. Available online: https://www.scirp.org/%28S%28czeh2tfqyw2orz553k1w0r45%29%29/reference/referencespapers.aspx?referenceid=2170065 (accessed on 1 April 2023).
38. El-Hames, A.S. Determination of groundwater availability in shallow arid region aquifers utilizing GIS technology: A case study in Hada Al-Sham, Western Saudi Arabia. *Hydrogeol. J.* **2004**, *13*, 640–648. [CrossRef]
39. *Aero Service. Final Operational Report of Airborne Magnetic*; Arabian Geophysical and Surveying Company: Dhahran, Saudi Arabia, 1966.
40. Miller, H.G.; Singh, V. Potential field tilt—A new concept for location of potential field sources. *J. Appl. Geophys.* **1994**, *32*, 213–217. [CrossRef]
41. Salem, A.; Williams, S.; Fairhead, D.; Smith, R.; Ravat, D. Interpretation of magnetic data using tilt-angle derivatives. *Geophysics* **2008**, *73*, L1–L10. [CrossRef]
42. Barbosa, V.; Silva, J.B.C.; Medeiros, W.E. Stability analysis and improvement of structural index estimation in Euler deconvolution. *Geophysics* **1999**, *64*, 48–60. [CrossRef]
43. Dadet, P.; Marchesseau, J.; Millon, R.; Motti, E. Mineral occurrences related to stratigraphy and tectonics in Tertiary sediments near Umm Lajj, eastern Red Sea area, Saudi Arabia. *Philos. Trans. R. Soc. Lond. Ser. A* **1970**, *267*, 99–106.
44. Reid, A.B.; Allsop, J.M.; Granser, H.; Millett, A.J.; Somerton, I.W. Magnetic interpretation in three dimensions using Euler deconvolution. *Geophysics* **1990**, *55*, 80–91. [CrossRef]
45. Bonnemaison, M.; Marcoux, E. Auriferous mineralization in some shear-zones: A three-stage model of metallogenesis. *Miner. Deposita* **1990**, *25*, 96–104. [CrossRef]
46. Eldosouky, A.M.; Elkhateeb, S.O.; Mahdy, A.M.; Saad, A.A.; Fnais, M.S.; Abdelrahman, K.; Andráš, P. Structural analysis and basement topography of Gabal Shilman area, South Eastern Desert of Egypt, using aeromagnetic data. *J. King Saud Univ. Sci.* **2021**, *34*, 101764. [CrossRef]

Disclaimer/Publisher's Note: The statements, opinions and data contained in all publications are solely those of the individual author(s) and contributor(s) and not of MDPI and/or the editor(s). MDPI and/or the editor(s) disclaim responsibility for any injury to people or property resulting from any ideas, methods, instructions or products referred to in the content.

minerals

MDPI

Article

Utilizing Remote Sensing and Satellite-Based Bouguer Gravity data to Predict Potential Sites of Hydrothermal Minerals and Gold Deposits in Central Saudi Arabia

Amr Abd El-Raouf [1,*], Fikret Doğru [2], Islam Azab [3], Lincheng Jiang [4], Kamal Abdelrahman [5], Mohammed S. Fnais [5] and Omar Amer [1]

[1] Geology Department, Faculty of Science, Zagazig University, Zagazig 44519, Egypt; omaramer@science.zu.edu.eg
[2] Construction, Oltu Vocational College, Ataturk University, Erzurum 25400, Turkey; fikretdogru@atauni.edu.tr
[3] Nuclear Materials, Authority, El-Maadi, Kattamyia, Cairo 530, Egypt; islam_nma2010@yahoo.com
[4] School of Emergency Management, Xihua University, Chengdu 610039, China; jianglc@zju.edu.cn
[5] Department of Geology and Geophysics, College of Science, King Saud University, P.O. Box 2455, Riyadh 11451, Saudi Arabia; khassanein@ksu.edu.sa (K.A.); mfnais@ksu.edu.sa (M.S.F.)
* Correspondence: ammohammed@science.zu.edu.eg

Abstract: This article aims to aid in exploring and forecasting hydrothermal minerals and gold deposits in Central Saudi Arabia (SA), with a focus on structural contexts. Remote sensing (RS) and satellite-based Bouguer gravity (SBG) data were integrated in order to create a mineral prediction map for the researched location. Data from the Landsat Operational Land Imager (OLI) and Shuttle Radar Topography Mission (SRTM) were transformed and enhanced using a variety of approaches. The delineation of hydrothermal alteration zones (HAZs) and highlighting of structural discontinuities in the OLI data were made possible using band ratios and oriented principal component analysis (PCA). Additionally, the underlying structural features were successfully exposed by processing the SBG using a variety of edge detection techniques, like the analytical signal (AS), total horizontal derivative (THD), tilt angle (TA), horizontal tilt angle (TDX), theta map (TM), horizontal derivative of the tilt derivative (HD_TDR), horizontal gradient of the tilt angle (HGTA), tilt angle of the analytical signal (TAAS), and soft sign function (SF). As a result, more prominent lineaments were found in the NW–SE, NNW–SSE, NE–SW, and NNE–SSW directions than in the N–S and E–W directions. The GIS incorporated surface/subsurface geological structure density maps with zones of hydrothermal alteration. It was found that the lineaments derived from the analysis of the RS and SBG data were more in line with the HAZs, which demonstrated the common connection between alteration zones and deep lineaments. The findings revealed a mineral prediction map with extremely low to extremely high probabilities. Overall, combining RS and SBG data effectively identified probable mineralization sites associated with hydrothermal processes and made it easier to create this study's final predictive mineralization map.

Keywords: remote sensing; Bouguer gravity; hydrothermal alteration; gold; Saudi Arabia

1. Introduction

The Arabian Shield (ASh) is considered an economically significant shield worldwide, as it has promising possibilities for exploring metallic ore deposits. The ASh of Saudi Arabia (SA) consists of stratiform, vein, and magmatic to late magmatic contact metamorphism deposits [1]. Over 800 occurrences of gold (Au) and other metal deposits are found throughout the ASh, including porphyry copper, volcanic-hosted massive sulfide (VHMS) (Al-Amar, Gabal Sayid, and Al-Nuqrah), and Au ore deposits, such as those in the Bulghah and Mahd Ad Dahab mines (in the production stage) [1,2].

Significant gold mineralization is found in the central zones of the Najd fault system (NFS), specifically in Ghadarah, Fawarah, Hamdah, and Gariat Avala. Major fault zones parallel to the Red Sea also run northward from the south, becoming more connected as they go deeper underground, and they overlook several gold mines, including the Wadi Bidah, Jadmah, Wadi Laif, and Mamilah mines (Figure 1a) [3].

The Arabian-Nubian Shield (ANS) is considered significant for gold exploration and mining in SA. It is crucial for relationships between gold genesis and orogenic tectonics. Based on the tectonic settings and gold host rocks, primary gold mineralization can be divided into three basic types [4], as described in the following paragraphs.

The first type includes volcano-sedimentary connections, such as the Siham Group, and epithermal deposits, like the Mahd Ad Dhahab and Al-Amar ore deposits, as well as volcanogenic massive sulfide (VMS) gold deposits.

Based on Al-Shanti [5], the second type of gold mineralization is found in listwaenite rocks, which were formed after ophiolitic rocks were carbonatized. These rocks have several suture zones. For the Saudi Ma'aden Mining Company (SMMC), Bi'r Tawilah (study area, e.g., Masarah and Al Mansourah) is a suitable candidate for gold-mineralization-hosted listwaenite in the Nabitah suture (NS) zone and the western section of the Afif terrane (AT) [4].

The third form of gold deposit is hosted by late- to post-tectonic (640–610 Ma) plutons of diorite–granite and/or their subvolcanic substitutes that intruded the Bani Ghayy and Murdama Groups, chiefly abundant in the western (AT) and eastern (NS) zones, such as in Bi'r Tawilah, Sukhaybarat, Bulghah, Zalm, Jabal Ghadarah, and Ad Duwayhi [6–10]. Mesothermal quartz-vein-type gold ore mineralization, developed in intraplate settings, controls these deposits, which are magmatically and/or structurally controlled [11].

The majority of gold is found as loose microscopic specks along arsenopyrite, pyrite, and occasionally chalcopyrite fractures, which were produced by CO2-rich ore fluids within these deposits, which are connected through quartz veins and stringers [4,9].

Traditional field geology surveys are extremely costly, time-consuming, and difficult for mineral exploration in hydrothermal alteration zones (HAZs). Furthermore, interpolations are widely used in the outcomes achieved. In this situation, the combination of RS and SBG data may be considered as a substitute method for carrying out regional geological mapping with tolerable precision in a manageable amount of time.

The major goal of the current research is to recognize the best locations for mineral resources and gold deposits, using a combination of surface and subsurface structure components and HAZ areas. RS data (Landsat 8 OLI and SRTM data) and SBG data were used in conjunction in order to identify HAZs and structural lineaments in the area under investigation.

Reconnaissance investigations frequently utilize remote sensing technology. Remote sensing is a crucial method for understanding several aspects, including geological, geomorphic, structural, and mineral deposits. Multiple generations of unmanned satellites, called Landsat, ranging from their initial generation to generation 9, have been developed and released by the National Aeronautics and Space Administration (NASA). These satellites collect vital RS data regarding mineral resources, structural aspects, and land use/land cover. Geomorphic and geological components are described in [9,12–23]. In order to emphasize the spectral contrasts between the bands, ratio images have been employed. This method has been applied in remote sensing in order to map lithology and HAZs, and to mark spectral differences [24], so that a high contrast range of spectral properties—not possible with separate bands—may be displayed.

Based on fluctuations in rock density, SBG data play a vital role in finding subsurface structures. These geological formations serve as conduits for mineral deposits connected to hydrothermal systems. An essential problem to address when examining potential field data concerns locating and relating subsurface density patterns to subsurface structures [25–29]. Mineral exploration and structural studies can use edge detection methods to delineate the boundaries of subsurface structures [29–32]. Many approaches

can be applied in order to detect structural edges, with most methods depending on the source field's derivatives [33,34]. Previously, the limits of sources buried at varying depths on an observational plane were explored using various enhancing filters [35,36]. Several studies have increased the accuracy with which filters detect the boundaries of buried HAZs [3,37,38]. Many edge detection strategies can be applied in order to achieve the goals of such investigations. The first-order vertical derivative (FVD), total horizontal derivative (THD) [23], analytical signal (AS), tilt derivative (TD) [39], tilt angle (TA), and theta filtering [40] are some of these methods. Recently, the horizontal derivative of the tilt derivative (HD_TDR), horizontal gradient of the tilt angle (HGTA), tilt angle of the analytical signal (TAAS), and soft sign function (SF), filters that are based on second-order derivatives of potential field data, were developed. These techniques effectively improve the resolution of the findings of boundary detection while avoiding the secondary boundary problem.

As a result, combining RS images and SBG data should aid in improving lithologic mapping, enhancing geologic structures, and identifying gold mineralization zones.

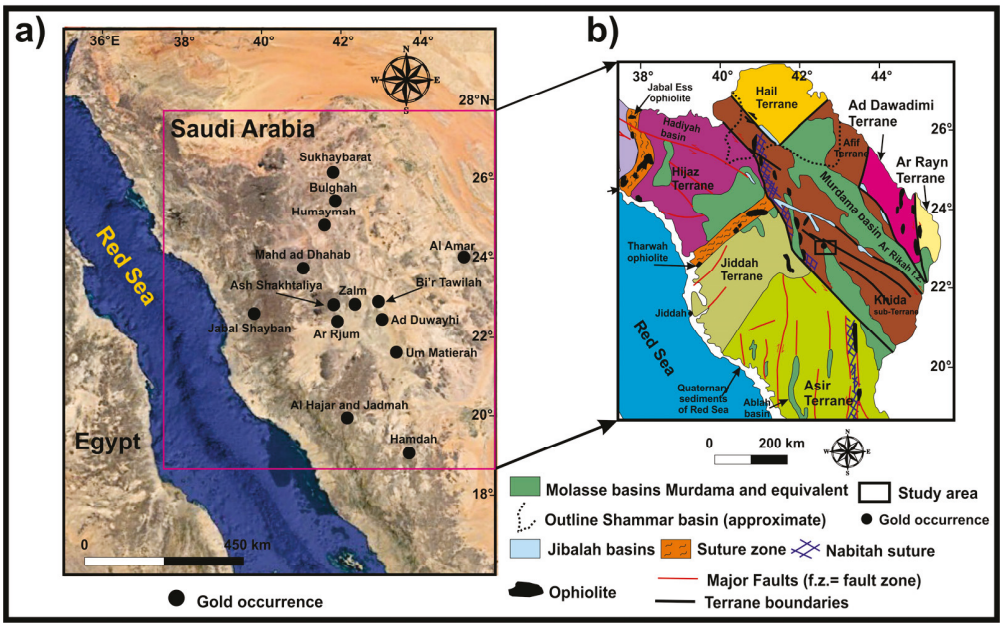


Figure 1. (**a**) Location map of the Arabian Shield (Ash) showing major ophiolite belts, tectonostratigraphic terranes, fault zones, sutures, and post-accretionary basins in Saudi Arabia. The locations of 14 significant gold deposits are shown and include our investigated site in Central Saudi Arabia and the Bi'r Tawilah gold mining area (Jabal Masarah, Al Mansourah, and Ghadarah). (**b**) A geological map of the Ash showing the study area location [41], with modifications [42,43].

2. Geological Outlines

2.1. Geological Setting

The region under investigation is situated in the central (ASh) area neighborhood, including the Bi'r Tawilah gold mining area and its surroundings. Along the Ad Dafinah faults that divide the Afif terrane, the area is located east of the Jeddah terrane [44,45]. Latitudes 22°00′ to 23°00′ N and longitudes 42°00′ to 43°30′ E serve as its boundaries (Figure 1b). The Hulyfah volcano-sedimentary pattern (Bani Ghayy and Siham Groups, 690 Ma and 620 Ma, respectively; [46]) make up the majority of the Bi'r Tawilah area (Figure 2). Younger syn-orogenic rocks (granodiorite and porphyritic rhyodacite) that are 710–685 Ma old intrude into this region. The Bani Ghayy Group comprises siltstone, greywacke, and conglomerate and is intercalated with metabasalts and pyroclastics. In contrast, the Siham Group comprises severely deformed and foliated chlorite, hornblende, and sericite ortho-schists. According to Al Jahadli [9], both groups underwent metamorphism into greenschist–lower amphibolite facies. Ortho-schists and molasse sediments are

the rocks that are visible in Jabal Bani Ghayy [47]. Gold and tungsten ore resources can be found at Bi'r Tawilah (Figure 2). The Bani Ghayy Group–Siham Group–N-striking thrust fault divides them [48].

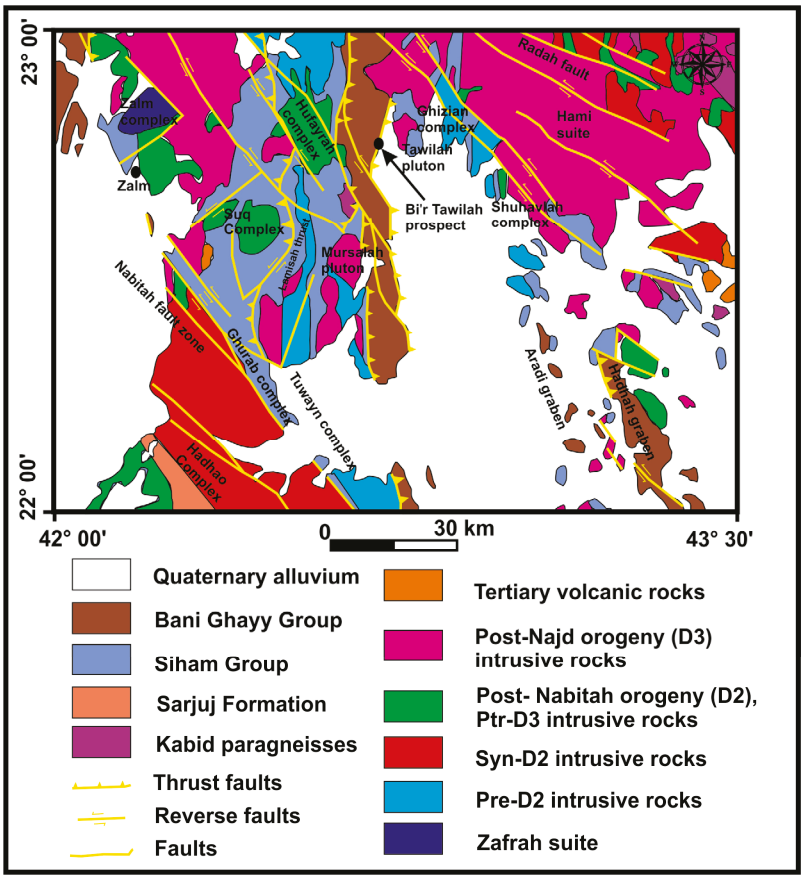


Figure 2. A geological map of the study area (modified from [47,49]).

A Pan-African example of gold mineralization, the Bi'r Tawilah gold mine in Central Saudi Arabia, includes hypogene and supergene minerals. The so-called "Nabitah orogenic zone" along the thrust fault (N–S) area hosts sulfidic gold deposits in the intermediate to felsic intrusions. Serpentines and associated listwaenites, porphyries, granites, and dioritic rocks are the four types of rock units that are present and are arranged from oldest to youngest. All kinds of rocks are subject to hydrothermal alteration, which includes chloritization, sericitization, carbonatization, and silicification [49].

2.2. Gold Mineralization and Structure Setting

Three gold mines (in the Bi'r Tawilah, Al Mansurah, and Masarah regions) are located within the research area. Mafic volcaniclastic rock units (Siham Group), conglomerate, and sandstone comprise most of the rock units in Bi'r Tawilah (the first area), with diorite and granodiorite only occasionally occurring at the surface. Jabal Ghadarh is a notable example of this. The N–S thrust fault (Bi'r Tawilah fault zone) deforms these rocks. Only one good barren quartz vein exposure, which is 55–120 cm thick and oriented NW, NE, and E–W, is present in the region. The Najd fault systems, which encompass the Bi'r Tawilah area, have structural data that are congruent with this [47].

Massive diamond drilling is mainly focused on listwaenite or carbonatized ultramafics, which have gold occurrences. The rocks made of listwaenite contain excellent gold occurrences. The boreholes in the Bi'r Tawilah region to the south reveal that minor ophiolitic serpentinite, diorite, deformed granodiorite, monzogranite, and porphyry intrusions constitute the principal lithologies present.

According to Surour et al. [49], the Bi'r Tawilah supergene zone exhibited the following characteristics: (1) the diorite was highly altered and had barren quartz stringers; (2) the granodiorite was affected by varying degrees of weathering; (3) the porphyry was weathered as indicated by the oxidized pyrite; (4) gold was found as inclusions in pyrite and silica in the deep horizons (i.e., hydrothermal alteration zones); and (5) in the weathered layers, supergene gold was discovered as the consequence of the oxidization of pyrite to goethite.

3. Materials and Methods

The present work utilized several analysis techniques to integrate the available datasets, including RS and SBG data [3,14,50], for mapping the structures and their related hydrothermal alteration zones (HAZs). These methods were used to connect the presence of mineral resources with the surface and subsurface structures delineated from the integrated approach. Figure 3 shows the integrated approach's workflow and each method's details.

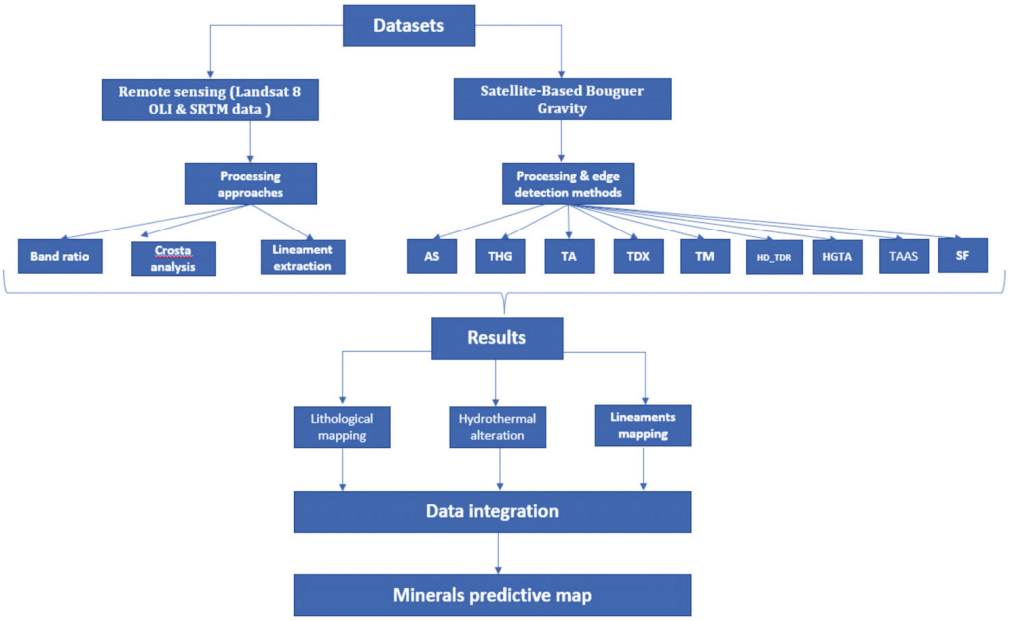


Figure 3. Workflow of the methods applied in the present study. Abbreviations are used in the table as follows: analytical signal (AS); total horizontal derivative (THD); tilt angle (TA); horizontal tilt angle (TDX); theta map (TM); horizontal derivative of tilt derivative (HD_TDR); horizontal gradient of tilt angle (HGTA); tilt angle of analytical signal (TAAS); and soft sign function (SF).

3.1. Remote Sensing Data

The Landsat-8 OLI (L8) dataset covering the investigated area originated from a mosaic of four scenes. The dataset was acquired on 4 July 2019 and was downloaded for free from the USGS Earth Explorer website (https://earthexplorer.usgs.gov, accessed on 20 July 2023). There are 11 bands in this dataset, each with various wavelengths and resolutions (Table S1).

For the L8 raw data to be prepared for further processing and to be in an adequate condition for investigation, pretreatment had to be carried out. Radiometric calibration, atmospheric correction, and minimum noise fraction (MNF) were all included in the preliminary processing.

Radiometric calibration and the Fast Line-of-Sight Atmospheric Analysis of Spectral Hypercubes (FLAASH) atmospheric correction model were applied using the ENVI software version 5.3 by L3Harris Geospatial USA (Broomfield, CO, USA), as described by Jahvar et al. [51], to calibrate the L8 data with the spectral radiance, subset them, and convert the digital number (DN) to reflectance.

MNF segregates noise in the data from the spectral information [52,53]. L8 bands in the initial space are converted to eigenspaces via MNF. A data space can be divided into two distinct regions: one region is characterized by large eigenvalues and coherent eigenimages, while near-unity eigenvalues and noise-dominated images represent the other region. Eliminating unwanted information from the data and only using coherent portions will improve the outcomes of spectral processing [53]. The MNF bands were converted into their initial data space minus the noise band(s) for bands containing eigenvalues less than 2, which were then regarded as noise [54]. There were only seven bands for which the MNF approach for the L8 subset covering the research area was employed.

3.1.1. Band Ratios (BRs)

The band ratio technique is applied mainly in geological applications [55–57]. The band ratio approach divides the digital data value of one band with high reflectance by the digital data value of another band with low reflectance [58–60]. This method reduces the negative impact of environmental details, such as the Earth's surface, while enhancing contrast and compositional data. Some characteristics that cannot be seen with raw data are highlighted by the shadow cast by the terrain's surface.

3.1.2. Crosta Analysis

To distinguish between hydrothermally altered minerals, Crosta analysis is used to decrease the number of spectral band inputs for principal component analysis (PCA). This is carried out to enhance the likelihood that the unwanted spectral bands will be identified, which can then be simply mapped onto just one of the principal component images. The main component images that directly emphasize the spectral characteristics of particular targets were chosen using the Feature-Orientated Principal Component Selection (FPCS) technique. This technique is used to examine the loadings of PCA eigenvectors to identify the components that capture information relevant to the target spectral signatures. The features that are most relevant to the theoretical spectral signatures of specific targets are then used to detect the targets in the image. The pixels in those selected principal component images that correspond to the targets are assigned as either dark or bright pixels, indicating the presence of the targets [61].

The USGS spectral database was used to determine the spectral characteristics of iron oxides and minerals that contain hydroxyl [62]. Bands 2, 5, 6, and 7 of the Landsat 8 OLI were chosen based on this spectral database to emphasize the spectral responses of iron-oxide-bearing and hydroxyl-bearing (clay) minerals.

3.1.3. Digital Elevation Model (DEM) of SRTM

The Shuttle Radar Topography Mission (SRTM) data were obtained using the radar C-band at 3 arcsec (90 m at the equator) during a collaborative effort by the National Aeronautics and Space Administration (NASA) and the National Geospatial-Intelligence Agency (NGA—previously known as the National Imagery and Mapping Agency, or NIMA), along with the participation of the German and Italian space agencies [63]. Digital elevation model (DEM) data extracted from the SRTM data [64] were used to recognize and extract geological lineaments by calculating and interpreting DEM derivatives, including shaded relief maps, slope maps, and traverse profiles [65].

Fill Sink

The resolution, or the separation among sample points, is a key factor in determining the correctness of DEM data [66]. Sink (and peak) refers to a standard error in DEM images brought on by resolution issues or by rounding elevation values to the closest integer. In the ArcGIS 10.9 environment, a method known as fill sink was used for the SRTM DEM data of the research region to remove sink errors. A hill shadow thematic map was created using the rectified image.

Shaded Relief

The topography is depicted visually on shaded relief thematic maps using gray values from raster imagery [59–61]. The borders separating regions that are darkened and those that are not shaded could be lineaments. Examination of the shade map obtained from the DEM also helps to characterize the lineaments. Therefore, a minimum–maximum range along a color ramp was added to a thematic shaded relief map that was created using the DEM. An azimuth of 135° (southeast), which represents the sun's position in relation to the horizon, was selected after examining the sun's various positions and relative angles since it may reveal the shaded and unshaded areas more clearly than other values. The sun's angle of elevation over the horizon was set to 45 degrees. The spatial analysis hill shading tool of the ArcMap mapping program was applied to complete the work.

Lineament Extraction

The PCI Geomatica 2014 program was used to automatically extract lineaments from the shaded relief image created from the SRTM DEM. The two primary processing stages used for automatic lineament extraction are described below. The first step is the recognition of edges that reveal regions of sharp variations in the values of nearby pixels, and the second step is the identification of the existence of lines [67,68]. These procedures mostly employ the PCI Geomatica software's LINE module, a popular package for automatically extracting lineaments [55].

An experimental test of automatic lineament extraction was conducted using various value ratios for each LINE module parameter. The test was run on an optical dataset to determine the best set of parameters that returned accurate results for the lines that were extracted [67]. These parameters were applied to the used data in accordance with the literature, and their validity was confirmed by visual assessment. Among this study's LINE module settings, the default, suggested, and defined values are all shown in Table S2.

3.2. Satellite-Based Bouguer Gravity Anomaly

This study used a high-resolution Earth gravity field model, SGG-UGM-2, as a satellite-based Bouguer gravity anomaly. The SGG-UGM-2 model is a combination of marine gravity data derived from satellite altimetry data and the Gravity Field and Steady-State Ocean Circulation Explorer (GOCE), the normal equation of the Gravity Recovery and Climate Experiment (GRACE), and EGM2008-derived continental gravity data up to degree 2190 and order 2159 [69]. The SGG-UGM-2 data are open-access and available at (http://icgem.gfz-potsdam.de/tom_longtime, accessed on 24 July 2023).

Edge Detection Operators

- Previous Edge Detection Methods

Boundary analysis operators are utilized to find the edge of the subsurface source. These methods are used for potential data, such as gravity and magnetic data. The formulae for these methods are presented below.

The analytical signal (AS) method is presented as the square root of the sum of the squares of the x, y, and z derivatives, which is known as the 3D AS [70]:

$$|\mathrm{AS}| = \sqrt{\left(\frac{\partial \mathrm{T}}{\partial \mathrm{x}}\right)^2 + \left(\frac{\partial \mathrm{T}}{\partial \mathrm{y}}\right)^2 + \left(\frac{\partial \mathrm{T}}{\partial \mathrm{z}}\right)^2} \quad (1)$$

In the result of the AS, the edge of a source is shown at the boundaries around the maximum values. The advantage of the AS method is that it is less dependent on the direction of the magnetization vector when using magnetic data. However, the AS method poorly balances the signals from shallow and deep anomalies [71].

The total horizontal gradient (THG) method is another common method, and the formula for the THG is given as [72]:

$$\mathrm{THG} = \sqrt{\left(\frac{\partial \mathrm{T}}{\partial \mathrm{x}}\right)^2 + \left(\frac{\partial \mathrm{T}}{\partial \mathrm{y}}\right)^2} \tag{2}$$

In the result of the THG, the edge of the source is shown at the maximum values. The THG method is less noise-sensitive but poorly balances the signals from shallow and deep anomalies [71].

The tilt angle (TA) shows the edge of the source at zero values. The TA method can generate a balanced image for sources at different depths. The limitation of the TA method is that it produces secondary edges around the true edge [71]. The formula for the TA is given as [39]:

$$\mathrm{TA} = \tan^{-1}\left(\frac{\left(\frac{\partial \mathrm{T}}{\partial z}\right)}{\sqrt{\left(\frac{\partial \mathrm{T}}{\partial \mathrm{x}}\right)^2 + \left(\frac{\partial \mathrm{T}}{\partial \mathrm{y}}\right)^2}}\right) \tag{3}$$

The TA method normalizes the vertical derivative (VDR) to the total horizontal derivative [73].

Another common technique in geophysical interpretation is the horizontal tilt angle (TDX), which is normalized to the absolute value of the vertical derivative [74]. The TDX method is represented as follows [75]:

$$\mathrm{TDX} = \tan^{-1}\left(\frac{\sqrt{\left(\frac{\partial \mathrm{T}}{\partial \mathrm{x}}\right)^2 + \left(\frac{\partial \mathrm{T}}{\partial \mathrm{y}}\right)^2}}{\left|\left(\frac{\partial \mathrm{T}}{\partial z}\right)\right|}\right) \tag{4}$$

Wijns et al. [40] proposed the theta map (TM) method, which produces balances between edges located at different source depths. The TM method shows the edge of a source at the minimum values. In addition, the TM method has secondary edges around the true edge, like the TA method. The TM method is given as follows [40]:

$$\mathrm{TM} = \cos^{-1}\left(\frac{\sqrt{\left(\frac{\partial \mathrm{T}}{\partial \mathrm{x}}\right)^2 + \left(\frac{\partial \mathrm{T}}{\partial \mathrm{y}}\right)^2}}{\sqrt{\left(\frac{\partial \mathrm{T}}{\partial \mathrm{x}}\right)^2 + \left(\frac{\partial \mathrm{T}}{\partial \mathrm{y}}\right)^2 + \left(\frac{\partial \mathrm{T}}{\partial z}\right)^2}}\right) \tag{5}$$

- Recent Edge Detection Methods

In recent years, many new boundary analysis methods have been proposed, such as the horizontal derivative of tilt derivative (HD_TDR) [76], horizontal gradient of tilt angle (HGTA) [77], soft sign function (SF) [78], and tilt angle of analytical signal (TAAS) [79] methods.

The HD_TDR method is like the analytical signal method but is sharper and generates better-defined maxima centered over the body edges of the source [76].

$$\mathrm{HD_TDR} = \sqrt{\left(\frac{\partial \mathrm{TDR}}{\partial \mathrm{x}}\right)^2 + \left(\frac{\partial \mathrm{TDR}}{\partial \mathrm{y}}\right)^2} \tag{6}$$

The horizontal gradient of tilt angle (HGTA) method is given as follows [77]:

$$\mathrm{HGTA} = \sqrt{\left(\frac{\partial \mathrm{TA}}{\partial \mathrm{x}}\right)^2 + \left(\frac{\partial \mathrm{TA}}{\partial \mathrm{y}}\right)^2} \tag{7}$$

The soft sign function (SF) method was proposed by [78] as follows:

$$SF = \frac{k \times \frac{\partial THG}{\partial z} - (k+2)\sqrt{\left(\frac{\partial THG}{\partial x}\right)^2 + \left(\frac{\partial THG}{\partial y}\right)^2}}{\sqrt{\left(\frac{\partial THG}{\partial x}\right)^2 + \left(\frac{\partial THG}{\partial y}\right)^2} + \left|k \times \frac{\partial THG}{\partial z} - (k+1)\sqrt{\left(\frac{\partial THG}{\partial x}\right)^2 + \left(\frac{\partial THG}{\partial y}\right)^2}\right|} \quad (8)$$

where $THG = \sqrt{\left(\frac{\partial T}{\partial x}\right)^2 + \left(\frac{\partial T}{\partial y}\right)^2}$, and $1 \leq k \leq 10$ will yield the best results [72].

The TAAS method shows the edges of the sources at the maximum values; however, the detected edges have low resolution. The formula for the TAAS is represented as [79]:

$$TAAS = \tan^{-1}\left(\frac{\frac{\partial AS}{\partial z}}{\left(\frac{\partial AS}{\partial x}\right)^2 + \left(\frac{\partial AS}{\partial y}\right)^2}\right) \quad (9)$$

4. Results and Discussion

4.1. Remote Sensing (RS) Data

4.1.1. Landsat 8 OLI Data

The investigation of the Landsat data allowed for the outlining of the HAZ areas. The spectral Sabin ratios (4/2, 6/5, 6/7) are represented in the RGB images and shown in Figure 4a [80]. The OH-bearing minerals (clay minerals, such as kaolinite, montmorillonite, and alunite) mainly manifested in a 6/7 ratio, appearing in the RGB images as blue-colored regions. The crimson hue of ferric minerals, such as limonite, hematite, and goethite, was mirrored in the band ratio 4/2. Areas with a high concentration of iron oxides were detected as reddish spots in the band ratio 6/5. A false-color composite map representing an alteration map for the research area was created using band ratios 6/7, 6/5, and 5 [81–83], with the HAZs denoted in yellow (Figure 4b).

The corresponding eigenvectors and eigenvalues of SPCA for iron oxide layouts are shown in Table S3, with band 4 (reflection) and band 2 (absorption) as distinctive bands for iron oxides and the typical PC4 for iron oxides. Both the eigenvectors and individual values of the hydroxyl minerals were calculated using the Crosta analysis of the Landsat 8 OLI. Table S4 shows that in PC4, there was a difference in eigenvector importing among bands 6 (-0.774) and 7 (0.504). As a result, the darkest pixels represented band 7 (0.59) and reflected the OH-bearing minerals. The hydrothermally changed portions emerged in a brilliant tone following the negation of PC4.

During the generation of the Crosta alteration image (Figure 4c,d), the iron oxide minerals, hydroxyl minerals, iron oxide minerals (F, H + F, H), and RGB images were shown in grayscale. The white pixels with bright reflections that identify alteration areas in the grayscale images are likely to be zones with the most future potential since they display both iron-stained and clay alterations. While hydroxyl minerals are placed in yellow to orange reflection color in the RGB images, areas rich in iron oxide minerals are identified in cyan to bluish coloration [83].

The grayscale image produced by ratioing bands 6 and 7 (6/7) traced clay and hydroxyl-mineral-bearing areas as white-colored areas or linear patterns scattered along possible tectonic elements and associated stream channels, implying that the distribution of these minerals may be structurally governed (Figure 4e,f) [84].

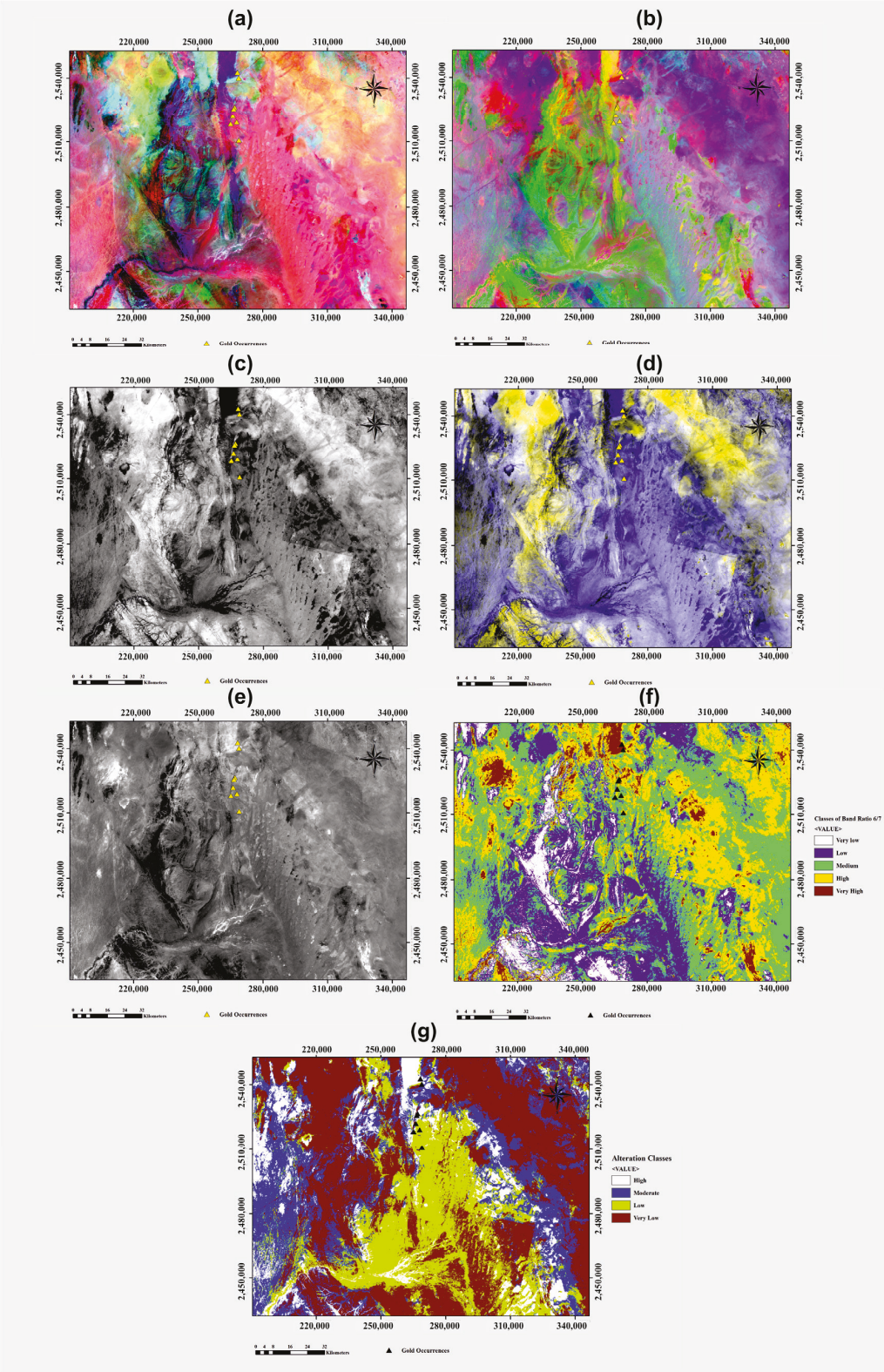


Figure 4. (**a**) Sabin band ratios in an RGB image. (**b**) Band ratios 6/7, 5/6, and 5 in an RGB image. (**c**) Crosta analysis (H, H + F, F) in a grayscale image. (**d**) RGB image. (**e**) Band ratio 6/7 for hydroxyl-bearing minerals in a grayscale image. (**f**) RGB image of band ratio 6/7 classes. (**g**) Hydrothermal alteration zone classes in the study area.

The images incorporate data from the band ratios and PCA-defined rock alteration caused by hydrothermal activity. These zones can be used to differentiate between locations with a high number of hydroxyl and iron oxide changes. As a result, the images were divided into five ranks. Figure 4g shows that the higher the rank, the better the mineral's favorable prospective grade. The richness of HAZs often indicates mineral alteration regions, particularly those rich in gold mineralization, which are frequently associated with highly sheared areas [85].

4.1.2. STRM DEM Data

The topographic variances varied from 857 to 1251 m (a.s.l.) according to the analysis of the SRTM DEM (Figure 5a). Additionally, the DEM offered geometry-related information not made available by previous RS approaches. The geological analysis of the Landsat photos and SRTM data revealed structures with lineaments (Figure 5b). From the findings of the lineament analysis, a total of 552 extracted lineaments from the STRM DEM are displayed in Figure 5c, along with a density map (Figure 5d) and a rose diagram showing the spatial distribution of the lineaments. The rose diagram is used to indicate the observed lineament trends, with patterns in the NW–SE, NNW–SSE, NE–SW, and NNE–SSW directions being considerably more apparent than those in the N–S and E–W directions (Figure 5c).

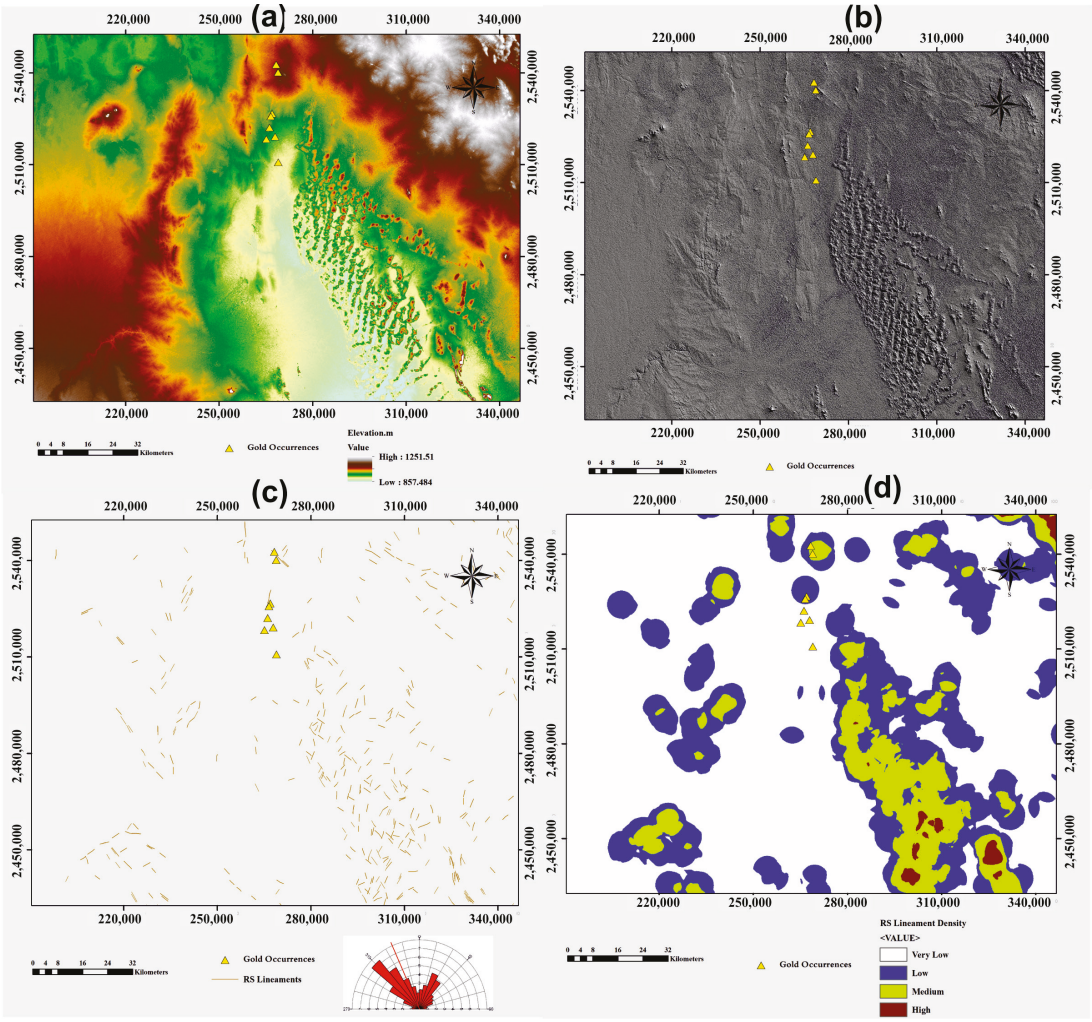


Figure 5. (**a**) The elevation map of the STRM DEM. (**b**) Shaded relief thematic map. (**c**) Elevations in the STRM DEM extracted lineament map. (**d**) Lineament density map.

Lineament density analysis was performed to determine the frequency of the lineaments per unit area. Also referred to as the lineament frequency, the lineament density is a measure of a collection of linear features in a location. This analysis led to the creation of a map (Figure 5d) that depicts the locations of the lineaments throughout the investigated area. According to [86], areas with a high lineament density are suitable for mineral prospecting.

4.2. Satellite-Based Bouguer Gravity (SBG) Data

In this study, the SGG-UGM-2 model was selected to obtain Bouguer gravity anomaly data between longitudes 42° and 43.3° and latitudes 22° and 23°, with a grid interval of 4 km. The Bouguer anomaly values changed from −62.8 to −99.6 mGal (Figure 6).

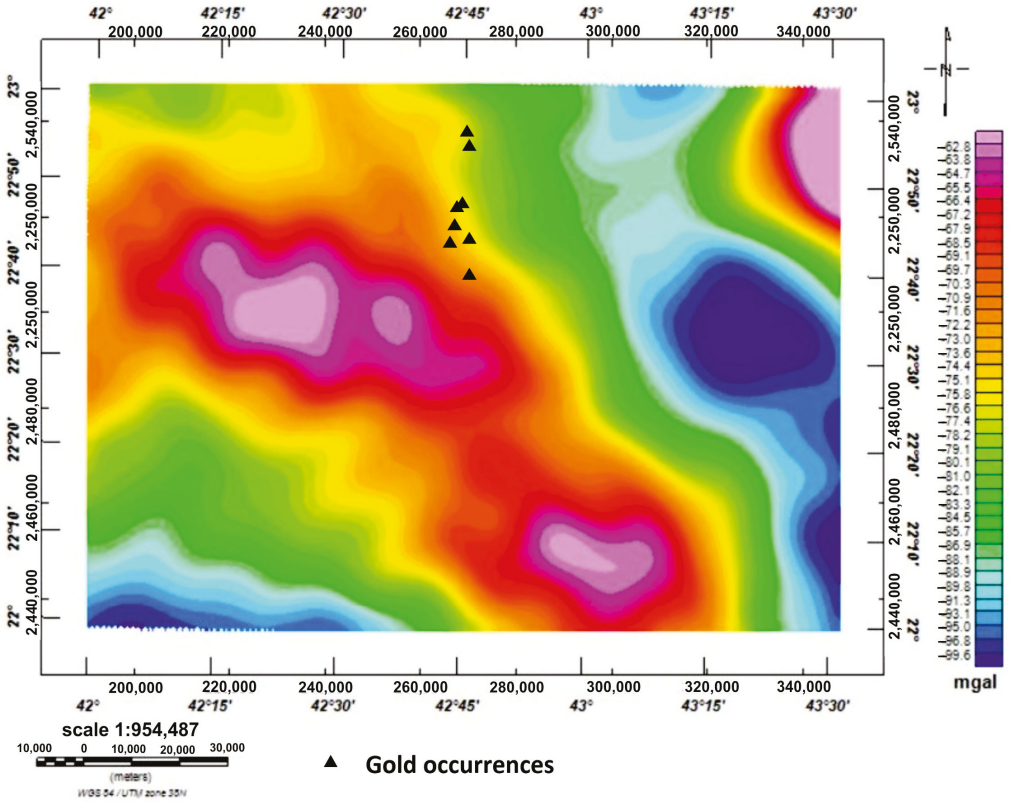


Figure 6. Bouguer gravity map of the study area.

Several threshold analysis operators were used, including the AS, THG, TA, TDX, and TM. Furthermore, modern edge recognition filters such as HD_TDR, HGTA, TAAS, and SF were used, and the findings were correlated with the research area's tectonic structure, according to the Hulyfah volcano-sedimentary pattern (Siham and Bani Ghayy Groups), which makes up most of the Bi'r Tawilah area and its surroundings. The Bouguer gravity map revealed higher values in the research region's central, southern, and northeastern parts. At the low–high-anomaly interface, −75.1 m Gal values were reported near the Bir Tawilah gold mining area (Figure 6).

The regional high-gravity anomalies are associated with crustal thickening in the research region's central, southern, and northeastern parts [87], implying that lithological crust changes cause this regional gravity anomaly gradient.

In the results of the AS method, the discontinuities cannot be seen, and the greatest values near the map's north reflect a northwest–southeast trend. This result could be explained by the AS's poor performance in recognizing shallow and deeper sources, and the discontinuities could be shallow sources in this location (Figure 7a).

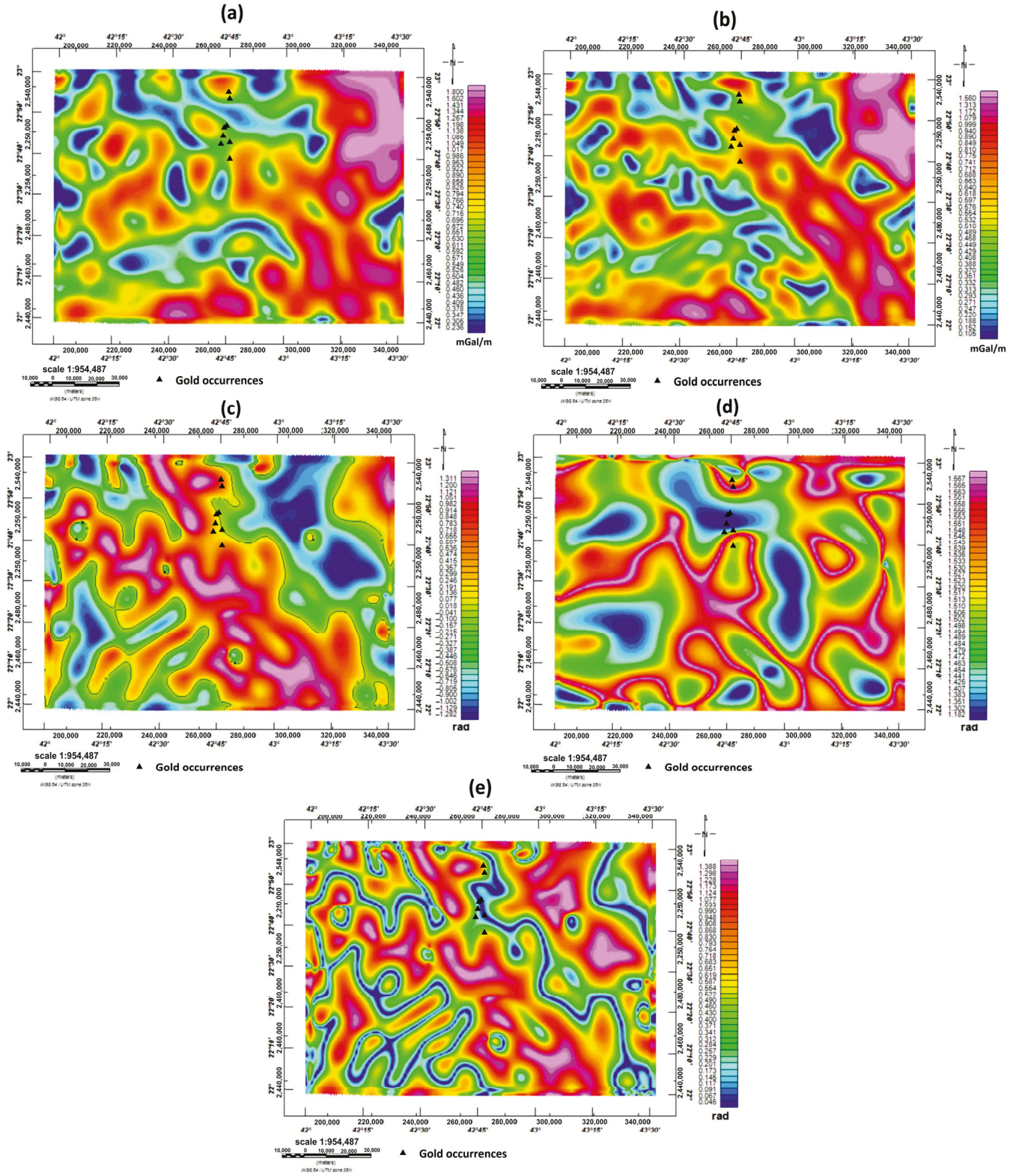


Figure 7. Boundary analysis results of the study area: (**a**) AS, (**b**) THG, (**c**) TA, (**d**) TDX, and (**e**) TM.

The NW–SE and NE–SW trends in the THG, TA, TDX, and TM data can, however, be seen clearly. The THD results are consistent with the nearby active and potential faults (Figure 7b–e). The maximum values depict the boundaries of tectonic plates and discontinuities. Additionally, although the TDX approach provides the edges at the maximum values (Figure 7d), the TA result displays the fault edges at the zero values rather than

the maximum values (Figure 7c). In the TM filter result, when the TM filter provides zero values, but the TDX filter yields maximum values at the exact locations, this may be connected to how the TM method produces secondary edges (Figure 7e). The TM and TDX maps have interconnected lineaments, which can make the interpretation more challenging.

The high-resolution SBG map underwent enhanced filtering using HD_TDR, HGTA, TAAS, and SF (Figure 8).

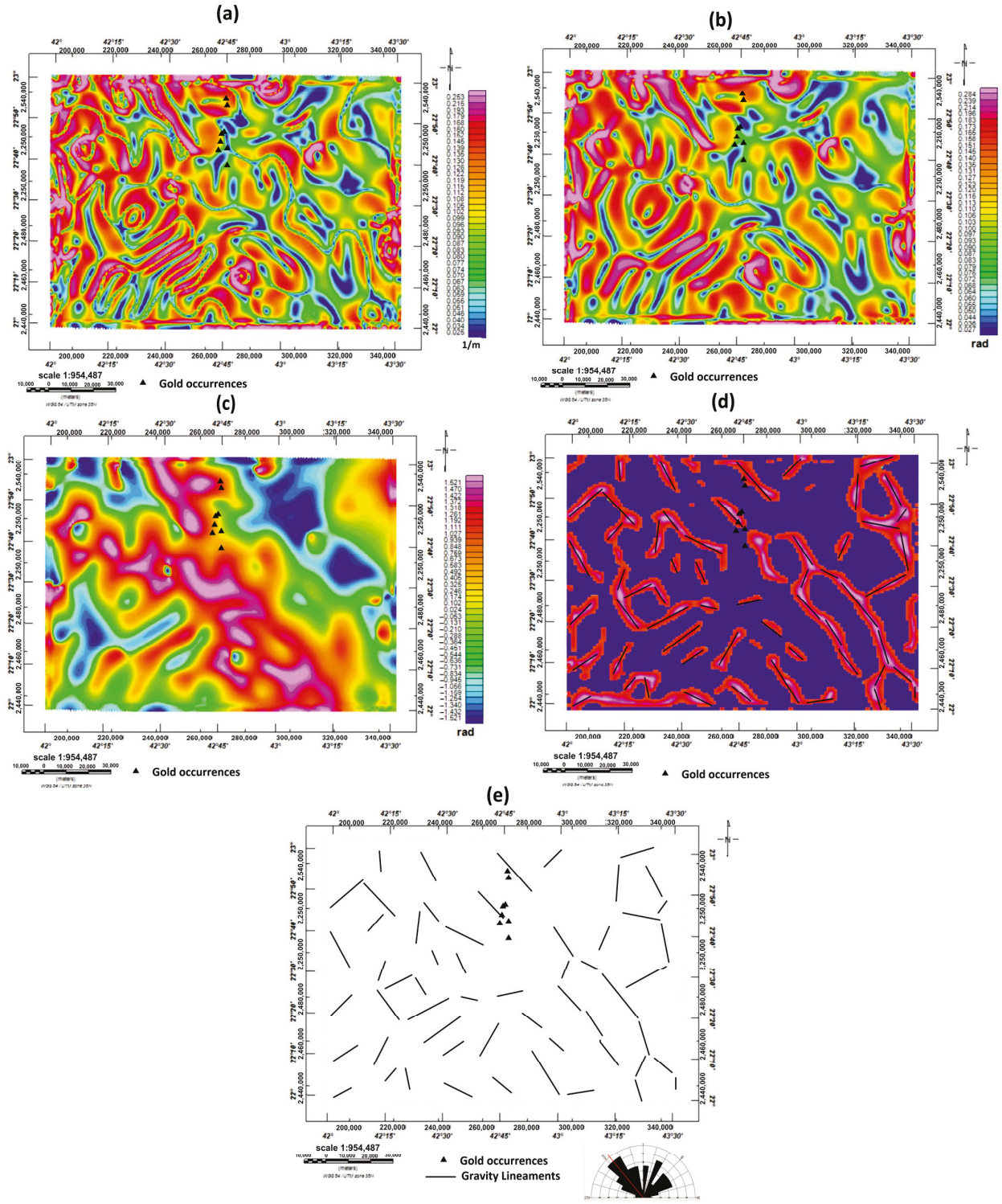


Figure 8. The results of recent boundary analysis methods: (**a**) HD_TDR, (**b**) HGTA, (**c**) TAAS, and (**d**) SF. (**e**) Extracted lineaments from the SBG data after applying advanced edge detection approaches.

The HGTA generated from the tilt angle filter is shown in Figure 8b, along with its effects and outputs. The lineaments brought about by lithological variation were visible along the tilt angle's zero-contour line, but this filter did not pick up on sharp edges [88].

The NE–SW, NW–SE, and N–S faults had prominent signatures on the HD_TDR and HGTA maps (Figure 8a,b). Therefore, they could not be used to identify the structural patterns in this situation. Strong filters called the TAAS and SF enable simultaneous equalization of signals with low and high amplitudes.

The geologic characteristics were considerably simpler to comprehend visually and qualitatively because the TAAS and SF maps (Figure 8c,d) provided a more detailed characterization of the features. A more exact length and width delineation can be seen on the SF map (Figure 8d). The visual comparison makes it simpler to understand the SF-derived lineaments. Subsurface linear structures detected in the research region according to the SF map (Figure 8e) exhibited lineaments, with the trends in the NW–SE, NNW–SSE, NE–SW, and NNE–SSW directions being more evident than those in the N–S and E–W directions. The lineament map derived from the subsurface gravity data highlighted the bulk of elongated NW–SE zones and their intersecting NE–SW trends (Figure 8e).

4.3. Integration of RS and SBG Results

Integrating multiple data sources in a spatial evaluation approach is essential in mineral prospect mapping [89]. To estimate the likely location of gold resources, a combined strategy has been used to characterize the areas of mineral occurrences [90]. This section combines the lineaments and HAZs produced from the RS and SBG data. This is helpful for investigation strategies in searching for minerals and serves as adequate evidence of mineralization.

By integrating the lineaments derived from the RS and SBG data, an integrative lineament map (Figure 9a) was constructed, which displays the critical surface and subsurface features (faults/fractures). Analysis of the RS- and SBG-derived lineaments revealed that the lineaments in the NW–SE, NNW–SSE, NE–SW, and NNE–SSW directions were more pronounced than those in the N–S and E–W directions. A density map was created using the data's recovered lineaments (Figure 9b), and we classified it into four classes. This map showed a high density of fracture/fault zones in the southeast of the research region (south of the Bir Tawilah gold mine) and a medium density in some sections of the western and eastern parts. The density map also showed a prominent NW–SE tendency that crossed the NE–SW trend.

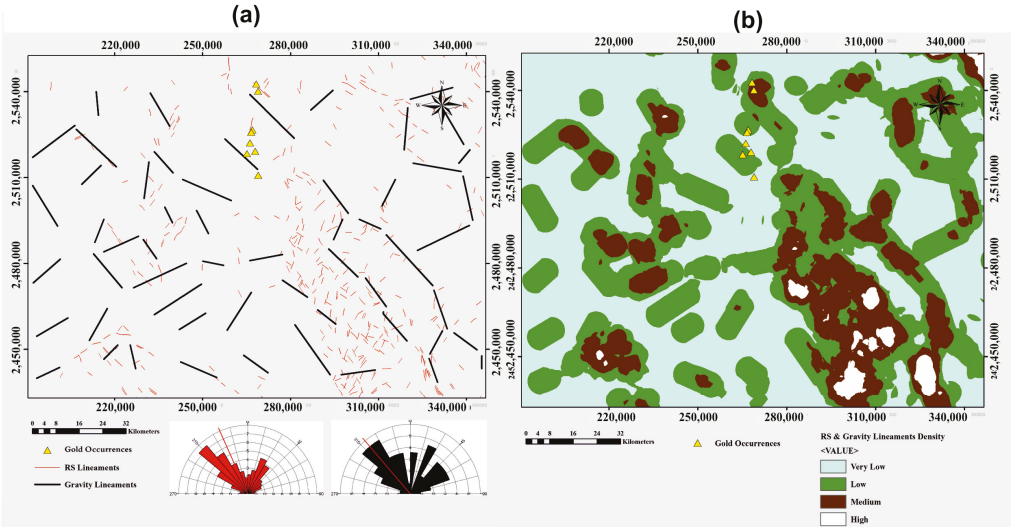


Figure 9. (**a**) An integrated lineament from the RS (black) and SBG (red) data. (**b**) Lineament density map from the RS and SBG data.

The geodynamic evolution of the studied area has been significantly controlled by the linear trends that have been found. These patterns, which govern the rock units and represent ideal locations for hydrothermal solutions, were confirmed in the Landsat data. The integrated and extracted lineaments from the RS and SBG data and the geological map were superimposed on the derived hygrothermal zone map to indicate the favorable and predicted sites of gold and hydrothermal mineralization (Figure 10). High-class sites indicate a desirable location and a greater density of mineral resources, considering that many mineral and gold deposits are linked to HAZs, including fluids that rise through fault lines and fissures.

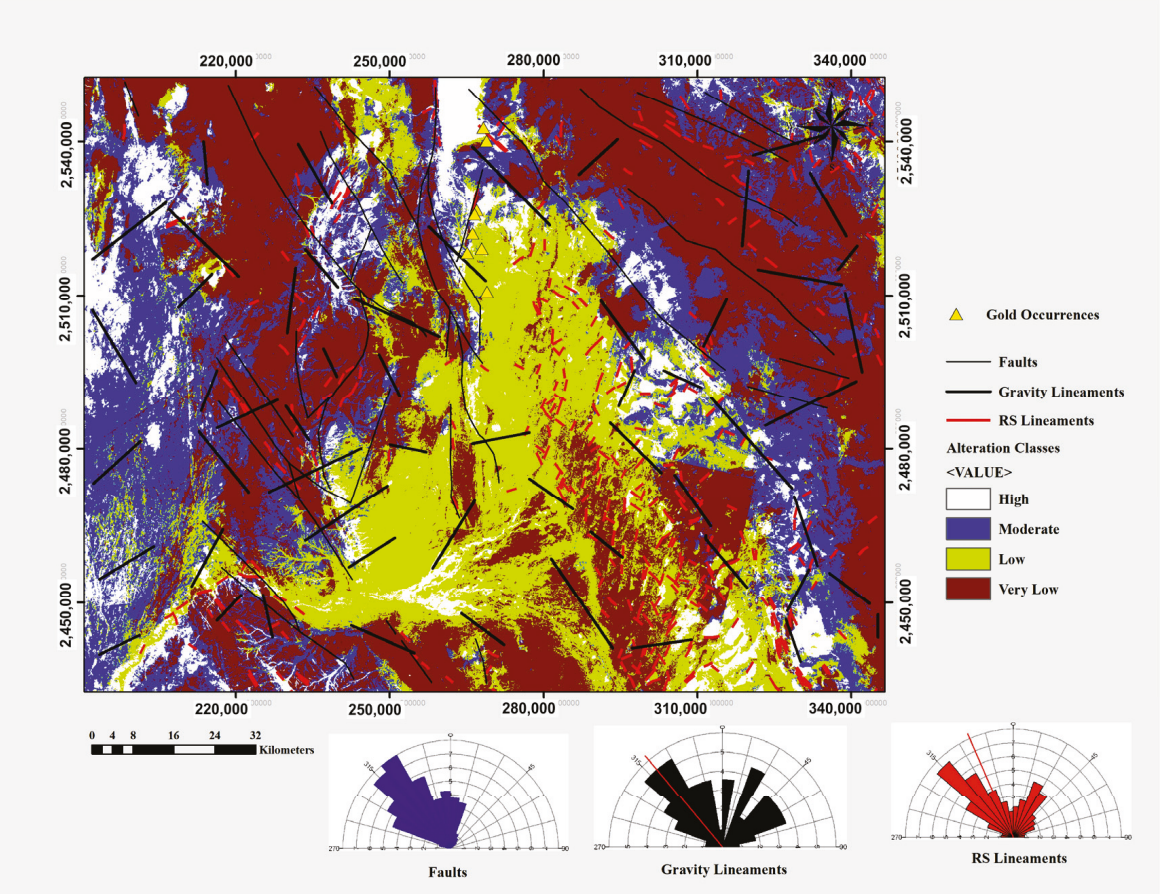


Figure 10. The map shows the hydrothermal alteration zone classes for the study area and is superimposed by the integrated lineaments from the geological map (black) and RS (gray) and SBG (red) data. The rose diagrams display the major and minor trends of the derived lineaments from the geological map and RS and SBG data analysis.

As a consequence of this, regions that have a greater lineament density, which is associated with tectonic/structural lithosphere deformation [91], are more likely to have deposits of gold mineralization. Therefore, the areas with the greatest change and lineament density are compatible with the most appropriate predicted mineralization regions. In addition, the location of the existing gold mines also correlates well with these locations. As a result, the predicted Au mineralization zones are found in the southeastern, eastern, and northern regions (Figure 10).

5. Conclusions

The research region is situated in the center of the Arabian Shield (Ash) and includes the Bi'r Tawilah gold mine area and its surrounding area, which is considered to be one of Saudi Arabia's largest gold mining areas. The current study's primary objective was to

identify the optimal locations of mineral resources and gold deposits by combining surface and subsurface structure components and hydrothermal alteration zone locations. The detection of HAZs and structural lineaments in the investigated area was achieved using an integrated approach based on remote sensing (RS) data (Landsat 8 OLI and SRTM data) and SBG data.

The merging of the RS and SBG data allowed for the detection of structural discontinuities and HAZs in the research area. In order to locate HAZs in the Landsat OLI data, image processing techniques including band ratios and PCA were applied. From the final image, four zones representing different degrees of alteration were identified. Lineaments were taken from the SRTM data analysis. Using the SBG data, several edge detection methods were utilized to build subsurface lineaments. The lineaments in the NW–SE, NNW–SSE, NE–SW, and NNE–SSW directions were more significant than those in the N–S and E–W directions, according to the analysis of the RS and SBG data's lineaments. The HAZs and lineament density were combined to create a mineral potential map that maximized the area of possible mineral resources.

The lineaments derived from the RS and SBG data analysis were found to be more compatible with the HAZs. This demonstrates that deep lineaments are frequently linked to alteration zones. This combination reflects the efficacy of using RS and SBG maps to explore gold occurrences and the associated hydrothermal metallic mineralization.

Supplementary Materials: The following supporting information can be downloaded at: https://www.mdpi.com/article/10.3390/min13081092/s1, Table S1: Spectral bands of the Landsat 8 satellite; Table S2: The values used for the parameters of the LINE module; Table S3: Eigenvectors and eigenvalues for iron-oxides mapping; and Table S4: Eigenvectors and eigenvalues for hydroxyl minerals mapping. References [92,93] are cited in the Supplementary Materials.

Author Contributions: Conceptualization, A.A.E.-R., F.D. and I.A.; methodology, A.A.E.-R., F.D. and I.A.; software, A.A.E.-R., F.D., I.A. and O.A.; validation, A.A.E.-R. and F.D.; formal analysis, A.A.E.-R., F.D. and I.A.; investigation, A.A.E.-R., F.D., I.A. and L.J.; resources, A.A.E.-R. and F.D.; data curation, A.A.E.-R., F.D. and I.A.; writing—original draft preparation, A.A.E.-R., F.D. and I.A.; writing—review and editing, A.A.E.-R., I.A., L.J. and O.A.; visualization, A.A.E.-R. and I.A.; supervision, A.A.E.-R. and I.A.; project administration, K.A. and M.S.F.; funding acquisition, K.A. and M.S.F. All authors have read and agreed to the published version of the manuscript.

Funding: This research was supported by the Researchers Supporting Project, number (IFKSUOR3-192-4), Ministry of Education, Saudi Arabia.

Data Availability Statement: Data are available from the corresponding authors upon reasonable request.

Acknowledgments: The authors extend their appreciation to the Deputyship for Research and Innovation, Ministry of Education, Saudi Arabia, for funding this research through project no. (IFKSUOR3-192-4). Also, we thank the editors and reviewers for their valuable comments and suggestions.

Conflicts of Interest: The authors declare no conflict of interest.

References

1. Darwish, M.A.; Butt, N.A. Mineral resource potential and its development in Saudi Arabia. *Eng. Sci.* **1996**, *8*, 107–120. [CrossRef]
2. Ministry of Planning KSA. *Fourth Development Plan (1985–1990)*; Ministry of Planning KSA: Riyadh, Saudi Arabia, 1985; pp. 167–184.
3. Eldosouky, A.M.; El-Qassas, R.A.Y.; Pham, L.T.; Abdelrahman, K.; Alhumimidi, M.S.; El Bahrawy, A.; Mickus, K.; Sehsah, H. Mapping Main Structures and Related Mineralization of the Arabian Shield (Saudi Arabia) Using Sharp Edge Detector of Transformed Gravity Data. *Minerals* **2022**, *12*, 71. [CrossRef]
4. Harbi, H.A.; Eldougdoug, A.A.; Al Jahdali, N.S. Evolution of the Arabian shield and associated mineralization. In Proceedings of the 9th Arab Conference of Mineral Resources, Jeddah, Saudi Arabia, 30 October–1 November 2006; pp. 1–11.
5. Al-Shanti, A.M.S. *Geology of the Arabian Shield*; Center for Scientific Publishing, King Abdlaziz University: Jeddah, Saudi Arabia, 1993.

6. Collenette, P.; Grainger, D.J. Mineral Resources of Saudi Arabia, not Including Oil, Natural Gas, and Sulfur. In *Ministry of Petroleum and Mineral Resources, Directorate General of Mineral Resources*; Ministry of Petroleum Saudi: Jeddah, Saudi Arabia, 1994.
7. Nehlig, P.; Salpeteur, I.; Asfirane, F.; Bouchot, V.; Eberlé, J.M.; Genna, A. The mineral potential of the Arabian shield: A reassessment. In Proceedings of the IUGS/UNESCO Meeting on the "Base and Precious Metal Deposits in the Arabian Shield", Jeddah, Saudi Arabia, 12–19 November 1999; pp. 12–19.
8. Leistel, J.M.; Al Jahdali, N.; Khalil, I.; Kattu, G.; Eberle, J.M.; Lambert, A.; Siddiqui, A.; Saleh, Y. *Results of Precious Metal Exploration in the Zalim Prospect, Kingdom of Saudi Arabia*; Ministry of Petroleum and Mineral Resources, Deputy Ministry for Mineral Resources: Jeddah, Saudi Arabia, 1999; Technical Report; BRGM-TR-99-14; 108p.
9. Al Jahdli, N.S. *Geology of Jabal Ghadarah Area, Bi'r Tawilah District with Special Emphasis on Listvinite as a Potential Source for Gold in the Kingdom of Saudi Arabia', M.Sc.*; King Abdulaziz University: Jeddah, Saudi Arabia, 2004.
10. Doebrich, J.L.; Zahony, S.G.; Leavitt, J.D.; Portacio, J.S., Jr.; Siddiqui, A.A.; Wooden, J.L.; Fleck, R.J.; Stein, H.J. Ad Duwayhi, Saudi Arabia: Geology and geochronology of a Neoproterozoic intrusion-related gold system in the Arabian Shield. *Econ. Geol.* **2004**, *99*, 713–741. [CrossRef]
11. Agar, R.A.; Stacey, J.S.; Whitehouse, M.J. *Evolution of Southern Afif Terrane: A Geochronologic Study*; Ministry of Petroleum and Mineral Resources, Deputy Ministry for Mineral Resources: Jeddah, Saudi Arabia, 1992; Open-File-Report; DGMR-OF-10-15; 46p.
12. Abdelkareem, M.; El-Baz, F. Characterizing hydrothermal alteration zones in Hamama area in the central Eastern Desert of Egypt by remotely sensed data. *Geocarto Int.* **2017**, *33*, 1307–1325. [CrossRef]
13. Ahmed, A.A.; Abdelkareem, M.; Asran, A.M.; Mahran, T.M. Geomorphic and lithologic characteristics of Wadi Feiran basin, Southern Sinai, Egypt, using remote sensing and field investigations. *J. Earth Syst. Sci.* **2017**, *126*, 85. [CrossRef]
14. Abdelkareem, M.; El-Din, G.M.K.; Osman, I. An integrated approach for mapping mineral resources in the Eastern Desert of Egypt. *Int. J. Appl. Earth Obs. Geoinf.* **2018**, *73*, 682–696. [CrossRef]
15. Sultan, M.; Arvidson, R.E.; Sturchio, N.C. Mapping of serpentinites in the Eastern Desert of Egypt by using Landsat thematic mapper data. *Geology* **1986**, *14*, 995–999. [CrossRef]
16. Abdelsalam, M.G.; Stern, R.J.; Berhane, W.G. Mapping gossans in arid regions with Landsat TM and SIR-C images: The Beddaho Alteration Zone in northern Eritrea. *J. Afr. Earth Sci.* **2000**, *30*, 903–916. [CrossRef]
17. Madani, A.A.; Rahman, E.M.A.; WZY, K.M.F.A.; Emam, A. Mapping of the hydrothermal alteration zones at Haimur gold mine area, South Eastern Desert, Egypt, using remote sensing techniques. *Egypt. J. Remote Sens. Space Sci.* **2003**, *6*, 47–60.
18. Ramadan, T.M.; Kontny, A. Mineralogical and structural characterization of alteration zones detected by orbital remote sensing at Shalatein District, SE Desert, Egypt. *J. Afr. Earth Sci.* **2004**, *40*, 89–99. [CrossRef]
19. Abdelkareem, M.; El-Baz, F. Mode of formation of the Nile Gorge in northern Egypt: A study by DEM-SRTM data and GIS analysis. *Geol. J.* **2015**, *51*, 760–778. [CrossRef]
20. El Khidir, S.O.; Babikir, I.A. Digital image processing and geospatial analysis of landsat 7 ETM+ for mineral exploration, Abidiya area, North Sudan. *Int. J. Geomat. Geosci.* **2013**, *3*, 645–658.
21. Amuda, O.S.; Adebisi, S.A.; Jimoda, L.A.; Alade, A.O. Challenges and possible panacea to the municipal solid wastes management in Nigeria. *J. Sustain. Dev. Stud* **2014**, *6*, 64–70.
22. Poormirzaee, R.; Oskouei, M.M. Use of spectral analysis for detection of alterations in ETM data, Yazd, Iran. *Appl. Geomat.* **2010**, *2*, 147–154. [CrossRef]
23. El-Din, G.K.; Abdelkareem, M. Integration of remote sensing, geochemical and field data in the Qena-Safaga shear zone: Implications for structural evolution of the Eastern Desert, Egypt. *J. Afr. Earth Sci.* **2018**, *141*, 179–193. [CrossRef]
24. Goetz, A.F.H.; Rock, B.N.; Rowan, L.C. Remote sensing for exploration; an overview. *Econ. Geol.* **1983**, *78*, 573–590. [CrossRef]
25. Kafadar, O. CURVGRAV-GUI: A graphical user interface to interpret gravity data using curvature technique. *Earth Sci. Inform.* **2017**, *10*, 525–537. [CrossRef]
26. Eldosouky, A.M.; Saada, S.A. Source edge detection (SED) of aeromagnetic data: Synthetic examples and a case study from Haimur area, south Eastern Desert, Egypt. *Arab. J. Geosci.* **2020**, *13*, 1–12. [CrossRef]
27. Pham, L.T.; Oksum, E.; Vu, M.D.; Vo, Q.T.; Du Le-Viet, K.; Eldosouky, A.M. An improved approach for detecting ridge locations to interpret the potential field data for more accurate structural mapping: A case study from Vredefort dome area (South Africa). *J. Afr. Earth Sci.* **2020**, *175*, 104099. [CrossRef]
28. Eldosouky, A.M.; Mohamed, H. Edge detection of aeromagnetic data as effective tools for structural imaging at Shilman area, South Eastern Desert, Egypt. *Arab. J. Geosci.* **2021**, *14*, 1–10. [CrossRef]
29. El-Raouf, A.A.; Doğru, F.; Abdelrahman, K.; Fnais, M.S.; El Manharawy, A.; Amer, O. Using Airborne Geophysical and Geochemical Methods to Map Structures and Their Related Gold Mineralization. *Minerals* **2023**, *13*, 237. [CrossRef]
30. Eldosouky, A.M.; Sehsah, H.; Elkhateeb, S.O.; Pour, A.B. Integrating aeromagnetic data and Landsat-8 imagery for detection of post-accretionary shear zones controlling hydrothermal alterations: The Allaqi-Heiani Suture zone, South Eastern Desert, Egypt. *Adv. Space Res.* **2019**, *65*, 1008–1024. [CrossRef]
31. Oksum, E.; Le, D.V.; Vu, M.D.; Nguyen, T.H.T.; Pham, L.T. A novel approach based on the fast sigmoid function for interpretation of potential field data. *Bull. Geophys. Ocean.* **2021**, *62*, 543–556.
32. Kharbish, S.; Eldosouky, A.M.; Amer, O. Integrating mineralogy, geochemistry and aeromagnetic data for detecting Fe–Ti ore deposits bearing layered mafic intrusion, Akab El-Negum, Eastern Desert, Egypt. *Sci. Rep.* **2022**, *12*, 15474. [CrossRef]

33. Pham, L.T. A comparative study on different filters for enhancing potential field source boundaries: Synthetic examples and a case study from the Song Hong Trough (Vietnam). *Arab. J. Geosci.* **2020**, *13*, 723. [CrossRef]
34. Pham, L.T. A high resolution edge detector for interpreting potential field data: A case study from the Witwatersrand basin, South Africa. *J. Afr. Earth Sci.* **2021**, *178*, 104190. [CrossRef]
35. Hang, N.T.T.; Thanh, D.D.; Minh, L.H. Application of directional derivative method to determine boundary of magnetic sources by total magnetic anomalies. *J. Sci. Earth* **2017**, *39*, 362–375. [CrossRef]
36. Pham, L.T.; Oksum, E.; Kafadar, O.; Trinh, P.T.; Nguyen, D.V.; Vo, Q.T.; Le, S.T.; Do, T.D. Determination of subsurface lineaments in the Hoang Sa islands using enhanced methods of gravity total horizontal gradient. *Vietnam J. Earth Sci.* **2022**, *43*, 395–409.
37. Eldosouky, A.M.; Pham, L.T.; Abdelrahman, K.; Fnais, M.S.; Gomez-Ortiz, D. Mapping structural features of the Wadi Umm Dulfah area using aeromagnetic data. *J. King Saud Univ.-Sci.* **2021**, *34*, 101803. [CrossRef]
38. Eldosouky, A.M.; Pham, L.T.; Mohmed, H.; Pradhan, B. A comparative study of THG, AS, TA, Theta, TDX and LTHG techniques for improving source boundaries detection of magnetic data using synthetic models: A case study from G. Um Monqul, North Eastern Desert, Egypt. *J. Afr. Earth Sci.* **2020**, *170*, 103940. [CrossRef]
39. Miller, H.G.; Singh, V. Potential field tilt—A new concept for location of potential field sources. *J. Appl. Geophys.* **1994**, *32*, 213–217. [CrossRef]
40. Wijns, C.; Perez, C.; Kowalczyk, P. Theta map: Edge detection in magnetic data. *Geophysics* **2005**, *70*, L39–L43. [CrossRef]
41. Nehlig, P.; Genna, A.; Asfirane, F.; Guerrot, C.; Eberlé, J.; Kluyver, H.; Lasserre, J.; Le Goff, E.; Nicol, N.; Salpeteur, N.; et al. A review of the Pan-African evolution of the Arabian Shield. *Geoarabia* **2002**, *7*, 103–124. [CrossRef]
42. Johnson, P.R.; Woldehaimanot, B. Development of the Arabian-Nubian Shield: Perspectives on accretion and deformation in the northern East African Orogen and the assembly of Gondwana. *Geol. Soc. Lond. Spéc. Publ.* **2003**, *206*, 289–325. [CrossRef]
43. Stern, R.J.; Johnson, P. Continental lithosphere of the Arabian Plate: A geologic, petrologic, and geophysical synthesis. *Earth-Sci. Rev.* **2010**, *101*, 29–67. [CrossRef]
44. Johnson, P.R. Tectonic development of the Arabian Shield: An overview. In *US Geological Survey Saudi Arabia Mission, IUGS/UNESCO Deposit Modelling Workshop*; Ministry of Petroleum and Mineral Resources, Deputy Ministry for Mineral Resources: Jeddah, Saudi Arabia, 1999.
45. Johnson, P.R. Post-amalgamation basins of the NE Arabian shield and implications for Neoproterozoic III tectonism in the northern East African orogen. *Precambrian Res.* **2003**, *123*, 321–337. [CrossRef]
46. Stacey, J.S.; Agar, R.A. U-Pb isotopic evidence for the accretion of a continental microplate in the Zalm region of the Saudi Arabian Shield. *J. Geol. Soc.* **1985**, *142*, 1189–1203. [CrossRef]
47. Agar, R.A. Geologic map of the Zalm quadrangle, sheet 22F, Kingdom of Saudi Arabia. *Saudi Arab. Deputy Minist. Miner. Resour. Geol. Map GM* **1989**, *89*, 41.
48. Sabir, H.; Labbé, J.F. Bi'r Tawilah tungsten prospect, Najd region, Kingdom of Saudi Arabia. *J. Afr. Earth Sci. (1983)* **1986**, *4*, 249–255. [CrossRef]
49. Surour, A.A.; Harbi, H.M.; Ahmed, A.H. The Bi'r Tawilah deposit, central western Saudi Arabia: Supergene enrichment of a Pan-African epithermal gold mineralization. *J. Afr. Earth Sci.* **2014**, *89*, 149–163. [CrossRef]
50. Zeinelabdein, K.A.E.; Elemam, M.S.; Ali, H.A.; Alhassan, O.M. An integrated analysis of Landsat OLI image and satellite gravity data for geological mapping in North Kordofan State, Sudan. *Am. J. Earth Sci.* **2014**, *1*, 25–32.
51. Javhar, A.; Chen, X.; Jovid, A.; Yunus, M.; Jamshed, A.; Eldiiar, D.; Zulfiyor, B. Evaluation of remote sensing techniques for lithological mapping in the southeastern Pamir using Landsat 8 OLI data. *Int. J. Geoinformatics* **2018**, *14*, 1–10.
52. Green, A.; Berman, M.; Switzer, P. Craig A transformation for ordering multispectral data in terms of image quality with implications for noise removal. *IEEE Trans. Geosci. Remote. Sens.* **1988**, *26*, 65–74. [CrossRef]
53. Vermillion, S.C.; Sader, S.A. Use of the minimum noise fraction (MNF) transform to analyze airborne visible/infrared imaging spectrometer (AVIRIS) data of northern forest types. *AVIRIS Workshop* **1999**, 7.
54. Boardman, J.W.; Kruse, F.A. Automated spectral analysis: A geologic example using AVIRIS data, north Grapevine Mountais. San Antonio. In Proceedings of the Tenth Thematic Conference, Geologic Remote Sensing, San Antonio, TX, USA, 9–12 May 1994; pp. I-407–I-418.
55. Amer, R.; Kusky, T.; Ghulam, A. Lithological mapping in the Central Eastern Desert of Egypt using ASTER data. *J. Afr. Earth Sci.* **2010**, *56*, 75–82. [CrossRef]
56. Ali, A.S.; Pour, A.B. Lithological mapping and hydrothermal alteration using Landsat 8 data: A case study in ariab mining district, red sea hills, Sudan. *Int. J. Basic Appl. Sci.* **2014**, *3*, 199. [CrossRef]
57. Mhamdi, H.S.; Raji, M.; Maimouni, S.; Oukassou, M. Fractures network mapping using remote sensing in the Paleozoic massif of Tichka (Western High Atlas, Morocco). *Arab. J. Geosci.* **2017**, *10*, 125. [CrossRef]
58. Goetz, A.F.H.; Rowan, L.C.; Kingston, M.J. Mineral Identification from Orbit: Initial Results from the Shuttle Multispectral Infrared Radiometer. *Science* **1982**, *218*, 1020–1024. [CrossRef]
59. Mars, J.C.; Rowan, L.C. Regional mapping of phyllic-and argillic-altered rocks in the Zagros magmatic arc, Iran, using Advanced Spaceborne Thermal Emission and Reflection Radiometer (ASTER) data and logical operator algorithms. *Geosphere* **2006**, *2*, 161–186. [CrossRef]
60. Pour, A.B.; Hashim, M. Hydrothermal alteration mapping from Landsat-8 data, Sar Cheshmeh copper mining district, south-eastern Islamic Republic of Iran. *J. Taibah Univ. Sci.* **2015**, *9*, 155–166. [CrossRef]

61. Loughlin, W.P. Principal component analysis for alteration mapping. *Photogramm. Eng. Remote Sens.* **1991**, *57*, 1163–1169.
62. Kokaly, R.F.; Clark, R.N.; Swayze Gregg, A.; Livo KEric Hoefen Todd, M.; Pearson Neil, C.; Wise Richard, A.; Benzel William Lowers Heather, A.; Driscoll Rhonda, L.; Klein Anna, J. *USGS Digital Spectral Library*; US Geological Survey: Reston, VA, USA, 2017. [CrossRef]
63. Rabus, B.; Eineder, M.; Roth, A.; Bamler, R. The shuttle radar topography mission—A new class of digital elevation models acquired by spaceborne radar. *ISPRS J. Photogramm. Remote. Sens.* **2003**, *57*, 241–262. [CrossRef]
64. Smith, M.J.; Clark, C.D. Methods for the visualization of digital elevation models for landform mapping. *Earth Surf. Process. Landf.* **2005**, *30*, 885–900. [CrossRef]
65. Ganas, A.; Athanassiou, E. A comparative study on the production of satellite orthoimagery for geological remote sensing. *Geocarto International* **2000**, *15*, 53–62. [CrossRef]
66. Environmental Systems Resource Institute. *ArcGIS Desktop Sofware, Release 10*; Environmental Systems Resource Institute: Redlands, CA, USA, 2012.
67. Adiri, Z.; El Harti, A.; Jellouli, A.; Lhissou, R.; Maacha, L.; Azmi, M.; Zouhair, M.; Bachaoui, E.M. Comparison of Landsat-8, ASTER and Sentinel 1 satellite remote sensing data in automatic lineaments extraction: A case study of Sidi Flah-Bouskour inlier, Moroccan Anti Atlas. *Adv. Space Res.* **2017**, *60*, 2355–2367. [CrossRef]
68. Thannoun, R.G. Automatic extraction and geospatial analysis of lineaments and their tectonic significance in some areas of Northern Iraq using remote sensing techniques and GIS. *Int. J. Enhanc. Res. Sci. Technol. Eng. Bull.* **2013**, *2*, 1–11.
69. Liang, W.; Li, J.; Xu, X.; Zhang, S.; Zhao, Y. A high-resolution Earth's gravity field model SGG-UGM-2 from GOCE, GRACE, satellite altimetry, and EGM2008. *Engineering* **2020**, *6*, 860–878. [CrossRef]
70. Roest, W.R.; Verhoef, J.; Pilkington, M. Magnetic interpretation using the 3-D analytic signal. *Geophysics* **1992**, *57*, 116–125. [CrossRef]
71. Prasad, K.N.D.; Pham, L.T.; Singh, A.P. Structural mapping of potential field sources using BHG filter. *Geocarto Int.* **2022**, *37*, 11253–11280. [CrossRef]
72. Cordell, L. Gravimetric expression of graben faulting in Santa Fe country and the Espanola basin. In *Guidebook to Santa Fe Country, 30th Field Conference*; New Mexico Geological Survey: Leroy Place Socorro, NM, USA, 1979; pp. 59–64.
73. Ferreira, J.; de Souza, J.; de Bongiolo, A.; de Castro, L.G. Enhancement of the total horizontal gradient of magnetic anomalies using the tilt angle. *Geophysics* **2013**, *78*, J33–J41. [CrossRef]
74. Ibraheem, I.M.; Haggag, M.; Tezkan, B. Edge Detectors as Structural Imaging Tools Using Aeromagnetic Data: A Case Study of Sohag Area, Egypt. *Geosciences* **2019**, *9*, 211. [CrossRef]
75. Cooper, G.; Cowan, D. Enhancing potential field data using filters based on the local phase. *Comput. Geosci.* **2006**, *32*, 1585–1591. [CrossRef]
76. Al-Badani, M.A.; Al-Wathaf, Y.M. Using the aeromagnetic data for mapping the basement depth and contact locations, at southern part of Tihamah region, western Yemen. *Egypt. J. Pet.* **2018**, *27*, 485–495. [CrossRef]
77. Verduzco, B.; Fairhead, J.D.; Green, C.M.; MacKenzie, C. New insights into magnetic derivatives for structural mapping. *Geophysics* **2004**, *23*, 116–119. [CrossRef]
78. Pham, L.T.; Eldosouky, A.M.; Abdelrahman, K.; Fnais, M.S.; Gomez-Ortiz, D.; Khedr, F. Application of the improved parabola-based method in delineating lineaments of subsurface structures: A case study. *J. King Saud Univ.-Sci.* **2021**, *33*, 101585. [CrossRef]
79. Cooper, G.R. Reducing the dependence of the analytic signal amplitude of aeromagnetic data on the source vector directionSignal amplitude of aeromagnetic data. *Geophysics* **2014**, *79*, J55–J60. [CrossRef]
80. Sabins, F.F. Remote sensing for mineral exploration. *Ore Geol. Rev.* **1999**, *14*, 157–183. [CrossRef]
81. Ramadan, T.M.; Sultan, S.A. Integration of geological, remote sensing and geophysical data for the identification of massive sulphide zones at Wadi Allaqi area, South Eastern Desert, Egypt. In Proceedings of the IGARSS 2003. 2003 IEEE International Geoscience and Remote Sensing Symposium. Proceedings (IEEE Cat. No. 03CH37477), Toulouse, France, 21–25 July 2003; pp. 2589–2592.
82. Gabr, S.S.; Diab, H.; Fattah, T.A.A.; Sadek, M.F.; Khalil, K.I.; Youssef, M.A. Aeromagnetic and Landsat-8 data interpretation for structural and hydrothermal alteration mapping along the Central and Southern Eastern Desert boundary, Egypt. *Egypt. J. Remote Sens. Space Sci.* **2021**, *25*, 11–20. [CrossRef]
83. Crosta, A.P. Enhancement of Landsat Thematic Mapper imagery for residual soil mapping in SW Minas Gerais State Brazil, a prospecting case history in greenstone belt terrain. In Proceedings of the 7th ERIM Thematic Conference on Remote Sensing for Exploration Geology, Calgary, AL, Canada, 2–6 October 1989.
84. Osinowo, O.O.; Gomy, A.; Isseini, M. Mapping hydrothermal alteration mineral deposits from Landsat 8 satellite data in Pala, Mayo Kebbi Region, Southwestern Chad. *Sci. Afr.* **2021**, *11*, e00687. [CrossRef]
85. Pour, A.B.; Hashim, M.; Hong, J.K.; Park, Y. Lithological and alteration mineral mapping in poorly exposed lithologies using Landsat-8 and ASTER satellite data: North-eastern Graham Land, Antarctic Peninsula. *Ore Geol. Rev.* **2019**, *108*, 112–133. [CrossRef]
86. Hubbard, B.M.; Thompson, T.J. *Lineament Analysis of Mineral Areas of Interest in Afghanistan: Automatically Delineated Lineaments using 30-m TM Imagery*; US Geological Survey: Reston, VA, USA, 2012; Open-File Report; 28p.
87. Melouah, O.; Eldosouky, A.M.; Ebong, E.D. Crustal architecture, heat transfer modes and geothermal energy potentials of the Algerian Triassic provinces. *Geothermics* **2021**, *96*, 102211. [CrossRef]

88. Pham, L.T.; Oksum, E.; Le, D.V.; Ferreira, F.J.; Le, S.T. Edge detection of potential field sources using the softsign function. *Geocarto Int.* **2022**, *37*, 4255–4268. [CrossRef]
89. Rigol-Sanchez, J.P.; Chica-Olmo, M.; Abarca-Hernandez, F. Artificial neural networks as a tool for mineral potential mapping with GIS. *Int. J. Remote Sens.* **2003**, *24*, 1151–1156. [CrossRef]
90. Woldai, T.; Pistocchi, A.; Master, S. Validation and sensitivity analysis of a mineral potential model using favourability functions. *Monash University Epress* **2006**, *2*, 1. [CrossRef]
91. Alexander, I.; Samuel, O.O.; Esther, C.M. Integrating Landsat-ETM and Aeromagnetic data for enhanced structural interpretation over Naragwata area, North-Central Nigeria. *Int. J. Sci. Eng. Res.* **2015**, *6*, 2229–5518.
92. Irons, J.R.; Dwyer, J.L.; Barsi, J.A. The next Landsat satellite: The Landsat data continuity mission. *Remote Sens. Environ.* **2012**, *122*, 11–21. [CrossRef]
93. Roy, D.P.; Wulder, M.A.; Loveland, T.R.; Woodcock, C.E.; Allen, R.G.; Anderson, M.C.; Helder, D.; Irons, J.R.; Johnson, D.M.; Kennedy, R.; et al. Landsat-8: Science and product vision for terrestrial global change research. *Remote Sens. Environ.* **2014**, *145*, 154–172. [CrossRef]

Disclaimer/Publisher's Note: The statements, opinions and data contained in all publications are solely those of the individual author(s) and contributor(s) and not of MDPI and/or the editor(s). MDPI and/or the editor(s) disclaim responsibility for any injury to people or property resulting from any ideas, methods, instructions or products referred to in the content.

minerals

MDPI

Article

Unconformities and Gold in New Zealand: Potential Analogues for the Archean Witwatersrand of South Africa

Dave Craw [1,*], Neil Phillips [2,3] and Julian Vearncombe [3,4]

[1] Geology Department, University of Otago, Dunedin 9010, New Zealand
[2] School of Geography, Earth and Atmospheric Sciences, University of Melbourne, Melbourne 3145, Australia; neil@phillipsgold.com.au
[3] Department of Earth Sciences, Stellenbosch University, Stellenbosch 7602, South Africa; julian@vearncombe.com
[4] Effective Investments Pty Ltd., South Perth 6951, Australia
* Correspondence: dave.craw@otago.ac.nz

Abstract: Possible young analogues for regionally extensive unconformities (100 to 400 km^2) in the gold-bearing Witwatersrand Supergroup (Archean, South Africa) occur in the South Island of New Zealand. Extensive marine unconformities in New Zealand show progression from an unconformity surface to conglomerate to clean well-sorted sandstone to marine mudstone, as is also found in the major Witwatersrand auriferous reef horizons. The hosting young sedimentary basins of the South Island rest on thin or thick crust on inboard and outboard foreland settings, with variable alluvial gold budgets. They expose the Cretaceous–Oligocene Waipounamu Erosion Surface unconformity that formed when most of New Zealand was subsiding, and Pleistocene–Holocene unconformities related to global sea level changes. The Witwatersrand gold-bearing reef sediments are a good match for such marine transgressions, but not alluvial fans or braided streams. Most Witwatersrand gold is immediately above planar unconformity surfaces and not restricted to, or concentrated in, erosion channels that are incised through the reefs. However, in modern alluvial fans or braided streams, gold is almost entirely in erosion channels on a smaller scale than the Witwatersrand gold reef packages and not spread across the planar unconformities. Alluvial fans and braid plains in New Zealand dilute gold with large volumes of gravel.

Keywords: gold; placer; Archean; unconformity; Cenozoic; marine; fluvial; tectonics

1. Introduction

The Witwatersrand Supergroup is the main component of a ~10-km-thick sedimentary basin with minimal igneous rocks but with Archean greenstone strata above and below [1–3]. Preserved basins of this thickness and composition are rare in the Archean. Within the Supergroup are multiple unconformities and a small number are well documented through deep drilling and mining [4]. These extensive planar surfaces can be 100 to 400 km^2 and are overlain immediately by reef packages of distinctive lithologies, with many containing economic gold. The scale and shape of the unconformities and their associated reef packages provide valuable information on the environment of sedimentary deposition and on possible origins of the mineral components of the reef. The Witwatersrand Supergroup has been deformed [5] and metamorphosed to greenschist facies throughout all its goldfields [6].

New Zealand's South Island, including both its onshore and offshore parts, is well studied by field mapping and geophysics, albeit with economically small placer gold mining. The value of using New Zealand as an analogue for sedimentary processes in the Witwatersrand basin was recognised in the 19th century [7] and extended more recently [8,9]. These authors focused on modern aeolian processes in marginal marine environments. No analogue is perfect, but the study of modern analogues such as New Zealand

provides a useful context in which to examine some features of the Archean Witwatersrand rocks. More specific geological links between New Zealand and the Witwatersrand basin are outlined in Section 2.2 below.

In this study, we present observations from four Cretaceous to Holocene sedimentary basins in New Zealand, all of which have local placer gold accumulations, to evaluate possible younger analogues of tectonic, lithological, sedimentological, and placer accumulation processes that may be relevant to the interpretation of the Witwatersrand gold. Sedimentation in the four New Zealand basins initially developed in the Cretaceous under an extensional tectonic regime, which has evolved to compressional tectonics from the Late Oligocene until the present. Consequently, these basins have a broadly similar geological history to the Witwatersrand basin of early extension, a compressional event, and are inferred to be foreland basins.

Despite the young age of the New Zealand basins, there have been variable amounts of post-depositional authigenic and diagenetic mineralogical alteration of the sediments. Some of these post-depositional processes occurred under low-oxygen geochemical conditions, which may be relevant to the low-oxygen conditions inferred for parts of the Archean Witwatersrand basin. Finally, we use the tectonic, sedimentary, and post-depositional alteration contexts of the New Zealand basins to evaluate the similarities and differences between modern geological processes and inferred processes relevant to gold mineralisation in the Witwatersrand basin. This paper looks at unconformities in general and especially those of the South Island, and the distribution and nature of the unconformities in the Witwatersrand, including their reef packages.

2. Approach and Methods

Our study primarily involves comparisons of relevant aspects of the Archean Witwatersrand Supergroup of South Africa to similar aspects of Cretaceous–modern New Zealand geology, particularly with respect to the nature and origin of unconformities. Hence, we use the published literature for these two contrasting regions and combine these established observations and interpretations in a novel way. To this end, we initially introduce key stratigraphic and structural features of the Witwatersrand Supergroup in general, and then document the similar features of young New Zealand geology. These parallel sets of observations are combined and evaluated in the Discussion section. Throughout the paper, we specifically separate processes of the formation of unconformities from placer gold accumulation processes that can locally accompany unconformity formation.

2.1. Witwatersrand Supergroup Background

As the dominant source of mined gold globally, the Witwatersrand Supergroup (Figures 1 and 2) has been extensively documented during mining, deep drilling, and seismic surveys. The resulting literature on the Witwatersrand gold deposits and the hosting rocks is vast and diverse, and a relevant fraction of this literature has been used in this study as a background context (see reference list). In particular, there have been over a century of publications providing reasons for which the major Witwatersrand reef packages might be marine [2,7,10–12]. However, there is still a strong influence of researchers who favour a non-marine fluvial setting [13–15].

2.2. Southern New Zealand as a Witwatersrand Analogue

The following general features of New Zealand make comparisons to the Witwatersrand a valuable exercise:

- New Zealand is a relatively small fragment of new continental crust (Figure 3a) that is broadly similar in size (~1000 km across) to that inferred for the proto-Kaapvaal craton (Figure 1a);
- The New Zealand crust hosts sedimentary basins (Figure 3) of similar scale (up to 7 km thick) to the Witwatersrand basin;

- The New Zealand sedimentary basins have a similar tectonic history to the West Rand and Central Rand Groups (lower Wits and upper Wits, respectively), with initial extension and subsidence followed by compression and uplift-related sedimentation (Figures 2a and 3; Table 1);
- The Miocene to Holocene history of compression-related sedimentation in New Zealand reflects foreland basins (Figure 3), with a range of features that are relevant to the Central Rand Group, which is also inferred to have been a foreland basin [16];
- The New Zealand sedimentary basins have many diverse unconformities within the sedimentary sequence, allowing comparison to the unconformities that are a key part of the Central Rand Group architecture (Figure 2b);
- Southern New Zealand has widespread primary and placer gold (Figure 3), so that the nature of placer gold deposits in young and active compressional basins can be readily observed;
- Phanerozoic examples are resolvable because of the contrasting marine and non-marine fossils in the various associated sediments.

To illustrate and quantify the key features of placer gold accumulation in the New Zealand context, we summarise extensive previous work on the geological and tectonic contexts of placer deposits in the sedimentary basins of the South Island in Table 1 [9,17–22]. More specific details of the South Island placer deposits in Table 1 and the text and figures herein have also been published previously [23–32].

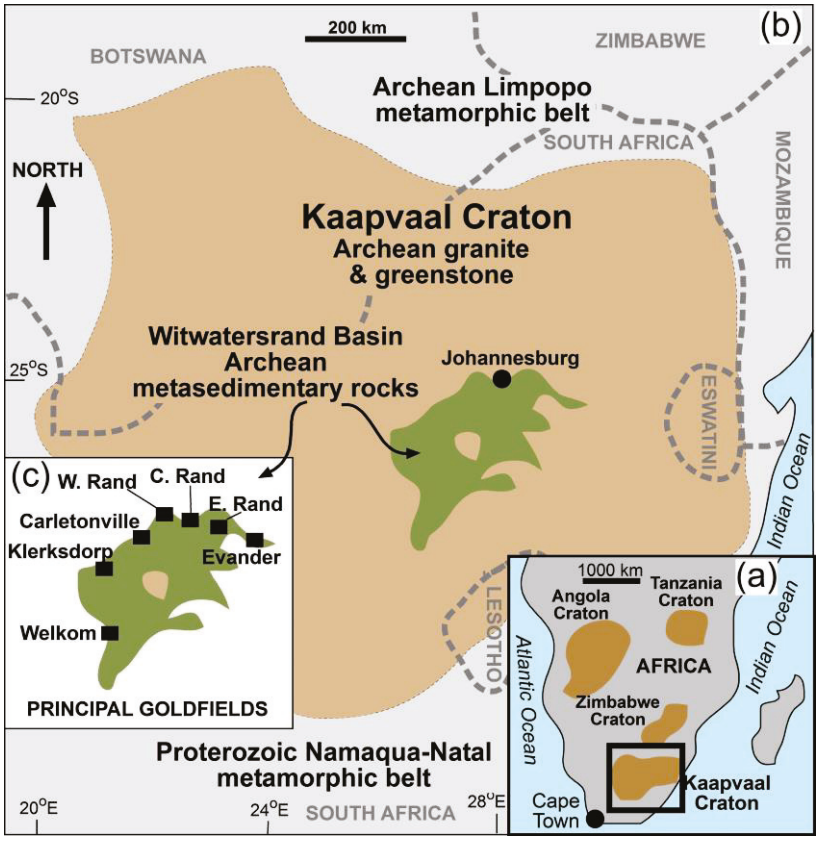


Figure 1. Location and geological setting for the Witwatersrand basin (**a**) in Southern Africa and (**b**) in the Archean Kaapvaal Craton, adapted from [33]. (**c**) Locations of principal goldfields.

Table 1. Summary of key features of New Zealand sedimentary basins relevant to placer gold deposits (references in text). Otago description includes Southland. QPC = quartz pebble conglomerate.

Basin	*Otago*	*Waiau*	*Canterbury*	*Westland*
Style	Foreland complex	Oblique foreland	Foreland	Inboard wedge
Tectonics	Compression	Transpression	Compression	Transpression
Age of foreland sediments	Miocene–Holocene	Miocene–Holocene	Miocene–Holocene	Miocene–Holocene
Crustal thickness	~25 km	~25 km	<20 km	>30 km
Basement rocks	Schist	Greywacke, crystalline	Greywacke	Schist, crystalline
Basement exposure	At and above sea level	Below sea level	Below sea level	At and below sea level
Precursor Cretaceous–Oligocene extensional sediments	Coastal, up to 1 km thick; eroded from inland	Locally >3 km thick	Locally >2 km thick	Mostly eroded; minor remnants
Placer ages	Cretaceous–Holocene	Miocene–Holocene	Modern	Pleistocene–Holocene
Fluvial placers	Abundant; 8 Moz production	Minor production	Negligible; dilution dominates	Common, post-glacial; 7 Moz production
Fluvial placer unconformity control	Basement; syn-sedimentary deformation and erosion	Local basement ribs	Local basement ribs	Local basement exposures; syn-sedimentary deformation and erosion
Beach placers	Rare, negligible production	Abundant; minor production	Negligible production	Common; moderate production
Gold source	Otago; Mesozoic veins in schist	Otago: Miocene veins ± Mesozoic veins	Southern Alps; Plio-Pleistocene veins	Southern Alps; Plio-Pleistocene veins
Placer recycling	Frequent, Cretaceous–Holocene uplift and erosion created QPCs	Common; Pleistocene uplift and erosion	No data	Common; Pleistocene sea-level changes
Age gap, source-to-placer	Wide; 50–110 Ma	Coeval to ~20 Ma	Coeval to ~5 Ma	Coeval to ~5 Ma
Placer hosts	Lithic conglomerates; Cretaceous–Pleistocene QPC	Lithic conglomerates and sands	Lithic conglomerates and sands	Lithic conglomerates and sands
Principal associated heavy minerals	Magnetite, hematite, garnet, zircon	Ilmenite, garnet, zircon, platinum	Zircon, epidote	Ilmenite, garnet, zircon
Gold particle sizes	2 to 0.1 mm flakes; rare cm nuggets	1 mm flakes to 0.1 mm toroids and spheroids	<0.5 mm flakes, incipient toroids	2 to 0.1 mm flakes; rare nuggets
Gold transport direction, Miocene–Holocene	Various; rivers from uplifted ranges across basin complex	SW orogen-parallel rivers; SE longshore drift	SE orogen-oblique rivers	NW orogen-normal rivers; NE longshore drift
Clay alteration in placers	Widespread in basement and sediments, Cretaceous–Pliocene	Localised in Pleistocene sediments and basement	Nil	Nil
Silica cementation associated with placers	Common in QPCs; recycled siliceous cobbles in Cretaceous–Holocene sediments	Nil	Nil	Nil
Authigenic pyrite in placers	Common, Cretaceous–Pliocene; minor detrital sulphides	Localised; Miocene–Pleistocene	Nil	Nil

2.3. Fluvial Channel Terminology

Fluvial channels are important features of non-marine placer gold deposits, and, in this study, we describe two principal types, initially in the context of young sedimentary systems in New Zealand, and then in the Witwatersrand deposits in the Discussion section. We refer to *braid channels* as the channels that carry most of the water and coarse sediment

in an active alluvial fan and downstream braid plain. These channels migrate laterally across a valley, with occasional lateral steps (avulsions). In contrast, *erosion channels* form by incision into the underlying substrate as a result of changing base levels and/or tectonic uplift. The two channel types are related, in that braid channels can evolve into erosion channels and braid channels dominate the wide erosional valley floors that have been incised into older sediments and/or basement rocks. Braid channels typically form with 1–2 m depth, whereas erosion channels can be tens to hundreds of metres in depth as tectonic uplift progresses. In the context of detrital gold accumulation to form non-marine placer deposits, it is the erosion channels that are most important, as they focus on longer-term water flow and the reworking of gold-bearing sediments to remove the finer components (winnowing) [22]. Resultant residual gold concentrations occur, with remnant coarse debris, at the bases of such channels (thalwegs), and these are the principal targets of placer mining [22]. Conversely, while rivers in braid channels can carry detrital gold, this setting generally lacks the repeated reworking of the sediments to concentrate gold, and, commonly, flood events in such channels cause the dilution of the gold with other debris.

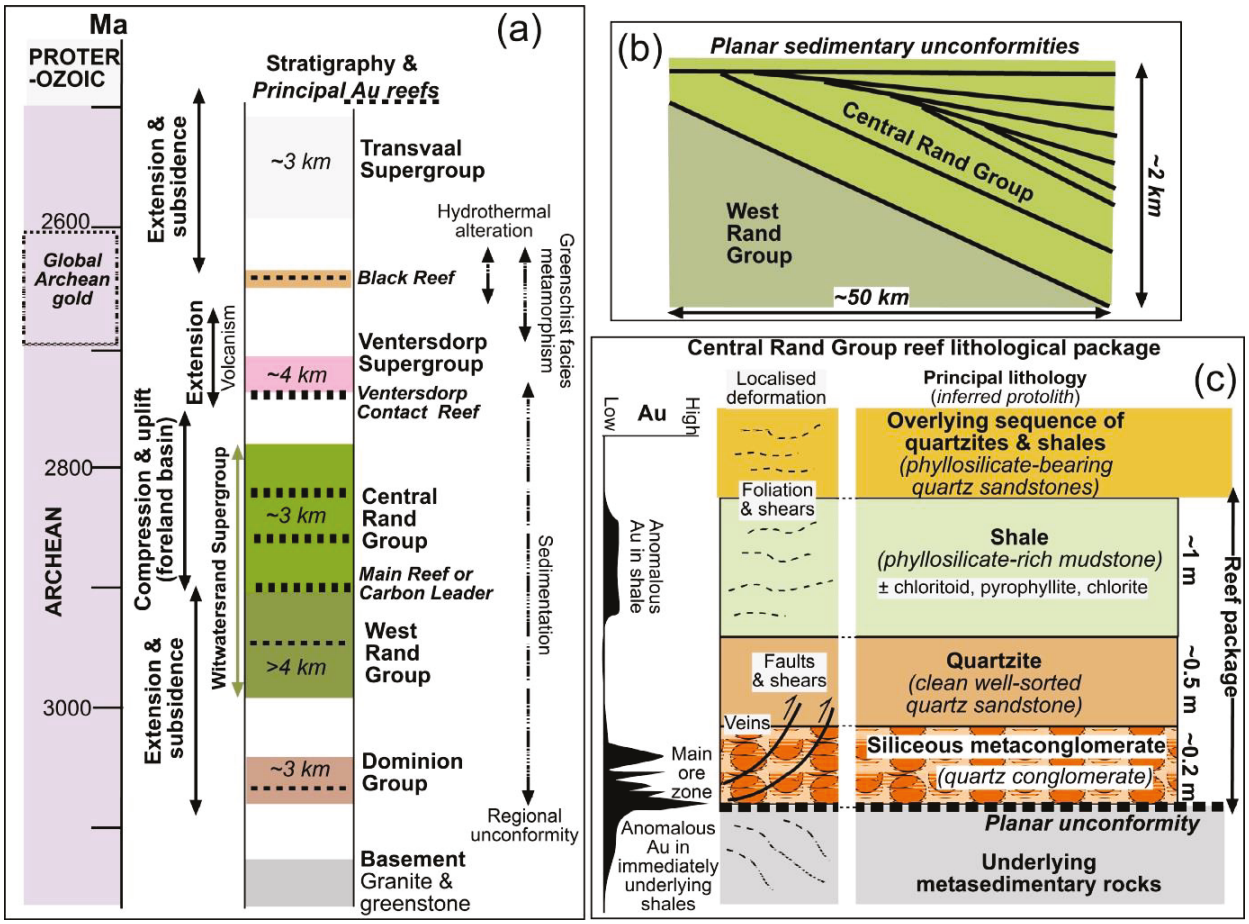


Figure 2. Stratigraphic, structural, and lithological setting of the Witwatersrand basin and the principal features of the unconformities in the sequence. (**a**) Generalised stratigraphic column with inferred tectonic settings through time, summarised from [2,33]. (**b**) Sketch section of numerous unconformities within in a single Central Rand Group goldfield, modified from [34]. (**c**) Principal present and inferred pre-metamorphic rock types at a typical unconformity in the Central Rand Group as in (**a**,**b**), sketched from [2], with generalised gold distribution summarised from [35].

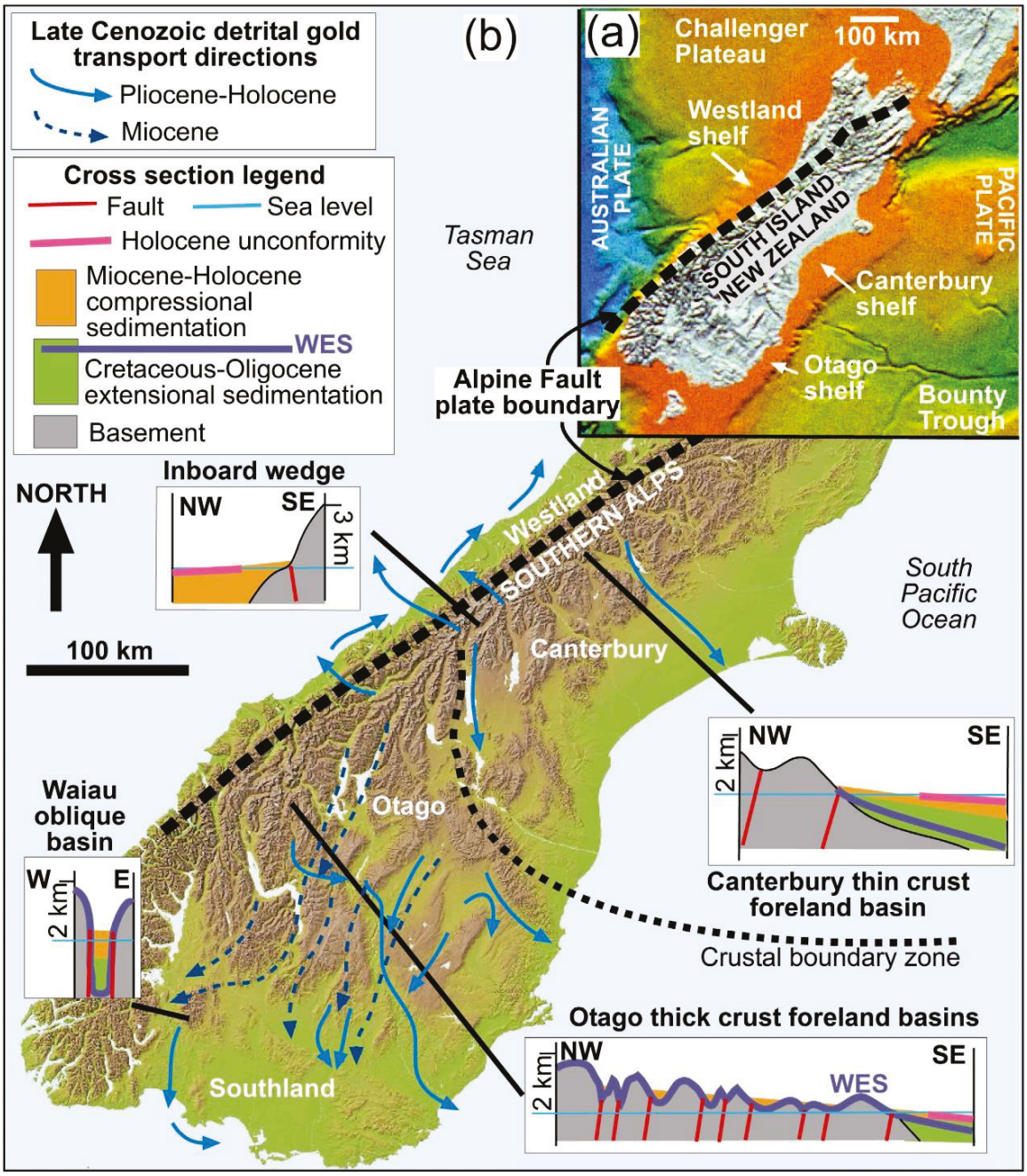


Figure 3. Tectonic setting of Cretaceous–Holocene sedimentary basins in Southern New Zealand. (**a**) Principal onshore and offshore topographic and structural features of the South Island of New Zealand on the Pacific–Australian tectonic plate boundary (DEM modified from niwa.co.nz). (**b**) Surface topography of the southern South Island (DEM modified from geographx.co.nz), with sketch cross-sections through the four principal sedimentary basins described in this paper (Table 1), with separate depositional components related to extensional and compressional tectonics. The two principal marine transgressional unconformities are indicated: WES = Waipounamu Erosion Surface (purple); the Holocene surface is pink. Transport directions of detrital gold are shown over time for Late Cenozoic compressional tectonics.

3. Observations on Archean Witwatersrand, South Africa

3.1. Witwatersrand Structure and Stratigraphy

The Archean Kaapvaal Craton underlies much of South Africa and is known from outcrop, geophysics, drilling, and spatially restricted mining (Figure 1). It comprises

greenstone belts, extensive granitic rocks, and some sedimentary basins that include the Witwatersrand Supergroup [2,3]. The ten-kilometre-thick Witwatersrand Supergroup was deposited on the proto-Kaapvaal Craton. During and after the sedimentary basin on the south side, the proto-Kaapvaal craton grew in the north by terrain accretion with the docking of island arcs at 2980 to 2960 Ma and the subsequent Limpopo Belt collisional orogeny at approximately 2672 to 2620 Ma [36]. The Limpopo collision is coincident with the global Archean gold event (Figure 2a) [37].

The Witwatersrand Supergroup is divided into a lower West Rand Group, dominated by 4 km of fine- to medium-grained clastic metasedimentary rocks, and an upper Central Rand Group of ~3 km of medium- to coarse-grained clastic rocks with minor shale units (Figure 2) [3]. The base of the Witwatersrand Supergroup is dated as younger than 2985 $\pm$ 14 Ma; the boundary between the West Rand Group and Central Rand Group is between 2914 and 2902 Ma, and the top of the Central Rand Group around 2780 Ma [38–40]. Two younger units, the Ventersdorp Contact Reef of ~2780 Ma and the Black Reef of ~2640 Ma, also contain significant gold. All these units precede the end of the global gold event of 2700 to 2600 Ma (Figure 2a) [37], the suggested global oxidation event at approximately 2450 to 2300 Ma [41], and the defined Archean–Proterozoic boundary of 2500 Ma. The significance of these ages is that several of the Archean basins, including the Witwatersrand, were already in place before the major global gold event.

The West Rand Group (lower Witwatersrand) has equal proportions of shelf mudstone and arenite of mainly marine origin. Laterally persistent magnetic shales and banded iron formations occur throughout the West Rand Group as 13 discrete units for over 200 km from Klerksdorp to the South Rand goldfield [42]. Gold and uraninite have been mined from several reefs in the West Rand Group and older Dominion Group rocks but in much smaller quantities than the Central Rand Group. The Central Rand Group (upper Witwatersrand) is almost 3 km thick and dominated by arenite, with thick conglomerate units more abundant towards the top, and an important marker, the 80-m-thick shale unit (Booysens Shale) [33].

The Witwatersrand goldfields are the largest and most productive gold deposits in the world [1]. Gold is present within the Witwatersrand Supergroup, which was initiated as an extensional basin, followed by sedimentation linked to compressional tectonics, which is commonly interpreted to have been a foreland basin [43,44]. Over 90% of the gold is within the upper third of the Witwatersrand Supergroup, closely associated with unconformities. Some of these unconformities are the focus of deformation structures that are temporally coincident with Limpopo tectonics [5,45–47]. On a smaller scale, gold is hosted in 0–2-m-thick reef packages on the unconformity surfaces. Many sedimentary features are still preserved in areas of low strain, but there has been substantial post-depositional structural, textural, and mineralogical alteration, and the sequence has metamorphosed to greenschist facies [6].

There has been controversy over the past 130 years about the origin of the gold, ranging from sedimentary placers, variably modified placers [48,49], and a relatively new syngenetic model [50] to hydrothermal processes akin to those in Archean greenstone gold deposits [33,51–53].

3.2. Unconformities in the Witwatersrand Supergroup

One of the most notable features of the architecture of the Central Rand Group in the Witwatersrand basin is some remarkably extensive planar unconformities that occur in the sequence (Figure 2b). These unconformities are the most thoroughly documented features of the basin because they host most of the economic gold and have been followed across tens of kilometres in mines for more than a century, with hundreds of km linking goldfields [3,4,54]. The planarity of these unconformities can be traced over hundreds of square kilometres within the basin.

Unconformities are common throughout the Witwatersrand Supergroup and vary from those with a discordance of several degrees, and with kms of lost sequence, to many with 0–2 degrees of discordance (Figure 2b) [34], and there are likely some that have

been overlooked where there is sparse drilling. The best-documented unconformities are mineralised in the upper Witwatersrand (where underground access, multiple drill holes, and seismic surveys provide constraints on the geometry of these planes). Underground access is poor in the lower Witwatersrand and the fewer drill holes are supplemented by surface mapping around Johannesburg and Klerksdorp. Towards the basin margin, the unconformities become stacked by repeated tilting during sedimentation, which is a feature of the mined areas [33]. The rock units above and below the unconformities are fully lithified, as expected at greenschist facies [2,33].

A subset of Witwatersrand unconformities has a distinctive 0–2 m overlying sedimentary sequence referred to as a reef package [6,35,55]. There is carbon on the surface of the major reef unconformities as carbon seams, veinlets, or nodules (called flyspeck carbon), and the great economic importance of gold with carbon means that the distribution of the latter has been mapped in detail across many tens of km^2 [2,56] and studied in detail [57]. Conglomerate overlies the carbon seam or unconformity and varies from a single layer of quartz pebbles to thicker single or multiple units of quartz pebble conglomerate. A distinctive quartz arenite is up to tens of cm thick and characterised by its distinctive glassy appearance of round, well-sorted quartz sand that is strongly lithified.

There are two contrasting depictions of reef packages in the literature (outlined above) that reflect different audiences and intent. Most publications and underground tours are designed to show reef packages with conglomerate and mineralisation, without complications of deformation or alteration (e.g., Figure 2c, right side). In contrast, foliated zones, breccias, faults, and dykes are common, and quartz veins are generally more abundant in reef packages compared to surrounding arenites (e.g., Figure 2c, left side). Several mesoscopic underground studies of reef packages document the higher strain in the reef packages compared to the bulk of the surrounding arenites. At a broad scale incorporating the study of many mines, the strain is reflected in reference to slate, phyllite, and crenulated schist for shale units in the heterogeneous reef package spanning various goldfields [6] and the K8, Black Bar, Green Bar, and Khaki shale units [15].

Specific studies at the top of the Witwatersrand Supergroup in the Ventersdorp Contact Reef (VCR) reveal a yellow phyllite in a high-strain zone with quartz veins in altered metabasalt juxtaposed with the VCR—the major reef in the Deelkraal mine [58]. The interface of the upper Witwatersrand and basal Ventersdorp Supergroups has been interpreted as a major rheological contrast exerting control over deformation, fluid flow, and gold distribution. The reef packages, such as the Carbon Leader and Basal Reef, have also been identified as the foci of large-scale alteration involving heterogeneous distributions of pyrophyllite and chloritoid in shales [33,45,47,52,59]. The mineralogical heterogeneity is explained by these authors as being caused by the substantial removal of Si, Fe, Mg, and Ca by fluids well after burial. At the Elandsrand mine, the Ventersdorp Contact Reef at the top of the Witwatersrand Supergroup is highly mineralised on a major angular unconformity but lacks some reef package characteristics. The deformation influences the reef thickness by structural duplication and by thinning. This research has been extended to other parts of the Ventersdorp Contact Reef [47,60]. Similar structural features [61] are also recorded in the Rand goldfields [62–66] and Evander [46], including bedding plane faults, quartz veins, ramps, duplexes, mylonitic schists, and phyllites. Two types of quartz veins are recorded in the reef package, both rheology-controlled: one is layer-parallel and can be hundreds of m in length, and the other is tens of cm in length and perpendicular to layering [2,10]. It is understandable that, in sedimentological studies, the detail of structural complexity is not emphasised, but where there is an absence of any reference to the existing published structural work, many readers are left unaware that deformation structures exist, are common, and are very important.

3.3. Gold and the Witwatersrand Unconformities

Most of the Witwatersrand gold has been mined from a small proportion of the unconformities, with some but not all of those overlain by a reef package. Because of the

mining, these unconformities are well constrained, as are their gold distributions (albeit confidential to the host company) and various mineral components in the conglomerate, arenite, and shale. Major reef horizons are as follows (Figures 1 and 2a) [2]:

- Welkom (Basal Reef);
- Klerksdorp (Vaal Reef, Ventersdorp Contact Reef, VCR);
- Carletonville (Main Reef group, e.g. Carbon Leader, VCR);
- West Rand (Main Reef group, Bird Reefs, Kimberley Reef, VCR);
- Central Rand (Main Reef group, Kimberley Reef);
- East Rand (Main Reef group, Kimberley Reef);
- Evander (Kimberley Reef).

The Main Reef group refers to some closely spaced reef packages near the base of the upper Witwatersrand (Central Rand Group). Minor reefs are on unconformities throughout the whole Witwatersrand Supergroup and there are auriferous conglomerate layers intermittently from the base of the Dominion Group to the Black Reef (Figure 2a). A reef package succession similar to the major Witwatersrand reefs also occurs in the Black Reef [67]. In the conglomerate units, gold is not necessarily confined to the base but may be common near the base, middle sections, or top (Figure 2c) [10,35]. Gold grains from Witwatersrand ores are around 0.01 mm to 0.05 mm, making them mostly invisible underground [45,53]. Coarser gold is rare and, when present, associated with some carbon and with quartz veins.

Within single goldfields, unconformities are several hundred km^2 in area; for example, the unconformity beneath the Ventersdorp Contact Reef is continuous for 450 km^2 [47]. If the currently accepted correlations [3] are correct, then the major unconformity surfaces span multiple goldfields and could be thousands of km^2 in total, although not economically mineralised throughout. Gold mineralisation on the major reefs is remarkably continuous across individual goldfields with semi-continuous stoping for 10 s km.

4. Cretaceous–Holocene Geology of South Island, New Zealand

4.1. Geological Setting

When seeking modern analogues for the Witwatersrand unconformities in the New Zealand setting, there are very few comparable features to choose from. We describe here the only two such features in the southern South Island, and both are of marine origin (Figures 4 and 5). The Waipounamu Erosion Surface formed during the Cretaceous–Oligocene marine transgression, and Pleistocene–Holocene sea level changes have created extensive planar surfaces offshore [18,68].

These surfaces have formed in active and evolving tectonic environments. New Zealand currently lies on the tectonic boundary between the Pacific Plate to the east and the Australian Plate to the west (Figure 3) [18]. The onshore boundary in the South Island, which is the focus of this paper, is the transpressional Alpine Fault (active Oligocene to recent; Figure 3). Compression-driven uplift on the southeastern side of this fault has created the Southern Alps, which has been rising since the inception of the fault zone in the Miocene. The erosion of these mountains, and other subsidiary compressional mountain ranges, provided the Miocene to Holocene sediment for the adjacent sedimentary basins (Figure 3 and Table 1) [17,18].

The mountains and basins are built on continental crust of varying thickness, a legacy of Cretaceous regional extension that initiated extensional sedimentary basins, and these basin sediments lie beneath the younger compressional components (Figure 3 and Table 1). The basement underlying the basins (Table 1) consists of regionally complex Paleozoic–Mesozoic metasedimentary rocks that range in metamorphic grade from prehnite–pumpellyite to amphibolite facies [17,18]. The regional extension of this basement continued into the Oligocene, resulting in the thinning of the Canterbury crust, and the basement rocks remain below sea level in most of the Canterbury foreland basin [18]. In contrast, the thicker crust beneath Otago and Southland has resulted in an emergent basement since the Miocene, and Miocene–Holocene sedimentation has occurred in multiple

small non-marine basins between ridges of older schist and greywacke rocks [25,29]. The narrow Waiau Basin in Western Southland was initiated as an extensional basin but has since undergone compression synchronous with Miocene–Holocene sedimentation [17]. On the west side of the South Island, the Westland inboard rivers flow steeply to the coast, and most sedimentation has occurred as an offshore wedge [18]. Only small, faulted slices of pre-Miocene extensional sediments are preserved locally onshore in Westland.

4.2. Planar Marine Unconformities

The most extensive planar unconformity is the Waipounamu Erosion Surface (WES, Figures 3–5) [68]. The low-relief unconformity surface dominates the presently exposed landscape of most of Otago and the eastern portions of the mountains at the edge of the Canterbury foreland basin, although it has since been disrupted by faulting and folding. This surface developed by marine planation as the sea transgressed across the subsiding landscape of the South Island during the extensional phase of sedimentary basin development (Figure 5a,b). The surface is time-transgressive, with initiation offshore to the east of the present landmass in the Cretaceous, and it evolved inland progressively, culminating in the essentially complete submergence of the land in the Oligocene. The original areal extent of the Waipounamu Erosion Surface was >100,000 km^2, encompassing the whole of the South Island and at least some of the North Island [68]. In the Southern Alps, Miocene to Holocene rapid uplift yielded the so-called "spiky mountain" landscape (Figures 3b and 4d) and facilitated sufficient erosion to remove all traces of the Waipounamu Erosion Surface there.

Remnants of the Waipounamu Erosion Surface are best preserved on the "lumpy" ranges of Central and Eastern Otago (Figure 4) and within remnants of the sedimentary sequences in Otago and Canterbury. The Waipounamu Erosion Surface transgressed over the top of extensional tectonic depressions that hosted fluvial sediments and associated coal-bearing strata, and it planed off intervening basement ridges [68].

The other principal planar unconformity in Southern New Zealand, also of marine origin, is in offshore shelf environments, where it formed during Late Pleistocene–Holocene marine transgression after periods of syn-glacial sea level low stands on both sides of the South Island [69,70]. The uplift of the South Island landmass was, and is, sufficiently rapid to prevent the Holocene marine transgression from encroaching large distances onshore, as the Waipounamu Erosion Surface did. However, the soft coastal sediments in Canterbury and Westland are being eroded rapidly (~1 m/year laterally; Figures 4 and 6) and large parts of the Otago shelf were formed by the planation of soft Miocene sediments (Figures 4c and 5e) [69–71]. Likewise, Cretaceous quartz pebble conglomerates on the Otago coast have been levelled and are still actively planned with landward erosion, contributing to the residual quartz gravel and sand on the Holocene unconformity surface (Figure 7a).

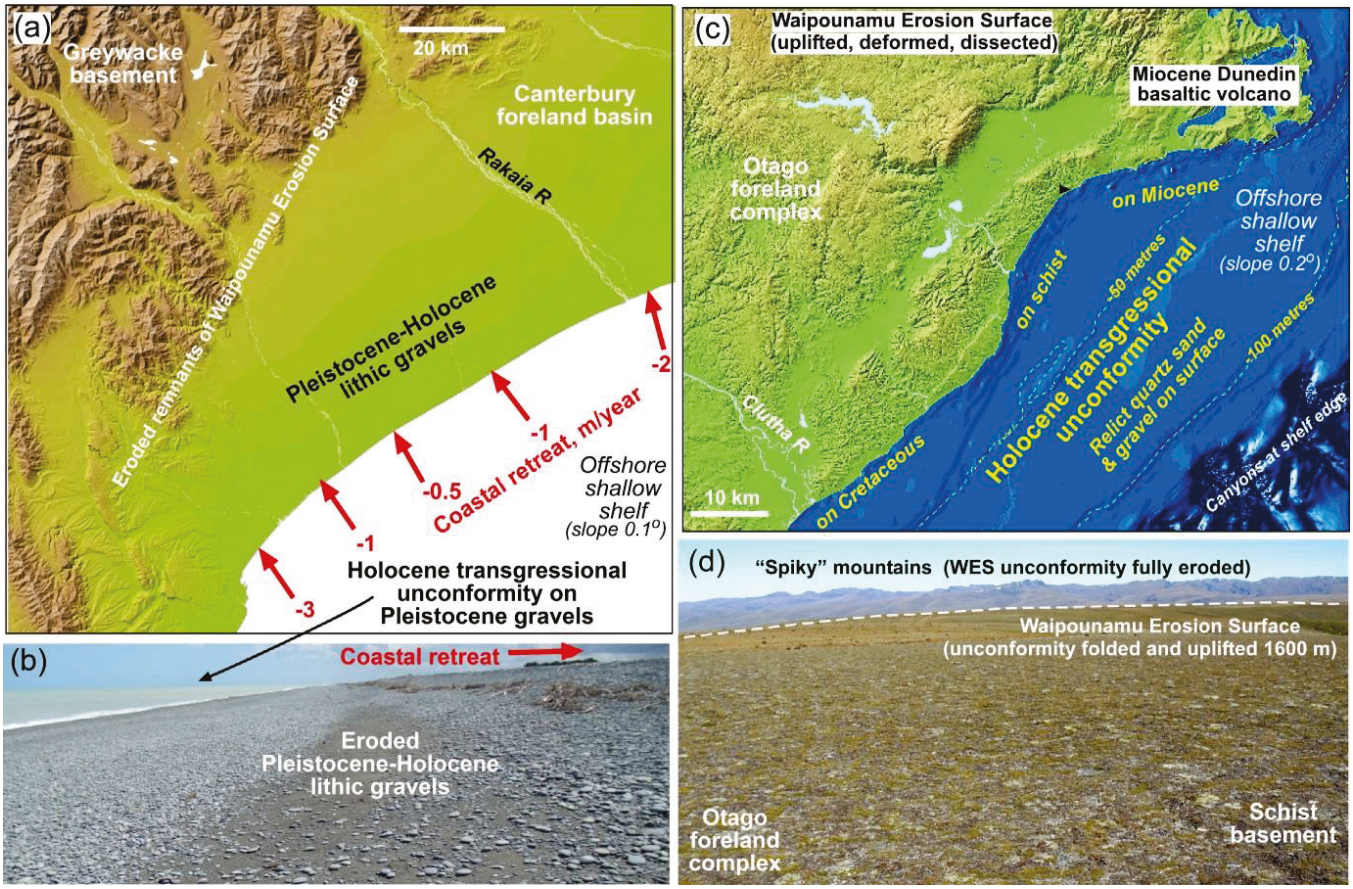


Figure 4. Contrasting appearances of the two principal marine transgressional unconformities on the eastern side of the South Island (Figure 3b). (**a**) Canterbury thin crust foreland basin has the Waipounamu Erosion Surface (WES) mostly below sea level, with uplifted and erosional remnants on the margins of the mountains. The Holocene unconformity is developing via coastal retreat at a rate of metres/year [71]. (**b**) Active Canterbury beach with lithic cobbles and sand derived from inland mountains and recycling of the immediately adjacent Pleistocene gravels that are being eroded during coastal retreat. (**c**) Topography of the Otago offshore shelf and immediate hinterland of the Otago foreland basin complex on thick crust. Low-relief shelf surface formed during Late Pleistocene–Holocene marine transgression, with extensive residual sand and gravel on surface [70]. Onshore land surface is dominated by the originally planar WES (Paleocene–Eocene in this area) that has been deformed and eroded. (**d**) Contrasting mountain range topography of inland Otago, with the Waipounamu Erosion Surface largely preserved (dashed line and foreground) on schist basement as rounded topography, and completely eroded from spiky mountains in the distance (west).

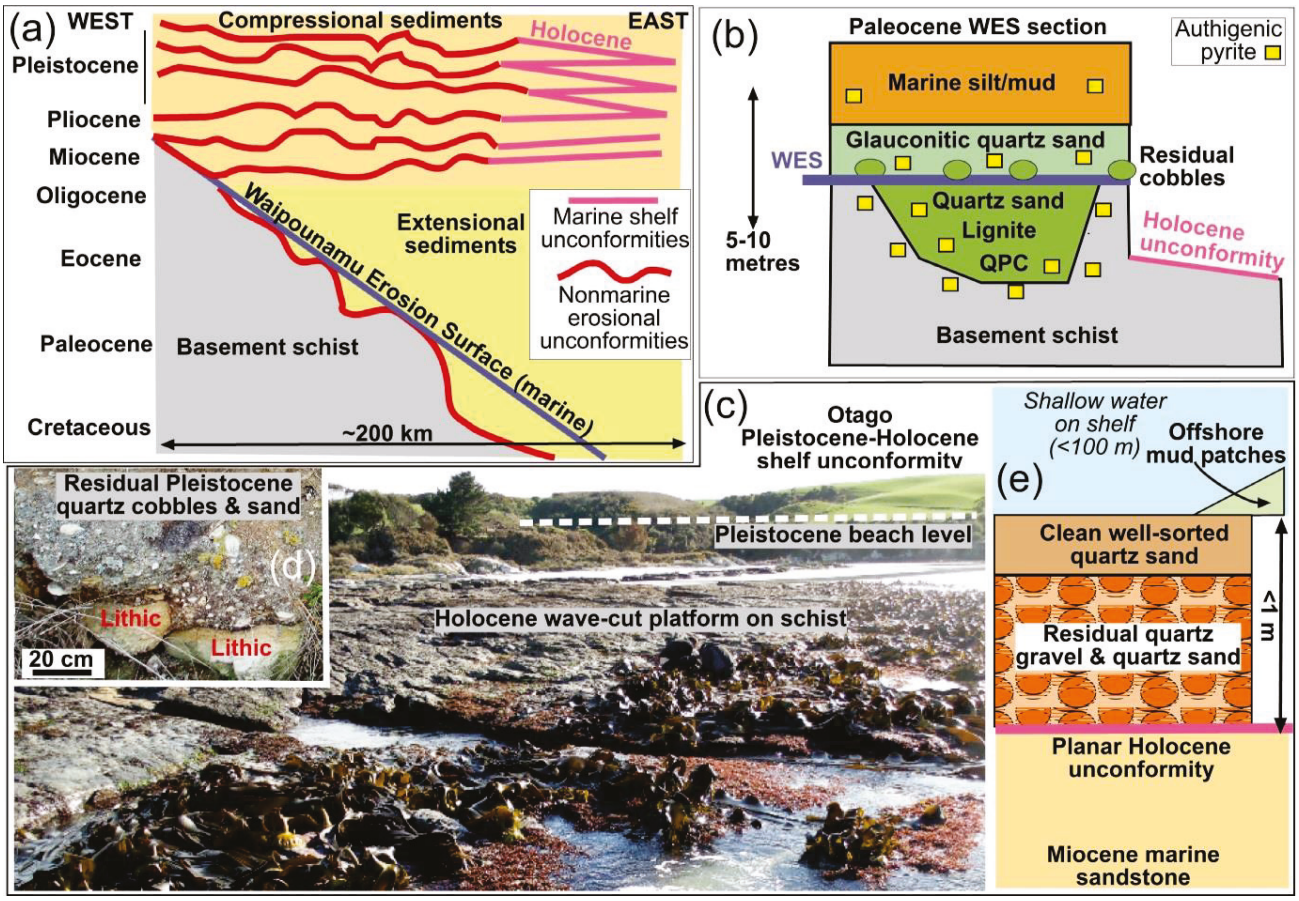


Figure 5. Geometry and lithology of unconformities in the Otago foreland basin complex (Figure 3b). (**a**) Interpretive cross-section (not to scale) comparing generalised unconformities within the sedimentary sequence. Miocene–Holocene onshore unconformity configurations are schematic and indicative of irregular and localised erosion and deposition. (**b**) Sketch section through the Paleocene Waipounamu Erosion Surface (WES) near the onshore east coast, showing principal lithologies. (**c**) Low-tide view of Holocene wave-cut platform incised during sea level rise. A similar Pleistocene beach terrace is indicated in background. (**d**) Residual quartz-rich sediments on schist basement unconformity at a Pleistocene beach terrace. (**e**) Sketch section through residual quartz sediments on the offshore Otago shelf [69].

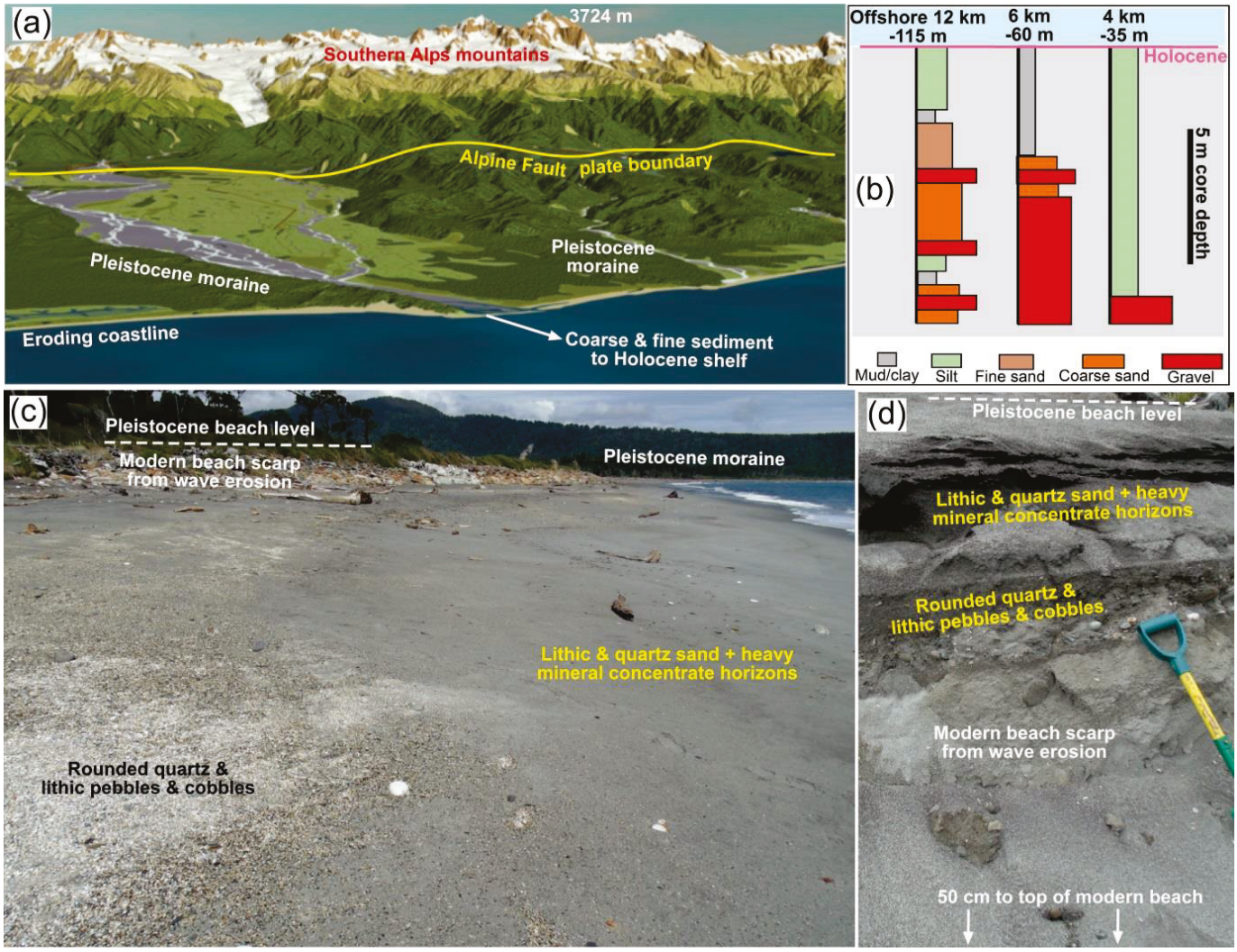


Figure 6. Present topography and sedimentation in the Westland inboard wedge (Figure 3b). (**a**) Oblique digital view of the onshore topography (from geographx.co.nz), showing the steep orogen-normal rivers that transport fresh lithic sediment to the coast and offshore shelf. (**b**) Sketch lithologic sections through the upper ten metres of Late Pleistocene–Holocene sediment on the offshore shelf, immediately below the Holocene transgressional unconformity, summarised from [32]. (**c**) Typical modern Westland beach with erosional scarp formed as the Holocene transgressional unconformity evolves shoreward. Residual lithic sediments have been reworked on the beach. (**d**) Close view of an erosional beach scarp, showing the lithological variations in the higher Pleistocene beach.

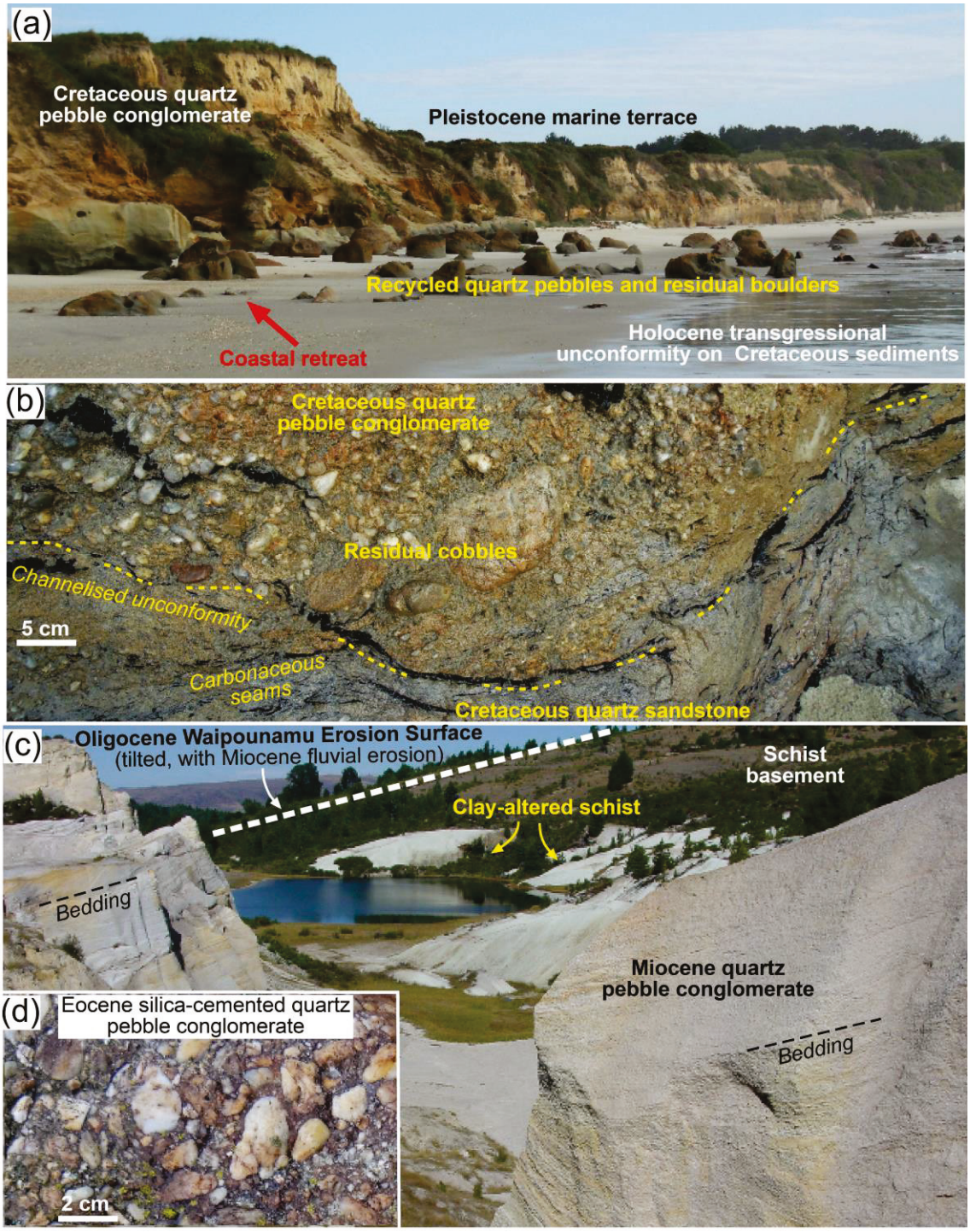


Figure 7. Outcrop features of quartz pebble conglomerates (QPC) in onshore Otago foreland basin complex [25,31]. (**a**) Cretaceous quartz pebble conglomerates coastal exposure that is being eroded and recycled on to the Holocene marine transgressional unconformity. (**b**) An internal unconformity within Cretaceous quartz pebble conglomerates sequence, with relict cobble accumulation. Carbonaceous material has been deformed and locally remobilised in the underlying sandstone. (**c**) Miocene quartz pebble conglomerates in an erosion channel in basement, with most pebbles recycled from Eocene (and ultimately Cretaceous) deposits. The Miocene conglomerate rests on the Waipounamu Erosion Surface schist basement, which has been tilted and dissected and has a groundwater-driven clay alteration zone (white). Exposures were created by placer mining extracting gold from the base of the channel. (**d**) Eocene quartz pebble conglomerates that has been silica-cemented by groundwater immediately above the Eocene Waipounamu Erosion Surface.

4.3. Non-Marine Unconformities

Non-marine unconformities in the South Island sedimentary basins are almost entirely fluvial in origin. They are numerous and widespread throughout all the non-marine parts of the sedimentary basins (Figure 5a). However, unlike the marine unconformities described above, the non-marine unconformities are highly irregular in geometry, are generally localised in scale (1–1000 m laterally), and are fluvial channels with a range of gradients (some very steep) and orientations related to the immediate eroding topography.

The erosion and recycling of pre-existing quartz pebble conglomerate sediments in the Otago sedimentary sequence has led to more rounded and better sorted quartz cobbles, pebbles, and sand, so that channelised unconformities are typically characterised by mature sediments with residual coarse clasts [20]. These processes occur at all scales from the metre scale, as in the internal unconformities in the Cretaceous fluvial sequence (Figure 7b) and in large (>50 m scale) erosion channels formed as the Eocene and Miocene recycling of quartz pebble conglomerates developed renewed deposits on low-relief surfaces in inland Otago (Figures 3 and 7c,d) [25]. Recycled quartz pebble conglomerate deposits formed locally through the Pliocene and Pleistocene on hill slopes in the inland Otago foreland basin.

With the increased uplift and associated steeper relief in the Pliocene and Pleistocene, large alluvial fans developed internal to and at the foot of the rising basement ranges (Figure 8). These fans were deeply channelised, with multiple unconformities on the 10–100 m scale in width and the 1–10 m scale in depth [25,29]. Sediments were dominated by coarse lithic gravels rather than quartz pebble conglomerates, although a minor component of recycled quartz pebble conglomerate debris persisted (Figure 8). The fans grew unconformably over older sediments and basement and extended for tens of km^2, but these underlying unconformities were also channelised (1–50 m scales). The ongoing uplift of mountain ranges also uplifted portions of early formed fans and resulted in the localised recycling of older gravels into younger fans (Figure 8d). New channelised unconformities developed during this process.

The Canterbury foreland basin is distinctly different from Otago in overall architecture, as most of the sediment from rising mountains has been deposited near sea level on a broad area of low relief formed by the coalescence of fluvial braid plains (Figure 9) [16]. To the west of this braid plain, a relatively narrow set of mountain ranges leads steeply back to the main Southern Alps. The broad braid plain has been formed through the Pliocene and Pleistocene by rivers with active gravel-dominated beds that are several kilometres wide, with braid channels that have migrated across the plain and intersected one another at various times. Modern rivers are currently cutting down through older gravels and recycling them but have a similar large-scale braided morphology (Figure 9a) [71]. The braid plain extended farther east during the Pleistocene, but coastal erosion is encroaching, and most sediment now heading offshore is fine-grained material that overlies the Holocene shelf unconformity (Figure 9b). Within the thick pile of lithic gravel that has resulted (Figure 9a–d), there are numerous fluvial unconformities that have formed on the scale of individual river courses: up to 3 km wide and ~100 km long (Figures 4a and 9a). These unconformities are highly channelised internally, with 10–100-m-deep erosion channels, especially near the rising mountain front (Figure 9a,d). Even the most distal portions of the active braid plain are incised up to 10 metres to leave broad-flanking Pleistocene terraces (Figure 9d) [18,71].

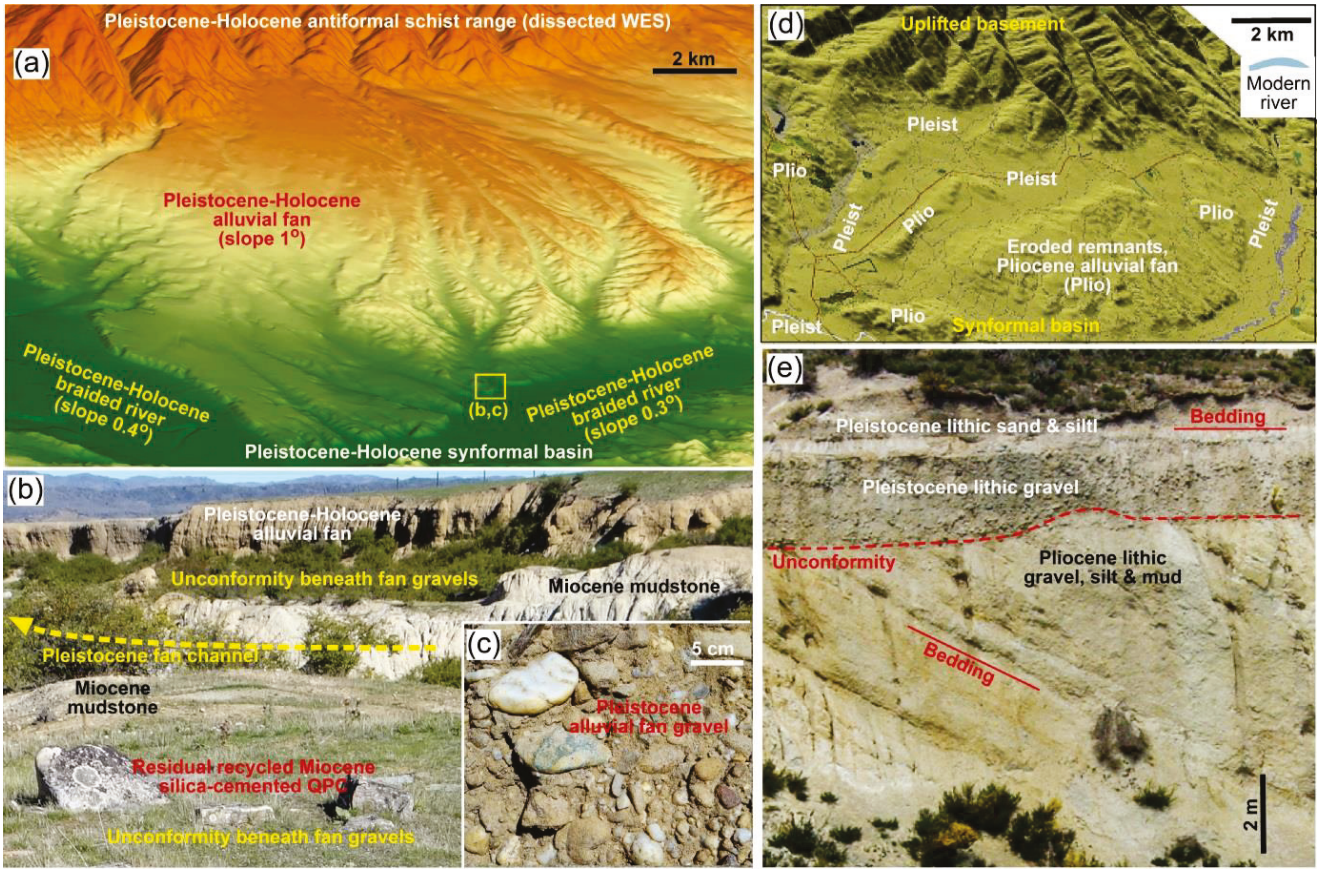


Figure 8. Onshore alluvial fans in the Otago foreland basin complex [25]. (**a**) Oblique digital topography of a large Pleistocene fan emanating from a rising antiformal range (vertical scale exaggerated ×2 for clarity). (**b**) Distal portion of fan in (**a**), showing unconformity between fan gravels and underlying Miocene sediments, exposed by placer gold miners following an erosion channel. Numerous large boulders of silica-cemented Miocene quartz pebble conglomerates litter the exposed unconformity. (**c**) Typical fan gravels in (**a**,**b**), showing abundant lithic sediments (brown) and recycled Miocene quartz pebble conglomerates (white). (**d**) Oblique digital topography of an inland basin margin, showing remnants of a large Pliocene alluvial fan (Plio) that has been eroded and recycled into Pleistocene fluvial deposits (Pleist). (**e**) Unconformity between deformed, tilted and eroded Pliocene distal fan sediments (below; fan as in (**d**)) and Pleistocene lithic sediments (above), in an outcrop exposed by down-cutting of a Holocene river.

At the edge of the mountain front, Pleistocene alluvial fans have spread eastwards to merge with the braid plain (Figure 9). These fans are even more channelised than the braid plains, and the internal unconformities are deeper, narrower, and more irregular than those on the braid plain. Farther inland, small basins and river valleys retain remnants of the Waipounamu Erosion Surface and associated marine sediments, but most of the inland area is underlain by an unaltered but deeply eroded basement where the Waipounamu Erosion Surface has been eroded to leave spiky mountains (Figure 4a) [18,68].

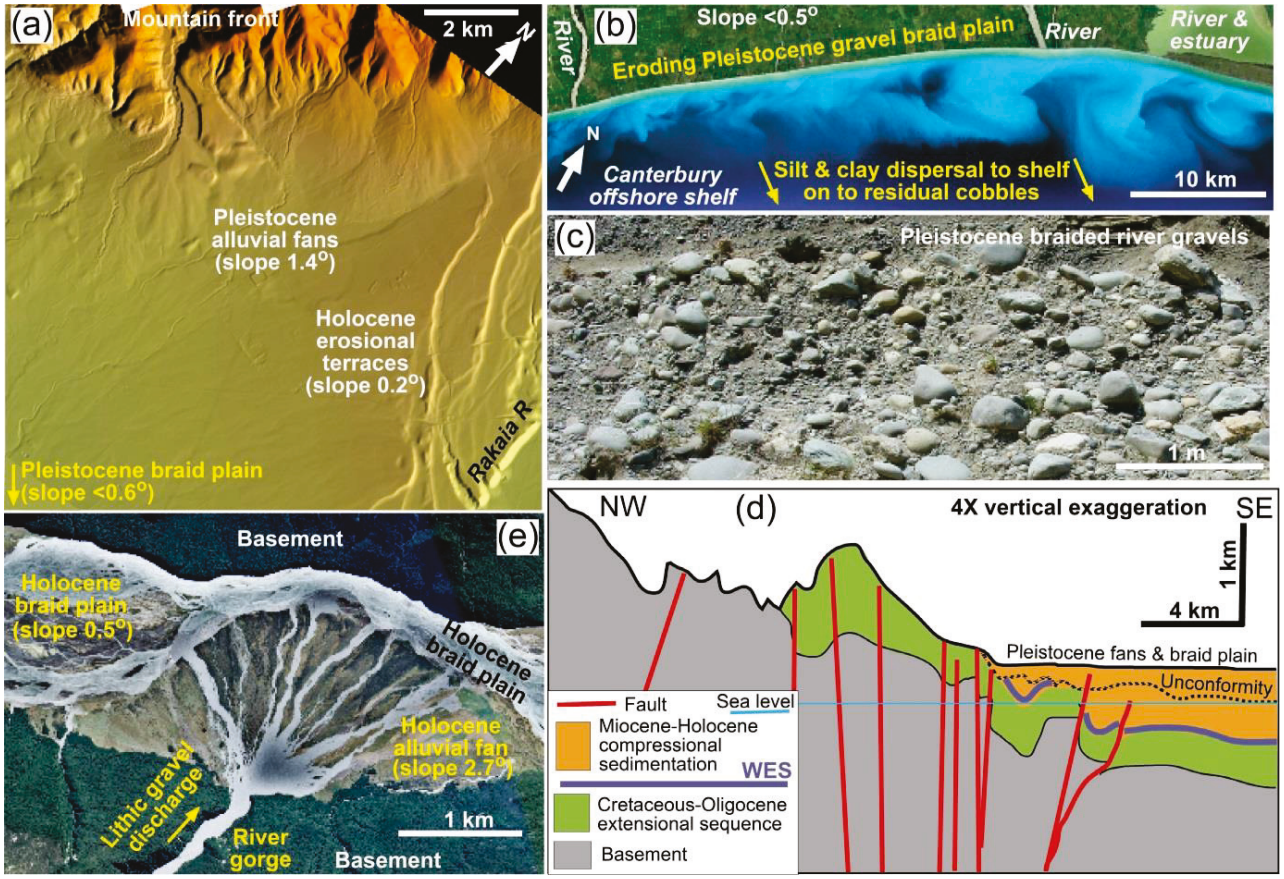


Figure 9. Onshore alluvial fans and associated braid plains in the Canterbury foreland basin. (**a**) Digital topography (exaggerated vertical scale) of the mountain front of the main Canterbury foreland basin, with typical fluvial slope angles of Pleistocene surfaces and terraces of a major Holocene river (right) that has a braid plain on the floor of a broad erosional channel cut >100 m into older gravels. (**b**) Aerial view (from Google Earth) of coastline at foot of the braid plain, with active plumes of fine sediments extending offshore onto the Holocene shelf unconformity that is transgressing coastwards (Figure 3a). (**c**) Typical braid channel gravels, with coarse rounded lithic cobbles in a matrix of lithic sand and silt. (**d**) Sketch cross-section, modified from [18], through the mountain front to the edge of the plains (as in (**b**)), with deformed Pleistocene gravels resting unconformably on deformed older basin sequence. (**e**) Aerial view (from Google Earth) of an active Holocene alluvial fan, with white active braid channels, extending from a steep side-stream into an active braid plain in an axial river in a glaciated inland valley.

4.4. Placer Gold Concentrations in New Zealand

Most placer gold in the South Island has been derived from Cretaceous orogenic (gold only) vein systems in greenschist facies schists [72]. Placer accumulations began during the Cretaceous tectonic extension, when basement ridges that were uplifted on extensional basin margins were eroded, shedding detrital gold into the fluvial system [31]. This gold was accompanied by abundant barren metamorphic quartz vein debris from the basement schist, and rounded quartz pebbles are a major component of the earliest placer deposits. Subsequent tectonic uplift and erosion has caused the recycling of gold and quartz pebbles, the addition of new quartz debris and gold, and ongoing transport and redeposition, numerous times throughout the subsequent history of Otago and Southland [20,25]. The addition of abundant lithic debris from rising mountains, especially from the Pliocene to Holocene, has resulted in the considerable dilution of gold in fluvial systems.

In addition to the gold sources in the Cretaceous Otago schist, auriferous quartz veins were emplaced in the rising Southern Alps, beginning in the Miocene in Otago and contin-

uing through the Pliocene and Pleistocene in the Canterbury–Westland mountains [21,22]. Detrital gold from these sources has contributed to placer accumulations in the Waiau Basin, the Canterbury foreland basin, and the Westland inboard wedge, primarily on beaches [9,21,22].

The all-time placer gold production from South Island sedimentary basins has been ~15 Moz (465 t), with ~8 Moz coming from fluvial placers of the Otago foreland basin complex and 7 Moz coming from the Westland inboard wedge [23]. The Westland placer gold was both fluvial and beach gold. The other major sources of gold are the operating Macraes orogenic (hard rock) mine, with all-time production exceeding 5 Moz from an endowment over 12 Moz [73], and ~3 Moz produced from orogenic deposits in Westland [23].

The onshore fluvial placer gold concentrations are focused in erosion channels within the fluvial sequences, from the Cretaceous to Holocene (Figures 8b and 10). Alluvial fans and downstream rivers that flow on the basement are the most significant sites for placer gold accumulation (Figure 7c, Figure 8a,b and Figure 10). Mining typically focused on the lowest part of the erosion channels (the thalweg), where coarse gravel hosted heavy mineral concentrations with gold (Figure 10a,b), and gold concentrations declined rapidly away from the thalweg both laterally and vertically. Likewise, other heavy minerals were not concentrated at shallower levels within these channels and on the channel margins, and any heavy minerals have been substantially diluted by silicate gravel and sand and/or a silt matrix. This is particularly true in relatively young (Pliocene–Holocene) sediments that are dominated by lithic debris. These essentially barren gravels were removed in mining merely to provide access to the thalweg material below (Figure 10c). Channels were unconformably incised into the underlying basement (Figure 10a,c) or soft sediment (Figures 8b and 10b,d) on scales from centimetres to tens of metres. In low-relief coastal environments, the channels are smaller and shallower, but heavy mineral concentrations are still preferentially found in the thalweg (Figure 10e), even if only a few cm deep (Figure 10f).

In overall gold production, marginal marine settings have been subordinate to the fluvial settings but constitute the most important placer accumulations associated with the Waiau, Westland, and Canterbury basins [9,23,30]. Gold in this setting occurs with other heavy minerals (including garnet, ilmenite) in localised seams (cm scale) on active beaches and in remnants of Pleistocene beaches both onshore and offshore (Figure 6c,d) [8,32]. These heavy mineral concentrates, with and without gold, are widespread at and immediately below the Pleistocene–Holocene offshore shelf unconformities [32,69]. Pleistocene beaches (above present sea level due to tectonic uplift or as high-stand levels) contain gold with heavy mineral concentrates in Westland and on the coast of the Waiau Basin, and these minerals are commonly recycled onto the Holocene unconformity at modern beaches [26,30,74]. Previous work on New Zealand analogues to Witwatersrand [8] has emphasised the importance of marginal marine processes in concentrating detrital gold, especially processes on the New Zealand beaches.

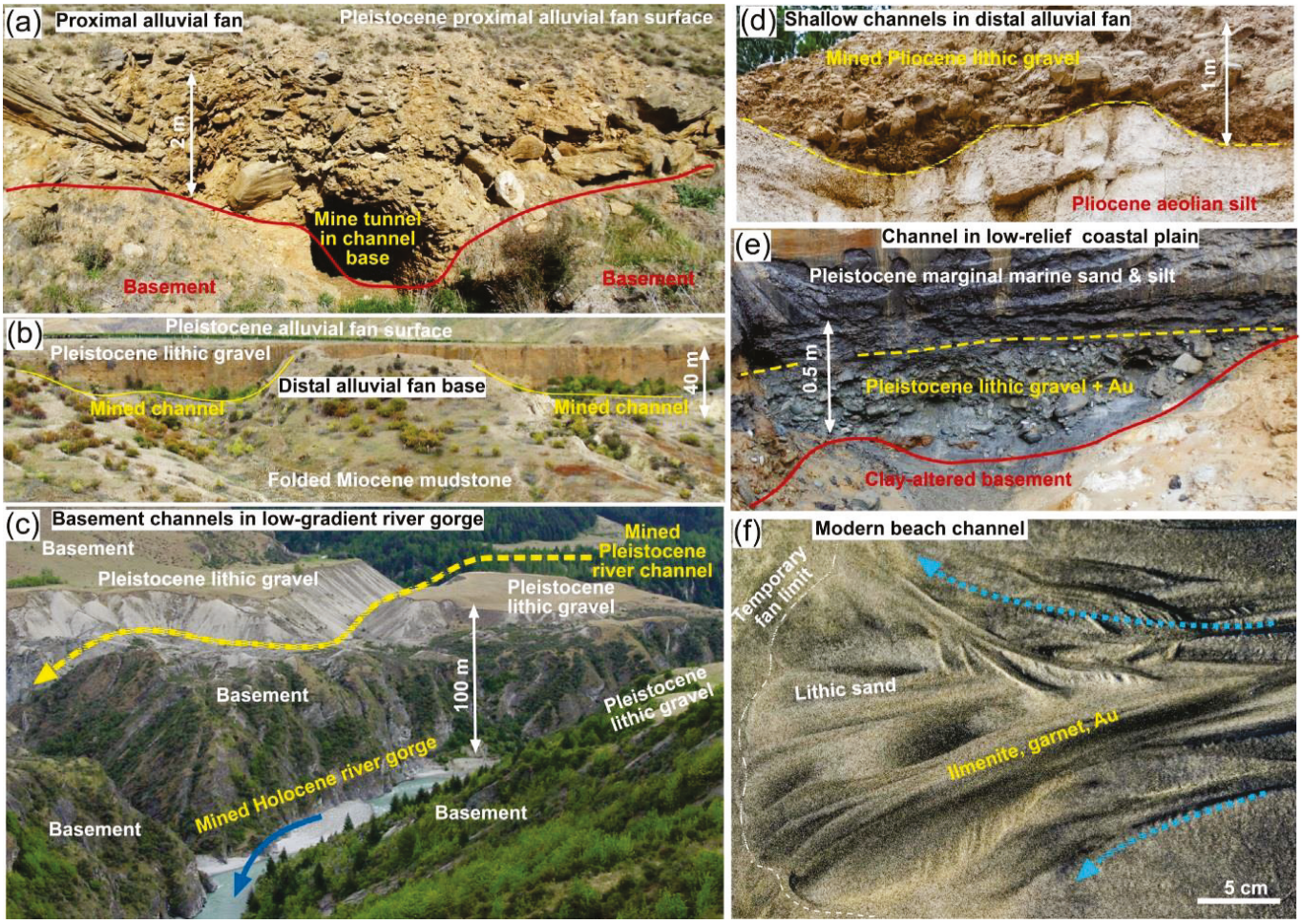


Figure 10. Examples of fluvial channels at unconformities that have been mined for gold in Late Cenozoic sedimentary sequence in the southern South Island. Examples (**a**–**d**) are in inland Otago foreland [22,25,29] and (**e**,**f**) are on the south coast, at the margin of the Waiau basin [30]. (**a**) Poorly sorted angular basement debris has accumulated in a proximal alluvial fan erosion channel, with gold concentration at the metre scale in channel thalweg (at tunnel). (**b**) Large-scale sluicing of distal Pleistocene fan gravels focused on the floors of erosion channels in underlying unconformity. (**c**) Mining in a narrow gorge followed Pleistocene and modern channel floors cut into basement. (**d**) Mine face in a Pliocene distal fan gravel, with gold concentrated with coarsest cobbles in channels eroded into consolidated silt. (**e**) Gravel erosion channel in basement beneath Pleistocene marginal marine sediments contains the only economic gold in a modern mine. (**f**) Small-scale heavy mineral concentrations (black sand with Au) are reworked into braid channels in temporary fans on a daily basis by shallow streams crossing a beach at low tide.

4.5. Mineral Transformations in Young Sediments

Shallow groundwater passage through Cretaceous–Pleistocene non-marine sediments, especially along unconformity zones where more permeable rocks occur, has resulted in post-depositional water–rock interactions that have transformed the minerals in the host rocks. The most prominent and widespread of these processes has affected basement rocks immediately below an unconformity and mineral changes and cementation in sediments immediately above the unconformity [75]. Some of these mineral changes have occurred under oxidising conditions, yielding ferric iron oxyhydroxides from labile iron minerals, but most have occurred under low-redox conditions in which ferrous iron-bearing secondary minerals have been formed. These processes involving shallow groundwater are similar to, and overlap with, the processes that form various components of the regolith in some continental areas [76,77].

The Otago and Southland basement rocks have been extensively altered to white kaolinite and green Fe^{2+}–smectite beneath Cretaceous–Pleistocene sediments on a scale of 1–20 metres (Figures 7c and 10e) [30,75]. Lithic clasts in overlying gravels have been variably converted into the same minerals, resulting in some clay cementation. Quartz pebble conglomerates overlying clay-bearing basement are commonly cemented by silica to form hard quartzite layers, in which the quartz clasts have been dissolved and recrystallised (Figure 7d). Elsewhere, the cementation of quartz pebble conglomerates by pyrite is common (Figure 11a). Most poorly sorted lithic gravel deposits with a lithic sand and silt matrix have developed some clay, leading to cementation, so that they become scarp-forming units (Figure 10a,b,d).

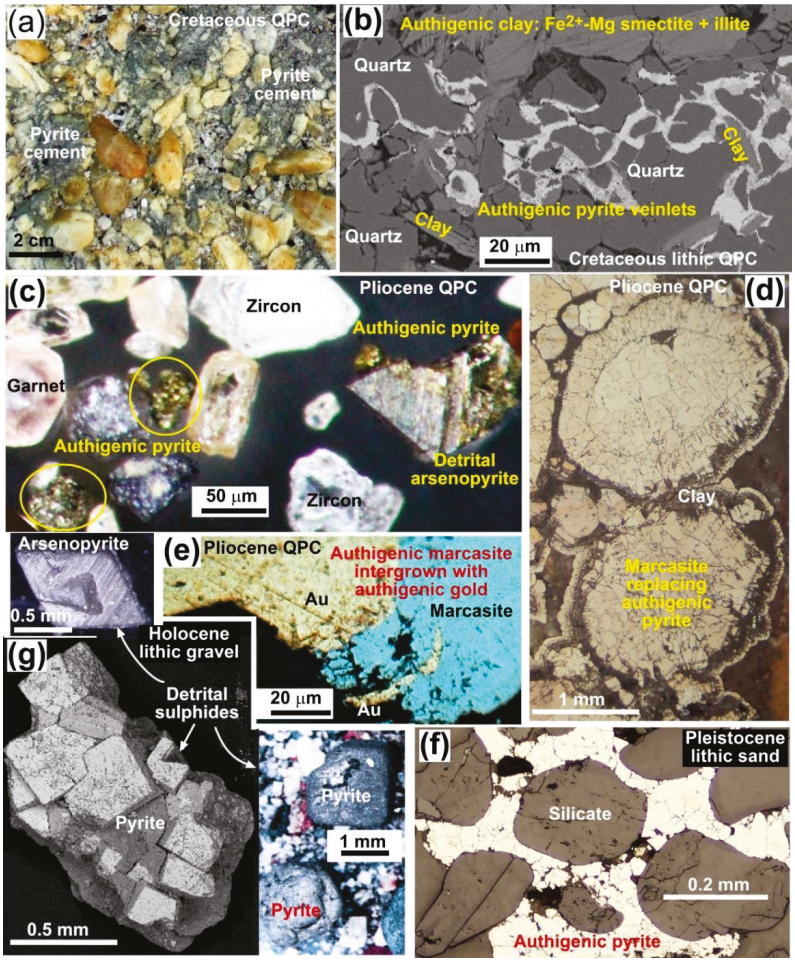


Figure 11. Principal textures of sulphide minerals in Cretaceous–Holocene terrestrial sediments [24,27,30,31] (**a**) Authigenic pyrite cement (grey) in Cretaceous quartz pebble conglomerate (QPC) overlying an internal unconformity on a coal seam. (**b**) Authigenic pyrite veinlets (light grey) form a network through groundwater-altered Cretaceous lithic quartz pebble conglomerates, with associate ferrous iron-bearing authigenic clays. (**c**) Disaggregated Pliocene quartz pebble conglomerates heavy mineral fraction, with fragments of authigenic pyrite and a particle of detrital arsenopyrite. (**d**) Authigenic pyrite grown in interstices of a Pliocene QPC and transformed into authigenic marcasite. Authigenic clay coating has been overgrown by marcasite in places. Polished section with partially crossed polars to enhance internal structure. (**e**) Intergrown authigenic gold and marcasite in Pliocene quartz pebble conglomerates. Marcasite has blue tinge because of carbon coat for electron microscopy. (**f**) Crystalline authigenic pyrite cement in Pleistocene lithic sand. (**g**) Detrital sulphides from Holocene lithic gravel near an exposed orogenic deposit [73,78]: partially rounded arsenopyrite (**top**), coarse angular pyrite (**left**), and rounded pyrite (**lower right**).

Low-redox clay formation is generally accompanied by authigenic pyrite (Figures 5b and 11b), the oxidation of which contributes to cementation by ferric oxyhydroxides. Nodules of crystalline pyrite have grown in sediment interstices authigenically (Figure 11c). The rapid erosion of rocks containing primary and authigenic sulphide minerals can lead to the preservation of detrital sulphides if they are rapidly deposited in water-saturated sediments (Figure 11g), and some detrital sulphides can persist in these sediments for thousands or even millions of years (Figure 11c) [24,78].

Detrital gold is malleable and the irregular primary shapes are rapidly transformed into flat flakes by fluvial pebble collision processes (Figure 12a–c). With ongoing fluvial transport, including recycling events, the flakes become thin and are commonly folded (Figure 12b,c) [27,28,79]. In addition, gold mobility in these same groundwaters has caused substantial shape changes to detrital flakes, producing pure gold overgrowths that are intergrown with authigenic clay (Figure 12d,e). Major shape changes also occur on beaches, where wind-driven sand blasting transforms fluvial flakes into those with a toroidal and spheroidal morphology (Figure 12f,g) [8,26,30].

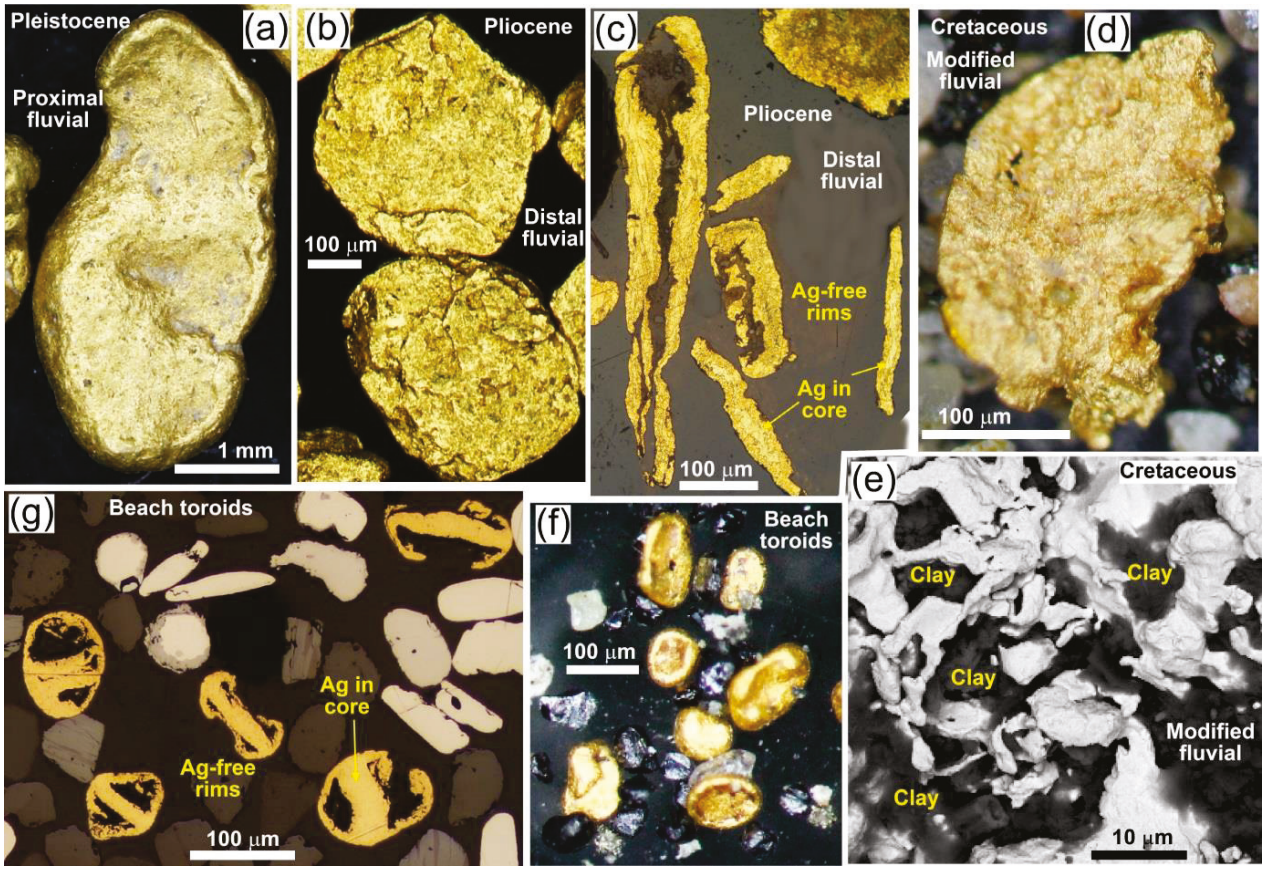


Figure 12. Typical morphological features of detrital gold in the southern South Island: (**a**–**e**) in inland Otago basin complex [27–29,31]; (**f**,**g**) at the margin of the Waiau basin [30]. (**a**) Proximal coarse particle derived from a supergene enrichment zone in Mesozoic schist and recycled through Miocene quartz pebble conglomerates into lithic Pleistocene gravels. (**b**) Distal thin fluvial flakes with folded rims from Pliocene quartz pebble conglomerates, recycled from Miocene quartz pebble conglomerates. (**c**) Sections through distal flakes (etched to show internal structure) that were recycled from Miocene quartz pebble conglomerates into Pleistocene lithic gravels. (**d**) Cretaceous fluvial flake with rough surface formed by authigenic gold remobilisation. (**e**) SEM image of complex plates of authigenic gold (white) that has overgrown authigenic clay on the exterior surface of Cretaceous fluvial gold. (**f**) Toroidal and spheroidal gold formed by sand blasting of fluvial flakes on Pleistocene–Holocene beaches. (**g**) Section through beach gold as in (**f**), accompanied by detrital platinum (white).

5. Discussion

5.1. Marine Transgression Unconformity Surfaces Globally

The New Zealand examples of marine unconformities that we have described are representative of many similar features throughout the Phanerozoic geological record around the world. The Late Pleistocene–Holocene transgressional unconformities on the offshore shelf areas of New Zealand are also found on many, possibly most, shallow marine shelf zones around the world, because of eustatic sea level changes associated with Pleistocene glacial cycles that culminated in a sea level rise from the Last Glacial Maximum. Beringia (Bering Sea between Russia and Alaska) and Doggerland (North Sea) are the most famous examples, for their relevance to human migration immediately before the Holocene transgression and marine unconformity formation. Low-relief continental areas are susceptible to large-scale marine planation, such as Southern Namibia and the Nullarbor Plains of Southern Australia. The latter example is one of the largest such surfaces in the world, with a polygenetic post-Miocene history that includes substantial marine planation in the Pliocene [80], and the offshore extension was last planed during the Holocene marine transgression.

The Phanerozoic examples described above are resolvable because of the contrasting marine and non-marine fossil material in the various associated sediments, as well as via direct observations of the Holocene surfaces. These fossil-based distinctions are not available for the Archean Witwatersrand basin. Instead, the principal evidence for the marine origin of the Witwatersrand unconformities lies in their planar nature and large extent, features that are clearly not associated with non-marine unconformities in New Zealand (Figures 7–9). The large-scale continuity of the overlying sediments in the upward-fining Witwatersrand reef package (Figure 2c) is also suggestive of a marine origin, as non-marine fluvial deposits in tectonic areas are typically discontinuous, as the New Zealand examples suggest. From this perspective, sections throughout New Zealand marine unconformities are broadly similar to a typical Witwatersrand reef package (Figure 2b,c versus Figures 5b and 6b). Based on these observations of both the New Zealand and Witwatersrand unconformities, we deduce that the extensive planar Witwatersrand unconformities that have been exposed by mining had a marine transgressional origin.

Early Witwatersrand workers, without the benefit of modern tectonics or sequence stratigraphy, considered non-marine settings before concluding that a marine origin for the Witwatersrand reefs was more likely [7,10,11,81–86]. There have also been more recent advocates of a marine environment for the Witwatersrand, e.g., [12,52]. Despite the importance of the depositional environment (marine or non-marine), many of these papers are overlooked in subsequent reviews, and a non-marine setting has been tacitly assumed, e.g., [1,15].

5.2. Gold Placers on Marine Unconformities

In New Zealand, the beaches on the western shelf are the most efficient placer-forming environments in the marine setting (Figure 6) [8,32,74,87]. These beach placers, characterised by abundant Fe-Ti oxide accumulations (*black sand*), are also widespread on the offshore Holocene unconformity, in areas up to 50 km wide and hundreds of km long. However, these black sands have undergone reworking by storm waves as they became submerged during the sea level rise. Black sand beach placers in the Westland inboard wedge also contain significant fine-grained (generally <0.5 mm) detrital gold. Despite the delivery of abundant fluvial gold to present and past shorelines, there is only minor gold on the offshore shelf sediments at and immediately above the Holocene unconformity. Typical gold concentrations in this region are less than 0.1 g/t, typical particle sizes are <0.2 mm, and no significant placer concentrations have been identified [32]. Apparently, beach-based concentrations have been at least partially dispersed and diluted by wave reworking as the beaches were submerged during marine transgression.

The other potentially placer-bearing Holocene marine unconformity in New Zealand is on the Otago shelf, offshore of the most productive fluvial deposits of the Otago foreland

basin complex. However, only minor fluvial gold is being transported by the low gradients of the rivers reaching this coast. For example, economic placer mining ceased ~90 km from the coast in the largest river (Clutha River, Figure 4c) [79]. Offshore gold exploration and surface sampling of the residual deposits on the Pleistocene–Holocene shelf (Figures 4c and 5e) have failed to find any significant placer gold concentrations. Instead, any potential heavy mineral concentrations are diluted in the nearshore region with barren sand deposits [69,70].

As with the Holocene marine unconformities, the Waipounamu Erosion Surface is notable for the general lack of placer gold accumulations despite the abundance of fluvial gold in the coeval onshore regions. Some placer gold accumulations developed in marine glauconitic sand immediately above the Waipounamu Erosion Surface, where fluvial braid channels of quartz pebble conglomerate were eroded at the retreating coastline, especially during the Eocene stage of transgression [20]. However, these placers are of only local extent (km scale), and most of the Waipounamu Erosion Surface is defined by barren residual sediments (Figure 5b) [68].

Elsewhere in the world, very few Pleistocene–Holocene marine transgressional unconformities have placer mineral concentrations. The Nome placer gold deposits, in the Bering Sea, are a notable exception [88]. Similarly, offshore Namibia has placer diamond deposits on the Pleistocene–Holocene shelf [89]. A distinctive feature of both examples is that they are on coastlines with low volumes of sediment input from the adjacent landmasses, which would otherwise dilute the heavy mineral suite.

5.3. Fluvial Processes and Placer Gold

The Witwatersrand basin has been postulated as being dominated by fluvial sediments, especially alluvial fans and braid plains [14,15,90], and many studies start with an assumption of the fluvial setting. However, fluvial environments in modern settings, especially foreland basins, are entirely different from the sedimentary record of the Witwatersrand basin, especially with respect to the unconformities that we interpret to be of marine origin (above). Fluvial environments in New Zealand foreland basin settings are characterised by a short (1–10 km) set of alluvial fans emanating from uplifted mountain ridges, and these fans merge downstream into braided rivers (10–100 km scales) that dominate the landscape (Figures 4, 6, 8 and 9). The gradients of most fans are typically low (1–2°; Figures 7a and 8a), although small, steeper fans (up to 3°) can develop locally at the foot of steep mountains, where erosion rates are high (Figure 9e). Farther downstream, braided rivers have even lower gradients (<0.5°; Figures 8 and 9).

The initial liberation of grains of gold from primary sources is limited during erosion at the heads of alluvial fans, and much of the gold remains encapsulated in lithic clasts. However, the recycling of uplifted paleo-placers readily provides gold to the fluvial system, and paleo-placers have been important sources of fluvial gold in the Otago foreland basin complex [20,22,79]. Once the detrital gold has moved to the distal parts of the alluvial fans and into the river system, transport in these low-gradient fluvial environments depends on the formation, folding, re-flattening, and refolding of flakes [26–28,79]. This gold is transported during flood events, along with lithic gravel, and the gold is widely dispersed through the gravel with little or no concentration [22].

Placer gold concentrations are invariably hosted in channels, and gold is best concentrated at or near an erosional unconformity at the base (the thalweg) of each channel (Figures 8 and 10). These unconformities are highly irregular in shape and extent, as they are repeatedly intersected by younger migrating erosional channels at all scales, from metres to tens of kilometres wide and metres to tens of metres deep. The thalwegs became enriched in gold and other heavy minerals as a result of extensive winnowing by repeated flood events, which removed most of the sediment and left only a residue [22]. Before winnowing, the gold is greatly diluted by abundant barren lithic debris. This dilution process is most effectively displayed in the Canterbury foreland basin, where abundant lithic gravels in alluvial fans and braid plains have no significant concentrations

of heavy mineral grains, including gold (Figure 9). The only (minor) gold concentrations occur on a beach near the mouth of the large Rakaia River (Figure 4a), where beach processes have allowed sufficient placer gold concentrations to be mined historically but on a small scale [9].

The relationship between placer gold and erosional fluvial channels on irregular unconformities is a worldwide phenomenon and has attracted mining for centuries [91–93]. We do not find these in the major Witwatersrand occurrences.

5.4. The Schematic Channels Interpreted in Witwatersrand Gold Mines

A significant shortcoming with all the sedimentological interpretations for the major Witwatersrand reefs is distinguishing schematic figures from quality data. The use of smoothed data without data points and lacking structural recordings means that correlations between gold and geology cannot be confirmed. Some maps from the 1970s with confidential gold data [34,94] are reproduced decades later, e.g., [50], with the gold data still confidential, despite the stopes being long closed.

The depiction of the major reefs being composed of linear channels [14,48,50] is difficult to rationalise with the planar orebodies because the planar character is well established by exploration drilling and actual mining. For the older mines of the Central Rand goldfield, a major sediment and gold entry point near Johannesburg is depicted with channels and gold distribution, e.g., [13] and many following publications. However, this interpretation is difficult to confirm without recorded gold grades or reef thickness data to reflect the sedimentology, and an understanding of the structural deformation. In the East Rand goldfield, there is a paucity of gold and sedimentological data due to several of the mines closing some years ago. In a rare example where actual gold grades are available, e.g., [50], the description of gold in channels is not convincing, the overall orebody appears planar, and structural deformation is overlooked. For the Central and East Rand goldfields, we suggest that some of the channels and entry points are derived from the genetic placer model, not solid data. The original entry points and channels [13] were meant to be conceptual and based upon their genetic biases; they have since been accepted as reality over time. The schema should only remain relevant whilst their assumed genetic model (placer) remains viable.

There are considerable sedimentological data for the stoped areas of the Basal Reef that are kilometres in width, and channels are drawn along the middle of higher-grade areas. A qualitative estimate using published maps suggests that most of the gold is between the schematic channels rather than within them [50]. Without recording deformational features, there remain multiple explanations for the measured bed thicknesses, with the original channels being only one possibility. Furthermore, there is no one-to-one relationship between gold and any channel thalweg; in fact, much of the gold appears to have been mined from outside the channel thalwegs. There are problems with the actual data for schematic channels, and these have been discussed previously [52,54]. There are undoubtedly linear channels in the Witwatersrand, but the geometry of the major economic gold distribution is planar and not primarily controlled by these channels.

5.5. Post-Depositional Changes

Onshore and offshore sediments are generally water-saturated after deposition, and observations of the New Zealand basin sediments show that chemical changes occur within the sediments on time scales of millions of years (Figures 8 and 10–12), with only shallow burial (<0.5 km in some cases). The formation of kaolinite in lithic sediments and basement rocks was extensive, especially in non-marine settings. Much of this alteration of sediments occurred under low-redox conditions, resulting in widespread authigenic pyrite deposition in both marine and non-marine sediments (Figures 5b and 11). Likewise, the authigenic formation of Fe^{2+}-bearing phyllosilicates occurred under the prevailing low-redox conditions: smectite in onshore deposits and glauconite in offshore deposits.

These latter mineral transformations involved silica mobility, with the dissolution of quartz clasts and quartz cementation.

In the Witwatersrand, it is difficult to determine the extent of the low-temperature mineral transformations that occurred before the metamorphic overprint. The sedimentary sequence has been metamorphosed to greenschist facies, with synchronous hydrothermal alteration at temperatures from 300 to 400 °C around 3 kbars or ~10 km depth [95]. These moderate-temperature processes induced extensive mineral transformations and lithification. Some of the authigenic processes described for the New Zealand basins are likely to have occurred in the Witwatersrand sequence. Quartz cementation, with the associated dissolution and shape changes of quartz clasts, probably occurred throughout the post-depositional history of the sediments. Quartz mobility is likely to have been especially pronounced in the quartz-rich sediments of the Witwatersrand reef packages, as is seen in New Zealand quartz pebble conglomerates and is pervasive in most Phanerozoic sedimentary sequences [96,97]. Likewise, some of the pyrite in New Zealand was authigenic to the unconformity zone soon after deposition. It is also possible that early formed authigenic pyrite, in non-marine sediments below an unconformity, was recycled as detrital pyrite clasts onto the marine unconformity of a reef package. The low-temperature recrystallisation of the authigenic pyrite occurred with increasing time and burial.

5.6. Critical Comparison: New Zealand Placers with Witwatersrand Gold

The Witwatersrand gold mine geology is distinctly different from the Phanerozoic channelised fluvial examples outlined above. We acknowledge that some erosion channels are present on and near the mined Witwatersrand unconformities, and some of these may be metres to several tens of metres deep and of unspecified width. However, there is little evidence of the significant enrichment of gold in the Witwatersrand thalwegs, even where the channels cut through a gold reef mined along an unconformity. The Witwatersrand unconformities are of primarily marine transgressional origin, albeit locally affected by fluvial channels. However, our observations of New Zealand and other global marine unconformities suggest that placer gold concentrations do not generally occur in offshore shelf environments. Hence, the Witwatersrand gold setting is paradoxical from a placer perspective: it is unlikely to be of fluvial origin because of the general lack of channels constraining the gold, and the gold is unlikely to be of placer origin in the marine transgression settings either.

Marine gold placers are relatively uncommon and account for 1% or less of global gold production. Nome is the largest goldfield in a marine environment, with production around 300 t, but this figure includes small auriferous quartz veins in a hinterland, detrital gold in creeks, gold in the back beach and active modern beach, and gold being dredged for 5 km offshore [88]. Westland NZ is also one of the largest but, as with Nome, much of its total production has come from onshore regions, adjacent to beach and marine accumulations. Neither Nome nor Westland is considered a viable analogue for the Witwatersrand.

6. Summary and Conclusions

Comparison with modern environments and especially the basins of the South Island, New Zealand suggests that the most productive Witwatersrand unconformities reflect marine transgressions. The planar Witwatersrand unconformity surfaces result from planation during marine incursions and are overlain by a reef package of conglomerates, followed by clean sandstone and then shale, reflecting deepening marine water (Figures 2c and 13). These Witwatersrand unconformity surfaces of 10 s to 100 s km^2 are much larger than most of the non-marine fluvial systems of braided rivers and particularly alluvial fans. The unconformities are directly responsible for two critical features that make Witwatersrand gold mineralisation so special: its high tonnage and its exceptional continuity. Globally, non-marine unconformities tend to have irregular geometry with variable gradients and orientation.

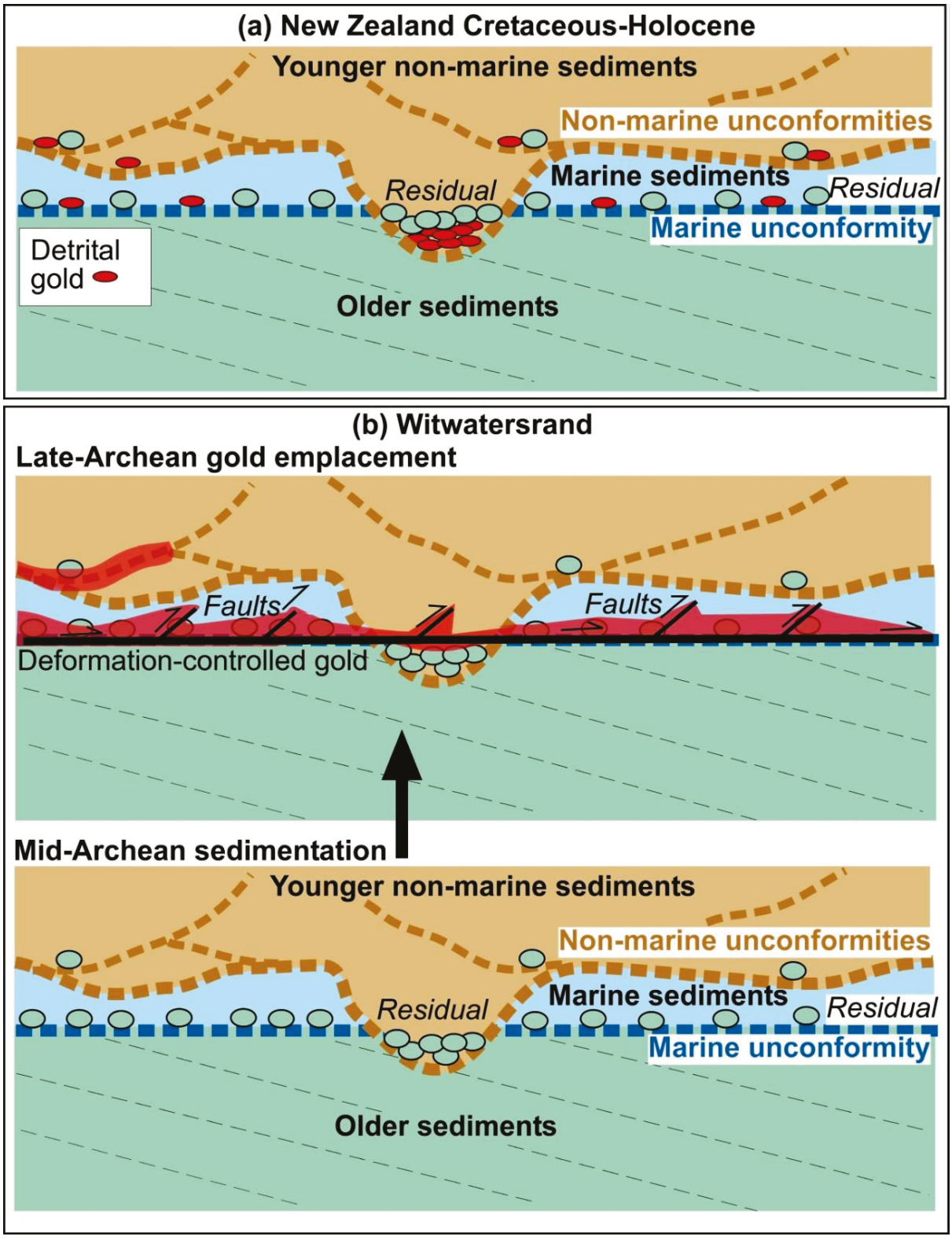


Figure 13. Cartoon summary of the comparisons of unconformity features between (**a**) Southern New Zealand and (**b**) Witwatersrand basin. Planar marine unconformities have residual conglomerates but little or no detrital gold. Non-marine unconformities are not planar, are highly channelised and irregular, and may have detrital gold in their thalwegs. Our conclusions emphasise the marine origin of the mid-Archean planar Witwatersrand unconformities, followed by late Archean hydrothermal gold mineralisation after deformation and metamorphism.

The planar Witwatersrand reefs do not match fluvial systems, which are highly channelised, or the much smaller beach deposits such as Nome Alaska or Westland NZ. Many of the channels and alluvial fan entry points shown on some Witwatersrand goldfield maps are schematic representations of a fluvial placer deposit and the locations of its entry points, fans, and channels in a conceptual model. However, we find little independent evidence for the entry points, and the planar distribution of gold does not match the geometry of the linear channels. In addition, it appears from past records that most gold has been mined from between the inferred channels. In the Witwatersrand, pressure solution has modified textures including pebbles, and the supposed preservation of original gold shapes, ventifacts, and driekanters (e.g., [8]) during greenschist facies metamorphism is speculative at best. The structural complexity has been significantly overlooked in sedimentological studies of Witwatersrand reef packages. Structural and alteration studies favour the gold being hydrothermal and tectonic, explaining the Witwatersrand appearance being unlike modern gold placers (Figure 13).

The world's great Phanerozoic gold placer deposits, predominantly around the Pacific margins, occur close to the bases of erosional channels, where gold grains can settle due to their density and size, and all the less dense rock particles can be removed by the winnowing energy of fluvial systems. However, the gold-rich proximal parts of these fluvial systems are unlikely to be preserved in tectonically active areas. More distal braided river deposits, with their vast amounts of moving sediment at the margins of orogens, are more likely to be preserved, but these systems commonly involve the dilution of gold rather than enrichment. Beach environments concentrate gold where there are local primary sources of auriferous quartz veins but, globally, they are highly subordinate to modern placer gold deposits in fluvial systems.

Author Contributions: Conceptual development: D.C. and N.P.; South African geological components: N.P. and J.V.; New Zealand components: D.C., N.P. and J.V. Manuscript draft: N.P. Manuscript development: D.C., N.P. and J.V. All authors have read and agreed to the published version of the manuscript.

Funding: D.C. was funded by the University of Otago.

Data Availability Statement: All data for this study are available for cited references as summarised in the text, figures, and tables.

Acknowledgments: Useful feedback was provided by Hartwig Frimmel and especially Terence McCarthy on an earlier draft of this manuscript, although they do not necessarily agree with all the conclusions. Stephen Read (University of Otago) crafted the DEM base maps in Figures 4, 8 and 9. Constructive comments from four journal reviewers improved the presentation. We thank the editors for the invitation to be part of this Special Issue.

Conflicts of Interest: The authors declare no conflict of interest.

References

1. Pretorius, D.A. Gold and uranium in quartz-pebble conglomerates. *Econ. Geol.* **1981**, *75*, 117–138.
2. Phillips, G.N.; Law, J.D.M. Witwatersrand goldfields: Geology, genesis and exploration. *SEG Rev.* **2000**, *13*, 439–500.
3. McCarthy, T.S. The Witwatersrand Supergroup. In *The Geology of South Africa*; Johnson, M.R., Anhaeusser, C.R., Thomas, R.J., Eds.; Geological Society of South Africa: Johannesburg, South Africa; Council of Geoscience: Pretoria, South Africa, 2006; pp. 155–186.
4. Winter, H.D.L.R.; Brink, M.C. Chronostratigraphic subdivision of the Witwatersrand Basin based on Western Transvaal composite columns. *S. Afr. J. Geol.* **1991**, *94*, 191–203.
5. Jolley, S.J.; Henderson, I.H.C.; Barnicoat, A.C.; Fox, N.P.C. Thrust-Fracture Network and Hydrothermal Gold Mineralization: Witwatersrand Basin, South Africa. In *Fluid Flow and Mineralization*; Special Publications; Mccaffrey, K.J.W., Lonergan, L., Wilkinson, J.J., Eds.; Geological Society: London, UK, 1999; Volume 155, pp. 153–165.
6. Phillips, G.N. Metamorphism of the Witwatersrand goldfields: Conditions during peak metamorphism. *J. Metamorph. Geol.* **1987**, *5*, 307–322. [CrossRef]
7. Bekker, G.F. *The Witwatersrand Banket, with Notes on Other Gold-Bearing Pudding Stones*; US Government Survey 18th Annual Report; US Government: Washington, DC, USA, 1897; Part V, pp. 153–184.
8. Minter, W.E.L. Irrefutable detrital origin of Witwatersrand gold and evidence of eolian signatures. *Econ. Geol.* **1999**, *94*, 665–670. [CrossRef]

9. Craw, D.; Youngson, J.H.; Leckie, D.A. Transport and concentration of detrital gold in foreland basins. *Ore Geol. Rev.* **2006**, *28*, 417–430. [CrossRef]
10. Graton, L.C. Hydrothermal origin of the Rand gold deposits: Testimony of the conglomerates. *Econ. Geol.* **1930**, *25*, 1–185. [CrossRef]
11. Verrezen, L. The facies technique of using sedimentology in valuation: A case study on the Vaal Reef palaeoplacer. *Geocongress* **1986**, *86*, 487–490.
12. Bailey, A.C.; Law, J.D.M.; Cadle, A.B.; Phillips, G.N. The Zandfontein Quartzite Formation, a marine deposit in the Central Rand Group, Witwatersrand Supergroup. *S. Afr. J. Geol.* **1990**, *93*, 135–146.
13. Brock, B.B.; Pretorius, D.A. Rand Basin Sedimentation and Tectonics. In *The Geology of Some Ore Deposits in Southern Africa*; Haughton, S.H., Ed.; Geological Society South Africa: Johannesburg, South Africa, 1964; pp. 549–599.
14. Minter, W.E.L. Detrital gold, uranium, and pyrite concentrations related to sedimentology in the Precambrian Vaal Reef placer, Witwatersrand, South Africa. *Econ. Geol.* **1976**, *71*, 157–176. [CrossRef]
15. Frimmel, H.E.; Minter, W.E.L. Recent developments concerning the geological history and genesis of the Witwatersrand gold deposits. *S. Afr. Soc. Econ. Geol. Spec. Publ.* **2002**, *9*, 17–45.
16. Catuneanu, O. Flexural partitioning of the Late Archaean Witwatersrand foreland system, South Africa. *Sed. Geol.* **2001**, *141*, 95–112. [CrossRef]
17. Turnbull, I.M.; Allibone, A.H. Geology of the Murihiku Area. In *1:250,000 Geological Map 20*; Institute of Geological & Nuclear Sciences: Lower Hutt, NZ, USA, 2003.
18. Cox, S.C.; Barrell, D.J.A. Geology of the Aoraki Area. In *1:250,000 Geological Map 15*; Institute of Geological & Nuclear Sciences: Lower Hutt, NZ, USA, 2007.
19. Craw, D.; Youngson, J.H.; Koons, P.O. Gold dispersal and placer formation in an active oblique collisional mountain belt, Southern Alps, New Zealand. *Econ. Geol.* **1999**, *94*, 605–614. [CrossRef]
20. Youngson, J.H.; Craw, D.; Falconer, D.M. Evolution of Cretaceous–Cenozoic quartz-pebble conglomerate gold placers during basin formation and inversion, southern New Zealand. *Ore Geol. Rev.* **2006**, *28*, 451–474. [CrossRef]
21. Upton, P.; Craw, D. Coeval emplacement and orogen-parallel transport of gold in oblique convergent orogens. *Tectonophysics* **2016**, *693*, 197–209. [CrossRef]
22. Roy, S.; Upton, P.; Craw, D. Gold in the hills: Patterns of placer gold accumulation under dynamic tectonic and climatic conditions. *Miner. Depos.* **2018**, *53*, 981–995. [CrossRef]
23. Williams, G.J. Economic Geology of New Zealand. *Australas. Inst. Min. Met. Monogr.* **1974**, *4*, 490.
24. Falconer, D.M.; Craw, D. Supergene gold mobility: A textural and geochemical study from gold placers in southern New Zealand. In: Supergene environments, processes and products. *Econ. Geol. Spec. Publ.* **2009**, *14*, 77–93.
25. Craw, D. River drainage reorientation during placer gold accumulation, southern New Zealand. *Miner. Depos.* **2013**, *48*, 841–860. [CrossRef]
26. Craw, D.; Mitchell, M.; McCann, R.; Reay, A. Compositional variations and morphological evolution in platinum beach placers, southern New Zealand. *Miner. Depos.* **2013**, *48*, 81–97. [CrossRef]
27. Craw, D.; Kerr, G.; Reith, F.; Falconer, D. Pleistocene paleodrainage and placer gold redistribution, western Southland, New Zealand. *N. Z. J. Geol. Geophys.* **2015**, *58*, 137–153. [CrossRef]
28. Craw, D.; Kerr, G.; Falconer, D. Mineralogy and provenance of auriferous Waimumu Quartz Gravels, Southland, New Zealand. *N. Z. J. Geol. Geophys.* **2015**, *58*, 281–295. [CrossRef]
29. Craw, D.; Hesson, M.; Kerr, G. Morphological evolution of gold nuggets in proximal sedimentary environments, southern New Zealand. *Ore Geol. Rev.* **2016**, *80*, 784–799. [CrossRef]
30. Craw, D.; Kerr, G. Physical and chemical evolution of a Pleistocene marginal marine gold paleoplacer deposit, southern New Zealand. *Ore Geol. Rev.* **2021**, *138*, 104341. [CrossRef]
31. Kerr, G.; Malloch, K.; Lilly, K.; Craw, D. Diagenetic alteration of a Mesozoic fluvial gold placer deposit, southern New Zealand. *Ore Geol. Rev.* **2017**, *83*, 14–29. [CrossRef]
32. Fraser, N. *Technical Report for Offshore Sampling of PP51979, West Coast*; NZ Petroleum and Minerals, Mineral Report Series MR4761; Seafield Resources Ltd.: Toronto, ON, Canada, 2011; p. 89.
33. Phillips, G.N.; Powell, R. Hydrothermal alteration in the Witwatersrand goldfields. *Ore Geol. Rev.* **2015**, *65*, 245–273. [CrossRef]
34. Minter, W.E.L.; Hill, W.C.N.; Kidger, R.J.; Kingsley, R.J.; Snowden, P.A. The Welkom Gold Field. In *Mineral Deposits of Southern Africa*; Anhaeusser, C.R., Maske, S., Eds.; Geological Society of South Africa: Johannesburg, South Africa, 1986; Volume 1, pp. 497–539.
35. Phillips, G.N. Anomalous gold in Witwatersrand shales. *Econ. Geol.* **1987**, *82*, 2179–2186. [CrossRef]
36. Vearncombe, J.R.; McNaughton, N.J.; Porter, J.; Zi, J.-W.; Talavera, C. Age of the Archaean Murchison belt and mineralisation, South Africa. *S. Afr. J. Geol.* **2021**, *124*, 315–342. [CrossRef]
37. Groves, D.I.; Goldfarb, R.J.; Robert, F.; Hart, C.J.R. Gold deposits in metamorphic belts: Overview of current understanding, outstanding problems, future research, and exploration significance. *Econ. Geol.* **2003**, *98*, 1–29.
38. Armstrong, R.A.; Compston, W.; Retief, E.A.; Williams, I.S.; Welke, H.J. Zircon ion microprobe studies bearing on the age and evolution of the Witwatersrand triad. *Precambrian Res.* **1991**, *53*, 243–266. [CrossRef]

39. Kositcin, N.; Krapěz, B. Relationship between detrital zircon age-spectra and the tectonic evolution of the Late Archaean Witwatersrand Basin, South Africa. *Precambrian Res.* **2004**, *129*, 141–168. [CrossRef]
40. Kositcin, N.; McNaughton, N.J.; Griffin, B.J.; Fletcher, I.R.; Groves, D.I.; Rasmussen, B. Textural and geochemical discrimination between zenotime of different origin in the Archaean Witwatersrand Basin, South Africa. *Geochim. Cosmochim. Acta* **2003**, *67*, 709–731. [CrossRef]
41. Gaucher, C.; Frei, R. The Archean-Proterozoic Boundary and Great Oxidation Event. In *Chemostratigraphy Across Major Chronological Boundaries*; Sial, A.N., Gaucher, C., Ramkumar, M., Ferreira, V.P., Eds.; American Geophys Union Monograph; American Geophysical Union: Washington, DC, USA, 2018; Volume 240, pp. 35–46.
42. Smith, A.J.B.; Beukes, N.J.; Gutzmer, J. The composition and depositional environments of Mesoarchean iron formations of theWest Rand Group of theWitwatersrand Supergroup, South Africa. *Econ. Geol.* **2013**, *108*, 111–134. [CrossRef]
43. Burke, K.; Kidd, W.S.; Kusky, T.M. Archean foreland basin tectonics in the Witwatersrand Basin, South Africa. *Tectonics* **1986**, *5*, 439–456. [CrossRef]
44. Catuneanu, O. Retroarc foreland systems—evolution through time. *J. Afr. Earth Sci.* **2004**, *38*, 225–242. [CrossRef]
45. Barnicoat, A.C.; Henderson, I.H.C.; Knipe, R.J.; Yardley, B.W.D.; Napier, R.W.; Fox, N.P.C.; Kenyon, A.K.; Muntingh, D.J.; Strydom, D.; Winkler, K.S.; et al. Hydrothermal gold mineralization in the Witwatersrand Basin. *Nature* **1997**, *386*, 820–824. [CrossRef]
46. Coward, M.P.; Spencer, R.M.; Spencer, C.E. Development of the Witwatersrand Basin, South Africa. In *Early Precambrian Processes*; Special Publications; Coward, M.P., Ries, A.C., Eds.; Geological Society: London, UK, 1995; Volume 95, pp. 243–269.
47. Jolley, S.J.; Freeman, S.R.; Barnicoat, A.C.; Phillips, G.M.; Knipe, R.J.; Pather, A.; Fox, N.P.C.; Strydom, D.; Birch, M.T.G.; Henderson, I.H.C.; et al. Structural controls on Witwatersrand gold mineralisation. *J. Struct. Geol.* **2004**, *26*, 1067–1086. [CrossRef]
48. Pretorius, D.A. The Geology of the Central Rand Goldfield. In *The Geology of Some Ore Deposits of Southern Africa*; Haughton, S.H., Ed.; Geological Society South Africa: Johannesburg, South Africa, 1964; Volume 1, pp. 63–108.
49. Frimmel, H.E.; Groves, D.I.; Kirk, J.; Ruiz, J.; Chesley, J.; Minter, W.E.L. The formation and preservation of the Witwatersrand goldfields, the World's largest gold province. *Econ. Geol.* **2005**, *100*, 769–797.
50. Frimmel, H.E.; Nwaila, G.T. Geologic evidence of syngenetic gold in the Witwatersrand Goldfields, South Africa. *Econ. Geol. Spec. Publ.* **2020**, *23*, 645–668.
51. Phillips, G.N.; Myers, R.E.; Palmer, J.A. Problems with the placer model for Witwatersrand gold. *Geology* **1987**, *15*, 1027–1030. [CrossRef]
52. Phillips, G.N.; Myers, R.E. The Witwatersrand goldfields. II: An origin for Witwatersrand gold during metamorphism and associated alteration. *Econ. Geol. Monogr.* **1989**, *6*, 598–608.
53. Barnicoat, A.C.; Phillips, G.M.; Law, J.D.M.; Walshe, J.L.; Phillips, G.N.; Fox, N.P.C. Refuting the Irrefutable: A New Look at a Well-Known Sample of Witwatersrand Gold Mineralisation. In Proceedings of the 2001: A Hydrothermal Odyssey Extended Abstracts, Townsville, Australia, 17–19 May 2001; Volume 59, pp. 16–17.
54. Phillips, G.N.; Myers, R.E.; Law, J.D.M.; Bailey, A.C.; Cadle, A.B.; Beneke, S.D.; Giusti, L. The Witwatersrand goldfields. I: Post-depositional history, syn-sedimentary processes, and gold distribution. *Econ. Geol. Monogr.* **1989**, *6*, 585–597.
55. Wiebols, J.H. Note on chloritoid in the Witwatersrand System. *Trans. Geol. Soc. S. Afr.* **1961**, *64*, 85–98.
56. Austin, M.A. Topographic Control of Facies in the Proterozoic Carbon Leader Placer. In Proceedings of the Geocongress '86; Extended Abstracts: An International Earth Science Congress, Johannesburg, South Africa, 7–11 July 1986; Geological Society of South Africa: Johannesburg, South Africa, 1986; pp. 437–440.
57. Parnell, J. Petrographic evidence for emplacement of carbon into Witwatersrand conglomerates under high fluid pressure. *Sed. Res.* **1999**, *69*, 164–170. [CrossRef]
58. Palmer, J.A.; Phillips, G.N.; McCarthy, T.S. Paleosols and their relevance to Precambrian atmospheric composition. *J. Geol.* **1989**, *97*, 77–92. [CrossRef] [PubMed]
59. Phillips, G.N. Widespread fluid infiltration during metamorphism of the Witwatersrand goldfields: Generation of chloritoid and pyrophyllite. *J. Metam. Geol.* **1988**, *6*, 311–332. [CrossRef]
60. Berlenbach, J.W. Aspects of bedding-parallel faulting associated with the Ventersdorp Contact Reef on the Kloof gold mine. *S. Afr. J. Geol.* **1995**, *98*, 335–348.
61. Jolley, S.J.; Stuart, G.W.; Freeman, S.R.; Knipe, R.J.; Kershaw, D.; Mcallister, E.; Barnicoat, A.C.; Tucker, R.F. Progressive evolution of a late orogenic thrust system, from duplex development to extensional reactivation and disruption: Witwatersrand Basin, South Africa. In *Deformation of the Continental Crust: The Legacy of Mike Coward*; Special Publications; Geological Society: London, UK, 2007; Volume 272, pp. 543–569.
62. Greenberg, R. Structure-gold relationships as revealed by some Witwatersrand mine survey plans. *Trans. Inst. Min. Metall.* **1964**, *73*, 1–10.
63. Pitts, P.A. Aspects of Shear Strain in the East Rand Basin. In *Natural Sciences*; Rand Afrikaans University: Johannesburg, South Africa, 1990; p. 145.
64. Mullins, M. Economic Gold Mineralisation in Shear Zones. In *Rand Leases Gold Mine: Other Reefs Symposium*; Extended Abstracts; Geological Society of South Africa: Johannesburg, South Africa, 1989; pp. 85–86.
65. Roering, C.; Smit, C.A. Bedding parallel shear thrusting and quartz vein formation in Witwatersrand quartzite. *J. Struct. Geol.* **1987**, *9*, 419–427. [CrossRef]

66. Coetzee, D.S.; Van Reenen, D.D.; Roering, C. Quartz vein formation, metamorphism, and fluid inclusions associated with thrusting and bedding-parallel shear in Witwatersrand quartzites, South Africa. *S. Afr. J. Geol.* **1995**, *98*, 371–381.
67. Els, B.G. The question of alluvial fans in the auriferous Archaean and Proterozoic successions of South Africa. *S. Afr. J. Geol.* **1998**, *101*, 17–26.
68. Landis, C.A.; Campbell, H.J.; Begg, J.G.; Mildenhall, D.C.; Paterson, A.M.; Trewick, S.A. The Waipounamu erosion surface: Questioning the antiquity of the New Zealand land surface and terrestrial fauna and flora. *Geol. Mag.* **2008**, *145*, 173–197. [CrossRef]
69. Carter, R.M.; Carter, L.; Williams, J.J.; Landis, C.A. Moderm and Relict Sedimentation on the South Otago Continental Shelf, New Zealand. In *New Zealand Oceanographic Institute Memoir*; New Zealand Oceanographic Institute Memoir: Wellington, New Zealand, 1985; Volume 93, p. 43.
70. Carter, L.; Carter, R.M. Holocene evolution of the nearshore sand wedge, South Otago continental shelf, New Zealand. *N. Z. J. Geol. Geophys.* **1986**, *29*, 413–424. [CrossRef]
71. Leckie, D.A. Canterbury Plains, New Zealand: Implications for sequence stratigraphic models. *AAPG Bull.* **1994**, *78*, 1240–1256.
72. Mortensen, J.K.; Craw, D.; MacKenzie, D.J.; Gabites, J.E.; Ullrich, T. Age and origin of orogenic gold mineralisation in the Otago Schist belt, South Island, New Zealand: Constraints from lead isotope and 40Ar/39Ar dating studies. *Econ. Geol.* **2010**, *105*, 777–793. [CrossRef]
73. Craw, D.; MacKenzie, D. Macraes Gold Deposit, New Zealand. In *Springer Briefs in World Mineral Deposits*; Springer: Cham, Switzerland, 2016; p. 130, ISBN 978-3-319-35158-2.
74. Ritchie, T.; Scott, J.; Craw, D. Garnet compositions track longshore migration of beach placers in western New Zealand. *Econ. Geol.* **2019**, *114*, 513–540. [CrossRef]
75. Chamberlain, C.P.; Poage, M.A.; Craw, D.; Reynolds, R.C. Topographic development of the Southern Alps recorded by the isotopic composition of authigenic clay minerals, South Island, New Zealand. *Chem. Geol.* **1999**, *155*, 279–294. [CrossRef]
76. Butt, C.R.M. Genesis of supergene gold deposits in the lateritic regolith of the Yilgarn Block, Western Australia. *Econ. Geol. Monogr.* **1989**, *6*, 460–470.
77. Anand, R.R.; Paine, M. Regolith geology of the Yilgarn craton. *Aust. J. Earth Sci.* **2002**, *49*, 3–162. [CrossRef]
78. Craw, D. Placer gold and associated supergene mineralogy at Macraes Flat, East Otago, New Zealand. *N. Z. J. Geol. Geophys.* **2017**, *60*, 353–367. [CrossRef]
79. Youngson, J.H.; Craw, D. Variation in placer style, morphology and gold particle behaviour down gravel-bed rivers: An example from the Shotover/Arrow-Kawarau-Clutha River system, Otago, New Zealand. *Econ. Geol.* **1999**, *94*, 615–634. [CrossRef]
80. James, N.P.; Bone, Y.; Carter, R.M.; Murray-Wallace, C.V. Origin of the late Neogene Roe Plains and their calcarenite veneer: Implications for sedimentology and tectonics in the Great Australian Bight. *Aust. J. Earth Sci.* **2006**, *53*, 407–419. [CrossRef]
81. Gregory, J.W. The Origin of the Gold in the Rand Banket. *Trans. Geol. Soc. S. Afr. Annex.* **1908**, *17*, 2–41.
82. Young, R.B. *The Banket: A Study of the Auriferous Conglomerates of the Witwatersrand and the Associated Rocks*; Gurney and Jackson: London, UK, 1917; p. 125.
83. Sharpe, J.M. The economic auriferous banket of Upper Witwatersrand Beds and their relationship to sedimentation features. *Geol. Soc. S. Afr. Trans.* **1949**, *52*, 265–300.
84. Brink, M.C. Tektoniese en Stratigrafiese Ontwikkeling van Die Witwatersrand-Supergroep en Verwante Gesteentes in Die Gebied Noord en oos van Klerksdorp. Ph.D Thesis, Randse Afrikaanse University, Johannesburg, South Africa, 1986; p. 330.
85. Verrezen, L. Sedimentology of the Vaal Reef Palaeoplacer in the Western Portion of Vaal Reef Gold Mine. Master's Thesis, Randse Afrikaanse Universiteit, Johannesburg, South Africa, 1987.
86. Cadle, A.; Bailey, A.; Law, J.; Phillips, G.N. How valid is the fluvial model for the Witwatersrand Basin? *Soc. Econ. Paleontol. Mineral.* **1987**, *4*, 11.
87. Christie, A.B. Exploration of Placer Titanomagnetite Iron Sand Deposits Offshore from the West Coast of the North Island. In *Mineral Deposits of New Zealand: Exploration and Research*; Christie, A.B., Ed.; Australasian Institute of Mining and Metallurgy: Carlton, Australia, 2016; Volume 31, pp. 443–450.
88. Sainsbury, C.L. Geology, ore deposits and mineral potential of the Seward Peninsula, Alaska. *US Bur. Mines Open File Rep.* **1975**, *73*, 108.
89. Coetzee, C.B. *Mineral Resources of the Republic of South Africa Handbook 7*; Geological Survey South Africa: Johannesburg, South Africa, 1976; pp. 17–30.
90. Pretorius, D.A. The depositional environment of the Witwatersrand gold fields: A chronologic review of speculations and observations. *Miner. Sci. Eng.* **1975**, *7*, 18–47.
91. Boyle, R.W. The geochemistry of gold and its deposits. *Geol. Surv. Can. Bull.* **1979**, *280*, 579.
92. Hughes, M.J.; Phillips, G.N.; Carey, S.P. Giant placers of the Victorian gold province. *SEG Newsl.* **2004**, *56*, 11–18. [CrossRef]
93. Garnett, R.H.T.; Bassett, N.C. Placer deposits. *Econ. Geol.* **2005**, *100*, 813–843.
94. Minter, W.E.L. A sedimentological synthesis of placer gold, uranium and pyrite concentrations in Proterozoic Witwatersrand sediments. In *Fluvial Sedimentology*; Miall, A.D., Ed.; Canadian Society of Petroleum Geologists: Calgary, AB, Canada, 1978; Volume 5, pp. 801–829.
95. Phillips, G.N.; Zhou, T.; Powell, R. Metamorphic temperature variations among Witwatersrand goldfields: Evidence from the pyrophyllite—chloritoid—chlorite mineral assemblage. *S. Afr. J. Geol.* **1997**, *100*, 393–404.

96. Nenna, F.; Aydin, A. The formation and growth of pressure solution seams in clastic rocks: A field and analytical study. *J. Struct. Geol.* **2011**, *33*, 633–643. [CrossRef]
97. Haile, B.G.; Line, L.H.; Klausen, T.G.; Olaussen, S.; Eide, C.H.; Jahren, J.; Hellevang, H. Quartz overgrowth textures and fluid inclusion thermometry evidence for basin-scale sedimentary recycling: An example from the Mesozoic Barents Sea Basin. *Basin Res.* **2020**, *33*, 1697–1710. [CrossRef]

Disclaimer/Publisher's Note: The statements, opinions and data contained in all publications are solely those of the individual author(s) and contributor(s) and not of MDPI and/or the editor(s). MDPI and/or the editor(s) disclaim responsibility for any injury to people or property resulting from any ideas, methods, instructions or products referred to in the content.

minerals

MDPI

Article

Controls, Expressions, and Discovery Potential of Gold Mineralization in the Central-Eastern Yilgarn Craton, Western Australia: New Insights from an Integrated Targeting Study

Oliver P. Kreuzer [1,2,*], Bijan Roshanravan [3,4], Amanda J. Buckingham [5,6], Daniel P. Core [5], Brian A. Konecke [5,7], Daniel McDwyer [8] and Roger Mustard [8]

[1] Corporate Geoscience Group (CGSG), P.O. Box 5128, Rockingham Beach, WA 6969, Australia
[2] Economic Geology Research Centre (EGRU), College of Science & Engineering, James Cook University, Townsville, QLD 4811, Australia
[3] Department of Mining Engineering, Birjand University of Technology, Birjand P.O. Box 97198-66981, Iran; bijan.roshanravan@gmail.com
[4] Department of Mining Engineering, Faculty of Engineering, University of Birjand, Birjand P.O. Box 97174-34765, Iran
[5] Fathom Geophysics Australia Pty Limited, P.O. Box 1253, Dunsborough, WA 6281, Australia; amanda@fathomgeophysics.com (A.J.B.); dan@fathomgeophysics.com (D.P.C.); brian@fathomgeophysics.com (B.A.K.)
[6] School of Earth and Oceans, The University of Western Australia, 35 Stirling Highway, Perth, WA 6009, Australia
[7] Department of Earth and Environmental Sciences, University of Michigan, 1100 N University Ave, Ann Arbor, MI 48109, USA
[8] St Barbara Limited, P.O. Box 1161, West Perth, WA 6872, Australia
* Correspondence: opkreuzer@gmail.com

Abstract

This paper presents the results of an integrated targeting study covering the central-eastern Archean Yilgarn Craton of Western Australia, a region renowned for its substantial gold endowment (>40 Moz Au). The cornerstones of this study included custom-built geophysical and remote sensing targeting tools, a new lithostructural interpretation of the area, a targeting model based on the mineral systems approach, and a best-practice mineral potential modeling (MPM) workflow employing five complementary modeling techniques. The geophysical targeting tools were used to identify proximity, association, and abundance relationships between gold mineralization and gravity ridges or edges, as well as 95th-percentile K/Th radiometric and remotely sensed goethite–clay–iron feature depth index ratio anomalies. The lithostructural interpretation revealed structural trends oblique or orthogonal to the NNW-SSE-striking greenstone belts, likely representing important structural controls on gold mineralization. Fry analysis, used to assess the spatial distribution of geological point patterns, showed similar directions of maximum gold occurrence alignment. Together, these observations proved to be strong predictors of gold prospectivity in the MPM component of this targeting study. The MPM not only identified most known gold occurrences but also highlighted several underexplored areas with significant potential. The highest-priority MPM targets represent roughly an order-of-magnitude reduction in search space, the hallmark of a well-performing and practically useful targeting methodology.

Keywords: exploration targeting; Fry analysis; gold; mineral potential modeling (MPM); mineral systems; structural controls; Yilgarn Craton

1. Introduction

The central-eastern Yilgarn Craton of Western Australia (Figure 1), the focus of this study, hosts a gold endowment exceeding 40.0 Moz Au [1], mainly contained within eleven orogenic gold deposits or deposit clusters of Archean age. Given this significant endowment, the presence of 78 operating gold mines, and the potential for new discoveries, the area has attracted considerable interest in both gold exploration [2] and gold-related research [3–13].

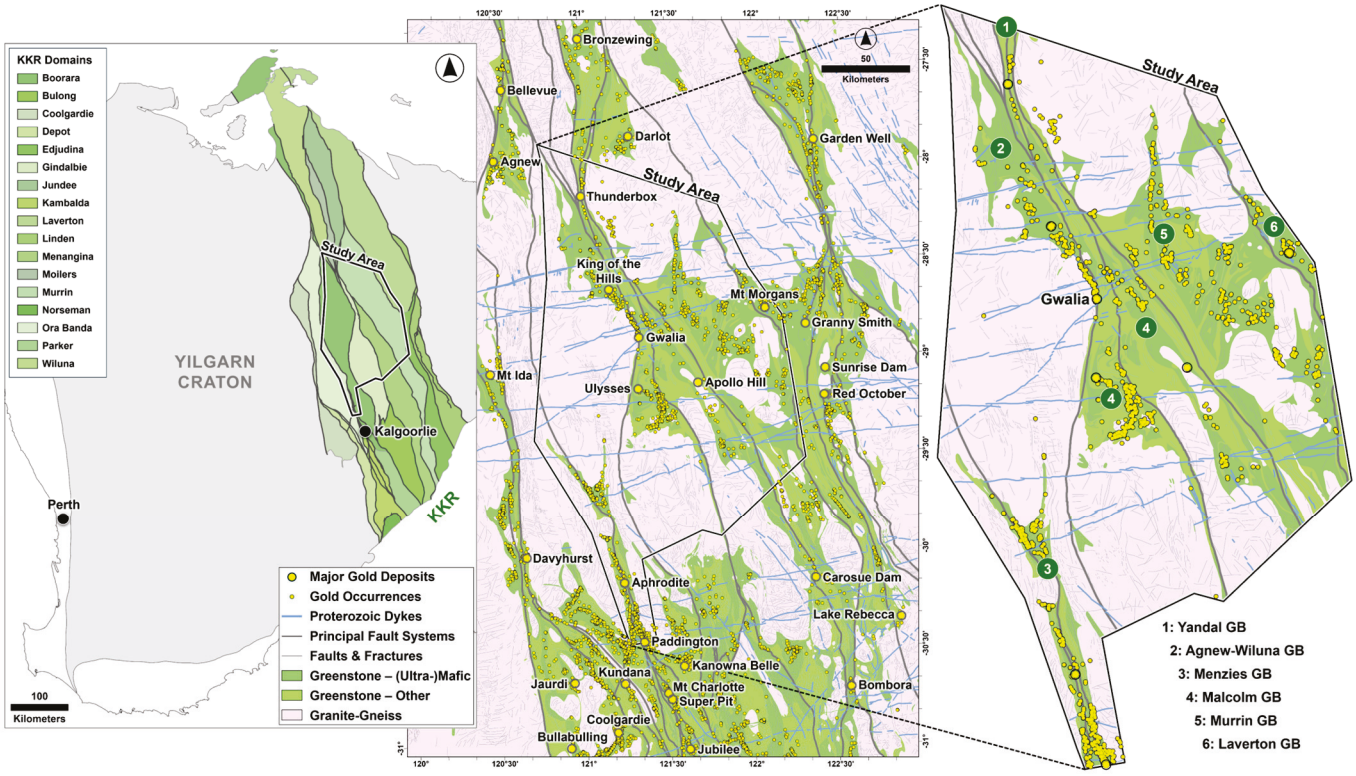


Figure 1. Location of the study area in the central-eastern Yilgarn Craton. A summary of the main gold deposit in the study area is provided in Table 1. Domain boundaries, geology, and gold occurrences are based on data sources listed in Table 2. Key to abbreviations: GB = greenstone belt; KKR = Kalgoorlie–Kurnalpi Rift.

Despite the region's economic importance, published targeting studies for orogenic gold deposits within all or parts of the central-eastern Yilgarn Craton are scarce and largely limited to works of a few authors [14–18]. In 2000, Groves et al. [14] developed a comprehensive conceptual targeting model that informed a knowledge-driven, vectorial fuzzy logic approach [19] to mineral potential modeling (MPM) over an area of ~17,000 km^2 in the southern Kalgoorlie Terrane, an area with minimal spatial overlap with the present study. The model was based on only two input datasets: known gold occurrences and a lithostructural (solid geology) map. The resulting MPM outputs were interpreted to suggest that gold mineralization is controlled by a limited set of critical factors, including proximity to NW-SE-striking granitoid–greenstone contacts, crustal-scale faults (particularly NW-SE-striking fault segments), NW-SE lithological contacts, anticlinal hinges, and chemically reactive host rocks.

In contrast to Groves et al. [14], the 2010 study by Czarnota et al. [15], which covered both the Kalgoorlie and Kurnalpi terranes (~130,000 km^2), benefited from a decade of advances in computing power, significant improvements in geographic information systems (GIS) and MPM, a greatly enhanced understanding of the geology of the Yilgarn Craton and its orogenic gold deposits, and the emergence of the mineral systems concept [20–22]

This framework marked a shift from descriptive, deposit-centric targeting toward a broader, scale-integrated approach focused on the processes of mineral deposit formation and their geodynamic context. Unlike the earlier study by Groves et al. [14], Czarnota et al. [15] developed numerous geological, geochemical, and geophysical predictor maps believed to represent mappable features of orogenic gold systems. However, instead of applying mathematical algorithms (i.e., MPM) to integrate these predictors, the authors used what they described as a "simple additive GIS treatment." This pseudo-MPM approach prevented the use of spatial statistics to assess the validity and performance of both the input predictor maps and the model. Instead, Czarnota et al. [15] defined an arbitrary buffer zone around areas of high gold prospectivity, which they claimed captured 75% of the known gold endowment within 5% of the modeled area. The buffer zone concept was also used to build potential occurrence maps along the Porcupine Fault, Abitibi gold province, Canada [23,24].

The most recent MPM study, by Witt et al. [16], produced gold prospectivity maps for both the Eastern Goldfields Superterrane (EGST; ~235,000 km^2) and the entire Yilgarn Craton (~680,000 km^2). The authors quantified spatial relationships between known gold endowment and a comprehensive set of regional geological, structural, geochemical, and geophysical criteria, from the best of which they generated prospectivity maps using a knowledge-driven fuzzy logic approach [25,26]. According to their spatial statistical analyses, the best regional-scale predictors of gold potential included proximity to mafic granite intrusions, areas of high fault density, regional fault bends, and greenstone belts.

This MPM-assisted targeting study, conducted over an area of ~27,150 km^2, differs from the earlier work in our key ways: (i) it is geophysically driven, using enhanced gravity and magnetic data to map the structural architecture, including cryptic basement features; (ii) it uses enhanced radiometric data and remotely sensed imagery to delineate prospective alteration systems; (iii) it establishes a new, internally consistent lithostructural framework that integrates those datasets into a single solid geology base for MPM; and (iv) it applies and cross-validates five complementary MPM techniques, spanning knowledge-driven, data-driven, and continuous methods. Together, these steps reduced the search space by an order of magnitude and revealed underexplored, gold prospective corridors largely invisible to traditional outcrop-based methods.

2. Geology

2.1. Eastern Goldfields Superterrane (EGST), Yilgarn Craton

2.1.1. Overview

The study area lies within the central-eastern Yilgarn Craton, a largely, poorly exposed Archean (~3730–2660 Ma) crustal block composed of extensive granite–greenstone and high-grade metamorphic gneiss terrains [27] (Figure 1). More specifically, it straddles the boundary between the Kalgoorlie and Kurnalpi terranes, which form part of the ~2960 to 2660 Ma EGST [7,12,28–30], one of the world's most significant and highly endowed Late Archean metallogenic provinces [8]. Each terrane of the EGST (from west to east: Kalgoorlie, Kurnalpi, Burtville, and Yamarna) represents a distinct, structurally bounded entity distinguished by major differences in stratigraphic age as well as the whole rock and isotopic geochemistry of its volcanic and intrusive rocks [28,31]. These terranes are further subdivided into lithostructural domains characterized by internally consistent stratigraphy and structural histories, and bounded by interconnected fault systems interpreted largely from geophysical data [31].

2.1.2. Geology and Structure

The greenstone belts and major fault systems of the EGST generally strike N-S to NNW-SSE. Deep seismic reflection data show that the principal fault systems, traceable in gravity and magnetic data for up to 700 km along strike, are E-dipping, crustal-scale structures that intersect the Mohorovičić discontinuity. The supracrustal volcanic and sedimentary successions defining the greenstone belts are preserved in synformal basins, up to seven kilometers thick, with stratigraphies typically dipping and facing away from granite domes that flank or core the belts [7]. As summarized by [10], greenstone sequences across the EGST display a broadly coherent stratigraphy, typically comprising (from base to top) (i) a basal volcanic package dominated by ~2720 to 2690 Ma komatiite and basalt; (ii) a sedimentary package dominated by ~2690 to 2670 Ma deep marine siliciclastic and volcaniclastic sedimentary rocks; and (iii) a ~2665 to 2655 Ma 'late-basin' fill package of fluvial and deep marine sedimentary rocks, resting unconformably on the older greenstone successions [32,33]. Older (~2960–2770 Ma) greenstone successions, composed mainly of intermediate to felsic and mafic–ultramafic volcanic rocks, have been identified in the Burtville Terrane and show lithological and temporal affinities with the Youanmi Terrane in the western Yilgarn Craton [7].

Granitoids are abundant and widespread throughout the EGST and can be classified into five principal groups [7,8,12,34]: (i) high-Ca granites, the most abundant group (~60% of all EGST granitoids), occur both within and outside greenstone belts. They are typically granite, granodiorite, or trondhjemite, with emplacement ages clustering at ~2800 Ma, 2740 to 2650 Ma, and 2685 to 2655 Ma; (ii) high field strength element (HFSE)-enriched granites represent 5 to 10% of Yilgarn granites, typically granite or granodiorite, occurring mostly internal or marginal to greenstone belts. Emplacement ages cluster at >2720 to 2665 Ma and 2700 to 2680 Ma; (iii) mafic granites also comprise 5 to 10% of Yilgarn granites. This group includes granite, granodiorite, tonalite, trondhjemite, and diorite, occurring mainly internal or marginal to greenstone belts. They are commonly spatially associated with gold mineralization, with emplacement ages between >2720 and 2650 Ma, though younger examples likely exist; (iv) low-Ca granites, the second most abundant group (~20%), occur mainly external to greenstone belts. They are typically granitic or granodioritic, emplaced between 2655 and 2630 Ma, and are interpreted as products of partial melting of high-Ca granite source rocks; and (v) syenitic granites, the least abundant group (<5%), are typically internal or marginal to greenstone belts. They are syenite or quartz syenite in composition, spatially associated with gold mineralization, and emplaced at 2650 Ma, and 2655 to 2645 Ma.

2.1.3. Deformation History

According to [7], poor rock exposure and strain partitioning make it difficult to correlate structural information across the EGST. Consequently, its structural evolution remains poorly constrained and the subject of ongoing debate. To address these challenges, Blewett et al. [7] conducted an integrated structural framework study combining over 10,000 new structural measurements with stratigraphic, magmatic, metallogenic, and geophysical data. Based on this synthesis, the authors proposed a six-stage (D_1–D_6) deformation history (Figure 2):

- D_1 (~2720–2670 Ma): ENE-WSW-directed extension marked by rifting and greenstone deposition.
- D_2 (~2670–2665 Ma): ENE-WSW-directed shortening associated with cessation of volcanism, development of NNW-SSE-trending upright folds, and N-S-to NE-SW-striking dextral strike–slip and reverse faults.

- D_3 (~2665–2655 Ma): NE-SW-directed extension and extensional doming involving deep crustal exhumation and formation of late basins that record the first deposition of granite detritus in the EGST.
- D_{4a} (~2655–2650 Ma): ENE-WSW-directed shortening resulting in tightening of earlier folds, WSW-directed thrusting along NNW-SSW-striking faults, and generation of NNW-SSE-trending upright folds and reverse faults.
- D_{4b} (~2655–2650 Ma): WNW-ESE-directed shortening characterized by reactivation and sinistral transpression along earlier NNW-SSE-striking faults and generation of ENE-WSW-striking thrust faults recording NW and SE transport.
- D_5 (~2650–2635 Ma): NE-SW-directed shortening marked by dextral strike–slip movement along N-S- to NNE-SSW-striking faults and thrusting along NNW-SSE- to NW-SE-striking faults.
- D_6 (<2630 Ma): Low-strain vertical shortening and horizontal extension marked by crenulation development.

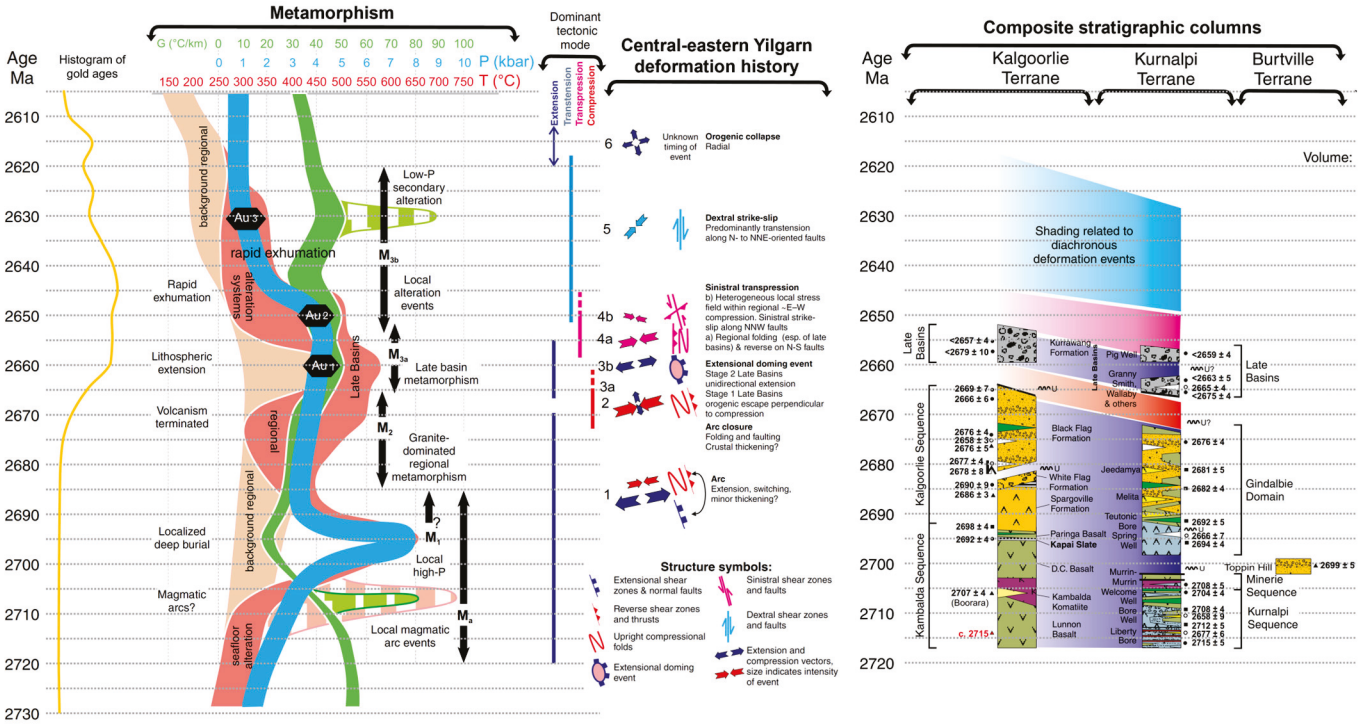


Figure 2. Yilgarn Craton time–space–event synthesis [35]. Adapted with permission from the Geological Survey of Western Australia. Copyright 2008, Government of Western Australia.

2.1.4. Metamorphic History

The EGST records metamorphic conditions ranging from sub-greenschist to granulite facies developed over ~130 Myr between ~2750 and 2620 Ma. A broadly conformable Neoarchean metamorphic history is indicated by regional isograds extending across terrane and domain boundaries [11,36]. Five regional metamorphic events have been identified across the EGST and temporally and spatially integrated with the structural framework of Blewett et al. [7] (Figure 2).

- M_a (>2750 Ma): Early, low-P/high-T upper-amphibolite to granulite facies assemblages are rare, restricted to magmatic arc-related ~2730 to 2810 Ma greenstone sequences in the western Burtville Terrane, and to HFSE granites and ~2675 to 2715 Ma greenstones of similar affinity in the Gindalbie Domain of the Kurnalpi Terrane.

- M_1 (~2750–2700 Ma): This event produced high-P/moderate-T assemblages preserved in narrow, upper amphibolite-grade zones along major, crustal-scale faults. The structural context, burial depth, and rapid exhumation suggest partial subduction and burial of buoyant magmatic arcs during arc accretion in subduction-like environments.
- M_2 (~2680–2670 Ma): A low-P/moderate-T event associated with contact metamorphism linked to emplacement of voluminous high-Ca granite melts into the upper crust, generated by partial melting of a subducted slab beneath the Kalgoorlie and Kurnalpi terranes. The M_2 event coincided with cessation of volcanism and D_2 crustal shortening.
- M_3 (~2665–2650 Ma): This event likely reflects lithospheric extension following subduction cessation with slab rollback and sag of the previously subducted plate causing extension of the overriding plate. The M_3 event coincided with D_3 metamorphic core complex formation.
- M_4 (~2650–2610 Ma): Low-P/high-T metamorphism was likely triggered by lower-crustal delamination, resulting in mantle upwelling and a thermal anomaly in the upper crust associated with widespread low-Ca granite magmatism.

2.1.5. Geodynamic Implications

Stratigraphic, structural, geochemical, and isotopic data support interpreting the Kalgoorlie, Kurnalpi, and Yamarna terranes of the EGST as failed intracontinental rift basins developed on older 'proto-Yilgarn' crust. These basins were later closed, uplifted, deformed, and metamorphosed during the ~2670 to 2630 Ma Kalgoorlie Orogeny [37,38].

2.2. Kalgoorlie–Kurnalpi Rift

The ~2720 to 2600 Ma Kalgoorlie–Kurnalpi Rift (Figure 1), identified by Witt et al. [12] based on stratigraphic, geochronological, and isotopic correlations across the Kalgoorlie and Kurnalpi terranes of the EGST, is interpretated to have formed in response to a major mantle input event that exploited weakened crust along the eastern margin of the Yilgarn proto-craton, comprising the South West, Narryer, and Youanmi terranes. According to [12], the genesis and evolution of the intracontinental Kalgoorlie–Kurnalpi Rift are consistent with spatially and temporally overlapping plume-related magmatism in the Kalgoorlie Terrane and west-directed subduction to the east of the Burtville Terrane. This geodynamic model, however, implies that plate tectonic processes comparable to modern-style plate tectonics operated as early as the Archean Eon, a contentious hypothesis that remains under active debate [39–41].

2.3. Kalgoorlie Terrane

The Kalgoorlie Terrane (Figures 1 and 3), the westernmost lithostructural element of the EGST, is bounded by the Ida–Waroonga fault system to the west and Ockerbury fault system to the east. The terrane is divided into ten domains, five of which (Boorara, Jundee, Moilers, Ora Banda, and Wiluna) occur within the study area. The terrane consists mainly of 2710 to 2660 Ma greenstones overlain by coarse clastic ('late basin') sequences dated at 2658 to 2655 Ma. Older (>2730 Ma) lithostratigraphic sequences appear restricted to the Norseman, Boorara, and Wiluna domains. Due to extensive cover, well-defined lithostratigraphic sequences have been established only in the southern Kalgoorlie Terrane, where greenstones are subdivided into the ~2710 to 2690 Ma Kambalda Sequence (tholeiitic and komatiitic mafic–ultramafic rocks) and the overlying, ~2690 to 2660 Ma Kalgoorlie Sequence (felsic volcaniclastic and epiclastic rocks with subordinate lavas). The late basin sequences consist mainly of poorly sorted, polymict conglomerates that grade upward into sandstone and siltstone. The Kalgoorlie Terrane greenstones form highly deformed,

curvilinear belts separated by variably deformed and metamorphosed granitoid rocks, emplaced principally between 2760 and 2620 Ma [7,28,36,42,43].

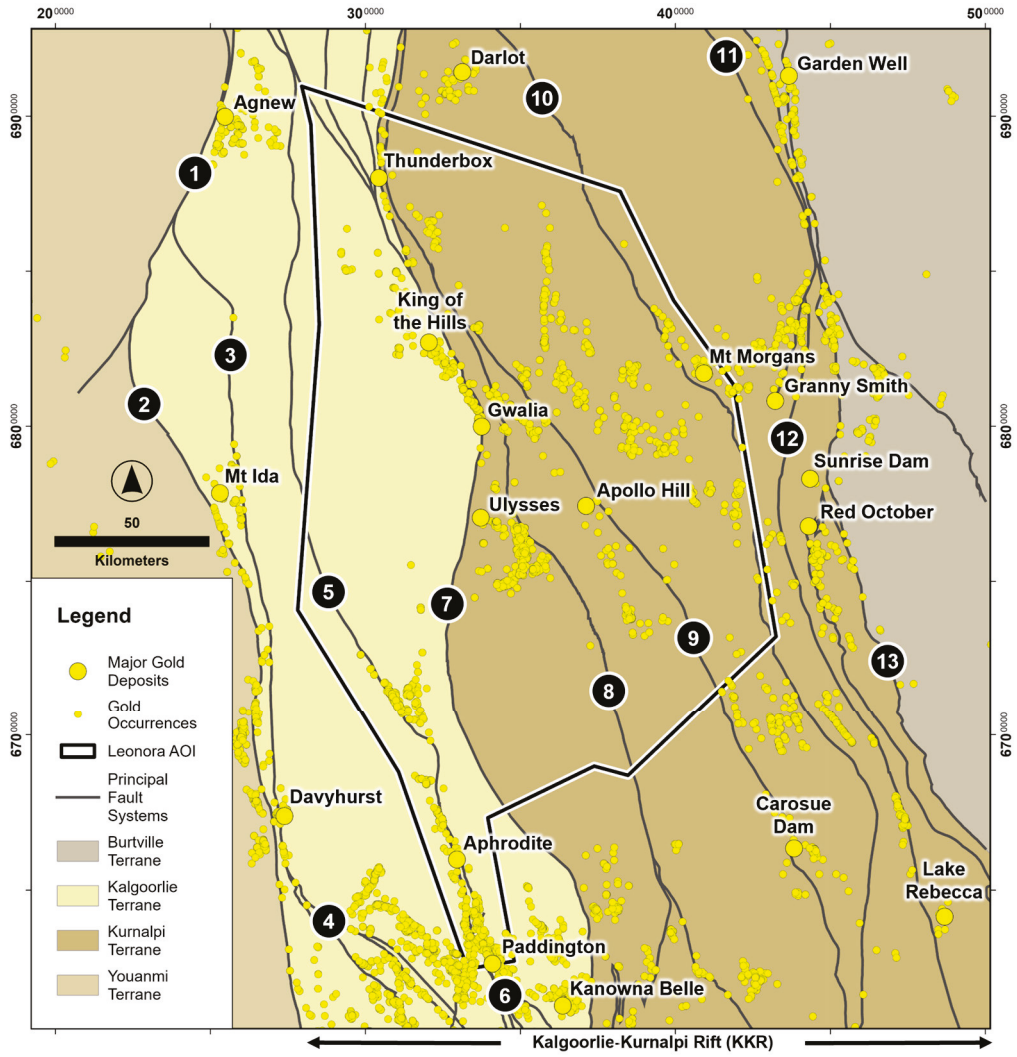


Figure 3. Terrane boundaries and major fault systems relevant to the study area. Names of major fault systems: 1 = Waroonga; 2 = Ida; 3 = Ballard; 4 = Zuleika; 5 = Menzies; 6 = Black Flag–Boorara–Abattoir; 7 = Ockerbury–McClure–Perseverance; 8 = Melita/Emu; 9 = Keith–Kilkenny; 10 = Celia; 11 = Laverton; 12 = Hootanui; 13 = Barnicoat. Terrane boundaries, faults and gold occurrences are based on data sources listed in Table 2.

2.4. Kurnalpi Terrane

The Kurnalpi Terrane (Figures 1 and 3), adjoining the Kalgoorlie Terrane to the east, is bounded to the west by the Ockerburry and to the east by the Hootanui fault system. It comprises seven domains, five of which (Edjudina, Gindalbie, Laverton, Menangina, and Murrin) occur within the study area. Lithostratigraphically, the Kurnalpi Terrane greenstones are subdivided into four main sequences: (i) The ~2800 Ma Laverton sequence, consisting of mafic–ultramafic volcanic rocks and banded iron formation with minor clastic sedimentary rocks intruded by felsic porphyries; (ii) the ~2715 to 2705 Ma Kurnalpi Sequence, comprising mafic volcanic and intrusive rocks, intermediate calc–alkaline igneous rocks, and feldspathic sedimentary units, with no clear stratigraphic equivalent in the Kalgoorlie Terrane; (iii) the ~2695 to 2675 Ma Minerie Sequence, composed of mafic–ultramafic volcanic rocks correlated with the Kambalda Sequence in the Kalgoorlie Terrane; and (iv) an unnamed, ~2690 to 2680 Ma sequence of bimodal rhyolite–basalt and felsic to inter-

mediate, calc–alkaline igneous rocks forming a linear belt along the western margin of the Gindalbie Domain. These greenstones are overlain by late basin sequences younger than ~2673 Ma, consisting mainly of turbidites with subordinary carbonaceous shale, sandstone, conglomerate, chert, and magnetic shale [7,28,42–44].

3. Gold Mineralization

3.1. Gold Endowment

In the EGST, gold was first discovered at Coolgardie in 1892 followed by Kalgoorlie in 1893. Since then, more than 20 deposits containing over one million ounces (Moz) of gold (Au) have been discovered in the region. Cumulative production exceeds 145 Moz Au, with the Golden Mile at Kalgoorlie accounting for 65 Moz Au (or ~45% of the total) [35,45]. Including unmined resources estimated at >125 Moz Au [1], the total endowment of the EGST exceeds 270 Moz Au. The study area contains >40.0 Moz Au of this endowment, largely within eleven major gold deposits and deposit clusters [1] (Figures 1 and 3; Table 1).

Table 1. Main gold deposits in the study area.

Deposit Name	Discovery (Year)	Endowment (Moz Au)	Absolute Age (Ma)	Geology and Mineralization
Paddington	1894	>11.7	Unk	Principal host rock(s): granophyric qtz-dolerite (greenschist facies); Mineralization style(s): closely spaced, 1 to 5 cm wide, subhorizontal, sheeted gold and sulfide (apy > py, sp > gn)-bearing qtz-dol-ank-ab veins, and a 3 m wide, steeply dipping, laminated, gold- and sulfide (apy > py, ccp, gn > sp)-bearing qtz-cb vein; Alteration type(s): carbonatization, chloritization, sericitization, silicification, sulfidation (apy, py, po); Metal association: Not reported (Au-As?); Ore control(s): D_2 kinematics and associated brittle–ductile structures; interaction of key structural elements (synclinal fold structure, location along the crustal-scale Bardoc Tectonic Zone), strong competency contrast between dolerite and surrounding ultramafic and sedimentary rocks
Gwalia	1896	>8.2	2755	Principal host rock(s): mafic schist, basalt (± pillowed) (lower amphibolite facies); Mineralization style(s): variably deformed, millimeter- to meter-scale, laminated and typically tightly folded and boudinaged gold- and sulfide (py, po > ccp)-bearing qtz-cb veins; Alteration type(s): carbonatization, biotitization, sericitization, silicification, sulfidation (py); Metal association: Not reported; Ore control(s): D_2 kinematics and associated ductile structures, interaction of key structural elements (mylonite zone, fold hinge of a large M-shaped fold, Poker/Gwalia Fault, bulge of the Raeside Batholith, proximity to crustal-scale Keith–Kilkenny fault system)
Mt Morgans	1896	>5.0	2650–2630	Principal host rock(s): banded iron formation (BIF) (greenschist facies); Mineralization style(s): structurally controlled, disseminated gold–sulfide (py > ccp) in BIF and along the margins of qtz-cb veins; Alteration type(s): silicification, carbonatization, sulfidation (py > po, ccp, sp); Metal association: Not reported; Ore control(s): $D_{4/5}$ kinematics and brittle(–ductile) structures, interaction of key structural elements (fault intersections, fold hinges developed on overturned anticlinal fold structure, dilational jog, proximity to crustal-scale Celia fault system), chemically reactive rock type (mag replacement by sulfides)

Table 1. *Cont.*

Deposit Name	Discovery (Year)	Endowment (Moz Au)	Absolute Age (Ma)	Geology and Mineralization
Tarmoola/King of the Hills	1897	>4.4	2650–2630	Principal host rock(s): trondhjemite, komatiite (greenschist facies); Mineralization style(s): sets of conjugate, 20 cm to 2 m wide, gold-, telluride-, sulfide (py, ccp, sp, gn)- and ±scheelite-bearing, laminated qtz-cb veins and breccias; Alteration type(s): silicification, carbonatization, sericitization, chloritization, albitization, and sulfidation (py, ccp, sp, ga); Metal association: Au-Sb-Mo-W ± Bi; Ore control(s): $D_{4/5}$ kinematics and associated brittle–ductile structures, interaction of key structural elements (proximity to local shear zones and crustal-scale Keith–Kilkenny fault system), strong competency contrast between trondhjemite and komatiite, fault–valve action; Note: Tarmoola/King of the Hills is the largest known granite-hosted gold deposit in the Yilgarn Craton
Thunderbox	1999	>4.4	Unk	Principal host rock(s): porphyritic dacite (upper greenschist facies); Mineralization styles: structurally controlled, disseminated gold–sulfide (apy, po > py, sp, gn) accumulations and mm to cm thick, boudinaged and folded gold- and sulfide (apy)-bearing qtz veins; Alteration styles: carbonatization, silicification, albitization and sulfidation (apy, po); Metal association: Not reported (Au-As?); Ore control(s): $D_{4/5}$ kinematics and brittle–ductile structures, interaction of key structural elements (local fold axes, Thunderbox shear zone, proximity to crustal-scale Perseverance fault system), strong competency contrast between porphyritic dacite and enclosing sedimentary and mafic volcanic rocks
Apollo Hill	1986	>2.0	Unk	Principal host rock(s): basalt (pillowed), dolerite, felsic volcaniclastic rocks; Mineralization style(s): Four sets of mm to cm thick, sheeted and stockwork-type, gold- and sulfide (py > ccp, sp, gn, po)-bearing qtz-cb veins; Alteration type(s): carbonatization, chloritization, sericitization, silicification, pyritization; Metal association: Not reported (Au-Ag-Cu-Pb-Zn?); Ore control(s): $D_{4/5}$(?) kinematics and associated brittle–ductile structures, interaction of key structural elements (Apollo-Ra shear zone, proximity to crustal-scale Keith–Kilkenny fault system), strong competency contrast, lithological contacts
Aphrodite	1996	>1.6	Unk	Principal host rock(s): volcaniclastic rocks, felsic to intermediate (dacitic) porphyries; Mineralization style(s): conjugate, mm to cm scale gold- and sulfide (py > apy)-bearing qtz veins and breccias; Alteration type(s): silicification, carbonatization, sericitization, biotitization and sulfidation (py > apy > gn, ccp, stb); Metal association: Not reported (Au-As-Sb?); Ore control(s): D_2 kinematics and associated brittle–ductile structures; interaction of key structural elements (local fold axes and crenulations, location along the crustal-scale Bardoc Tectonic Zone), strong competency contrast, chemically reactive sedimentary rock

Table 1. *Cont.*

Deposit Name	Discovery (Year)	Endowment (Moz Au)	Absolute Age (Ma)	Geology and Mineralization
Ulysses	1993	>1.6	Unk	Principal host rock(s): qtz-dolerite (sills), basalt; Mineralization style(s): stacked, shear zone-hosted, gold- and sulfide-bearing qtz veins; Alteration type(s): silicification, carbonatization, sericitization, albitization, sulfidation (py, po > ccp) ± biotitization, chloritization; Metal association: Not reported; Ore control(s): $D_{4/5}$(?) kinematics and associated brittle–ductile structures; interaction of key structural elements (fault intersections with dolerite sills), strong competency contrast
Menzies	1891	>1.4	Unk	Principal host rock(s): metasedimentary rock, basalt, amphibolite ± porphyritic granodiorite; Mineralization style(s): locally stacked, shear zone-hosted, gold- and sulfide (py > apy)-bearing qtz veins and zones of brecciation; Alteration type(s): biotitization, chloritization, sericitization, silicification, sulfidation (py, po) ± carbonatization; Metal association: Au-As; Ore control(s): $D_{4/5}$(?) kinematics and associated brittle–ductile structures; interaction of key structural elements (shear fabric, proximity to Menzies shear zone, location along the crustal-scale Bardoc Tectonic Zone)
Wonder	1890s	>0.9	Unk	Principal host rock(s): syenogranite (Bundarra Batholith) with partially assimilated greenstone rafts (mafic roof pendants); Mineralization style(s): gold- and sulfide (py > ccp, gn)-bearing qtz veins; Alteration type(s): silicification, carbonatization, sericitization, propylitization (hem), sulfidation (py) ± chloritization; Metal association: Not reported; Ore control(s): $D_{4/5}$(?) kinematics and associated brittle–ductile structures; interaction of key structural elements (local faults, granite margin, proximity to the crustal-scale Keith–Kilkenny fault system), strong competency contrast between granite and mafic greenstone rafts
Zoroastrian	1894	>0.6	Unk	Principal host rock(s): granophyric dolerite; Mineralization style(s): steeply dipping and flat-lying, gold- and sulfide (apy, py, po)-bearing qtz stockwork veins; Alteration type(s): silicification, carbonatization, sericitization, chloritization, sulfidation (apy, py, po); Metal association: Not reported; Ore control(s): $D_{4/5}$(?) kinematics and associated brittle–ductile structures; interaction of key structural elements (narrow synclinal fold structure, constriction zone between two granite domes, location along the crustal-scale Bardoc Tectonic Zone), strong competency contrast between dolerite and surrounding sedimentary, mafic and ultramafic rocks

Sources: Paddington = [5], Gwalia = [9,46], Mt Morgans = [47], Tarmoola/King of the Hills [4,9], Thunderbox = [48], Apollo Hill = [49], Aphrodite = [50], Ulysses [51,52], Menzies = [53], Wonder = [54,55], Zoroastrian = [56,57]. Gold endowment data were compiled from the above sources and [1]. Mineral abbreviations [58,59]: ab = albite, ank = ankerite, apy = arsenopyrite, cb = carbonate mineral; ccp = chalcopyrite, dol = dolomite, gn = galena, hem = hematite, mag = magnetite, po = pyrrhotite, py = pyrite, qtz = quartz, sp = sphalerite. Other abbreviations: Unk = unknown.

3.2. Gold Deposit Styles

The EGST hosts a diverse range of gold deposit styles controlled by various structural settings and hosted in multiple rock types spanning metamorphic grades from sub-greenschist to amphibolite facies. Despite this diversity, their shared characteristics strongly

suggest that gold deposits within the EGST, and broader Yilgarn Craton, formed as part of regionally extensive gold mineralizing systems active during different stages of the late Archean evolution of the craton [60,61].

According to Tripp et al. [62], gold mineralization occurs in structurally and/or lithologically controlled lodes, typically as quartz ± carbonate veins, breccias, or disseminations enveloped by gold-related wall-rock alteration. Gold is present in all rock types, though it occurs most commonly in basalt and dolerite, and least commonly in large granitoid bodies [16,62]. Structural control was the dominant factor influencing mineralization, across scales, governing both hydrothermal fluid flow and the architecture and localization of gold deposition [62].

3.3. Gold Depositional Events

The EGST experienced multiple, protracted gold mineralization events during the late Archean, associated with both extensional and compressional deformation episodes within a ~60 Myr timeframe between ~2670 and 2630 Ma [5,7–9,12,15,62]. Although gold deposition occurred during most EGST deformation events [7], the formation of the largest deposits is attributed to three key stages (Figure 2) [7,8,15]:

- D_3 (~2665–2655 Ma): Development of the EGST crustal architecture during NE-SW-directed extension and metamorphic core complex formation. Major crustal-penetrating fault systems were established at this stage, linking the upper crust to a metasomatized mantle, as evidenced by the first emplacement of mafic and syenitic granites. This mantle connection likely introduced significant heat at the crustal–mantle boundary, promoting mantle-to-crust metal transfer. An important D_3 deposit in the study area is Gwalia (>8.2 Moz Au).
- D_4 (~2655–2650 Ma): The extensional crustal framework formed during D_3 was inverted during D_4, a brittle–ductile deformation event comprising an initial phase of ENE-WSW-directed shortening (D_{4a}) followed by WNW-ESE-directed shortening (D_{4b}). This phase coincided with a shift from high- to low-Ca granite magmatism driven by crustal melting and represents the most significant gold mineralization event in the EGST. Strike–slip deformation and reactivation of pre-existing structural heterogeneities during D_{4b} served as highly effective fluid-focusing mechanisms. The most prominent D_4 deposit is the Golden Mile (>65 Moz Au), located ~35 km south of the study area.
- D_5 (~2650–2635 Ma): A subsequent stress field reorientation induced NE-SW-directed shortening accompanied by dextral strike–slip, thrusting, and low-Ca granite emplacement. Gold mineralization was primarily controlled by brittle structures. A key D_5 deposit is Sunrise Dam (>10.3 Moz Au), located ~20 km east of the study area.

4. Materials and Methods

4.1. Study Background

The study described in this paper was conducted in late 2021. It was commissioned by the Australian mining company St Barbara Limited, which also defined the layout of the study area. At that time, the central-eastern Yilgarn Craton hosted St Barbara's Leonora operations, comprising the Gwalia underground mine and a 1.4 Mtpa processing plant, along with nearby gold development and exploration projects. In 2023, the Leonora operations were sold to another Australian gold miner, Genesis Minerals Limited [63].

4.2. Methodology

This study employed a systematic, six-step workflow (Figure 4) that integrates geological understanding with advanced geospatial analysis for gold exploration targeting. The first step involved reviewing orogenic gold deposit models within the study area and the broader Yilgarn Craton to establish the conceptual basis for a mineral systems

targeting framework [20–22,64–66], based on the critical processes in orogenic gold formation and their mappable expressions. Geophysical and remote sensing datasets were then filtered and enhanced to extract structural information and hydrothermal alteration signatures [67,68], which were incorporated into a new lithostructural (solid geology) interpretation. Building on this framework, mineral potential modeling (MPM) was conducted using a multi-technique approach that combined continuous, data-driven, and knowledge-driven methods, enabling cross-validation and comparison of the resulting prospectivity maps [69]. The final stage synthesized these results to identify and prioritize gold exploration targets across the central-eastern Yilgarn Craton.

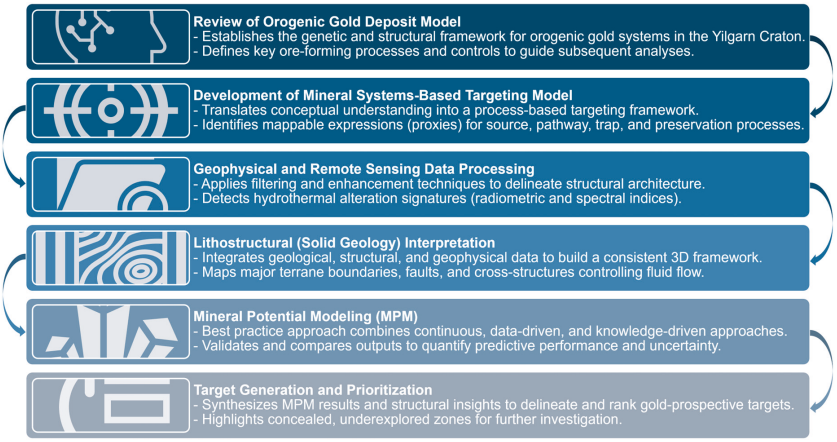


Figure 4. Schematic flowchart illustrating the methodological workflow adopted in this study.

4.3. Geoscience and Exploration Data

The geoscience and exploration data used in this study came from two principal sources (Table 2): open-access repositories maintained by the Geological Survey of Western Australia (GSWA) and proprietary company data.

Table 2. Types and sources of datasets used in this study.

Category	Data Type/Name	Source	Comments
Gold occurrences	Mines and mineral deposits (MINEDEX)	GSWA	Data available from DEMIRS Data and Software Centre: https://dasc.dmirs.wa.gov.au/
	MINEDEX operating mines map		
Geology	1:100,000 state interpreted bedrock geology of Western Australia		
	1:500,000 interpreted bedrock geology of Western Australia		
	1:100,000 geological series maps		
	1:500,000 state regolith geology		
	In-house Eastern Yilgarn Craton geology map	SBM	Confidential dataset
	pmd*CRC 1:100,000 solid geology map, eastern Yilgarn Craton	[15]	Data or data links provided in quoted references
	Yilgarn Craton metamorphic facies map	[11,36]	
Geochemistry	Yilgarn Craton εNd (juvenile crust) map	[34]	
Drilling	Mineral exploration drill holes (open file)	GSWA	Confidential dataset
	Leonora drill hole database	SBM	https://dasc.dmirs.wa.gov.au/
Geophysics	400 m Bouguer gravity merged grid of Western Australia 2020 version 1	GSWA	Data available from MAGIX Online: https://geodownloads.dmp.wa.gov.au/downloads/geophysics/72203/, https://geodownloads.dmp.wa.gov.au/downloads/geophysics/72204/ and https://geodownloads.dmp.wa.gov.au/downloads/geophysics/72205/
	40 m reduced to the pole (RTP) magnetic merged grid of Western Australia 2021 version 1		
	Radiometric grids (80 m) of Western Australia		
Remote Sensing	ALOS World 3D—30 m (AW3D30) ALOS Global Digital Surface Model	OpenTopography	Data available from https://opentopography.org/
	Sentinel-2 (blue, green, red, and near-infrared (NIR) bands at 10 m and other bands at 20 m resolution)	European Space Agency	Data available from https://dataspace.copernicus.eu

Key to abbreviations: DEMIRS = Department of Energy, Mines, Industry Regulation and Safety; GSWA = Geological Survey of Western Australia; pmd*CRC = Predictive Mineral Discovery Cooperative Research Centre; SBM = St Barbara Limited. The data repositories listed here were last accessed on 8 October 2025.

4.4. Processing and Interpretation of Geophysical and Remote Sensing Data

4.4.1. Geophysical Data and Processing

Geophysical data were downloaded in grid format (Table 2) and windowed to the study area, allowing for adequate buffer zones. Minimal processing was required, as the datasets were available as merged products with the appropriate data reduction already applied, providing complete coverage of the study area at various spatial resolutions (i.e., cell sizes). Access to objective, 'blanket-coverage' geophysical data of sufficient spatial resolution is essential for exploration targeting in areas where prospective bedrock is concealed by significant cover, such as in the central-eastern Yilgarn Craton. Moreover, geophysical data are well suited to mapping the expressions of mineralizing processes and are therefore a fundamental component of a mineral systems-type targeting approach.

Three types of geophysical data were sourced and processed for inclusion in this targeting study [70]: (i) Gravity data, which respond to variations in rock density and reflect subsurface density contrasts. Gravity surveys are therefore considered 'depth penetrative' methods. (ii) Magnetic data, which respond to variations in rock magnetism, primarily controlled by magnetic susceptibility. Like gravity data, they reflect subsurface contrasts. (iii) Radiometric data, which measure surface variations in naturally occurring gamma radiation, primarily emitted by radioactive isotopes of potassium (K), thorium (Th), and uranium (U).

In the EGST, gravity gradients show a clear association with faults that host gold deposits [71]. The extraction of gravity gradients from gridded gravity data has been performed in various ways since the method was first introduced in the late 1970s [72,73]. In this study, we adapted the phase congruency approach of Kovesi [74], using the differential upward continuation operator of Jacobson [75] instead of log-Gabor filters. This resulted in a multi-scale feature detection filter for potential field (gravity and magnetic) data. Topological features [76] extractable from gridded potential field data at multiple scales are as follows: (i) edges (i.e., maximum gradient curves), representing traces of physical property boundaries across gravity or magnetic data grids, typically arising from structural breaks such as faults, shear zones, or lithological contacts. (ii) Ridges (i.e., surface maxima or peak curves), corresponding to ridgeline features in gravity and magnetic data grids. Gravity ridges, for example, indicate peak gravity responses. In granite–greenstone terranes, these ridges often coincide with the thickest, dense, mafic–ultramafic rock units, effectively mapping structurally thickened sequences in the central parts of inverted greenstone basins. (iii) Valleys (i.e., surface minima), corresponding to valley-line features in gravity or magnetic data grids. Magnetic valleys often coincide with faults or fault corridors where primary magnetite has been partially or completely destroyed by fluid–rock interaction.

Radiometric data, by contrast, are particularly effective for detecting and mapping outcropping hydrothermal alteration systems. Studies by de Quadros et al. [77], Herbert et al. [78], and Shebl et al. [79] have demonstrated the utility of this technique for identifying zones of gold-related white mica (sericite) alteration through computations involving normalized radiometric data and their ratios.

4.4.2. Remote Sensing Data and Processing

ALOS digital elevation data [80] were downloaded in grid format (Table 2) and processed similarly to the geophysical data described above. The topographic data represent the Earth's surface morphology, where elevation highs often correspond to units more resistant to weathering. Thus, even in ancient peneplained cratonic settings such as the Yilgarn Craton, topographic data can aid in mapping outcropping or subcropping bedrock, structural trends in exposed rock, and areas affected by past or present mining. Surface topography may also reflect geological processes relevant to exploration targeting, especially in well-exposed neotectonic terrains. In this study, the topographic data provided important input for both

the lithostructural interpretation (mapping of outcropping and subcropping bedrock and structural trends) and the interpretation of the radiometric and remote sensing data (matching of anomalies with areas of outcropping and subcropping bedrock, and mine workings).

Multi-spectral Sentinel-2 data were downloaded as multiband grids (Table 2) and clipped to the study area. Several salt lakes within the area were manually delineated and removed to avoid false positives during processing. Spectral indexes were then calculated to highlight goethite and other ferric-iron-bearing phases (Band4/Band2) and clay minerals (Band11/Band12). The iron feature depth (IFD), a remote sensing index used to map the presence and abundance of iron-bearing minerals, was computed to emphasize potential weathering sulfides in the regolith [81]. The calculation of IFD involved determining the expected value at Band 8A of the Sentinel-2 data by performing a linear interpolation between Band 6 and Band 11. The ratio was then computed between the expected Band 8A value and the measured Band 8A value. This process measures absorption on Band 8A, which is associated with the presence of iron in minerals such as jarosite. The three indexes (goethite, clay, and IFD) were combined into a cyan–magenta–yellow (CMY) ternary image, which was converted to CIELab, a color space defined by the Commission Internationale de l'Eclairage (CIE), to calculate the Euclidean distance to black [82]. Black areas in the CMY image correspond to zones where all three indexes are high, indicating probable clay alteration and weathering sulfides. The distance-to-black values were then inverted so that higher values represent areas where all three indexes are relatively high. The resulting inverse distance grid was thresholded and polygonized.

4.4.3. Lithostructural (Solid Geology) Map

The workflow used to interpret the geophysical data and produce the solid geology map followed the approach outlined by [83]. It involved (i) constructing form lines, (ii) identifying magnetic rock units, (iii) characterizing geophysical domains, (iv) integrating geophysical interpretations with supporting data (e.g., geological maps), (v) defining structural elements, (vi) mapping and interpretating lithology, and (vii) developing an integrated lithostructural framework.

4.5. Mineral Systems Concept

The targeting model developed in this study was based on the mineral systems approach [20–22,64,84] and implemented following the methodologies described in [64,68,85,86]. In essence, the mineral systems concept views mineral deposits as localized expressions of a sequence of geological processes operating across multiple temporal and spatial scales: (i) source processes extract essential mineral deposit components (melts and/or fluids, metals, and ligands) from crustal or mantle sources; (ii) transport processes move these components from source to trap regions via melts and/or fluids; (iii) trap processes focus melt and/or fluid flow into physically and/or chemically receptive, deposit-scale sites; (iv) deposition processes enable efficient metal extraction from melts and/or fluids passing within the traps; and (v) preservation processes maintain the accumulated metals over time.

Where one or more of these critical processes fail to operate, a mineral deposit cannot form or be preserved. The probabilistic nature of the mineral systems framework aligns well with MPM [64,85,86], which relies on mathematical algorithms. A further strength of the mineral systems approach is its capacity to provide a robust yet flexible framework for developing a holistic, process-based targeting model and for identifying, mapping, or querying expressions of key mineralizing processes within available geoscience datasets [22,87].

4.6. Fry Analysis

Fry analysis [88] is a straightforward geometrical method for visualizing spatial patterns in point data. It records the distance and bearing from each point in a dataset to

every other point, either manually or computationally. For n points, this yields $n(n-1)$ spatial relationships. These point translations are displayed in autocorrelation (Fry) plots and Rose diagrams, which enhance subtle spatial trends and reveal directions of maximum continuity in mineral deposit alignments [89–91]. In this study, we used DotProc 1.0, a Fry analysis freeware programmed by A. Kuskov, A. Mikhailov, and P. Dirks.

4.7. Background to Mineral Potential Modeling (MPM)

MPM, first introduced in the late 1980s alongside the rise of Geographic Information Systems (GIS) [92,93], has since evolved into a robust, cost- and time-efficient exploration targeting tool with strong big data analytics capabilities. MPM can concurrently handle, integrate, process, and model diverse and often large datasets, including geological, geophysical, geochemical, remote sensing, and drilling data. It is particularly well suited for effective screening and target generation across large search areas, from individual mineral districts or belts to entire countries or continents. In general, MPM comprises four main stages [21,87,94–97]: (i) the genetic model stage identifies the key geological processes responsible for the formation of the targeted deposit type to establish a conceptual model; (ii) the targeting model stage translates the genetic model into a targeting model in which critical ore-forming processes are expressed by mappable criteria (also referred to as spatial proxies, predictor maps, or targeting elements); (iii) the mathematical model stage integrates the predictor maps using weighted mathematical algorithms; and (iv) the target identification and prioritization stage maps and ranks the most prospective areas.

Mathematical modeling approaches are generally categorized as knowledge-driven, data-driven, hybrid (data- and knowledge-driven), or continuous methods employing logistic functions [26,94,98]. The choice of weighting methods depends largely on data availability, specifically the number of known mineral occurrences supporting the targeting model (prospect locations). Data-rich 'brownfield' regions, typically well explored around known mineral deposits, favor data-driven weighing methods. In contrast, data-poor 'frontier', 'grassroots', or 'greenfields' regions often require knowledge-driven approaches reliant on expert judgement [93,94]. Continuous weighting methods, by comparison, require neither prospect locations nor expert input, using continuous spatial evidence to achieve a superior predictive performance relative to discretized data [98].

In this study, we applied a multi-technique MPM framework [69] incorporating continuous (fuzzy gamma [99]; geometric average [100]; improved index overlay [101]), data-driven (random forest, RF [102]), and knowledge-driven (best-worst method-sum additive weighting, BWM-SAW [103–105]) modeling techniques.

5. Data Integration and Examination

5.1. Insights from the Enhancement Filtering of Geophysical and Remote Sensing Data

Enhancement filtering of gravity data revealed two critical insights into the proximity, association, and abundance relationships between gravity features and gold occurrences. Belt-parallel gravity ridges act as proxies for greenstone basin centers or zones of thicker mafic–ultramafic material along greenstone keels and root zones (Figure 5). A confidential, continent-scale gravity enhancement study for Australia demonstrated that a large proportion of Yilgarn gold (and nickel) deposits show strong proximity, association, and abundance relationships with gravity ridges. A similar pattern is evident in the study area, where most gold occurrences, except those wholly within intrusive rocks, exhibit comparable relationships with gravity ridges observable at multiple scales (Figure 6). Gravity edges represent discontinuities such as faults, shear zones, or major lithological boundaries. In the study area, the Thunderbox, King of the Hills, Gwalia, and Ulysses gold deposits all occur along a curvilinear, belt-parallel gravity edge that can be traced for >230 km along its strike, extending north beyond the

study area boundary. Notably, this gravity linear coincides only locally with the Perseverance–Ockerbury–McClure fault system but shows strong spatial correspondence with the basement granite–greenstone contact (Figure 6). Similar, semi-parallel lineaments elsewhere in the study area may represent attractive first-pass exploration targets.

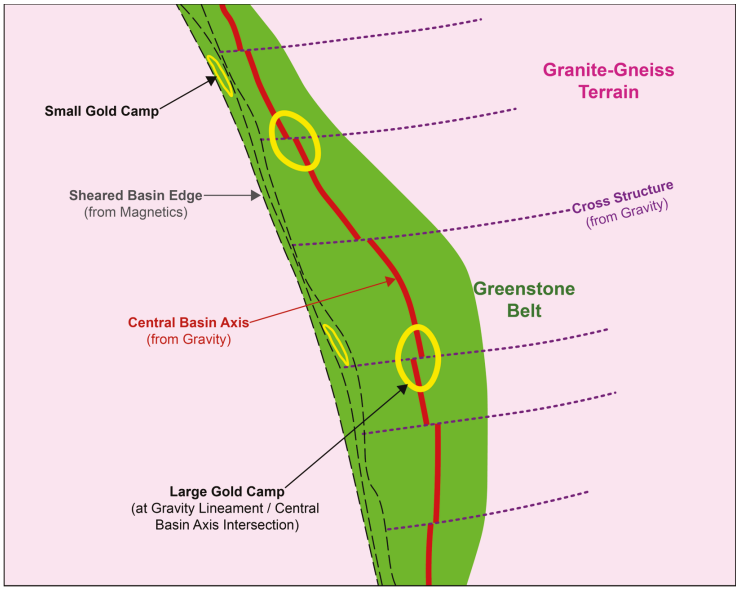


Figure 5. Schematic model for gold targeting in greenstone belt-hosted systems (modified from [106]). In this model, large, multi-million-ounce gold camps form in the central parts of now-inverted 'greenstone basins', particularly where these are intersected by cross-structures. Structurally thickened mafic–ultramafic rock packages in the central basin areas are mapped as gravity ridges (Figure 6), whereas strongly deformed basin margins, typically associated with smaller gold deposits, are mapped as gravity edges (Figure 7).

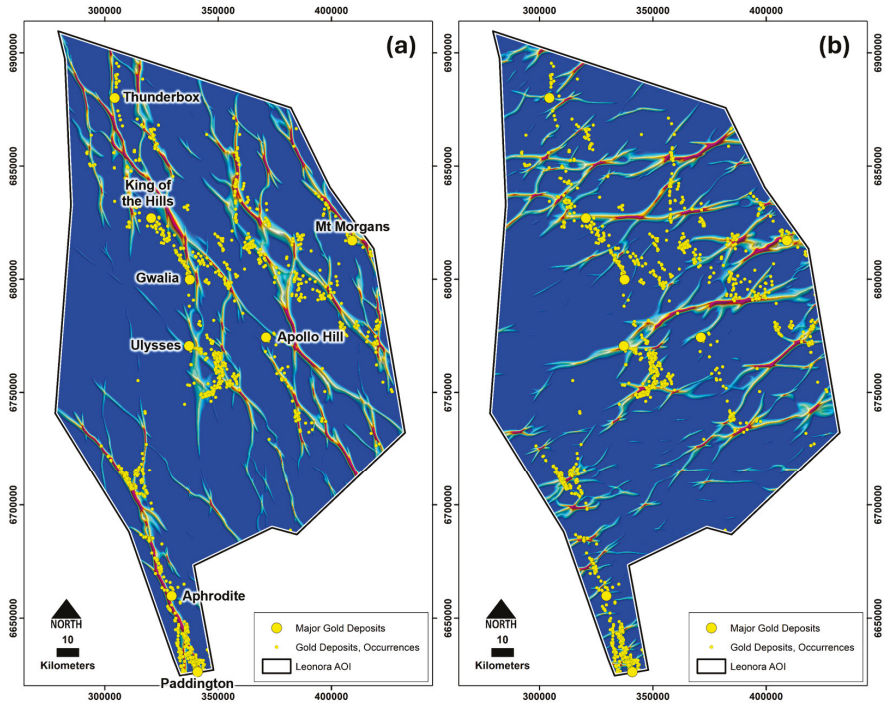


Figure 6. Gravity ridges (800 m scale) serve as proxies for centers of now-inverted greenstone basins or zones of thickened mafic material along greenstone keels and root zones. (**a**) Belt-parallel gravity ridges. (**b**) Cross-belt gravity ridges. High values (red colors) indicate high data confidence whilst low values (blue colors) indicate low data confidence. See text for details.

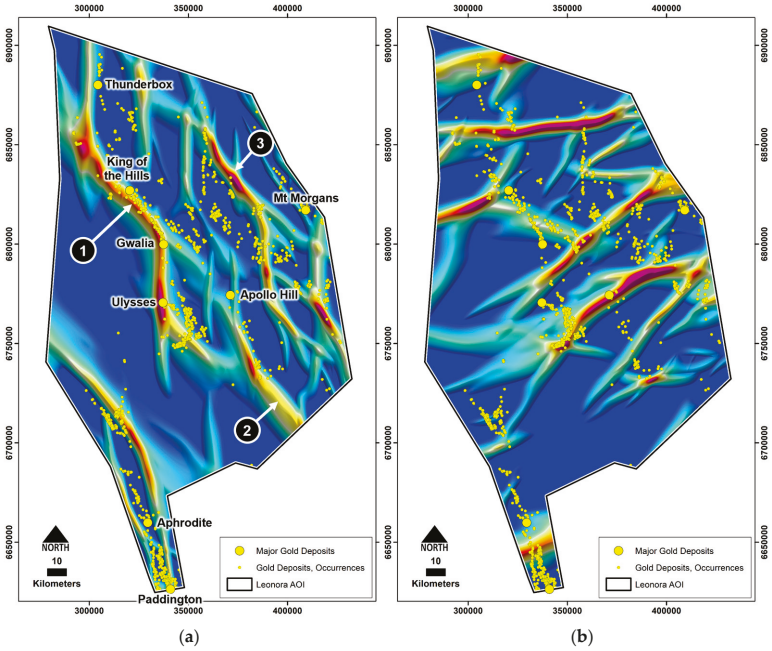


Figure 7. Gravity edges (3200 m scale) represent major faults or lithological boundaries. (**a**) Belt-parallel gravity edges. (**b**) Cross-belt gravity edges. Label #1 marks a curvilinear, belt-parallel gravity edge traceable for over 230 km and likely extending beyond the study area. The Thunderbox, King of the Hills, Gwalia, and Ulysses gold deposits all occur along this feature. Notably, this gravity edge does not coincide spatially with the nearby Ockerbury–McClure–Perseverance fault system but instead aligns with a granite–greenstone contact. Semi-parallel gravity edges, particularly those labeled #2 and #3, may represent promising exploration targets. High values (red colors) indicate high data confidence whilst low values (blue colors) indicate low data confidence. See text for details.

Magnetic edges typically mark faults, shear zones, or lithological boundaries. Within the study area, magnetic edge enhancement filtering highlights (i) proterozoic dolerite dykes, (ii) certain intrusive contacts, and (iii) segments of major and subsidiary shear and/or fault zones. Notably, all larger gold deposits coincide with magnetic edges (Figure 8).

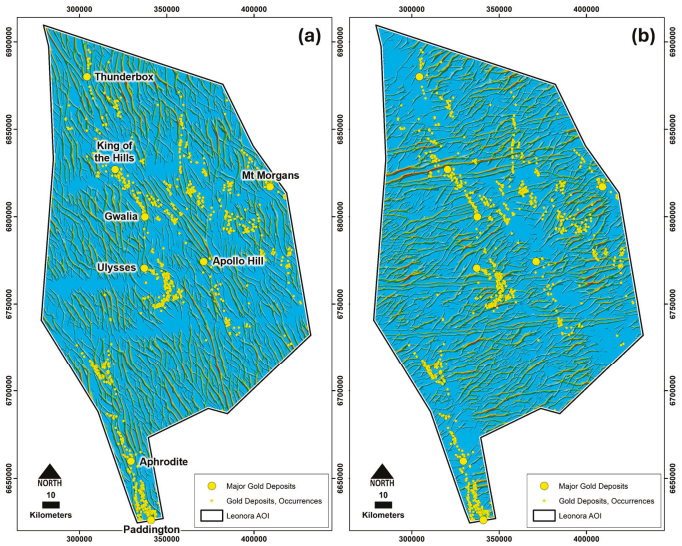


Figure 8. Magnetic edges (800 m scale) represent faults or lithological boundaries. (**a**) Belt-parallel magnetic edges. (**b**) Cross-belt magnetic edges. Lithostructural features visible here include Proterozoic dolerite dykes and selected intrusive contacts and faults. High values (red colors) indicate high data confidence whilst low values (blue colors) indicate low data confidence. See text for details.

Where exposed at the surface or in open-cut mines, orogenic gold systems in the study area show spatial proximity, association, and abundance relationships with (i) domains exhibiting high (≥95th percentile) K/Th ratios derived from radiometric data, and (ii) goethite–clay–iron feature depth index (IFD) anomalies extracted from remote sensing imagery.

Overall, the integration of advanced geophysical and remote sensing data modeling enabled the mapping of potential ore-controlling structures and ore signatures, significantly enhancing the toolkit for gold targeting in the central-eastern Yilgarn Craton. The semi-automated filtering methods applied to these datasets helped reduce bias and inconsistencies inherent in purely human-based interpretations.

5.2. Lithostructural (Solid Geology) Interpretation

The main objective of the lithostructural interpretation was to produce a coherent base map for MPM and target generation. Priority was given to developing a new structural framework that integrates the results of geophysical enhancement and filtering. Whilst the interpretation incorporated and respected elements of previous solid geology maps produced by the Geological Survey of Western Australia, pmd*CRC, and St Barbara Limited (Table 2), particularly regarding geological boundaries, the overall structural framework was reconstructed from the ground up, guided by the newly derived geophysical evidence.

In the study area, form lines (Figure 9a) delineate stratigraphy and schistosity in greenstones, compositional layering in granitoids, and schistosity in gneissic units. Although form line orientations vary considerably, NNW-SSE trends predominate, reflecting the principal stratigraphic and tectonic grain of the greenstone sequences. Local variations are mainly attributable to folding on the kilometer to multi-kilometer scale.

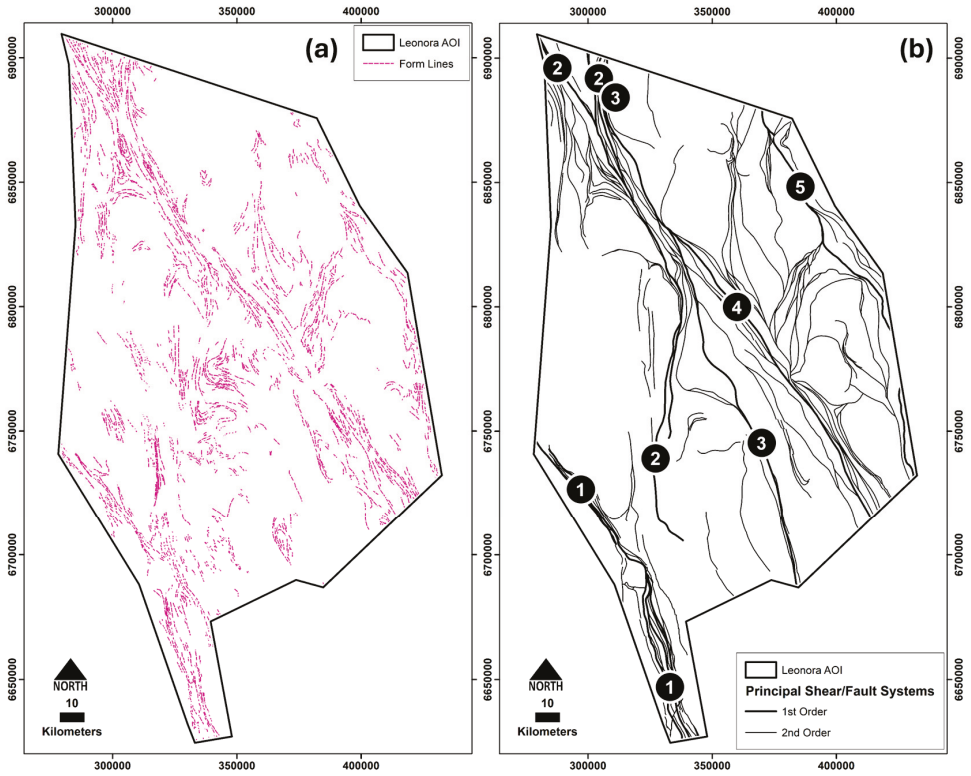


Figure 9. *Cont.*

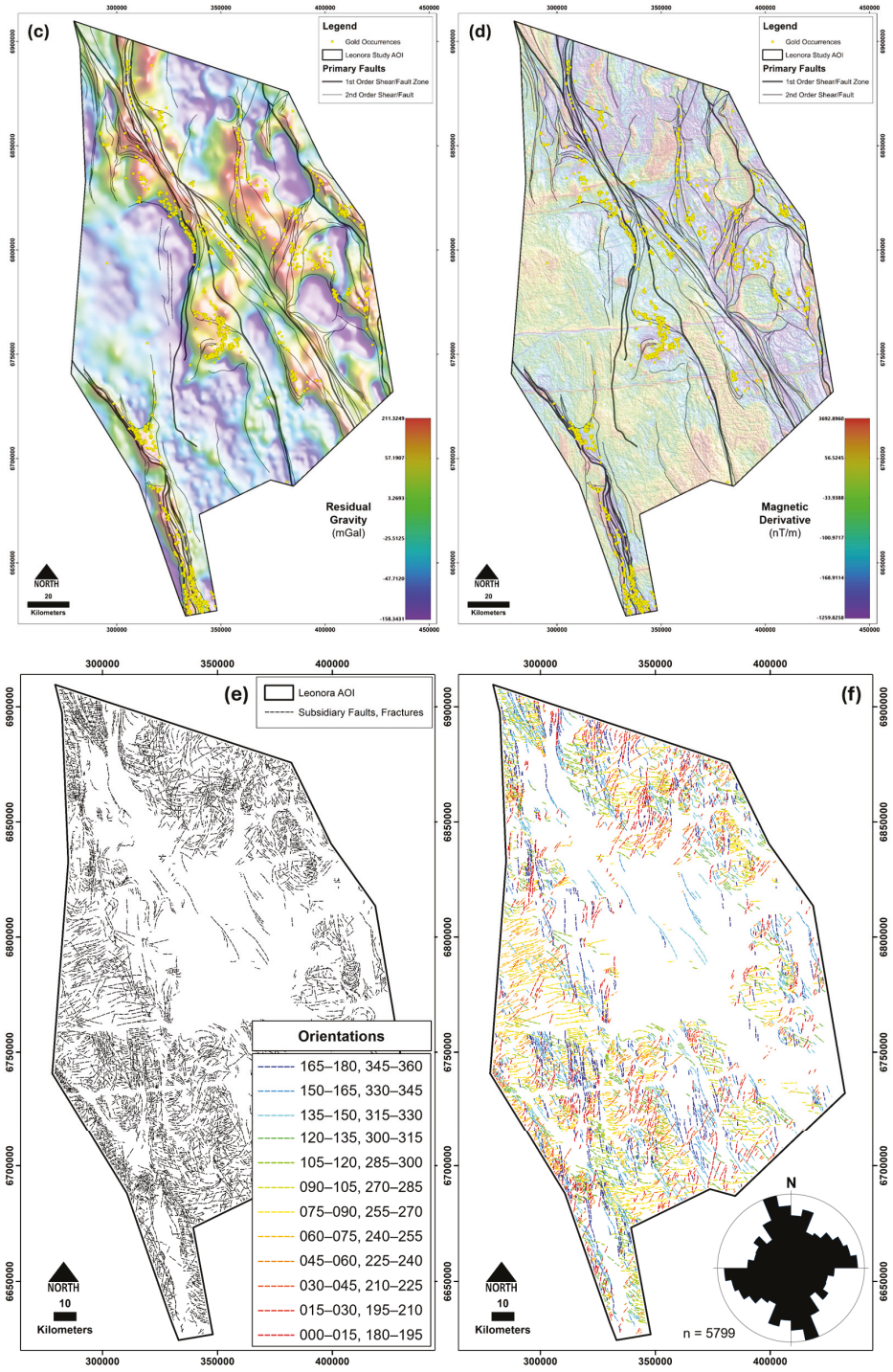


Figure 9. Lithostructural (solid geology) interpretation. (**a**) Form lines. (**b**) First- and second-order fault systems. First-order fault systems: 1 = Menzies–Boorara fault system (separating the Ora Banda and Boorara domains of the Kalgoorlie Terrane); 2 = Ockerburry–McClure–Perseverance fault system (separating the Kalgoorlie and Kurnalpi terranes); 3 = Melita–Emu fault system (separating the Gindalbie and Menangina domains of the Kurnalpi Terrane); 4 = Keith–Kilkenny fault system (separating the Menangina and Murrin domains of the Kurnalpi Terrane); 5 = Celia fault system (separating the Murrin and Edjudina/Laverton domains of the Kurnalpi Terrane). First- and second-order fault systems draped over (**c**) gravity data (0–6400 m differential upward continuation of the Bouguer anomaly grid) and (**d**) magnetic data (1VD of the RTP). (**e**) Fault and fracture systems. (**f**) Fault and fracture systems color-coded by dominant orientation, thereby highlighting several structural corridors with prevailing N-S, E-W, NE-SW, and NW-SE trends. Inset: Rose diagram showing mean orientations of fault and fracture systems in the study area.

The major, first- and second-order faults within the study area (Figure 9b–d), likely the products of D_3 deformation and subordinate to earlier, N-S-striking D_1 master faults (cf. Figure 3 in [7]), include the (i) the Menzies–Boorara fault system separating the Ora Banda and Boorara domains of the Kalgoorlie Terrane; (ii) the Ockerburry–McClure–Perseverance fault system dividing the Kalgoorlie and Kurnalpi terranes; (iii) the Melita–Emu fault system separating the Gindalbie and Menangina domains of the Kurnalpi Terrane; (iv) the Keith–Kilkenny fault system dividing the Menangina and Murrin domains of the Kurnalpi Terrane; and (v) the Celia fault system separating the Murrin and Edjudina/Laverton domains of the Kurnalpi Terrane.

The subsidiary third- and fourth-order fault and fracture network defines several structural corridors with dominant N-S, E-W, NE-SW, and NW-SE orientations (Figure 9e,f). These corridors, oblique or orthogonal to the general NNW-SSE trend of the greenstone belts, likely played a key role in focusing fluid flow and controlling the gold mineralization. This interpretation is supported by Fry analysis results, which indicated preferred gold occurrence alignments along NNW-SSE, N-S to NNE-SSW, NE-SW, and NW-SE trends (Figure 10).

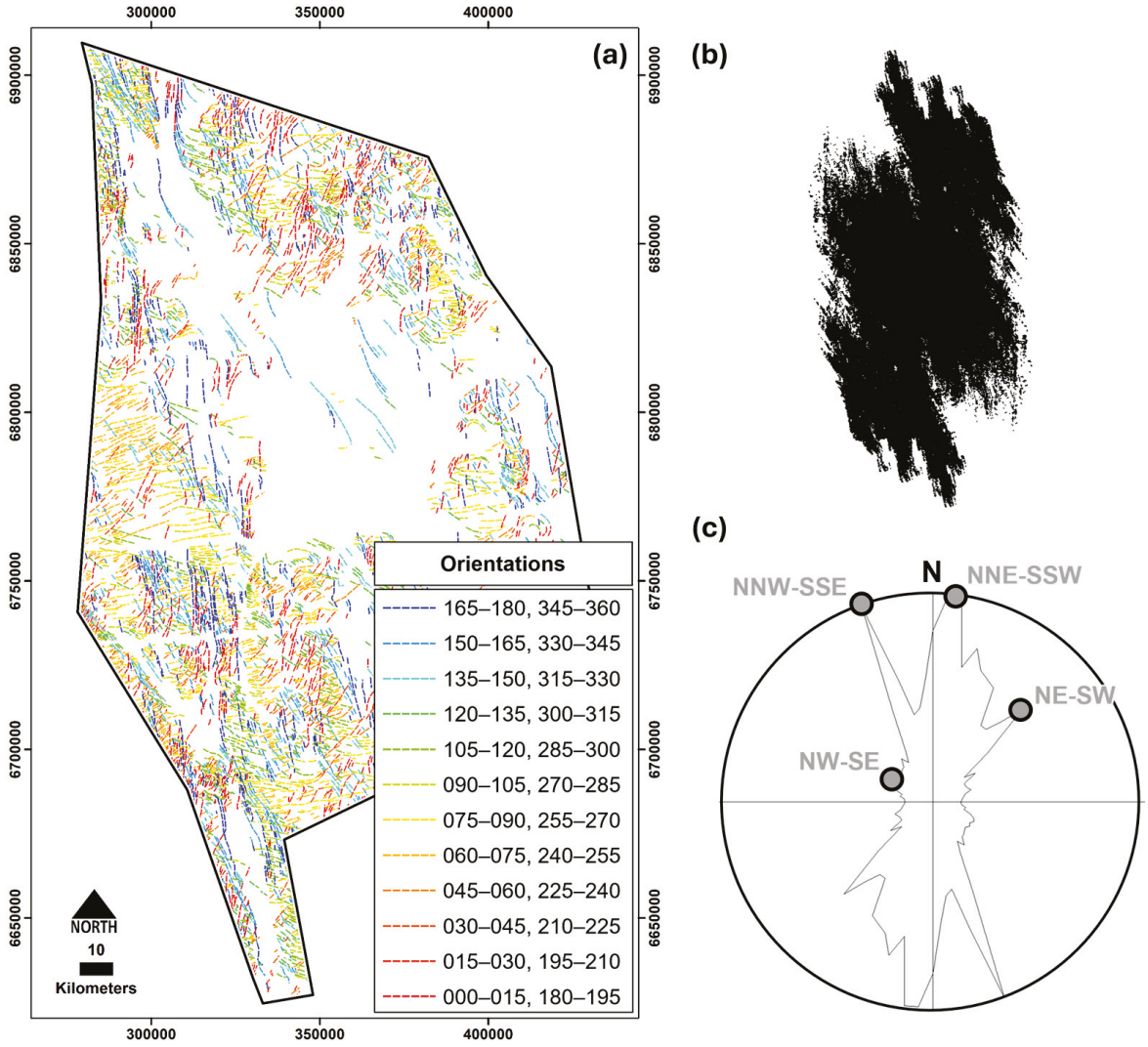


Figure 10. Fry analysis. (**a**) Structural framework and gold occurrences used in the analysis. (**b**) Fry plot showing translations of all gold occurrences (center-to-center distances and directions). (**c**) Rose diagram illustrating frequency distributions and dominant gold occurrence alignments: NNW-SSE, NNE-SSW, NE-SW, and NW-SE.

Lithologically, the study area can be divided into two broad Archean domains (Figure 11), namely felsic to intermediate granite–gneiss, and greenstone terrain. Intrusive rocks dominate, covering ~62% of the study area (plan view). These include large regional and deformed gneissic ('external' or 'basement') granitoid plutons, typically of monzogranitic composition, often delineated by well-defined gravity lows. Smaller 'internal' plutons intruding the greenstone belts range in composition from granitic to gabbroic.

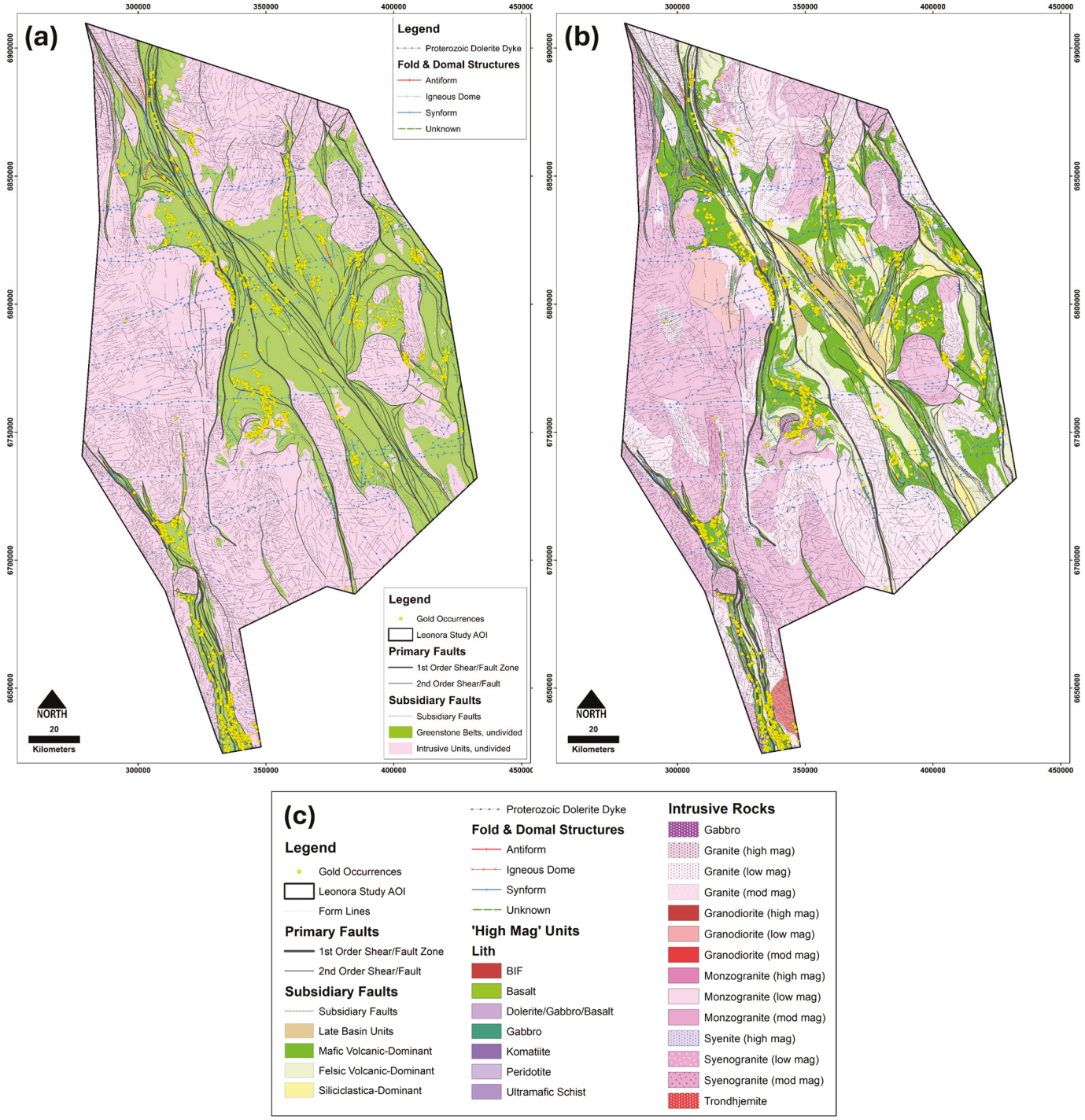


Figure 11. Lithostructural (solid geology) interpretation—final map product. (**a**) Simplified version showing undivided granite and greenstone units. (**b**) Detailed version showing lithological subdivisions. (**c**) Legend for (**b**).

The greenstones, generally associated with gravity highs, are classified into four broad lithological groups: (i) Late basin sequences comprising polymictic to oligomictic conglomerate and sandstone. (ii) Sedimentary siliciclastic sequences consisting of felsic volcaniclastic sandstone, siltstone ± conglomerate, chemical sedimentary rocks, and interleaved felsic volcanic rocks. (iii) Felsic to intermediate volcanic sequences comprising rhyolite to rhyodacite, andesite, felsic volcaniclastic, and siliciclastic rocks ± felsic and mafic volcanic rocks, interleaved with coeval basalt and dolerite. (iv) Mafic to ultramafic volcanic sequences consisting of basalt, komatiite, peridotite, serpentinite, and mafic–ultramafic chlorite, tremolite, and fuchsite-andalusite schists ± coeval dolerite and gabbro. Within all the above sequences are narrow, curvilinear units marked by strong positive magnetic anomalies, typically comprising banded iron formation (BIF), basalt, dolerite, gabbro, komatiite, peridotite, or ultramafic schist.

The study area is also traversed by numerous E-W- to ENE-WSW-striking dolerite intrusions belonging to the Paleoproterozoic (~2408–2401 Ma) Widgiemooltha dyke swarm [107,108] (Figure 11). These dykes are easily identifiable in magnetic datasets due to their strong magnetic contrast and linear geometry. Two groups are distinguished: (i) 2408 ± 3 Ma dykes that produce positive magnetic anomalies and typically strike ~075°, and (ii) 2401 ± 1 Ma dykes that produce negative magnetic anomalies and generally strike ~085°. The contrasting magnetic polarities reflect emplacement during different paleomagnetic regimes. Composed of solidified mantle-derived melts, the dykes are interpreted to have exploited pre-existing crustal heterogeneities, marking deep-seated, mantle-tapping structures of Archean origin that were reactivated during the Proterozoic. Notably, many gold occurrences, particularly the larger deposits, are situated along or within 5 km of the dyke swarm corridors.

6. Targeting Model

Developing an effective targeting model requires careful consideration of several interrelated factors [21,68,109,110]:

- The geological processes responsible for forming the targeted mineral deposit type [20,65,84,111,112].
- The mappable expressions of these processes in available geoscience and exploration datasets [84,113].
- The spatial and temporal scales at which these processes occurred and can be mapped [113,114].
- Geological uncertainty and human bias [65,115].

In this study, we adopted a mineral systems approach to exploration targeting [21], structuring our model around the key processes controlling orogenic gold formation and their corresponding mappable expressions, as summarized in Table 3.

Table 3. Orogenic gold deposit targeting model.

Critical Processes	Constituent Processes	Targeting Criteria (Proxies)	Rationale for Proxies	Proxies Used for MPM
Source	Availability of energy to drive and sustain the mineral system	Source processes related to orogenic Au systems are cryptic in nature: – They operate at the broad regional scale, commonly involve the lower crust and upper mantle, and, thus, are often theorical in nature as are their proxies	Broad consensus exists in terms of orogenic Au systems of the Yilgarn Craton being formed in convergent margin settings, particularly in accretionary orogens, which, if mineralized, involve the following ingredients [34,116,117]: – High-heat flow environment that was sustained by mantle upwelling and associated, deep-seated magmatic processes – Fertile metasomatized upper lithospheric mantle that provided a prolific Au source – Translithospheric plumbing systems that focused magmas and fluids into the upper crust – Geodynamic switches from rifting to arc/back-arc accretion to craton collision that triggered regional extension or shortening events – Chemically important ligands for Au transport, such as hydrosulfide or chloride complexes that were liberated by metamorphic or magmatic devolatilization, respectively – Juvenile input linked to crustal thinning that allowed magmatism to tap younger, mantle-derived sources Ground-preparation is equally important, with mineralized orogens typically comprising the following [11,34,65]: – Lithospheric architecture, including lithospheric discontinuities – Attenuated greenstone belt terrain – Heterogenous strain distribution and steep metamorphic gradients – Large domains of sub-greenschist to lower amphibolite facies of metamorphic grade	Proximity to the following: – Domains of juvenile crust (εNd-values of −0.2 to 2.4) – Regional gravity highs – Greenstone belts – Domains of favorable metamorphic grade (sub-greenschist to lower amphibolite facies)
	Availability of fertile Au source region			
	Availability of melts and fluids to extract Au from source region			
	Availability of ligands to enhance Au solubility			
	Favorable geodynamic/tectonic (“ground-preparation”) history			
Transport	Fundamental translithospheric structures	First-order fault systems	– Serve as melt/fluid pathways – Facilitate Au transfer from the mantle/lower crust into the upper crust	Proximity to the following: – Principal faults – Subsidiary faults – Proterozoic dolerite dykes – Fold hinges – Late basin conglomerates – Flanks of granitoid bodies – Basement granitoids – Granitoid domes – Lithological contacts – Areas of demagnetization – Remotely sensed alteration systems – Domains of high K/Th values (≥95th percentile) – Mafic–ultramafic volcanic rocks – Felsic to intermediate volcanic rocks – Siliciclastic and sedimentary rocks – Internal granitoids – ‘High mag units’ – Known gold occurrences
	Crustal structures	Second-order fault systems	– Serve as melt/fluid pathways – Facilitate Au transfer from the lower into the upper crust	
		Regional folds	– Play an important role as hinge-parallel fluid pathways in fold–thrust belts, in particular anticlinal folds [118]	
		Domes	– Permeability is generally enhanced on flanks, apex, and nose regions of granite-cored domes and provides a focusing mechanism for Au mineralizing fluids	
		Greenstone constriction zones	– Present areas where fault or shear zones converge and greenstone volumes are structurally attenuated	
		Late basins	– Late basins are filled with (highly) permeable conglomerate units – They are typically developed in the hangingwalls of major fault systems	
		Proterozoic dolerite dyke swarms	– Can be traced for hundreds of kilometers and mark deep-seated, mantle-tapping structures, that facilitated the ascent of mantle melts – May represent long-lived, reactivated Archean discontinuities	

Table 3. *Cont.*

Critical Processes	Constituent Processes	Targeting Criteria (Proxies)	Rationale for Proxies	Proxies Used for MPM
Trap	Transient catastrophic rock failure and concomitant structurally controlled, and highly focused fluid flow	Second- and higher-order faults	– Fry analysis indicates that Au deposits have proximity, association, and abundance relationships with NNW-SSE-, N-S- to NNE-SSW-, NE-SW-, and NW-SE-striking faults	Density of the following: – Principal faults – Principal fault intersections – Proterozoic dolerite dykes – Lithological contacts – NNW-SSE- and ENE-WSW-striking gravity ridges – NNW-SSE- and ENE-WSW-striking gravity edges
		Fault irregularities – Dilational or contractional bends/jogs – Fault splays, tips, and wings – En-echelon fracture zones	– Fluid flow within fault zones is controlled by gradients in permeability and hydraulic head, which are highest at fault splays, bends, jogs, and intersections, localities commonly mineralized within orogenic Au systems [119]	
		Structural intersections and intersection density	– Common association between high fracture density and Au mineralization throughout terranes and geological time indicates a fundamental underlying ore control [120] – High-density fracturing is commonly accompanied by enhanced fluid flow during fault–fracture mesh development, producing regional-scale fluid pressure gradients that focus hydrothermal fluids into preferentially fractured areas	
		Fold structures	– Common association between folds and Au mineralization with the location of orogenic Au deposits often controlled by plunging fold hinges, fold noses, or limbs [121] – Truncated folds are particularly favorable structural settings for Au mineralization with many large Au deposits hosted in such settings (e.g., Golden Mile, Timmins, Damang, Callie, Bendigo)	
		Ductile structures – Boudinage – Stretching lineation – Deflections in schistosity	– Boudinage, stretching lineations, and deflections in schistosity have little or no expressions in the available geophysical data and are generally not (comprehensively) recorded in the readily available 1:100,000 or 1:250,000-scale government mapping	
		Competency contrasts	– May give rise to local zones of dilation and permeability, focusing fluid flow at or close to lithological contacts [122] – In the Yilgarn Craton, strong competency contrasts typically exist between greenstone units and internal granitoid/diorite/dolerite dykes, plugs, and stocks	
		Lithological complexity	– Areas of lithological heterogeneity are characterized by geological diversity, which may be expressed, for example, by complex stratigraphic architecture, presence of small stocks, porphyries, or dykes, or occurrence of mantle magmas	
Deposition	Physicochemical destabilization of Au-bearing fluids	Phase separation	– Linked to sudden fluid pressure drops as predicted by the fault–valve model [123]	
		Fluid–rock interaction	– Orogenic Au systems typically form from reduced, near-neutral, low-salinity, CO_2-rich, H_2S-bearing fluids in which Au is transported in the form of $Au(HS)^{2-}$ complexes – Au deposition involves destabilization of these complexes due to fluids interacting with iron-rich rocks to form (arseno-)pyrite [124]	
		Fluid mixing	– Orogenic Au deposits form along geochemical gradients as two or more end-member fluids, at least one of which is Au-bearing, which interact with one another [8,15]	

Table 3. *Cont.*

Critical Processes	Constituent Processes	Targeting Criteria (Proxies)	Rationale for Proxies	Proxies Used for MPM
	Geodynamics	Tectonic setting, crustal depth, and timing of Au deposit formation and post-Au deformation history	– The long-term preservation potential of orogenic Au systems is high because of their late orogenic timing, formation at crustal depths of typically >5 km, and within stable, thick, and buoyant lithospheric blocks [121]	Not used in this study: – The abundance and widespread distribution of Au occurrences is taken to indicate a good degree of preservation across the entire study area
Preservation	Peneplanation and climate	Peneplained, tectonically stable cratonic environments in (semi-) arid climate zones	– Peneplained cratonic blocks in (semi-)arid climate zones like the Yilgarn Craton are characterized by relatively low erosional activity, a factor that promotes the preservation of Au deposits – However, deep weathering (typically 100 to <300 m deep in the Yilgarn Craton) leads to oxidation, creating an upper oxidized and leached zone and a thicker, underlying saprolitic, clay-rich zone [125]	

7. Mineral Potential Modeling (MPM)

7.1. Statistical Evaluation of Predictor Maps

The predictive performance of each predictor map was statistically evaluated using a reference dataset comprising 1773 gold occurrences, referred to as mineral deposit locations (MDLs), and 1773 unmineralized sites, referred to as non-deposit locations (NDLs). The MDLs include gold deposits, occurrences, and mineralized drill intercepts. The NDLs were selected based on the following criteria: (i) spatial randomization; (ii) sufficient distance from known gold occurrences, and (iii) location outside of the gold-permissive tract.

Two statistical methods were applied to assess predictor map performance: (i) the normalized density index (N_d) [126,127], illustrated in prediction-area plots (Figure S1), and (ii) the area under the receiver operating characteristic curve (AUC) [127,128] (Figure S2). Predictor maps meeting the thresholds of $N_d > 1.00$ [126] and $AUC > 0.50$ [128] were considered suitable for inclusion in the MPM process (Table 4).

Table 4. Statistical parameters for the predictor maps as derived from prediction-area plots and receiver operating characteristic curves.

Predictor Map	P_r (%)	O_a (%)	N_d	AUC
Proximity to known gold occurrences	100	0	Infinity	1.000
Proximity to greenstone belts	69	31	2.230	0.965
Proximity to domains of favorable metamorphic grade	69	31	2.230	0.950
Proximity to felsic to intermediate volcanic rocks	59	41	1.440	0.948
Proximity to regional gravity highs	71	29	2.450	0.931
Proximity to mafic–ultramafic volcanic rocks	69	31	2.230	0.922
Proximity to basement granitoids	71	29	2.450	0.858
Proximity to 'high mag units'	66	34	1.940	0.852
Proximity to areas of demagnetization	62	38	1.630	0.851
Proximity to subsidiary faults	66	34	1.940	0.833
Proximity to remotely sensed alteration systems	72	28	2.570	0.824
Proximity to lithological contacts	68	32	2.120	0.800
Proximity to fold hinges	59	41	1.440	0.794
Proximity to internal granitoids	64	36	1.770	0.788
Density of principal faults	61	39	1.560	0.786
Proximity to principal faults	64	36	1.770	0.778
Density of lithological contacts	58	42	1.380	0.758
Density of ENE-WSW-striking gravity ridges	63	37	1.700	0.746
Density of NNW-SSE-striking gravity ridges	59	41	1.440	0.715
Density of principal fault intersections	59	41	1.440	0.700
Proximity to siliciclastic and sedimentary rocks	64	36	1.770	0.691
Density of ENE-WSW-striking gravity lineaments	59	41	1.440	0.669
Proximity to flanks of granitoid bodies	59	41	1.440	0.639
Density of NNW-SSE-striking gravity lineaments	56	44	1.270	0.611
Proximity to domains of juvenile crust (εNd-values of -0.2 to 2.4)	52	48	1.080	0.611
Proximity to domains of high K/Th values ($\geq$95th percentile)	55	45	1.220	0.560
Proximity to Proterozoic dolerite dykes	52	48	1.080	0.537
Density of Proterozoic dolerite dykes	51	49	1.040	0.515

Key to abbreviations: P_r = prediction rate, O_a = prediction area, $N_d = Pr/Oa$, AUC = area under the receiver operating characteristic curve.

7.2. Continuously Weighted Mineral Potential Models

Gold prospectivity in the Leonora district was modeled using three continuous integration techniques: (i) fuzzy gamma [99], (ii) geometric average [100], and (iii) improved index overlay [101]. Predictor maps were weighted using logistic [98] and small fuzzification functions [129,130], producing fuzzy membership scores within the interval [0, 1] for the proxy variables (Figures S5–S36).

The MPM outcomes for the Leonora district, generated from these integration functions, are shown in Figure 12a–c.

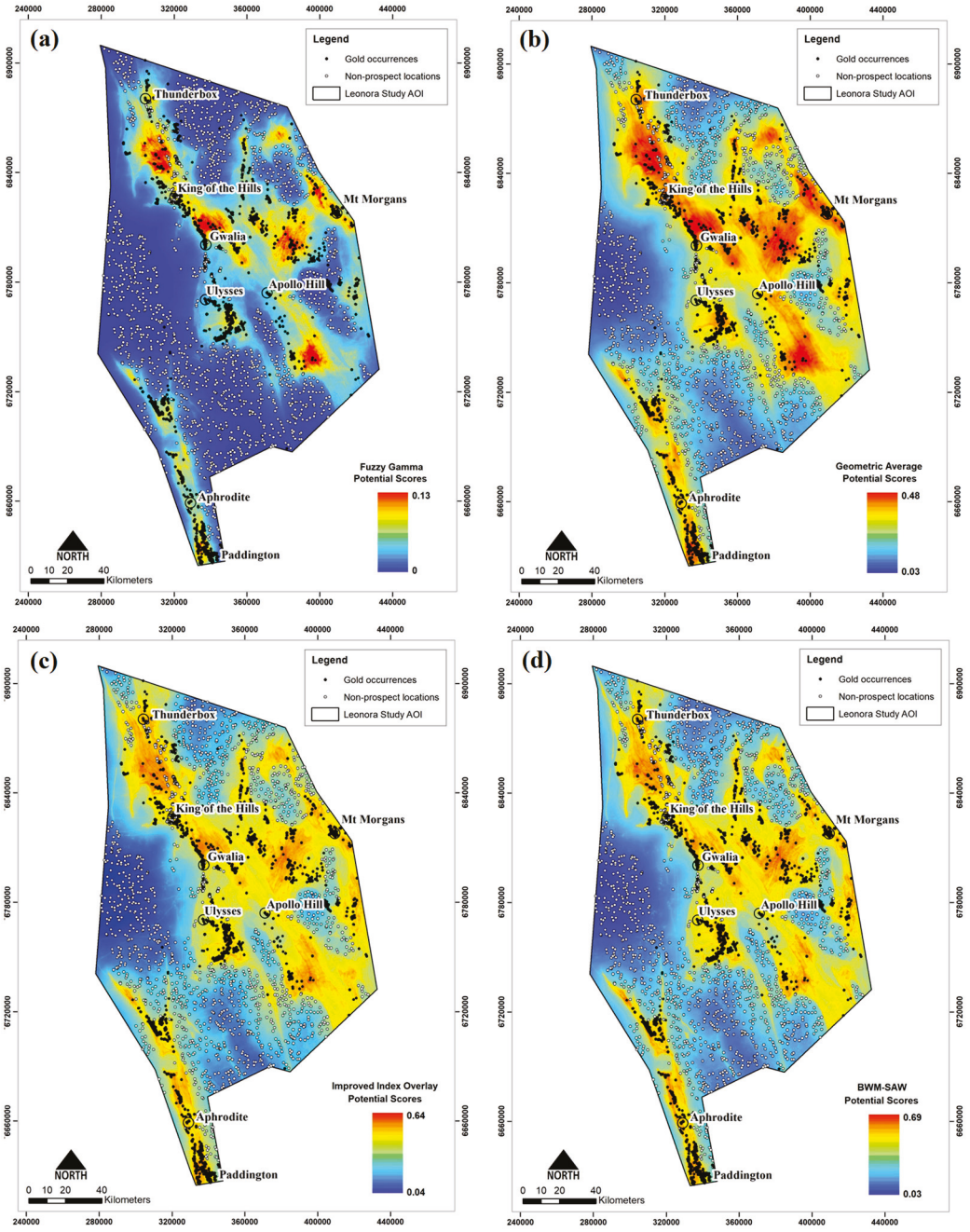


Figure 12. *Cont.*

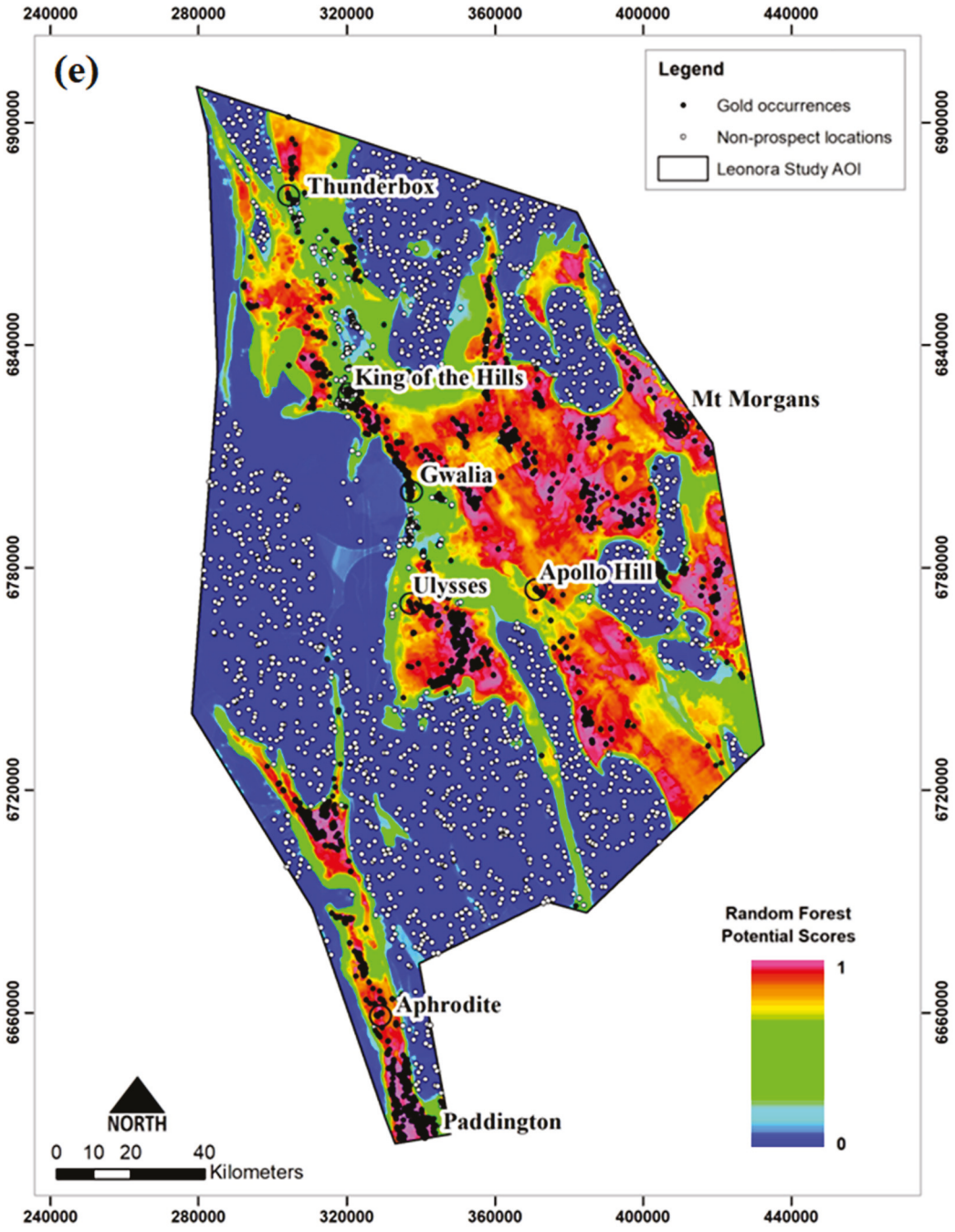


Figure 12. Gold potential maps. (**a**) Fuzzy gamma. (**b**) Geometric average. (**c**) Improved index overlay. (**d**) BMW-SAW. (**e**) Random forest.

7.2.1. Continuous Fuzzy Gamma Model

Continuously weighted fuzzy spatial predictors can be integrated using fuzzy operators [26]. In this study, the fuzzy gamma operator, which combines the *SUM* and *PRODUCT* operators, was applied to achieve fine-tuned calibration of various inputs [131]:

$$\mu_C = [1 - \prod_{i=1}^{n}(1 - \mu_i)]^{\gamma} \times [\prod_{i=1}^{n} \mu_i]^{1-\gamma} \quad (1)$$

For each cell, μ_i represents the fuzzy score of the ith input spatial predictor, and μ_C denotes the resulting potential score obtained through the combination procedure, with

the parameter constrained to the interval $(0 \leq \gamma \leq 1)$. A gamma value of 0.9 was adopted in this analysis.

7.2.2. Geometric Average Technique

The geometric average provides an effective multi-criteria decision-making (MCDM) framework for coherently integrating continuously weighted predictor maps in MPM. Following the mathematical formulation in Equation (2), the geometric average (G_A) for each spatial cell is computed as the nth root of the product of the corresponding proxy values [100]:

$$G_A(F_1, F_2, \ldots, F_n) = \sqrt[n]{\prod_{i=1}^{n} F_i} = \sqrt[n]{F_1 F_2 \ldots F_n} \quad (2)$$

For each spatial cell, n denotes the total number of predictor maps, while F_i represents the fuzzy weight corresponding to the ith predictor map. Equation (2) was adapted to the specific conditions of the study area as follows:

$$G_{Gold}(F_1, F_2, \ldots, F_{28}) = \sqrt[28]{\prod_{i=1}^{28} F_i} = \sqrt[28]{F_1 F_2 \ldots F_{28}} \quad (3)$$

In this formulation, $F_1, F_2, \ldots, F_{28}$ denote the fuzzy scores assigned to the evidential values within their respective predictor maps. After calculating the gold potential value (G_{Gold}) for each unit cell across the study area, the resulting outputs were spatially mapped to construct the geometric average gold potential model.

7.2.3. Improved Index Overlay Model

The Improved Index Overlay is an enhanced form of the data-driven index overlay method applied in both brownfield and greenfield MPM [101]. Unlike conventional or earlier data-driven approaches, this technique assigns weights to each predictor map using a modified Shannon's entropy algorithm, thereby removing dependence on expert judgement or known mineral occurrences. The detailed workflow of this weighting procedure is described in [101]. Using this approach, predictor map weights were objectively determined (Table 5), showing that lithological contact density is the most influential predictor map, whereas proximity to principal faults has the lowest relative significance.

After calculating the predictor map weights via the modified Shannon's entropy algorithm, the maps were integrated using the Improved Index Overlay framework as follows:

$$I_{IO} = \frac{\sum_{i}^{n} W_{vi} W_i}{\sum_{i}^{n} W_i} \quad (4)$$

where for all cells within the study area, I_{IO} denotes the Improved Index Overlay score, W_i represents the weight of the ith predictor map assigned by the entropy algorithm, and W_{vi} corresponds to the continuous cell value of the ith predictor map derived from logistic or small fuzzification functions. In this study, Equation (4) was formulated as follows:

$$I_{IO} = \frac{WV_1W_1 + WV_2W_2 + \ldots + WV_{28}W_{28}}{W_1 + W_2 + \ldots + W_{28}} \quad (5)$$

Here, $W_1, W_2, \ldots, W_{28}$ denote the entropy-based weights of the predictor maps, representing the continuous evidential values assigned to each cell within the respective predictor maps.

Table 5. Predictor map weights as determined by the modified Shannon's entropy method.

Predictor Map	Entropy (*e*)	Normalized Entropy Value (*h*)	Weight (*W*)
Density of lithological contacts	6095	0.0106	0.9894
Proximity to basement granitoids	7645	0.0133	0.9867
Proximity to felsic to intermediate volcanic rocks	8618	0.0150	0.9850
Density of principal fault intersections	14,307	0.0249	0.9750
Density of Proterozoic dolerite dykes	15,560	0.0271	0.9729
Density of principal faults	15,964	0.0278	0.9722
Proximity to greenstone belts	16,756	0.0292	0.9708
Proximity to domains of favorable metamorphic grade	17,192	0.0300	0.9700
Proximity to regional gravity highs	17,325	0.0302	0.9698
Density of NNW-SSE-striking gravity lineaments	18,651	0.0325	0.9675
Density of ENE-WSW-striking gravity ridges	20,723	0.0361	0.9639
Density of ENE-WSW-striking gravity lineaments	20,805	0.0363	0.9637
Density of NNW-SSE-striking gravity ridges	21,253	0.0371	0.9629
Proximity to mafic–ultramafic volcanic rocks	21,418	0.0373	0.9627
Proximity to fold hinges	23,135	0.0403	0.9597
Proximity to siliciclastic and sedimentary rocks	23,344	0.0407	0.9593
Proximity to domains of high K/Th values ($\geq$95th percentile)	23,608	0.0412	0.9588
Proximity to domains of juvenile crust (εNd-values of -0.2 to 2.4)	23,831	0.0415	0.9585
Proximity to internal granitoids	24,255	0.0423	0.9577
Proximity to lithological contacts	24,480	0.0427	0.9573
Proximity to remotely sensed alteration systems	25,084	0.0437	0.9563
Proximity to 'high mag units'	25,400	0.0443	0.9557
Proximity to known gold occurrences	25,649	0.0447	0.9553
Proximity to flanks of granitoid bodies	25,836	0.0450	0.9550
Proximity to areas of demagnetization	25,900	0.0452	0.9548
Proximity to Proterozoic dolerite dykes	26,630	0.0464	0.9536
Proximity to subsidiary faults	26,876	0.0469	0.9531
Proximity to principal faults	27,249	0.0475	0.9525

7.3. Best–Worst Simple Additive Weighting (BWM–SAW) Mineral Potential Model

Among knowledge-driven MPM techniques, multi-criteria decision-making (MCDM) approaches are particularly valued for their efficiency [97,132–135]. In these methods, weights are typically assigned to predictor maps using either matrix-based or comparison-based procedures. Notably, the simple additive weighting (SAW) method [103] and the best–worst method (BWM) [105] are well-established examples of these approaches, both of which have been successfully applied in MPM studies [97,132–135].

In this study, a hybrid MCDM framework, namely BWM–SAW [134], was employed in conjunction with the overall performance (O_p) index [136–138]. The O_p index is derived from an improved prediction-area (P–A) plot incorporating three fundamental criteria: (i) occupied area curve, (ii) NDL prediction rate curve, and (iii) MDL prediction rate curve [136]. The BWM technique was used to objectively quantify the weights of the decision criteria represented by the predictor maps (Table 4). The O_p index then served to determine the weights of the predictor maps and to identify the best and worst predictors (Figure S33, Table 6). Based on these results, the others-to-worst (OW) and best-to-others

(BO) vectors were established (Tables S1 and S2) according to the O_p values listed in Table 6. The optimal weights $(W_1^*, W_2^*, \ldots, W_n^*)$ and ξ^* were obtained by solving the following problem [134]:

$$\begin{aligned} &\min \xi \\ &\text{s.t.} \\ &\left|W_B - a_{Bj} W_j\right| \le \xi, \text{ for all } j \\ &\left|W_j - \mathrm{a}_{jW} W_W\right| \le \xi, \text{ for all } j \\ &\sum_j W_j = 1 \\ &W_j \ge 0, \text{ for all } j \end{aligned} \tag{6}$$

where a_{Bj} represents the precedence of the best decision criterion B over the decision criterion j, a_{jW} demonstrates the precedence of the decision criterion j over the worst decision criterion W, and ξ^* is the optimal consistency value. For this study, Problem (6) was formulated as shown in Equation (7):

$$\begin{aligned} &\min \xi \\ &\text{s.t.} \\ &|W_1 - 2W_2| \le \xi, \text{ for all } j \\ &|W_1 - 2W_3| \le \xi, \text{ for all } j \\ &|W_1 - 2W_4| \le \xi, \text{ for all } j \\ &\quad \vdots \\ &|W_1 - 9W_{28}| \le \xi, \text{ for all } j \\ &|W_2 - 5W_{28}| \le \xi, \text{ for all } j \\ &|W_3 - 5W_{28}| \le \xi, \text{ for all } j \\ &|W_4 - 5W_{28}| \le \xi, \text{ for all } j \\ &\quad \vdots \\ &|W_{27} - 2W_{28}| \le \xi, \text{ for all } j \\ &\sum_j W_j = 1 \\ &W_j \ge 0, \text{ for all } j \end{aligned} \tag{7}$$

Table 6. Improved prediction-area plot parameters for the effective predictor maps.

Effective Predictor Maps	**Parameters**						
	P_m	P_n	$100 - P_m$	$100 - P_n$	TP_r	FP_r	O_p
0to known gold occurrences (DC_1)	100	46	0	54	1	0.46	0.54
Proximity to regional gravity highs (DC_2)	71	43	29	57	0.71	0.43	0.28
Proximity to basement granitoids (DC_3)	71	43	29	57	0.71	0.43	0.28
Proximity to greenstone belts (DC_4)	69	42	31	58	0.69	0.42	0.27
Proximity to domains of favorable metamorphic grade (DC_5)	69	43	31	57	0.69	0.43	0.26
Proximity to mafic–ultramafic volcanic rocks (DC_6)	69	44	31	56	0.69	0.44	0.25
Proximity to subsidiary faults (DC_7)	66	42	34	58	0.66	0.42	0.24
Proximity to remotely sensed alteration systems (DC_8)	72	48	28	52	0.72	0.48	0.24
Proximity to 'high mag units' (DC_9)	66	43	34	57	0.66	0.43	0.23
Proximity to principal faults (DC_{10})	64	43	36	57	0.64	0.43	0.21
Proximity to lithological contacts (DC_{11})	68	47	32	53	0.68	0.47	0.21
Density of ENE-WSW-striking gravity ridges (DC_{12})	63	45	37	55	0.63	0.45	0.18

Table 6. *Cont.*

Effective Predictor Maps	Parameters						
	P_m	P_n	$100 - P_m$	$100 - P_n$	TP_r	FP_r	O_p
Proximity to internal granitoids (DC_{13})	64	47	36	53	0.64	0.47	0.17
Density of principal faults (DC_{14})	61	45	39	55	0.61	0.45	0.16
Proximity to siliciclastic and sedimentary rocks (DC_{15})	64	48	36	52	0.64	0.48	0.16
Proximity to areas of demagnetization (DC_{16})	62	46	38	54	0.62	0.46	0.16
Proximity to fold hinges (DC_{17})	59	47	41	53	0.59	0.47	0.12
Proximity to felsic to intermediate volcanic rocks (DC_{18})	59	48	41	52	0.59	0.48	0.11
Density of NNW-SSE-striking gravity ridges (DC_{19})	59	48	41	52	0.59	0.48	0.11
Density of ENE-WSW-striking gravity lineaments (DC_{20})	59	48	41	52	0.59	0.48	0.11
Density of principal fault intersections (DC_{21})	59	48	41	52	0.59	0.48	0.11
Proximity to flanks of granitoid bodies (DC_{22})	59	48	41	52	0.59	0.48	0.11
Density of lithological contacts (DC_{23})	58	49	42	51	0.58	0.49	0.09
Density of NNW-SSE-striking gravity lineaments (DC_{24})	56	49	44	51	0.56	0.49	0.07
Proximity to domains of juvenile crust (DC_{25})	52	47	48	53	0.52	0.47	0.05
Proximity to domains of high K/Th values (DC_{26})	55	50	45	50	0.55	0.5	0.05
Proximity to Proterozoic dolerite dykes (DC_{27})	52	50	48	50	0.52	0.5	0.02
Density of Proterozoic dolerite dykes (DC_{28})	51	51	49	49	0.51	0.51	0.00

Key to abbreviations: P_m = hits, P_n = false alarms, 100-P_m = misses, 100-P_n = correct rejections, TP_r = true positive rate, FP_r = false positive rate, O_p = overall performance, DC = decision criterion.

Optimal weights $(W_B^*, W_1^*, \ldots, W_W^*)$ and ξ^* were obtained by solving Equation (7) (Table S3). For $a_{BW} = a_{13} = 9$, the resulting consistency index was 5.23 [134], and the consistency ratio $0.009/5.25 = 0.002$, indicating excellent consistency. Following the assignment of predictor weights, the SAW method was applied to rank all decision alternatives. A decision matrix $B_{1201497 \times 28}$ was built comprising 1,201,497 decision alternatives, each corresponding to a cell within the predictor maps, and 28 decision criteria. Alternatives were ranked via the step-by-step SAW procedure described by [134]. The resulting BWM-SAW gold potential model for the Leonora district is shown in Figure 12d.

7.4. Random Forest (RF) Mineral Potential Model

An increasing number of recent studies have demonstrated the effectiveness of RF-based MPM, consistently showing its superior performance compared to a wide range of previously applied supervised machine learning techniques [66,69,86,138–143]. The enhanced performance of RF is largely due to its ability to mitigate overfitting and improve predictive accuracy through the bootstrap aggregation (bagging) approach [102]. RF is an ensemble-based machine learning algorithm that generates multiple random subsets of training data, each used to construct an unpruned decision tree [102]. In this framework, bootstrapping with replacement is applied to the spatial proxy values at mineral deposit and non-deposit locations (labeled data). Approximately two-thirds of the labeled data (in-bag samples) are used to train each tree, while the remaining out-of-bag (OOB) samples are used to estimate model error and impurity. In summary, the RF model represents an ensemble of unpruned decision trees, each built from distinct training subsets that capture different underlying patterns (existent patterns).

The implementation of RF requires specifying two main hyperparameters: (i) the number of decision trees (n) in the ensemble and (ii) the number of predictor variables (m) considered at each node split [102]. In this study, n = 1000 and m = 9 were adopted follow-

ing the procedure outlined in [139]. The relative importance of predictor variables was quantified using the mean decrease in the Gini impurity index (M_G) and the mean decrease in accuracy (M_a). The M_G index measures each variable's contribution to improving node homogeneity and, consequently, the model's overall discriminative power. M_a, on the other hand, is derived from OOB error, and reflects accuracy-based predictor relevance. As noted by [102], higher M_a and M_G values indicate greater predictor importance. Figure S34 shows the relative significance of predictor variables in the RF model: Proximity to volcanic rocks of felsic to intermediate composition is the least significant predictor, whereas proximity to juvenile crust (based on M_a) and proximity to basement granitoids (based on M_G) are the most significant.

Figure 12e presents the RF-based gold potential model generated from 27 validated fuzzified predictor maps (Figures S5b–S31b), excluding the "proximity to known gold occurrences" map to minimize exploration bias. The associated training error curve (Figure S35) shows a steady decline in model error with an increasing tree number, from an initial mean squared error of ~0.065 for the first tree to about 0.028 at the 1000th iteration.

8. Discussion

8.1. Geological and Structural Implications

One of the key geological observations in this study is that gold occurrences display proximity, association, and abundance relationships with structures oriented orthogonally or at high angles to the dominant NNW-SSW grain of the terrane- and domain-bounding fault systems and regional schistosity within the greenstone belts.

Notably, a spatial relationship was observed between gold occurrences, particularly the larger deposits, and E-W-striking magnetic edges, which correspond to geological features such as Proterozoic dolerite dyke corridors (Figure 8). A similar relationship was reported by Isles et al. [144] for the Yilgarn Craton as a whole, where most major gold districts exhibit "intriguing spatial associations" with Proterozoic dykes. Isles et al. interpreted this association as evidence that the dykes occupy much older planes of weakness formed prior to, or contemporaneous with, Archean gold mineralization. We concur with this interpretation and suggest that Proterozoic dyke swarms, which can be easily traced in magnetic and gravity data, delineate important yet cryptic basement structures, some of which, or segments thereof, likely played a critical role in localizing gold mineralization. This interpretation is supported by spatial statistical analyses conducted in this study, which yielded $AUC > 0.52$ and $N_d > 1.04$ for predictor maps representing Proterozoic dolerite dyke proximity and density (Table 4). Following published criteria [126,128], any predictors with $AUC > 0.50$ and $N_d > 1.00$ are considered statistically valid, confirming a meaningful spatial relationship between gold occurrences and Proterozoic dolerite dykes, or, more precisely, the structures that host them.

Secondly, we identified N-S, E-W, NE-SW, and NW-SE structural trends, represented by subsidiary, late-tectonic (likely $D_{4/5}$), low-displacement faults and fractures that are oblique or orthogonal to the dominant NNW-SSW structural grain. Fry analysis revealed similar directions of maximum gold occurrence alignment, suggesting that these structures exerted significant control on gold localization. Some coincide with NE-SW- and NW-SE-striking low-displacement faults and fractures interpreted by [145], termed Perkins Discontinuities. These planar boundaries mark abrupt terminations of mineralization continuity, typically observed at hand-sample to deposit scales. According to [145], the Perkins Discontinuities identified at the Aphrodite deposit and surrounding area predate mineralization, resulting in an asymmetric gold distribution across these typically unmineralized faults and fractures. A detailed lithostructural interpretation of the Bardoc area by [146] showed that Aphrodite lies within a ~5 km wide, NE-SW-striking corridor defined by a series of fractures and

low-displacement (<100 to 300 m) dextral faults (Figure 13). These structures, together with less common NW-SE-striking ones, cut obliquely across the dominant NNW-SSE trend of the Bardoc Tectonic Zone. Deposit-scale studies at Aphrodite reported cross-structures of similar orientation, including the NW-SE-striking, moderately NE-dipping Epsilon orebody [50] and numerous, weakly mineralized ENE-WSW (070°) and WNW-ESE (130°)-striking quartz–carbonate ± pyrite veins [50,147]. We infer that the intersection of the dominant NNW-SSE trend with subordinate NE-SW (±22.5°) and NW-SE (±22.5°) structures created a high-permeability network that strongly influenced gold localization, not only at Aphrodite but also in other areas where similar structural interactions occur. Further detailed studies across multiple scales and sites are required to better constrain the role of these cross-structures in controlling gold mineralization and ore geometry.

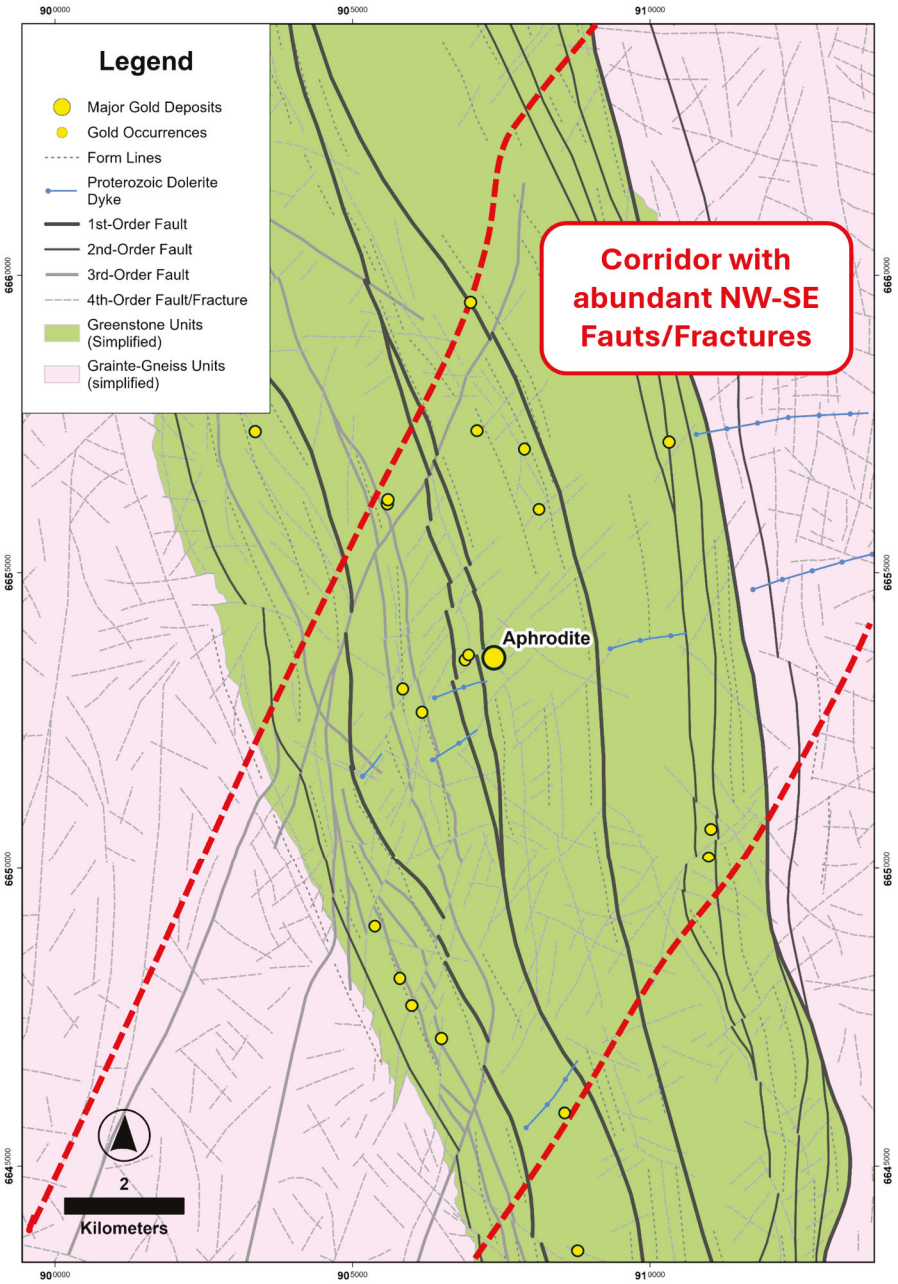


Figure 13. Location of the Aphrodite gold deposit cluster within a ~5 km wide, NE-SW-striking corridor defined by a series of fractures and low-displacement (<100 to 300 m) faults exhibiting apparent dextral kinematics.

8.2. Geophysical and Remote Sensing Implications

Magnetic and gravity data are the most widely used and available geophysical datasets for regional targeting of orogenic gold mineralization in the Yilgarn Craton. Greenstones typically exhibit strong magnetic and density contrasts relative to the surrounding granites. High-resolution magnetic data effectively map greenstone belt fabrics, with fabric-parallel features commonly representing faults, shear zones, or stratigraphic boundaries. In contrast, 'cross-fabric' features, widespread across the craton, most often correspond to cross-cutting fault–fracture systems or mafic dykes. Gravity data, though generally of coarser resolution, remain useful for delineating greenstone distribution, relative thicknesses, and major cross-structures. The main objective of the semi-automated geophysical filtering in this study was to highlight geological features in a consistent and relatively unbiased manner. This was achieved is by extracting features of specific orientations (Figures 6–8), as different orientations often correspond to distinct deformation styles or events. The phase congruency algorithm extracts features in eight different orientations (0°, 22.5°, 45°, 67.5°, 90°, etc.), which can then be combined to highlight particular structural trends. For example, the fabric-parallel features in Figures 6a, 7a and 8a were produced by combining the 0° and 167.5° orientations to highlight NNW-SSE to N-S trends, typically corresponding to belt-parallel fault or shear zones and stratigraphic contacts. Gold-bearing structures are generally parallel the host greenstone fabric, whereas cross-structures influence grade continuity and distribution. Isolating these structural types separately enhanced targeting effectiveness. Importantly, the phase congruency method is relatively amplitude-independent, allowing subtle features to be detected, which is critical since orogenic gold systems are not always associated with strongly magnetic bodies. Rather, their geophysical signatures vary widely due to differences in host rocks, structural settings, mineralization styles, ore minerals, and alteration assemblages.

Direct detection of unweathered orogenic gold systems using Sentinel-2 data is challenging. Pyrite, a common alteration mineral phase, cannot typically be detected through satellite remote sensing. However, Sentinel-2 can detect its weathering products, such as goethite and jarosite [81,148]. Pyrite oxidation generates acidic conditions that promote clay formation during silicate weathering [149]. Given the extensive weathering and oxidation of the Yilgarn Craton [150], any exposed gold mineralization is expected to be associated with ferric iron phases and clays. In the study area, zones showing coincident highs in goethite, clay, and IFD indices correlate well with known mineralization. While single remote sensing products often yields many false positives, this issue was reduced using a CMY ternary combination of the goethite, clay, and IFD indices. This approach efficiently and accurately highlights areas with coincident anomalies while automated extraction minimizes interpreter bias or inconsistency. The main limitation of this method, however, is that Sentinel-2 can only detect surface mineralization. Any significant cover will obscure signals from underlying rocks.

8.3. Mineral Potential Modeling (MPM) Implications

8.3.1. Predictor Map Performance

The significance of predictor maps in MPM can be viewed from two complimentary perspectives. In the pre-modeling stage, emphasis is placed on identifying and selecting the most effective predictor maps for integration into a potential model (Table 4). In the post-modeling stage, predictor maps are ranked according to their relative contribution to the prediction of potential values (Figure S34). Careful selection of high-performing predictor maps prior to modeling minimizes systemic uncertainty and ensures that the model is based on robust and geologically meaningful variables. Conversely, post-modeling evaluation allows the exclusion of predictors with limited or negligible predictive capacity, refining subsequent model iterations. This iterative process enhances the overall efficiency

and robustness of the modeling framework while enabling a comparative assessment of successive models to evaluate the sensitivity of results to predictor map selection.

It is strongly recommended to use a combination of statistical analysis tools to identify the most effective predictor maps and quantify their contribution to potential value prediction. Using multiple performance metrics enables a more accurate comparison, differentiation, and informed decisions regarding the retention or exclusion of predictor maps. For example, both the "proximity to fold hinges" (predictor M1) and "proximity to flanks of granitoid bodies" (predictor M2) maps achieved identical N_d scores of 1.440. However, their *AUC* scores distinguish them, with M1 scoring ~1.24 times higher than M2. Relying solely on the N_d index would not have revealed this difference, whereas incorporating *AUC* clearly demonstrated the superiority of M1. Similarly, as shown in Figure S34, the predictor map for "proximity to areas of demagnetization" ranks 21st by M_a, but 9th by M_G. To achieve more precise and robust comparisons, it is advisable to integrate additional performance metrics, such as entropy or information gain.

8.3.2. Multi-Technique Approach

The robustness of MPM is highly dependent on the quality of the underlying genetic model and the accurate translation of key genetic processes into mappable targeting criteria. Since the conceptual model forms the core of the MPM process, most stochastic uncertainty arises from inappropriate selection of predictor maps. Although these issues can be reduced through mineral systems modeling, both systemic and stochastic uncertainties can be further mitigated by adopting a multi-technique approach to MPM. This approach (i) ensures optimal use of available empirical and conceptual information, (ii) allows comparison, contrast, and cross-validation of MPM results, and (iii) better constrains exploration targets by integrating outputs from diverse numerical models [69,114]. As demonstrated in [69,86,97], a multi-technique MPM strategy not only yields more robust exploration targets but also provides insights unattainable through any single modeling technique, while contributing to the development and calibration of new analytical tools and techniques.

In addition to these advantages, combining multiple techniques with the development of diverse gold potential models (Figure 12) also enables the assessment of model performance. To this end, we applied the improved P-A plot procedure of Roshanravan et al. [136]. Based on Figure S36 and the performance statistics reported in Table 7, the RF algorithm to MPM delivered the best-performing gold potential model for the study area (overall performance, O_p = 0.52) (Figure 12e). Notably, the RF-derived potential model exhibits distinct spatial patterns compared to those produced by the other techniques (Figure 12). This variation, which enhances prediction reliability in this study, reflects an intrinsic property of the RF algorithm: namely, its ensemble of regression trees generated through bootstrap sampling, with final predictions derived from the average outputs, thereby reducing variance and improving robustness.

Table 7. Improved prediction-area (P-A) plot parameters for the different gold potential models.

	Fuzzy Gamma	**Geometric Average**	**Improved Index Overlay**	**BWM-SAW**	**RF**
P_m (Hits)	77	78	79	88	88
P_n (False Alarms)	42	43	42	41	36
$100-P_{\mathrm{m}}$ (Misses)	23	22	21	12	12
$100-P_{\mathrm{n}}$ (Correct Rejection)	58	57	58	59	64
True Positive Rate (TP_r)	0.77	0.78	0.79	0.88	0.88
False Positive Rate (FP_r)	0.42	0.43	0.42	0.41	0.36
Overall Performance (O_p)	0.35	0.35	0.37	0.47	0.52

8.3.3. Predictor Map Sensitivity

Several predictor maps used in this study have the potential to introduce bias into the MPM because they (i) represent 'self-fulfilling prophecies' (e.g., proximity to gold occurrences) that artificially enhance prospectivity near known deposits; (ii) show interdependencies with other predictors (e.g., proximity to greenstone belts or granitoid flanks) due to spatial overlap; (iii) are ineffective in areas of cover (e.g., proximity to remotely sensed alteration systems or domains of high K/Th values) where signals fail to penetrate the regolith; and/or (iv) do not uniformly or objectively represent the entire study area (e.g., proximity to fold hinges) owing to inconsistent mapping scales or data resolutions.

Given that such biases can significantly affect outcomes [114], we assessed model sensitivity to selected predictor maps. Specifically, we used the best-performing RF approach to generate two alternative gold potential maps for the study area by varying the number and type of input predictors: Alternative RF Model 1, excluding proximity to (a) gold occurrences, (b) greenstone belts, (c) granitoid flanks, (d) fold hinges, (e) remotely sensed alteration systems, and (f) high K/Th domains; and Alternative RF Model 2, excluding only (a) to (c). Both models achieved an excellent overall performance (O_p) ranging from 0.49 (Alternative RF Model 1) to 0.54 (Alternative RF Model 2), comparable with or slightly exceeding that of the original RF model (O_p = 0.52). The results are not only statistically but also visually similar, with minimal discernible differences between the original and alternative RF-derived gold prospectivity maps (Figure 14).

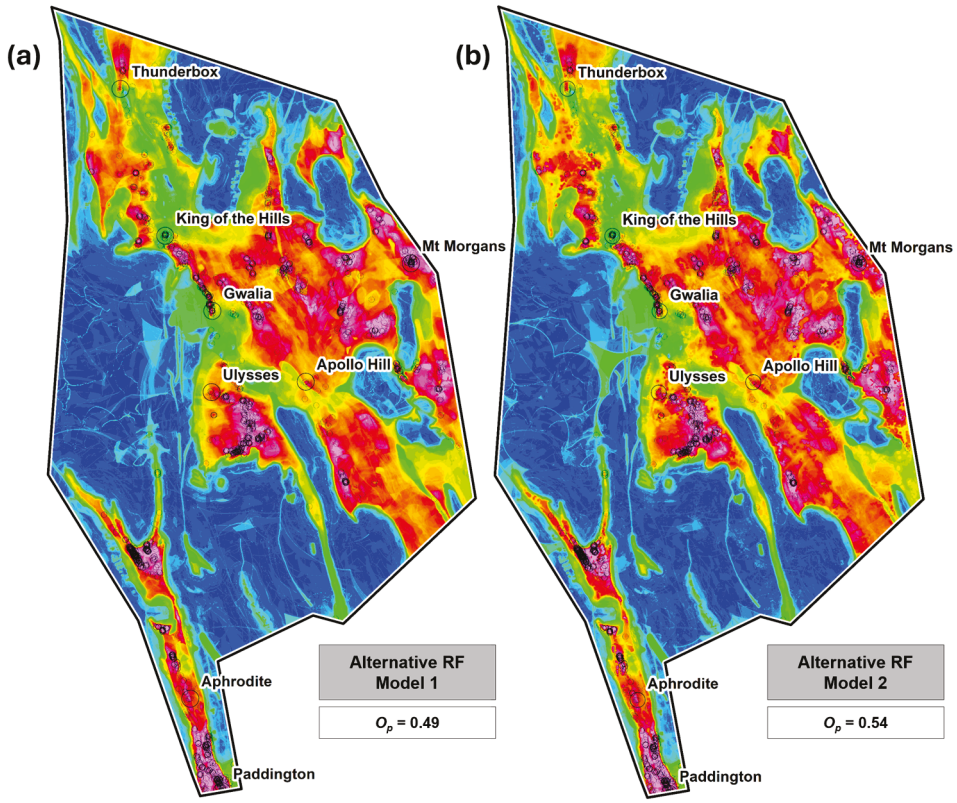


Figure 14. Alternative random forest (RF) gold prospectivity models generated to test sensitivity and performance with respect to selected predictor maps. (**a**) Alternative RF Model 1 excludes proximity to known gold deposits, greenstone rocks, remotely sensed alteration systems, fold hinges, granitoid flanks, and domains with high K/Th. (**b**) Alternative RF Model 2 proximity to known gold deposits, greenstone rocks, and granitoid flanks. Overall performance (O_p) values of the alternative models are comparable to, and for (**b**), even higher than the O_p of the original RF model. See text for details and Figure 12e for a color legend.

8.3.4. Using Fractal Thresholding for Target Generation

The concentration-area (C-A) fractal technique [151], a well-established method for classifying continuous spatial data [66,101,127,134,152–154], was applied to prioritize areas of gold potential derived from the best-performing RF model. Two thresholds (Figure S37), representing major slope changes and corresponding to higher potential scores and data populations more strongly associated with mineralization, were identified at 0.830 (2nd-order target areas) and 0.958 (1st-order target areas). These thresholds were used to generate a ternary-class exploration targeting map, categorizing model outputs into domains of high, moderate, and low gold potential (Figure 15). The delineated target areas show a strong spatial correlation with known gold occurrences and key predictors in the underlying genetic and targeting models for orogenic gold systems. As shown in Figure 15, the prioritized high-potential (1st order) target areas represent an order-of-magnitude (>13 times) reduction in search space, a hallmark of a robust, practically effective targeting method [114].

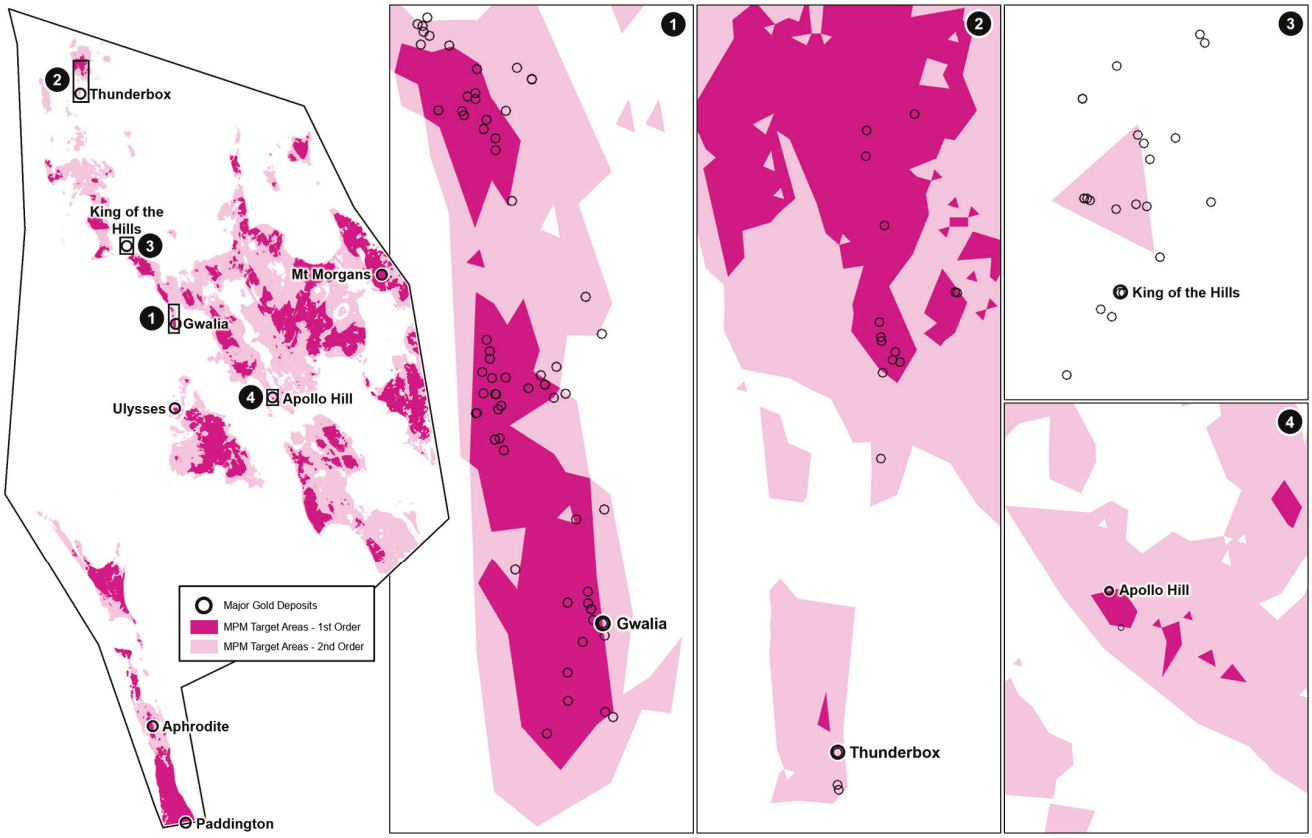


Figure 15. Map of prioritized MPM target areas showing the major gold deposits within the study area. Insets provide detailed views of selected areas.

Beyond delineating high-priority targets, the MPM results served three additional purposes: (i) providing context and constraints for prioritizing future gold exploration, (ii) identifying the most prospective ground held by competitors to inform potential investment, acquisition, or joint-venture opportunities, and (iii) supporting the monitoring of mineral tenement status and identification of new vacant ground for acquisition.

8.4. Targeting Implications

8.4.1. Role of MPM as a Targeting Tool

Since its inception in the late 1960s and early 1970s [113], MPM has evolved significantly, both methodologically and as an effective targeting tool. According to [85], while

methodological and technological advances have been comprehensively addressed and widely published, practical applications of MPM remain limited in the literature, aside from the presentation of mineral potential maps. Notable case studies where modeling results were used for further analysis or where comprehensive targeting models and quality targets were developed include [69,85,86,95,155–159].

As summarized by [69], the 2020 discovery of the Gonneville Ni-Cu-PGE deposit, located ~70 km northeast of Perth, Western Australia (Figure 1), represents the first world-class discovery that is, at least partly, attributable to MPM, validating its effectiveness as a targeting tool and providing proof-of-concept for this technology. The greenfield discovery, made by Chalice Mining Limited [160], was guided by a Ni-Cu-PGE prospectivity map produced by Geoscience Australia [161], which also opened up an entirely new search space for such orthomagmatic sulfide deposits along the >1000 km long, underexplored western margin of the Archean Yilgarn Craton.

Despite their capabilities, MPM-generated prospectivity maps do not guarantee discovery success and should not be viewed as 'treasure maps'. Instead, they serve as starting points for 'treasure hunts'. MPM is best regarded as another tool within the 'exploration toolbox', specifically, a decision support tool for delineating, ranking, and prioritizing exploration targets based on modeled prospectivity. It is also important to recognize that prospectivity maps represent a snapshot in time, reflecting both the current conceptual understanding of the targeted mineral deposit type and the quality and availability of supporting data at the time of modeling. As new or improved data become available, results will invariably change, typically for the better [66].

8.4.2. Assessment of MPM Target Areas

The RF model, the best-performing MPM approach in this study, identified all large (>1 Moz) gold deposits and deposit clusters in the study area, including Paddington, Gwalia, Mt Morgans, Tarmoola/King of the Hills, Thunderbox, Apollo Hill, Aphrodite, Ulysses, and Menzies (Figures 14 and 15). It also correctly delineated most smaller gold occurrences, with 83.93% of deposits within anomalies covering only 7.69% of the total area [86,140,162]. This demonstrates the excellent predictive performance of the RF model.

Areas modeled as having high gold potential, but lacking known occurrences and exhibiting the same mappable features as mineralized zones, clearly warrant further investigation, particularly where underexplored. One way to assess exploration maturity is to examine existing exploration data, especially drilling records as drilling provides the most definitive subsurface test. Reverse circulation and diamond core holes are particularly informative. Areas with a high drilling density typically indicate intensive exploration and a good understanding of subsurface geology, making the presence of undiscovered deposits unlikely. In contrast, areas with sparse or shallow drilling (<100 m) may remain underexplored.

Open-file drilling data were obtained primarily from the Geological Survey of Western Australia (GSWA) and supplemented by confidential data provided by St Barbara Limited (SBM) (Table 2). The GSWA database includes over 231,000 records, while the SBM dataset comprises more than 77,000 records (Table 8), with some overlap between them. The GSWA records are open-file only, meaning confidential holes are excluded. Despite these limitations, the combined datasets provide a reasonably complete picture of drilling within the study area. Although, the greenstone belts may appear well tested at first glance (Figure 16b), this impression changes when only reverse circulation and diamond drill collars are plotted. The resulting map reveals that large portions of the greenstone belts remain untested at depth (Figure 16c).

Table 8. Summary statistics for the open-file Geological Survey of Western Australia (GSWA) and confidential St Barbara Limited (SBM) drill hole databases.

Parameters	GSWA Database	SBM Database	Comments
Number of drill holes	231,760	77,675	
Main hole type			
RC	84,078 (36%)	19,874 (26%)	Only 39% of all drill holes completed in the study area are RC or DD holes, whereas 56% represent geochemical drill holes comprising RAB, AC, and AUG holes.
RAB	62,377 (27%)	43,180 (56%)	
AC	52,905 (23%)	8875 (11%)	
AUG	14,276 (6%)	889 (1%)	
DD	7043 (3%)	1827 (2%)	
Other	11,081 (5%)	3030 (4%)	
Hole depth—all drill holes			
Min	0.0 m	0.0 m	The median value demonstrates that 50% of all drill holes completed in the study area have hole lengths of only 39 m or less.
Max	2895.6 m	2895.6 m	
Median	39.0 m	36.0 m	
Mean	50.5 m	53.9 m	
Hole depth—RC holes			
Min	0.0 m	0.0 m	Of the 80,078 RC holes in the GSWA database, 31,713 (~40%) targeted Au whilst 32,666 (~41%) targeted Ni ± Co; the remaining holes targeted mostly base metals ± Au.
Max	1043.1 m	624.6 m	
Median	41.0 m	69.0 m	
Mean	53.1 m	81.3 m	
Hole depth—DD holes			
Min	0.0 m	6.0 m	Of the 7043 DD holes in the GSWA database, 3511 (~50%) targeted Au ± Ag, Ni; the remaining holes targeted mostly base metals ± Au.
Max	2895.6 m	2895.6 m	
Median	211.9 m	220.0 m	
Mean	292.8 m	403.0 m	

Key to abbreviations: AC = aircore; AUG = auger; DD = diamond core; RAB = rotary air blast; RC = reverse circulation.

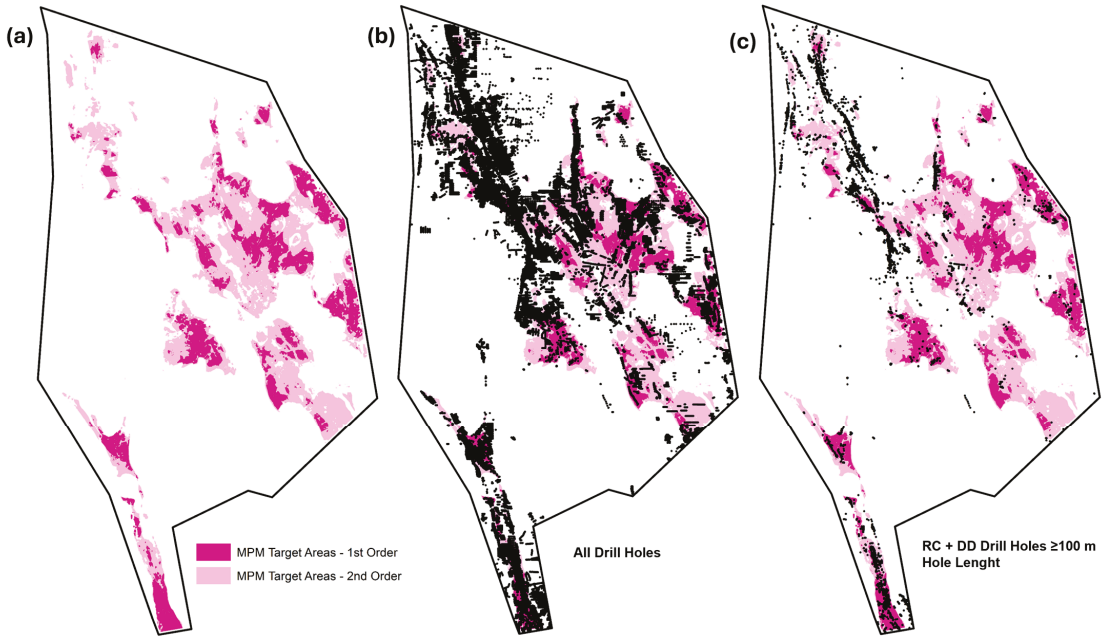


Figure 16. Prioritized MPM target areas (**a**) overlain with the collars of all open-file drill holes (**b**) and the collars of reverse circulation (RC) and diamond core (DD) holes ≥100 m in length. Each black dot represents a drill collar location. Map (**c**) shows that many high-priority areas remain poorly tested or untested by bedrock drilling, particularly below vertical depths of ~90 to 100 m.

Our review of previous drilling (Figure 17) identified six broad areas of high gold potential with relatively low drill hole densities, particularly when considering only reverse circulation and diamond core drill holes ≥100 m in length. These areas exhibit many of the targeting criteria outlined in Table 4 and, therefore, represent attractive exploration targets.

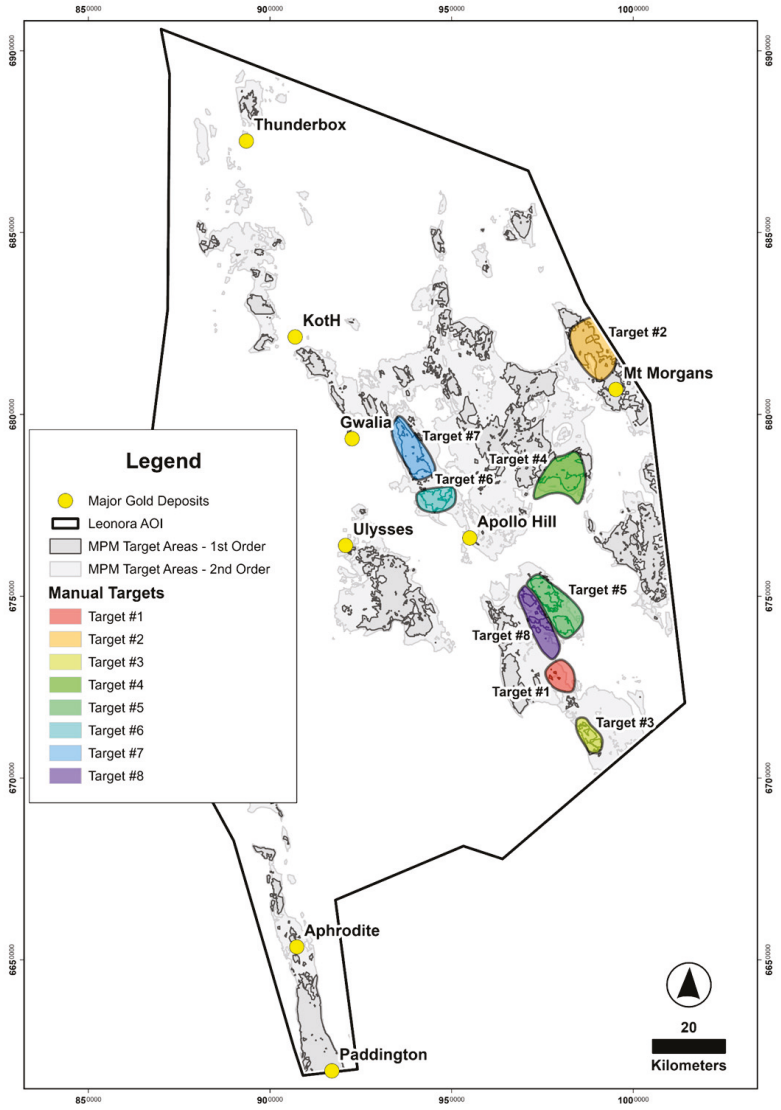


Figure 17. 'Manual targets' generated from prioritized MPM target areas. Target descriptions are given in Table 9.

A manual analysis [95,163] delineated eight discrete targets within the broader prioritized MPM target areas (Table 9; Figure 17). With one exception, all manual targets are located along NNW-SSE-trending, '800 m scale' gravity ridges, features that map thicker portions of greenstone belts and commonly coincide with significant gold deposits. As shown in Figure 6, many large gold deposits occur on or near these 800 m scale NNW-SSE-trending ridges.

The two highest ranked manual targets are particularly noteworthy:

- Target #1: This target covers a cluster of poorly tested intrusions of the McAuliffe Well Syenite, which intruded mafic volcanic-dominated greenstone sequences, abut the first-order Keith–Kilkenny fault system, and are crosscut by E-W- to NW-SW-striking dolerite dykes. Shallow rotary air blast (RAB) drilling by Saracen Gold Mines Proprietary Limited (maximum hole depth of 45 m) returned intercepts of up to 1.00 m

@ 12.28 g/t Au from 9.00 m (hole YER143), 1.00 m @ 6.94 g/t Au from 10.00 m (hole YER158), and 2.00 m @ 2.20 g/t Au from 9.00 m (hole YER159), defining surficial, saprolite-hosted gold mineralization over an area of ~400 × 300 m at the Dingo prospect. The nearby Bull Terrier prospect returned intercepts of 16.00 m @ 2.59 g/t Au from 105.00 m (hole YBD-2) and 16.00 m @ 1.52 g/t Au from 60.00 m, including 1.00 m @ 211.70 g/t Au from 65.00 m (hole YRC-63) [164,165]. No deeper or more systematic exploration drilling appears to have been undertaken across the McAuliffe Well Syenite intrusive cluster. Moreover, the area is held by several exploration companies, and this fragmented ownership, apparently persisting for decades, has likely hindered a more integrated exploration approach.

- Target #2: This target comprises prospective mafic and felsic volcanic-dominated greenstone sequences, containing chemically reactive banded iron formations (BIFs) and syenite intrusions, located along strike from the Mt Morgans gold production center. Previous drilling returned intersections of up to 6.70 m @ 13.15 g/t Au from 95.00 m (hole MRC036), 5.90 m @ 7.24 g/t from 79.00 m (hole MRC003), and 2.90 m @ 5.41 g/t Au from 112.00 m (hole MRC028), defining a modest resource of >150 koz Au @ 1.40 g/t Au at the Korong-Waihi prospect. The mineralization remains open along strike and at depth, with no drilling below a vertical depth of 150 m [166,167]. As with target #1, fragmented ownership currently hinders a more integrated exploration approach.

Table 9. 'Manual targets' generated from RF-derived MPM targets. Targets are labelled according to their ranking ranging from #1 (highest-ranked) to #8 (lowest-ranked).

Target ID	Name	Rationale	Exploration and Ownership
#1	Dingo	Lithostructural target comprising a cluster of poorly tested intrusions of the McAuliffe Well Syenite; partially covered by Lake Raeside; hosts Dingo and Bull Terrier Au occurrences; proximal to 1st-order Keith–Kilkenny fault system; located along an NNW-SSE-trending gravity ridge	Shallow saprolite drilling only although open-file drill hole data appear to be incomplete; best historic drill intercept: 1.00 m @ 12.28 g/t Au; disjointed ownership
#2	Westralia North	Lithostructural target comprising BIF units and syenite intrusions; Korong and Akicia Au occurrences; proximal to 1st-order Celia fault system; located along an NNW-SSE gravity ridge; along strike from the Mt Morgans Au deposit	No deep drilling >150 m vertical; best historic drill intercept: 6.70 m @ 13.15 g/t Au; disjointed ownership
#3	Mt Boyce	Lithostructural target; largely soil covered; no reported Au occurrences in 2021; proximal to 1st-order Keith–Kilkenny fault system; located along an NNW-SSE-trending gravity ridge	No deep drilling >100 m vertical; best historic drill intercept: 2.00 m @ 34.50 g/t Au
#4	Mt Redcastle	Lithostructural target in 'nose region' of a large granite dome and comprising internal granitoids; hosts several known Au occurrences; proximal to unnamed 2nd-order fault system; located along NW-SE-trending gravity ridge	No deep drilling >100 m; disjointed ownership
#5	Mt Remarkable	Lithostructural target covering part of the Pig Well Basin; no reported Au occurrences in 2021; proximal to 1st-order Keith–Kilkenny fault system; located along an NNW-SSE-trending gravity ridge	Drilling is mostly associated with the Marvellous Au occurrence; best historic drill intercept: 82.00 m @ 0.83 g/t Au; disjointed ownership; partly located within an extensive registered site of Aboriginal cultural heritage

Table 9. *Cont.*

Target ID	Name	Rationale	Exploration and Ownership
#6	Twenty Six Well	Lithostructural target; largely soil covered; no reported Au occurrences in 2021; proximal to 1st-order Keith–Kilkenny fault system; located along an NNW-SSE-trending gravity ridge	Minimal drilling; disjointed ownership
#7	Malcolm	Lithostructural target comprising BIF units; hosts numerous Au occurrences over a strike length of 10 km; located in between the 1st-order Keith–Kilkenny and Melita-Emu fault systems; located along an NNW-SSE-trending gravity ridge	Limited drilling; best historic drill intercept: 11.00 m @ 1.75 g/t Au + 10.00 m @ 1.26 g/t Au; disjointed ownership
#8	Lake Raeside	Lithostructural target covering part of the Pig Well Basin; largely covered by lake Raeside; proximal to 1st-order Keith–Kilkenny fault system; located along an NNW-SSE-trending gravity ridge	Minimal drilling; disjointed ownership; partly located within an extensive registered site of Aboriginal cultural heritage

Key to abbreviations: BIF = banded iron formation.

8.5. Post-Study Target Validation

The MPM and targeting study described in this paper was completed in late 2021. A brief review of subsequent exploration activity revealed three 2024 to 2025 drilling campaigns whose results independently validate several of this study's predicted targets.

Saturn Metals Limited conducted aircore (AC) drilling that returned 13.0 m @ 1.32 g/t Au from 56.0 m (including 4.0 m @ 4.31 g/t Au from 56.0 m; hole AHAC04641) and 12.0 m @ 0.72 g/t Au from 40.0 m (including 4.0 m @ 1.57 g/t Au from 44.0 m; hole AHAC2616) from two parallel gold-bearing structures, Aquarius West and Aquarius East [168]. These coincide with priority MPM target zones and manual Target #5 (Figure 18). The Aquarius gold trend extends along a ~26 km NNW-SSE corridor, defined by additional mineralized intercepts such as 3.0 m @ 8.51 g/t Au from 102.0 m (hole MBAC0629) and 36.0 m @ 0.48 g/t Au from 24.0 m (including 3.0 m @ 1.65 g/t Au from 57.0 m; hole MBRC049). The trend follows an NNW-SSE gravity edge parallel to the Keith–Kilkenny fault zone and aligned with a complex granite–greenstone contact.

Arika Resources Limited completed reverse circulation (RC) and diamond core (DD) drilling at its Yundamindra project (Figure 19), where ~97% of historic holes were <50 m deep. The new drilling defined mineralized zones at the open-ended Pennyweight Point (e.g., 14.0 m @ 15.48 g/t Au from 46.0 m, hole YMRC077; 30.0 m @ 3.86 g/t Au from 89.0 m, hole YMRC069; 36.0 m @ 2.14 g/t Au from 104.0 m, hole 25YMD001) and Landed at Last prospects (e.g., 4.0 m @ 41.56 g/t Au from 52.0 m, hole 25AYRC007; 30.0 m @ 2.26 g/t Au from 26.0 m, hole YMRC050; 14.8 m @ 3.10 g/t Au from 87.0 m, hole 25YMD003) [169]. These prospects lie entirely within first-order MPM target zones, coinciding with a complexly faulted greenstone constriction wedged between two granitic batholiths. They also align with NNW-SSE and NNE-SSW gravity edges and coincide with distinct, remotely sensed goethite–clay–iron feature depth index (IFD) anomalies.

Genesis Minerals Limited is conducting infill and extensional drilling at the Admiral deposit (0.3 Moz Au; Figure 20) to confirm strike and depth continuity among several shallow open-pits, aiming to define a single large system. Recent RC drill results include 17.0 m @ 2.98 g/t Au from 154.0 m (hole 25USRC1685), 17.0 m @ 1.84 g/t Au from 1.0 m (hole 25USRC1661), 16.0 m @ 1.88 g/t Au from 135.0 m (hole 25USRC1683), 9.0 m @ 3.30 g/t Au from 175.0 m (hole 25USRC1677), and 11.0 m @ 2.73 g/t Au from 177.0 m (hole 25USRC1681) [170]. The Admiral open-pits occur within a first-order MPM target zone and coincide with belt-parallel and orthogonal gravity ridges, as well as K/Th radiometric and remotely sensed goethite–clay–iron feature depth index anomalies.

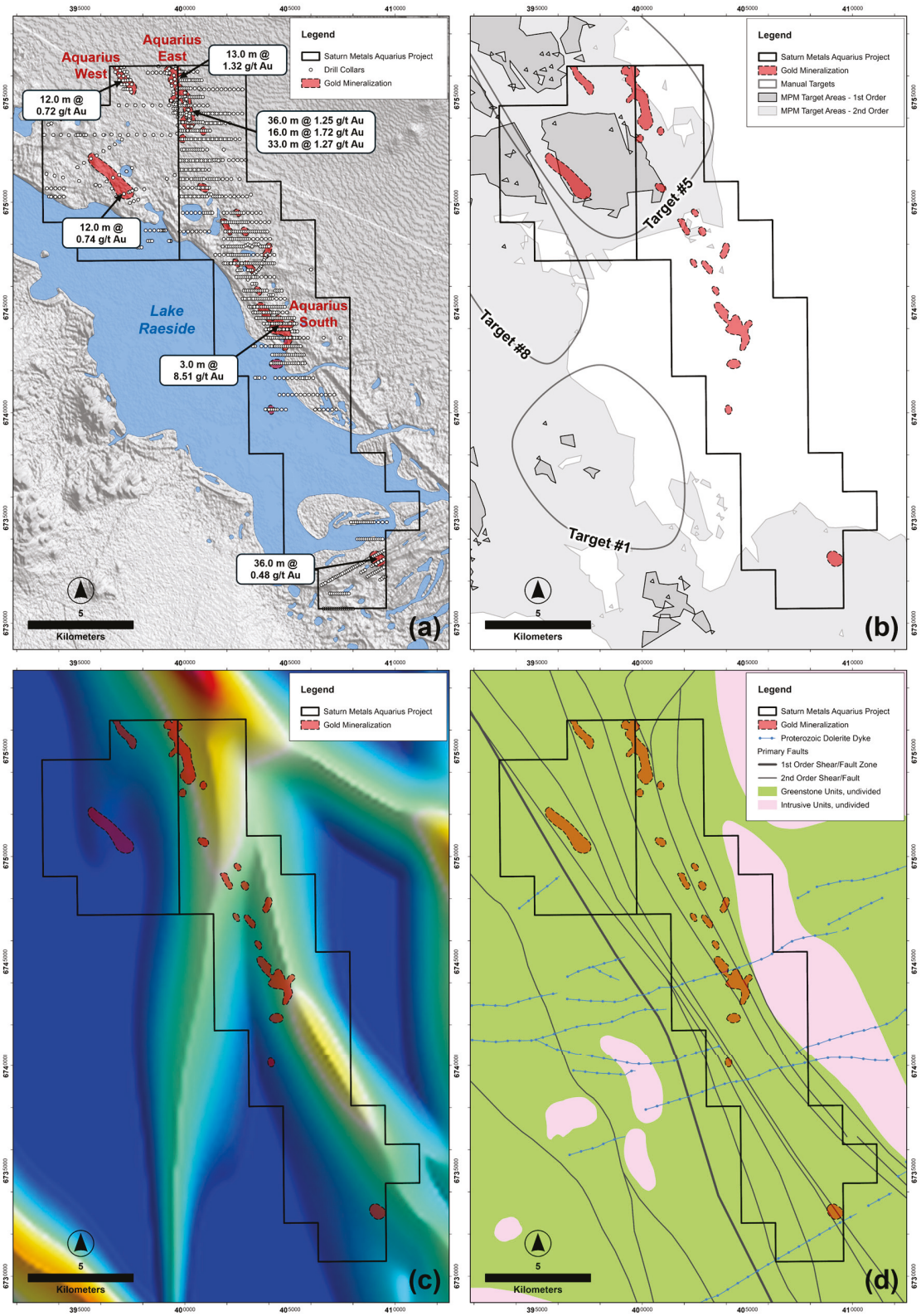


Figure 18. Post-study target validation using recent exploration results from the Aquarius gold trend [168]. (**a**) Map of gold mineralized zones interpreted from drill intersections with downhole assays ≥0.4 g/t Au, showing drill collars and selected significant intercepts. Background: digital elevation model (2:1 vertical exaggeration). (**b**) Relationship between the Aquarius gold trend and MPM and manual targets generated in this study. (**c**) Belt-parallel gravity edges (800 m scale). High values (red colors) indicate high data confidence whilst low values (blue colors) indicate low data confidence. (**d**) Simplified geological map of the area.

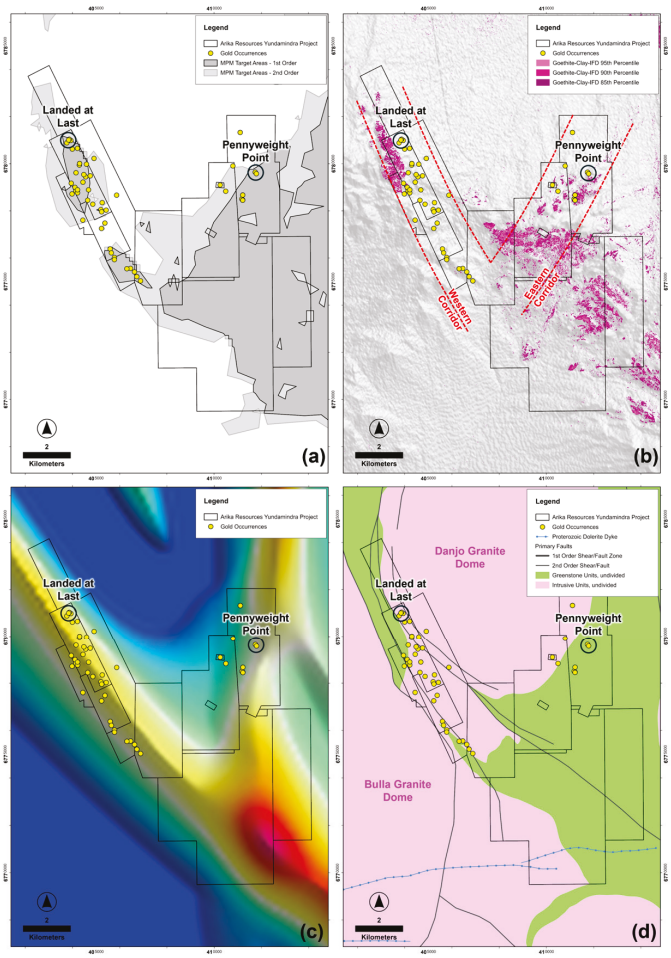


Figure 19. Post-study target validation using recent exploration results from the Western and Eastern Corridor gold trends, Yundamindra [169]. (**a**) Relationship between the Landed at Last and Pennyweight Point gold discoveries and MPM targets generated in this study. (**b**) Goethite–clay–iron feature depth index (IFD) anomalies derived from Sentinel-2 imagery. Background: digital elevation model (2:1 vertical exaggeration). (**c**) Belt-parallel gravity edges (800 m scale). High values (red colors) indicate high data confidence whilst low values (blue colors) indicate low data confidence. (**d**) Simplified geological map of the area.

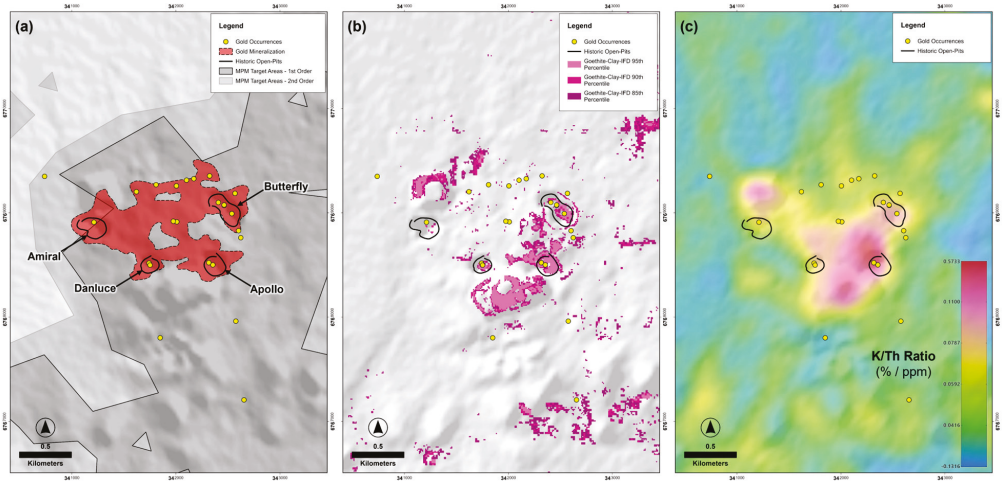


Figure 20. Post-study target validation using recent exploration results from the Admiral group of open-pits [170]. Background: digital elevation model (2:1 vertical exaggeration). (**a**) Relationship between the drill-indicated gold mineralization and MPM targets generated in this study. (**b**) Goethite–clay–IFD anomalies derived from Sentinel-2 imagery. (**c**) K/Th radiometric ratio anomaly.

9. Summary and Conclusions

This study of Archean orogenic gold systems in the central-eastern Yilgarn Craton illustrates that a geophysically informed lithostructural framework, when combined with a mineral systems-based targeting model and a suite of complementary prospectivity algorithms, provides a powerful tool for gold exploration.

Enhancement filtering of gravity, magnetic, radiometric, and remote sensing data revealed cryptic structures and alteration systems that correlate with known gold deposits and extend into underexplored areas.

The solid geology map produced in this study formed the foundation for a multi-technique mineral potential modeling (MPM) workflow incorporating five complementary prospectivity methods spanning knowledge-driven, data-driven, and continuous approaches. The best-performing random forest (RF) model accurately predicted most known gold occurrences while significantly reducing and prioritizing the search space for new targets.

The key strengths of this approach are its reproducibility, explicit integration of deep-seated and cross-structure architectures, and capacity to test multiple weighting schemes to minimize bias. Overall, the results confirm that combining a detailed geophysical interpretation with mineral systems-based prospectivity modeling is an effective strategy for identifying concealed gold corridors and reducing exploration risk. The methodology is readily transferable to other commodities and geological provinces worldwide.

In summary, the following conclusions can be drawn from this study:

1. Structural controls: Cross-cutting N-S, NE-SW, and NW-SE fault and fracture corridors overprint the greenstone belt-parallel fabric and consequently aligned with clusters of gold occurrences. Supported by Fry analysis, these oblique structures likely represent key fluid-focusing zones that controlled mineralization.
2. Geophysical insights: Gravity and magnetic data reveal concealed structural controls. Belt-parallel gravity ridges correspond to thickened mafic–ultramafic roots of inverted greenstone basins, the most prospective settings for multi-million-ounce systems. Gravity edges and magnetic edges delineate fault zones and granite–greenstone contacts. Major deposits such as Thunderbox, King of the Hills, Gwalia, Ulysses, and Paddington occur along these edges, indicating previously unrecognized cryptic crustal boundaries.
3. Integrated geological framework: Enhanced gravity, magnetic, radiometric, and remote sensing filters clarified subtle but continuous fault zones, alteration halos, and greenstone basin keels not visible in published maps. These datasets were synthetized into a new, geophysically constrained lithostructural framework for mineral targeting.
4. Mineral potential modeling (MPM): Five complementary techniques were applied, with the random forest (RF) model performing best and detecting ~84% of known deposits while reducing the prospective search area to <8% of the total. Key predictive variables included proximity to (i) gravity ridges and edges, (ii) cross-structure density, (iii) alteration indices (high K/Th, Fe-oxide-clay ratios), (iv) greenstone belts, and (v) internal granitoid margins. Several underexplored, highly prospective corridors were delineated, particularly along concealed gravity-defined trends.
5. Exploration implications: Deep-seated trans-lithospheric and cross-belt faults are confirmed as primary ore controls in the Yilgarn Craton. Integrating geophysical enhancement, structural reconstruction, and mineral systems-based modeling provides a quantitative, reproducible framework for regional-scale targeting. This approach effectively maps cryptic crustal architecture, reducing both the exploration risk and search space.

Supplementary Materials: The following supporting information can be downloaded at https://www.mdpi.com/article/10.3390/min15121255/s1, Figures S1 and S2: Prediction-area plots for the predictor maps used in this study; Figures S3 and S4: Receiver operating characteristic curves for the predictor maps used in this study; Figures S5–S32: Predictor maps used in this study; Figure S33: Improved prediction-area plots for the predictor maps used in this study; Figure S34: Measure of predictor variable importance derived by RF technique; Figure S35: Evolution of mean squared error curve; Figure S36: Improved prediction-area plot for the mineral potential models generated in this study; Figure S37: Concentration-area fractal plot for the superior RF mineral potential model; Table S1: Others-to-worst pairwise comparison vector based on the O_p index; Table S2: Best-to-others pairwise comparison vector based on the O_p index; Table S3: Optimal weights (W^*) derived from the BWM approach.

Author Contributions: Conceptualization, O.P.K., D.M. and R.M.; methodology, O.P.K., B.R., A.J.B., D.P.C., B.A.K. and D.M.; software, B.R., A.J.B., D.P.C. and B.A.K.; validation, O.P.K., B.R., A.J.B., D.P.C. and B.A.K.; formal analysis, O.P.K., B.R., A.J.B., D.P.C. and B.A.K.; investigation, O.P.K., B.R., A.J.B., D.P.C. and B.A.K.; resources, O.P.K., B.R., A.J.B., D.P.C. and B.A.K.; data curation, O.P.K., B.R., A.J.B., D.P.C. and B.A.K.; writing—original draft preparation, O.P.K., B.R., A.J.B., D.P.C. and B.A.K.; writing—review and editing, O.P.K., B.R., A.J.B., D.P.C., D.M. and R.M.; visualization, O.P.K., B.R., A.J.B., D.P.C. and B.A.K.; project administration, O.P.K. and D.M.; funding acquisition, O.P.K. All authors have read and agreed to the published version of the manuscript.

Funding: This research was funded by St Barbara Limited (https://stbarbara.com.au/). D.M. and R.M. are employees of St Barbara Limited.

Data Availability Statement: The sources of the publicly available datasets analyzed in this study are specified in Table 1. Confidential company data cannot be made publicly available.

Acknowledgments: Genesis Minerals Limited (https://genesisminerals.com.au/) is thanked for permission to publish the results of this work. Particular thanks go to Andrew Chirnside, Group Manager Geology & Exploration at Genesis Minerals Limited, for his support and assistance. The authors also thank the three anonymous reviewers for their valuable insights and feedback, which helped to strengthen this work.

Conflicts of Interest: Oliver P. Kreuzer was a co-owner of Corporate Geoscience Group. Bijan Roshanravan was contracted by Corporate Geoscience Group. Amanda J. Buckingham, Daniel P. Core and Brian A. Konecke were employed by Fathom Geophysics Australia Pty Limited. Daniel McDwyer and Roger Mustard were employed by St Barbara Limited. The paper reflects the views of the scientists and not the company.

Abbreviations

The following abbreviations are used in this manuscript:

Au	Gold
DEMIRS	Department of Energy, Mines, Industry Regulation and Safety
EGST	Eastern Goldfields Superterrane
GSWA	Geological Survey of Western Australia
IFD	Iron feature depth
KotH	King of the Hills gold deposit
koz	Thousand ounces
MA	Time ago in millions of years
Moz	Million ounces
MPM	Mineral potential modeling
Mtpa	Millions of tons per annum
Myr	Time span in millions of years
SBM	St Barbara Limited

References

1. Geological Survey of Western Australia. *Gold Investment Opportunities*; Government of Western Australia, Department of Energy, Mines, Industry Regulation and Safety: East Perth, Australia, 2023; 2p.
2. Phillips, G.N.; Vearncombe, J.R.; Eshuys, E. Gold production and the importance of exploration success: Yilgarn Craton, Western Australia. *Ore Geol. Rev.* **2019**, *105*, 137–150. [CrossRef]
3. Williams, P.R.; Nisbet, B.W.; Etheridge, M.A. Shear zones, gold mineralization and structural history in the Leonora district, Eastern Goldfields Province, Western Australia. *Aust. J. Earth Sci.* **1989**, *36*, 383–403. [CrossRef]
4. Duuring, P.; Hagemann, S.G.; Cassidy, K.F.; Johnson, C.A. Hydrothermal alteration, ore fluid characteristics, and gold depositional processes along a trondhjemite-komatiite contact at Tarmoola, Western Australia. *Econ. Geol.* **2004**, *99*, 423–451. [CrossRef]
5. Morey, A.A.; Weinberg, R.F.; Bierlein, F.P. The structural controls of gold mineralisation within the Bardoc Tectonic Zone, Eastern Goldfields Province, Western Australia: Implications for gold endowment in shear systems. *Miner. Depos.* **2007**, *42*, 583–600. [CrossRef]
6. Weinberg, R.F.; Van Der Borgh, P. Extension and gold mineralization in the Archean Kalgoorlie terrane, Yilgarn craton. *Precambrian Res.* **2008**, *161*, 77–88. [CrossRef]
7. Blewett, R.S.; Czarnota, K.; Henson, P.A. Structural-event framework for the eastern Yilgarn Craton, Western Australia, and its implications for orogenic gold. *Precambrian Res.* **2010**, *183*, 203–229. [CrossRef]
8. Czarnota, K.; Champion, D.C.; Goscombe, B.; Blewett, R.S.; Cassidy, K.F.; Henson, P.A.; Groenewald, P.B. Geodynamics of the eastern Yilgarn Craton. *Precambrian Res.* **2010**, *183*, 175–202. [CrossRef]
9. Jones, S.A. Contrasting structural styles of gold deposits in the Leonora Domain: Evidence for early gold deposition, Eastern Goldfields, Western Australia. *Aust. J. Earth Sci.* **2014**, *61*, 881–917. [CrossRef]
10. Jones, S.A. 2730-2670 Ma rifting triggers sagduction prior to the onset of orogenesis at ca 2650 Ma: Implications for gold mineralisation, Eastern Goldfields, Western Australia. *Aust. J. Earth Sci.* **2024**, *71*, 647–672. [CrossRef]
11. Goscombe, B.; Foster, D.A.; Blewett, R.; Czarnota, K.; Wade, B.; Groenewald, B.; Gray, D. Neoarchean metamorphic evolution of the Yilgarn craton: A record of subduction, accretion, extension and lithospheric delamination. *Precambrian Res.* **2019**, *335*, 105441. [CrossRef]
12. Witt, W.K.; Cassidy, K.F.; Lu, Y.J.; Hagemann, S.G. The tectonic setting and evolution of the 2.7 Ga Kalgoorlie–Kurnalpi Rift, a world-class Archean gold province. *Miner. Depos.* **2020**, *55*, 601–631. [CrossRef]
13. Jones, S.A.; Cassidy, K.F.; Davis, B.K. Unravelling the D1 event: Evidence for early granite-up, greenstone-down tectonics in the Eastern Goldfields, Western Australia. *Aust. J. Earth Sci.* **2021**, *68*, 1–35. [CrossRef]
14. Groves, D.I.; Goldfarb, R.J.; Knox-Robinson, C.M.; Ojala, J.; Gardoll, S.; Yun, G.Y.; Holyland, P. Late-kinematic timing of orogenic gold deposits and significance for computer-based exploration techniques with emphasis on the Yilgarn Block, Western Australia. *Ore Geol. Rev.* **2000**, *17*, 1–38. [CrossRef]
15. Czarnota, K.; Blewett, R.S.; Goscombe, B. Predictive mineral discovery in the eastern Yilgarn Craton, Western Australia: An example of district scale targeting of an orogenic gold mineral system. *Precambrian Res.* **2010**, *183*, 356–377. [CrossRef]
16. Witt, W.K.; Ford, A.; Hanrahan, B.; Mamuse, A. *Regional-Scale Targeting for Gold in the Yilgarn Craton: Part 1 of the Yilgarn Gold Exploration Targeting Atlas*; Report 125; Geological Survey of Western Australia: East Perth, Australia, 2013; 130p.
17. Witt, W.K.; Ford, A.; Hanrahan, B. *District-Scale Targeting for Gold in the Yilgarn Craton: Part 2 of the Yilgarn Gold Exploration Targeting Atlas*; Report 132; Geological Survey of Western Australia: East Perth, Australia, 2015; 276p.
18. Witt, W.K. *Deposit-Scale Targeting for Gold in the Yilgarn Craton: Part 3 of the Yilgarn Gold Exploration Targeting Atlas*; Report 158; Geological Survey of Western Australia: East Perth, Australia, 2016; 182p.
19. Knox-Robinson, C.M. Vectorial fuzzy logic: A novel technique for enhanced mineral prospectivity mapping, with reference to the orogenic gold mineralisation potential of the Kalgoorlie Terrane, Western Australia. *Aust. J. Earth Sci.* **2000**, *47*, 929–941. [CrossRef]
20. Wyborn, L.A.I.; Heinrich, C.A.; Jaques, A.L. Australian Proterozoic mineral systems: Essential ingredients and mappable criteria. In Proceedings of the 1994 AusIMM Annual Conference: Australian Mining Looks North—The Challenges and Choices, Darwin, NT, Australia, 5–9 August 1994; pp. 109–115.
21. McCuaig, T.C.; Beresford, S.; Hronsky, J. Translating the mineral systems approach into an effective exploration targeting system. *Ore Geol. Rev.* **2010**, *38*, 128–138. [CrossRef]
22. McCuaig, T.C.; Hronsky, J.M.A. The mineral system concept—The key to exploration targeting. *Soc. Econ. Geol. Spec. Publ.* **2014**, *18*, 153–175. [CrossRef]
23. Rabeaut, O.; Legault, M.; Cheilletz, A.; Jébrak, M.; Royer, J.J.; Cheng, L.Z. Gold potential of a hidden Archean fault zone: The case of the Cadillac–Larder Lake fault. *Explor. Min. Geol.* **2010**, *19*, 99–116. [CrossRef]
24. Rabeau, O.; Royer, J.J.; Jébrak, M.; Cheilletz, A. Log-uniform distribution of gold deposits along major Archean fault zones. *Miner. Depos.* **2013**, *48*, 817–824. [CrossRef]

25. An, P.; Moon, W.M.; Rencz, A. Application of fuzzy set theory to integrated mineral exploration. *Can. J. Explor. Geophys.* **1991**, *27*, 1–11.
26. Bonham-Carter, G.F. *Geographic Information Systems for Geoscientists: Modelling with GIS*; Pergamon: Oxford, UK, 1994; 416p.
27. Huston, D.L.; Blewett, R.S.; Champion, D.C. Australia through time: A summary of its tectonic and metallogenic evolution. *Episodes* **2012**, *35*, 23–43. [CrossRef]
28. Cassidy, K.F.; Champion, D.C.; Krapež, B.; Barley, M.E.; Brown, S.J.A.; Blewett, R.S.; Groenewald, P.; Tyler, I.M. *A Revised Geological Framework for the Yilgarn Craton, Western Australia*; Record 2006(8); Geological Survey of Western Australia: East Perth, Australia, 2006; 15p.
29. Wyche, S.; Fiorentini, M.L.; Miller, J.L.; McCuaig, T.C. Geology and controls on mineralisation in the Eastern Goldfields region, Yilgarn Craton, Western Australia. *Epis. J. Int. Geosci.* **2012**, *35*, 273–282. [CrossRef]
30. Masurel, Q.; Thébaud, N. Deformation in the Agnew-Wiluna greenstone belt and host Kalgoorlie Terrane during the c. 2675–2630 Ma Kalgoorlie Orogeny: ∼45 Ma of horizontal shortening in a Neoarchean back-arc region. *Precambrian Res.* **2024**, *414*, 107586. [CrossRef]
31. McCuaig, T.C.; Miller, J.M.; Beresford, S. *Controls on Giant Mineral Systems in the Yilgarn Craton—A Field Guide*; Record 2010(26); Geological Survey of Western Australia: East Perth, Australia, 2010; 159p.
32. Krapež, B.; Barley, M.E.; Brown, S.J. Late Archaean synorogenic basins of the Eastern Goldfields Superterrane, Yilgarn Craton, Western Australia: Part I. Kalgoorlie and Gindalbie Terranes. *Precambrian Res.* **2008**, *161*, 135–153. [CrossRef]
33. Wyche, S. *Geological Setting of Mineral Deposits in the Eastern Yilgarn Craton—A Field Guide*; Record 2014(10); Geological Survey of Western Australia: East Perth, Australia, 2014; 56p.
34. Mole, D.R.; Fiorentini, M.L.; Cassidy, K.F.; Kirkland, C.L.; Thébaud, N.; McCuaig, T.C.; Doublier, M.P.; Duuring, P.; Romano, S.S.; Maas, R.; et al. Crustal evolution, intra-cratonic architecture and the metallogeny of an Archaean craton. In *Ore Deposits in an Evolving Earth*; Jenkin, G.R.T., Lusty, P.A.J., McDonald, I., Smith, M.P., Boyce, A.J., Wilkinson, J.J., Eds.; Special Publications, Geological Society: London, UK, 2015; Volume 393, pp. 23–80.
35. Czarnota, K.; Blewett, R.S.; Goscombe, B. *Structural and Metamorphic Controls on Gold Through Time and Space in the Central Eastern Goldfields Superterrane—A Field Guide*; Record 2008(9); Geological Survey of Western Australia: East Perth, Australia, 2008; 66p.
36. Goscombe, B.; Blewett, R.S.; Czarnota, K.; Groenewald, B.; Maas, R. *Metamorphic Evolution and Integrated Terrane Analysis of the Eastern Yilgarn Craton: Rationale, Methods, Outcomes and Interpretation*; Record 2009(23); Geoscience Australia: Canberra, Australia, 2009; 270p.
37. Masurel, Q.; Thébaud, N.; Saptoka, J.; De Paoli, M.C.; Drummond, M.; Smithies, R.H. Stratigraphy of the Agnew-Wiluna greenstone belt: Review, synopsis, and implications for the late Mesoarchean to Neoarchean geological evolution of the Yilgarn Craton. *Aust. J. Earth Sci.* **2022**, *69*, 1149–1176. [CrossRef]
38. Weinberg, R.F.; Moresi, L.; Van der Borgh, P. Timing of deformation in the Norseman-Wiluna belt, Yilgarn craton, Western Australia. *Precambrian Res.* **2003**, *120*, 219–239. [CrossRef]
39. Brown, M.; Johnson, T.; Gardiner, N.J. Plate tectonics and the Archean Earth. *Annu. Rev. Earth Planet. Sci.* **2020**, *48*, 291–320. [CrossRef]
40. Windley, B.F.; Kusky, T.; Polat, A. Onset of plate tectonics by the Eoarchean. *Precambrian Res.* **2021**, *352*, 105980. [CrossRef]
41. Kuang, J.; Morra, G.; Yuen, D.A.; Kusky, T.; Jiang, S.; Yao, H.; Qi, S. Metamorphic constraints on Archean tectonics. *Precambrian Res.* **2023**, *397*, 107–195. [CrossRef]
42. Blewett, R.S.; Czarnota, K. *Tectonostratigraphic Architecture and Uplift History of the Eastern Yilgarn Craton*; Record 2007(15); Geological Survey of Western Australia: East Perth, Australia, 2007; 114p.
43. Krapež, B.; Barley, M.E. Late Archaean synorogenic basins of the Eastern Goldfields Superterrane, Yilgarn Craton, Western Australia: Part III. Signatures of tectonic escape in an arc-continent collision zone. *Precambrian Res.* **2008**, *161*, 183–199. [CrossRef]
44. Yilgarn Craton—Geology, Structure and Mineralisation (PorterGeo). Available online: https://portergeo.com.au/database/mineinfo.asp?mineid=mn1626 (accessed on 12 July 2025).
45. KCGM Operations (Northern Star Resources Limited). Available online: https://www.nsrltd.com/our-assets/kcgm-operations/ (accessed on 28 July 2025).
46. Sons of Gwalia, Gwalia, Tower Hill (PorterGeo). Available online: https://portergeo.com.au/database/mineinfo.asp?mineid=mn761 (accessed on 2 August 2025).
47. Vielreicher, R.M.; Groves, D.I.; Ridley, J.R.; McNaughton, N.J. A replacement origin for the BIF-hosted gold deposit at Mt. Morgans, Yilgarn Block, WA. *Ore Geol. Rev.* **1994**, *9*, 325–347. [CrossRef]
48. Bennett, M.A. Thunderbox gold and Waterloo nickel deposits. In *Gold and Nickel Deposits in the Norseman-Wiluna Greenstone Belt, Yilgarn Craton, Western Australia—A Field Guide*; Record 2014(16); Neumayr, P., Harris, M., Beresford, S.W., Eds.; Geological Survey of Western Australia: East Perth, Australia, 2014; 166p.
49. Castle, M. Independent geologist's report on the Apollo Hill gold project in Western Australia. In *Prospectus Saturn Metals Limited ACN 619 488 498*; Saturn Metals Limited: West Perth, Australia, 2018; pp. 53–132.

50. Standing, J.; Outhwaite, M.; Fay, C.; Martin, D.; McCormack, B. Aphrodite geological campaign 2018. In *Confidential Report to Spitfire Materials Limited, Model Earth Proprietary Limited*; March 2018; 59p.
51. Harris, M.; Fleming, S.; Dudfield, L.; Savage, B. Melita project—Ulysses gold deposit, Western Australia. In *Regolith Expression of Australian Ore Systems—A Compilation of Geochemical Case Histories and Conceptual Models*; Butt, C.R.M., Cornelius, M., Scott, K.M., Robertson, I.D.M., Eds.; Cooperative Research Centre for Landscape Environments and Mineral Exploration (CRC LEME); 3p. Available online: https://crcleme.org.au/RegExpOre/Ulysses.pdf (accessed on 2 August 2025).
52. Genesis Minerals Limited. Ulysses mineral resource soars 137% to 760,000 ounces. In *Australian Securities Exchange (ASX) Announcement Dated 09 October 2018*; Genesis Minerals Limited: Perth, Australia, 2018; 17p.
53. Witt, W.K. *Gold Mineralization in the Menzies-Kambalda Region, Eastern Goldfields, Western Australia*; Report 39; Geological Survey of Western Australia: East Perth, Australia, 1993; 165p.
54. Martinick McNulty Pty Limited. Notice of intent to mine the Wonder orebody. In *Department of Energy, Mines, Industry Regulation and Safety (DEMIRS), Government of Western Australia, GeoDocs, Document MP3808, 09 October 2001*; Martinick McNulty Pty Limited: West Perth, Australia, 2001; 79p. Available online: https://geodocs.dmirs.wa.gov.au/Web/documentlist/9/EARS_regi_id/17195 (accessed on 2 August 2025).
55. Allchurch, J.D. Celtic Project, Annual report covering 01/04/2016 to 31/03/2017, combined reporting number C28/2012 for P37/8306, P37/8382, P37/8383, P37/8384, P37/8385, P37/8386, M37/350, M37/488, M37/513, M37/514 and M37/638. In *Department of Energy, Mines, Industry Regulation and Safety (DEMIRS), Government of Western Australia, WAMEX Mineral Reporting System, Report Number A114129, 21 September 2017*; S R Mining Pty Limited and Bligh Resources Limited: Fremantle, WA, Australia, 2017; 17p. Available online: https://wamex.dmp.wa.gov.au/Wamex/Search/ReportDetails?ANumber=114129 (accessed on 2 August 2025).
56. Schmitt, L.A. The Dolerite-Hosted Zoroastrian Gold Deposit, Yilgarn Craton, Western Australia: Lithogeochemistry, Alteration Zonation Patterns and Source of Sulfur. Maser's Thesis, Oulu Mining School, University of Oulu, Oulu, Finland, 2017; 91p.
57. Dunbar, P.; Fairfield, P. Independent technical assessment & valuation report, Bardoc Gold Limited Scheme Booklet. In *Australian Securities Exchange (ASX) Announcement Dated 23 February 2022*; Bardoc Gold Limited: North Fremantle, WA, Australia, 2022; 328p.
58. Kretz, R. Symbols for rock-forming minerals. *Am. Mineral.* **1983**, *68*, 277–279.
59. Siivola, J.; Schmid, R. A systematic nomenclature for metamorphic rocks: 12. List of mineral abbreviations. In *Recommendations by the IUGS Subcommission on the Systematics of Metamorphic Rocks*; Web Version 01.02.07.; International Union of Geological Sciences (IUGS) Subcommission on the Systematics of Metamorphic Rocks (SCMR): Beijing, China, 2007; 5p.
60. Groves, D.I. The crustal continuum model for late-Archaean lode-gold deposits of the Yilgarn Block, Western Australia. *Miner. Depos.* **1993**, *28*, 366–374. [CrossRef]
61. Groves, D.I.; Ridley, J.R.; Bloem, E.M.J.; Gebre-Mariam, M.; Hagemann, S.G.; Hronsky, J.M.A.; Knight, J.T.; McNaughton, N.J.; Ojala, J.; Vielreicher, R.M.; et al. Lode-gold deposits of the Yilgarn block: Products of Late Archaean crustal-scale overpressured hydrothermal systems. In *Early Cambrian Processes*; Special Publications, 95(1); Coward, M.P., Ries, A.C., Eds.; Geological Society of London: London, UK, 1995; pp. 155–172.
62. Tripp, G.I.; Tosdal, R.M.; Blenkinsop, T.; Rogers, J.R.; Halley, S. Neoarchean Eastern Goldfields of Western Australia. In *Geology of the World's Major Gold Deposits and Provinces*; Sillitoe, R.H., Goldfarb, R.J., Simmons, S.F., Eds.; Society of Economic Geologists: Littleton, CO, USA, 2020; pp. 709–734.
63. St Barbara Limited. St Barbara agrees to sale of Leonora assets to Genesis Minerals for total consideration of $600 million. In *Australian Securities Exchange (ASX) Announcement Dated 17 April 2023*; St Barbara Limited: West Perth, Australia, 2023; 5p.
64. Knox-Robinson, C.M.; Wyborn, L.A.I. Towards a holistic exploration strategy: Using geographic information systems as a tool to enhance exploration. *Aust. J. Earth Sci.* **1997**, *44*, 453–463. [CrossRef]
65. Kreuzer, O.P.; Etheridge, M.A.; Guj, P.; McMahon, M.E.; Holden, D.J. Linking mineral deposit models to quantitative risk analysis and decision-making in exploration. *Econ. Geol.* **2008**, *103*, 829–850. [CrossRef]
66. Kreuzer, O.P.; Roshanravan, B. Transforming LCT pegmatite targeting models into AI-powered predictive maps of lithium potential for Western Australia and Ontario: Approach, results and implications. *Minerals* **2025**, *15*, 397. [CrossRef]
67. Buckingham, A.J.; Core, D.P.; Hart, C.J.R.; Jenkins, S. *TREK Project Area Gravity Compilation, Enhancement Filtering and Structure Detection*; Geoscience BC Report 2017-14; Geoscience BC: Vancouver, BC, Canada, 2017; 34p.
68. Kreuzer, O.P.; Buckingham, A.; Mortimer, J.; Walker, G.; Wilde, A.; Appiah, K. An integrated approach to the search for gold in a mature, data-rich brownfields environment: A case study from Sigma-Lamaque, Quebec. *Ore Geol. Rev.* **2019**, *111*, 102977. [CrossRef]
69. Roshanravan, B.; Kreuzer, O.P.; Buckingham, A.; Keykhay-Hosseinpoor, M.; Keys, E. Mineral potential modelling of orogenic gold systems in the Granites-Tanami Orogen, Northern Territory, Australia: A multi-technique approach. *Ore Geol. Rev.* **2023**, *152*, 105224. [CrossRef]

70. Dentith, M.; Mudge, S.T. *Geophysics for the Mineral Exploration Geoscientist*; Cambridge University Press: Cambridge, UK, 2014; 454p.
71. Bierlein, F.; Murphy, F.C.; Weinberg, R.F.; Lees, T. Distribution of orogenic gold deposits in relation to fault zones and gravity gradients: Targeting tools applied to the Eastern Goldfields, Yilgarn Craton, Western Australia. *Miner. Depos.* **2006**, *41*, 107–126. [CrossRef]
72. Cordell, L. Gravimetric expression of graben faulting in Santa Fe country and the Espanola Basin, New Mexico. In *Guidebook to Santa Fe Country: Thirtieth Field Conference, October 4–6, 1979*; Ingersoll, R.V., Ed.; New Mexico Geological Society: Socorro, NM, USA, 1979; pp. 59–64.
73. Grauch, V.J.S.; Cordell, L. Limitations of determining density or magnetic boundaries from the horizontal gradient of gravity or pseudogravity data. *Geophysics* **1987**, *52*, 118–121. [CrossRef]
74. Kovesi, P.D. Image features from phase congruency. *Videre: J. Comput. Vis. Res.* **1999**, *1*, 1–26.
75. Jacobsen, B.H. A case for upward continuation as a standard separation filter for potential-field maps. *Geophysics* **1987**, *52*, 1138–1148. [CrossRef]
76. Cazals, F.; Pouget, M. *Topology Driven Algorithms for Ridge Extraction on Meshes*; Raport Recherche 5526; Institut National de Recherche en Sciences et Technologies du Numérique (INRIA): Sophia Antipolis, France, 2005; 29p.
77. de Quadros, T.F.; Koppe, J.C.; Strieder, A.J.; Costa, J.F.C. Gamma-ray data processing and integration for lode-Au deposits exploration. *Nat. Resour. Res.* **2003**, *12*, 57–65. [CrossRef]
78. Herbert, S.; Woldai, T.; Carranza, E.J.M.; van Ruitenbeek, F.J. Predictive mapping of prospectivity for orogenic gold in Uganda. *J. Afr. Earth Sci.* **2014**, *99*, 666–693. [CrossRef]
79. Shebl, A.; Abdellatif, M.; Badawi, M.; Dawoud, M.; Fahil, A.S.; Csámer, Á. Towards better delineation of hydrothermal alterations via multi-sensor remote sensing and airborne geophysical data. *Sci. Rep.* **2023**, *13*, 7406. [CrossRef]
80. Japan Aerospace Exploration Agency. ALOS World 3D 30 Meter DEM, Version 3.2, Jan 2021. Distributed by OpenTopography. Available online: https://doi.org/10.5069/G94M92HB (accessed on 18 November 2022).
81. Mielke, C.; Boesche, N.K.; Rogass, C.; Kaufmann, H.; Gauert, C.; de Wit, M. Spaceborne mine waste mineralogy monitoring in South Africa, applications for modern push-broom missions: Hyperion/OLI and EnMAP/Sentinel-2. *Remote Sens.* **2014**, *6*, 6790–6815. [CrossRef]
82. ISO/CIE. Colorimetry—Part 4: CIE 1976 L*a*b* Colour Space. International Standard, ISO/CIE 11664-4:2019. Available online: https://cdn.standards.iteh.ai/samples/74166/8056d4c35bb24b54a6a7761c51f2575f/ISO-CIE-11664-4-2019.pdf (accessed on 1 October 2025).
83. Siddorn, J.P.; Williams, P.R.; Isles, D.J.; Rankin, L.R. Integrated geologic-geophysical interpretation of district-scale structural frameworks: Systematic approaches for targeting mineralizing systems. In *Applied Structural Geology of Ore-Forming Hydrothermal Systems*; Reviews in Economic Geology, 21; Rowland, J.V., Rhys, D.A., Eds.; Society of Economic Geologists: Littleton, CO, USA, 2020; pp. 271–313.
84. Hagemann, S.G.; Lisitsin, V.A.; Huston, D.L. Mineral system analysis: Quo vadis. *Ore Geol. Rev.* **2016**, *76*, 504–522. [CrossRef]
85. Kreuzer, O.P.; Miller, A.V.; Peters, K.J.; Payne, C.; Wildman, C.; Partington, G.A.; Puccioni, E.; McMahon, M.E.; Etheridge, M.A. Comparing prospectivity modelling results and past exploration data: A case study of porphyry Cu–Au mineral systems in the Macquarie Arc, Lachlan Fold Belt, New South Wales. *Ore Geol. Rev.* **2015**, *71*, 516–544. [CrossRef]
86. Roshanravan, B.; Kreuzer, O.P.; Bruce, M.; Davis, J.; Briggs, M. Modelling gold potential in the Granites-Tanami Orogen, NT, Australia: A comparative study using continuous and data-driven techniques. *Ore Geol. Rev.* **2020**, *125*, 103661. [CrossRef]
87. Kreuzer, O.P.; Yousefi, M.; Nykänen, V. Introduction to the special issue on spatial modelling and analysis of ore-forming processes in mineral exploration targeting. *Ore Geol. Rev.* **2020**, *119*, 103391. [CrossRef]
88. Fry, N. Random point distributions and strain measurement in rocks. *Tectonophysics* **1979**, *60*, 89–105. [CrossRef]
89. Vearncombe, J.R.; Vearncombe, S. The spatial distribution of mineralization; applications of Fry analysis. *Econ. Geol.* **1999**, *94*, 475–486. [CrossRef]
90. Kreuzer, O.P.; Blenkinsop, T.G.; Morrison, R.J.; Peters, S.G. Ore controls in the Charters Towers goldfield, NE Australia: Constraints from geological, geophysical and numerical analyses. *Ore Geol. Rev.* **2007**, *32*, 37–80. [CrossRef]
91. Carranza, E.J.M. Controls on mineral deposit occurrence inferred from analysis of their spatial pattern and spatial association with geological features. *Ore Geol. Rev.* **2009**, *35*, 383–400. [CrossRef]
92. Agterberg, F.P. Computer programs for mineral exploration. *Science* **1989**, *245*, 76–81. [CrossRef]
93. Bonham-Carter, G.F.; Agterberg, F.P.; Wright, D.F. Integration of geological datasets for gold exploration in Nova Scotia. *Digit. Geol. Geogr. Inf. Syst.* **1989**, *10*, 15–23.
94. Carranza, E.J.M. *Geochemical Anomaly and Mineral Prospectivity Mapping in GIS—Handbook of Exploration and Environmental Geochemistry 11*; Elsevier: Amsterdam, The Netherlands, 2008; 351p.
95. Joly, A.; Porwal, A.K.; McCuaig, T.C. Exploration targeting for orogenic gold deposits in the Granites-Tanami Orogen: Mineral system analysis, targeting model and prospectivity analysis. *Ore Geol. Rev.* **2012**, *48*, 349–383. [CrossRef]

96. Porwal, A.K.; Carranza, E.J.M. Introduction to the special issue: GIS-based mineral potential modelling and geological data analyses for mineral exploration. *Ore Geol. Rev.* **2015**, *71*, 477–483. [CrossRef]
97. Roshanravan, B.; Kreuzer, O.P.; Buckingham, A. BWM-MARCOS: A new hybrid MCDM approach for mineral potential modelling. *J. Geochem. Explor.* **2025**, *269*, 107639. [CrossRef]
98. Yousefi, M.; Nykänen, V. Data-driven logistic-based weighting of geochemical and geological evidence layers in mineral prospectivity mapping. *J. Geochem. Explor.* **2016**, *164*, 94–106. [CrossRef]
99. Yousefi, M.; Carranza, E.J.M. Fuzzification of continuous-value spatial evidence for mineral prospectivity mapping. *Comput. Geosci.* **2015**, *74*, 97–109. [CrossRef]
100. Yousefi, M.; Carranza, E.J.M. Geometric average of spatial evidence data layers: A GIS-based multi-criteria decision-making approach to mineral prospectivity mapping. *Comput. Geosci.* **2015**, *83*, 72–79. [CrossRef]
101. Aryafar, A.; Roshanravan, B. Improved index overlay mineral potential modeling in brown- and greenfields exploration using geochemical, geological and remote sensing data. *Earth Sci. Inform.* **2020**, *13*, 1275–1291. [CrossRef]
102. Breiman, L. Random forests. *Mach. Learn.* **2001**, *45*, 5–32. [CrossRef]
103. Hwang, C.-L.; Yoon, K. (Eds.) Methods for multiple attribute decision making. In *Multiple Attribute Decision Making*; Springer: Berlin/Heidelberg, Germany, 1981; pp. 58–191.
104. Afshari, A.; Mojahed, M.; Yusuff, R.M. Simple additive weighting approach to personnel selection problem. *Int. J. Innov. Manag. Technol.* **2010**, *1*, 511.
105. Rezaei, J. Best-worst multi-criteria decision-making method. *Omega* **2015**, *53*, 49–57. [CrossRef]
106. Gold Road Resources Limited. Company presentation. In *Australian Securities Exchange (ASX) Announcement Dated 23 May 2013*; Gold Road Resources Limited: West Perth, Australia, 2013; 26p.
107. Pisarevsky, S.A.; De Waele, B.; Jones, S.; Söderlund, U.; Ernst, R.E. Paleomagnetism and U-Pb age of the 2.4 Ga Erayinia mafic dykes in the south-western Yilgarn, Western Australia: Paleogeographic and geodynamic implications. *Precambrian Res.* **2015**, *259*, 222–231. [CrossRef]
108. Wingate, M.T.D. Mafic dyke swarms and large igneous provinces in Western Australia get a digital makeover. In *GSWA 2017 Extended Abstracts—Promoting the Prospectivity of Western Australia, Record 2017/2*; Geological Survey of Western Australia: East Perth, Australia, 2017; pp. 4–8.
109. McCuaig, T.C.; Kreuzer, O.P.; Brown, W.M. Fooling ourselves—Dealing with model uncertainty in a mineral systems approach to exploration. In Proceedings of the 9th Biennial SGA Meeting "Mineral Exploration and Research: Digging Deeper", Dublin, Ireland, 20–23 August 2007; pp. 1435–1438.
110. Hronsky, J.M.A.; Groves, D.I. Science of targeting: Definition, strategies, targeting and performance measurement. *Aust. J. Earth Sci.* **2008**, *55*, 3–12. [CrossRef]
111. Lord, D.; Etheridge, M.A.; Willson, M.; Hall, G.; Uttley, P.J. Measuring exploration success: An alternative to the discovery-cost-per-ounce method of quantifying exploration success. *Soc. Econ. Geol. (SEG) Newsl.* **2001**, *45*, 1 and 10–16. [CrossRef]
112. Penney, S.R.; Allen, R.M.; Harrisson, S.; Lees, T.C.; Murphy, F.C.; Norman, A.R.; Roberts, P.A. A global-scale exploration risk analysis technique to determine the best mineral belts for exploration. *Trans. Inst. Min. Metall.* **2004**, *133*, B183–B196. [CrossRef]
113. Porwal, A.K.; Kreuzer, O.P. Introduction to the special issue: Mineral prospectivity analysis and quantitative resource estimation. *Ore Geol. Rev.* **2010**, *38*, 121–127. [CrossRef]
114. Hronsky, J.M.; Kreuzer, O.P. Applying spatial prospectivity mapping to exploration targeting: Fundamental practical issues and suggested solutions for the future. *Ore Geol. Rev.* **2019**, *107*, 647–653. [CrossRef]
115. Bárdossy, G.; Fodor, J. Traditional and new ways to handle uncertainty in geology. *Nat. Resour. Res.* **2001**, *10*, 179–187. [CrossRef]
116. Hronsky, J.M.; Groves, D.I.; Loucks, R.R.; Begg, G.C. A unified model for gold mineralisation in accretionary orogens and implications for regional-scale exploration targeting methods. *Miner. Depos.* **2012**, *47*, 339–358. [CrossRef]
117. Groves, D.I.; Santosh, M.; Müller, D.; Zhang, L.; Deng, J.; Yang, L.Q.; Wang, Q.F. Mineral systems: Their advantages in terms of developing holistic genetic models and for target generation in global mineral exploration. *Geosystems Geoenvironment* **2022**, *1*, 100001. [CrossRef]
118. Sibson, R.H. Hinge-parallel fluid flow in fold-thrust belts: How widespread? *Proc. Geol. Assoc.* **2005**, *116*, 301–309. [CrossRef]
119. Cox, S.; Knackstedt, M.; Braun, J. Principles of structural control on permeability and fluid flow in hydrothermal systems. *Rev. Econ. Geol.* **2001**, *14*, 1–24.
120. Tripp, G.I.; Vearncombe, J.R. Fault/fracture density and mineralization: A contouring method for targeting in gold exploration. *J. Struct. Geol.* **2004**, *26*, 1087–1108. [CrossRef]
121. Groves, D.I.; Santosh, M.; Goldfarb, R.J.; Zhang, L. Structural geometry of orogenic gold deposits: Implications for exploration of world-class and giant deposits. *Geosci. Front.* **2018**, *9*, 1163–1177. [CrossRef]
122. Sibson, R.H.; Scott, J. Stress/fault controls on the containment and release of overpressured fluids: Examples from gold-quartz vein systems in Juneau, Alaska; Victoria, Australia and Otago, New Zealand. *Ore Geol. Rev.* **1998**, *13*, 293–306. [CrossRef]

123. Sibson, R.H. Fault-valve behavior and the hydrostatic-lithostatic fluid pressure interface. *Earth-Sci. Rev.* **1992**, *32*, 141–144. [CrossRef]
124. McQueen, K.G. Ore deposit types and their primary expressions. In *Regolith Expression of Australian Ore Systems: A Compilation of Exploration Case Histories with Conceptual Dispersion, Process and Exploration Models*; Butt, C.R.M., Robertson, I.D.M., Scott, K.M., Cornelius, M., Eds.; Cooperative Research Centre for Landscape Environments and Mineral Exploration (CRCLEME): Bentley, Australia, 2005; pp. 1–14.
125. Phillips, G.N.; Thomson, D.F.; Kuehn, C.A. Deep weathering of deposits in the Yilgarn and Carlin gold provinces. In Proceedings of the Regolith '98 Conference: New Approaches to an Old Continent, Kalgoorlie, Australia, 2–9 May 1998; pp. 1–22. Available online: https://crcleme.org.au/Pubs/Monographs/regolith98/1-phillips_et_al.pdf (accessed on 2 August 2025).
126. Mihalasky, M.J.; Bonham-Carter, G.F. Lithodiversity and its spatial association with metallic mineral sites, Great Basin of Nevada. *Nat. Resour. Res.* **2001**, *10*, 209–226. [CrossRef]
127. Roshanravan, B.; Agajani, H.; Yousefi, M.; Kreuzer, O.P. Generation of a geochemical model to prospect podiform chromite deposits in north of Iran. In Proceedings of the 80th EAGE Conference and Exhibition, Copenhagen, Denmark, 11–14 June 2018.
128. Nykänen, V.; Lahti, I.; Niiranen, T.; Korhonen, K. Receiver operating characteristics (ROC) as validation tool for prospectivity models—A magmatic Ni-Cu case study from the central Lapland greenstone belt, northern Finland. *Ore Geol. Rev.* **2015**, *71*, 853–860. [CrossRef]
129. Tsoukalas, L.H.; Uhrig, R.E. *Fuzzy and Neural Approaches in Engineering*; John Wiley & Sons: New York, NY, USA, 1997; 606p.
130. Nykänen, V.; Groves, D.I.; Ojala, V.J.; Eilu, P.; Gardoll, S.J. Reconnaissance-scale conceptual fuzzy-logic prospectivity modelling for iron oxide copper-gold deposits in the northern Fennoscandian Shield, Finland. *Aust. J. Earth Sci.* **2008**, *55*, 25–38. [CrossRef]
131. Zimmermann, H.J. *Fuzzy Set Theory—And Its Applications*; Kluwer Academic Publishing: Dordrecht, The Netherlands, 1996; 399p.
132. Karbalaei-Ramezanali, A.; Feizi, F.; Jafarirad, A.; Lotfi, M. Application of best-worst method and additive ratio assessment in mineral prospectivity mapping: A case study of vein-type copper mineralization in the Kuhsiah-e-Urmak Area, Iran. *Ore Geol. Rev.* **2020**, *117*, 103268. [CrossRef]
133. Feizi, F.; Karbalaei-Ramezanali, A.A.; Farhadi, S. FUCOM-MOORA and FUCOM-MOOSRA: New MCDM-based knowledge-driven procedures for mineral potential mapping in greenfields. *SN Appl. Sci.* **2021**, *3*, 358. [CrossRef]
134. Aryafar, A.; Roshanravan, B. BWM-SAW: A new hybrid MCDM technique for modeling of chromite potential in the Birjand district, east of Iran. *J. Geochem. Explor.* **2021**, *231*, 106876. [CrossRef]
135. Riahi, S.; Fathianpour, N.; Tabatabaei, S.H. Improving the accuracy of detecting and ranking favorable porphyry copper prospects in the east of Sarcheshmeh copper mine region using a two-step sequential Fuzzy-Fuzzy TOPSIS integration approach. *J. Asian Earth Sci.* **2023**, *10*, 100166. [CrossRef]
136. Roshanravan, B.; Aghajani, H.; Yousefi, M.; Kreuzer, O.P. An improved prediction-area plot for prospectivity analysis of mineral deposits. *Nat. Resour. Res.* **2019**, *28*, 1089–1105. [CrossRef]
137. Roshanravan, B.; Kreuzer, O.P.; Buckingham, A.; Keys, E. On data quality in mineral potential modelling: A case study using Random Forest and fractal techniques. In Proceedings of the 84th EAGE Annual Conference & Exhibition, Vienna, Austria, 5–8 June 2023.
138. Roshanravan, B.; Kreuzer, O.P. An optimized XGBoost approach to prospectivity modelling of orogenic gold systems in the Granites-Tanami Orogen, Australia. In Proceedings of the 86th EAGE Annual Conference & Exhibition, Toulouse, France, 1–5 June 2025.
139. Rodriguez-Galiano, V.F.; Chica-Olmo, M.; Chica-Rivas, M. Predictive modelling of gold potential with the integration of multisource information based on random forest: A case study on the Rodalquilar area, Southern Spain. *Int. J. Geogr. Inf. Sci.* **2014**, *28*, 1336–1354. [CrossRef]
140. Carranza, E.J.M.; Laborte, A.G. Random forest predictive modeling of mineral prospectivity with small number of prospects and data with missing values in Abra (Philippines). *Comput. Geosci.* **2015**, *74*, 60–70. [CrossRef]
141. Sun, T.; Chen, F.; Zhong, L.; Liu, W.; Wang, Y. GIS-based mineral prospectivity mapping using machine learning methods: A case study from Tongling ore district, eastern China. *Ore Geol. Rev.* **2019**, *109*, 26–49. [CrossRef]
142. Xiang, J.; Xiao, K.; Carranza, E.J.M.; Chen, J.; Li, S. 3D mineral prospectivity mapping with random forests: A case study of Tongling, Anhui, China. *Nat. Resour. Res.* **2020**, *29*, 395–414. [CrossRef]
143. Zhang, S.; Carranza, E.J.M.; Xiao, K.; Wei, H.; Yang, F.; Chen, Z.; Xiang, J. Mineral prospectivity mapping based on isolation forest and random forest: Implication for the existence of spatial signature of mineralization in outliers. *Nat. Resour. Res.* **2022**, *31*, 1981–1999. [CrossRef]
144. Isles, D.J.; Cooke, A.C. Spatial associations between post-cratonisation dykes and gold deposits in the Yilgarn Block, Western Australia. In Proceedings of the 2nd International Dyke Conference—Mafic Dykes and Emplacement Mechanisms, Adelaide, Australia, 12–16 September 1990; pp. 157–162.
145. Cowan, E.J.; Hobbs, B.E. Perkins Discontinuities: Structurally controlled grade patterns diagnostic of epigenetic gold mineralisation at the deposit-scale. *Aust. J. Earth Sci.* **2025**, *72*, 660–700. [CrossRef]

146. Kreuzer, O.P. Bardoc gold study. In *Confidential Report to St Barbara Limited, Corporate Geoscience Group*; February 2023; 85p.
147. Crameri, K. Structural Controls on Mineralisation Within the Alpha Lode at the Aphrodite Deposit, Western Australia. Bachelor (Honours) Thesis, University of South Australia, Adelaide, Australia, 2002; 63p.
148. Ge, W.; Cheng, Q.; Jing, L.; Wang, F.; Zhao, M.; Ding, H. Assessment of the capability of Sentinel-2 imagery for iron-bearing minerals mapping: A case study in the Cuprite area, Nevada. *Remote Sens.* **2020**, *12*, 3028. [CrossRef]
149. Kimpe, C.D.; Miles, N. Formation of swelling clay minerals by sulfide oxidation in some metamorphic rocks and related soils of Ontario, Canada. *Can. J. Soil Sci.* **1992**, *72*, 263–270. [CrossRef]
150. Anand, R.R.; Butt, C.R.M. A guide for mineral exploration through the regolith in the Yilgarn Craton, Western Australia. *Aust. J. Earth Sci.* **2010**, *57*, 1015–1114. [CrossRef]
151. Cheng, Q.; Agterberg, F.P.; Ballantyne, S.B. The separation of geochemical anomalies from background by fractal methods. *J. Geochem. Explor.* **1994**, *51*, 109–130. [CrossRef]
152. Afzal, P.; Yasrebi, A.B.; Saein, L.D.; Panahi, S. Prospecting of Ni mineralization based on geochemical exploration in Iran. *J. Geochem. Explor.* **2017**, *181*, 294–304. [CrossRef]
153. Nezhad, S.G.; Mokhtari, A.R.; Rodsari, P.R. The true sample catchment basin approach in the analysis of stream sediment geochemical data. *Ore Geol. Rev.* **2017**, *83*, 127–134. [CrossRef]
154. Keykhay-Hosseinpoor, M.; Porwal, A.; Rajendran, K.; Panja, S. Mineral system modeling of lithium-cesium-tantalum (LCT)-type pegmatites: Regional-scale exploration targeting and uncertainty analysis in the Sanandaj-Sirjan zone, Western Iran. *J. Geochem. Explor.* **2025**, *279*, 107885. [CrossRef]
155. Partington, G. Developing models using GIS to assess geological and economic risk: An example from VMS copper gold mineral exploration in Oman. *Ore Geol. Rev.* **2010**, *38*, 197–207. [CrossRef]
156. Chudasama, B.; Porwal, A.; Kreuzer, O.P.; Butera, K. Geology, geodynamics and orogenic gold prospectivity modelling of the Paleoproterozoic Kumasi Basin, Ghana, West Africa. *Ore Geol. Rev.* **2016**, *78*, 692–711. [CrossRef]
157. Chudasama, B.; Kreuzer, O.P.; Thakur, S.; Porwal, A.; Buckingham, A. Surficial uranium mineral systems in Western Australia: Geologically-permissive tracts and undiscovered endowment. In *Quantitative and Spatial Evaluations of Undiscovered Uranium Resources*; IAEA-TECDOC-1861; International Atomic Energy Agency: Vienna, Austria, 2018; pp. 446–614.
158. Bruce, M.; Kreuzer, O.P.; Wilde, A.; Buckingham, A.; Butera, K.; Bierlein, F. Unconformity-type uranium systems: A comparative review and predictive modelling of critical genetic factors. *Minerals* **2020**, *10*, 738. [CrossRef]
159. Partington, G.A.; Peters, K.J.; Czertowicz, T.A.; Greville, P.A.; Blevin, P.L.; Bahiru, E.A. Ranking mineral exploration targets in support of commercial decision making: A key component for inclusion in an exploration information system. *Appl. Geochem.* **2024**, *168*, 106010. [CrossRef]
160. Chalice Mining Limited. Significant nickel-palladium discovery confirmed at Julimar. In *Australian Securities Exchange (ASX) Announcement Dated 15 April 2020*; Chalice Mining Limited: West Perth, Australia, 2020; 19p. Available online: https://chalicemining.com/wp-content/uploads/2022/12/6975195.pdf (accessed on 8 September 2025).
161. Dulfer, H.; Skirrow, R.G.; Champion, D.C.; Highet, L.M.; Czarnota, K.; Coghlan, R.; Milligan, P.R. *Potential for Intrusion-Hosted Ni-Cu-PGE Sulfide Deposits in Australia: A continental-Scale Analysis of Mineral System Prospectivity*; Record 2016(01); Geoscience Australia: Canberra, Australia, 2016; 97p.
162. Porwal, A.; Carranza, E.J.M.; Hale, M. Knowledge-driven and data-driven fuzzy models for predictive mineral potential mapping. *Nat. Resour. Res.* **2003**, *12*, 1–25. [CrossRef]
163. Kreuzer, O.P.; Markwitz, V.; Porwal, A.K.; McCuaig, T.C. A continent-wide study of Australia's uranium potential: Part I: GIS-assisted manual prospectivity analysis. *Ore Geol. Rev.* **2010**, *38*, 334–366. [CrossRef]
164. Roberts, F.I.; Witt, W.K.; Westaway, J. *Gold Mineralization in the Edjudina-Kanowna Region, Eastern Goldfields, Western Australia*; Report 90; Geological Survey of Western Australia: East Perth, Australia, 2004; 277p.
165. Blina Minerals NL. Acquisition of Dingo gold project. In *Australian Securities Exchange (ASX) Announcement Dated 05 May 2017*; Blina Minerals NL: West Perth, Australia, 2017; 14p. Available online: https://announcements.asx.com.au/asxpdf/20170505/pdf/43j1p43h2x9km6.pdf (accessed on 8 September 2025).
166. Verity Resources Limited. Resource upgrade drilling completed. In *Australian Securities Exchange (ASX) Announcement Dated 04 August 2025*; Verity Resources Limited: Kew East, Australia, 2025; 7p. Available online: https://wcsecure.weblink.com.au/pdf/VRL/02974515.pdf (accessed on 8 September 2025).
167. Verity Resources Limited. Historical drill validation study confirms high grade zones at Monument gold project. In *Australian Securities Exchange (ASX) Announcement Dated 12 September 2025*; Verity Resources Limited: Kew East, Australia, 2025; 28p. Available online: https://wcsecure.weblink.com.au/pdf/VRL/02992609.pdf (accessed on 8 September 2025).
168. Saturn Metals Limited. Regional aircore drill results widen a second major gold trend at the Apollo Hill project. In *Australian Securities Exchange (ASX) Announcement Dated 15 May 2025*; Saturn Metals Limited: West Perth, Australia, 2025; 17p.

169. Arika Resources Limited. Unlocking high-impact discoveries in the Leonora-Laverton goldfields. In *Australian Securities Exchange (ASX) Announcement Dated 18 September 2025*; Arika Resources Limited: Perth, Australia, 2025; 19p.
170. Genesis Minerals Limited. Strong drilling results at Laverton and Leonora support strategy to drive organic growth. In *Australian Securities Exchange (ASX) Announcement Dated 01 September 2025*; Genesis Minerals Limited: Perth, Australia, 2025; 30p.

Disclaimer/Publisher's Note: The statements, opinions and data contained in all publications are solely those of the individual author(s) and contributor(s) and not of MDPI and/or the editor(s). MDPI and/or the editor(s) disclaim responsibility for any injury to people or property resulting from any ideas, methods, instructions or products referred to in the content.

minerals

MDPI

Article

Geochemical Overprinting and Secondary Placer Crystal Formation in the La Cholla District, Quartzsite, Arizona, USA: Evidence from Copper Isotopes, Morphology, and Trace Elements

Erik B. Melchiorre [1,2,*], Ryan Mathur [3], George Kamenov [4] and Jorge Paredes [1]

[1] Department of Geology, California State University, 5500 University Parkway, San Bernardino, CA 92407, USA; jparedes@csusb.edu
[2] Department of Earth Sciences, University of California Riverside, 900 University Avenue, Riverside, CA 92521, USA
[3] Department of Geology, Juniata College, 1700 Moore Street, Huntingdon, PA 16652, USA; mathurr@juniata.edu
[4] Department of Geological Sciences, University of Florida, Gainesville, FL 32611, USA; kamenov@ufl.edu
* Correspondence: emelch@csusb.edu or emelch@ucr.edu; Tel.: +1-909-537-7745

Abstract: Geochemical overprinting on placer gold deposits produces complex deposits with apparently paradoxical geochemical and morphological attributes. The La Cholla placer gold deposits near Quartzsite, Arizona, USA, contain sharp and often undamaged gold crystals within high-energy gravels as a result of postdepositional recrystallization by localized hot springs. Geothermal fluids emanated from a basin-bounding fault and left a distinct signature that includes recrystallized gold with low Pb and δ^{65}Cu > 1.14‰, secondary uraninite and carnotite, travertine deposits, and mounds of highly silicified placer gravels. Surrounding these deposits are placer gravels with angular gold morphology and geochemistry indicative of flash-flood pulse placers with a lode gold source <5 km and gold particles with low Pb and δ^{65}Cu < 0.77‰. The multitude of small local lode gold source veins is likely related to specialized fluid migration along mid-Tertiary detachment faults. The unroofing of these veins at 5 to 17 Ma by high-angle Basin and Range faulting led to extensive placer development, with subsequent localized modification by geothermal fluid migration along the same faults. This study documents geochemical overprinting and modification of placer deposits and bears upon the study of other placers containing crystalline gold and uranium mineralization. Similar deposits may document past geothermal activity and identify structural fluid conduits and steep paleo-topographic gradients.

Keywords: gold; placer; gold crystals; copper isotope; uranium; Arizona

1. Introduction

The investigation of lode and placer gold deposit genesis bears directly on the exploration and extraction of this economically prized and industrially important metal. Natural "native gold" alloys of Au + Ag ± Cu (hereafter referred to as native primary gold) within lode ore deposits is well understood, and is generally interpreted as having a shallow hydrothermal origin ([1,2] and references therein). Placer gold is native gold within secondary sedimentary deposits, and its occurrence has been credited to primary, secondary, and a combination of primary and secondary formations [3]. In the simplest and most historically accepted theory of placer formation, a gold mass forms as a lode deposit during a hydrothermal event and survives physical and chemical weathering as native gold particles due to the low chemical reactivity and malleability of gold [1,4]. However, a secondary, accretionary origin for some placer gold has been suggested by observations of bacterioform gold, high-purity gold overgrowths, and nanoparticulate

gold in biomats [3,5–9]. Other authors have rejected low-temperature or biogeochemical nugget growth and suggested an abiological, high-temperature (100 s of °C) origin within lode deposits [10]. The recent consensus of many workers is that the processes of both primary and secondary models likely play a role in placer gold formation, with the specific contribution of each end member varying from location to location [3,11–13].

Studies of placer gold deposits have used morphology [14–16], trace element chemistry [14,17], biogeochemistry [3,7], and stable isotopes to understand deposit genesis. For example, placer gold alloy typically contains lead [18,19] in quantities sufficient to permit measurement of the lead isotope signal to provide insights into potential source(s) and process(es) that contributed to placer formation [14,20,21].

In particular, gold nuggets found in placers at Rich Hill, Arizona, contain thousands of ppm Pb and virtually no U [20]. Distinct Pb isotope values between vein and placer gold at Rich Hill indicated that the placer nuggets formed within the placer environment [20]. Therefore, comparison of isotope signatures between different types of native gold can provide important information about the origin of gold in the placer deposits.

In this study we take advantage of a recent resurgence in small-scale placer gold mining in the La Cholla District to obtain unique and historically rare access to these mining claims and samples. We utilize the mode of occurrence, morphology, elemental compositions, and Cu isotopes in the different types of native gold occurring in these placers to decipher the origin and evolution of native gold.

2. History and Geological Setting

The La Cholla District is located 10 km (6.2 miles) southwest of the town of Quartzsite in the Basin and Range Province of western Arizona, USA (Figure 1). Official placer gold production for all three adjoining districts of the greater Quartzsite area, from 1862 to present, is estimated at over 4665 kg (150,000 troy ounces) ([21] and references therein). Production for the La Cholla placers was poorly recorded but estimated at less than 746 kg (24,000 troy ounces) [22]. However, the real total production is likely much higher, as considerable amounts of gold went unreported in this remote district with a significant population of foreign miners [22–24]. The La Cholla District, and especially the Gold Eye Mine area within it, is noted for a localized abundance of very-well-crystalized gold within the placer deposits (Figure 2). Modern placer operations in the past two decades by Larry Schreiner (Beehive Mining), Steve Hunt (Gold Eye Mine), Terry Barnes (Melfern Mine), and metal detecting by countless others have yielded over 10 kg (over 300 troy ounces) of gold, including hundreds of individual euhedral gold crystals <1 g, with one massive cluster of physically damaged crystals recovered in 2019 weighing 280 g (9 troy ounces) (Figures 2 and 3).

The placer deposits at La Cholla were known to Europeans by at least the early 1800s, well before the "official" discovery in 1862. Many sources refer to "old Spanish diggings" that were encountered by the prospectors in the 1860s (e.g., [25,26]). Later work suggests that these placer diggings in La Cholla, and shallow prospect shafts in the nearby Plomosa District, were excavated by French fur trappers who were overwintering in the warmer climate of Arizona. A summary of the evidence provided in [25] includes stories by native peoples of revenge killings between themselves and Europeans in the 1830s to 1840s and artifacts from France such as coins, a sword, and a mirror (the latter two with French hallmarks). Some of these artifacts have been preserved in the collections of the Yuma and Quartzsite Historical Societies. In the 2000s, the location and extent of these older workings in the La Cholla District were mapped in a mining history project [26] that utilized a combination of historical and contextual evidence. Placer gold from the greater Quartzsite region is poorly studied and understood, with few published studies [26,27].

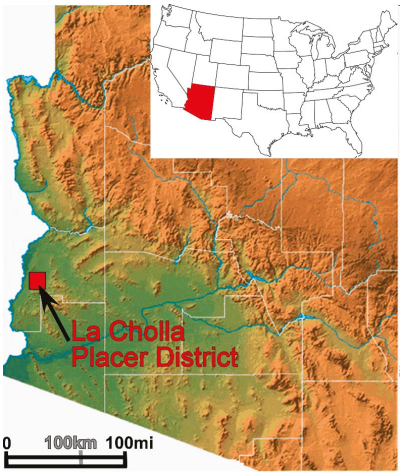


Figure 1. Index map of the location of the La Cholla District (red square), with inset map of the United States showing the location of Arizona in red (modified from [26]).

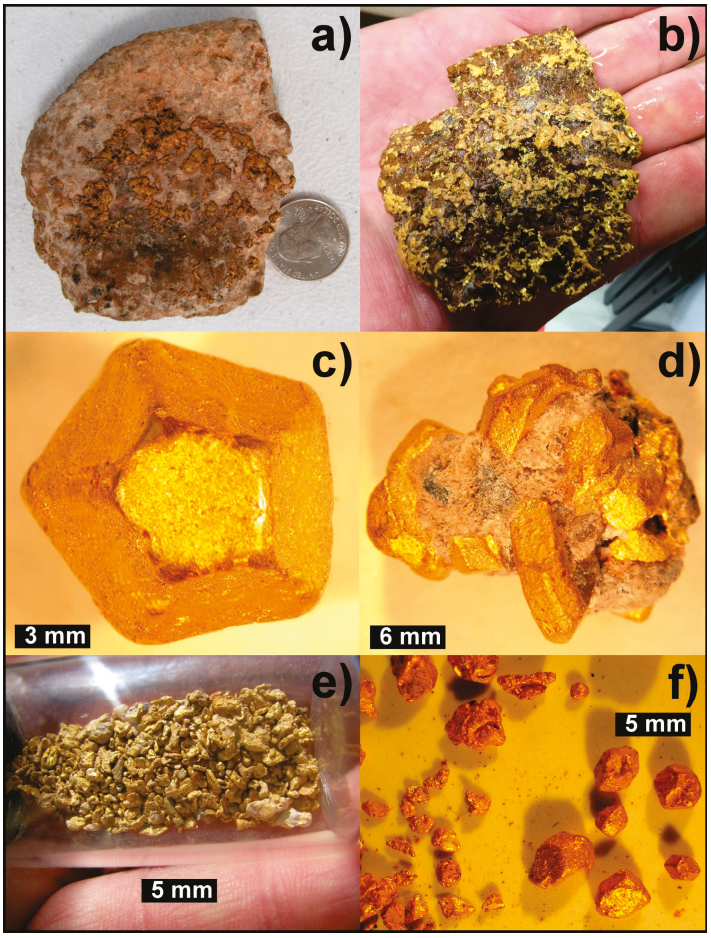


Figure 2. Examples of placer gold from the La Cholla placers: (**a**) A mass of caliche containing a 280 g (9 troy ounce) cluster of gold crystals. Coin is 24.26 mm. (**b**) The same cluster after removal of caliche with weak acid, highlighting damaged outer crystals and sharp internal crystal masses. Hand for scale. (**c**) Example of a 9 mm single crystal of gold from the placer deposit. (**d**) An 18 mm long cluster of crystals from the placer deposit showing tan caliche and silicified matrix. (**e**) A vial with raw dry-wash gold from the La Cholla placers, showing angular gold. Vial is 15 mm diameter. (**f**) Side-by-side comparison of angular gold (left) and damaged crystal gold (right) from the same day of operations at site 2019. All photos by author (EM).



Figure 3. Example of a portable wet recovery plant at Beehive Mining's operations in 2020. This plant is typically moved annually to new sites to access new deposits. A small loader at right loads paydirt into the yellow hopper to feed a conveyer to the cylindrical trommel (center-right). Gold is recovered from washed sediment in a sluice (center). Settling pans for water recycling are on the left.

The geological and geochemical setting of the La Cholla Placers was documented with field mapping of placer lithology/mineralogy, unit thickness, and depositional indicators. Locations of placer gold sampling are presented in Figure 4, while corresponding data are in Table 1. While much of the placer unit is weakly to moderately cemented by caliche (soil carbonate) and has angular gold particles, localized zones occur with abundant gold crystals and heavily silicified sediments with little to no caliche (Figure 5). For the purposes of this study, we refer to these cemented and altered gold-bearing sediments as "placers" to denote both their origin and method of mining. Within these silicified zones, striking bright yellow carnotite [$K_2(UO_2)_2(VO_4)_2 \bullet 3H_2O$] occurs as sparse coatings both on clasts and along postsilicification fractures (Figure 6). From the unconsolidated and caliche-cemented placers, two small particles of uraninite [UO_2] were identified in "black sand" placer concentrates. Lead also occurs abundantly within the unconsolidated and caliche-cemented placer unit, with nodules of argentiferous galena encrusted by cerussite (1 mm to 10 cm) being abundant enough to have been mined historically as their own resource [25]. These galena/cerussite nodules should not be confused with anthropogenic lead bullet fragments that are often found in heavy mineral separates from many modern placer operations.

Table 1. Morphological measurements and calculations, plus major and minor element concentrations for placer gold particles examined in this study. * denotes samples which were also analyzed by ICP-MS, with associated data presented in Table 2. † Flatness index (FI) was calculated using the formula FI = length + width/2 X thickness or (X + Y)/2Z) in the nomenclature below. ‡ Distance was calculated using the flatness index, as described in Section 3. "Inclusion" classification is for gold with >30% mineral inclusions by visual estimation.

Sample Number	X (cm)	Y (cm)	Z (cm)	T/W	W/L	FI †	Distance (km) ‡	Au (wt%)	Ag (wt%)	Cu (mg/kg)
Crystals										
2019 R1	0.42	0.36	0.32	0.89	0.86	1.22	1.05	99.95	0.05	76
2019 R2	0.40	0.38	0.24	0.63	0.95	1.63	1.18	99.78	0.22	58
2019 R3 *	0.29	0.27	0.18	0.67	0.93	1.56	1.15	99.01	0.98	95
2019 R4	0.31	0.28	0.23	0.82	0.90	1.28	1.07	98.59	1.40	18
2018 R1	0.38	0.35	0.27	0.77	0.92	1.35	1.08	97.89	2.10	86
2018 R2	0.51	0.39	0.31	0.79	0.76	1.45	1.11	98.15	1.84	73
2018 R3	0.69	0.61	0.42	0.69	0.88	1.55	1.15	97.43	2.56	89
2017 R1	0.25	0.22	0.19	0.86	0.88	1.24	1.06	99.73	0.26	79
2017 R2	0.32	0.30	0.29	0.97	0.94	1.07	1.03	99.02	0.97	111
2016 R1	0.41	0.40	0.39	0.98	0.98	1.04	1.03	99.31	0.68	88
2016 R2	0.60	0.51	0.42	0.82	0.85	1.32	1.08	99.36	0.63	79
2016 R3 *	0.55	0.46	0.39	0.85	0.84	1.29	1.07	96.04	3.94	191
2016 R4	0.38	0.34	0.32	0.94	0.89	1.13	1.04	98.89	1.11	36
2016 R5	0.48	0.42	0.35	0.83	0.88	1.29	1.07	99.07	0.92	116
2016 R6	0.31	0.29	0.27	0.93	0.94	1.11	1.03	99.88	0.11	93
2016 R7	0.27	0.26	0.19	0.73	0.96	1.39	1.10	95.92	4.07	61
2016 R8	0.42	0.40	0.38	0.95	0.95	1.08	1.03	98.85	1.14	93
2015 R1	0.41	0.32	0.31	0.97	0.78	1.18	1.04	98.67	1.32	117
2015 R2	0.25	0.20	0.20	1.00	0.80	1.13	1.04	98.71	1.28	125
2015 R3	0.26	0.23	0.18	0.78	0.88	1.36	1.09	99.23	0.76	151
2015 R4 *	0.25	0.23	0.17	0.74	0.92	1.41	1.10	99.30	0.68	134
2015 R5	0.31	0.28	0.19	0.68	0.90	1.55	1.15	97.10	2.88	157
2015 R6	0.27	0.21	0.18	0.86	0.78	1.33	1.08	98.90	1.09	141
2015 R7	0.23	0.20	0.17	0.85	0.87	1.26	1.06	99.26	0.72	126
2014 R1	0.39	0.35	0.28	0.80	0.90	1.32	1.08	99.14	0.85	116
2014 R2	0.22	0.21	0.19	0.90	0.95	1.13	1.04	98.68	1.31	142
2014 R3	0.21	0.17	0.16	0.94	0.81	1.19	1.05	99.10	0.89	93
2014 R4	0.19	0.16	0.15	0.94	0.84	1.17	1.04	99.75	0.24	38
2014 R5	0.24	0.20	0.17	0.85	0.83	1.29	1.07	98.90	1.10	71
2013 R1	0.21	0.19	0.17	0.89	0.90	1.18	1.04	98.62	1.37	127
2013 R2	0.19	0.16	0.15	0.94	0.84	1.17	1.04	99.85	0.14	146
2013 R3	0.20	0.18	0.17	0.94	0.90	1.12	1.04	99.57	0.42	98
2013 R4	0.19	0.17	0.16	0.94	0.89	1.13	1.04	98.83	1.15	150
2013 R5	0.20	0.18	0.17	0.94	0.90	1.12	1.04	99.28	0.70	131
Angular										
2019 A1	0.59	0.37	0.21	0.57	0.63	2.29	1.62	94.02	5.95	221
2019 A2	0.67	0.43	0.25	0.58	0.64	2.20	1.55	95.79	4.19	185
2019 A3	0.52	0.37	0.20	0.54	0.71	2.23	1.57	95.13	4.85	197
2019 A4	0.87	0.41	0.29	0.71	0.47	2.21	1.56	95.89	4.09	210
2019 A5	0.75	0.36	0.25	0.69	0.48	2.22	1.57	94.77	5.20	216
2018 A1	0.42	0.28	0.14	0.50	0.67	2.50	1.82	96.07	3.84	822
2018 A2	0.71	0.41	0.22	0.54	0.58	2.55	1.87	94.90	4.99	1109
2018 A3	0.62	0.39	0.17	0.44	0.63	2.97	2.37	95.68	4.23	835
2018 A4	0.72	0.48	0.22	0.46	0.67	2.73	2.07	95.30	4.63	710
2018 A5	0.68	0.52	0.23	0.44	0.76	2.61	1.94	95.27	4.64	892

Table 1. *Cont.*

Sample Number	X (cm)	Y (cm)	Z (cm)	T/W	W/L	FI †	Distance (km) ‡	Au (wt%)	Ag (wt%)	Cu (mg/kg)
2017 A1 *	0.42	0.34	0.18	0.53	0.81	2.11	1.48	96.50	3.48	209
2017 A2	0.57	0.32	0.15	0.47	0.56	2.97	2.36	98.19	1.77	388
2017 A3 *	0.46	0.34	0.12	0.35	0.74	3.33	2.89	99.10	0.86	425
2016 A1 *	0.61	0.39	0.27	0.69	0.64	1.85	1.30	93.96	5.94	1038
2016 A2	0.74	0.43	0.32	0.74	0.58	1.83	1.29	95.75	4.19	640
2015 A1	0.52	0.23	0.21	0.91	0.44	1.79	1.27	94.20	5.75	487
2015 A2	0.60	0.35	0.25	0.71	0.58	1.90	1.33	94.93	5.03	437
2015 A3 *	0.58	0.22	0.20	0.91	0.38	2.00	1.40	95.81	4.13	612
2015 A4	0.60	0.25	0.21	0.84	0.42	2.02	1.42	92.12	7.82	541
2015 A5	0.76	0.28	0.23	0.82	0.37	2.26	1.60	95.89	4.04	662
2015 A6	0.65	0.35	0.29	0.83	0.54	1.72	1.23	92.07	7.86	765
2015 A7	0.68	0.38	0.29	0.76	0.56	1.83	1.29	93.07	6.89	371
2014 A1 *	0.52	0.39	0.14	0.36	0.75	3.25	2.76	97.59	2.39	199
2014 A2 *	0.53	0.39	0.15	0.38	0.74	3.07	2.50	96.31	3.67	149
2014 A3	0.52	0.41	0.15	0.37	0.79	3.10	2.54	97.03	2.95	192
2014 A4	0.61	0.50	0.13	0.26	0.82	4.27	4.60	98.14	1.84	171
2014 A5	0.65	0.52	0.14	0.27	0.80	4.18	4.41	98.98	1.01	128
2013 A1	0.45	0.32	0.13	0.41	0.71	2.96	2.36	98.10	1.86	427
2013 A2 *	0.39	0.30	0.12	0.40	0.77	2.88	2.25	99.26	0.70	470
2013 A3	0.54	0.39	0.15	0.38	0.72	3.10	2.54	99.02	0.94	395
2013 A4	0.51	0.36	0.13	0.36	0.71	3.35	2.91	96.02	3.94	400
2013 A5	0.51	0.35	0.15	0.43	0.69	2.87	2.24	98.37	1.59	479
Inclusions										
2019 I1	0.55	0.37	0.20	0.54	0.67	2.30	1.63	94.23	5.63	1397
2019 I2	0.52	0.34	0.19	0.56	0.65	2.26	1.60	95.69	4.21	1072
2019 I3	0.63	0.39	0.17	0.44	0.62	3.00	2.41	94.87	5.04	934
2019 I4	0.41	0.38	0.18	0.47	0.93	2.19	1.55	95.32	4.62	630
2019 I5	0.51	0.36	0.16	0.44	0.71	2.72	2.06	95.34	4.58	837
2017 I1 *	0.39	0.35	0.14	0.40	0.90	2.64	1.97	98.38	1.05	5722
2015 I1	0.41	0.29	0.18	0.62	0.71	1.94	1.36	98.13	1.79	808
2015 I2	0.43	0.31	0.20	0.65	0.72	1.85	1.30	97.39	2.54	698
2015 I3	0.57	0.35	0.19	0.54	0.61	2.42	1.75	97.69	2.24	723
2015 I4	0.58	0.33	0.18	0.55	0.57	2.53	1.85	99.09	0.84	752
2014 I1	0.51	0.22	0.12	0.55	0.43	3.04	2.46	99.04	0.91	561
2014 I2	0.95	0.54	0.21	0.39	0.57	3.55	3.23	99.50	0.44	623
2013 I1 *	0.52	0.38	0.22	0.58	0.73	2.05	1.43	96.95	2.94	1101
2013 I2	0.57	0.45	0.23	0.51	0.79	2.22	1.56	95.81	4.13	593
2013 I3	0.60	0.38	0.21	0.55	0.63	2.33	1.66	96.35	3.60	512
2013 I4	0.73	0.61	0.31	0.51	0.84	2.16	1.52	96.52	3.45	355

Table 2. ICP-MS trace element data for select placer gold particles. Units are mg/kg.

Elem.	2013 A2	2015 R4	2016 R3	2019 R3	2014 A1	2014 A2	2015 A3	2016 A1	2017 A1	2017 A3	2013 I1	2017 I1
V	0.078	0.150	0.050	0.148	0.015	0.273	0.110	0.107	0.057	0.073	0.186	0.062
Cr	0.063	0.032	0.025	0.063	0.030	0.104	0.058	0.077	0.037	0.104	0.052	0.035
Mn	<0.1	<0.1	<0.1	<0.1	<0.1	<0.1	<0.1	<0.1	<0.1	<0.1	<0.1	<0.1
Fe	<0.2	7.49	<0.2	<0.2	4.90	0.66	0.40	<0.2	<0.2	0.67	<0.2	1.98
Ni	<0.007	<0.007	<0.007	<0.007	<0.007	<0.007	0.018	<0.007	<0.007	<0.007	<0.007	<0.007
Cu	487	528	101	102	206	162	630	1122	234	436	1049	5788
Zn	0.207	<0.02	0.024	<0.02	0.816	<0.02	0.036	0.381	<0.02	0.468	0.090	0.488
Sr	<0.01	<0.01	<0.01	<0.01	<0.01	<0.01	<0.01	<0.01	<0.01	<0.01	<0.01	<0.01
Ba	<0.025	0.349	<0.025	<0.025	<0.025	<0.025	<0.025	<0.025	<0.025	<0.025	<0.025	<0.025
La	0.001	0.004	0.001	<0.0001	0.003	0.003	0.002	<0.0001	0.001	<0.0001	0.002	0.001
Ce	0.001	0.002	0.002	0.001	0.006	0.002	0.003	<0.0001	0.003	0.001	0.003	0.001

Table 2. *Cont.*

Elem.	2013 A2	2015 R4	2016 R3	2019 R3	2014 A1	2014 A2	2015 A3	2016 A1	2017 A1	2017 A3	2013 I1	2017 I1
Pr	<0.0001	0.001	0.001	<0.0001	0.001	0.001	0.001	<0.0001	<0.0001	<0.0001	<0.0001	<0.0001
Nd	<0.0008	0.003	0.001	0.001	0.004	<0.0008	0.003	<0.0008	<0.0008	<0.0008	<0.0008	<0.0008
Sm	<0.0007	<0.007	<0.0007	<0.007	<0.0007	<0.007	<0.0007	0.001	<0.0007	<0.007	<0.0007	<0.007
Eu	<0.0012	<0.0012	<0.0012	<0.0012	<0.0012	<0.0012	<0.0012	<0.0012	<0.0012	<0.0012	<0.0012	<0.0012
Gd	<0.0043	<0.0043	<0.0043	<0.0043	<0.0043	<0.0043	<0.0043	<0.0043	<0.0043	<0.0043	<0.0043	<0.0043
Tb	<0.0001	<0.0001	<0.0001	<0.0001	<0.0001	<0.0001	<0.0001	<0.0001	<0.0001	<0.0001	<0.0001	<0.0001
Dy	<0.0003	<0.0003	<0.0003	<0.0003	<0.0003	<0.0003	0.002	<0.0003	<0.0003	<0.0003	<0.0003	<0.0003
Ho	<0.0001	<0.0001	<0.0001	<0.0001	<0.0001	<0.0001	<0.0001	<0.0001	<0.0001	<0.0001	<0.0001	<0.0001
Er	<0.0003	<0.0003	<0.0003	<0.0003	<0.0003	<0.0003	<0.0003	<0.0003	<0.0003	<0.0003	<0.0003	<0.0003
Tm	<0.0001	<0.0001	<0.0001	<0.0001	<0.0001	<0.0001	<0.0001	<0.0001	<0.0001	<0.0001	<0.0001	<0.0001
Yb	<0.0004	<0.0004	<0.0004	<0.0004	<0.0004	<0.0004	<0.0004	<0.0004	<0.0004	<0.0004	<0.0004	<0.0004
Lu	<0.0001	<0.0001	<0.0001	<0.0001	<0.0001	<0.0001	<0.0001	<0.0001	<0.0001	<0.0001	<0.0001	<0.0001
Pb	0.071	0.227	0.088	0.025	1.882	71.231	0.121	0.042	0.011	0.380	0.038	0.458
Th	0.016	0.010	0.008	0.020	0.007	0.036	0.020	0.015	0.011	0.014	0.012	0.010
U	<0.0001	<0.0001	0.002	<0.0001	<0.0001	<0.0001	0.004	<0.0001	<0.0001	0.001	<0.0001	<0.0001

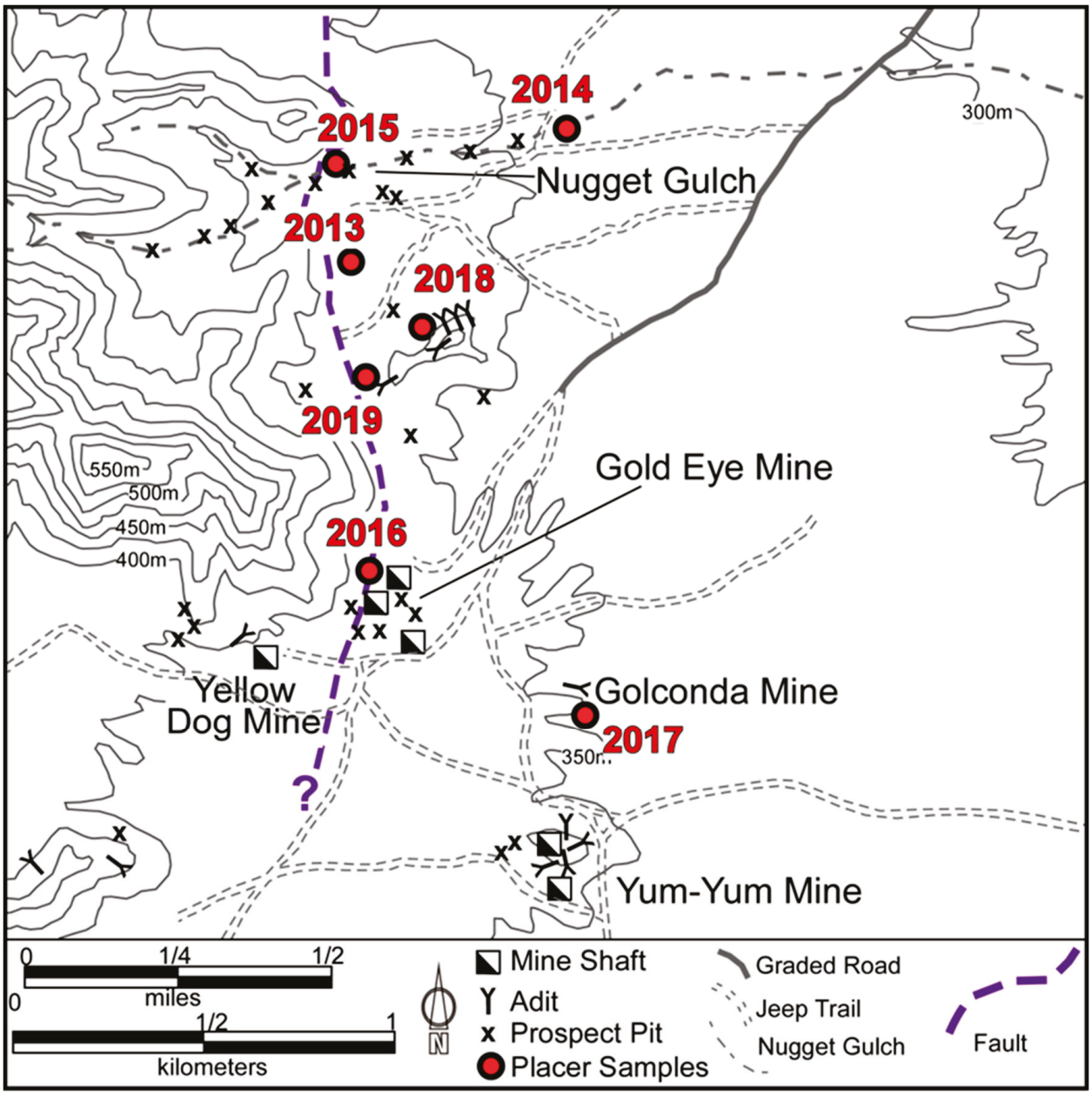


Figure 4. Map of La Cholla placers showing location of placer samples from this study (red dots) and major mines and landmarks. Dashed purple line is the approximate trace of the major range-bounding fault.

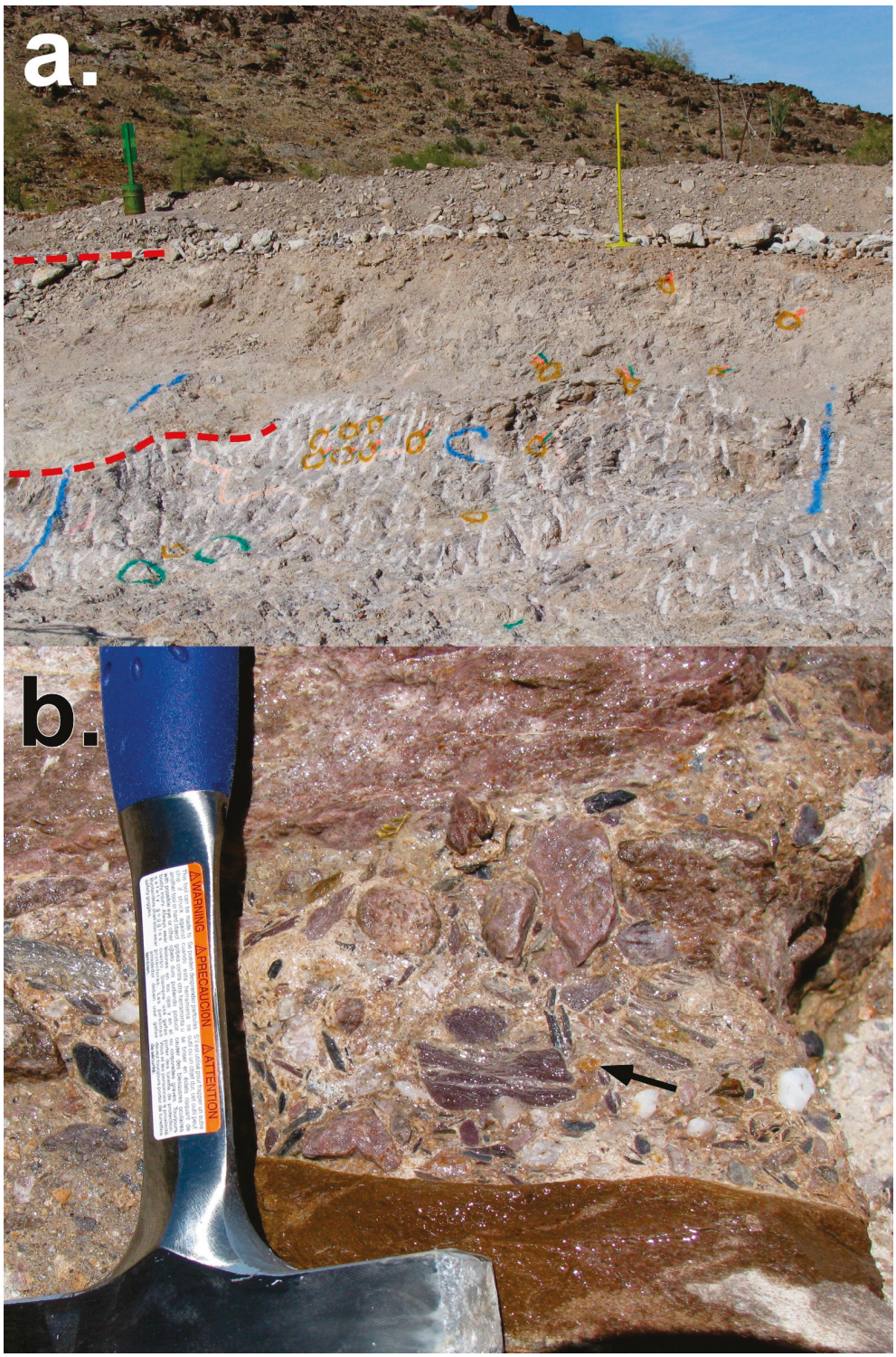


Figure 5. Photos of La Cholla placers at the Gold Eye Mine (site 2016). (**a**) Section of an active mining face in placer gravels. Green post on left is 1 m (field of view is ~8 m, L to R). From the top, separated by red dashed lines on left: modern slope-wash gravels, older caliche-cemented gravels, and at bottom of section, silica-cemented gravels. Orange spray-painted circles on outcrop mark metal detector "hits" where gold crystals or nuggets were later recovered. White vertical lines in silica-cemented unit are from a backhoe-mounted jackhammer. (**b**) Detail of silica-cemented gravels, wetted with water to highlight detail. A 6 mm gold crystal is exposed at the black arrow. Rock hammer for scale.

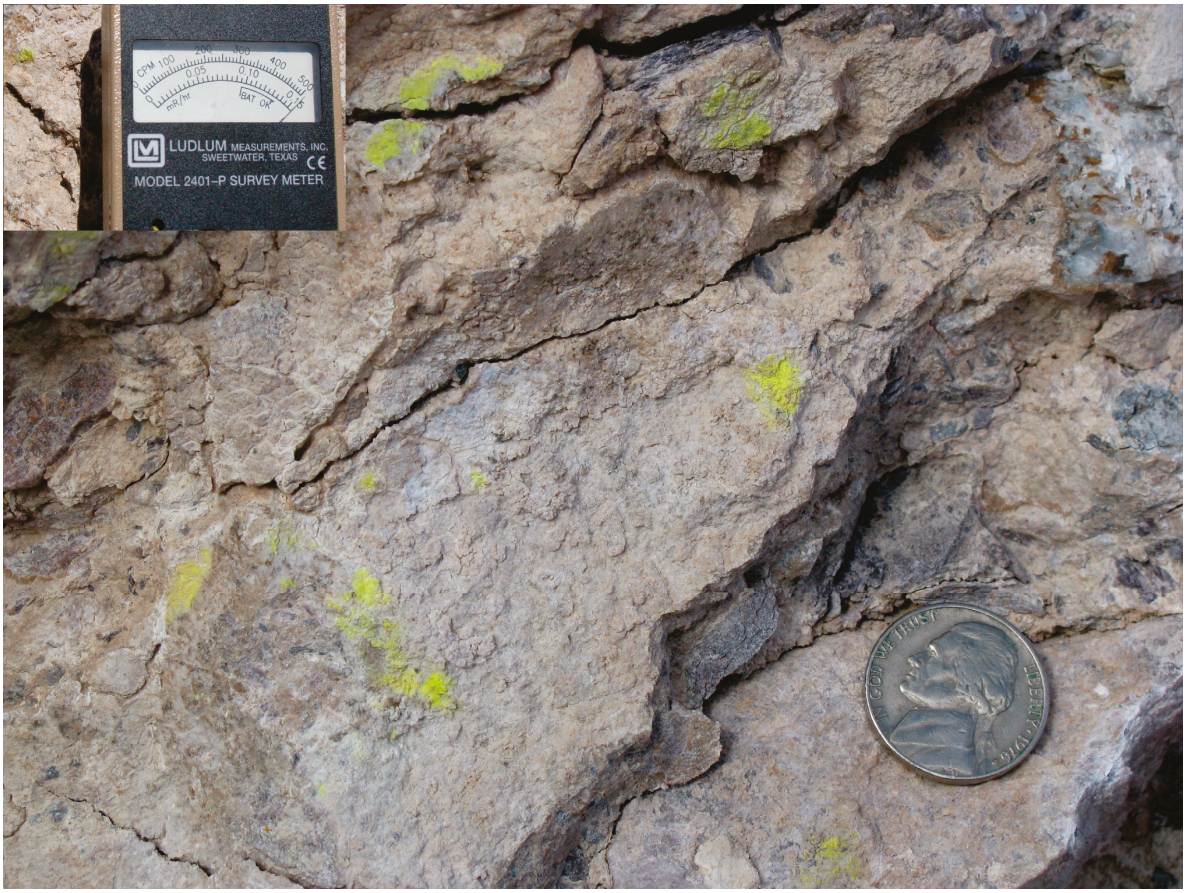


Figure 6. Silica- and caliche-impregnated sand and gravel placer unit at La Cholla. The caliche coating conceals unit texture in most places. Yellow coatings are the uranium mineral carnotite. Coin is 21.21 mm diameter. Inset photo is a α–β–γ radiation survey meter on the same outcrop showing a reading exceeding 0.15 mR/h (500 counts per minute).

Known lode gold sources for placers at La Cholla include dozens of small veins of quartz + siderite + gold ± pyrite ± chalcopyrite ± iron oxides or quartz + tourmaline ± gold. The specific location of individual veins is not mapped or recorded here, at the request of mining claim owners. These veins are generally less than 1 m wide and persist for 10s of m along strike, and they have been opened by dozens of shallow prospect shafts and adits. The largest lode mines were the Yum Yum and Beehive, with a combined production of 8.5 kg (275 troy ounces) of gold [23,24,26,28]. These lode gold deposits occur within the Jurassic McCoy Mountains Formation [29]. In the study area, this complex sequence of south-dipping metasedimentary rocks includes a tan metaconglomerate-to-quartzite overlain by a distinctive purple-to-green phyllitic schist. Felsic volcanic rocks of Jurassic age occur within the north end of the district [30] but host fewer of the lode gold veins.

3. Materials and Methods

This study examines placer gold recovered during modern placer mining operations and was facilitated by the willingness of several mine owners to permit scientific study of their gold. Samples were obtained from each of the seven study area localities employing the methodology described below. It was not practical to obtain additional samples for this study due to the elevated price of gold, difficulty in maintaining access to claims, and time required for obtaining sterile samples and new samples from within cemented deposits using only hand tools.

Samples of gold were recovered from placer deposits by utilizing a combination of methods. Samples of 0.25 to 1 g were recovered for geochemical and shape analyses using

the portable wet recovery plants operated by individual mine owners. In these operations, a "Bobcat" loader feeds placer gravels into a wet spray trommel to separate oversize gravels. The oversize gravels are later examined with a metal detector for the collection of the rare oversize gold. The trommel fines are processed in a recirculating sluice with riffles and gold matting, with cleanup by hand panning of concentrates. These plants can process 2 to 10 cubic yards of material per day, with capacity limited by water quality and water availability. Three cascading rectangular 2 × 3 m metal settling basins recycle the plant water, and operations end each day when water becomes too muddy and inhibits gold recovery (Figure 3).

Additional samples were recovered using a Keene Engineering vibrostatic dry washer (Chatsworth, CA, USA). Similarly, larger gold (>0.50 g) was recovered with a MINELAB GP-Extreme metal detector under dry conditions. In zones of placer sediment that were heavily silicified and cemented, metal detector "hits" were marked and samples removed later by hand with a hammer and chisel. All samples were recovered by, or in the presence of, one of the authors. Samples were not cleaned prior to analysis.

Secondary gold structures and morphologies of placer gold samples were measured and imaged using established methods [31]. Morphological measurements and observations were performed on individual gold particles using microtweezers and a binocular microscope with digital camera. Samples for additional shape and surface chemical analyses were mounted with double-sided carbon tape on their flattest side to expose the maximum surface area. A LEO Zeiss 1540XB Field Emission Gun-Scanning Electron Microscope (SEM) (Carl Zeiss AG, Jena, Germany) was used to generate secondary electron (SE) and backscatter electron (BSE) images using an acceleration voltage of 2 or 15 kV, respectively. Concavities on gold particle surfaces were targeted, as these regions were most likely to contain and preserve exterior-projecting mineral inclusions and fragile bacterioform gold structures.

Additional SEM imaging of the exterior and interior surfaces of representative gold particles was performed with a Fisher-Phenom ProX SEM employing the same settings detailed above. A Cameca SX-100 at the University of Arizona was used for Electron Probe Micro-Analyzer (EPMA) probe measurements of gold (major) and silver–copper (minor) element abundances, using standard off-peak interference and matrix corrections [32,33]. Following shape analysis and grain exterior observations, samples were mounted on a postmount with double-sided carbon tape and lightly polished to expose grain interiors for major and minor element analysis. Some of these samples were later removed for ICP-MS and copper isotope analyses. Some samples were embedded in low-volatile epoxy and deeply polished to explore potential rim chemistry variations, using sequential grits down to a 0.3 micron diamond abrasive. Great care was taken to minimize sample preparation artifacts such as deposition of polishing debris into fractures or pores, localized smearing which can obscure internal chemistry or physical features, and cross-contamination [34,35]. The error associated with the in situ EPMA element microprobe analyses is less than ±0.1 wt%.

For trace element analyses, native gold nuggets were dissolved in precleaned Teflon beakers with 4 mL ultrapure Aqua Regia on a hot plate for 24 h. A small fraction of the resultant Aqua Regia solution was further diluted with 5% HNO_3 to achieve final dilution of around 2000×. Precise final dilution factor was determined by weight for each sample. Trace element analyses were performed on an Element2 HR-ICP-MS (Thermo Finnigan, San Jose, CA, USA) at medium resolution. Quantification of the results was achieved via external calibration using a set of gravimetrically prepared dilutions of commercial ICP-MS standards (SPEX CertiPrep, Inc., Metuchen, NJ, USA).

Native gold samples were processed similar to the techniques in [36], where two ion-exchange chromatography was used to purify the copper from the gold-rich matrix. The gold was dissolved in Teflon beakers with 4 mL of ultrapure Aqua Regia at 140 °C for 24 h. These solutions were dried, and concentrations of copper were measured from these solutions on an ICP-OES at Pennsylvania State University to determine the

amount of solution to dry for purification by ion exchange chromatography. Approximately 10 micrograms of copper was used for ion exchange chromatography, as defined in [37].

Copper isotope ratios were measured on the Neptune (Thermo brand, Schaumburg, IL, USA) at Pennsylvania State University. The instrument was in low resolution mode and the solution concentrations were at 100 ppb. This generated a 5 V signal on ^{63}Cu. Mass bias was corrected for using standard–sample–standard bracketing with the NIST 976 international isotope standard. One block of 30 ratios was measured for each sample, and this procedure was repeated so that the reported values are an average of 60 ratios. The reported values are in the traditional per mil format compared to the NIST 976. Errors for the analyses are 0.08‰ (2Θ) and are calculated by the overall variations of the NIST standard for the duration of the measurement session (described in [37]). Replicate values all fall within this reported range. An internal standard (USD 1 cent coin from 1838) had δ65Cu = +0.05‰ (±0.07, 2σ, n = 3) within the error of the value reported in [37].

Morphological analyses were performed on physical measurements using the methods and reporting nomenclature outlined in detail in [38–43]. Flatness index (FI) was calculated using the formula FI = length + width/2 X thickness or (X + Y)/2Z) [42].

4. Results

The thickness of the placer gravels is just 0.5 m (1.6 ft) in the west against the southern Dome Rock Mountains bedrock but over 30 m (100 ft) thick as measured in mine shafts to the east. Throughout most of these thicker sections, gold is irregularly distributed and fine-grained, averaging 0.2 g/m^3 where sampled. In the thicker sections of placer, a richer zone averaging 1 g/m^3 was encountered at about mid-depth within a bed of coarser sediment, while the richest zone is just above bedrock with grades above 1 g/m^3 and containing the coarsest gold. The placer gravels contain zones of strong silicification and calcite cementing where they extend over a major high-angle range-bounding fault (Figure 4). Remnants of small pods of travertine are also found in the gravels over this fault, though much more has been mined historically for production of lime to whitewash the early adobe buildings of the region.

The four main methods used to examine the placer gold from the La Cholla placers are morphological measurements using a binocular microscope or SEM; major and minor element characterization of gold grain outer surfaces and interiors using EPMA; trace element characterization of gold particles using ICP-MS; and copper isotope measurements. Biological observations, amplifications, and culturing with subsequent biomolecular sequencing of the isolate were performed on samples collected under sterile conditions. However, this work is beyond the scope of the present study and requires additional analyses.

Results of morphological analyses are presented in Figure 7 and Table 1. Surface textures [36] varied from highly irregular and angular to regular and rounded and include a wide range of putative (bio)geochemical forms and textures. Gold from the silicified gravels, and their physical weathering products located directly down the modern topographic gradient, are dominantly regular and smooth surfaced three-dimensional euhedral crystals with sharp faces (e.g., Figure 2c,d). Paradoxically, these same silicified deposits contain abundant rounded fist- to pea-sized cobbles and gravel, suggestive of a high-energy depositional environment (Figure 3b).

Gold particles from unconsolidated and caliche-cemented gravels have surface angularity and are considerably flattened and elongate. The angular placer gold particles examined with SEM imaging exhibit deep pockets which contain matlike structures with a strong morphological resemblance to bacterial mats and surfaces replete with a wide range of putative biomorphic forms. Where present, impact striation marks were dull and weathered, suggesting prolonged exposure to chemical weathering after they were created. These striations are not shiny and fresh, as is often observed when damage occurs during mining.

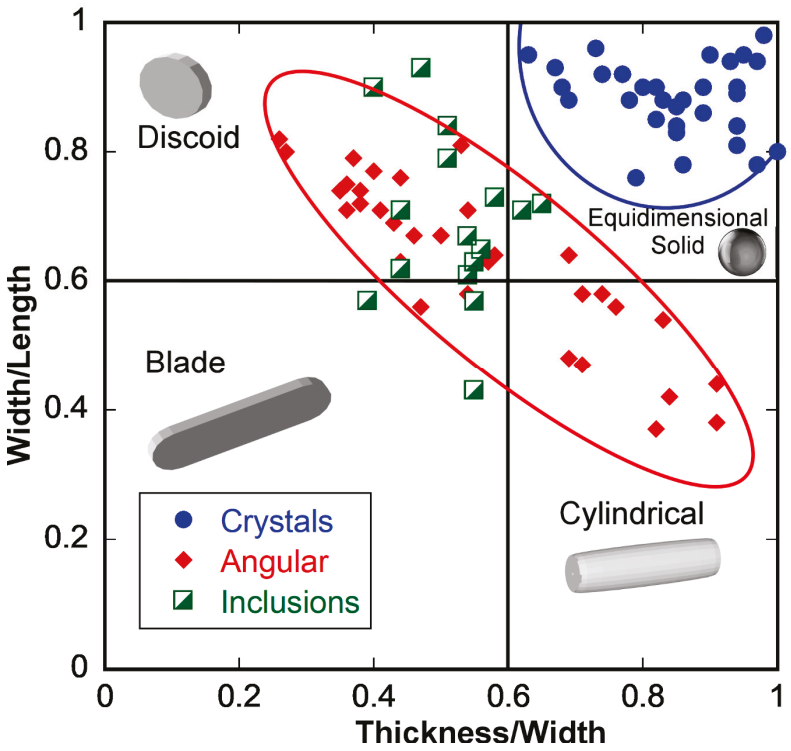


Figure 7. Zingg plot of the morphology of placer gold from the La Cholla placers. Examples of idealized morphology are presented in gray.

A subset of the angular gold grouping is "inclusion gold" that contains inclusions of other minerals at >30% by volume within gold otherwise exhibiting the same angular gold group characteristics. The inclusion grouping gold has inclusions of siderite, iron oxides, metal sulfides (pyrite, chalcopyrite, galena), quartz, mica, and on rare occasions tourmaline. Where present, the tourmaline crystals are observed intact and penetrating the interiors of gold particles (Figure 8). Morphology of this gold grouping is similar to the angular grouping, and where it differs, this is attributed to external projections of the inclusions.

Major and minor element data for gold grain interior surfaces are presented in Table 1. The crystal shape population (n = 34) ranged from 99.95 to 95.92 wt% gold, with an average of 98.82%. Silver ranged from 4.07 to 0.05 wt% silver, with an average of 1.17%. Copper ranged from 191 to 18 mg/kg, with an average of 103 mg/kg. The angular gold group (n = 32) ranged from 99.26 to 92.07 wt% gold, with an average of 96.04%. Silver ranged from 7.86 to 0.07 wt% silver, with an average of 3.91%. Copper ranged from 1109 to 128 mg/kg, with an average of 468 mg/kg. The inclusion gold group (n = 16) ranged from 99.5 to 94.23 wt% gold, with an average of 96.89%. Silver ranged from 5.63 to 0.44 wt% silver, with an average of 3.00%. Copper ranged from 5722 to 355 mg/kg, with an average of 1082 mg/kg ppm.

Trace element characterization of gold particles using ICP-MS is presented in Table 2. All trace elements except copper have very low abundance. Of particular note are the exceedingly low levels of Pb and U measured within the gold particles. Copper concentrations range from 101 mg/kg to 5788 mg/kg, consistent with EPMA values reported for La Cholla placer gold particles.

Copper isotope measurement for individual placer gold particles (Table 3) ranged from a δ^{65}Cu high of +4.95‰ to a low of +0.14‰. Distribution of values is bimodal, with the crystal grouping >1.14‰ and the angular and inclusion grouping <0.77‰. Samples in Table 3 are either for the same particles also found in Table 1 (e.g., 2014 A2) or for separate particles not presented in Table 1 (e.g., 2014 Angular).

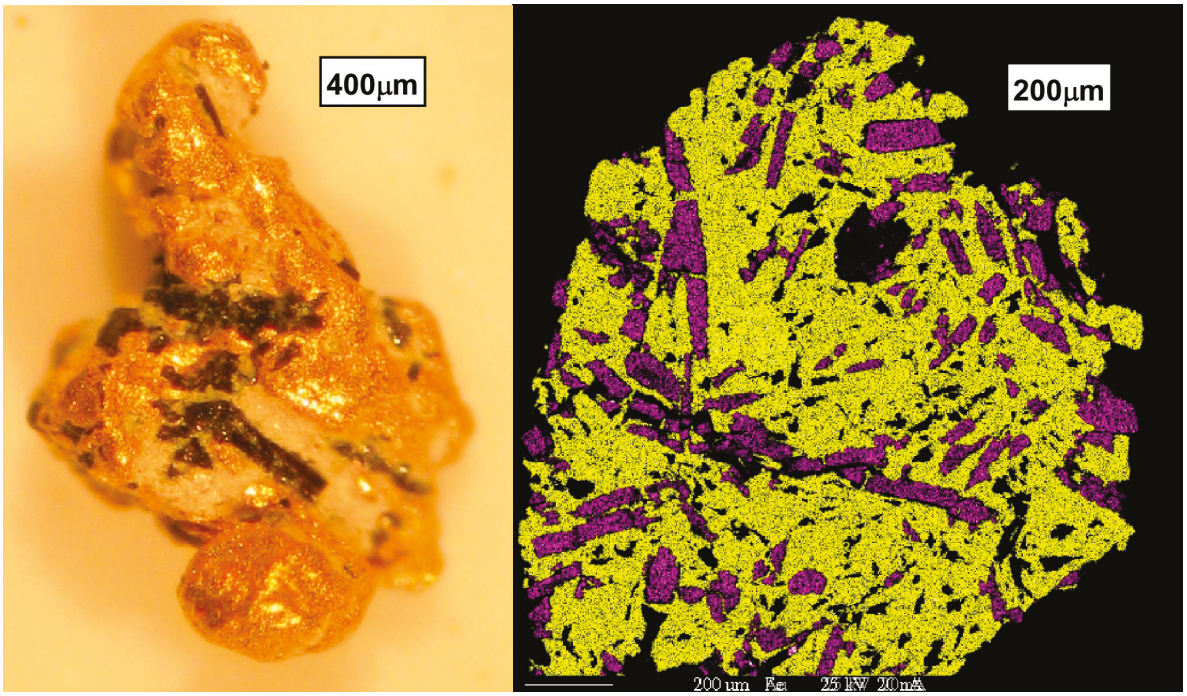


Figure 8. Inclusion gold morphology showing tourmaline inclusions. (L) The exterior of a small gold particle showing black elongate crystals of tourmaline. (R) SEM-EDX element map for a polished interior section of gold showing iron (red) and semiquantitative boron (blue) abundance, highlighting tourmaline as purple within a gold (yellow) matrix. Black interior spots are quartz.

Table 3. Copper isotope data for select placer gold particles.

Sample	δ^{65}Cu
2013 Crystal	1.17
2015 Crystal	1.14
2016 Crystal	1.79
2015 R4 (Crystal)	4.94
2014 Angular	0.23
2015 Angular	0.62
2017 Angular	0.53
2019 Angular	0.77
2014 A1	0.41
2017 A3	0.14
2014 A2	0.26
2016 A1	0.54
2017 I1	0.14

5. Discussion

5.1. Geology of the La Cholla Placers

The La Cholla placers can be divided into two main units: placer gravels that are strongly cemented by silicification and placers that are weakly cemented by caliche or are unconsolidated (Figure 5). The latter placer deposits contain angular to rounded clasts of local bedrock up to 1 m in diameter and suggest an environment of deposition that was very energetic. These are most likely pulse placers [40] that have accumulated from multiple generations of desert flash-flood events.

It is notable that the placers that are silicified and those with the most competent calcite cement both occur along a major high-angle range-bounding fault that delineates the eastern side of the southern Dome Rock Mountains. Travertine pods and mounds up to 4 m are also found directly above this same fault (Figure 9) and nearby down the modern

topographic gradient. Remnants of many these deposits are often hard to identify as most were mined for production of lime whitewash that was used historically for the adobe walls of buildings in the region [25]. Similar and larger travertine deposits up to 8 m were found in gravels of "Lime Kiln Gulch" along a major high-angle range-bounding fault a few miles away that marks the western side of the southern Dome Rock Mountains. These travertine deposits are likely fossil thermal springs that mark the surface expression of hydrothermal fluids emerging from depth along the basin-bounding faults.



Figure 9. A mound of light-colored travertine sits in contrast against dark McCoy Mountains metasedimentary rocks. Mound is approximately 4 m across. Inset photo shows detail of 25 cm long travertine clasts.

5.2. Morphology of La Cholla Gold

The surface morphology of the particles of gold from the angular grouping is typical of shorter transport distances in arid climates [14] and has features such as brittle mineral inclusions, angular forms, and percussion impact markings that are typical of debris-flow pulse placers [40]. Similarly, analysis of angular gold morphology on a Zingg plot (Figure 7) reveals a continuous trend of forms ranging from cylindrical to discoid. This range and trend has been attributed to placer gold morphologies driven by high-energy events [15]. Extensive scanning electron microscope, backscatter electron, and elemental mapping imaging of this gold is presented in [26].

The placer gold particles from the crystal grouping are, unsurprisingly, distinct three-dimensional forms that are likely dictated by crystal habit. Variation in morphology is mainly controlled by minor deformation caused by very short transport distances. The presence of these well-formed and often undamaged crystals of soft gold alloy (Figure 2c,d) within a high-energy deposit (Figure 5b) suggests that the formation of the crystals post-dates the deposition of the gravels. Yet, the intense silicification of the crystal-bearing placer unit precludes crystal deposition after the silicification event. This leaves the silicification event as a prime suspect for deposition of these placer gold crystals.

Morphology may also be used to estimate transport distance of placer gold particles (e.g., [4,41,42]). Specifically, morphology has been used to determine the distance placer gold has traveled, as gold is known to become flatter with increasing transport distance and more elongate in high-energy environments. These same trends are observed in the angular gold particles of the La Cholla placers. Quantification of transport distance may be estimated using the flatness index (FI), where the formula FI = ((length + width)/2 × thickness) is used [42]. In this paper, we consolidate historical data from other placer districts and

sources [41–43] to calculate a best-fit equation where transport distance (km) = 1.2833 + (FI − 0.57662) + (FI^2 × 0.31718). It is acknowledged that this equation is a generalization for placer gold and that the placer gold alloy composition, local climate variation, chemistry of the water of transportation, mineralogy of the sediment load, and other factors will influence the reliability of this approximation of transport distance due to their effects on chemical and physical weathering rates. Nevertheless, we present transport distance estimates here, as the differences between these estimates and even the absolute values are informative in understanding potential sources of the placer gold.

For the angular gold grouping, estimated transport distances from the lode source range from 1.2 to 4.6 km, with an average of 2.1 km. The inclusion gold subgrouping has similar values, ranging from 1.3 to 3.2 km, with an average of 1.8 km. The crystal grouping of placer gold ranges from 1.0 to 1.2 km, with an average of 1.1 km. It should come as no surprise that the gold crystals which likely formed in situ within the placer have such small estimated transport distances; this suggests an error of distance estimation of approximately 1 km.

Using the range-bounding fault as a reference line (Figure 4), it is possible to plot the average transport distance estimate for each sample site vs. the measured distance of that site from the fault (Figure 10). As expected, the estimated distance from the lode source of the placer gold increases with increasing distance down the elevation gradient and away from the fault. The Y-intercept suggests that the lode source of the placer gold lies at least 1.5 km uphill to the west of the fault. This is consistent with the known locations of quartz ± siderite ± gold and quartz ± tourmaline ± gold veins in the southern Dome Rock Mountains, and specifically the patented claims of the Beehive lode located just to the west of the area in Figure 4.

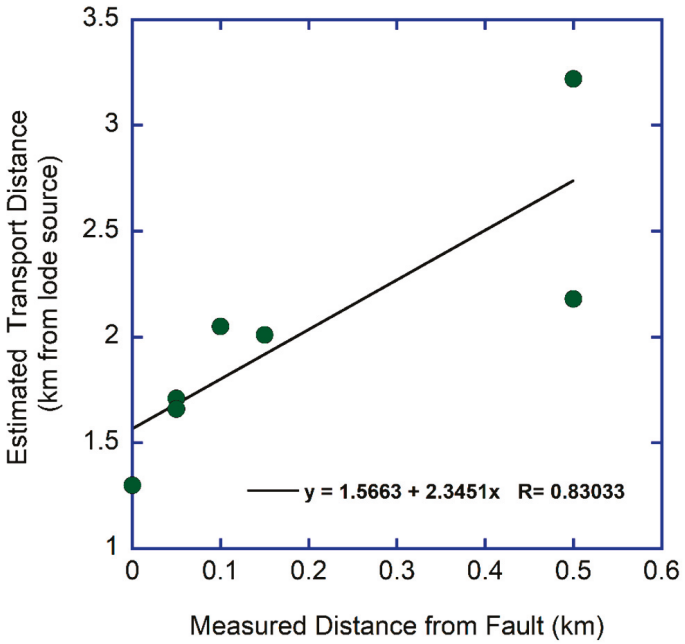


Figure 10. Plot of estimated transport distance for angular placer gold particles (calculated from flatness index) vs. measured distance from the range-bounding fault. Plot is for average transport distance by sample site and not for individual particles.

5.3. Geochemistry of La Cholla Placer Gold

5.3.1. Abundances of Silver and Copper in Gold Alloy and Inclusion Significance

The placer gold morphology groups from the La Cholla placers have major and minor element abundances within the gold alloy of the interiors of the particles that form distinct populations (Figure 11). Crystals generally have the lowest copper values and a wide range of gold–silver alloying trends, tending towards higher gold purity. Angular gold typically

has higher copper than the crystals and gold–silver alloying trends tending towards less elevated gold purity. Inclusion gold has the highest copper values, with one exceptionally elevated sample. As care was taken to avoid measurements on or adjacent to inclusions, this is likely due to microinclusions or diffusion from inclusions of copper phases. The inclusion gold otherwise exhibits a gold–silver alloying trend similar to the angular gold particles.

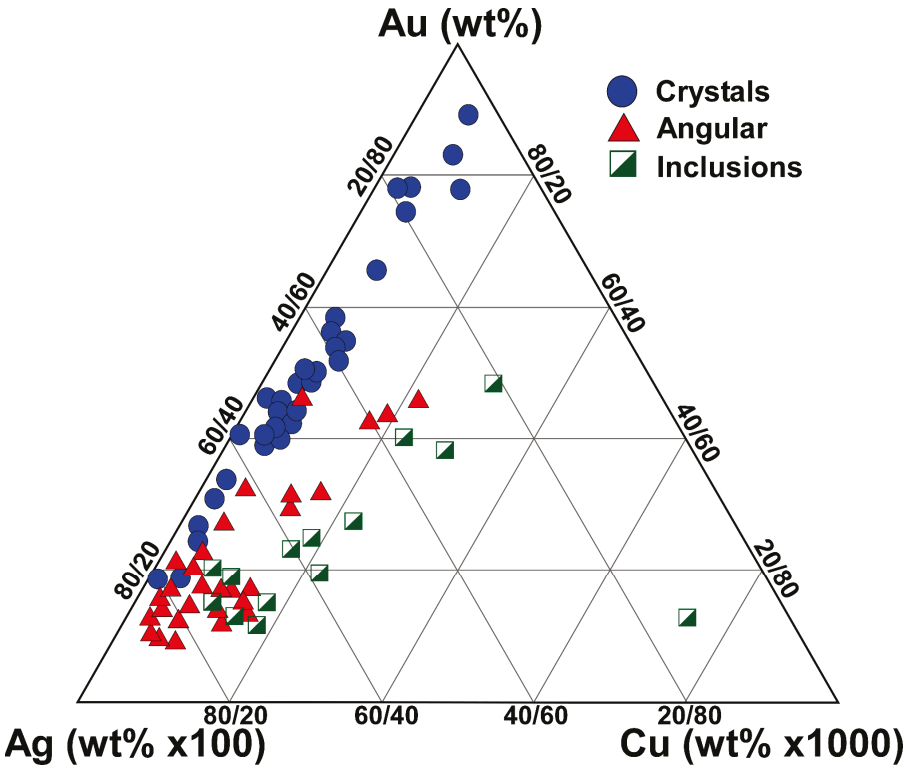


Figure 11. Ternary plot of major and minor elemental abundances for individual gold particles measured in this study. Silver abundance has been amplified by ×100 and copper by ×1000 to highlight differences and relationships between different gold morphology groups.

Significantly, the continuous and overlapping gold–silver alloying trend between the angular placer gold particles and the placer crystals hints at a genetic link between these gold morphology groupings. This trend is consistent with gold crystal formation from dissolution of angular gold, with selective removal of some silver and copper.

For angular and inclusion gold, the elemental abundances display a relationship with the estimates of transport distance calculated from morphology (Figure 12). With increasing transport distance, gold purity increases, while silver and copper decrease. This has been observed in many districts around the world [1,4,15].

Inclusions of minerals within placer gold particles provide an additional link to source regions (Figure 8). Inclusions within gold crystals were limited to fine, rounded quartz particles and crack fillings of silica. Angular and inclusion gold groupings always have inclusions in varying amounts and speciation. While quartz is the most abundant inclusion observed, sulfides are quite common (e.g., pyrite, chalcopyrite). In some angular and inclusion gold, pseudomorphs of siderite (iron carbonate) and iron oxides after pyrite are quite common. Inferred lode sources of gold above the placers display similar vein mineralogy. It is likely that primary vein mineralogy included sulfides and gold, as is typical for base metal epithermal veins in this part of Arizona. But the deep and localized carbonate alteration of some of these veins to form abundant siderite hints at a later hydrothermal event. The genetic link between visible native gold and siderite was clearly understood by early miners who methodically tested virtually every quartz–siderite vein with prospect pits and shafts. Indeed, the Yum Yum Mine is noted for spectacular specimens

of chocolate-brown siderite riddled with native gold that are on display at the Arizona Mining and Mineral Museum in Phoenix.

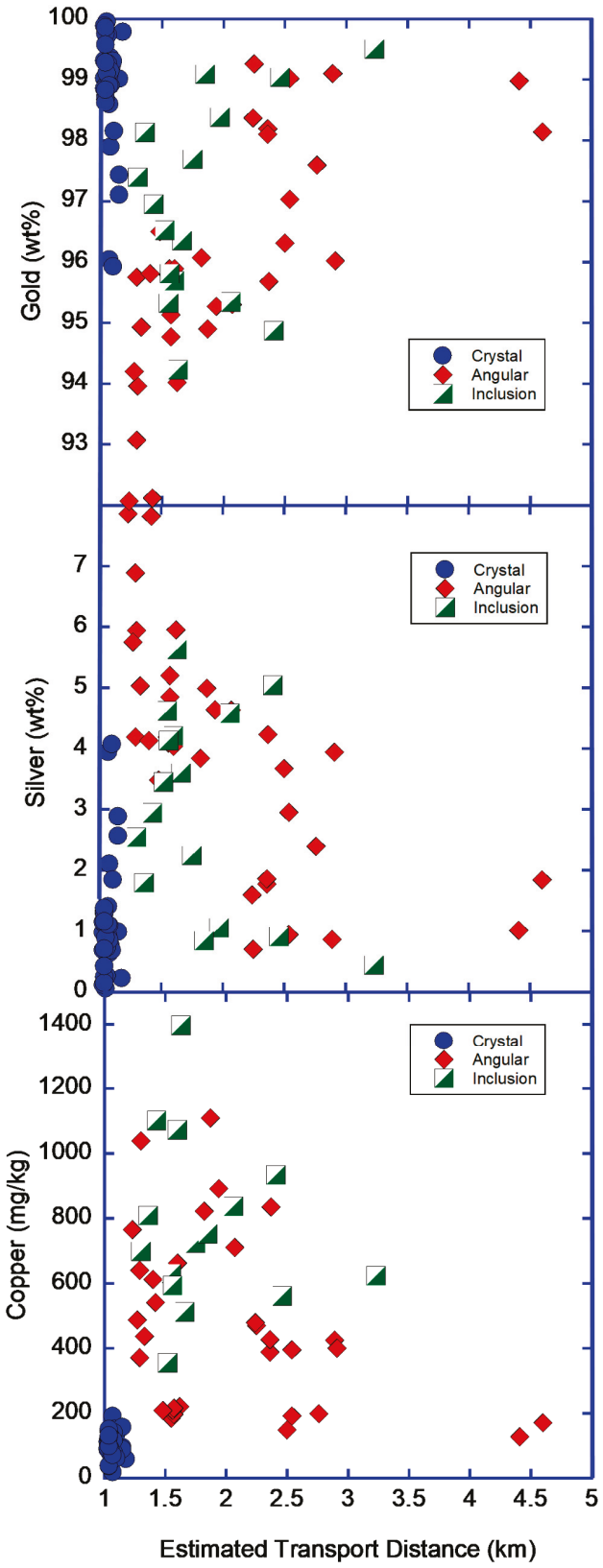


Figure 12. Plot of estimated transport distance for placer gold particles (calculated from flatness index) vs. elemental abundances for individual gold particles measured in this study.

Placer and lode gold is also found in association with tourmaline (Figure 8). Much recent work has been undertaken to examine the genetic relationship between gold and tourmaline within veins of orogenic gold deposits [44–46]. While an examination of this relationship at La Cholla was precluded by the small number of placer gold particles with tourmaline inclusions, future investigators may find this fertile ground to examine if older orogenic deposits predate the detachment-related base metal and gold veins.

5.3.2. Uranium and Lead Elemental Abundances

A surprising discovery was the very low levels of U and Pb within placer gold of the La Cholla placers (Table 2). It was initially hypothesized that levels of these elements would be elevated in the gold particles, based upon the abundance of lead (as galena and cerussite) in lode and placer deposits of the district and region and the observation of the uranium mineral carnotite [$K_2(UO_2)_2(VO_4)_2 \bullet 3H_2O$] within portions of the placers.

The La Cholla gold samples show extremely low concentrations of trace elements (Table 2). Only Cu is present at 100s to 1000s of mg/kg levels (Tables 1 and 2). ICP-MS analyses revealed Pb < 0.46 mg/kg in 75% of the samples, with the remaining two samples at 1.8 and 71 mg/kg (Table 2). Uranium concentrations were mostly below the detection limit (<0.0001). Only three samples showed detectable U concentrations between 0.001 and 0.004 mg/kg (Table 2). The observed extremely low U content in the native gold samples agrees with other works [18,20]. However, the observed very low Pb content in the La Cholla placer gold is unusual compared to the 450–10,300 mg/kg Pb observed in native gold samples from Rich Hill, Arizona [20]. This observation potentially indicates that the processes responsible for the formation of the La Cholla placer gold are different compared to the Rich Hill placers.

The low levels of uranium in the placer gold at La Cholla are more striking when the abundance of carnotite within the silicified placers is considered. Uranium is well-known to occur as detrital fragments in some late Archean to early Proterozoic gold placers (e.g., [47,48]), though the La Cholla placers are considerably younger. Uraninite particles were also observed in the "black sand" concentrates from the unconsolidated and caliche-cemented La Cholla placers, though a local bedrock source has yet to be identified. Insights on the significance of the uranium occurrence lie in the distribution and speciation of the uranium at La Cholla. Uraninite clearly occurs as detrital particles in the unconsolidated and caliche-cemented placers but has not been found within the silicified placers. Conversely, carnotite occurs in abundance within the silicified placers but is not found within the unconsolidated and caliche-cemented placers. The formation of carnotite within calcrete (caliche) has been well studied (e.g., [49,50]). These studies differentiate between carnotite sandstone deposits that form due to a redox front and caliche carnotite deposits that form due to the effect of carbonate solutions on uranium and vanadium solubility. Carbonated fluids are excellent at transporting uranium and vanadium over a wide range of pH, whereas uncarbonated solutions will favor precipitation of carnotite down to a pH < 4 (Figure 3 in [49]). The highly carbonated thermal waters which produced travertine mounds within the placer gravels would provide the ideal mechanism to transport dissolved uranium and vanadium.

These same carbonated thermal waters would leach uranium and vanadium from bedrock but also contribute to the oxidation of the base metal quartz veins to produce siderite–quartz veins. The highly carbonated fluids would also interact with any placer gold encountered and locally dissolve and reprecipitate some of the placer gold as crystals. After emerging from the vents, excess fluids would soak into the surrounding gravels and migrate along bedrock channels to precipitate uraninite where reducing organic debris was encountered. At a later point, the fluids at some of these vents changed to lower pH/Eh and higher temperatures and elevated dissolved silica content. This change in fluid chemistry replaced the original carbonate alteration with strong silicification and permitted carnotite precipitation within the gravels.

5.3.3. Copper Isotope Values

There is a distinct copper isotope difference between the angular ($\delta^{65}Cu = +0.54 \pm 0.22$) and crystalline ($\delta^{65}Cu = +2.8 \pm 1.0$) gold samples. Oxidation of copper over a large range of temperatures and pressures is known to generate fluids that are enriched in the ^{65}Cu isotope. Both empirical [51–56] and theoretical [57,58] data demonstrate this occurrence. The lower $\delta^{65}Cu$ copper isotope values are similar to those found in epithermal gold deposits [59,60] and most likely represent the primary signature of the gold originating from local base metal veins. The carbonated hydrothermal overprinting event at La Cholla was most likely oxidative in nature and "leached" heavier Cu from the preexisting lode vein minerals. Zones where alteration was intense produced recrystallized placer gold with a heavier copper isotope signal inherited from the oxidation of the base metal veins and older angular placer gold. Slightly heavier copper isotope values in angular placer gold may indicate the degree to which the parent vein was subjected to carbonate alteration to produce siderite–gold veins, the degree of limited interaction of these fluids with angular placer gold, or both. However, the formation of the younger crystalline placer gold is associated with these carbonated hydrothermal fluids as recorded by their distinctly heavier $\delta^{65}Cu$ values.

5.4. Origin and Evolution of the La Cholla Placer Gold Deposits

It is well-known that in primary lode deposits, a succession of superimposed ore-forming events produce telescoping and complex deposits (i.e., hybrid deposits types; [61]). The La Cholla placers are an excellent example of similar complex deposit history and overprinting within a secondary placer deposit.

Gold mineralization in the greater La Cholla District and districts to the north have a clear association with migration of specialized fluids along mid-Tertiary detachment faults (e.g., Copperstone Deposit, [62]). These mid-Tertiary primary lode gold deposits were subsequently unroofed by erosion related to continued detachment faulting and later 5 to 17 Ma high-angle Basin and Range faulting, and they began producing placer gold deposits.

Volcanism during this same period (e.g., [63]) produced thermal springs along these high-angle faults, which served as convenient conduits for deep, warm, mineral-rich fluids. Geochemical constraints suggest that the original placers were locally intruded and altered by geothermal fluids emanating from these faults. Similar localized geothermal alternation of placer deposits may be documented in the "White Placers" of Rich Hill, Arizona, USA, and the White Channel sediments of the Klondike region, Yukon Territory, Canada [14,64–66]. Originally, these fluids at La Cholla were warm and carbonate-rich, resulting in leaching of uranium and lead, mobilization of placer gold, and precipitation of travertine mounds. Later, these fluids became warmer and Si-dominant, resulting in cementation of portions of the placers with silica, recrystallization of placer gold as gold crystals, and precipitation of U and V as carnotite. The result is a complex placer deposit consisting of the original placer with overprinting by carbonate and later silica alteration events. Significantly, these geothermal alterations of the original placer produced localized recrystallization of placer gold as distinct, sharp crystals within the placer gravels. They also leached select elements (U, Pb, V) from the placer deposit and produced localized secondary uranium mineralization.

6. Conclusions

This study of geochemical overprinting and modification of placer deposits bears directly upon the study of other placers, especially those containing crystalline gold and uranium mineralization. The geochemical overprinting of placer deposits has produced much controversy due to the apparently paradoxical evidence recorded within them. This has also caused decades of debate regarding the genesis of very old placer deposits.

In the La Cholla placer gold deposits near Quartzsite, Arizona, USA, geochemical overprinting on placer gold deposits produced complex deposits with sharp and often undamaged gold crystals within high-energy gravels as a result of postdepositional re-

crystallization by localized hot spring systems. The geothermal fluids emanated from a basin-bounding fault and left a distinct geochemical signature that includes recrystallized gold, secondary uraninite and carnotite, travertine deposits, and mounds of highly silicified placer gravels. Surrounding these deposits are more typical placer gravels with angular placer gold morphologies and geochemistry indicative of flash-flood pulse placers with a lode gold source within 5 km of the deposit. The multitude of small local lode gold source veins is likely related to specialized fluid migration along mid-Tertiary detachment faults. The unroofing of the deposit by 5 to 17 Ma high-angle Basin and Range faulting led to extensive placer development with subsequent localized modification by geothermal fluid migration along the same faults.

Future workers should utilize the evidence provided by similar overprinting on placer deposits to infer conditions of deposit formation and evolution. These interpretations may include evidence of past geothermal activity, the presence of previously undiscovered structures which served as fluid conduits, and areas of steep paleo-gradients of topography.

Author Contributions: Methodology, E.B.M., R.M. and G.K.; formal analysis, E.B.M., R.M., G.K. and J.P.; investigation, J.P.; writing—original draft preparation, E.B.M. and J.P.; writing—review and editing, E.B.M., R.M. and G.K.; supervision, G.K.; funding acquisition, G.K. All authors have read and agreed to the published version of the manuscript.

Funding: Instrumentation was provided and supported by the National Science Foundation, EAR-0115884 and EAR-0941106. XRF instrumentation was provided by a grant from the W.M. Keck Foundation. Support was also provided by a NASA Astrobiology Institute Minority Institution Research Sabbatical (NAI-MIRS) program award to the lead author and an institutional grant by CSUSB. CSUSB provided internal funding to support undergraduate participation in this research activity.

Data Availability Statement: The data presented in this study are available in the article. Additional data is not available, at request of the mine owners.

Acknowledgments: This study would not have been possible without the generous support of mine owners Larry Schreiner and Steve Hunt. Their support of field work on their mining claims, provision of samples, and open communication about the nature of the deposits they were mining were invaluable. The lead author also thanks his colleagues of the Minority Institution Astrobiology Collaborative (MiAC) for providing the supportive environment that made this work possible. We thank Ken Domanik at the University of Arizona for help with probe analyses. James Pelley provided support for SEM imaging. Additional field support was provided by Blake Harmon and the Quartzsite Metal Detecting Club and undergraduate students from CSUSB.

Conflicts of Interest: The authors declare no conflict of interest.

References

1. Boyle, R.W. *The Geochemistry of Gold and Its Deposits: Together with a Chapter on Geochemical Prospecting for the Element*; Geological Survey of Canada: Ottawa, ON, Canada, 1979; 280p, ISBN 0-660-19591-7.
2. Saunders, J.A.; Unger, D.L.; Kamenov, G.D.; Fayek, M.; Hames, W.E.; Utterback, W.C. Genesis of Middle Miocene Yellowstone-hotspot-related bonanza epithermal Au-Ag deposits, Northern Great Basin, USA. *Min. Dep.* **2008**, *43*, 715–734. [CrossRef]
3. Reith, F.; Fairbrother, L.; Nolze, G.; Wilhelmi, O.; Clode, P.L.; Gregg, A.; Parsons, J.E.; Wakelin, S.A.; Pring, A.; Hough, R.; et al. Nanoparticle factories: Biofilms hold key to gold dispersion and nugget formation. *Geology* **2010**, *38*, 843–846. [CrossRef]
4. Lindgren, W. *Tertiary Gravels of the Sierra Nevada of California*; Professional Paper 78; US Geological Survey: Washington, DC, USA, 1911; 226p.
5. Watterson, J.R. Artifacts resembling budding bacteria produced in placer-gold amalgams by nitric acid leaching. *Geology* **1994**, *20*, 1144–1146. [CrossRef]
6. Mossman, D.J.; Reimer, T.; Durstling, H. Microbial processes in gold migration and deposition: Modern analogues to ancient deposits. *Geosci. Can.* **1999**, *26*, 131–140.
7. Reith, F.; Lengke, M.F.; Falconer, D.; Craw, D.; Southam, G. Winogradski Review: The geomicrobiology of gold. *Int. Soc. Microb. Ecol. J.* **2007**, *1*, 567–584. [CrossRef]
8. Hough, R.M.; Butt, C.R.M.; Fisher-Buhner, J. The crystallography, metallography and composition of gold. *Elements* **2009**, *5*, 297–302. [CrossRef]
9. Southam, G.; Lengke, M.F.; Fairbrother, L.; Reith, F. The biogeochemistry of gold. *Elements* **2009**, *5*, 303–307. [CrossRef]

10. Hough, R.M.; Butt, C.R.M.; Reddy, S.M.; Verrall, M. Gold nuggets: Supergene or hypogene? *Austr. J. Earth Sci.* **2007**, *54*, 959–964. [CrossRef]
11. Fairbrother, L.; Brugger, J.; Shapter, J.; Laird, J.; Southam, G.; Reith, F. Supergene gold transformation: Biogenic secondary and nano-particulate gold from arid Australia. *Chem. Geol.* **2012**, *320*, 17–31. [CrossRef]
12. Craw, D.; Lilly, K. Gold nugget morphology and geochemical environments of nugget formation, southern New Zealand. *Ore Geol. Rev.* **2016**, *79*, 301–315. [CrossRef]
13. Stewart, J.; Kerr, G.; Prior, D.; Halfpenny, A.; Pearce, M.; Hough, R.; Craw, D. Low temperature recrystallisation of alluvial gold in paleoplacer deposits. *Ore Geol. Rev.* **2017**, *88*, 43–56. [CrossRef]
14. Melchiorre, E.B.; Kamenov, G.D.; Sheets-Harris, C.; Andronikov, A.; Leatham, W.B.; Yahn, J.; Lauretta, D.S. Climate-induced geochemical and morphological evolution of placer gold deposits at Rich Hill, Arizona, USA. *Geol. Soc. Am. Bull.* **2017**, *129*, 193–202. [CrossRef]
15. Melchiorre, E.B.; Henderson, J. Topographic gradients and lode gold sourcing recorded by placer gold morphology, geochemistry, and mineral inclusions in the east fork San Gabriel River, California, USA. *Ore Geol. Rev.* **2019**, *109*, 348–357. [CrossRef]
16. Masson, F.X.; Beaudoin, G.; Laurendeau, D. Multi-method 2D and 3D reconstruction of gold grain morphology in alluvial deposits: A review and application to the Rivière du Moulin (Québec, Canada). *Geol. Soc. Lond. Spec. Publ.* **2022**, *516*, 337–352. [CrossRef]
17. Melchiorre, E.B.; Orwin, P.M.; Reith, F.; Rea, M.A.D.; Yahn, J.; Allison, R. Biological and geochemical development of placer gold deposits at Rich Hill, Arizona, USA. *Minerals* **2018**, *8*, 56. [CrossRef]
18. Pettke, T.; Frei, R. Isotope systematics in vein gold from Brusson, Val d'Ayas (NW Italy), Pb/Pb evidence for a Piemonte metaophiolite Au source. *Chem. Geol.* **1996**, *127*, 111–124. [CrossRef]
19. Kamenov, G.D.; Saunders, J.A.; Hames, W.E. Mafic Magmas as Sources for Gold in Middle-Miocene Epithermal Deposits of Northern Great Basin, USA: Evidence from Pb Isotopic Compositions of Native Gold. *Econ. Geol.* **2007**, *102*, 1191–1195. [CrossRef]
20. Kamenov, G.D.; Melchiorre, E.B.; Ricker, F.N.; DeWitt, E. Insights from Pb Isotopes for Native Gold Formation during Hypogene and Supergene Processes at Rich Hill, Arizona. *Econ. Geol.* **2013**, *108*, 1577–1589. [CrossRef]
21. Jones, E.L. *Gold Deposits Near Quartzsite, Arizona*; U.S. Geological Survey Bulletin 620; US Government Printing Office: Washington, DC, USA, 1915; pp. 45–57.
22. Blake, W.P. Report of the Territorial Geologist. In *Report of the Governor of Arizona for 1899*; Arizona Territorial Government: Phoenix, AZ, USA, 1899; pp. 42–153.
23. Tenney, J.B. *Unpublished Field Notes*; Arizona Bureau of Mines: Tucson, AZ, USA, 1933.
24. Wilson, E.D. *Arizona Gold Placers and Placering*, 5th ed.; Bulletin 160; Arizona Bureau of Mines and Mineral Technology: Tucson, AZ, USA, 1952; p. 148.
25. Keiser, W. *Lost Mines and Prospectors' Lore*; Yuma County Historical Society, Inc.: Yuma, AZ, USA, 1978; p. 49.
26. Melchiorre, E.B. *Gold Atlas of Quartzsite, Arizona: Volume 2, Southern Dome Rock Mountains*; Rock Doc Publications: San Bernardino, CA, USA, 2013; p. 298.
27. Velasquez, C.M.L. Geochemical Classification of Placer and Lode Gold Deposits within the Northern Dome Rock Mountains of the Quartzsite Mining District. Master's Thesis, California State University, San Bernardino, AZ, USA, 2012.
28. Wilson, E.D.; Cunningham, J.B.; Butler, G.M. *Arizona Lode Gold Mines and Gold Mining*; Bulletin 137; Arizona Bureau of Mines and Mineral Technology: Tucson, AZ, USA, 1952; p. 261.
29. Harding, L.E.; Coney, P.J. The geology of the McCoy Mountains Formation, southeastern California and southwestern Arizona. *Geol. Soc. Am. Bull.* **1985**, *96*, 755–769. [CrossRef]
30. Tosdal, R.M.; Haxel, G.B.; Wright, J.E.; Jenney, J.P.; Reynolds, S.J. Jurassic geology of the Sonoran Desert region, southern Arizona, southeastern California, and northernmost Sonora: Construction of a continental-margin magmatic arc. *Geol. Evol. Ariz. Ariz. Geol. Soc. Dig.* **1989**, *17*, 397–434.
31. Shuster, J. Structural and chemical characterization of placer gold grains: Implications for bacterial contributions to grain formation. *Geomicro. J.* **2015**, *32*, 158–169. [CrossRef]
32. Armstrong, J.T. Quantitative analysis of silicates and oxide minerals: Comparison of Monte-Carlo, ZAF and Phi-Rho-Z procedures. In *Proceedings of the Microbeam Analysis Society*; Newbury, D.E., Ed.; San Francisco Press: San Francisco, CA, USA, 1988; pp. 239–246.
33. Donovan, J.J.; Snyder, D.A.; Rivers, M.L. An improved interference correction for trace element analysis. *Microbeam An.* **1993**, *2*, 23–28. [CrossRef]
34. Knight, J.B.; McTaggart, K.C. *Composition of Gold from Southwestern British Columbia: British Columbia*; Geological Fieldwork 1988, Paper Vol. 1989-1; Ministry of Energy, Mines and Petroleum Resources: Ottawa, ON, Canada, 1989; pp. 387–394.
35. Douma, Y.; Knight, J.B. Mounting samples in methylmethocrylate for SEM and EMP analysis. *J. Sed.* **1994**, *A64*, 675–677. [CrossRef]
36. Saunders, J.A.; Mathur, R.; Kamenov, G.D.; Shimizu, T.; Brueseke, M.E. New isotopic evidence bearing on bonanza (Au-Ag) epithermal ore-forming processes. *Miner. Depos.* **2015**, *51*, 1–11. [CrossRef]
37. Mathur, R.; Titley, S.; Barra, F.; Brantley, S.; Wilson, M.; Phillips, A.; Munizaga, F.; Maksaev, V.; Vervoort, J.; Hart, G. Exploration potential of Cu isotope fractionation in porphyry copper deposits. *J. Geochem. Explor.* **2009**, *102*, 1–6. [CrossRef]

38. Blott, S.J.; Pye, K. Particle shape: A review and new methods of characterization and classification. *Sedimentology* **2008**, *55*, 31–63. [CrossRef]
39. Zingg, T. Beitrag zur schotteranalyse. *Schweiz. Mineral. Petrogr. Mitt.* **1935**, *15*, 39–140.
40. McCulloch, R.; Lewis, B.; Keill, D.; Shumaker, M. *Applied Gold Placer Exploration and Evaluation Techniques*; Special Publication 115; Montana Bureau of Mines and Geology: Butte, MT, USA, 2003; p. 115.
41. Hérail, G.; Fornari, M.; Viscarra, G.; Miranda, V. Morphological and chemical evolution of gold grains during the formation of a polygenic fluviatile placer: The Mio- Pleistocene Tipuani placer example (Andes, Bolivia). *Chron. Rech. Min.* **1990**, *500*, 41–49.
42. Loen, J.S. Use of placer gold characteristics to locate bedrock gold mineralization. *Explor. Min. Geol.* **1995**, *4*, 335–339.
43. Cailleux, A.; Tricart, J. Introduction to the study of sand and pebbles. *Cent. Doc. Univ. Paris* **1959**, *3*, 194–202.
44. Fontem, N.K.; Suh, C.E.; Ngatcha, R.B.; Shemang, E.M.; Vishiti, A.; Melchiorre, E.; Fon, A.N. Tourmaline occurrence and gold mineralization at a granitoid-metasediment contact in the Upper Lom Basin, east Cameroon. *SN Appl. Sci.* **2023**, *5*, 141. [CrossRef]
45. Guo, M.; Liu, J.; Zhai, D.; de Fourestier, J.; Liu, M.; Zhu, R. Tourmaline as an indicator of ore-forming processes: Evidence from the Laodou gold deposit, Northwest China. *Ore Geol. Rev.* **2023**, *154*, 105304. [CrossRef]
46. Faye, C.I.; Ndiaye, A.A.; Dia, I.; Gueye, M.; Moritz, R. Geological, geophysical and surface geochemical guides for gold exploration in the Falémé Volcanic Belt, West African Craton, Senegal. *J. Geochem. Explor.* **2023**, *245*, 107145. [CrossRef]
47. Minter, W.E.L. Detrital gold, uranium, and pyrite concentrations related to sedimentology in the Precambrian Vaal Reef placer, Witwatersrand, South Africa. *Econ. Geol.* **1976**, *71*, 157–176. [CrossRef]
48. Hallbauer, D.K. *Geochemistry and Morphology of Mineral Components from the Fossil Gold and Uranium Placers of the Witwatersand*; US Geological Survey Professional Paper 1161-A-BB; US Government Printing Office: Washington, DC, USA, 1981.
49. Mann, A.W. *Chemical Ore Genesis Models for the Precipitation of Carnotite in Calcrete*; Commonwealth Scientific and Industrial Research Organisation Paper CSIRO-FP-7; Commonwealth Scientific and Industrial Research Organisation: Canberra, Australia, 1974.
50. Mann, A.W.; Deutscher, R.L. Genesis principles for the precipitation of carnotite in calcrete drainages in Western Australia. *Econ. Geol.* **1978**, *73*, 1724–1737. [CrossRef]
51. Borrok, D.M.; Nimick, D.A.; Wanty, R.B.; Ridley, W.I. Isotopic variations of dissolved copper and zinc in stream waters affected by historical mining. *Geochim. Cosmochim. Acta* **2008**, *72*, 329–344. [CrossRef]
52. Ehrlich, S.; Butler, I.; Halicz, L.; Rickard, D.; Oldroyd, A.; Matthews, A. Experimental study of the copper isotope fractionation between aqueous Cu (II) and covellite, CuS. *Chem. Geol.* **2004**, *209*, 259–269. [CrossRef]
53. Kimball, B.E.; Mathur, R.; Dohnalkova, A.C.; Wall, A.J.; Runkel, R.L.; Brantley, S.L. Copper isotope fractionation in acid mine drainage. *Geochim. Cosmochim. Acta* **2009**, *73*, 1247–1263. [CrossRef]
54. Li, D.; Liu, S.-A. Copper Isotope Fractionation during Basalt Leaching at 25 °C and pH = 0.3, 2. *J. Earth Sci.* **2022**, *33*, 82–91. [CrossRef]
55. Mathur, R.; Ruiz, J.; Titley, S.; Liermann, L.; Buss, H.; Brantley, S.L. Cu isotopic fractionation in the supergene environment with and without bacteria. *Geochim. Cosmochim. Acta* **2005**, *69*, 5233–5246. [CrossRef]
56. Zhao, Y.; Xue, C.; Liu, S.-A.; Mathur, R.; Zhao, X.; Yang, Y.; Dai, J.; Man, R.; Liu, X. Redox reactions control Cu and Fe isotope fractionation in a magmatic Ni–Cu mineralization system. *Geochim. Cosmochim. Acta* **2019**, *249*, 42–58. [CrossRef]
57. Fujii, T.; Moynier, F.; Abe, M.; Nemoto, K.; Albarède, F. Copper isotope fractionation between aqueous compounds relevant to low temperature geochemistry and biology. *Geochim. Cosmochim. Acta* **2013**, *110*, 29–44. [CrossRef]
58. Seo, J.H.; Lee, S.K.; Lee, I. Quantum chemical calculations of equilibrium copper (I) isotope fractionations in ore-forming fluids. *Chem. Geol.* **2007**, *243*, 225–237. [CrossRef]
59. Duan, J.; Tang, J.; Li, Y.; Liu, S.-A.; Wang, Q.; Yang, C.; Wang, Y. Copper isotopic signature of the Tiegelongnan high-sulfidation copper deposit, Tibet: Implications for its origin and mineral exploration. *Miner. Depos.* **2016**, *51*, 591–602. [CrossRef]
60. Saunders, N.J.; Barling, J.; Harvey, J.; Halliday, A.N. Heterogeneous nickel isotopic compositions in the terrestrial mantle—Part 1: Ultramafic lithologies. *Geochim. Cosmochim. Acta* **2020**, *285*, 129–149. [CrossRef]
61. Sillitoe, R.H. Erosion and collapse of volcanoes: Causes of telescoping in intrusion-centered ore deposits. *Geology* **1994**, *22*, 945–948. [CrossRef]
62. Salem, H.M. Geochemistry, Mineralogy, and Genesis of the Copperstone Gold Deposit. Ph.D. Thesis, The University of Arizona, La Paz County, AZ, USA, 1993; p. 211.
63. Reynolds, S.J.; Welty, J.W.; Spencer, J.E. Volcanic history of Arizona: Fieldnotes. *Ariz. Bur. Geol. Miner. Technol.* **1986**, *16*, 1–5.
64. Dufresne, M.B. Origin of Gold in the White Channel Sediments of the Klondike Region, Yukon Territory. Master's Thesis, University of Alberta, Edmonton, AB, Canada, 1986; p. 181.
65. Dufresne, M.B.; Morison, S.R.; Nesbitt, B.E. Evidence of hydrothermal alteration in White Channel sediments and bedrock of the Klondike area, west-central Yukon. *Yuk. Geol.* **1986**, *1*, 44–49.
66. Tempelman-Kluit, D.J. *White Channel Gravel of the Klondike. Yukon Exploration and Geology 1981, Exploration and Geological Services Division*; Yukon Indian and Northern Affairs Canada: Whitehorse, YT, Canada, 1982; p. 79.

Disclaimer/Publisher's Note: The statements, opinions and data contained in all publications are solely those of the individual author(s) and contributor(s) and not of MDPI and/or the editor(s). MDPI and/or the editor(s) disclaim responsibility for any injury to people or property resulting from any ideas, methods, instructions or products referred to in the content.

minerals

MDPI

Article

Soil Geochemistry Combined with Particulate Gold Microchemistry Provides Evidence of Eluvial Gold Genesis and Anthropogenic Hg Use in Eastern Cameroon Goldfields

Akumbom Vishiti [1,2,*], Cheo Emmanuel Suh [3,4], Ralain Bryan Ngatcha [4,5], Erik B. Melchiorre [6], Elisha Mutum Shemang [7], Benjamin Odey Omang [8], Terence Cho Ngang [4], Fernando Castro Valdez [6] and Sharila Gillian Sekem [4]

1 Department of Civil Engineering, The University Institute of Technology (IUT), University of Douala, Douala P.O. Box 8698, Littoral Region, Cameroon
2 Laboratory of Geosciences, Natural Resources and Environment, Department of Earth Sciences, Faculty of Science, University of Douala, Douala P.O. Box 24157, Littoral Region, Cameroon
3 Economic Geology Unit, Department of Geology, University of Buea, Buea P.O. Box 63, South West Region, Cameroon; suhemmanuel@uniba.cm
4 Department of Geology, Mining and Environmental Science, The University of Bamenda, Bambili P.O. Box 39, North West Region, Cameroon; bryanngatcha@gmail.com (R.B.N.); terence.cho@rwth-aachen.de (T.C.N.); gilliansekem@gmail.com (S.G.S.)
5 Department of Geology, Life and Earth Sciences Institute (PAULESI), Pan African University, Ibadan 200132, Oyo State, Nigeria
6 Department of Geological Sciences, California State University, 5500 University Parkway, San Bernardino, CA 92407, USA; emelch@csusb.edu (E.B.M.)
7 Department of Earth and Environmental Sciences, Botswana International University of Science and Technology, Private Bag 16, Palapye 10071, Botswana; shemange@biust.ac.bw
8 Department of Geology, University of Calabar, Calabar PMB 1115, Cross River State, Nigeria; benjaminomang@unical.edu.ng
* Correspondence: vakumbom@gmail.com

Abstract: The identification of trace element anomalies in soils has been proven to assist semi-mechanized small-scale gold operations. This study employs soil geochemistry combined with the microchemical signature of particulate gold from the Batouri goldfield to (1) vector possible gold-endowed lithologies introducing particulate gold into the overlying regolith, and (2) assess anthropogenic Hg used in purification of both primary and alluvial/eluvial gold by artisans. The soil geochemistry shows irregularly distributed anomalies of elevated Cu especially in the saprolite soil layer. Whereas in the lateritic soil layer, a Au-Ag-Hg metal association is reported for the first time in this gold district and could be linked to anthropogenic Hg used in gold recovery. Particulate gold recovered from the soil varies in shape from euhedral and irregular to sub-rounded, indicating a proximal lode source. The gold grains range in size from nano-particles to >300 µm and are Au-Ag alloys. The gold particles reveal inclusions such as quartz, silicate, zircon and ilmenite suggesting that the grains were dislodged from quartz veins within the granitic basement. Systematic variation in the microchemical signature of the gold grains is suggestive of spatial and temporal evolution of the mineralizing fluid. These results are consistent with investigations from similar geologic settings worldwide and validate the combined utility of gold fingerprinting and pathfinder elements in soil to examine deposit genesis in other gold districts globally.

Keywords: geochemistry; soil; particulate gold; morphology; microchemistry; anthropogenic Hg; Cameroon

1. Introduction

Historically, many small scale and artisanal gold mining regions have produced significant negative environmental impacts [1,2]. In fact, soil contamination represents a

major environmental problem in gold mining sites [3]. Contaminants such as metals and metalloids in soils typically originate from geogenic sources. However, they could also result from anthropogenic activities especially with the occurrence of Acid Mine Drainage (AMD) phenomenon [4] and the use of hazardous products in the gold extraction process such as sulfuric acids mercury and arsenic by gold miners [2,5,6]. In some regions, these impacts continue to the present day. This is exacerbated in jurisdictions where the regulatory framework governing toxic metal use in gold processing is weak. Such is the case of the eastern Cameroon goldfield, where new small scale gold mining pits are being opened almost every year. This has raised the area's worth and potential for gold exploration. In the south eastern region of Cameroon where the Batouri goldfield is located, gold production began in 1934 [7]. Primary gold mineralization in the Batouri goldfield is inferred to be hosted in quartz veins in wide brittle/ductile shear zones and Neoproterozoic granites, and it is likely to be buried in deeper crustal levels [8–10]. However, uplift, weathering and erosion may have brought the mineralization close to the surface [8–10]. Moreover, supergene processes such as weathering, erosion and sedimentation can modify primary gold resources [11,12]. Secondary gold resources in particular result primarily from the physical weathering of gold from primary lode sources [13,14]. Deep chemical weathering and laterite formation may further mobilize and concentrate these physically weathered gold particles [15]. This chemical weathering includes a combination of remobilization through dissolution–re-precipitation, grain coarsening and differential chemical weathering that produces gold-rich grain rims through the depletion of silver from the gold alloy [16–18]. According to [12], gold resources in the weathering blanket are often economically profitable as they present easily accessible targets since they are composed of poorly consolidated material that is readily mineable. Several models postulate that one or two mushroom-shaped dispersion zones from the mineralized vein may be present in deep weathering profiles where gold is redistributed. In lateritic residuum and the upper part of the mottled zone in humid and tropical rainforest environments, a gold mineralization halo is often observed (e.g., [19]). Gold dissolution by acidic and saline groundwater and re-precipitation farther in the saprolite layer can be related to post laterite remobilization in semi-arid environments [20]. The liberated gold from the primary sources migrates along various pathways as gold chloride and thiosulfate complexes and are dispersed by complex mechanisms into the soil horizons [21].

In areas such as Batouri, which is characterized by a thick weathering cover developed over a range of granitic basement rock lithologies truncated by quartz veins, understanding the resulting secondary dispersion trend in the soil is vital in the search for primary sources concealed by the overburden. The determination of element associations and distribution trends can be performed through integrated geochemical data analysis and interpretation of textural properties of the hypogene mineralization. However, soil geochemistry applied to gold exploration can be challenging owing to the fact that native gold is chemically and physically resistant, suggesting that gold dispersion in the surficial environment occurs mainly in the particulate form [22] or in localized microbial biofilms as nanoparticulate gold [23]. New mineral leases are legally accessible in the eastern part of the Batouri gold district, necessitating the need for identification of gold-rich horizons in the regolith through data collection and deposit genesis models.

In this geochemical study, trace elements in the soils are measured to identify abnormally elevated values which can guide exploration and provide environmental geochemical assessment. Furthermore, gold particles from various soil horizons were investigated physically and chemically to identify differences in primary gold particle composition and composition of gold particles tainted by anthropogenic activities.

2. Regional and Local Geology

Batouri is a segment of the Adamawa-Yadé geological domain (AYD; Figure 1), which in itself is an integral part of the Neoproterozoic Fold Belt of Cameroon (NFBC) [24,25]. The

NFBC developed due to the convergence and eventual collision of three crustally stable blocks: the Congo–São Francisco Craton, the West African Craton [24] and the Sahara metacraton.

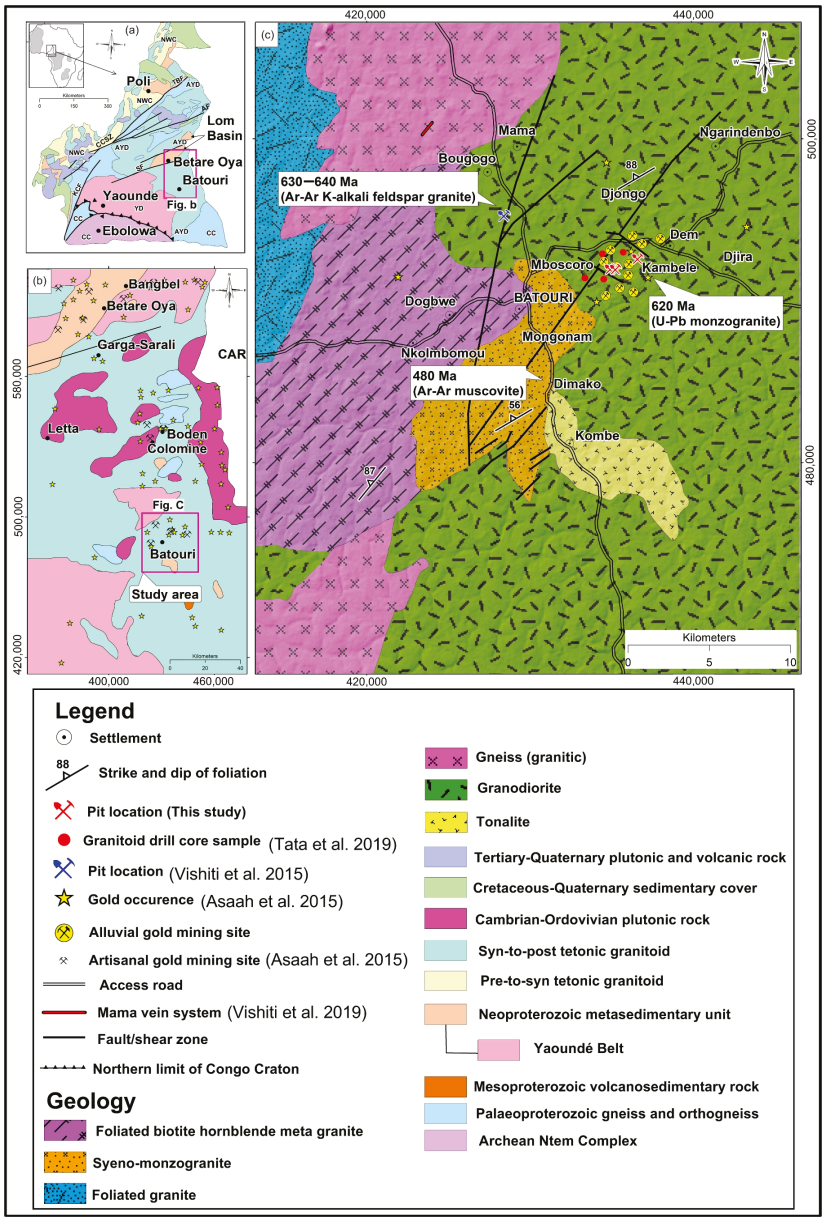


Figure 1. (**a**) Geological map of Cameroon (modified after [10,26]). The Central Cameroon Shear Zone (CCSZ) is defined by a system of NE trending faults comprising Tchollire-Banyo Fault (TBF), Adamawa Fault (AF), Sanaga Fault (SF) and Kribi-Campo Fault (KCF). (**b**) Regional geological map of south eastern Cameroon showing artisanal gold mining sites and other reported gold indications (modified after [27]). (**c**) Geology of the Batouri goldfield. The area is characterized by a predominant NE-SW trending shear zone. It is composed predominantly of Pan African granitoids and has a thick lateritic cover. CC = Congo Craton, YD = Yaoundé Domain, NWC = North West Cameroon Domain. Granitoid drill core samples [9], pit location [13], gold occurrence and artisanal gold mining site [10], Mama vein system [8].

The region is therefore dominated by translational tectonics evidenced by strike-slip shear zones defining a zone of sub-horizontal deformation termed the Central Cameroon Shear Zone (CCSZ). Most of the shear zones have NNE-SSW to ENE-WSW strike patterns. The CCSZ splays into a number of anastomosing networks of faults that include the Adamawa fault and associated brittle structures depicted in Figure 1a [26,28]. According

to [24,25,29], the AYD experienced polyphase deformation through to the Pan African event. Consequently, lithologic units within the domain bear pre-tectonic, syn-tectonic and post-tectonic imprints. These are largely high-K, calc-alkaline rocks [9,10,30,31] interspersed with low- to medium-grade metamorphic rocks of volcano–sedimentary protoliths [32–34].

Hypogene gold in the Batouri area is linked to quartz veins hosted by various granitic facies [9,10] that show evidence of pervasive alteration by crustal fluid circulation [8–10,35]. Gold is either dispersed in the quartz matrix or confined as stringers along foliations in the granites [8–10]. The gold grades within the granite alteration halo vary from 2 ppm to 103 ppm [8,9,13,14,35,36]. The granites are subduction-related and 640–620 Ma old [10], similar to those farther afield in the AYD [30,31,34,35,37] and southern Chad [38]. This class of granite-related gold deposits contributes to about 32% of the world's gold reserve [39–43]. Artisanal gold mining has been ongoing in the Batouri goldfield (Figure 1b) since the 1930s [7]. At the moment, the indigenous people and multinational companies mine gold using artisanal and semi-mechanical techniques. Typically, mining for gold is performed right on river banks, in quartz veins and on the weathering blanket, resulting in diverse environmental consequences (Figure 2).

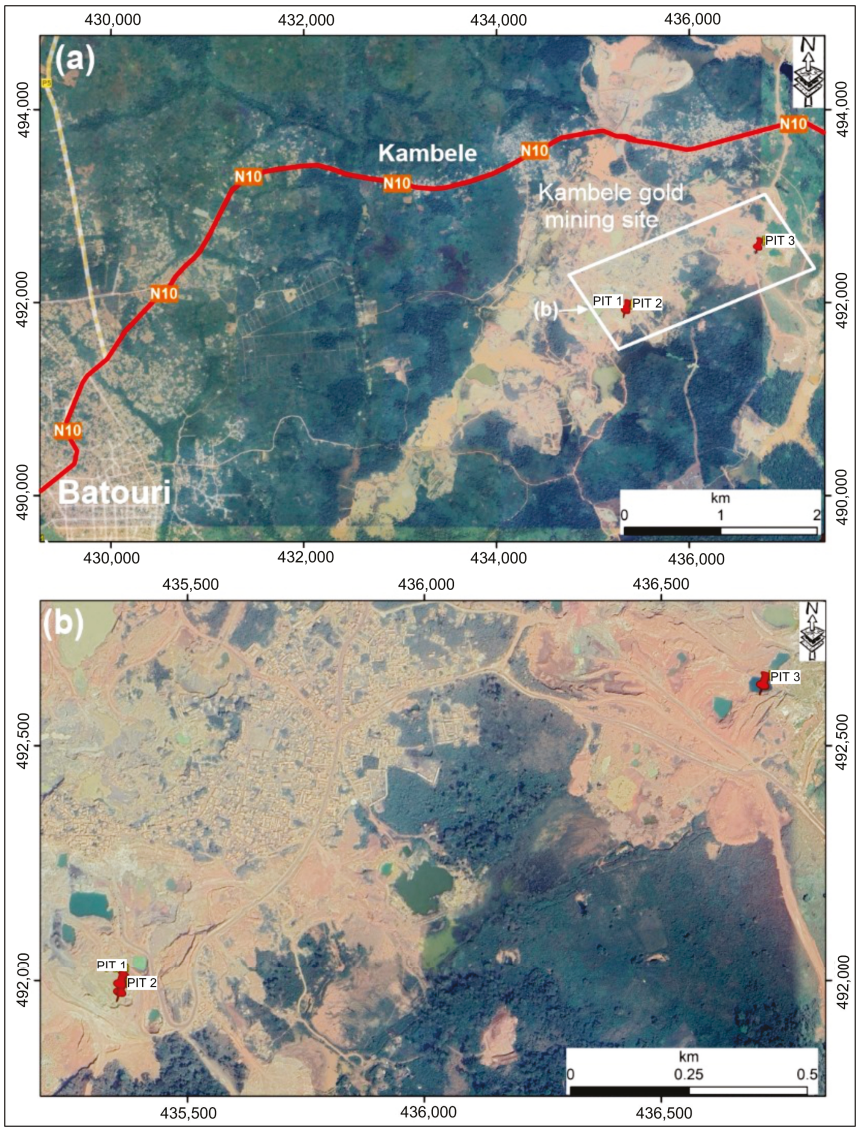


Figure 2. (**a**,**b**) Satellite image of the Batouri goldfield indicating the position of the pits sampled. The area is highly deforested, and the color of surface water is now pale yellow.

3. Materials and Methods

3.1. Sample Collection

The Batouri goldfield has experienced a flurry of gold exploration and exploitation activities by artisans in the past two decades (Figure 3a). At its eastern limit, new artisanal mining sites and mineral leases are becoming available each year. Samples used in this study are principally soils obtained from three (03) exploration pits (Figures 3b and 4) sunk down to the bedrock and the deepest pit was 21 m deep. This exposed soil horizons that were subsequently carefully logged and sampled (Figure 4). Pit logging involved identifying the various soil layers using features such as layer thickness, color, texture and structure. Each layer was then sampled separately by chipping along the walls of the pit in order to obtain a representative sample (Figure 4d). Each sample collected through this channel chip sampling method was thoroughly mixed, made into a cone and quartered for a microchemical analysis and geochemistry.

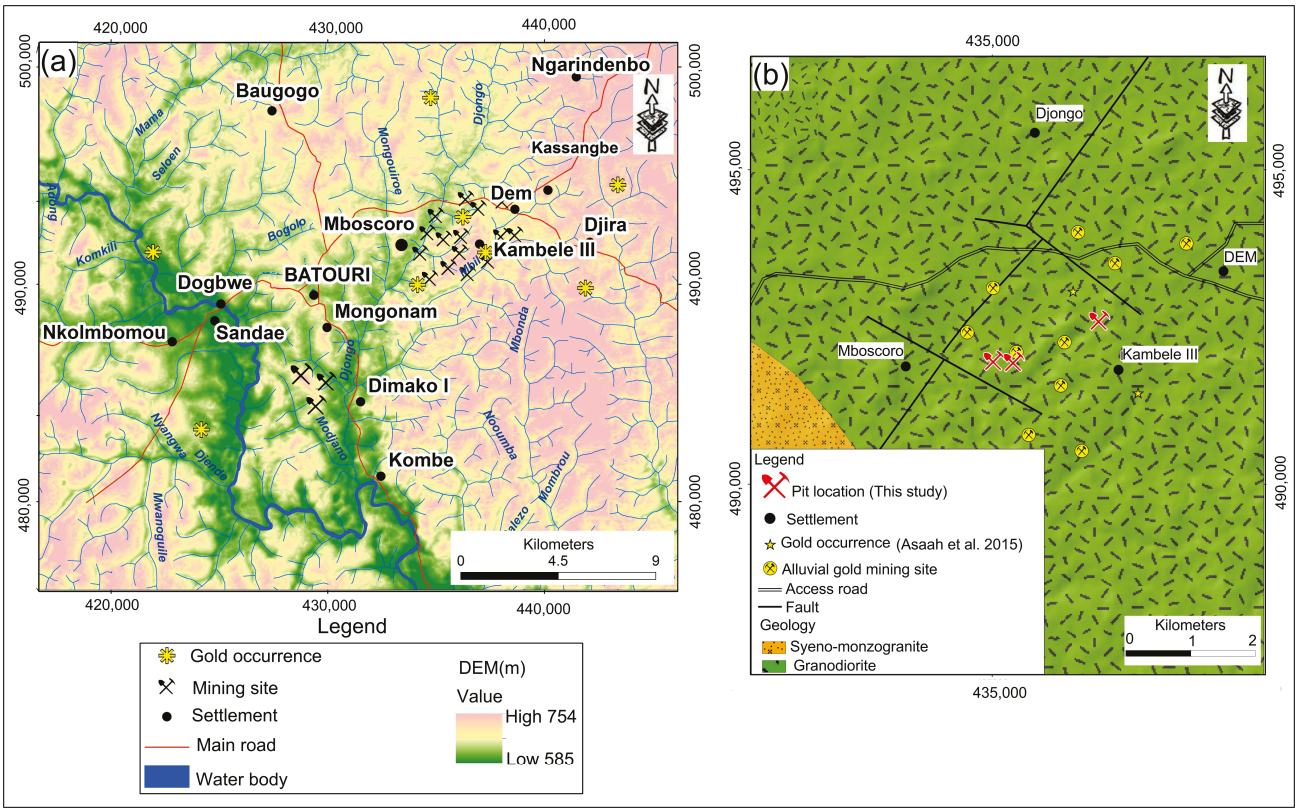


Figure 3. (**a**) Map of the Batouri area showing a dendritic drainage pattern and artisanal mining sites. (**b**) Map of the study area showing the position of studied pits. Gold occurrence [10].

3.2. Panning, Gold Grain Morphology and Microchemical Characterization

Subsamples of 25% by weight from the pits were processed by panning to obtain a heavy mineral concentrate containing particulate gold. Gold particles (50) from the overburden examined in this study were recovered from the saprock in PIT01 at a depth between 13 and 20 m, the saprolite layer of PIT03 at a depth from 13 to 21 m and the lateritic layer of the same pit at depths less than 4 m (Figure 5). The individual gold particles were then handpicked under a binocular microscope. Panning of the other horizons did not yield gold particles.

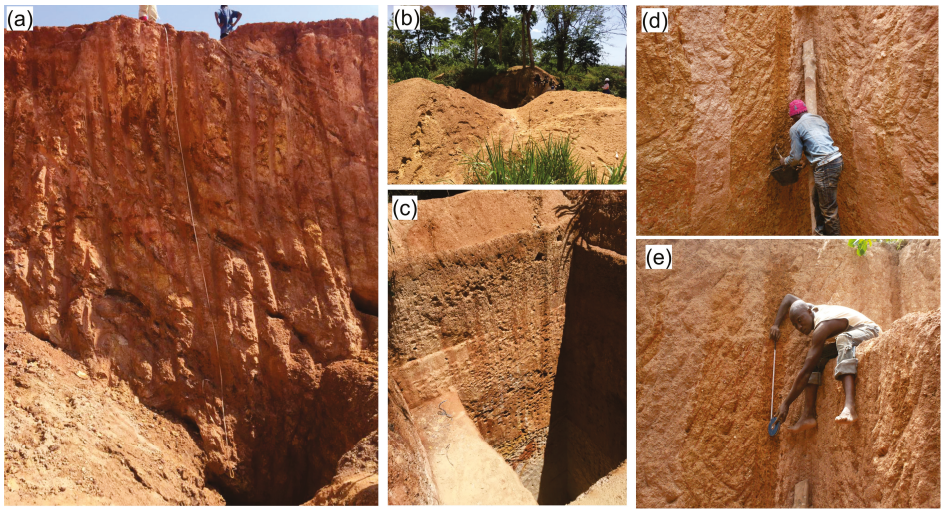


Figure 4. (**a**–**c**) Exploration and mining pits in the Batouri goldfield. (**d**) Channel sampling method along the pit wall. (**e**) Procedure of measuring the thickness of the mottled zone.

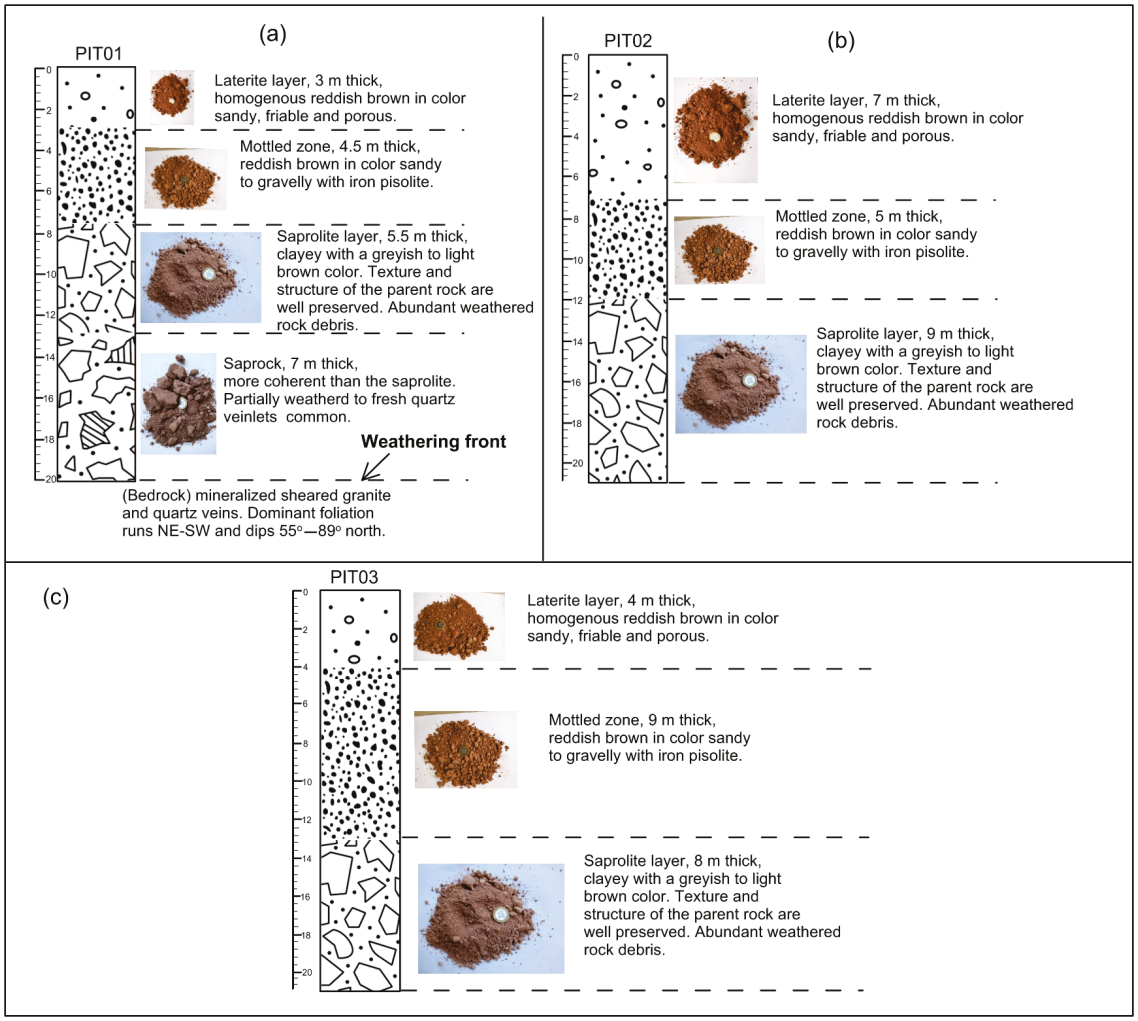


Figure 5. Soil horizons exposed within the three studied exploration pits in the eastern Batouri goldfield. The vertical scale represents depths in meters. From the top to the bottom, the profiles vary from the lateritic layer through the mottled zone, the saprolite and the saprock layers. Note that the size of the coin used for scale in the photograph is 24 mm. (**a**) Profile of pit 1, (**b**) Profile of pit 2, (**c**) Profile of pit 3.

Gold grains mounted in epoxy resin were polished down to a 0.3 μm grit to expose grain interiors, following the method described in [44]. For grain morphological study, a Fisher-Phenom XL scanning electron microprobe (SEM) was used to generate secondary electron (SE) and backscatter electron (BSE) images at the California State University, San Bernardino, USA. The instrument was operated with an acceleration voltage of 15 kV. Furthermore, scanning electron microprobe (SEM) imaging, mapping and an energy dispersive spectroscopy (EDS) analysis of the gold particles were performed with the same instrument as documented in [44]. The composition of the gold grains from the concentrates was determined using an additional electron microprobe analyzer equipped with wavelength dispersive spectrometry (WDS). The WDS was calibrated against a set of purchased house standards of gold–silver–copper alloy metals prior to gold grain analysis. The error associated with the trace element analyses is less than ±0.2 wt.%. A laboratory standard was run after every 10 analyses to ensure quality control on the data. The gold fineness was calculated using the formula Au × 1000/Ag + Au [45].

3.3. Bulk Geochemistry

The second quarter of the soil sample was manually mixed thoroughly to yield a homogenous sample (~4 kg each). The homogenized samples were then quartered. For each 1 kg of sample, 250 g were pulverized and about 50 g of the powder reserved for geochemical analysis. The stream sediment and soil samples for geochemical analysis were shipped to the ACME analytical Laboratories, Vancouver, BC, Canada. A 0.5 g sample of powder quartered from the samples collected from the various layers in the pits was analyzed for Au +53 elements using the inductively coupled plasma mass spectrometry (ICP-MS) technique. The analytical technique permits a detection limit of 0.2 ppb for Au. Randomly selected samples were analyzed twice for quality control, while blanks and in-house (SAND-VAN) blanks were used to correct for any aliquot impurity. The DSII and OREAS International Standards were used in calibrating the equipment. While the major elements show detection limits that range from 0.001 to 0.02 wt.%, the trace element reveals limits of detection that vary between 0.0002 and 20 ppm. The geochemical trends during weathering were determined as a function of the degree of chemical weathering using the chemical index of alteration (CIA). The CIA was calculated using the method proposed by [46] ($Al_2O_3/(Al_2O_3 + CaO + Na_2O + K_2O) \times 100$). The mass balance method was used to further demonstrate chemical changes between the various layers. Element gains and losses were calculated using the immobile element method of [47] with TiO_2 as the least mobile element. The mass change for a given element in an altered rock is calculated using the following equation:

$$\Delta C_{TiO2 \cdot J} = 100 \times [(C_{J \cdot A}/C_{J \cdot F})/(C_{TiO2 \cdot A}/C_{TiO2 \cdot F})] - 1$$

where $C_{J \cdot A}$ is the concentration of the element in the altered rock, $C_{J \cdot F}$ is the concentration of the element in the fresh/parent rock. Chemical variations in the average concentration of elements in the regolith were determined using the Isocon plot of [48]. The composition of the average fresh granite from [9] was used as a reference for the mass balance calculation.

4. Results

4.1. Description of the Soil Profile

The weathering profile in the Batouri goldfield presents an undisturbed succession of weathering horizons (Figure 5). From the bedrock to the surface, the weathering blanket reaches a thickness of 21 m. It varies upwards from the saprock at the bottom through the saprolite, mottled zone to the lateritic layer at the top; although, the saprock layer is absent in PIT02 and PIT03. The main characteristics of the profiles in Batouri are illustrated in Figure 5. The lateritic layer varies in thickness from 3 to 7 m. It is friable, porous, homogenous and reddish brown in color and reveals a characteristic ferralitic soil matrix. This layer grades downwards to the mottled zone which varies in thickness from 4.5 to 9 m. It is composed of iron-rich pisoliths scattered in a sparse sandy-clayey matrix. It ranges in color from brown to reddish brown. This layer progressively changes into the saprolite

layer. The saprolite layer at the base of the profile varies from 5.5 to 9 m in thickness. It ranges in color from grayish to light brown and consists essentially of clay, rock fragments, quartz debris and mica. The primary fabric of the parent rock is only partially preserved, but its mineralogy is essentially the same as that of the saprock layer, although with more clay content in the matrix. Partially weathered quartz veinlets are common. This horizon gradually changes at its lower limit into the saprock. The saprock, which is 7 m thick as exposed, characterizes the base of PIT01. It is pale cream in color and preserves the structure and texture of the parent rock. Within this horizon, quartz and muscovite survive towards the top while feldspar totally disappears. This layer is more coherent than the saprolite layer. Quartz veins exposed in this horizon show a characteristic stock work texture with a general NE-SW trend. The quartz veins are weakly to moderately brecciated and locally contain late Fe-Mn oxide, clay infill and visible millimeter size gold flakes.

4.2. Chemical Trends and Element Mobility in the Weathering Blanket

The major and trace element composition of soil from the weathering horizons is presented in Table 1. The samples were not analyzed for SiO_2 since its ubiquitous abundance and distribution in stream sediment and granite-derived soils do not define haloes. The weathering profiles show CIA values that range from 72 to 99. In the (Al_2O_3 − (CaO + Na_2O) − K_2O) diagram ([49]; Figure 6), a single weathering trend parallel to the A-K line is identified: from an intermediate weathering state towards a pure kaolinitic pole (Al_2O_3). This is coupled with a consistent gain in Fe_2O_3 (Figures 7 and 8). Lateralization in the regolith is marked by enrichment in Fe_2O_3 with a concentration of 17.15 wt.% in the lateritic layer of PIT01. It is accompanied by a slight increase in Al_2O_3, SO_3 and P_2O_5, and a remarkable depletion in MgO, CaO, Na_2O and K_2O as expected from the replacement of plagioclase and K-feldspar (Figure 7). Along with the addition of Au, other metal elements (e.g., Cu, Pb, Zn and Ba) are also enriched. It is worth nothing that Ba is only enriched in the saprolite and saprock horizons in PIT01. Besides slight enrichment in U, Rb and Sr within the profile, the concentrations of LILE are low. Most HFSEs such as Ga, Th, Hf and Zr show enrichments in the regolith (Figure 8). Lateralization is also marked by slight enrichments in Ag, As, Mo and Y (Figure 8, Table 1).

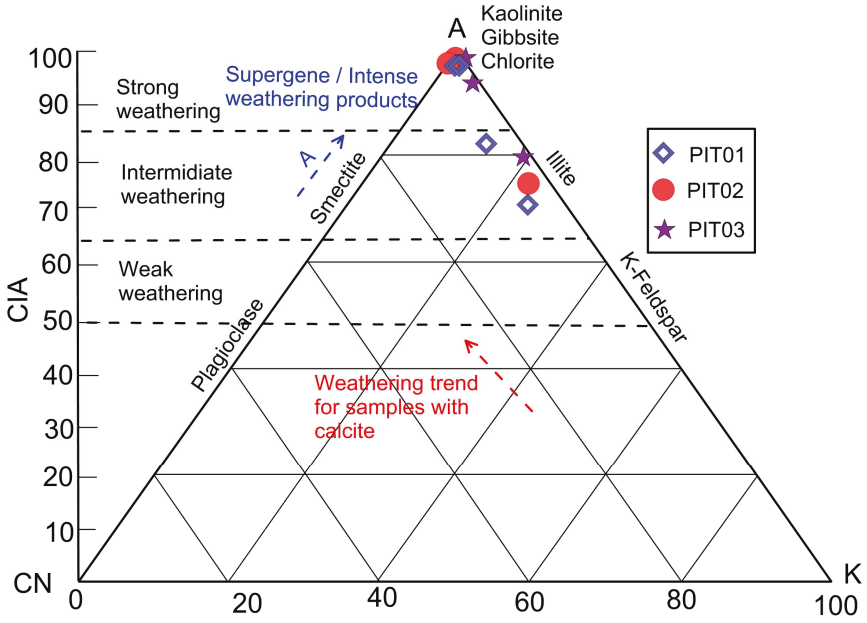


Figure 6. Ternary A-CN-K diagram used as a proxy to the alteration state of the regolith in the Batouri area. The regolith goes from a weak weathering state to an intermediate weathering state towards a theoretical kaolinite pole (Al_2O_3). Note that the samples investigated reveal a weathering trend that follows the A-K line.

Table 1. Geochemical composition of soil horizons from exploration pits in the Batouri goldfield.

		SOIL									
	DL	**PIT01**				**PIT02**			**PIT03**		
		LAT	**MOT**	**SAP**	**SAPROCK**	**LAT**	**MOT**	**SAP**	**LAT**	**MOT**	**SAP**
Elements											
Al_2O_3wt%	0.01	2.76	1.70	0.18	0.60	2.15	1.00	0.33	2.79	0.82	0.22
Fe_2O_3	0.01	17.15	4.06	1.38	9.71	10.04	1.96	0.32	8.97	2.92	12.88
MgO	0.01	0.01	0.02	bdl	0.03	0.02	0.01	bdl	0.01	bdl	bdl
CaO	0.01	0.01	0.01	0.01	0.02	0.02	0.02	bdl	0.01	bdl	bdl
Na_2O	0.001	<0.01	<0.01	<0.01	0.01	bdl	0.01	bdl	bdl	bdl	<0.01
K_2O	0.01	0.02	0.02	0.06	0.09	0.04	0.05	0.11	0.02	0.05	0.05
TiO_2	0.001	0.04	0.02	0.06	0.02	0.02	<0.01	bdl	0.04	0.01	0.03
P_2O_5	0.001	0.04	0.01	0.19	0.25	0.03	0.01	0.01	0.02	0.01	0.12
SO_3	0.02	bdl	bdl	bdl	bdl	bdl	bdl	bdl	bdl	bdl	bdl
CIA		99	98	85	72	97	93	74	99	94	80
ppm											
Au	0.0002	<1	<1	>100	3	<1	1	<1	<1	<1	>100
Ag	0.002	<1	<1	53	1	<1	<1	<1	<1	<1	85
As	0.1	19	4	bdl	100	40	21	9	67	30	253
Ba	0.5	7	10	165	151	14	15	22	7	9	19
Be	0.1	1	<1	1	3	<1	<1	<1	<1	<1	1
Bi	0.02	<1	<1	<1	<1	<1	<1	<1	<1	<1	<1
B	20	bdl	bdl	bdl	bdl	bdl	bdl	bdl	bdl	bdl	bdl
Co	0.1	1	1	14	20	1	1	<1	1	<1	7
Cs	0.02	<1	<1	<1	<1	<1	<1	<1	1	<1	<1
Cr	0.5	250	23	12	25	132	17	3	106	32	112
Cu	0.01	6	8	9	31	27	17	10	22	6	22
Cd	0.01	bdl	bdl	<1	<1	<1	bdl	bdl	bdl	bdl	<1
Ga	0.1	23	13	bdl	8	16	7	1	20	7	3
Ge	0.1	bdl	bdl	bdl	bdl	bdl	bdl	bdl	bdl	bdl	bdl
Hf	0.02	<1	<1	<1	bdl	<1	<1	<1	1	<1	<1
Hg	0.005	<1	<1	4	10	<1	<1	<1	<1	<1	3
In	0.02	<1	<1	<1	<1	<1	<1	bdl	<1	<1	<1
Li	0.1	1	2	1	1	1	2	1	2	1	<1
Mo	0.01	2	1	<1	2	2	1	<1	2	1	4
Mn	1	100	110	695	762	94	35	13	104	40	242
Nb	0.02	<1	<1	bdl	<1	<1	<1	bdl	<1	<1	bdl
Ni	0.1	3	3	3	12	3	2	1	4	1	10
Pb	0.01	47	22	136	157	36	15	8	15	6	39
Pd	0.01	bdl	bdl	bdl	bdl	bdl	bdl	bdl	bdl	bdl	bdl
Pt	0.002	bdl	bdl	<1	bdl	bdl	bdl	bdl	bdl	bdl	<1
Rb	0.1	3	3	2	4	7	5	4	4	4	2
Re	0.001	bdl	bdl	bdl	bdl	bdl	bdl	bdl	bdl	bdl	bdl
Sb	0.02	<1	<1	1	2	<1	<1	<1	<1	<1	2
Sc	0.1	13	8	13	17	10	5	1	13	4	12
Se	0.1	1	bdl	bdl	1	1	bdl	bdl	<1	<1	bdl
Sn	0.1	2	2	1	1	2	1	<1	2	1	3
Sr	0.5	2	3	28	25	3	2	1	3	1	12
Ta	0.05	bdl	bdl	bdl	bdl	bdl	bdl	bdl	bdl	bdl	bdl
Te	0.02	<1	bdl	bdl	<1	<1	bdl	bdl	<1	bdl	bdl
Th	0.1	38	13	626	431	21	9	7	21	13	265
Tl	0.02	<1	<1	1	<1	<1	<1	<1	<1	<1	bdl
U	0.1	3	2	7	6	2	1	<1	3	1	7
V	1	537	88	30	145	259	41	5	232	74	227
W	0.1	<1	bdl	bdl	3	1	<1	bdl	bdl	bdl	1
Y	0.01	3	7	82	59	3	5	4	6	4	22
Zn	0.1	10	10	154	66	24	14	5	15	3	21
Zr	0.1	22	7	3	1	14	5	2	24	9	3
La	0.5	10	38	2438	1968	20	41	56	22	26	1288
Ce	0.1	70	136	>2000	>2000	75	82	88	57	67	>2000

Abbreviations: LAT = laterite, MOT = mottled zone, SAP = saprolite, SAPROCK = saprock layer, DL = detection limit, bdl = below detection limit.



Figure 7. Histograms showing the gain/loss of major oxides and trace elements in the different layers of the pits dug in the Batouri goldfield [47]. Calculations are based on the immobile element method with TiO_2 as the least mobile element. The average concentration of major oxides and trace elements of the three pits were used. (**a**–**d**) represent the major element data for the layers, while (**a-1**–**d-1**) represent their trace element counterparts.

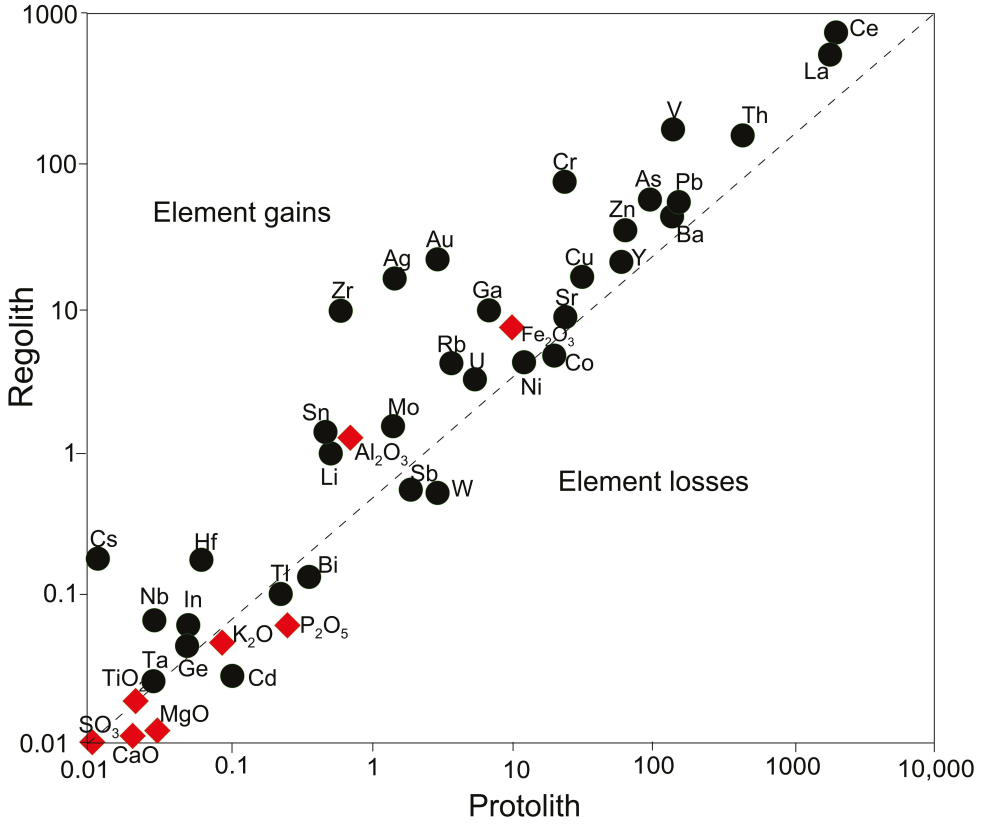


Figure 8. Isocon diagrams [48] of the Batouri weathering blanket. The concentrations of major elements are in wt.% (oxides) and ppm (trace elements) and scaled to fit on the plot. The dashed lines = constant mass reference. Isocon diagram shows the average composition of protolith against the average composition of the regolith.

In the regolith, gold also shows a strong positive correlation with Ag (r = 0.97) and a moderate correlation (r = 0.51–0.73) with As, Sb, Sr, Th, Y and Zn (Table 2).

Table 2. Pearson's linear correlation coefficient (r) matrix for gold and other elements from the weathering profile in the Batouri goldfield (elements with strong correlation to Au are marked in bold). The 0.5 threshold was used as a 'marker' for Au.

	Au	Ag	As	Ba	Ce	Co	Cr	Cu	Mo	Mn	Pb	Rb	Sb	Sr	Th	V	W	Zn	Zr
Au	1.00																		
Ag	**0.97**	1.00																	
As	**0.51**	0.69	1.00																
Ba	0.44	0.28	−0.02	1.00															
Ce	**0.78**	0.75	0.57	0.78	1.00														
Co	0.46	0.39	0.31	0.92	0.90	1.00													
Cr	−0.07	0.02	0.20	−0.38	−0.20	−0.26	1.00												
Cu	0.00	0.08	0.54	0.23	0.36	0.44	0.04	1.00											
Mo	0.34	0.52	0.87	−0.27	0.29	0.05	0.64	0.43	1.00										
Mn	0.49	0.37	0.18	0.97	0.87	0.98	−0.25	0.34	−0.05	1.00									
Pb	0.40	0.27	0.09	0.95	0.80	0.95	−0.13	0.34	−0.06	0.98	1.00								
Rb	−0.64	−0.64	−0.34	−0.28	−0.55	−0.35	−0.04	0.41	−0.26	−0.36	−0.28	1.00							
Sb	**0.53**	0.57	0.69	0.67	0.92	0.89	−0.05	0.60	0.46	0.80	0.77	−0.37	1.00						
Sr	**0.62**	0.50	0.22	0.96	0.91	0.96	−0.28	0.30	−0.03	0.98	0.95	−0.41	0.80	1.00					
Th	**0.73**	0.60	0.23	0.93	0.92	0.91	−0.25	0.20	0.00	0.95	0.90	−0.49	0.76	0.99	1.00				
V	−0.12	−0.04	0.21	−0.29	−0.14	−0.14	0.98	0.10	0.63	−0.14	−0.02	−0.07	0.05	−0.20	−0.19	1.00			
W	−0.01	0.04	0.45	0.54	0.60	0.78	−0.09	0.72	0.25	0.65	0.67	0.03	0.83	0.57	0.46	0.06	1.00		
Zn	**0.64**	0.44	−0.09	0.90	0.72	0.75	−0.28	0.06	−0.26	0.85	0.83	−0.32	0.48	0.90	0.92	−0.26	0.20	1.00	
Zr	−0.39	−0.37	−0.18	−0.50	−0.57	−0.52	0.74	−0.06	0.26	−0.44	−0.37	0.20	−0.47	−0.50	−0.49	0.71	−0.38	−0.35	1.00

4.3. Gold Concentrations along the Weathering Profile

Gold distribution in the various layers of each pit varies considerably (Table 1 and Figure 9). All the weathering blanket layers are gold-bearing; although, no systematic gold

enrichment is recorded (Figure 9). The saprock in PIT01 was measured to have a gold content of 3 ppm. The quartz vein itself identified within the saprock was not analyzed to avoid the nugget effect as millimeter size gold flakes were observed within the veins. The highest gold concentration (100 ppm) is recorded in the saprolite layers of PIT01 and PIT03. The mottled zone shows a maximum gold content of 1 ppm in PIT02, greater than that recorded in the saprolite horizon within the same pit. The opposite is true for PIT01 and PIT03. The lateritic layer shows a gold content that reaches a maximum concentration of <1 ppm.

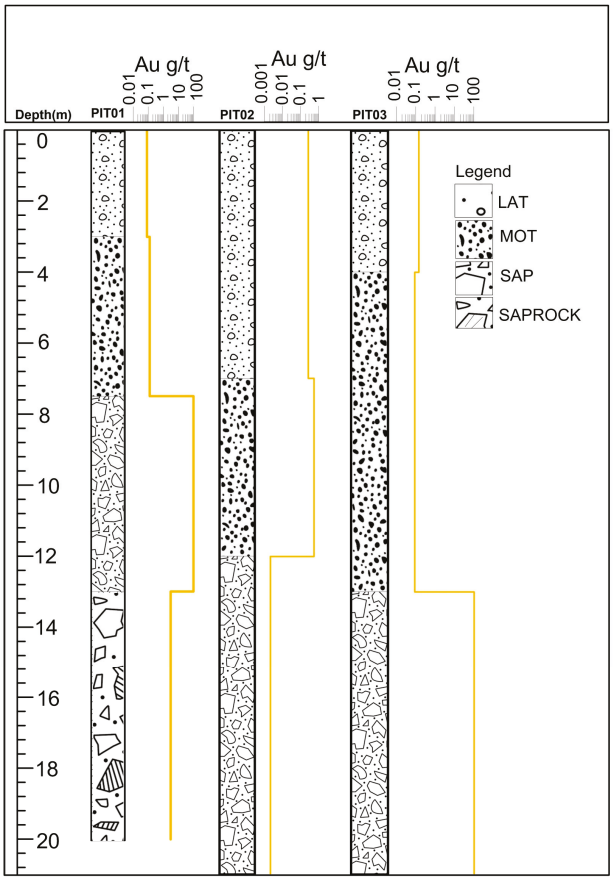


Figure 9. Profiles exposed in the Batouri goldfield, indicating the variation of Au concentration with depth. Note that the saprolite layer of PIT01 and PIT03 reveal a gold high of 100 ppm.

4.4. Gold Grain Morphology, Surface Characteristics and Microchemistry

Gold grains from the saprock, saprolite and laterite layers display a variation in their shapes and sizes. Backscatter electron (BSE) images of the gold grains and gold microchemistry are presented in Figures 10 and 11. Grains from the saprock layer are generally crystalline to angular in shape (Figure 10a–g). The grains vary from irregular and euhedral with clear crystal faces to sub-rounded with rough edges. Their surfaces have grooves and ridges and are often coated by iron-manganese-oxide clays in association with zircon, ilmenite and quartz (Figures 10a–j and 11a). The saprock gold particles are >20 µm in the longest dimension. The gold grains (Figure 11a) show a Ag concentration that ranges from 2.68 to 4.87 wt.% and Au values that reach a maximum of 97.32 wt.%. A single analysis identified Cu with a concentration of 0.70 wt.%.

Gold grains from the saprolite layer vary from sub-rounded to elongated to irregular and range in size from nanoparticulate to >300 µm (Figures 10i–l and 11e,f). They exhibit irregular and pitted surfaces expressed as cavities, most of which are filled with clay (silicates) minerals and quartz. Heavy mineral associations include zircon (Figure 10i–k).

Backscatter electron (BSE) images of gold particles with representative analytical points are presented in Figure 11e,f. The concentration of Au and Ag varies from the cores to the

rims of the gold grains analyzed, with copper detectable in few analytical spots (Figure 11e,f). The rims show Au contents as high as 85.13 wt.% and Ag contents of 14.87 wt.%. The cores show Ag contents as high as 26.68 wt.% and Au contents that range from 73.32 to 92.35 wt.%. This is coupled with Cu contents that reach a maximum of 7.70 wt.% (Figure 11e,f).

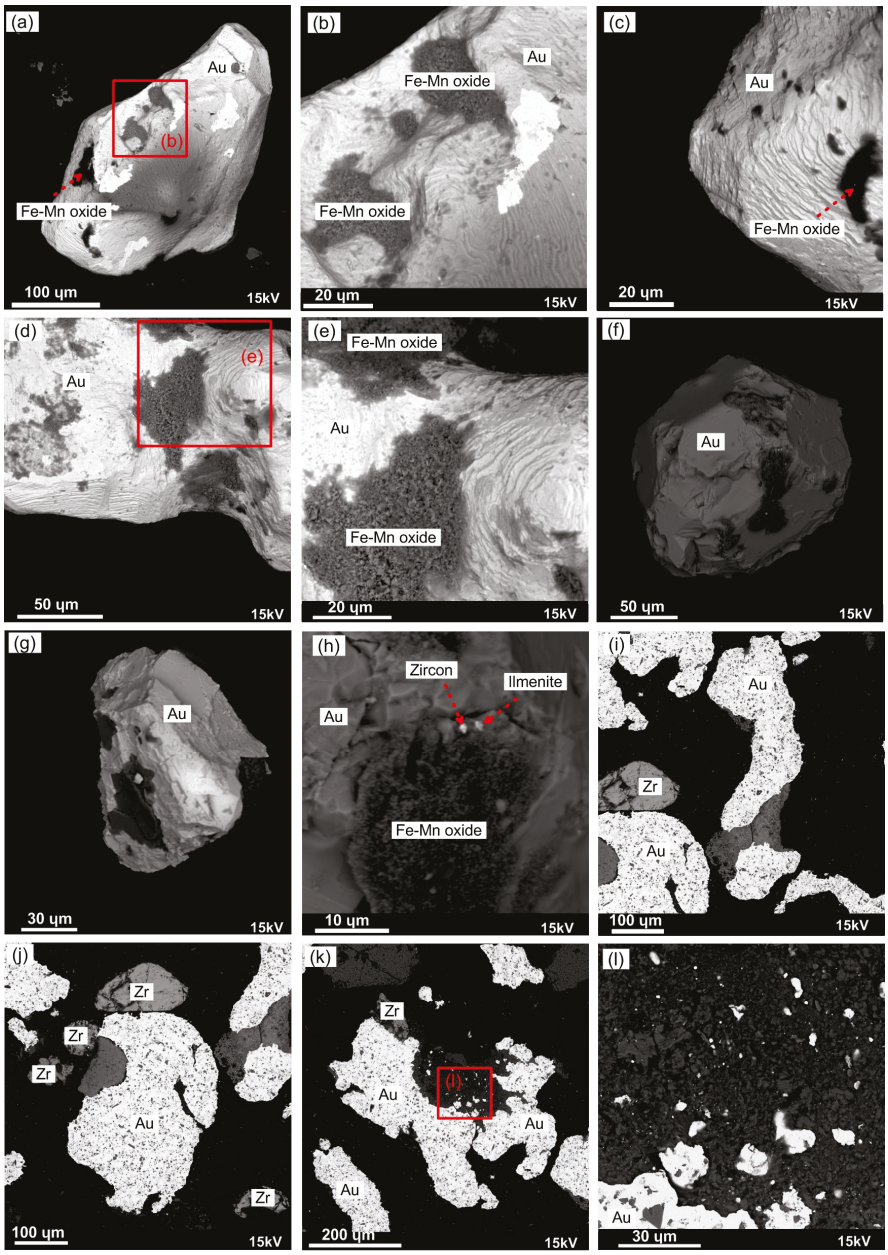


Figure 10. Scanning Electron Microscope (SEM) images (**a**–**g**) and Backscattered Electron (BSE) images (**i**–**l**) of gold grains from the saprock and saprolite layers indicating their morphology and surface features. (**a**–**g**) Gold grains from the saprock are generally crystalline to angular in shape and are greater than 20 µm in size. Notice the ridges, channels and Fe-Mn-O coatings on the grains. The brighter areas on the surface of the gold grains indicate areas where the iron-manganese-oxide coating has flaked. (**h**) Inclusions of ilmenite and zircon in gold grains from the saprock. (**i**–**l**) Gold grains from the saprolite layer are generally irregular; although, elongated and sub-rounded grains are present. They are characterized by pitted surfaces and vary in size from nano-particles to 200 µm. Abbreviations: Au = gold, Zr = zircon, Fe-Mn oxide = iron manganese oxide.

Gold grain	PIT N°	Layer	Grain N°	Shape	Point	Position	Content, wt. %															
							Au	Ag	Al	Ba	C	Cu	Gd	Fe	Hg	Mn	N	Nb	Nd	O	Si	Total	Fineness
(a)	PIT01	Saprock	1	angular	1	core	94.44	4.87				0.70										100.01	950.96
					2	core	97.32	2.68				0.00										100	973.20
					3												9.19	17.14		73.67		100	
					4					7.94	2.53		11.54			44.59		10.60		20.53		97.73	
					region 1		71.57									4.60				23.83		100	1000.00
					region 2		71.12									4.79				24.09		100	1000.00
					map		85.34	4.58	0.47			0.00		1.98		7.01					0.63	100.01	949.07
(b)	PIT03	Laterite	5	irregular	1				20.47					5.35								99.18	
					2	rim	100	0.00				0.00							64.46		18.01	100	1000.00
					3	rim	82.68	17.32				0.00										100	826.80
					4	core	86.63	11.49				1.88										100	882.90
					5	rim	81.84	16.57				1.58										99.99	831.62
					6	core	70.26	11.26				0.00			18.48							100	861.87
					7	rim	100	0.00				0.00			0.00							100	1000.00
					8	core	80.17	19.82				0.00			0.00							99.99	801.78
(c)	PIT03	Laterite	6	irregular	5	rim	75.00	3.64				3.86			16.69							99.19	953.71
					6	rim	65.61	3.33				0.00			31.00							99.94	951.70
					7	rim	97.41	2.59				0.00			0.00							100	974.10
					8	core	81.24	14.00				4.76			0.00							100	853.00
(d)	PIT03	Laterite	7	irregular	1															53.93	45.63	99.56	
					2	rim	90.34	9.66				0.00										100	903.40
					3	core	80.81	19.91				0.00										100.72	802.32
					4				3.39					24.85						28.55	43.21	100	
					5	core	73.26	26.74				0.00										100	732.60
					6	rim	75.26	10.58				0.00			14.16							100	876.75
(e)	PIT03	Saprolite	4	sub-rounded	1	rim	85.13	14.87				0.00										100	851.30
					2	core	85.25	14.75														100	852.50
					3	core	92.35	0.00				7.65										100	1000.00
					4	core	76.53	15.77				7.70										100	829.14
					5	core	77.74	22.26				0.00										100	777.40
				irregular	6	core	85.88	14.12				0.00										100	858.80
					7	core	73.32	26.68				0.00										100	733.20
					8	core	86.39	13.61				0.00										100	863.90
(f)	PIT03	Saprolite	8	irregular	1															59.27	40.38	99.65	
					2				15.29					37.98						32.27	14.56	100	
					3	core	81.51	18.47				0.00										100	815.10
					4	core	83.20	16.80				0.00										100	832.00
					map		57.56		13.90		12.89			6.66							8.99	99.97	1000

Figure 11. Scanning electron microscope (SEM) and backscattered electron (BSE) images of gold grains from the saprock, saprolite and lateritic layers of the Batouri goldfield. The composition of the respective gold grains and associated inclusion entombed in them is also presented. Gold grains from the saprolite and lateritic horizons are zoned and show characteristic pitted surfaces. The gold grains are alloyed mainly with Ag; although, a few analyses have identified Cu. Grains from the lateritic horizon show Hg with concentrations as high as 31 wt.%. (**a**) Representative gold grain from the saprock layer. (**b**–**d**) Representative gold grains from the laterite horizon. (**e**,**f**) Representative gold grains from the saprolite horizon.

Gold grains recovered from the lateritic horizon vary from irregular and elongated to sub-rounded in shape (Figure 11b–d). They are generally <200 µm. They show characteristic pitted surfaces and a "brain-like" look due to abundant microcavities and pores (Figure 11b,c). The concentration of gold in the rim ranges from 65.61 to 100 wt.%, while the Ag content varies between 0.00 and 17.32 wt.%. In the core, the concentration of Au reaches a maximum of 86.63 wt.%, while the Ag content varies between 11.26 and 26.74 wt.%. It is observed that the concentration of gold increases towards the rims, while the Ag content increases towards the core. Sporadic high contents of Hg (maximum of 31 wt.%) have been identified in some of the grains (Figure 11). Energy-dispersive spectroscopy (EDS) patterns and EMPA maps of gold grains recovered from the regolith are presented in (Figure 12).

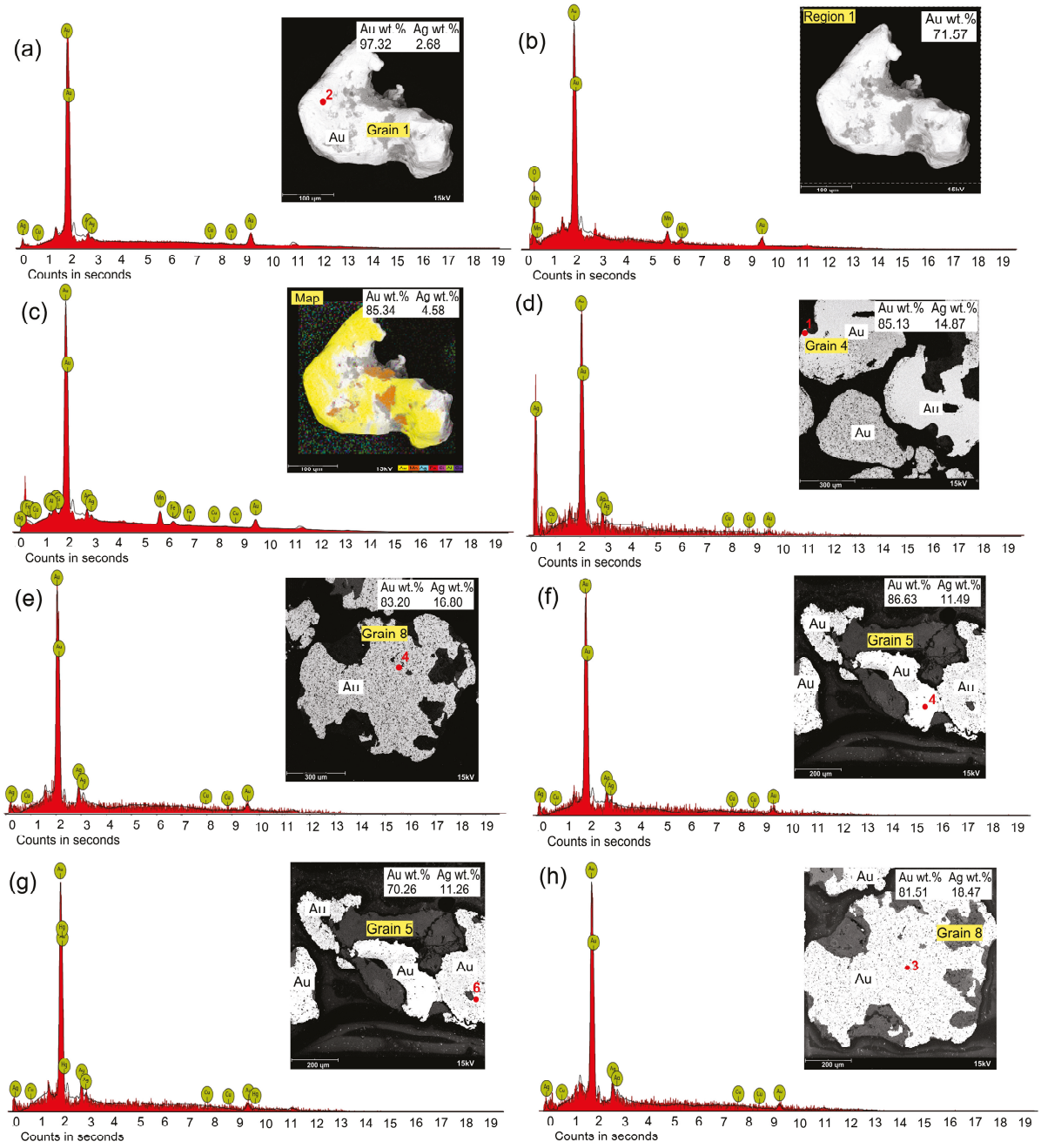


Figure 12. Energy-dispersive spectroscopy (EDS), scanning electron microscope (SEM) map and backscattered electron (BSE) images of gold grains from the saprock layer in PIT01 (**a**–**c**), saprolite layers (**d**,**e**,**h**) in PIT03, (**f**,**g**) laterite layer in PIT03 of the Batouri goldfield showing the typical alloy composition. (**a**) Au-Ag-Cu alloy. (**b**) Mn-O-Au. (**c**) Au-Ag-Mn-Fe-Si-Al-Cu. (**d**) Au-Ag-Cu alloy. (**e**) Au-Ag alloy. (**f**) Au-Ag-Cu alloy. (**g**) Au-Ag-Hg alloy. (**h**) Au-Ag alloy.

4.5. Characterization of Inclusion Signatures

Inclusions within the gold grains are illustrated in Figures 10, 11 and 13. The inclusions are generally irregular in shape with a maximum size less than ~200 µm. Compositionally, the mineral inclusions are composed of quartz, zircon, ilmenite, silicate and clay minerals (Figures 10, 11 and 13).

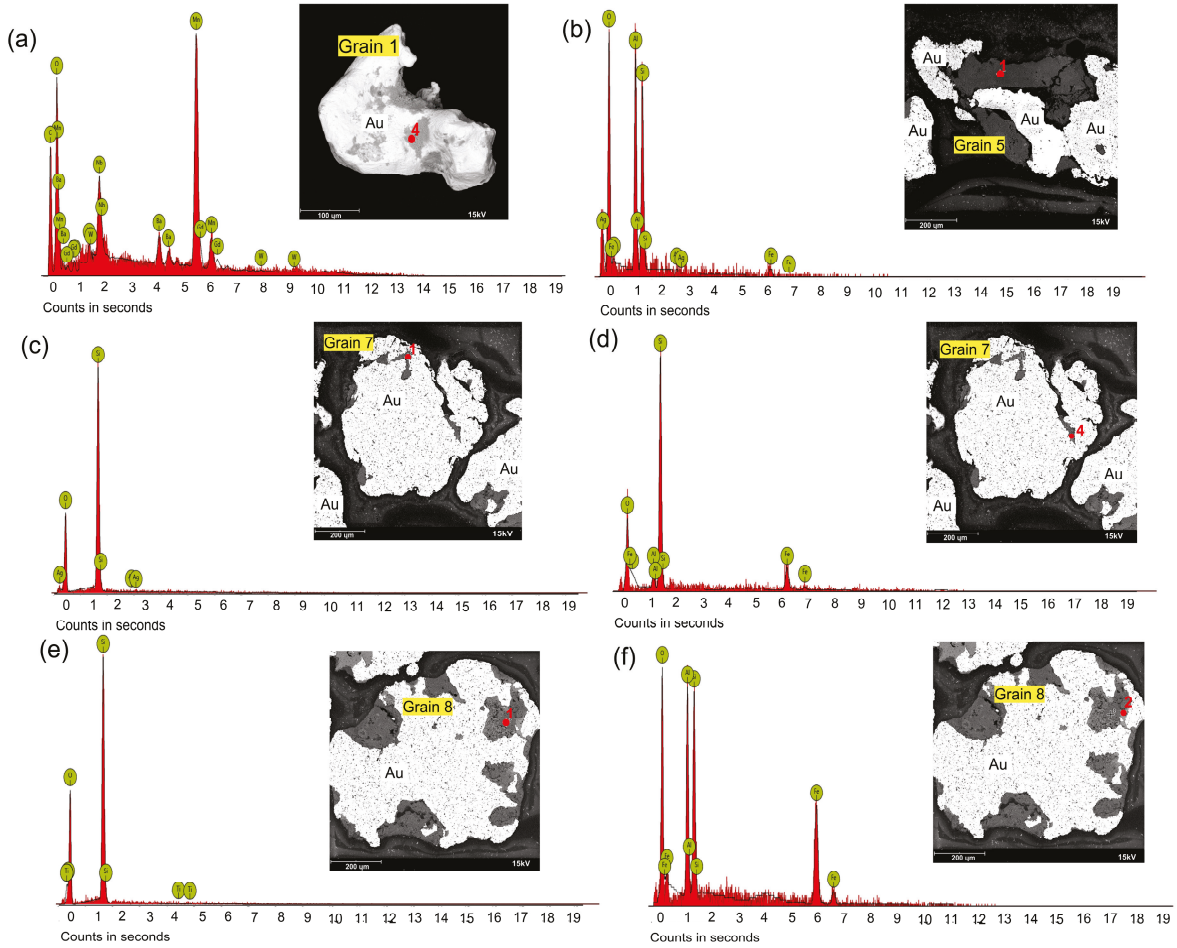


Figure 13. Energy-dispersive spectroscopy (EDS), scanning electron microscope (SEM) and backscattered electron (BSE) images of the polished sections of gold grains from the saprock and saprolite layers from the Batouri goldfield indicating coating material and inclusions in the gold grains. (**a**) C, Mn, O, Ba, Nb, W, Gd. (**b**) Fe, Ag, Al, Si, O. (**c**) Si, O, Ag. (**d**) Fe, O, Si, Al. (**e**) Si, Ti, O. (**f**) Fe, Al, Si, O. Grains 1, 5, 7 and 8 represents the gold grains analyzed and the numbers in them indicate analytical points.

5. Discussion

5.1. Geochemical Characterization of the Weathering Blanket

The succession of the weathering horizons exposed in the Batouri goldfield results from weathering related to the regolith landform regime in which they are situated [11–13]. The soil cover consists of four horizons, namely, from the bottom to the top, saprock, saprolite, mottled zone and the lateritic layer (Figure 5). The soil profile here is similar to that described by [19] in the Dimako area, [13] in the Batouri north goldfield, [12] in Couriège French Guiana developed on amphibolites but varies significantly from profiles described by [50] in the Bétaré Oya goldfield, which is developed upon the schistose parent rock. The saprock and saprolite horizons that preserve textures of the granitic basement rock point towards a purely residual inheritance [12]; although, selected biogenic concentrations of elements such as Au and Mn have been noted in similar environments [51]. The nature of the mottled zone and the lateritic layer is more difficult to apprehend as primary textures are almost destroyed. The lateritic layer has been reworked. According to [12], the upwards evolution from the saprolite to the mottled zone is primarily typical of in situ deep weathering. Thus, such textures are produced by the leaching of primary lithostructure and local segregation of Fe [52].

The transformation of protolith to the regolith (Figure 8) does not generally lead to large changes in element concentrations. Elements close to the isocon correspond to small

gains and losses [48]. However, Fe_2O_3 was consistently enriched during intermediate to intensely weathered activities in the Batouri area. This marks the process of lateritization in the regolith (Figures 7 and 8). According to [10,35], the basement rocks in this area have high magnetic susceptibility values and are magnetite series granitic rocks. This explains the elevated Fe_2O_3 concentration in the soil. The intermediate to intense weathering conditions revealed by the soil is marked by clay minerals (Figure 6, kaolinite, gibbsite, chlorite, illite). The soil show similarities in mineral composition (as determined by the X–ray diffraction technique) with lateritic soil developed on granite in the eastern region of Cameroon [53,54]. It is worth noting that the formation of the regolith seems to be accompanied by the segregation of elements such as Au-As-Ce-Cu-Pb-Rb-Sr-Y-Zn indicating contribution from felsic bedrock, while the Cr-V content can be attributed to subordinate mafic lithologies (Figure 8; [9,55]). The in situ character of the saprock/saprolite and mottled zone studied is further supported by enrichments in high field strength elements (HFSE) such as Ga, Th, Hf and Zr representing the least mobile element derived from the chemically homogenous basement rock (Table 1). Fresh granitic samples reported by [9] yield similar HFSE. Such enrichment in the regolith is produced by the leaching and loss of most highly mobile cations such as Si, Mg, Na, Ca, K and Ba during intense chemical weathering typical in tropical environments [12]. Since barium is chemically unstable in the surface environment, elevated barium in the weathering blanket (e.g., PIT01) suggests a close proximity to the source [56]. The weathering blanket's abundance of P, Zr and Ba is a reflection of the accessory minerals monazite, apatite and zircon found in the underlying granites. Therefore, it can be suggested that the weathering profile exposed in the Batouri goldfield is derived from a protolith that is chemically homogeneous.

5.2. Gold Grain Distribution along the Weathering Blanket

Gold redistribution in the supergene environment is primarily mediated by residual enrichments, chemical and biological dissolution/reprecipitation and physical transport [19]. Climate, bedrock composition and geomorphological factors all influence the style and intensity of gold mobilization [57]. As a result, the variation in gold grades in the studied profiles, along with the compositional and morphological features of gold, enable the mobility of gold during weathering to be assessed. It has been noted that within weathering profiles developed in equatorial environments, chemical dispersion of gold only occurs in the lateritic horizon and the upper portion of the mottled zone, while dispersion in the saprolite stays quite limited [58]. The reverse is true in the studied profiles which show a variation in the concentration of gold. The saprolite horizons in PIT01 and PIT03 reveals the highest concentration of gold at 100 ppm, while the saprock reveals a gold content of 3 ppm, the mottled zone in PIT02 shows a maximum gold content of 1 ppm and the lateritic horizon of the same pit reveals a gold content of <1 ppm. Thus, there is no discernable systematic enrichment in the concentration of gold from the bottom to the top of the pits. The high gold content in the saprock and saprolite layers coupled with the occurrence of gold in all the soil layers argues against any significant Au dissolution, remobilization and precipitation within the weathering cycle. Rather, the redistribution of gold in the particulate form is evident. This is similar to results by [13] in the Batouri north goldfield and [14] in the Kambélé gold mining area but significantly differs from profiles described by [50] developed on the schist basement in the Bétaré Oya gold district. In soil profiles where Au remobilization and chemical precipitation of authigenic gold is evident, Au is usually dissolved from the higher horizons and reprecipitated from unstable complexes to form mottled zone and saprolite haloes at depth (e.g., [19,59]). The fact that the saprock and the saprolite horizons with high gold contents and the lateritic horizon also recovered particulate gold with the nano size fraction goes further to support the dispersion of gold in the particulate form in the Batouri goldfield. This is also affirmed by the absence of circular pits on surfaces or irregular gold grain shapes following gold dissolution after exposure to weathering solutions and the absence of secondary gold spherolites on surfaces of primary gold [16,17].

It is also possible that gold microbiology plays a role in the gold distribution in these profiles. It is well known that bacterioform gold is linked with high-purity gold overgrowths and nanoparticulate gold in association with Fe-and Mn-rich biomats (e.g., [60]). These same features associated with biogenic gold are also noted in the samples from this study. The magnitude of any biological contribution to gold enrichment is not clear and remains to be examined. Regardless of the exact contribution and timing of biological precipitation or overprinting on pre-existing native gold, bacterioform nano-particulate gold similar to that of other localities [51] is present in these samples.

5.3. Gold Microchemical Signature and Grain Transportation

The microchemical signature of detrital gold has been widely used to link its features to possible hypogene sources in regional exploration schemes [61,62], similar to those documented in this study. The criteria used in such studies include grain morphology, alloy elements and the diversity of inclusion minerals in the gold particles (e.g., [63–68]). The morphology of gold grains can also aid in identifying proximity to the primary mineralization [69].

Gold particles recovered in this study vary in terms of texture from one soil horizon to the other. We have shown that gold particles from the saprock are generally crystalline to angular with clear crystal faces, rough edges, grooves and ridges (Figures 10 and 11). Gold particles from the saprolite horizon are generally irregular and elongated to sub-rounded (Figures 10 and 11). Such observations point to either a limited dispersion of gold from the primary source or restricted exposure to chemical weathering time since being dislodged from the hypogene source (Figures 10a–g and 11a; [70]). The grains' principal inclusions, surface features such as ridges, cavities and rough and etched pits, indicate that they were likely recently derived from the primary source. Mechanical weathering influences are also minimal. The sub-rounded nature of the gold grains recovered from the soil profile implies that gold grain roundness can also develop in soil profiles and not only in alluvial systems. Gold grains forming the laterite horizon show vermiform microtextures and pitted surfaces with microcavities (Figure 11b–d). This is similar to secondary particulate gold reported [6] in the Inagli Pt-Au placer deposit in Russia, where in this study, the gold grains show no evidence of intricate secondary growth features such as dendrites and filaments, which are pervasive in authigenic gold (e.g., [71]). The microfabrics observed in the gold particles do not indicate any supergene contributions; thus, the gold grains are detrital and not authigenic in origin.

Mineral inclusion suites have been widely used to link gold to their possible primary sources for the purpose of exploration [65]. In the Batouri goldfield, ore mineral inclusions were scarce; nevertheless, gangue minerals provide an avenue for this study (Figures 10, 11 and 13). Gold grains from the saprock layer are coated with Fe-Mn oxides, while ilmenite and zircon are common heavy minerals in the horizon. This is associated with elevated contents of Ba, Cu, C, Gd, Nb, O, Mn, Fe Al, Si and W which can be attributed to minerals such as silicates, oxides and REE minerals (Figures 11 and 13). The saprolite layer shows an intimate association with silicates, clay and quartz. Weathering of the granite hosting lode mineralization released gold into the regolith. This is in agreement with the bulk geochemical data discussed above, which pointed to the redistribution of gold in the solid state in the soil. Iron oxide inclusions containing Cr and V reported for the first time in the Essabikoula area within the Ntem complex have been attributed to the interaction between hot reducing hydrothermal fluid and local mafic lithologies [55].

The Au alloy composition as indicated in the gold grains is mainly binary (Au-Ag, Figure 14a); although, few analytical spots reveal a ternary Au-Ag-Cu composition in the saprolite and laterite horizons with Cu contents that reach a maximum of 7.70 wt.% (Figures 11 and 14b). In the Cameroon goldfields, such high Cu content is reported for the first time. Systematic changes in alloy composition in gold detrital particles within a single hydrothermal system point to the evolution of the hydrothermal fluids in space and time [72]. It is possible that the lode source had multiple mineralizing events that produced a range of native gold generations. Some of the gold grains on the lode were

more Cu-rich than others. This assertion is supported by Cu contents as high as 874 ppm in the hydrothermally altered basement granitoids [9,67].The composition of gold grains from this study is here compared with gold mineralization in the quartz vein and bedrock of the eastern Cameroon goldfield and granite hosted gold mineralization in Bigorne, Iberian Variscan belt, western Europe (Figure 14a,b). The detrital grains have core compositions consistent with their derivation directly from hypogene mineralization and support the interpretation of the grains in the weathering blanket as inherited relic grains from the primary mineralization [13,68]. The gold grains have a fineness value that varies from 732 to 1000 (Figure 14c) with an average value of 888.

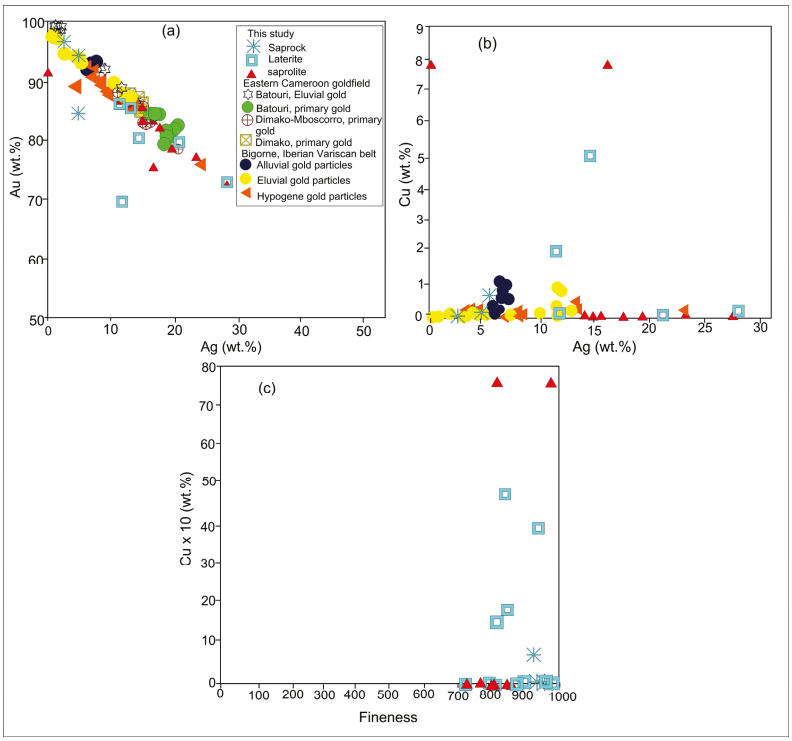


Figure 14. (**a**) Co-variance of Ag and Au for gold particles from the Batouri goldfield compared with primary gold grains from the eastern region and gold particles from Bigorne deposits [67]. Gold grains from Batouri are characterized by low Ag and high gold contents. (**b**) Variation in the concentration of Ag and Cu in gold grains from the Batouri goldfield. Note a Cu content as high as 7.7 wt%. (**c**) Purity of the gold grains from the saprock and saprolite layers as represented by gold grain finesses in the cores and rims.

A majority of the values cluster within the lower limit (Figure 14c). High Ag content recorded in the core (Figure 11) and rim portions of the grains suggests limited rates of physical and chemical weathering resulting in negligible Ag leaching and point to the presence of electrum, a natural alloy of gold with >20 wt.% Ag sourced from a Ag-enriched primary deposit.

5.4. Impact of Anthropogenic Activities

Anthropogenic activity in artisanal and small scale gold mining sites is an important source of contamination to the environment. In the eastern Cameroon goldfield, mining sites such as Bétaré Oya and Kambélé are noted for soil, stream sediment and surface water contamination mainly resulting from anthropogenic activities [2,73]. While the soil and sediment show elevated contents of Co, Cd, Cu, As, Cr, Pb and Zn [2], surface waters show metallic elements in the following descending order Fe > Mn > Pb > Cr > Cd [73]. In this study, the Au-Ag alloy grains from the lateritic horizon show high Hg content (Figures 11 and 12g). The Hg contents identified in the gold grains vary from 18.48 in

the core to between 16.69 and 31 wt.% in the rims of the grains. This high Hg content is reported for the first time in the gold district. The Au-Ag-Hg compound has been reported in the hypogene environment [72]. Orogenic gold with high Hg content have also been reported by [61,62]. According to [61,62], Hg high in gold grains is indicative of an orogenic setting/low-temperature hydrothermal activity emplaced at high structural levels. The Au-Ag-Hg alloy has also been reported in supergene conditions as a result of the introduction of anthropogenic Hg during mining operations [5,6]. The earliest records of Hg use in amalgamation were from Egypt and China more than 3000 years ago [74]. Mercury has been used in inexpensive, easy and rapid approaches for extracting gold from its ore and soil [75]. Notably, owing to weak legislation, poor engagement, contribution of artisanal miners and easily accessible and robust black market for Hg usage in the artisanal and semi mechanized gold miming (ASGM) will continue to persist [76,77]. The high content of Hg identified in samples from this study is considered to be from anthropogenic sources; although, some of the measurements were performed in the core of the grains and as amalgam coatings on the grain exteriors.

The abundance of Hg within the lateritic horizon and not within lower stratigraphic horizons, in conjunction with an abundant source from mining operations, strongly suggests that this Hg has anthropogenic origins. However, naturally occurring Hg from the upper geochemical halo of orogenic deposits is well documented [61,62]. Furthermore, the presence of Hg alloys and Hg minerals within the interior of gold grains without clear internal migratory pathways can support the case for a natural source (e.g., [78]). The implications of natural Hg towards understanding ore deposit type, genesis and evolution warrant further investigation at this site. Future work with measurements of Hg isotopes may provide insights on the relative contributions of these two potential sources. Regardless of origin, the abundance of Hg in these deposits remains an environmental concern for both the health of miners and the regional ecosystem.

5.5. Implication to Gold Exploration in the Regolith

The exploration for gold in weathered and covered terrains commonly relies on sampling and analyzing in situ material [12]. A detailed characterization of the regolith is required in order to better comprehend the physico-chemical changes along the profile and distinguish remobilized material from that developed in place [13,50,79,80]. The data presented in this study suggest that gold remained in the solid form during its dispersion, owing to its chemical stability. The results also show that the horizons with visible and recoverable gold grains also have high gold assay values, indicating the detrital nature of the particles. From the bulk geochemical data, the distribution of Au in all the horizons and the fact that the saprock and the saprolite horizons are enriched in gold, as well as the occurrence of quartz inclusions in the gold grains, these indicate quartz-vein-related hypogene mineralization within the granitic basement. It is also worth noting the usefulness of pathfinder elements such as Pb, Cu, As, Bi, Te and Ag as they may positively correlate with Au [81]. In the Batouri goldfield, Ag shows a strong positive correlation with Au and thus can be identified as the pathfinder element for gold in the area. Bulk assay data combined with gold microchemical features in regolith material deliver a potent exploration technique in tropical terrains.

6. Conclusions

The following conclusions can be drawn from this study:

1. Pits dug in the Batouri goldfield exposed an in situ profile comprising various layers from the bottom to top as follows: saprock layer, saprolite, mottled zone and the laterite layer. It is clear that the lateritic layer has been reworked. The saprock layer in PIT01 is characterized by quartz veins that show gold flakes.
2. The soil samples define a single weathering array corresponding to intermediate weathering evolving towards the kaolinitic end.

3. Regolith evolution involved the development of laterite with elevated Fe content and enriched in Au-As-Ba-Ce-Cu-Pb-Rb-Sr-Y-Zn, pointing to inputs from the felsic basement, while Cr-V are related to mafic lithologies. High concentrations of chemically unstable Ba in the weathering blanket (e.g., PIT01) also affirm the proximity to the primary source.
4. Gold grains show surface features that attest to their derivation from proximal sources. They are associated with inclusions of gangue minerals such as quartz, silicates, zircon and ilmenite inferred to be inherited from the underlying granitic basement rock.
5. All horizons identified show the presence of gold; however, the concentration varies from top to bottom in a non-systematic manner. Gold essentially survived the rigors of the weathering cycle in the particulate form as explained by the 3 ppm Au in the saprock and 100 ppm Au in the saprolite. All the soil layers should therefore be taken into account during succinct regolith exploration efforts in this area.
6. The gold grains are not authigenic in origin, and the concentration of Au is uniform along the core, solution fissures and rims, while that of Ag increases towards the core. These grains are alloyed with Ag and define a single compositional population similar to grains from the bedrock.
7. Gold grains from the lateritic horizon show a Au-Ag-Hg assemblage. The Hg high is identified for the first time in the Batouri goldfield. Such elevated contents of Hg indicate modification due to human activities especially with the use of hazardous Hg-based products in the gold extraction process.

Author Contributions: Conceptualization, C.E.S.; Data curation, F.C.V.; Funding acquisition, C.E.S., E.B.M. and E.M.S.; Field Investigation, A.V., R.B.N., B.O.O., T.C.N. and S.G.S.; Methodology, A.V., C.E.S. and E.B.M.; Resources, C.E.S.; Supervision, C.E.S.; Validation, C.E.S. and E.B.M.; Writing—original draft, A.V.; Writing—review and editing, A.V., C.E.S., R.B.N., E.B.M., E.M.S., B.O.O., T.C.N., F.C.V. and S.G.S. All authors have read and agreed to the published version of the manuscript.

Funding: Research Modernization Allowance scheme of the Ministry of Higher Education, Cameroon.

Data Availability Statement: The data presented in this study are available in the article. Additional data are not available.

Acknowledgments: A.V. and C.E.S. acknowledge support from the Cameroon Government through the Research Modernization Allowance scheme of the Ministry of Higher Education that enabled them to fund the M.Sc. dissertation of S.G.S., whose data form part of this contribution. C.E.S., E.M.S. and E.B.M. acknowledge the collaboration framework through which some of the data reported here were acquired. Comprehensive reviews by three anonymous reviewers contributed immensely to the improvement of this contribution.

Conflicts of Interest: The authors declare no conflicts of interest.

References

1. Orji, O.U.; Ibiam, U.A.; Awoke, J.N.; Obasi, O.D.; Uraku, A.J.; Alum, E.U.; Eze, A.G. Assessment of levels and health risks of trace metals in soils and food crops cultivated on farm lands near enyigba mining sites, Ebonyi state, Nigeria. *J. Food Protect.* **2021**, *84*, 1288–1294. [CrossRef] [PubMed]
2. Elvine Paternie, E.D.; Hakkou, R.; Ekengele Nga, L.; Bitom Oyono, L.D.; Ekoa Bessa, A.Z.; Oubaha, S.; Khalil, A. Geochemistry and geostatistics for the assessment of trace elements contamination in soil and stream sediments in abandoned artisanal small-scale gold mining (Bétaré-Oya, Cameroon). *Appl. Geochem.* **2023**, *150*, 105592. [CrossRef]
3. Bailey, A.S.; Jamieson, H.E.; Radkova, A.B. Geochemical characterization of dust from arsenic-bearing tailings, Giant Mine, Canada. *Appl. Geochem.* **2021**, *135*, 105119. [CrossRef]
4. Reyes, A.; Cuevas, J.; Fuentes, B.; Fernandez, E.; Arce, W.; Guerrero, M.; Letelier, M.V. Distribution of potentially toxic elements in soils surrounding abandoned mining waste located in Taltal, Northern Chile. *J. Geochem. Explor.* **2021**, *220*, 106653. [CrossRef]
5. Falconer, D.M.; Craw, D.; Youngson, J.H.; Faure, K. Gold and sulphide minerals in tertiary quartz pebble conglomerate gold placers, Southland, New Zealand. *Ore Geol. Rev.* **2006**, *28*, 525–545. [CrossRef]
6. Svetlitskaya, T.V.; Nevolko, P.A.; Kolpakov, V.V.; Tolstykh, N.D. Native gold from the Inagli Pt–Au placer deposit (the Aldan Shield, Russia): Geochemical characteristics and implications for possible bedrock sources. *Miner. Depos.* **2018**, *53*, 323–338. [CrossRef]
7. Gazel, J.; Gérard, G. *Carte Géologique de Reconnaissance du Cameroun au 1/500,000, Feuille Batouri-Est avec Notice Explicative*; Mémoire Direction des Mines et de la Géologie, Yaoundé, Cameroon; Science and Education Publishing: Newark, DE, USA, 1954.

8. Vishiti, A.; Etame, J.; Suh, C.E. Features of gold-bearing quartz veins in an artisanal mining dominated terrain, Batouri Gold District, Eastern region of Cameroon. *Episodes* **2019**, *42*, 199–212. [CrossRef]
9. Tata, E.; Suh, C.E.; Vishiti, A.; Shemang, E.M.; Fon, A.N.; Ateh, K.I.; Chombong, N.N. Wallrock alteration categories and theirgeochemical signatures in gold-bearing Neoproterozoic granitoids, Batouri Gold District, southeastern Cameroon. *Geochem. Explor. Environ. Anal.* **2019**, *19*, 269–288. [CrossRef]
10. Asaah, A.V.; Zoheir, B.; Lehmann, B.; Frei, D.; Burgess, R.; Suh, C.E. Geochemistry and geochronology of the ~620 Magold-associated Batouri granitoids, Cameroon. *Inter. Geol. Rev.* **2015**, *57*, 1485–1509. [CrossRef]
11. Anand, R.R.; Hough, R.M.; Salama, W.; Aspandiar, M.F.; Butt, C.R.M.; Gonzalez-Alvarez, I.; Metelka, V. Gold and pathfinder elements in ferricrete gold deposits of the Yilgarn Craton of Western Australia: A review with new concepts. *Ore Geol. Rev.* **2019**, *104*, 294–355. [CrossRef]
12. Combes, V.; Teitler, Y.; Eglinger, A.; André-Mayer, A.-S.; Heuret, A.; Pochon, A.; Cathelineau, M.; Gibert, P. Diversity of supergene gold expressions and implications for gold targeting in an equatorial regolith (AMG's Couriège Exploration Prospect, French Guiana). The Geological Society of London Recent Advances in Understanding Gold Deposits: From Orogeny to Alluvium. *Geol. Soc. Lond. Spec. Publ.* **2022**, *516*, SP516-2021-40.
13. Vishiti, A.; Suh, C.E.; Lehmann, B.; Egbe, J.A.; Shemang, E.M. Gold grade variation and particle microchemistry in exploration pits of the Batouri Gold District, SE Cameroon. *J. Afr. Earth Sci.* **2015**, *111*, 1–13. [CrossRef]
14. Etutu, M.E.M.; Mafany, G.T.; Suh, C.E. Application of multi-element soil geochemistry and particulate gold exploration in the Kambele plain, Batouri Gold District, Southeast Cameroon. In *Recent Research on Geomorphology, Sedimentology, Marine Geosciences and Geochemistry, Advances in Science, Technology & Innovation*; Springer: Cham, Switzerland, 2022.
15. Craw, D.; Kerr, G. Geochemistry and mineralogy of contrasting supergene gold alteration zones, southern New Zealand. *J. Appl. Geochem.* **2017**, *5*, 19–34. [CrossRef]
16. Bamba, O.; Parisot, J.C.; Grandin, G.; Beauvais, G. Ferricrete genesis and supergene gold behavior in Burkina Faso, West Africa. *Geochem. Explor. Environ. Anal.* **2002**, *2*, 3–14. [CrossRef]
17. Larizzatti, H.; Oliveria, S.M.B.; Butt, C.R.M. Morphology and composition of gold in a lateritic profile, Fazenda Pison Garimpo, Amazon, Brazil. *J. South Am. Earth Sci.* **2008**, *25*, 359–376. [CrossRef]
18. Falconer, D.M.; Craw, D. Supergene gold mobility: A textural and geochemical study from gold placers in southern New Zealand. *Econ. Geol. Spec. Publ.* **2009**, *14*, 77–93.
19. Suh, C.E.; Lehmann, B. Morphology and electron-probe micro analysis of residual gold-grains at Dimako, southeast Cameroon. *Neues Jahrb. Für Mineral. Monatshefte* **2003**, *6*, 225–275.
20. Freyssinet, P.H.; Butt, C.R.M.; Morris, R.C.; Piantone, P. Ore-forming processes related to lateritic weathering. In *Economic Geology 100th Anniversary Volume*; Hedenquist, J.W., Thomson, J.F.H., Goldfarb, R.J., Richards, J.P., Eds.; Society of Economic Geologists Inc.: Littleton, CO, USA, 2005; pp. 681–722.
21. Zotov, A.; Kuzmin, N.; Reukov, V.; Tagirov, B. Stability of $AuCl_2$—From 25 to 1000 °C at pressures to 5000 bar and consequences for hydrothermal gold mobilization. *Minerals* **2018**, *8*, 286. [CrossRef]
22. Reis, A.P.; Silva, E.F.; Sousa, A.J.; Patinha, C.; Martins, E.; Guimaraes, C.; Azevedo, M.R.; Nogueira, P. Geochemical associations and their spatial patterns of variation in soil tungsten deposit: A pilot analysis data from the Marrancos gold. *Geochem. Explor. Environ. Anal.* **2009**, *9*, 319–340. [CrossRef]
23. Shuster, J.; Reith, F.; Cornelis, G.; Parsons, J.E.; Parsons, J.M.; Southam, G. Secondary gold structures: Relics of past biogeochemical transformations and implications for colloidal gold dispersion in sub tropical environments. *Chem. Geol.* **2017**, *450*, 154–164. [CrossRef]
24. Toteu, S.F.; Penaye, J.; Djomani, Y.P. Geodynamic evolution of the Pan-African belt in central Africa with special reference toCameroon. *Can. J. Earth Sci.* **2004**, *41*, 73–85. [CrossRef]
25. Van Schmus, W.R.; Oliveira, E.P.; Da Silva Filho, A.F.; Toteu, S.F.; Penaye, J.; Guimaraes, I.P. Proterozoic links between the Borborema Province, NE Brazil, and the Central African Fold Belt. *Geol. Soc. Lond. Spec. Publ.* **2008**, *294*, 69–99. [CrossRef]
26. Toteu, S.F.; Van Schmus, R.W.; Penaye, J.; Michard, A. New U-Pb and Sm-Nd data from north central Cameroon and its bearing on the Pre-Pan-African history of Central Africa. *Precambrian Res.* **2001**, *108*, 45–73. [CrossRef]
27. Milesi, J.P.; Toteu, S.F.; Deschamps, Y.; Feybesse, J.L.; Lerouge, C.; Cocherie, A.; Penaye, J.; Tchameni, R.; Moloto-A-Kenguemb, G.; Kampunzu, H.A.B.; et al. An overview of the geology and major ore deposits of Central Africa: Explanatory note for the 1:4,000,000 map "geology and major ore deposits of Central Africa". *J. Afr. Earth Sci.* **2006**, *44*, 571–595. [CrossRef]
28. Njiekak, G.; Dorr, W.; Tchouankoue, J.-P.; Zulauf, G. U–Pb zircon and microfabric data of (meta) granitoids of western Cameroon: Constraints on the timing of pluton emplacement and deformation in the Pan-African belt of central Africa. *Lithos* **2008**, *102*, 460–477. [CrossRef]
29. Tchameni, R.; Pouclet, A.; Penaye, J.; Ganwa, A.A.; Toteu, S.F. Petrography and geochemistry of the Ngaoundéré Pan-African granitoids in Central North Cameroon: Implications for their sources and geological setting. *J. Afr. Earth Sci.* **2006**, *44*, 511–529. [CrossRef]
30. Ateh, K.I.; Suh, C.E.; Shemang, E.M.; Vishiti, A.; Tata, E.; Chombong, N.N. New LA-ICP MS U-Pb Ages, Lu-Hf Systematics and REE Characterization of Zircons from a Granitic Pluton in the Betare Oya Gold District, SE Cameroon. *J. Geosci. Geomat.* **2017**, *5*, 267–283.
31. Ngatcha, R.B.; Okunlola, O.A.; Suh, C.E.; Ateh, K.I.; Hofmann, A. Petrochemical characterization of Neoproterozoic Colomine granitoids, SE Cameroon: Implications for gold mineralization. *Lithos* **2019**, *344–345*, 175–192. [CrossRef]

32. Ganwa, A.A.; Siebel, W.; Frisch, W.; Shang, K.C.; Ekodeck, E.G. Geochemistry and geochronology of the Meiganga metadiorite: Implication on the timing of D2 deformational phase in Adamawa-Yade Domain in Cameroon. *Int. J. Biol. Chem. Sci.* **2011**, *5*, 1754–1767. [CrossRef]
33. Tchakounte, J.N.; Eglinger, A.; Toteu, S.F.; Zeh, A.; Nkoumbou, C.; Mvondo-Ondoa, J.; Penaye, J.; Wit, M.; Barbey, P. The Adamawa-Yade domain, a piece of Archaean crust in the Neoproterozoic Central African Orogenic belt (Bafia area, Cameroon). *Precambrian Res.* **2017**, *299*, 210–229. [CrossRef]
34. Ngatcha, R.B.; Suh, C.E.; Okunlola, O.A.; Nunoo, S.; Ateh, K.I.; Elburg, M.; Hofmann, A. Crustal modeling from Pan-African granites of the Colomine Gold District, SE Cameroon: Insights from zircon U-Pb dating and Lu-Hf isotope systematic. *J. Afr. Earth Sci.* **2022**, *187*, 104441. [CrossRef]
35. Suh, C.E.; Lehmann, B.; Mafany, G.T. Geology and geochemical aspects of lode gold mineralization at Dimako-Mboscorro, SE Cameroon. *Geochem. Explor. Environ. Anal.* **2006**, *6*, 295–309. [CrossRef]
36. Asaah, A.V. Lode Gold Mineralization in the Neoproterozoic Granitoids of Batouri. Ph.D. Dissertation, Southeastern Cameroon, Technische Universität Clausthal, Clausthal-Zellerfeld, Germany, 2010; 187p.
37. Ndonfack, K.I.A.; Xie, Y.; Zhong, R.; Yomeun, B.S.; Cui, K.; Shan, X. Tectonic evolution of Neoproterozoic rocks, eastern Cameroon: Implication for gold mineralization in the Bétaré Oya and Woumbou-Colomine-Kette districts. *Precambrian Res.* **2022**, *368*, 106475. [CrossRef]
38. Tchameni, R.; Doumnang, J.C.; Deudibaye, M.; Branquet, Y. On the occurrence of gold mineralization in the Pala Neoproterozoic formations, South-Western Chad. *J. Afr. Earth Sci.* **2013**, *84*, 36–46. [CrossRef]
39. Large, R.R.; Allen, R.L.; Blake, M.D.; Herrmann, W. Hydrothermal alteration and volatile element halos for the Rosebery Klens volcanic-hosted massive sulfide deposit, western Tasmania. *Econ. Geol.* **2001**, *96*, 1055–1072. [CrossRef]
40. Salvi, S.; Amponsah, P.O.; Siebenaller, L.; Béziat, D.; Baratoux, L.; Jessell, M. Shear related gold mineralization in Northwest Ghana: The Julie deposit. *Ore Geol. Rev.* **2016**, *78*, 712–717. [CrossRef]
41. ElMonsef, M.A.; Slobodník, M.; Salem, I.A. Hydrothermal evolution of granitoid hosted gold mineralization in gidami area: An example for orogenic-gold deposits in Egypt. *J. Afr. Earth Sci.* **2018**, *146*, 132–149.
42. Frimmel, H.E. Earth's continental crustal gold endowment. *Earth Plan. Sci. Lett.* **2008**, *267*, 45–55. [CrossRef]
43. Lipson, R. The promise and perils of porphyry deposits in the future of gold production. *SEG Discov.* **2014**, *98*, 1–21. [CrossRef]
44. Melchiorre, E.B.; Henderson, J. Topographic gradients and lode gold sourcing recorded by placer gold morphology, geochemistry, and mineral inclusions in the east fork San Gabriel River, California, USA. *Ore Geol. Rev.* **2019**, *109*, 348–357. [CrossRef]
45. Hallbaer, D.K.; Utter, T. Geochemical and morphological characteristics of gold particles from recent river deposits and the fossil placer of the Witwatersrand. *Miner. Depos.* **1977**, *12*, 293–306. [CrossRef]
46. Nesbitt, H.W.; Young, G.M. Formation and diagenesis of weathering profiles. *J. Geol.* **1989**, *97*, 129–147. [CrossRef]
47. MacLean, W.H.; Kranidiotis, P. Immobile elements as monitors of mass transfer in hydrothermal alteration: Phelps Dodge massive sulfide deposit, Matagami, Quebec. *Econ. Geol.* **1987**, *82*, 951–962. [CrossRef]
48. Grant, J.A. Isocon analysis: A brief review of the method and applications. *Phys. Chem. Earth Parts A/B/C* **2005**, *30*, 997–1004. [CrossRef]
49. Rollinson, H.R. *Using Geochemical Data: Evaluation, Presentation, Interpretation*; Routledge: London, UK, 2014.
50. Fon, A.N.; Suh, C.E.; Vishiti, A.; Ngatcha, R.B.; Ngang, T.C.; Shemang, E.M.; Egbe, J.A.; Lehmann, B. Gold dispersion in tropical weathering profiles at the Belikombone gold anomaly(Bétaré Oya gold district), east Cameroon. *Geochemistry* **2021**, *81*, 125770. [CrossRef]
51. Melchiorre, E.B.; Orwin, P.M.; Reith, F.; Rea, M.A.D.; Yahn, J.; Allison, R. Biological and geochemical development of placergold deposits at Rich Hill, Arizona, USA. *Minerals* **2018**, *8*, 56. [CrossRef]
52. Ghosh, S.; Guchhait, S. Characterization and evolution of primary and secondary laterites in north western Bengal Basin, West Bengal, India. *J. Palaeogeogr.* **2015**, *4*, 203–230. [CrossRef]
53. Nzabakurikiza, A.; Onana, V.L.; ZeA, N.; Mvindi, A.T.Z.; Ekodeck, G.E. Geological, geotechnical, and mechanical characterization of lateritic gravels from Eastern Cameroon for road construction purposes. *Bull. Eng. Geol. Environ.* **2016**, *76*, 1549–1562. [CrossRef]
54. Doum, J.M.; Fuh, G.C.; Fadil-Djenabou, S.; Onana, V.L.; Ndjigui, P.D.; Armstrong-Altrin, J.S. Characterization and potential application of gley sols and feral sols for ceramic industry: A case study from Dimako (Eastern Cameroon). *Arab. J. Geosci.* **2020**, *13*, 1074. [CrossRef]
55. Dongmo, F.W.N.; Chapman, R.J.; Bolarinwa, A.T.; Yongue, R.F.; Banks, D.A.; Olajide-Kayodea, J.O. Microchemical characterization of placer gold grains from the Meyos Essabikoula area, Ntem complex, southern Cameroon. *J. Afr. Earth Sci.* **2019**, *151*, 189–201. [CrossRef]
56. Moles, N.R.; Chapman, R.J. Integration of detrital gold microchemistry, heavy mineral distribution, and sediment geochemistry to clarify regional metallogeny in glaciated terrains: Application in the Caledonides of southeast Ireland. *Econ. Geol.* **2019**, *114*, 207–232. [CrossRef]
57. Webster, J.G.; Mann, A.W. The influence of climate, geomorphology and primary geology on the supergene migration of gold and silver. *J. Geochem. Explor.* **1984**, *22*, 21–42. [CrossRef]
58. Butt, C.R.M. The development of regolith exploration geochemistry in the tropics and sub-tropics. *Ore Geol. Rev.* **2015**, *73*, 380–393. [CrossRef]

59. Freyssinet, P. Gold dispersion related to ferricrete pedogenesis in South Mali: Application to geochemical exploration. *Chron. Miner. Res. Explor.* **1993**, *510*, 25–40.
60. Reith, F.; Fairbrother, L.; Nolze, G.; Wilhelmi, O.; Clode, P.L.; Gregg, A.; Parsons, J.E.; Wakelin, S.A.; Pring, A.; Hough, R.; et al. Nano particle factories: Biofilms hold key to gold dispersion and nugget formation. *Geology* **2010**, *38*, 843–846. [CrossRef]
61. Chapman, R.J.; Leake, R.C.; Moles, N.R.; Earls, G.; Cooper, C.; Harrington, K.; Berzins, R. The application of microchemical analysis of gold grains to the understanding of complex local and regional gold mineralization: A case study in Ireland and Scotland. *Econ. Geol.* **2000**, *95*, 1753–1773.
62. Chapman, R.J.; Leake, R.C.; Moles, N.R. The use of microchemical analysis of alluvial gold grains in mineral exploration: Experiences in Britain and Ireland. *J. Geochem. Explor.* **2000**, *71*, 241–268. [CrossRef]
63. Townley, B.K.; Hérail, G.; Maksaev, V.; Palacios, C.; de Parseval, P.; Sepulveda, F.; Orellana, R.; Rivas, P.; Ulloa, C. Gold grain morphology and composition as an exploration tool: Application to gold exploration in covered areas. *Geochem. Explor. Environ. Anal.* **2003**, *3*, 29–38. [CrossRef]
64. Chapman, R.J.; Moles, N.R.; Bluemel, B.; Walshaw, R.D. Detrital gold as an indicator mineral. In *Recent Advances in Understanding Gold Deposits: From Orogeny to Alluvium*; Torvela, T., Lambert-Smith, J.S., Chapman, R.J., Eds.; Geological Society, London, Special Publications; Geological Society of London: London, UK, 2022; p. 516.
65. Chapman, R.J.; Mortensen, J.K.; Allan, M.M.; Walshaw, R.D.; Bond, J.; MacWilliam, K.A. New approach to characterizing deposit type using mineral inclusion assemblages in gold particles. *Econ. Geol.* **2022**, *117*, 361–381. [CrossRef]
66. Chapman, R.J.; Mortensen, J.K. Application of microchemical characterization of placer gold grains to exploration for epithermal gold mineralization in regions of poor exposure. *J. Geochem. Explor.* **2006**, *91*, 1–26. [CrossRef]
67. Moles, N.R.; Chapman, R.J.; Warner, R.B. The significance of copper concentrations in natural gold alloy for reconnaissance exploration and understanding gold-depositing hydrothermal systems. *Geochem. Explor. Environ. Anal.* **2013**, *13*, 115–130. [CrossRef]
68. Leal, S.; Lima, A.; Noronha, F. Characterization of heavy mineral concentrates and detrital gold particles from the Bigorne granite-hosted gold deposit in the Iberian Variscan Belt. *Geol. Soc. Lond. Spec. Publ.* **2021**, *516*, 202–217. [CrossRef]
69. Grant, A.H.; Lavin, O.P.; Nicol, I. The morphology and chemistry of transported grains as an exploration tool. *J. Geochem. Explor.* **1991**, *40*, 73–94. [CrossRef]
70. Dubé, B.; Gosselin, P. Greenstone-hosted quartz carbonate vein deposits. In *Mineral Deposits of Canada: A Synthesis of Major Deposit-Types, District Metallogeny, the Evolution of Geological Provinces, and Exploration Methods*; Good fellow, W.D., Ed.; Geological Association of Canada, Mineral Deposits Division, Special Publication; Geological Association of Canada: St. John's, NL, Canada, 2007; Volume 5, pp. 49–73.
71. Lange, I.M.; Gignoux, T. Distribution, characteristics, and genesis of high fineness gold placers, Nine mile Valley, Central-Western Montana. *Econ. Geol.* **1999**, *94*, 375–386. [CrossRef]
72. Goldfarb, R.J.; Pitcairn, I. Orogenic gold: Is a genetic association with magmatism realistic? *Miner. Depost.* **2023**, *58*, 5–35. [CrossRef]
73. Elisabeth Sylvie, N.M.; Ekoa Bessa, A.Z.; Ayissi Mbomo, R.E.; Akono, J.V.; Dairou, B.; Pierre, K. Evaluation of surface water contamination and its impacts on health in the mining districts of Kambélé and Bétaré-Oya (Eastern-Cameroon). *Heliyon* **2024**, *10*, 29189. [CrossRef] [PubMed]
74. Hylander, L.D.; Meili, M. 500 years of mercury production: Global annual inventory by region until 2000 and associate demissions. *Sci. Total Environ.* **2003**, *304*, 13–27. [CrossRef]
75. *UNEP Reducing Mercury Use in Artisanal and Small Scale*; United Nations Environmental Program, United Nations: New York, NY, USA, 2012; p. 76.
76. Sousa, R.; Veiga, V.; Zyl, V.D.; Telmer, K.; Spiegel, S.; Selder, J. Policies and regulations for Brazil's artisanal gold mining sector: Analysis and recommendations. *J. Clean Prod.* **2011**, *19*, 742–750. [CrossRef]
77. Clifford, M.J. Future strategies for tackling mercury pollution in artisanal gold mining sector: Making the Minamata convention work. *Futures* **2014**, *62*, 106–112. [CrossRef]
78. Melchiorre, E.B.; Mathur, R.; Kamenov, G.; Paredes, J. Geochemical Overprinting and Secondary Placer Crystal Formation in the La Cholla District, Quartzsite, Arizona, USA: Evidence from Copper Isotopes, Morphology, and Trace Elements. *Minerals* **2023**, *13*, 1444. [CrossRef]
79. Butt, C.R.M.; Lintern, M.; Anand, R.R. Evolution of regoliths and landscapes in deeply weathered terrain—Implications for geochemical exploration. *Ore Geol. Rev.* **2000**, *16*, 167–183. [CrossRef]
80. Sawadogo, B.; Bamba, O.; Chardon, D. Landform-regolith mapping in the West African context. *Ore Geol. Rev.* **2020**, *126*, 103782. [CrossRef]
81. Sunkari, E.D.; Appiah-Twum, M.; Lermi, A. Spatial distribution and trace element geochemistry of laterites in Kunche area: Implication for gold exploration targets in NW, Ghana. *J. Afr. Earth Sci.* **2019**, *158*, 103519. [CrossRef]

Disclaimer/Publisher's Note: The statements, opinions and data contained in all publications are solely those of the individual author(s) and contributor(s) and not of MDPI and/or the editor(s). MDPI and/or the editor(s) disclaim responsibility for any injury to people or property resulting from any ideas, methods, instructions or products referred to in the content.

minerals

MDPI

Article

Evolution of the Ore-Bearing Fluid of Alin Sb–Au Orebodies in Shuixie Cu–Co Orefield, SW China: Constraints on the Rare Earth Element and Trace Element Components of Auriferous Pyrite and Host Rock

Guo Li [1], Shanshan Ru [1,2,*], Chuandong Xue [1,*] and Wei Wang [1]

[1] Department of Earth Sciences, Kunming University of Science and Technology, Kunming 650093, China; liguo@stu.kust.edu.cn (G.L.); 20191101001@stu.kust.edu.cn (W.W.)
[2] City College, Kunming University of Science and Technology, Kunming 650093, China
* Correspondence: 20140045@kust.edu.cn (S.R.); xuechuandong@kust.edu.cn (C.X.)

Abstract: The Shuixie Cu–Co polymetallic orefield, located in western Yunnan Province (southeastern margin of the Qinghai–Tibet Plateau), is renowned for its Cu–Co mineralization. A recent resource reassessment identified Sb–Au and Cu–Co–Bi (Sb–Au) orebodies as genetically associated with primary Cu–Co mineralization. The mineralization characteristics and microscopic observations indicate that gold mineralization in the Sb–Au orebodies follow a pulsating fluid injection model. The model includes four pulses: (1) euhedral gold-poor pyrite (PyI_1) precipitation; (2) margin-parallel growth of gold-rich pyrite (PyI_2) on PyI_1; (3) continued growth of gold-rich pyrite (PyI_3) along PyI_2; and (4) outermost concentric gold-rich pyrite (PyI_4) formation. This study examined gold-bearing pyrite in orebodies and host rocks. In situ laser ablation inductively coupled plasma mass spectrometry (LA–ICP–MS) analysis of pyrite and inductively coupled plasma mass spectrometry (ICP–MS) whole-rock trace element analysis were conducted to track the ore-forming fluid evolution. Compared with CI chondrite, pyrites from all pulses were enriched in LREEs over HREEs. The pyrite REE distribution curves exhibited right-skewed patterns, reflecting LREE enrichment. The Hf/Sm, Nb/La, and Th/La ratios were generally below 1, indicating high-field-strength element depletion. These results suggest a Cl-rich, F-poor ore-forming fluid. The pyrite trace elements showed enrichment in the chalcophile elements (e.g., Cu and Pb) and exceptionally high Bi levels compared with the continental crust. The chalcophile elements (e.g., Zn and Cd) were depleted, whereas iron-group elements (e.g., Co) were enriched and Ni was depleted. The pyrite δCe values (0.87–1.28, mean = 1.01) showed weak anomalies, indicating a reducing ore-forming environment. The δEu values of pyrite during pulses 1 to 4 ranged widely, from 0.2–3.01 (mean of 1.17), 0.27–1.39 (0.6), and 0.41–1.40 (0.96) to 0.4–1.36 (0.84), respectively, suggesting an initial temperature decline and subsequent increase in the ore-forming fluid. Significant variations were found in the Y/Ho, Zr/Hf, and Nb/Ta ratios across pulses, indicating the potential involvement of high-temperature hydrothermal fluids or late-stage alteration during ore formation. The Y/Ho ratio of pyrite overlapped most closely with that of the continental crust of China, indicating a close relationship between the ore-forming fluids and the crust.

Keywords: Au-bearing pyrite; REE; trace element; ore field; Sb–Au orebodies; Lanping Basin

1. Introduction

The Sanjiang Composite Orogenic Belt (SCOB), located on the southeastern edge of the Tibetan Plateau, is a key part of the global Tethyan metallogenic domain. Its Cenozoic tectonic–magmatic activities and polymetallic mineralization have long been a focus of international mineral deposit studies [1–3] (Figure 1). The Lanping Basin, a mid-Cenozoic intracontinental strike–slip basin in the southern segment of the orogenic belt, records the distant effects of the India–Eurasia plate collision. Additionally, its complex hydrothermal mineralization system has produced polymetallic resources, including copper, lead, zinc, antimony, and gold, making it a natural laboratory for exploring the metallogenic mechanisms of continental collision zones [1,3]. The recent discovery of the Alin gold deposit in the western part of the basin revealed the potential for the superposition of orogenic gold deposits and shallow low-temperature hydrothermal systems. This provides a key case for understanding the metallogenic diversity along the eastern Tethyan margin [4,5]. Despite extensive global research on orogenic gold deposits (e.g., craton greenstone belts) and shallow, low-temperature hydrothermal systems (e.g., the circum-Pacific belt), the coupling mechanisms between the two in intraplate strike–slip environments remain controversial [6]. The morphology, crystal features, and trace element content of pyrite are closely linked to the physicochemical properties of ore-forming fluids including sulfur fugacity, temperature, and cooling rate [7–10]. Hydrothermal pyrite, a direct sample for studying mineralization fluids, reflects the properties of ore-forming fluids and their material sources through its REE distribution, trace element content, and ratios [11–14].

The uniqueness of the Alin gold deposit lies in the unclear source of the mineralizing fluid. Existing isotopic data only preliminarily suggest the involvement of magma fluids [5], but lack quantitative constraints on crust–mantle interactions. The mechanism of element occurrence is unclear. As the primary gold-bearing mineral, pyrite's rare earth element (REE) distribution pattern and trace element ratios have not yet been revealed in terms of their role in fluid evolution. This study used micro-region in situ analytical techniques to systematically analyze the distribution patterns of REE and trace element combinations in pyrite from the Alin gold deposit. The aims were to (1) reveal the material sources and evolution of metallogenic fluids, filling the geochemical gap in fluid studies in the western margin of the Lanping Basin, and (2) establish the coupling relationships between REEs and elements such as Au, As, and Sb, providing new evidence for understanding the extraordinary element enrichment mechanism in collision-zone gold deposits.

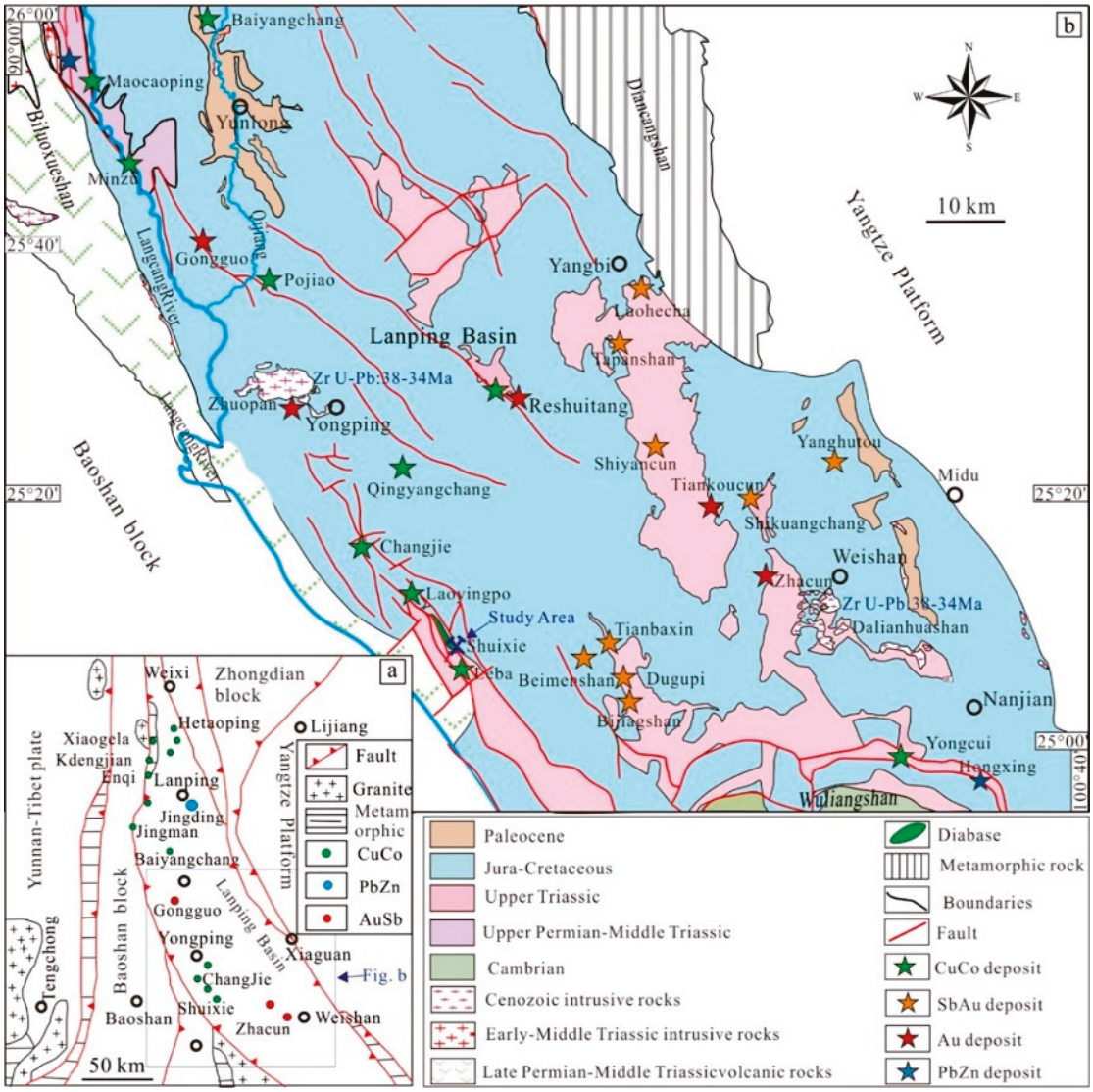


Figure 1. Regional tectonic map (**a**) (modified from [15]) and simplified geological map (**b**) (modified from [15,16]) of the Yongping–Weishan Cu–Co–Au–Sb metallogenic belt in western Yunnan Province, SE Xizang–Qinghai Plateau.

2. Geological Setting

2.1. Regional Geological Background

The Shuixie Cu–Co polymetallic orefield is situated at the southwestern edge of the Meso–Cenozoic Lanping Basin, on the southeastern Xizang–Qinghai Plateau. It is an important part of the Sanjiang Composite Orogenic Belt (SCOB) (Figure 1a). The tectonic framework of the Lanping Basin is shaped by the Baoshan–Tengchong Block to the west, the Yangtze Platform to the east, and the Meso–Cenozoic Simao Basin to the south. Permian to Cretaceous sedimentary strata are exposed within and along the margins of the basin (Figure 1b). Geological surveys have shown that the SCOB, including the Lanping Basin, evolved through several phases: the Paleo–Tethys continental marginal arc basin, the Neo–Tethys back-arc foreland basin, and the ongoing Cenozoic intracontinental collisional belt between the Indian and Eurasian continents. These processes led to the widespread development of Triassic arc magmatic belts, Mesozoic red-bed basins, and Eocene to Oligocene alkali-rich porphyry belts [1–3,15–17]. These processes are associated with tectonic, sedimentary, metamorphic, and magmatic activities, creating a distinct polymetallic metallogenic zone.

The Yongping–Weishan Cu–Co–Sb–Au polymetallic mineralization belt lies in the southwest of the Lanping Basin and is rich in Cu, Co, Sb, Au, and associated minerals such as siderite, barite, and fluorite (Figure 1b). Notable deposits include the Baiyangchang Cu–Ag–Pb–Zn deposit in Yunlong County, the Gongguo Cu–Co–Au, Reshuitang Cu–Au–Pb–Zn, Qingyangchang and Changjie Cu–Co–Ag, and Laoyingpo and Shuixie Cu–Co–Au deposits in Yongping County, and the Tianbaxin–Bijianshan–Dugupi Sb–fluorite and Zhacun Au–Sb–Pb–Zn deposits in Weishan County (Figure 1b). Himalayan–aged (38–34 Ma) potassic intrusive bodies are associated with hornfels development in the surrounding sandy siltstones and small-scale Cu–Pb–Zn–Au polymetallic mineralization at the Zhuopan pluton in Yongping County, Lianhuashan and Gejiumu plutons in Weishan County, and Guduo and Jiedingshan plutons in Midu County (Figure 1b).

The Shuixie orefield is part of the Yongping–Weishan region, a prospective area for gold, copper, cobalt, antimony, mercury, arsenic, iron, and rare earth elements. Over more than fifty years of geological exploration, more than ten medium-to small-sized Cu–Co and Cu deposits have been discovered including the Shuixie Jie, Xiaotuanshan, Caiyuanzi, Shangbielie, Qingtian, Zhifanghe, and Alin deposits [4,5].

2.2. Deposit Geology

The Alin deposit lies on the eastern flank of the Alin anticline. The deposit contains outcrops of the Upper Triassic Maichuqing Formation (T_3m), Lower Jurassic Yangjiang Formation (J_1y), and Middle Jurassic Huakaizuo Formation (J_2h) (Figure 2). A detailed stratigraphic description is provided in Figure 2. The main faults in the area are F_1, F_2, F_3, F_4, F_5, and F_6. Of these, F_2 and F_4 are NNE-trending, F_1 is NNW-trending, and F_3 is EW-trending. F_1 is the primary controlling fault of the Alin deposit, with a total length of 1.7 km, and is a reverse fault. F_2, the second largest fault after F_1, also controls mineralization in the area. It is displaced by F_3 in the northern part and has a total length of 1.8 km. F_3 is a right–lateral reverse fault, 2.9 km long, extending from Mingcaoshan in the west to beyond the mining area in the east [18]. No igneous rock outcrops are observed. The Alin anticline is the largest fault-derived structure in the mining area. It is a tilted syncline, with its hinge rising toward the southwest and extending near the western side of the Alin mineralization belt. The Alin syncline lies southeast of the Alin anticline, roughly parallel to it. Gold is currently mainly mined from the 1760 and 1700 tunnels at the Alin deposit. The orebodies occur in vein-like and layered forms, primarily in the T_3m, which consists of grayish-white feldspar-quartz sandstone and gray-black to black carbonaceous mudstone in fault breccia zones. It also occurs in the J_2h and J_1y, containing purple to purplish-red, dark medium-grained sandstone, quartz sandstone, and feldspar-quartz sandstone. The mineralized breccia consists mainly of feldspar-quartz sandstone fragments and fault clay (Figure 3). The thickness of the orebodies ranges from 6 to 11.98 m, with a length of up to 130 m. The ore exhibits dense, massive, banded, impregnated, vein-like, networked, and breccia structures, with euhedral, subhedral, and anhedral grains as well as textures of replacement, dissolution, and cataclasis (Figure 3). The gold (Au) grade ranges from 0.26 to 36.35 g/t, with a maximum of 120.0 g/t and an average of 4.02 g/t [18]. This study focused on the Sb–Au orebodies in the 1700-, 1715-, and 1760-level tunnels (Figure 3). The main metal minerals are pyrite, arsenopyrite, stibnite, sphalerite, and trace chalcopyrite. The gangue minerals are primarily barite, rhodochrosite, dolomite, calcite, quartz, feldspar, and biotite (Figure 4). Secondary minerals include limonite and azurite.

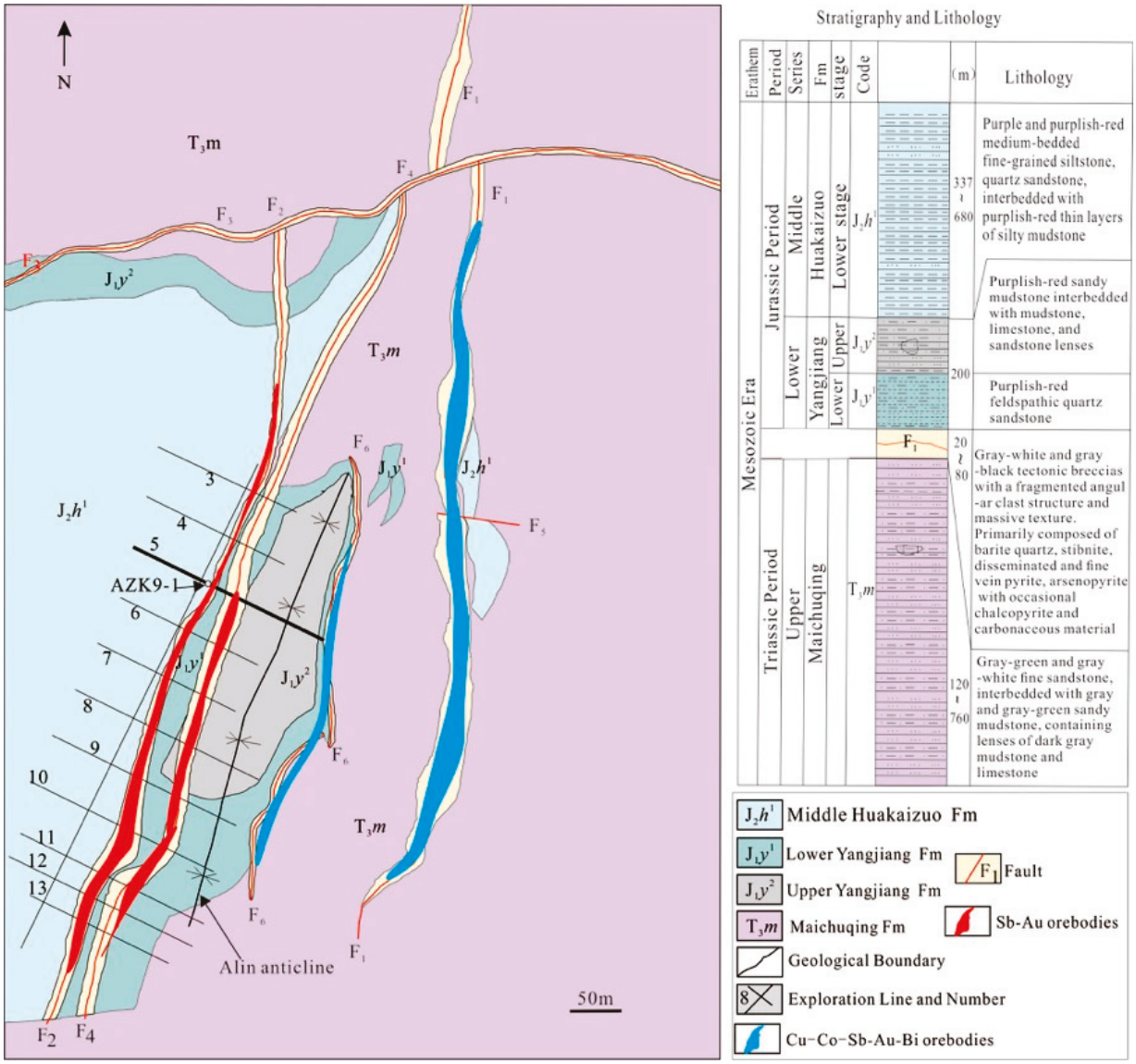


Figure 2. Geological map of the Cu–Co–Au–Sb mineralized district in Yongping Changjie–Shuixie (modified from [5,18]). Abbreviation: Fr—Formation.

The Shuixie Alin Sb−Au orebodies follow a pulsating fluid injection model, based on field geological observations, petrographic identification, and BSE morphology analysis. The mineralization consists of five pulses, four of which exhibit gold mineralization, characterized by alternating precipitation of pyrite and arsenopyrite: (I) pulses 1, with barite (minor)–pyrite–arsenopyrite; (II) pulses 1, with pyrite—arsenopyrite; (III) pulse 3, with pyrite–arsenopyrite– stibnite (minor); (IV) pulse 4, with pyrite–arsenopyrite–quartz; and (V) pulse 5, characterized by a large amount of stibnite [5].

During pulse 1, barite (trace), pyrite (PyI_1), and arsenopyrite ($ApyI_1$) are precipitated, with weak gold mineralization. Arsenopyrite and pyrite in the host rock occur as euhedral−subhedral crystals (Figure 4c–e). In the orebodies, they predominantly appear as subhedral crystals, often with a pyrite ring–core structure (Figure 4f–j). During pulse 2, pyrite (PyI_2) and arsenopyrite ($ApyI_2$) crystallize, showing stronger gold mineralization. Without arsenopyrite and pyrite crystals from this pulse can be observed in the host rock. In the orebodies, pyrite mainly appears as euhedral or fragmented crystals, growing along arsenopyrite ($ApyI_2$) and forming the primary ring in a ring−core pyrite structure (Figure 4f,h–j). Pulse 3 precipitates pyrite (PyI_3), arsenopyrite ($ApyI_3$), and stibnite (trace),

with the strongest gold mineralization. These pyrites are identified only in the orebodies, mainly as euhedral pyrite, cut or intergrown with arsenopyrite (Figure 4f and g), forming secondary rings in a ring–core pyrite structure (Figure 4h–j). The final pulse of gold mineralization (IV) consists of pyrite (PyI_4), arsenopyrite ($ApyI_4$), and quartz, with relatively strong mineralization. They mainly occur as the outermost rings of the ring–core structure, with crystal forms similar to those of pulses 2 and 3 (Figure 4h–j). For further details on the ore mineral features, see Li et al. [5].

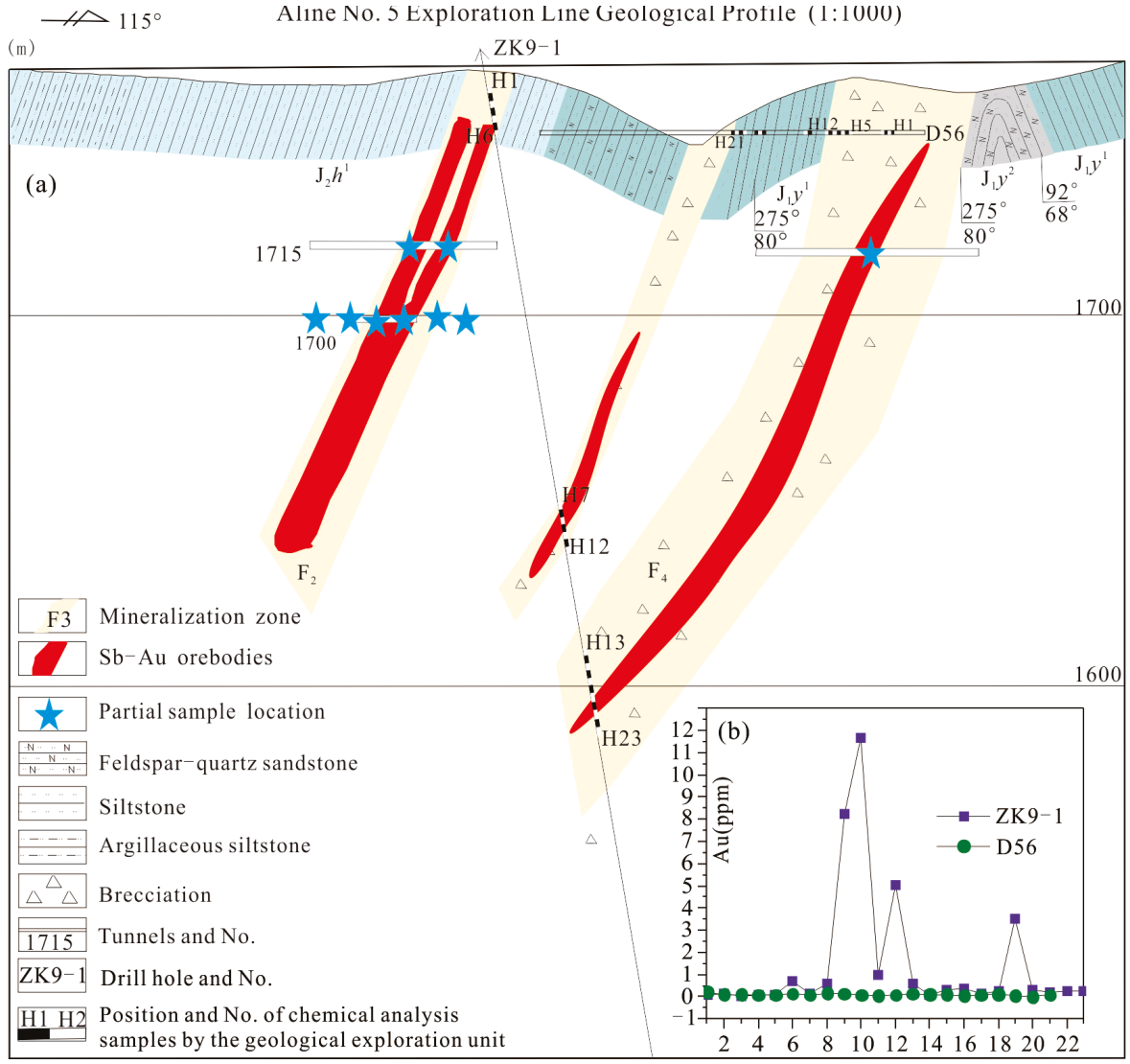


Figure 3. (**a**) Representative exploration profile of the Alin deposit [18]. (**b**) The exploration unit tested the gold (Au) grade of the samples [18].

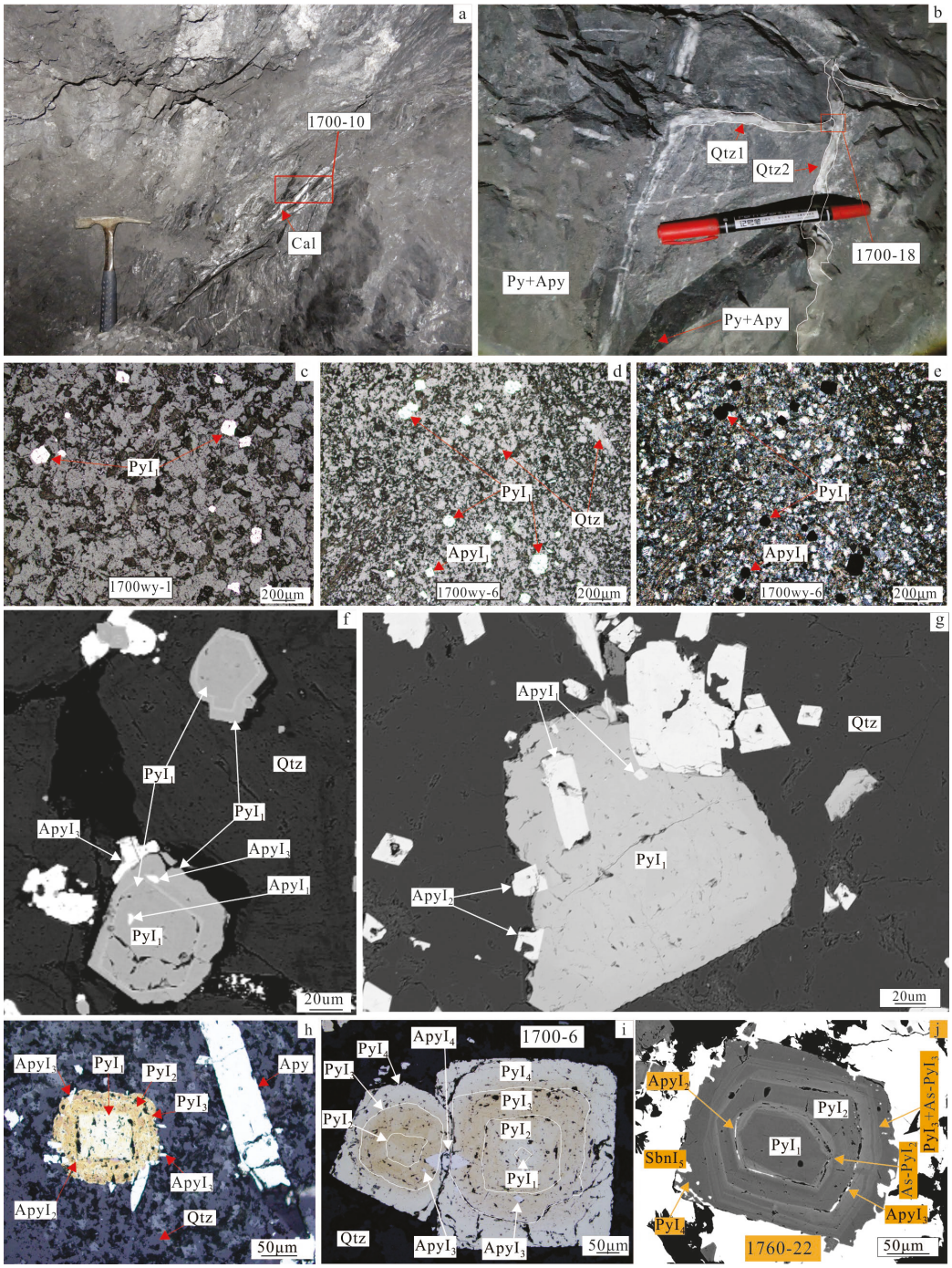


Figure 4. Photographs of the mineral assemblage of the Sb–Au orebodies (**i**,**j**) (from [5]). (**a**,**b**) Orebodies and sampling location corresponding to the sketch map, showing strong barite and stibnite mineralization; (**c**–**e**) Euhedral PyI_1 and $ApyI_1$ grains in a quartz matrix within the country rock; (**f**,**g**) Fine euhedral–subhedral arsenopyrite ($ApyI_1$) as mineral inclusions in subhedral pyrite (PyI_1); (**h**) Level III secondary proliferative ring–core structure, formed subhedral PyI_1 overgrown by a subhedral rim of pyrite PyI_2, PyI_2 overgrown by a subhedral ring of pyrite (PyI_3), and arsenopyrite ($ApyI_2$) as mineral inclusions in pyrite (PyI_2); (**i**) Level IV secondary proliferative ring–core structure euhedral PyI_1 overgrown by a euhedral–subhedral rim of PyI_2 and PyI_3, $ApyI_3$ as mineral inclusions in PyI_3, and PyI_3 overgrown by a euhedral ring of PyI_4; (**j**) Irregular PyI_3 wrapping fine $ApyI_3$ cut by long columnar $ApyI_4$, forming a quaternary proliferative ring structure composed of PyI_4, $ApyI_4$, and $SbnI_5$; Abbreviations: Apy = arsenopyrite; As − Py = pyrite with high arsenic content; Py = pyrite; Qtz = quartz; Sbn = stibnite; PyI_1–PyI_4 = pyrite during pulses 1–4, respectively; $ApyI_1$–$ApyI_4$ = arsenopyrite during pulses 1–4, respectively.

3. Sample and Analytical Methods

The samples from the Alin Sb–Au orebodies in this study were collected during the horizontal mining stage. Systematic samples from both the orebodies and host rock were collected. The samples were taken from the 1700 tunnel. All samples were cut into thin sections for microscopic observation and backscattered electron (BSE) imaging. The pyrite mineralization stages in different samples were divided into pulses. Each pulse of pyrite was delineated with an oil-based pen, followed by microscopic photography. Finally, in situ LA–ICP–MS analysis was conducted. The host rock samples were ground and analyzed for whole-rock trace elements and REEs.

3.1. LA-ICP-MS Analysis

The trace element analysis of pyrite was conducted by LA–ICP–MS at Sample Solution Analytical Technology Co. Ltd., Wuhan, China. Detailed operating conditions for the laser ablation system and the ICP–MS instrument and data reduction were the same as described by [19]. Laser sampling was performed using a GeolasPro laser ablation system that consisted of a COMPexPro 102 ArF excimer laser (wavelength of 193 nm and maximum energy of 200 mJ) and a MicroLas optical system. An Agilent 7700e ICP–MS instrument was used to acquire ion-signal intensities. Helium was applied as a carrier gas. Argon was used as the make-up gas and mixed with the carrier gas via a T-connector before entering the ICP. A "wire" signal smoothing device is included in this laser ablation system [20]. The spot size and frequency of the laser were set to 32 μm and 5 Hz, respectively. The trace element compositions of the sulfides were calibrated against various reference materials (NIST 610 and NIST 612) without using an internal standard [21]. The sulfide reference material of MASS–1 (USGS) was used as the unknown sample to verify the accuracy of the calibration method. Each analysis incorporated a background acquisition of approximately 20–30 s, followed by 50 s of data acquisition from the sample. An Excel–based software ICPMSDataCal 11.8 was used to perform offline selection and integration of the background and analyzed signals, time-drift correction, and quantitative calibration for trace element analysis [21].

3.2. Trace Element Analysis of Whole Rock

Trace element analysis of the whole rocks was conducted on an Agilent 7700e ICP–MS at Wuhan Sample Solution Analytical Technology Co. Ltd., Wuhan, China. The detailed sample-digesting procedure was as follows: (1) Sample powders (200 mesh) were placed in an oven at 105 °C and dried for 12 h; (2) 50 mg of the sample powder was accurately weighed and placed in a Teflon bomb; (3) 1 mL of HNO_3 and 1 mL of HF were slowly added into the Teflon bomb; (4) the Teflon bomb was put into a stainless steel pressure jacket and heated to 190 °C in an oven for >24 h; (5) after cooling, the Teflon bomb was opened, placed on a hotplate at 140 °C, and evaporated to incipient dryness, then, 1 mL of HNO_3 was added and evaporated to dryness again; (6) 1 mL of HNO_3, 1 mL of MQ water, and 1 mL of 1 ppm internal standard solution In were added, and the Teflon bomb was resealed and placed in the oven at 190 °C for >12 h; and (7) the final solution was transferred to a polyethylene bottle and diluted to 100 g via the addition of 2% HNO3.

4. Results

4.1. Rare Earth Elements

The in situ rare earth element (REE) results for pyrite and the host rock are presented in Table S1. The measured results were standardized using the CI chondrite standard [22], as illustrated in Figure 5. Significant differences in the REE geochemical characteristics were observed between the pyrite of each pulse and the host rocks. (I) The ΣREE content

of the host rocks ranged from 260.26 × 10^{-6} to 773.11 × 10^{-6}, with an LREE/HREE ratio of 2.92 to 3.85, indicating LREE enrichment. The $(La/Yb)_N$ values ranged from 8.14 to 11.36, $(La/Lu)_N$ from 8.19 to 10.92, and $(Ce/Yb)_N$ from 5.84 to 8.47. The LREE−HREE fractionation was minimal, with $(La/Sm)_N$ values ranging from 3.43 to 4.05, and (Gd/Yb)N from 1.47 to 1.80. The LREEs exhibited slightly more differentiation than the HREEs. The δEu values ranged from 0.68 to 0.82, with an average of 0.73, and the δCe values ranged from 0.92 to 1.00, with an average of 0.96 (Figure 5e, Table S1). (II) For pulse 1 pyrite, the ΣREE content ranged from 4.49 × 10^{-6} to 21.48 × 10^{-6} with an LREE/HREE ratio of 0.96 to 3.54, indicating LREE enrichment. The $(La/Yb)_N$ values ranged from 3.36 to 121.21, $(La/Lu)_N$ from 1 to 43.62, and $(Ce/Yb)_N$ from 1.85 to 91.12. A significant LREE−HREE fractionation was observed, with $(La/Sm)_N$ between 0.52 and 4.29, and $(Gd/Yb)_N$ between 1.12 and 15.71. The LREEs exhibited less differentiation than the HREEs. The δEu values ranged from 0.20 to 3.01, with an average of 1.17, and the δCe values ranged from 0.69 to 1.10, with an average of 0.99 (Figure 5a, Table S1). (III) For pulse 2 pyrite, the ΣREE range was 7.8 × 10^{-6}~57.94 × 10^{-6}. Compared with pulse 1, both the ΣREE content and range increased. The LREE/HREE ratio ranged from 0.87 to 6.73, with the LREEs generally being more enriched. The $(La/Yb)_N$ value ranged from 1.46 to 28.53, $(La/Lu)_N$ from 1.15 to 23.85, and $(Ce/Yb)_N$ from 0.39 to 23.21. A large fractionation between the LREEs and HREEs was observed, with $(La/Sm)_N$ values between 2.15 and 4.25, and $(Gd/Yb)_N$ between 0.15 and 4.91. The variation in the LREEs was smaller than in the HREEs. The δEu value ranged from 0.27 to 1.39, with an average of 0.60, and the δCe value ranged from 0.35 to 1.52, with an average of 0.99 (Figure 5, Table S1). (IV) For pulse 3 pyrite, the ΣREE content ranged from 18.77 × 10^{-6} to 84.40 × 10^{-6}. Compared with pulse 2, both the ΣREE content and range increased. The LREE/HREE ratio ranged from 1.7 to 5.55, with the LREEs being more enriched. The $(La/Yb)_N$ value ranged from 3.0 to 16.55, $(La/Lu)_N$ from 2.83 to 14.51, and (Ce/Yb)N from 2.83 to 14.51. A significant fractionation between the LREEs and HREEs was observed, with (La/Sm)N values ranging from 1.92 to 5.85 and (Gd/Yb)N from 0.46 to 1.42. The variation in LREEs was greater than that in HREEs. The δEu value ranged from 0.41 to 1.40, with an average of 0.96, and the δCe value ranged from 0.85 to 1.72, with an average of 1.28 (Figure 5c, Table S1). (V) For pulse 4 pyrite, the ΣREE content ranged from 3.19 × 10^{-6} to 54.79 × 10^{-6}. Compared with pulse 3, both the ΣREE content and ranges decreased. The LREE/HREE ratio ranged from 1.65 to 6.22, with the LREEs being more enriched. The $(La/Yb)_N$ value ranged from 2.22 to 17.59, $(La/Lu)_N$ from 2.25 to 9.75, and $(Ce/Yb)_N$ from 2.35 to 12.59. Significant fractionation between the LREEs and HREEs was observed, with (La/Sm)N values ranging from 2.18 to 4.08 and (Gd/Yb)N from 0.45 to 1.19. The variation in LREEs was greater than that in the HREEs. The δEu value ranged from 0.40 to 1.36, with an average of 0.84, and the δCe value ranged from 0.79 to 1.49, with an average of 1.13 (Figure 5d, Table S1).

4.2. Trace Elements

The trace element concentrations are presented in Table S1. The results were standardized using the continental crust standard [23], as shown in Figure 6. The trace elements were classified into iron-group elements (V, Cr, Co, and Ni), rare elements (Li, Sc, Y, Zr, Nb, Hf, etc.), radioactive elements (Th and U), tungsten–molybdenum group elements (Mo and W), and sulfur-loving elements (Cu, Zn, Cd, Tl, Pb, etc.) according to Zawaritsky's scheme [24,25]. The iron-group elements in pyrite varied significantly from pulse 1 to 4. V and Cr were depleted at all stages, with depletion being smaller during pulses 1 to 3 compared with pulse 4. Co and Ni were enriched in all pulses, particularly in pulse 1. However, Co was depleted at some points in pulses 1, 2, and 3, while Ni was mostly depleted in pulses 3 and 4. The Co/Ni ratio ranged from 0.18 to 30.35 across all pulses,

with nearly half of the data points below 1, and 20 out of 27 points below 5. The rare element concentrations in pyrite were depleted in all pulses. The radioactive elements in pyrite were generally depleted across all pulses. The tungsten–molybdenum group elements exhibited significant variation in all pulses. Mo was depleted, while W was enriched in all pulses, with the enrichment factors (K) mostly greater than 1. Chalcophile elements were the primary ore-forming elements. Cu and Pb were enriched in all pulses, with enrichment factors (K) typically between 1 and 10. Tl was depleted in pulse 1 but enriched in the other pulses, whereas Zn and Cd were depleted across all pulses. The iron-group elements in the host rocks showed little variation across the orebodies. V, Cr, Co, and Ni were depleted in both the upper and lower parts, but their concentrations were similar to those of the continental crust standard. The rare element concentrations showed minor depletion, similar to those of the iron-group elements. The radioactive elements were generally enriched, with the enrichment factors (K) just above 1. Due to experimental limitations, the tungsten–molybdenum group elements (Mo and W) were not tested in the host rocks. The enrichment–depletion characteristics of the chalcophile elements (Cu, Pb, Tl, Zn, and Cd) were similar to those observed in pyrite. Notably, Bi exhibited extraordinary enrichment in both the surrounding rocks and pulses, with their enrichment factors (K) ranging from 10 to 100, and even exceeding 100.

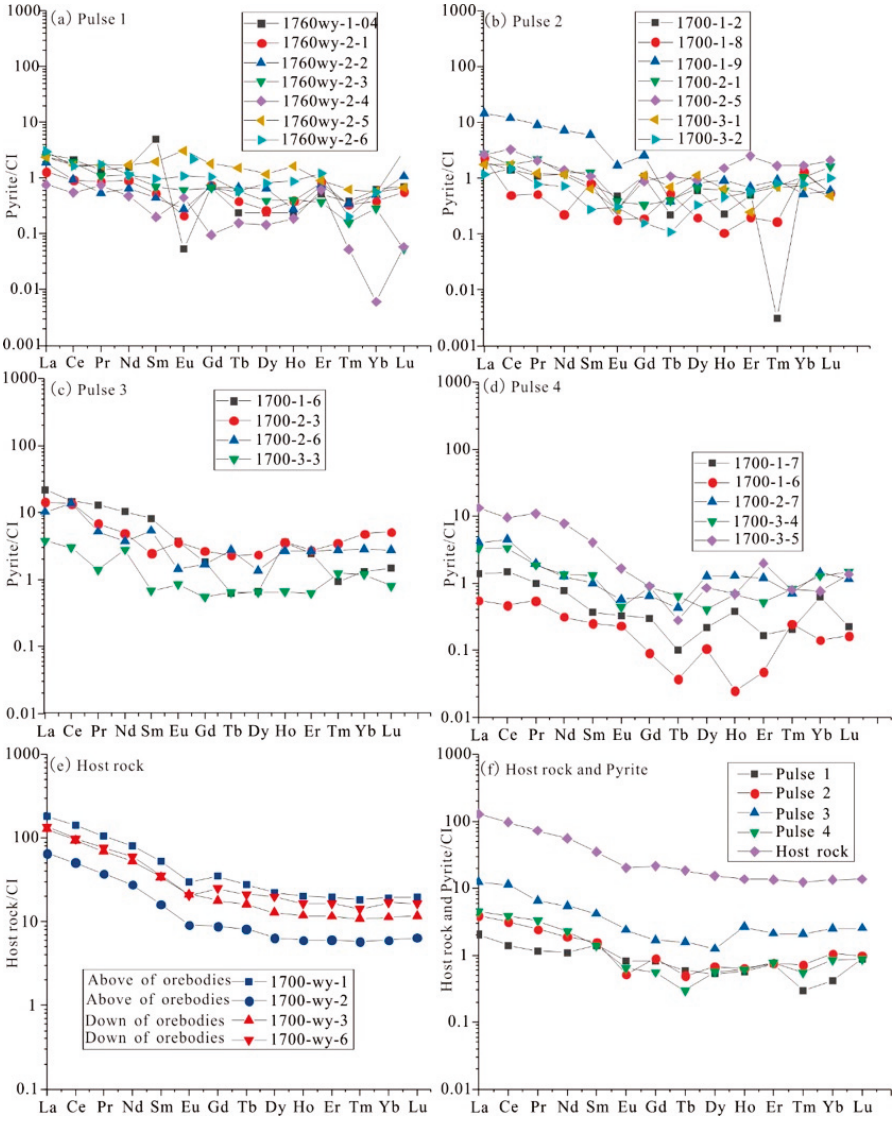


Figure 5. CI chondrite-normalized REE patterns of pyrite (normalization values after [22]).

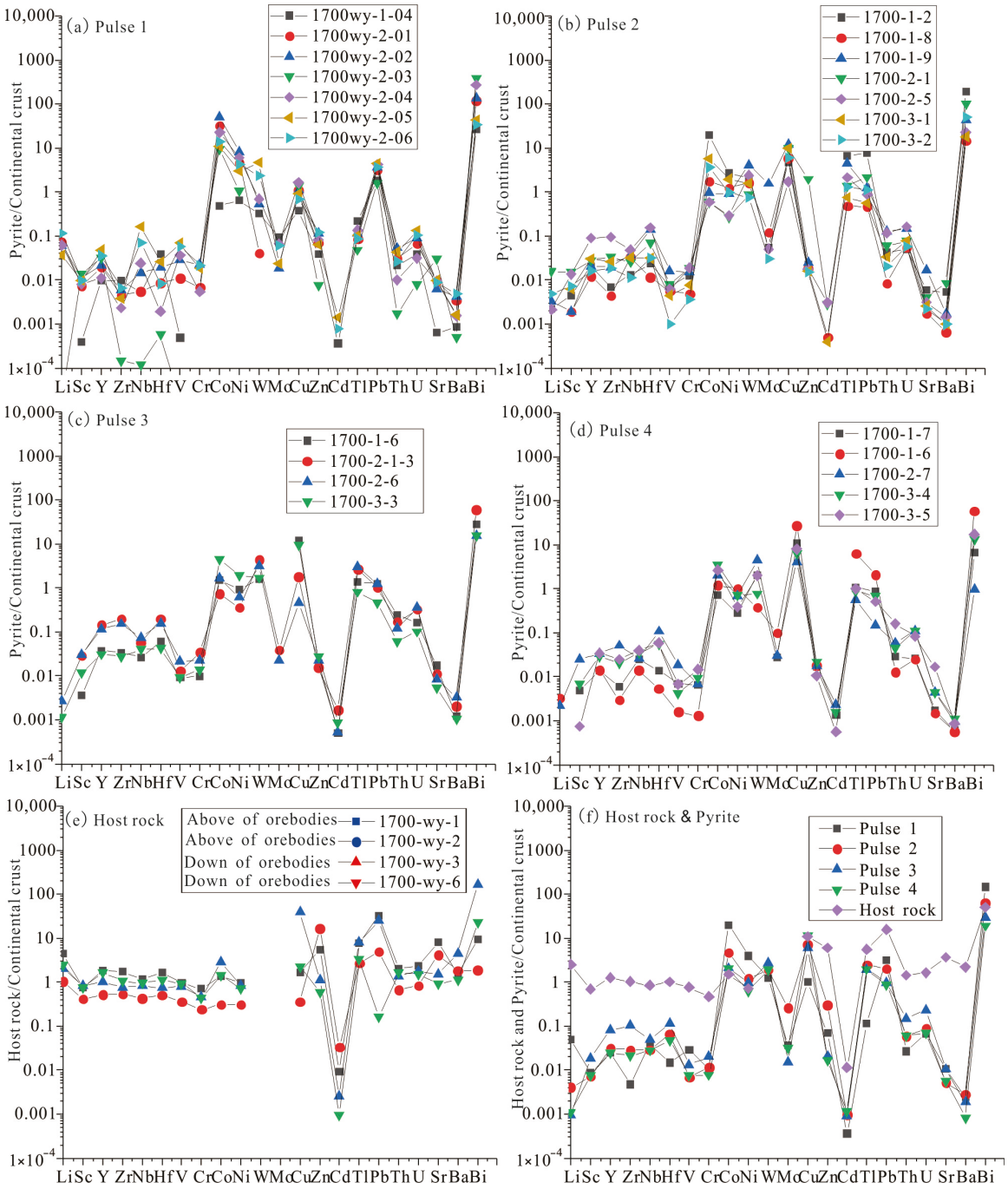


Figure 6. Continental crust-normalized trace element patterns of pyrite (normalization values based on [23]).

5. Discussion

5.1. The Composition of Ore-Forming Fluid

The average rare earth element (REE) content of each pulse of pyrite is shown in Figure 7. The average ΣREE content increased from pulse 1 (12.78×10^{-6}) to pulse 2 (19.63×10^{-6}), peaked at pulse 3 (58.59×10^{-6}), and then decreased at pulse 4 (21.03×10^{-6}). Both individual data points and average values indicated that the ΣREE content was much lower than the host rock's average (528.21×10^{-6}). All pyrite pulses showed enrichment of the LREEs over HREEs, with varying degrees of LREE-HREE fractionation. For instance, pulse 1 exhibited a large fractionation between the LREEs and HREEs, with smaller variation within the LREEs compared with that within the HREEs. In

contrast, pulse 3 showed a greater fractionation between the LREEs and HREEs, with more variation within the LREEs than within the HREEs, likely due to temperature changes that alter the physicochemical properties of the hydrothermal fluids or the influence of external fluids. Our arsenopyrite As atom data indicated average precipitation temperatures of 240 °C, 220 °C, 235 °C, and 230 °C for pulses 1 to 4, respectively [5]. This is consistent with previous temperature measurements (142–230 °C) of quartz fluid inclusions from the Shuixie deposit [24]. The average ΣREE content in the host rock (528.21×10^{-6}) showed a greater enrichment of the LREEs, with a small LREE-HREE fractionation and slightly more variation within the LREEs than in the HREEs.

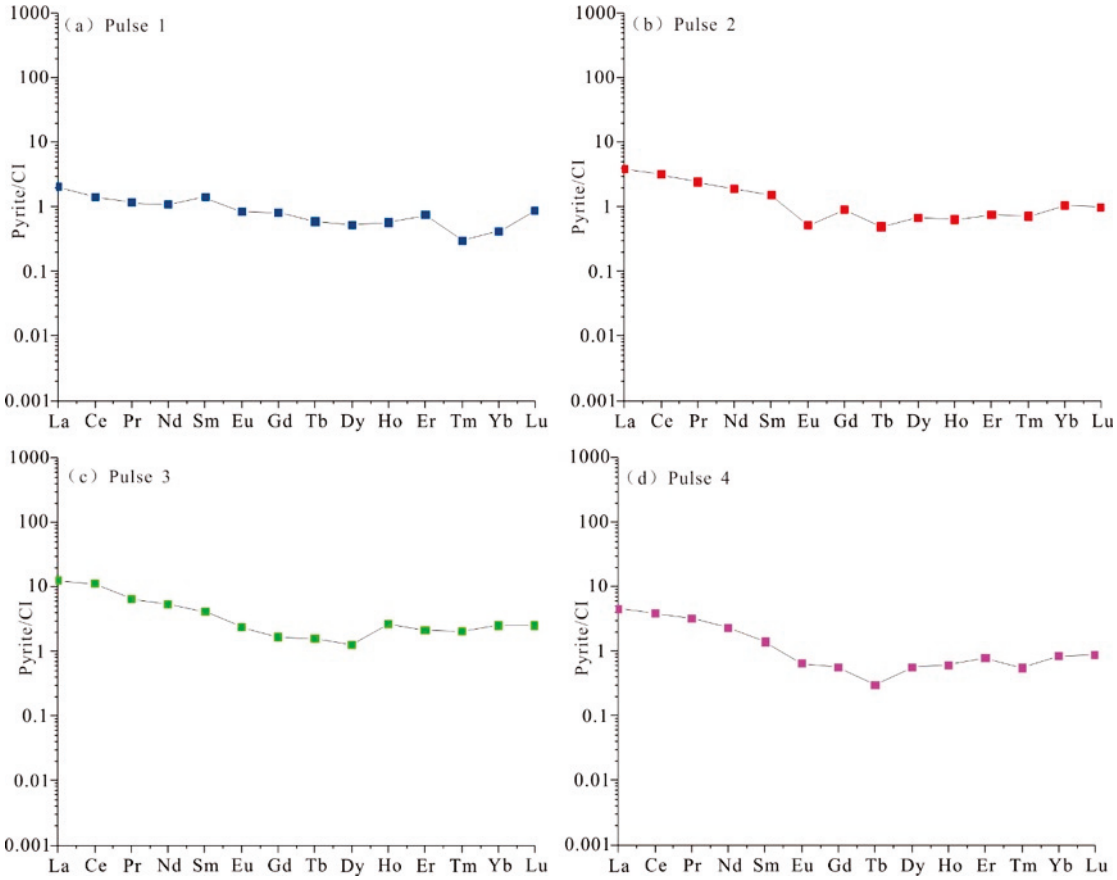


Figure 7. Average continental crust-normalized trace element patterns of pyrite (normalization values based on [23]).

Previous studies have shown that REE ions can form complexes with ions such as carbonate (CO_3^{2-}), chloride (Cl^-), fluoride (F^-), nitrate (NO_3^-), and sulfate (SO_4^{2-}), leading to compounds such as carbonates, sulfates, and chlorides. This represents a key form of REE occurrence in nature [25]. The REE distribution curves for pyrite from various pulses in the Alin Sb–Au orebodies were mostly right-skewed, indicating LREE enrichment (Figure 5). This suggests that the ore-forming fluids contain a significant amount of F^- or Cl^- [26–28]. High field strength elements (HFSEs), including HREEs, Nb, Ta, and Ce, have small ionic radii and high ionic charges, leading to strong ionic fields. The distribution of REEs and HFSEs is primarily controlled by their content in pyrite-forming fluids, with little influence from the crystal structure. If the ore-forming fluid is rich in Cl^-, the Hf/Sm, Nb/La, and Th/La ratios are generally less than 1. In contrast, F^--enriched fluids with concentrated HFSEs show Hf/Sm, Nb/La, and Th/La ratios greater than 1 [27]. Table S1 shows that most of the Hf/Sm, Nb/La, and Th/La values for pyrite from the Alin gold

deposit were less than 1, with only a few exceeding 1, suggesting that the ore-forming fluid is rich in Cl^- and low in F^- [24–26].

Each pulse of pyrite in the Alin Sb–Au orebodies was enriched in chalcophile elements such as Cu and Pb, and relatively depleted in Zn and Cd, showing an exceptionally high enrichment of Bi, while the iron-group elements were enriched in Co but depleted in Ni. The HFSEs, including Th, U, Ta, Nb, Zr, and Hf, were relatively depleted. The large ion lithophile elements (LILEs), such as Sr, Ba, and Rb, were also relatively depleted (Figure 5). The tungsten–molybdenum group elements (Mo and W) exhibited varying patterns of enrichment and depletion at different pulses. The trace element characteristics of pyrite suggest that the ore-forming fluid is enriched in sulfur-loving elements such as Cu, Pb, and Bi (Figure 6). The field observations, hand specimens, and microscopic analysis revealed that, in addition to pyrite, the ore minerals included small amounts of chalcopyrite, sphalerite, and galena, consistent with the trace element enrichment. In the host rock, the enrichment and depletion patterns of chalcophile elements, such as Cu, Pb, Tl, Zn, and Cd, mirrored those in pyrite. The iron-group elements showed minimal variation between the upper and lower parts of the ore body, with V, Cr, Co, and Ni depleted in both, though their depletion was not significant when compared with the standard crustal values. The REEs exhibited similar depletion patterns to those of the iron-group elements. The radioactive elements typically showed enrichment, with their enrichment coefficients (K) slightly exceeding 1. Notably, Bi showed exceptional enrichment in both the surrounding rock and all pulses, with K values ranging from 10 to 100, occasionally exceeding 100. The trace elements in pyrite displayed characteristics of ore-forming fluid element enrichment.

5.2. Evolution of Ore-Bearing Fluid

Eu^{2+} is stable in high-temperature reducing hydrothermal fluids, leading to positive Eu anomalies. In contrast, low-temperature reducing conditions result in negative Eu anomalies due to the instability of Eu^{2+}. Under oxidizing conditions, Ce^{3+} oxidizes to Ce^{4+}, separating from other elements and causing Ce anomalies [26]. The δCe values of pyrite in different pulses varied significantly, with an average around 1 (ranging from 0.87 to 1.28, mean = 1.01), showing no significant Ce anomaly. This finding suggests a reducing environment during pyrite mineralization, consistent with the presence of pyrite and arsenopyrite as the main gold-bearing minerals in the Alin Sb–Au orebodies. Pyrite's REE profile showed negative Eu anomalies, with δEu values ranging from 0.6 to 1.17 (Figure 8). The δEu average values for pulses 1 to 4 were 1.17, 0.60, 0.96, and 0.84, respectively, indicating considerable variation. For pyrite crystallized during pulse 1 (PyI_1), the number of δEu values greater than and less than 1 were roughly equal, suggesting a high formation temperature and a complex formation environment. The pyrite precipitated during pulses 2 and 3 exhibited a general negative Eu anomaly, with only a few points greater than 1, indicating a lower temperature compared with that during pulse 1. The pyrite precipitated during pulse 4 showed a similar number of δEu values greater than and less than 1, suggesting a high temperature. The temperature decreased from pulses 1 to 3, and then increased during pulse 4, consistent with the formation temperatures (240 °C, 220 °C, 235 °C, and 230 °C for pulses 1 to 4, respectively) determined based on the arsenopyrite atomic percentages [5] and quartz fluid inclusions [24], suggesting the possible involvement of external high-temperature hydrothermal fluids during the later stages of mineralization. The host rock of the Alin Sb–Au orebodies showed a narrow range of δCe values (0.92−1.0, mean = 0.96) and δEu (0.68−0.82, mean = 0.73) values, exhibiting an overall negative anomaly. Whether these anomalies can reflect the physicochemical conditions of mineralization requires further investigation.

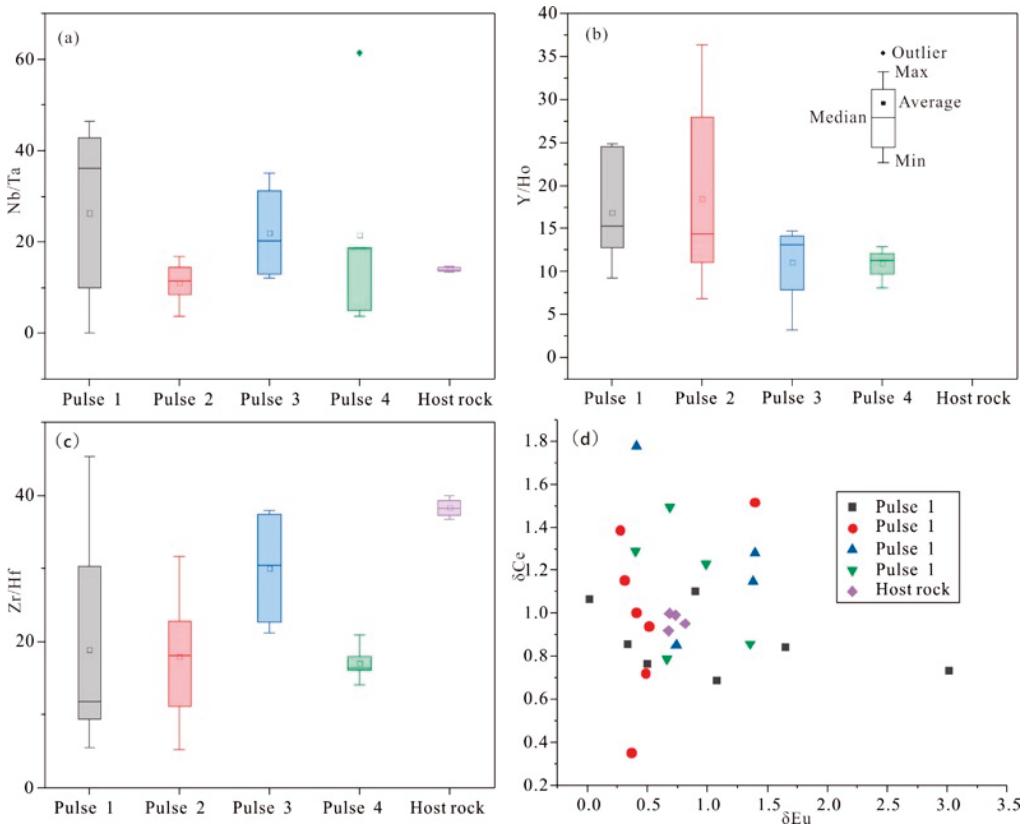


Figure 8. Ore-forming fluid characteristics: (**a**) Nb/Ta ratios of pyrite in each pulse; (**b**) Y/Ho ratios of pyrite in each pulse; (**c**) Zr/Hf ratios of pyrite in each pulse; and (**d**) δCe–δEu values of pyrite in each pulse.

Co and Ni replace Fe in pyrite mainly through isomorphous substitution. Co, being closer to Fe on the periodic table, is more easily incorporated into the pyrite lattice than Ni. The Co/Ni ratio offers insights into the mineralization conditions and pyrite formation [29,30]. Co is more temperature sensitive than Ni, making the Co/Ni ratio useful for indicating the formation temperature of minerals. A lower Co/Ni ratio typically corresponds to a lower formation temperature [31,32]. During pulse 1 of the Alin Sb–Au orebodies, only one pyrite sample had a Co/Ni ratio below 1, while the others were significantly higher, suggesting a higher crystallization temperature. During pulse 2, the Co/Ni ratio of pyrite ranged from 0.34 to 11.4, with a mean of 3.5. The ratio was roughly balanced between values greater than 1 and those less than 1, indicating a lower precipitation temperature compared with that of pulse 1. During pulse 3, the Co/Ni ratio of pyrite ranged from 0.4 to 2.6, with a mean of 1.33, suggesting a lower precipitation temperature than during pulse 2. During pulse 4, the Co/Ni ratio of pyrite ranged from 1.55 to 5.43, with a mean of 3.56, suggesting a higher precipitation temperature than during pulses 2 and 3. The variation in mineralization temperature in the Aling gold deposit, from high to low and back to high, suggests that higher-temperature hydrothermal fluids may have been mixed in during pulse 4. This hypothesis is supported by large-scale stibnite precipitation during the late stages of mineralization [5].

The Y/Ho, Zr/Hf, and Nb/Ta ratios remained stable within the same hydrothermal system due to the similar ionic radii and valence states of the Y−Ho, Zr−Hf, and Nb−Ta. When disturbed by hydrothermal activity or metasomatism, these element pairs exhibited distinct differentiation. Within the same sample, these ratios showed varying values and wide ranges [32–34]. The Y/Ho, Zr/Hf, and Nb/Ta values of the Alin Sb–Au orebodies varied widely across pulses (Figure 8a–c), suggesting that the ore-forming hydrothermal

system in each pulse may have been disturbed, possibly due to metasomatism or external hydrothermal fluids.

Figure 8b shows the Y/Ho ratios of pyrite under different pulses of the Alin Sb–Au orebodies. Excluding an outlier of 176.58 from pulse 4, the ratios ranged from 3.24 to 36.38, with an average of 15.60. Pulse 2 exhibited the broadest range of Y/Ho ratios. The average Y/Ho values of the pulses increase, then decreased, and finally increased again. The Y/Ho ratio of chondrites is approximately 28, the mantle ranges from 25 to 30, seawater ranges from 40 to 70, and the Y/Ho ratio in China's continental crust ranges from 20 to 35 [26,33,35,36]. The Y/Ho ratios of pyrite at all pulses of Alin closely matched those of the continental crust of China, indicating a strong relationship between the ore-forming fluids and the crust. The Zr/Hf and Nb/Ta ratios of pyrite in each pulse of the Aling gold deposit, shown in Figure 8a,c, exhibited large variations. The average Zr/Hf values of the pulses decreased, and then increased, while the Nb/Ta values decreased, then increased, and finally decreased again.

6. Conclusions

1. The ore-forming fluids were low in Cl^- and F^-, but enriched by sulfur-loving elements such as Cu, Zn, Cd, Pb, and Bi and iron-group elements such as Co.
2. The physical and chemical conditions during mineralization were marked by a reducing environment. Initially, the temperature decreased from pulse 1 to pulse 4, and then increased again.
3. The temperature increase during pulse 4 may have resulted from the influx of Sb-bearing high-temperature hydrothermal fluids, causing a metasomatic effect.

Supplementary Materials: The following supporting information can be downloaded at: https://www.mdpi.com/article/10.3390/min15050491/s1. Table S1: Data of gold-bearing pyrite and host rock rare earth elements and trace elements from the Shuixie Arlin Sb–Au deposit. (All data in this paper are shown in Table S1).

Author Contributions: G.L.: Conceptualization, Methodology, Investigation, Methodology, Writing—original draft, Writing—review and editing, Visualization; S.R.: Conceptualization, Methodology, Data curation, Writing—original draft, Writing—review and editing, Investigation, Formal analysis, Visualization, Supervision; Funding acquisition, Project administration; C.X.: Conceptualization, Methodology, Data curation, Writing—original draft, Writing—review and editing, Investigation, Formal analysis, Visualization, Supervision; Funding acquisition, Project administration; W.W.: Writing—review and editing, Investigation, Formal analysis. All authors have read and agreed to the published version of the manuscript.

Funding: The authors declare that this study received funding from the Scientific Research Foundation of the Yunnan Education Department (grant no. 2023J0131), the Provincial Talent Training Program (grant no. KKSY201556033), the Second Tibetan Plateau Scientific Expedition and Research Project (2021QZKK0301), and the National Natural Science Foundation of China (42163007, 41373049). The authors (Shanshan Ru and Chuandong Xue) were the applicants for funding. The funders (Shanshan Ru and Chuandong Xue) were involved in the study design, collection, analysis, interpretation of data, the writing of this article and the decision to submit it for publication.

Data Availability Statement: Data are contained within the Supplementary Materials.

Conflicts of Interest: The authors declare that they have no known competing financial interests or personal relationships that could have appeared to influence the work reported in this paper.

References

1. Hou, Z.Q.; Zaw, K.; Pan, G.T.; Mo, X.X.; Xu, Q.; Hu, Y.Z.; Li, X.Z. Sanjiang Tethyan metallogenesis in SW China: Tectonic setting, metallogenic epochs and deposit types. *Ore Geol. Rev.* **2007**, *31*, 48–87. [CrossRef]
2. Wu, Z.H.; Barosh, P.J.; Wu, Z.H. Vast early Miocene lakes of the central Tibetan Plateau. *Geol. Soc. Am. Bull.* **2008**, *120*, 1326–1337.
3. Wang, C.M.; Chen, J.Y.; Yang, L.F.; Zhang, R.; Du, B.; Shi, K.X. Tectonic–fluid–mineral system in the Lanping basin, Sanjiang Tethys. *Acta Petrol. Sin.* **2017**, *33*, 1957–1977. (In Chinese with English abstract)
4. Feng, Z.J.; Xue, C.D.; Wei, A.Y.; Wang, W.; Li, G. Discovery of gold deposit in the Shuixie Zhifanghe copper–cobalt district in Yongping County, western Yunnan Province, SW China. *Geol. China* **2024**, *51*, 2. (In Chinese with English abstract)
5. Li, G.; Xue, C.D.; Feng, Z.J.; Wang, W.; Wei, A.Y. In situ elemental and sulfur isotopic variations of Au–bearing iron–sulfides from newly unearthed Alin gold deposit in the Shuixie Cu–Co orefield (Western Yunnan Province), SE Tibet: Insights into enrichment processes of invisible gold. *Ore Geol. Rev.* **2025**, *178*, 106477. [CrossRef]
6. Chen, G.Y.; Sun, D.S.; Chang, L.; Zang, W.S.; Wang, J.; Lu, A.H. Morphogenesis of Pyrite. *Geoscience* **1987**, *1*, 60–76. (In Chinese with English abstract)
7. Hou, J.; Xu, T.; Lu, Q.T.; Zheng, M.; Bai, Z.M. The fine upper crustal stracture below the Qin-Hang and Wuyishan metallogenic belts revealed by double beamforming ambient noise tomgraphy. *Chin. J. Geophys.* **2011**, *65*, 3881–3889.
8. Sun, D.S.; Chen, G.Y. Morphogenesis of Pyrite. *Bull. Mineral. Petrol. Geochem.* **1987**, *3*, 139–140. (In Chinese with English abstract)
9. Henderson, P. *Rare Earth Element Geochemistry*; Elsevier Science Publishers: Amsterdam, The Netherlands, 1984; pp. 1–510.
10. Reich, M.; Kesler, S.E.; Utsunomiya, S.; Christopher, S.; Stephen, L. Solubility of gold in arsenian pyrite. *Geochim. Cosmochim. Acta* **2005**, *69*, 2781–2796. [CrossRef]
11. Large, R.R.; Danyushevsky, L.; Hollit, C.; Maslennikov, V.; Meffre, S.; Gilbert, S.; Bull, S.; Scott, R.; Emsbo, P.; Thomas, H.; et al. Gold and trace ele ment zonation in pyrite using a laser imaging technique: Implic ations for the timing of gold in orogenic and Carlin-style sedi ment hosted deposits. *Econ. Geol.* **2009**, *104*, 635–668. [CrossRef]
12. Mao, G.Z.; Hua, R.M.; Gao, J.F.; Li, W.; Zhao, K.; Long, G.; Lu, H. Existing forms of REE in gold bearing pyrite of the Jinshan gold deposit, Jiangxi Province, China. *J. Rare Earths* **2009**, *27*, 1079–1087. [CrossRef]
13. Schade, J.; Cornell, D.H.; Theart, H.F.J. Rare-earth element and isotopic evidence for the genesis of the Prieska massive sulfide deposit, South Africa. *Econ. Geol.* **1989**, *84*, 49–63. [CrossRef]
14. Wu, L.X.; Liu, H.D.; Hou, J.H.; Wang, Q.H.; Chen, H. The rare earth elements and trace elements of gold–bearing pyrite from Jiangjiayao gold deposit, Shandong Province. *Geol. China* **2020**, *2*, 1–24.
15. Yang, T.N.; Yan, Z.; Xue, C.D.; Xin, D.; Dong, M.M. India indenting Eurasia: A brief review and new data from the Yongping Basin on the SE Tibetan Plateau. *Geosciences* **2021**, *11*, 518. [CrossRef]
16. Yang, T.N.; Dong, M.M.; Xue, C.D. Coherent chemical variation trends of the 55–25 Ma magmatic rocks in SE Tibet: N–S direction lithospheric stretching of Eurasia during early stage of India–Eurasia Collision. *Acta Geol. Sin.* **2023**, *97*, 1283–1305. [CrossRef]
17. Liang, M.J.; Yang, T.N.; Xue, C.D.; Xin, D.; Yan, Z.; Liao, C.h.e.n.; Han, X.u.e.; Xie, Z.P.; Xiang, K. Complete deformation history of the transition zone between oblique and orthogonal collision belts of the SE Tibetan Plateau: Crustal shortening and rotation caused by the indentation of India into Eurasia. *J. Struct. Geol.* **2022**, *156*, 104545. [CrossRef]
18. *Resource Reserves Verification Report of Xiaotuanshan from Shuixie Copper–Cobalt Deposit, Yongping County, Yunnan Province*; Yongping Mining Co., Ltd.: Dali, China, 2023. (In Chinese with English abstract)
19. Zong, K.Q.; Klemd, R.; Yuan, Y.; He, Z.Y.; Guo, J.L.; Shi, X.L.; Liu, Y.S.; Hu, Z.C.; Zhang, Z.M. The assembly of Rodinia: The correlation of early Neoproterozoic (ca. 900 Ma) high–grade metamorphism and continental arc formation in the southern Beishan Orogen, southern Central Asian Orogenic Belt (CAOB). *Precambrian Res.* **2017**, *290*, 32–48. [CrossRef]
20. Hu, Z.C.; Zhang, W.; Liu, Y.S.; Gao, S.; Li, M.; Zong, K.Q.; Chen, H.H.; Hu, S.H. "Wave" Signal–Smoothing and Mercury–Removing Device for Laser Ablation Quadrupole and Multiple Collector ICPMS Analysis: Application to Lead Isotope Analysis. *Anal. Chem.* **2015**, *87*, 1152–1157. [CrossRef]
21. Liu, Y.S.; Hu, Z.C.; Gao, S.; Gunther, D.; Xu, J.; Gao, C.G.; Chen, H.H. In situ analysis of major and trace elements of anhydrous minerals by LA−ICP−MS without applying an internal standard. *Chem. Geol.* **2008**, *257*, 34–43. [CrossRef]
22. Sun, S.; McDonough, W.F. Magmatism in ocean basin. In *Chemical and Isotopic Systematics of Ocean Basalts: Implications for Mantle Composition and Processes*; Saunders, A.D., Norry, M.J., Eds.; Geological Socity London Special Publish: London, UK, 1989; Volume 42, pp. 313–345.
23. Gao, S.; Luo, T.C.; Zhang, B.R.; Zhang, H.F.; Han, Y.W.; Zhao, Z.D.; Hartmut, K. Texture and composition of Eastern China crust. *Sci. China (Ser. D)* **1999**, *29*, 204–213. (In Chinese)
24. Han, Y.W.; Ma, Z.D.; Zhang, H.F.; Zhang, B.R.; Li, F.L.; Gao, S.; Bao, Z.Y. *Geochemistry*; Geological Publishing House: Beijing, China, 2003; pp. 1–370. (In Chinese with English abstract)
25. Li, F.; Huang, D.Y.; Pu, W.M. On the geological characteristics and genesis of Shuixie copper deposit in Yongping. *Yunnan Geol.* **1994**, *13*, 341–349.

26. Chen, B.H.; Wang, Z.L.; Li, H.L.; Li, J.K.; Li, J.L.; Wang, G.Q. Evolution of ore fluid of the Taishang gold deposit, Jiaodong: Constraints on REE and trace element component of auriferous pyrite. *Acta Petrol. Sin.* **2014**, *30*, 2518–2532. (In Chinese with English abstract)
27. Oreskes, N.; Einaudi, M.T. Origin of rare earth element–enriched hematite breccias at the Olympic Dam Cu–U–Au–Ag deposit, Roxby Downs, South Australia. *Econ. Geol.* **1990**, *85*, 1–28. [CrossRef]
28. Keppler, H. Constraints from partitioning experiments on the composition of subduction–zone fluids. *Nature* **1996**, *380*, 237–240. [CrossRef]
29. Chen, M.H.; Wu, L.L.; Uttly, P.J.; Norman, T.; Zheng, J.M.; Qin, Y.Z. REE features of arsenian pyrite and vein quartz and their fulid inclusions in Jingfeng (Liannigou) gold deposit, Guizhou provice, China. *Acta Petrol. Sin.* **2007**, *23*, 2423–2433.
30. Hu, Y.; Chen, M.H.; Dong, Q.J.; Huang, Q.W. Trace Elements Features of the Vein Quartzs, Arsenian Pyrites and Their Fluid Inclusions in Jinfeng (Lannigou) Gold Deposit, Guizhou Province, China. *Geol. J. China Univ.* **2009**, *15*, 506–516. (In Chinese with English abstract)
31. Sheng, J.F.; Li, Y. A study of minor elements in minerals from polymetallic deposits in the central part of the da hinggan mountains. *Miner. Depos.* **1999**, *34*, 57–64.
32. Yuan, Q.; Ge, W.S.; Ding, H.; Chen, J.; Jia, H.X.; Huang, G.; Zhang, J.R. Geochemical Characteristics of REE and Trace Elements of Pyrite: Constraint on the Ore–Forming Fluid of the Lvyuan Gold Deposit, Eastern Junggar. *Bull. Mineral. Petrol. Geochem.* **2017**, *36*, 628–636.
33. Bau, M.; Dulski, P. Comparative study of yttrium and rare–earth element behaviours in fluorine–rich hydrothermal fluids. *Contrib. Mineral. Petrol.* **1995**, *119*, 213–223. [CrossRef]
34. Yaxley, G.M.; Green, D.H.; Kamenetsky, V. Carbonatitemetasomatism in the Southeastern Australian Lithosphere. *J. Petrol.* **1998**, *39*, 1917–1930. [CrossRef]
35. Chi, Q.H.; Yan, M.C. *Applied Geochemistry Element Abundance Pamphlet*; Geological Publishing House: Beijing, China, 2007; pp. 8–114. (In Chinese with English abstract)
36. Barrat, J.A.; Zanda, B.; Moynier, F.; Bollinger, C.; Liorzou, C.; Bayon, G. Geochemistry of CI chondrites: Major and trace elements, and Cu and Zn isotopes. *Geochim. Cosmochim. Acta* **2012**, *83*, 79–92. [CrossRef]

Disclaimer/Publisher's Note: The statements, opinions and data contained in all publications are solely those of the individual author(s) and contributor(s) and not of MDPI and/or the editor(s). MDPI and/or the editor(s) disclaim responsibility for any injury to people or property resulting from any ideas, methods, instructions or products referred to in the content.

minerals

MDPI

Article

Analysis of Structural Position of Carlin-Type Gold Deposits with Lineament Analysis of Remote Sensing Data Using pyLEFA Software

Sergei Shevyrev * and Natalia Boriskina

Far East Geological Institute, Far Eastern Branch of Russian Academy of Sciences, Vladivostok 690022, Russia; boriskina2000@mail.ru
* Correspondence: shevirev@mail.ru

Abstract: Previous research on Carlin-type gold deposits in North America and China has revealed peculiarities in their genesis, distribution, and prospectivity. However, pinpointing these deposits within known ore districts and prospective areas is a complex and resource-demanding task. Studying the structural and geological characteristics of Carlin-type deposits in areas with a longer history of exploration using machine learning techniques is crucial, especially considering the potential for discovering Carlin-type deposits in Russia. Crustal fracturing fields detected in space imagery and digital relief models can serve as a foundation for prospectivity mapping of Carlin-type deposits, even without evidence of magmatic sources of ore matter. The detection of disjunctive features, observed as linear elements (lineaments) in remote sensing images of the Earth, allows for a quantitative description of the Earth's crust permeability to ore-bearing magmas and fluids. This can be accomplished using open source pyLEFA software. Optical detection methods facilitate this process, while the assessment of heterogeneity in the distribution of fracture field parameters is achieved using unsupervised learning and classification. Machine learning based on datasets produced with pyLEFA enables the assessment of the contribution of predictor variables to the result. The knowledge acquired can be applied to areas with the potential for discovering Carlin-type deposits.

Keywords: Carlin-type deposits; lineaments; geoinformatics; object detecting; machine learning

1. Introduction

Carlin-type gold deposits are geologically significant altered metasomatic bodies within carbonate rocks, holding substantial gold reserves and resources. Initially described in the Nevadan metallogenic province (USA), similar deposits are also found in the Verkhoyansk (Russia) and South China (China) metallogenic provinces [1–4]. Carlin-type deposits often appear in nodes or linear groups (trends), and small surface areas can host significant resources at depth [2].

The largest known Carlin-type deposits (CTDs) are in the western United States and southwestern China. Enormous world-level CTDs in north-central Nevada host over 6000 t of gold and are exceeded only by the South African Witwatersrand [2,5,6]. Nevadan CTD account for ~75% of US and ~9% of annual worldwide Au production, making the USA the fourth-largest gold producer [5,7–9]. The second-largest concentration of gold of Carlin type is the Dian-Qian-Gui area in southwestern China, where about 200 deposits or occurrences were found, including several large (>20 t Au) and super-large (>100 t Au)

reservoirs of over 1000 t of Au [10,11]. The Carlin trend is the leading source of Nevada's gold production, with 2227 tons extracted as of 2008 [12].

The Nevadan metallogenic province is located at the junction of the Pacific and North American platforms. According to the authors of [1,13,14], the American platform is a complex accretionary orogen formed as a result of the rifting of the Rodinia supercontinent and the accumulation of Proterozoic-Paleozoic and early Mesozoic strata of carbonate, terrigenous, siliceous, and shale composition from a passive continental margin. The late Mesozoic and Cenozoic periods saw changes in the tectonic regime, with the subduction of a young oceanic slab and ongoing thrust faulting of the ancient continental plate. Early Mesozoic subduction resulted in the formation of magmatic arcs and massive I- and S-type intrusions of Jurassic (160–140 Ma) and Cretaceous (120–80 Ma) age. The magmatism of that period is associated with Au porphyry deposits with W, Mo, Cu, Pb, Zn, and Ag [13]. In the early Paleocene (~65 Ma), plutonic magmatism migrated easterly. This extension was accompanied by subaerial volcanism, which formed basalt-rhyolite bimodal assemblages in the middle Eocene (~45 Ma), succeeded by silicic caldera complexes and associated epithermal Au-Ag deposits in the Oligocene and Miocene [15,16]. Thrust faulting led to the division of orogenic belts into autochthonous (carbonate-terrigenous) and allochthonous (siliceous-terrigenous) sequences that were originally united at the sedimentation zone of Antler Rise, which exhibits typical CTD trends and hosts large Mesozoic granitoids [16].

The current literature suggests that the geodynamic settings for the formation of CTD may involve the presence of a long-lived hotspot [2] or a sub-crustal (mantle) source [4]. The Nevadan metallogenic province is located over the sizable positive gravity anomaly "of the North Nevada Rift", which was supposedly formed by the rise of the mantle and weakening of the Earth's crust, controlled by local gradient zones and corresponding deep faults [1]. Also, the Nevadan province has thermal anomalies and hot springs, which marks fluid and energy flows from the mantle [17]. It is believed that the forming of world-class CTDs involves two asthenospheric sources: the subslab source, which metasomatically refertilizes the subslab lithospheric mantle; and the subcrustal source, which drives mantle upwelling. Decompression in these areas affected by large transform faults can be followed by melting in the mantle and asthenosphere. These melts can contribute to the formation of crustal primary magmatic chambers when migrating through the mantle wedge subcontinental asthenosphere, the upper mantle, and the foundation of the Earth's crust. Above these chambers, volcanic-plutonic systems may form, providing favorable conditions for the localization of porphyry mineralization. In remote parts, CTDs may also occur in these locations [18,19].

In the context of hotspot theory, over the past 100 million years, the North American continent has drifted westward relative to the then-existing hotspot system [2]. Between 60 and 43 million years ago, the hotspot's influence on the continent was shielded by the shallow subducting slab of the Farallon oceanic plate. Magmas and fluids accumulated beneath this slab until its breakdown around 42 million years ago. The main phase of mineralization occurred between 40 and 36 million years ago, when the Nevadan metallogenic province was positioned above the Yellowstone plume [2].

The goal of this study is to examine the potential of applying remote sensing and machine learning methods for predicting areas prospective for CTDs using cost-effective technologies. The K-means unsupervised classification method was used for the classification of the area and targeting for exploration [20]. Prospective zoning was made using a technique developed by Sergei Shevyrev, i.e., pyLEFA (pythonic Lineament Extraction and Fracture Analysis) 0.61a, a free and open source remote sensing software [21,22]. This cross platform software extracts lineaments from georeferenced images using the Hough transform method [23]. It can export lineaments into the vector ESRI Shape format, com-

pute parameters that describe lineament coverage, and combine them into data tables for machine learning. If prospectivity mapping of the area and modeling for exploration targeting (referencing Nevadan metallogenic province) prove to be viable, this approach could be applied to outline primary exploration targets for CTDs in less studied areas.

2. Materials and Methods

The location of presumed material sources and the role of crustal infrastructure in fluid migration have predefined the role of optical recognition methods for prospectivity mapping. The material source for the formation of CTDs is deep-seated [2,5,24,25]. It is emphasized that a superposition of three factors is crucial: the presence of an enriched gold-bearing mantle zone; an accretionary orogen with sutures penetrating the basement; and an ascending fluid flow from the sub-slab and supra-slab asthenosphere along the fault and extensional zones [4]. These patterns of distribution make the structural features of the area significant for predicting Carlin-type deposits and their discovery in Russia and other parts of the world. Identifying the features of the fracture network structure makes it possible to predict the placement of ore substance accumulations of a similar genesis at the scale of ore objects and nodes.

For our structural study, the Carlin district (Basin and Range Province) and the adjacent area were chosen as a benchmark for studying CTDs (Figure 1). The study area is located on the eastern edge of the Pacific and comprises long-lived convergent zones with alternating extensional and compressional tectonic settings [4,13]. Faults, thrusts, alternating magmatic fronts, and bimodal volcanic series have been described here. The deposit trends are mostly oriented northwest (Carlin, Alligator Ridge, Battle Mountain Eureka, Jarrett Canyon), which corresponds to the orientation of magmatic fronts and is orthogonal to the main geological and geomorphological structures. Contemporary research suggests that the linear placement of the CTD is predetermined by the arrangement of Archean basement faults which were reactivated by later tectono-magmatic events [4,13].

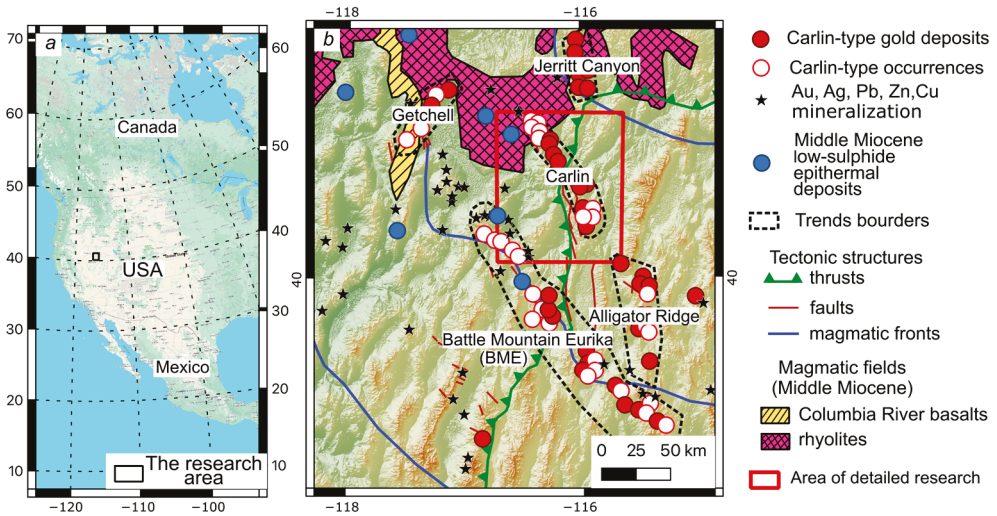


Figure 1. The research area on a geographical map of North America (**a**). Tectonic map of the Western North American gold province with Carlin-type deposit trends (**b**), adapted from [4,5].

The Carlin trend is hosted by sedimentary, volcanic, and volcano-sedimentary rocks of varying ages (Figure 2). In addition to stratigraphically undifferentiated pre-Cenozoic sedimentary rocks, Jurassic, Paleogene, and Neogene formations are known in the study area; these layers were formed in an active continental margin setting. The observed tectonic structure of the ore fields began forming around 40 million years ago, coinciding with the initial formation of grabens in the study area [2]. This process was marked by

faulting at different levels of the crust and andesitic volcanism in marginal basins. New faults were formed, and existing ones in the cover and basement were reactivated. The rock sequences hosting the mineralization include large volumes of thinly layered dolomitic limestones and marls. Alterations accompanying the mineralization development involved volume loss, increased rock permeability, and silicification. The permeable jasperoid rock structure, typical for CTD, was created by partial leaching of dolomite grains [2,26]. The thrust faults play a special role in deposit formation, acting as structural traps for ascending fluids. Impermeable clay-siltstone rocks of allochthons overlying carbonate autochthons served as impermeable barriers in this process [27].

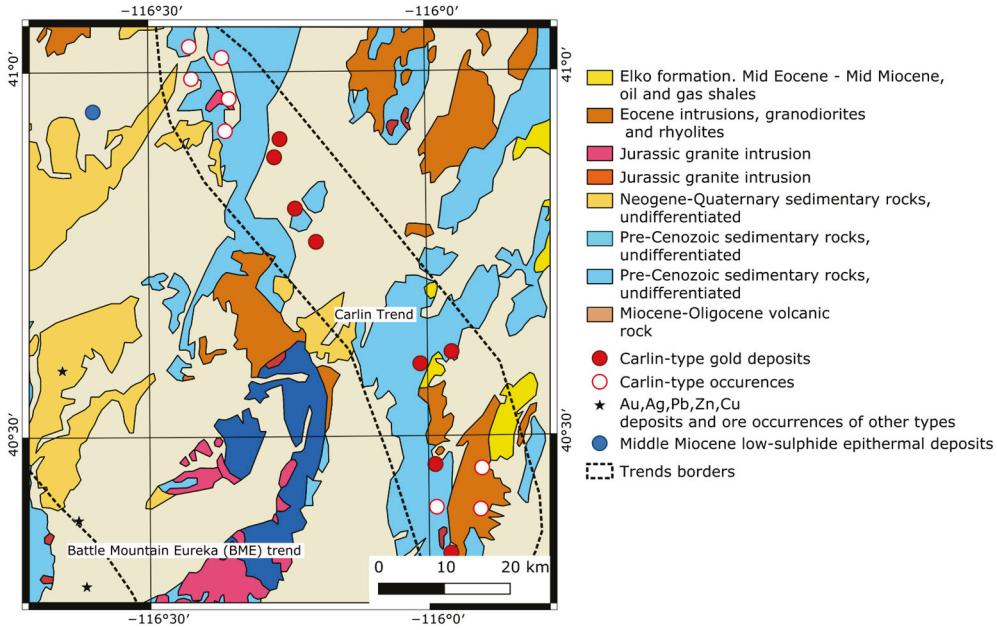


Figure 2. Geological map of the research area, adapted from [25].

Despite the noticeable presence of magmatic rocks in the structure of Carlin-type deposit trends (see Figure 2), there is no genetic link between the ores and magma or associated secondary alterations [2,4]. Carlin-type gold deposits and occurrences are characterized by the following metasomatic transformations: decarbonatization, silicification, argillitization, and dolomitization. For magmatic rocks located in fault zones, sericitization has been described. These metasomatic alterations are associated with fault zones and areas of increased fracturing [2]. Recent decades have seen a breakthrough in satellite technologies for Earth studies. Remote sensing methods provide information about physical fields, crustal composition, and tectonics [28–30].

Morphological analysis and lineament recognition are traditionally used to identify fault networks in the Earth's crust [31–36]. The description of the crustal fracture structure in the study area was performed using the pyLEFA 0.61a software. A graphic representation of the application's algorithm is provided in Figure 3. It comprises three stages and fifteen actions, including optional ones.

To explore the functionality to be added in future versions of the pyLEFA 0.61a software, prototyping was conducted to process data tables covering the spatial distributions of the fracturing parameters in the study area. This involved applying the k-means unsupervised classification algorithm [20], mapping the classes of coverage areas to ore deposits and ore-bearing structures, and analyzing the contribution of predictor variables to the resulting classes of averaging windows with varying prospectivity [37].

To assess the spatial distribution of crustal permeability and, consequently, the relative prospectivity of the area, data from the Landsat 9 mission, provided by NASA and the U.S.

Geological Survey, were used [38]. pyLEFA 0.61a can also process georeferenced optical images and digital relief models. The scale of features to be extracted and, consequently, the crustal discontinuities to be studied are limited by the spatial resolution of the images. Data processing was conducted using the pyLEFA 0.61a software [21], which is based on computer vision technology utilizing probabilistic Hough transform [23,39,40]. The cross-platform pyLEFA application, written in Python, features a graphical user interface built on the QT library (Figure 4). It can open georeferenced remote sensing images and operates with objects in the metric coordinate system of the Mercator projection; however, support for data in geographic coordinates is not guaranteed. Various topologies of vector shape files are supported. A key feature introduced in pyLEFA 0.61a is the ability to use point layers to compute raster heat maps. This feature is used to generate and save data tables that correlate linear element pattern parameters (predictors) with point density (target variable). The tables are saved in CSV format (comma-separated values) and can be used for engineering graphics, machine learning, and hypothesis testing (see Figure 4).

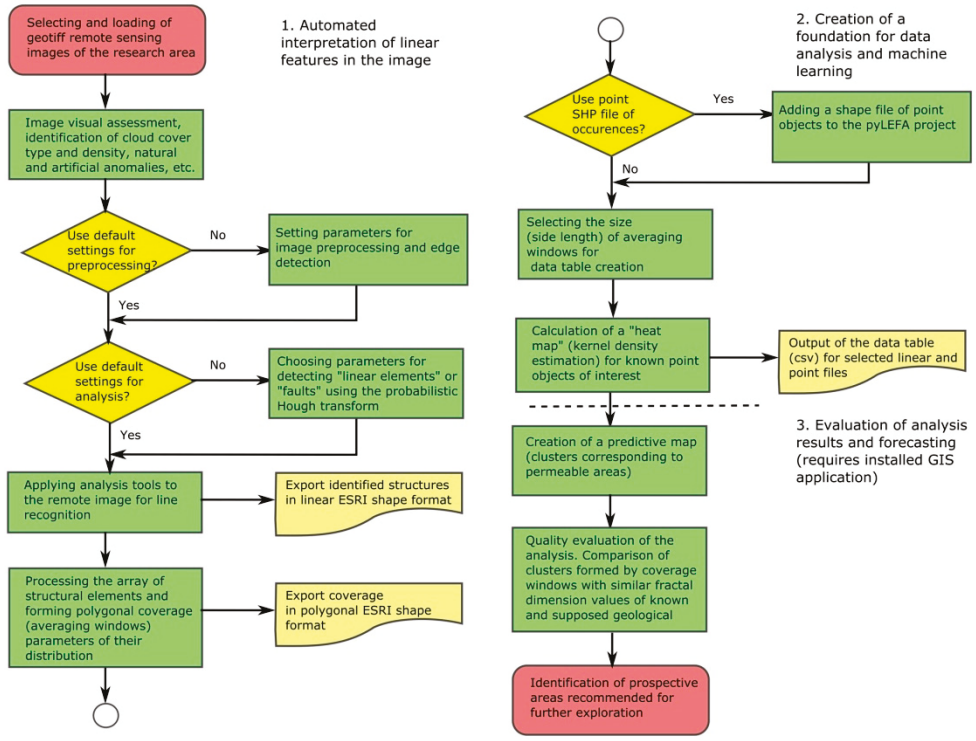


Figure 3. Algorithm for remote structure analysis in pyLEFA 0.61a software.

In pyLEFA, starting from version 0.6a, users can save and load projects that contain references to the files they are working with (buttons 1–3, see Figure 4). A project consolidates files related by the covered area and the spectrum of the tasks being addressed, including geotiff and ESRI shape files. The project file (with a *.lefa extension) is an XML format record containing information about the original "parent" file for the vector file being considered (if the file was created in pyLEFA), a reference to it on the disk, and information about the content. For vector data, the topological type is also specified.

Routine use of the program involves starting with the addition of georeferenced TIFF files for analysis (button 4; see Figure 4). It is also possible to enhance the project with an existing vector file containing linear or point features (button 5; see Figure 4). Analysis settings for the raster file can be accessed from the "View" menu → "Settings" (see Figure 4). Recognition is performed by edge detection on the image using the Canny method, along with specifying the Hough transform and Canny edge detection parameters (Table 1). The table presents the adjustable parameters for the image processing used for "line" and "fault"

detection, i.e., the maximum tolerated value to keep the detected line from separation (Gap Length), the minimum length of the line to be detected (Line Length), the threshold of the Hough Transform accumulator necessary for line detection (Detection Threshold), and the standard deviation for Canny edge detection Gaussian [41,42].

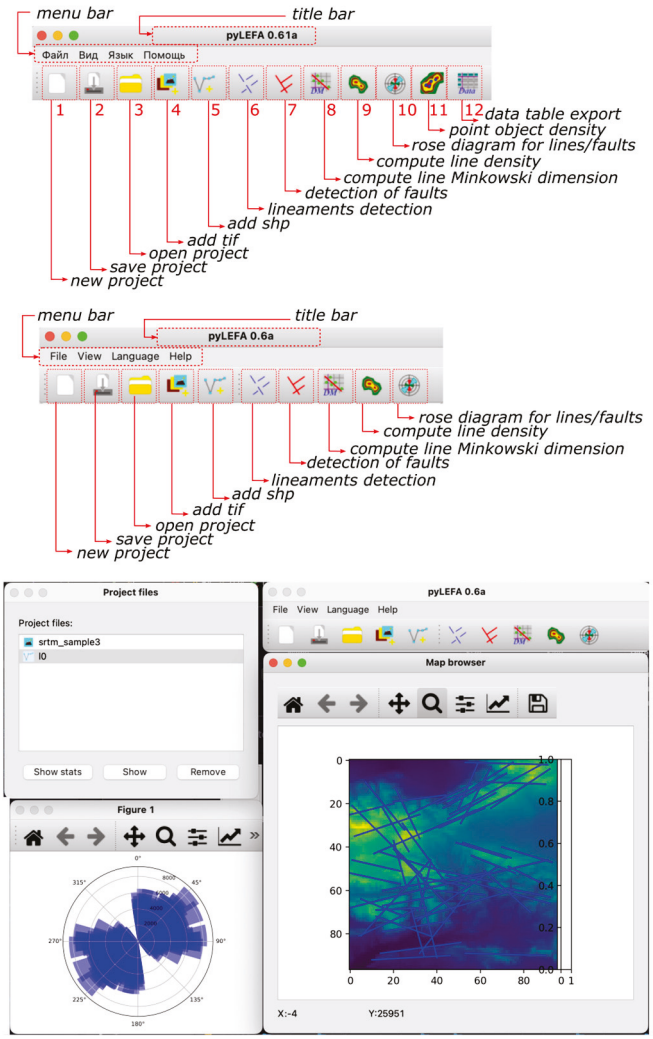


Figure 4. Interface of the pyLEFA 0.61a program with the functions of individual buttons indicated.

Table 1. Hough Transform Parameters for Identifying Linear Features on Landsat 9 OLI Image (Band 9) of the Carlin Trend in PyLEFA 0.61a.

№	Order of Identified Linear Features	Parameter			
		Sigma for Canny (n*0.1)	Detection Threshold	Line Length (min.)	Gap Length
1	First-order linear elements (“lines”)	15	10	50	10
2	Second-order elements (“faults”)	–	30	200	10

This process enables the recognition of lineaments in remote images from Landsat 9 OLI satellite photographs (Figure 5). A visual comparison of the identified structural elements, trend boundaries, and ore deposits confirmed the hypothesized link between deep-seated faults and the formation of CTD [4,5,25]. As can be seen in Figure 5, lineaments of the first order (“lines”) in the N and NE direction dominate among the detected ones. Their direction is orthogonal to Mesozoic subduction and thrust faulting (NW), which supposedly indicates that the age and origin of these features are related to changes in

the tectonic regime. Produced by processes on a planetary scale, these detected linear elements could be deep-seated. Meanwhile, linear objects of the second order ("faults") correspond to the directions of known faults and sometimes coincide with them (NW) (cf. Figures 1 and 5).

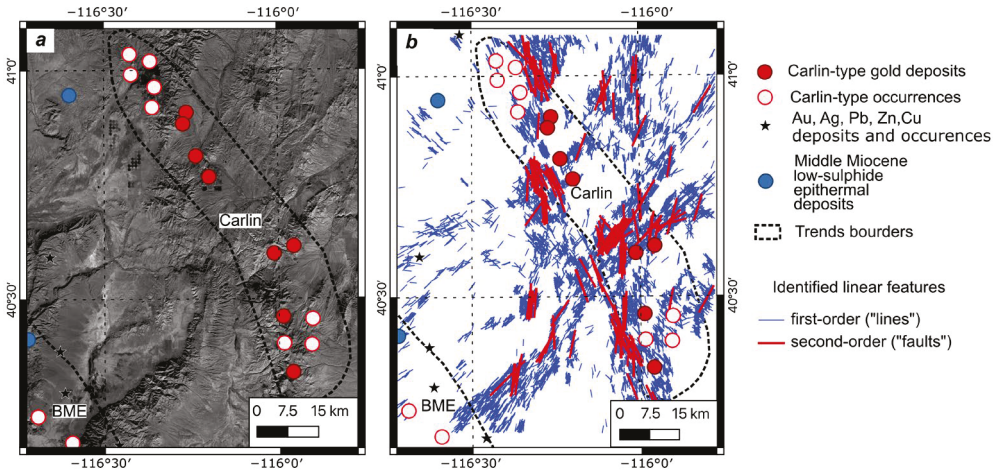


Figure 5. Landsat 9 OLI satellite image (band 7, path 041, row 032), captured on 11 September 2023 (**a**) and its interpretation scheme in pyLEFA 0.61a (**b**). For other symbols, see Figure 1.

The number of identified objects and their lengths are determined using parameters from the probabilistic Hough transform process. Users can set threshold values (peak intensity in Hough space), the minimum length of detectable lines, and the allowable gap in pixels forming a line. Since the settings for binarization and recognition significantly influence the analysis results, users have the option of saving these settings to an external file and loading them later. Configuration files (*.lpf) placed in the "lines" subdirectory of the "presets" folder within the program directory will be automatically loaded upon startup and will appear in the corresponding dropdown list of this tab.

The initially identified pattern of first-order lineaments, considered as "tectonic fractures", is used for the subsequent identification of second-order lineaments, interpreted as "tectonic faults". These terms are placed in quotes because the results of optical image recognition can be misinterpreted as purely tectonic features. This can occur due to false recognition of roads, power lines, contrails from airplanes, or other linear features that do not reflect the structure of the Earth's crust or the condition of rock formations. It is important to remember that the interpretation of identified elements requires validation with data obtained from other sources or fieldwork.

In the program, users can adjust the Hough transform parameters for the detection of second-order lineaments, referred to as "faults". Hough transform is applied to the binarized pattern of first-order lineaments directly identified from the satellite image. The parameters for this pattern can also be saved as presets (located in the presets/faults directory within the program directory). The binarization of raster images, a necessary step for object recognition, can be performed using Canny transformation (with one adjustable parameter) or "flow detection" [43]. The identified linear elements of both orders are saved as georeferenced ESRI shape files (*.shp), and they can also be opened within the program. A layer (if specified) serves as a background for displaying the lines on the basis of which they were generated.

A visual assessment of the rose diagrams for the directions of the first and second-order lineaments (Figure 6) indicates their alignment with the northwest (dominant) orientation of the geological and geomorphological structures of the region, confirming the accuracy of the identified linear elements and the nature of their corresponding features. For layers

containing identified linear elements, it is possible to generate polygonal coverage layers that provide a parametric description of the pattern of first or second-order lineaments. These coverage layers are ESRI shape polygonal layers, where the square polygons of the averaging windows correspond to rows in the attribute table of the file, containing calculated values for the windows such as the Minkowski fractal dimension or total line length (in meters). The size of the averaging windows is user-defined. Coverage polygon classes are computed for parameters describing the pattern of the first-order linear features, as represented across the entire study area. Determining the number of classes and their boundary values can be a complex task which is often left to the subjective judgment of the user. To define the number of classes and the boundaries of these values, the concentration-area (C-A) curve method described by Yousefi and Carranza [44] is applied.

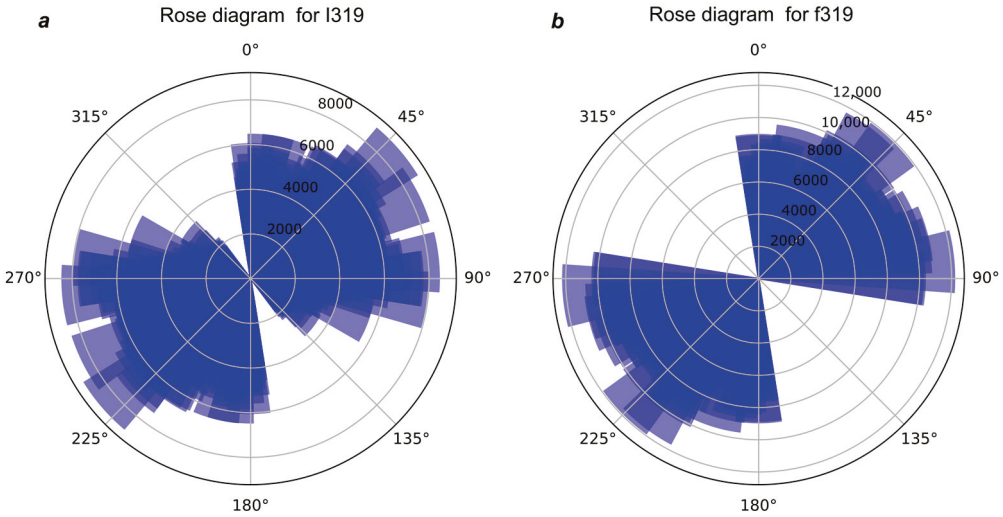


Figure 6. Rose diagrams of lineaments identified for the Carlin trend and adjacent area: (**a**) first-order ("fractures"); (**b**) second-order ("faults").

This method identifies a parameter value for which the area corresponding to values equal to or greater than the given one changes sharply, coinciding with a break on the C-A curve. This analysis is implemented as experimental Python scripts and has not yet been incorporated into pyLEFA 0.61a, but the scripts themselves are available for download [45]. The C-A curve method involves plotting a curve in logarithmic coordinates for a predictor variable, showing the logarithms of threshold values against the area covered on the map. Class boundaries are determined by the presence of n inflection points on this curve, with the number of classes being n + 1 (Figure 7). Calculations were performed for the initially obtained first-order lineaments covering the entire study area. Using the computed C-A curves (Figure 7a,b), eight classes were identified for the line density of first-order lineaments, and nine classes for the Minkowski fractal dimension. The color gradations of the averaging windows of the coverage layer reflect the distribution of the calculated parameter values.

From Figure 8, it is evident that there is only a partial match between CTD sites and the classes with the highest parameter values that describe the pattern of the identified linear features. Thus, determining a threshold value to separate squares with prospective and non-prospective areas is challenging. To delineate the area's permeability for ore-bearing fluids, which is indirectly reflected in the pattern of the identified linear features, an unsupervised machine learning method, k-means classification, is employed [20].

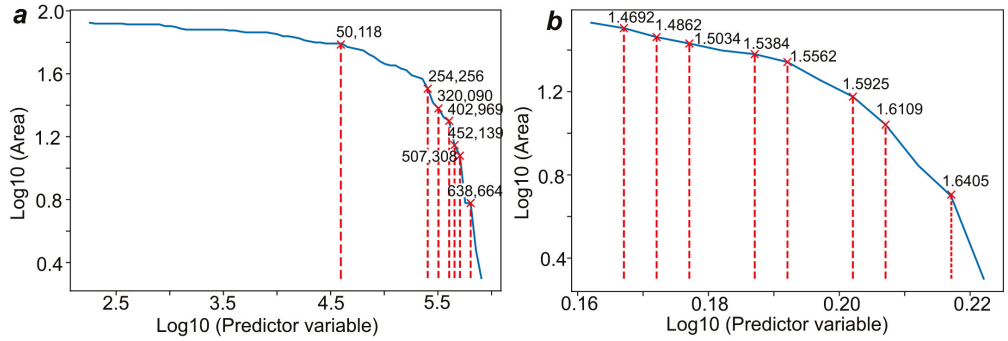


Figure 7. C-A curves for parameters describing the pattern of first-order lines for density (**a**) and the Minkowski fractal dimension (**b**). The breakpoint values are indicated above the curve's inflection point (oblique crosses).

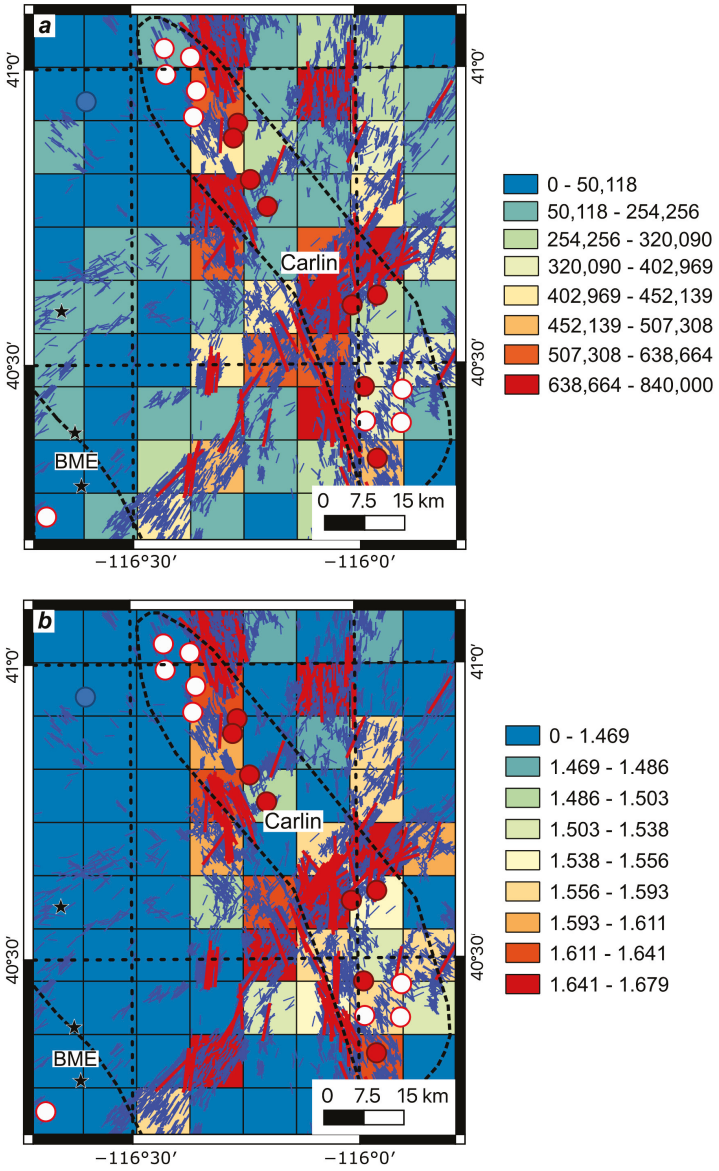


Figure 8. Distribution of first-order line pattern parameters for the area adjacent to the Carlin trend. Density of first-order lines (**a**) and Minkowski fractal dimension of the first order (**b**). Layout created in QGIS; class boundaries are defined according to Figure 7. For other symbols, see Figures 1 and 5.

An interesting practical feature of the program is the previously mentioned data integration of the density and the Minkowski fractal dimension, which is either uploaded

into the program or generated by it for vector layers of linear features and point value density distribution, with output provided as a CSV file (comma-separated values). This opens up new possibilities, as the program can analyze not only lineaments but also geological boundaries, dikes, veins, and other linear features.

In addition to the parameter values of the coverage, the generated table includes metric coordinates of the averaging window boundaries used for calculations and the coordinates of the centroid points. An interesting feature is that the densities (total line lengths within an averaging window) and fractal dimensions can also be included in the table for any linear vector layers arbitrarily loaded into the project. Table generation is performed to average the windows of a user-specified size. The density distribution field of point features under study is loaded into the table as the target variable. While calculating the point feature density, the program creates a "heat map", i.e., a raster geotiff file that contains values that are inverse to the distances from the points of the loaded image to the point features of the loaded file, known as kernel density estimation [46]. Values are computed within the limits defined by the user-specified "calculation radius". By creating a table based on the calculated layers and point features, it is possible to construct predictive and descriptive machine learning models to identify patterns in the distribution of the point features and the main factors of their placing. This capability enables the program to be used to develop machine learning models, i.e., k-means in this particular research case. The first 10 entries in the data table for averaging windows measuring 10 km are shown in Table 2.

Table 2. Header and first 10 entries of the data table for k-means clustering in case study.

id	X_left	Y_top	X_right	Y_bottom	X_centroid	Y_centroid	l3l9_dens	f3l9_dens	l3l9_mink	f3l9_mink	dep_po
0	523305	4549283	533295	4539293	528300	4544288	0	0	0	0	0
1	523305	4539293	533295	4529303	528300	4534298	20010	0	0.9943	0	0.0344
2	523305	4529303	533295	4519313	528300	4524308	69840	0	1.2197	0	0
3	523305	4519313	533295	4509323	528300	4514318	5040	0	0.8001	0	0
4	523305	4509323	533295	4499333	528300	4504328	40980	0	1.0458	0	0
5	523305	4499333	533295	4489343	528300	4494338	76140	0	1.3709	0	0.0516
6	523305	4489343	533295	4479353	528300	4484348	65940	0	1.3015	0	0.0137
7	523305	4479353	533295	4469363	528300	4474358	87030	0	1.4034	0	0.0145
8	523305	4469363	533295	4459373	528300	4464368	13560	0	1.0905	0	0.0834
9	523305	4459373	533295	4449383	528300	4454378	16740	0	1.2695	0	0.0877

Note: Geometric parameters include X_left, Y_top, X_right, Y_bottom, X_centroid, and Y_centroid, which represent the coordinates of the sides and centroids of the averaging windows. Predictors are identified as l3l9_dens and l3l9_mink, representing the density and Minkowski fractal dimension calculated for first-order linear elements within the windows; f3l9_dens and f3l9_mink represent the density and Minkowski fractal dimension calculated for second-order linear elements. The target variable is dep_po, which refers to the density distribution of mineralizations.

The calculation of predictor variables and the creation of data tables based on them allow comparisons to be made of the parameters describing the pattern of lineaments (predictors) with the kernel density distribution of the studied point features [46]. This approach is applicable not only for predicting mineralization but also for other purposes. Such a method opens up opportunities to use a wide range of machine learning and artificial intelligence techniques in the study of lineament patterns for the discovery and assessment of regularities and interrelationships.

In this study, the k-means unsupervised classification method [20] was applied to segment the coverage squares of the averaging windows based on the density and connectivity of first and second-order lineaments. The choice of this method was driven by the fact that class identification is performed independently of the target variable values and is solely linked to changes in the lineament values themselves. Subsequently, if a connection between the target variable values and the classes of the averaging windows can be estab-

lished, it would verify both the tectonic nature of the identified features and the role of fracture tectonics identified from satellite imagery in the formation of Carlin-type deposits.

Developing a machine learning model requires a preliminary assessment of the relationships both among predictor variables and between these variables and the target variable (Figure 9). Significant correlations are observed between some predictor variables (Pearson correlation coefficient values >0.7) due to the fact that second-order lineaments are derived from first-order features (Figure 9a). The density of first-order lines is related to the density of second-order lines (>0.83). The Minkowski fractal dimension is associated with density, as greater lengths of linear features within an averaging window indicate a higher degree of self-similarity of the pattern. A weak correlation was found between the density of second-order lineaments and their Minkowski fractal dimension (0.43). There is no linear correlation between predictors and the density of deposit occurrences (−0.17 to 0.21). The pairwise correlation of variables shows (Figure 9b) that forming a spindle-shaped cloud of figurative points (indicating a near-linear dependency) is possible only for the density of first and second-order linear features, as well as their Minkowski fractal dimensions.

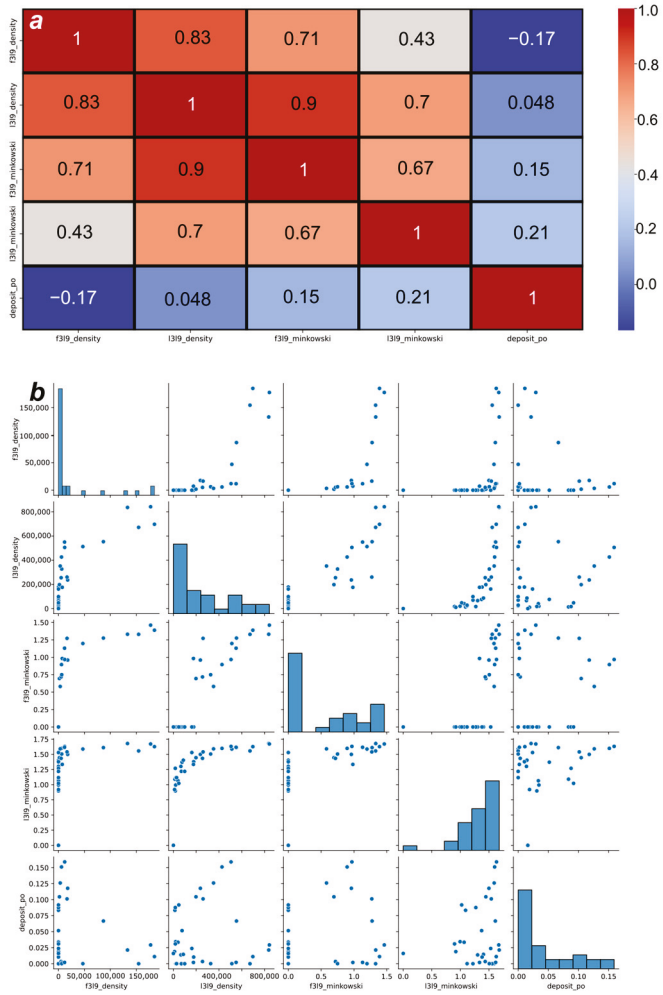


Figure 9. Analysis of the relationships between predictor variables and the target variable. Heat map of the data table (**a**) and pairwise correlation of the data table (**b**). See Table 2 for variable labels.

The elbow method was used to determine the optimal number of k-means clusters, which allows comparisons to be made of the number of classes and the amount of "distortion", defined as the sum of squared distances between class observations and their centroid [47]. In other words, selecting the optimal number of classes involves identifying a point where further increasing the number of classes no longer significantly de-

creases the distortion (Figure 10a). Using this method, four classes of averaging windows were determined.

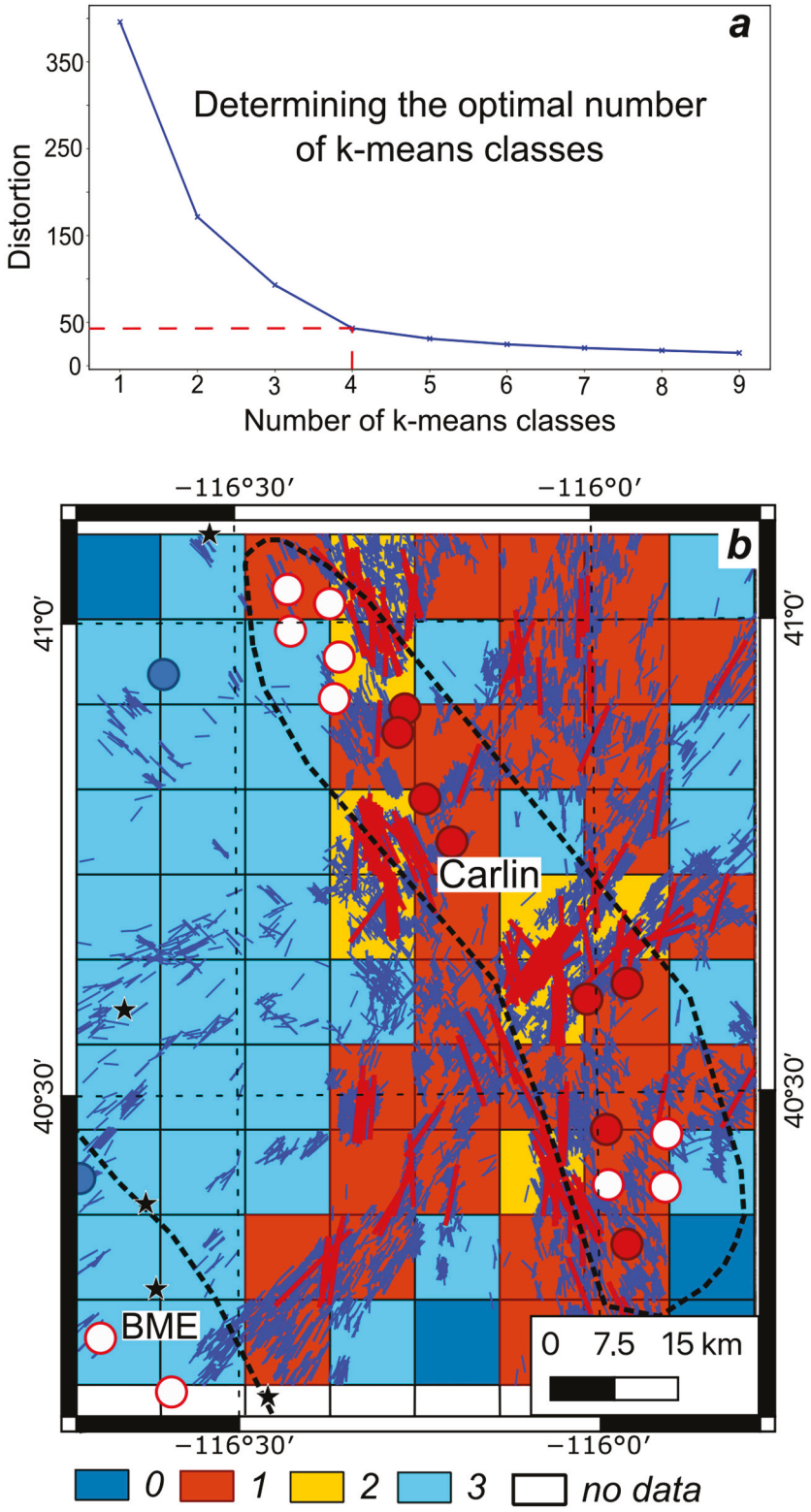


Figure 10. K-means classification for averaging the windows of the area: determination of the number of classes using the elbow method (**a**); coverage of the area with averaging windows for which k-means classes are defined (**b**). Numbers indicate k-means classes.

For the square averaging windows, k-means classification was performed using only predictor variables, without mapping to the target variable. Experimental script sets

for the development of new components of the pyLEFA program were used for these calculations [45], and a schematic map was created (Figure 10b). Since the classification utilized only variables describing the density and fractal dimension of first and second-order line patterns, if their correlation with ore-bearing potential is justified, then the classes of averaging windows will describe fracturing and, consequently, the permeability of the Earth's crust. This indicates the need to verify their applicability for predicting Carlin-type gold deposits. A visual comparison shows that Carlin-type deposits correspond to class 1 averaging windows (Figure 10b), while occurrences are mainly concentrated within class 1 and 2 windows. Accordingly, class 0 and 3 averaging windows are preliminarily assessed by us as non-prospective.

3. Results

The application of the k-means unsupervised classification method enabled the zoning of the area adjacent to the Carlin trend (Nevada, USA) into four distinct classes (see Figure 10). By comparing these classes with known hydrothermal ore deposits, they were categorized by permeability: classes 0 and 3 are relatively impermeable, and classes 1 and 2 are relatively permeable (see Figure 10).

To understand and evaluate the importance of predictors in k-means classification, a method proposed by Alghofaili [37] was used to assess the contribution of predictor variables to the identified classes. This approach leverages the Random Forest Classifier to determine the significance of each predictor in the formation of clusters, indicating the impact of the corresponding natural factors on the results (Figure 11).

An analysis of the weights table for predictors calculated for linear features in satellite imagery (Figure 11a) indicates that in the prospective averaging window classes (classes 1 and 2), the most significant factors are the density and Minkowski fractal dimension of second-order linear features ("faults"). These same predictors, when calculated for linear elements, are of secondary importance, as illustrated by the bar chart (Figure 11b). Additionally, in the non-prospective coverage window classes (classes 0 and 3), second-order linear features ("faults") are absent.

The revealed connections, validated by actual mineralization occurrences, demonstrated that the processing of Landsat 9 images with pyLEFA 0.61a software can facilitate first-pass prospectivity mapping for deposits controlled by crustal fracturing. The resulting division of the area based on the unsupervised k-means method proved that the obtained linear element density and interconnectivity are responsible for the distribution of CTD. Thus, this method can be transferred to other areas.

The result of evaluating the coverage of averaging windows over the study area can be presented as a confusion matrix, where columns represent the model's results and rows show the correspondence (or lack thereof) with actual data (Table 3). The obtained confusion matrix reflects only approximate model performance. The actual sizes and contours of known deposits and occurrences were not considered in the study. Provisionally prospective averaging windows (classes 1 and 2) located within ore-bearing trends but not containing any deposit or occurrence marked as a point object are counted as "false positives" in the part of the table reflecting point objects (columns 1 and 2). Identified "false positives" and "false negatives" may present a distorted view of the actual situation, as the future discovery of ore objects in these areas could change the perceived ore-bearing nature of the study area. Considering averaging windows that partially or entirely fall within ore-bearing trends provides more reliable performance metrics for the model (Table 3, columns 3 and 4).

a №	Predictors	Weight	k-means class.
0	l3l9_density	0.6103	0
1	l3l9_minkowski	0.3707	0
2	f3l9_density	0.0117	0
3	f3l9_minkowski	0.0073	0
4	f3l9_density	0.4562	1
5	f3l9_minkowski	0.3446	1
6	l3l9_density	0.1885	1
7	l3l9_minkowski	0.0107	1
8	f3l9_density	0.4461	2
9	f3l9_minkowski	0.326	2
10	l3l9_density	0.2236	2
11	l3l9_minkowski	0.0043	2
12	l3l9_density	0.3031	3
13	l3l9_minkowski	0.2595	3
14	f3l9_density	0.2575	3
15	f3l9_minkowski	0.1799	3

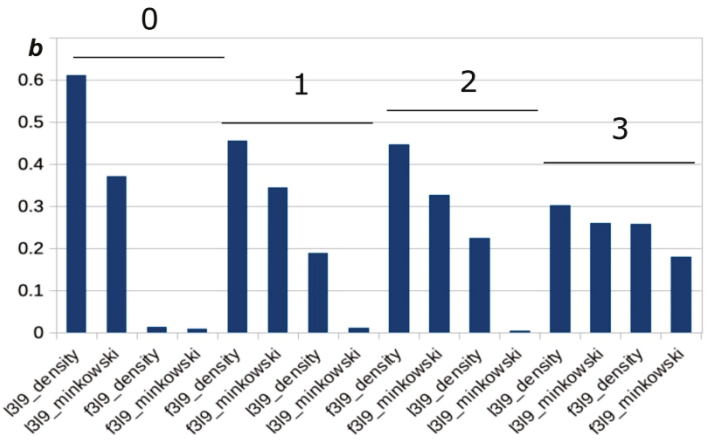


Figure 11. Predictors for k-means unsupervised classification and its significance (weight), shown as a table (**a**) and as a bar chart (**b**). Blue rectangles indicate weight, numbers correspond to Figure 10.

Table 3. Confusion matrix for the results of the semi-automatic classification of the averaging windows in the research area.

Facts	For Point Objects		For Trend Boundaries	
	1	2	3	4
	'Non-Prospective'	**'Prospective'**	**'Non-Prospective'**	**'Prospective'**
'Non-Prospective'	44 True Negative	32 False Positive	38 True Negative	16 False Positive
'Prospective'	6 False Negative	8 True Positive	12 False Negative	24 True Positive

To evaluate the quality of dividing the research area into provisionally prospective and non-prospective sections, machine learning metrics were calculated [48]. The results of these metrics are shown in Table 4. The metrics in the "Value (points)" row were calculated assuming that averaging windows were considered prospective only if they included ore objects. In contrast, the metrics in the "Value (trends)" row were obtained by considering objects as prospective if they fell within trend boundaries or intersected these boundaries.

Table 4. Metrics for Predictive Assessment of the Research Area.

№	Metric	Acc	TPR	PPV	FScore	TNR	FPR	Kappa	BA
1	Value (Points)	0.60	0.67	0.2	0.31	0.59	0.41	0.01	0.63
2	Value (Trends)	0.69	0.67	0.6	0.63	0.7	0.3	0.27	0.69

Note: Acc—Accuracy, TPR—True Positive Rate, PPV—Precision, FScore—F-measure, TNR—True Negative Rate, FPR—False Positive Rate, Kappa—Kappa Statistic, BA—Balanced Accuracy.

4. Discussion

When evaluating our classification of the research area into provisionally "prospective" and "non-prospective" averaging windows, a higher classification quality was established for the identification of prospective windows (classes 1 and 2) when compared to the boundaries of ore-bearing trends (Table 4, row 2). Several metrics support this finding. The accuracy and precision, which indicate how well the classified objects match reality, were significantly higher, with a 25% lower false positive rate. The kappa statistic was substantially higher for the assessment aligned with trend boundaries. A kappa value of 0.01 indicates no agreement in assigning objects to the binary classes of "prospective" and "non-prospective", whereas kappa = 0.27 suggests a satisfactory degree of agreement [49]. The balanced accuracy was also higher in the second case (0.69 vs. 0.63). Thus, the evaluation of the classification using quantitative metrics suggested that the developed approach is applicable for delineating prospective permeable areas of the Earth's crust.

The described technology is viable and could be applied in other regions if the crucial role of crustal fractures that could be identified as linear elements is supported by mineralization concepts. Also, the data table output from the pyLEFA software (as distinct from the lineament coverage parameters) can integrate geochemical, geophysical, and point occurrence data, making optical features recognition applications expandable. Despite the fact that the lineaments extracted from the remote sensing image using the optical recognition method could be partially masked by diluvium or vegetation coverage, the technology for their analysis may be formalized for use in cost-effective first pass prospectivity analyses based on machine learning technologies. The unsupervised and easily explainable method of classification, the k-means, can classify a territory into a formal number of classes; the connection with a target variable describing the presence of mineralization occurrence could be measured with the Alghofaili method [37]. Classes with greater prospectivity could then be considered as the primary targets for costly field surveying. Transferred to other regions, this approach could be the foundation for the future development of a non-biased decision-making instrument for mineral prospectivity analysis.

5. Conclusions

This study zoned the Carlin trend and its surrounding area based on the detection of first and second-order lineaments, the calculation of their parameters, and an export of the resulting data as a table. The k-means machine learning model created to classify the area is an unsupervised model, meaning it uses only predictor variables and does not consider the calculated kernel density distribution of point objects as a target variable. Despite this, the classification of square averaging windows proved applicable for the delineation of the area of the Carlin ore trend, as demonstrated by the model's quality assessment metrics. Identifying individual mineralizations with this model is challenging, since it does not account for the actual area and reserves of deposits. The present case study demonstrates the applicability of the proposed approach for the preliminary division of the study area and the planning of more detailed work.

The experience gained by using the pyLEFA program to generate a dataset for machine learning can be utilized to predict objects and areas in other regions, and the data obtained during prototyping may be implemented in new versions of pyLEFA.

Author Contributions: Conceptualization, S.S. and N.B.; methodology, S.S.; software, S.S.; validation, S.S. and N.B.; formal analysis, S.S. and N.B.; investigation, S.S. and N.B.; resources, S.S.; writing—original draft preparation, S.S.; writing—review and editing, S.S. and N.B.; visualization, N.B. All authors have read and agreed to the published version of the manuscript.

Funding: This research received no external funding.

Data Availability Statement: This study utilized freely available Landsat 9 OLI satellite data [50]. The pyLEFA software for lineament analysis is available on the program's official website [51] and source codes [22], and the scripts for performing the coverage data classification and constructing C-A curves are available in the program's prototyping repository section [45].

Acknowledgments: We would like to thank the reviewers for their helpful comments.

Conflicts of Interest: The authors declare no conflicts of interest.

References

1. Hofstra, A.H.; Cline, J.S. Goldin 2000. Paper 5: Characteristics and models for Carlin-type gold deposits. *Rev. Econ. Geol.* **2000**, *13*, 163–220.
2. Volkov, A.V.; Sidorov, A.A. Thegeological-genetic model of Carlin-type gold deposits. *Lithosphere* **2016**, *6*, 145–165.
3. Volkov, A.V.; Galyamov, A.L. Geophysical model of the Earth's crust, geodynamic conditions and prospects for discovering Carlin-type ore deposits in the Arctic zone of the Republic of Sakha (Yakutia). *Arct. Ecol. Econ.* **2020**, *1*, 82–94. [CrossRef]
4. Khomich, V.G.; Boriskina, N.G. Eventual solution to the problems of gold ore trends localization in the Carlin province (Nevada, USA). *Int. J. Earth Sci.* **2021**, *110*, 2043–2055. [CrossRef]
5. Muntean, J.L.; Cline, J.S.; Simon, A.C.; Longo, A.A. Magmatic hydrothermal origin of Nevada's Carlin-type gold deposits. *Nat. Geosci.* **2011**, *4*, 122–127. [CrossRef]
6. Saunders, J.A.; Hofstra, A.H.; Goldfarb, R.J.; Reed, M.H. 13.15—Geochemistry of Hydrotherma lGold Deposits. In *Treatiseon Geochemistry*, 2nd ed.; Holland, H.D., Turekian, K.K., Eds.; Elsevier: Amsterdam, The Netherlands, 2014; pp. 383–424. [CrossRef]
7. Muntean, J.L.; Davis, D.A.; Ayling, B. *The Nevada Mineral Industry 2016: Nevada Bureau of Mines and Geology*; Special Publication: MI-2016 (2017); Nevada Bureau of Mines and Geology University of Nevada Reno: Reno, NV, USA, 2017; pp. 1–187.
8. Richardson, C.A.; Seedorff, E. Exploring for structurally concealed Carlin-type mineralization: A case study from the northern Shoshone Range, Nevada, USA. *Ore Geol. Rev.* **2023**, *163*, 105738. [CrossRef]
9. Huff, D.; Fithian, M.T.; Fulton, A.; Holley, E.A. Alteration, Gold Deportment, Quartz Textures, and Fluid Characteristics in the Red Dot Depositat Marigold Mine, Nevada. *Econ. Geol.* **2024**, *119*, 1587–1609. [CrossRef]
10. Hu, R.Z.; Peng, J.T.; Ma, D.S.; Su, W.C.; Shi, C.H.; Bi, X.W.; Tu, G.C. Epoch of large-scale low-temperature mineralizations in south western Yangtze massif. *Miner. Depos.* **2007**, *26*, 583–596. (In Chinese with English abstract)
11. Huang, Y.; Hu, R.; Bi, X.; Fu, S.; Peng, K.; Gao, W.; Oyebamiji, A.; Zhaanbaeva, A. Low-temperature thermochronology of the Carlin-type gold deposits in south western Guizhou, China: Implications for mineralization age and geological thermal events. *Ore Geol. Rev.* **2019**, *115*, 103178. [CrossRef]
12. Price, J.G.; Coyner, A.R.; Muntean, J.; Driesner, D. Update on Nevada Mineral Production and Exploration. Available online: https://data.nbmg.unr.edu/Public/freedownloads/misc/presentations/NWMAupdate09.pdf (accessed on 13 December 2024).
13. Hronsky, J.M.A.; Groves, D.I.; Loucks, R.R.; Begg, G.C. A unified model for gold mineralisation in accretionary orogens and impli-cations for regional-scale exploration targeting methods. *Miner. Depos.* **2012**, *47*, 339–358. [CrossRef]
14. Cline, J.S. Nevada's Carlin-Type Gold Deposits: What We've Learned During the Past 10 to 15 Years. In *Diversity in Carlin-Style Gold Deposits*; Muntean, J.L., Ed.; Reviews in Economic Geology: Littleton, CO, USA, 2018; Volume 20, pp. 7–38. [CrossRef]
15. Manning, A.H.; Hofstra, A.H. Noble gas data from Gold field and Tonopa hepithermal Au-Ag deposits, ancestral Cascades Arc, USA: Evidence for a primitive mantle volatile source. *Ore Geol. Rev.* **2017**, *89*, 683–700. [CrossRef]
16. Muntean, J.L. *Diversity in Carlin-Style Gold Deposits*; Reviews in Economic Geology: Littleton, CO, USA, 2018; pp. 1–363. [CrossRef]
17. Kuchai, V.K.; Vesson, R.L. Fixed hot zone, types of orogenesis and Cenozoic tectonics of the USA West. *Geotectonics* **1980**, *2*, 49–62.
18. Richards, J.P. Post subduction porphyry Cu-Au and epithermal Au deposits: Products of remelting of subduction-modified lithosphere. *Geology* **2009**, *37*, 247–250. [CrossRef]
19. Khomich, V.; Shcheka, S.; Boriskina, N. Geodynamic factors in the formation of large gold-bearing provinces with Carlin-type deposits on continental margins in the North Pacific. *AIMS Geosci.* **2023**, *9*, 672–696. [CrossRef]
20. Scikit-Learn. K-Means Clustering. Available online: https://scikit-learn.org/stable/modules/generated/sklearn.cluster.KMeans.html (accessed on 5 December 2024).
21. Shevyrev, S.L. pyLEFA Pythonic Lineament Extraction and Fracture Analysis. Available online: http://lefa.geologov.net (accessed on 13 December 2024).

22. Users of pyLEFA 0.61a software. Incomplete List of Research Papers. Available online: http://lefa.geologov.net/our_users/ (accessed on 11 January 2025).
23. Ershov, E.I. *Fast Hough Transform as a Tool for Analyzing Two-Dimensional and Three-Dimensional Images in Problems of Searching for Lines and Linear Clustering*; Publishing House of IITPRAS: Moscow, Russia, 2018; pp. 1–118.
24. Volkov, A.V.; Galyamov, A.L.; Lobanov, K.V. Prospects for discovery of new large strategic metals deposits in the Arctic zone of Russia. *Proc. Annu. Fersman Sci. Sess. Geol. Inst. Kola Sci. Cent. Russ. Acad. Sci.* **2020**, *17*, 89–96. [CrossRef]
25. Henry, C.D.; John, D.A.; Leonardson, R.W.; McIntosh, W.C.; Heizler, M.T.; Colgan, J.P.; Watts, K.E. Timing of rhyolite intrusion and Carlin-type gold mineralization at the Cortez Hills Carlin-type Deposit, Nevada, US. *Econ. Geol.* **2023**, *118*, 57–91. [CrossRef]
26. Cline, J.S.; Hofstra, A.H.; Muntean, J.L.; Tosdal, R.M.; Hicke, K.A. Carlin-type gold deposits in Nevada: Critical geologic characteristics and viable models. In *Economic Geology 100th Anniversary Volume*; Hedenquist, J.W., Thompson, J.F.H., Goldfarb, R.J., Richards, J.P., Eds.; Society of Economic Geologists: Littleton, CO, USA, 2005; pp. 451–484.
27. Nutt, C.J.; Hofstra, A.H. Alligator Ridge District, East-Central Nevada: Carlin-Type Gold Mineralization at Shallow Depths. *Econ. Geol.* **2003**, *98*, 1225–1241. [CrossRef]
28. Srivastava, S.; Divekar, A.V.; Anilkumar, C.; Naik, I.; Kulkarni, V.; Pattabiraman, V. Comparative analysis of deep learning image detection algorithms. *J. Big Data* **2021**, *8*, 66. [CrossRef]
29. Yang, L.; Driscol, J.; Sarigai, S.; Wu, Q.; Chen, H.; Lippitt, C.D. Google Earth engine and artificial intelligence (AI): A comprehensive review. *Remote Sens.* **2022**, *14*, 3253. [CrossRef]
30. Eppelbaum, L.V.; Khabarova, O.; Birkenfeld, M. Advancing archaeo-geophysics through integrated informational-probabilistic techniques and remote sensing. *J. Appl. Geophys.* **2024**, *227*, 105437. [CrossRef]
31. Gil'manova, G.Z.; Goroshko, M.V.; Rybas, O.V.; Didenko, A.N. Lineament analysis of morphostructures of the Uchur-Maya basin (Southeastern Siberian Platform) from SRTM Data: Relationship with metallogeny. *Int. J. Geosci.* **2012**, *3*, 1176–1186. [CrossRef]
32. Hashim, M.; Ahmad, S.; Johari, M.A.; Pour, A.B. Automatic lineaments extraction in a heavily vegetated region using Landsat Enhanced Thematic Mapper (ETM+) imagery. *Adv. Space Res.* **2013**, *51*, 874–890. [CrossRef]
33. Miller, M.S.; Becker, W.T. Reactivated lithospheric-scale discontinuities localize dynamic uplift of the Moroccan Atlas Mountains. *Geology* **2014**, *42*, 35–38. [CrossRef]
34. Elmahdy, S.I.; Mohamed, M.M. Mapping of tectolineaments and investigate the irassociation with earthquakes in Egypt: A hybrid approach using remote sensing data. *Geomat. Nat. Hazards Risk* **2016**, *7*, 600–619. [CrossRef]
35. Meixner, J.; Grimmer, J.C.; Becker, A.; Schill, E.; Kohl, T. Comparison of different digital elevation models and satellite imagery for lineament analysis: Implications for identification and spatial arrangement of fault zones in crystalline basement rocks of the southern Black Forest (Germany). *J. Struct. Geol.* **2018**, *108*, 256–268. [CrossRef]
36. Hamann, J.S.; Baranskaya, A.V.; Geissler, W.H.; Baranov, B.V.; Tsukanov, N.V. Digital topographic analysis and lineament interpretation south of the Lena Delta, North Siberia: Landscape expression of it stectonic activity. *Geomorphology* **2024**, *457*, 109228. [CrossRef]
37. Alghofaili, Y. Interpretable K-Means: Clusters Feature Importances. Towards Data Science. Available online: https://towardsdatascience.com/interpretable-k-means-clusters-feature-importances-7e516eeb8d3c (accessed on 14 June 2024).
38. Landsat Mission. Available online: https://www.usgs.gov/landsat-missions (accessed on 19 May 2024).
39. Khalifani, F.M.; Bahroudi, A.; Aliyari, F.; Abedi, M.; Yousefi, M.; Mohammadpour, M. Generation of an efficient structural evidence layer for mineral exploration targeting. *J. Afr. Earth Sci.* **2019**, *160*, 103609. [CrossRef]
40. Aisabokhae, J.; Alimi, S.; Adeoye, M.; Oresajo, B. Geological structure and hydrothermal alteration mapping for mineral deposit prospectivity using airborne geomagnetic and multispectral data in Zuru Province, northwestern Nigeria. *Egypt. J. Remote Sens. Space Sci.* **2023**, *26*, 231–244. [CrossRef]
41. Straight Line Hough Transform. Scikit-Image Website. 2024. Available online: https://scikit-image.org/docs/0.24.x/auto_examples/edges/plot_line_hough_transform.html (accessed on 10 January 2024).
42. Probabilistic Hough Line Transform. Scikit-Image Website. 2024. Available online: https://scikit-image.org/docs/stable/api/skimage.transform.html#skimage.transform.probabilistic_hough_line (accessed on 10 January 2024).
43. Shevyrev, S.L. Algorithm of morphological analysis and identification of stream order in digital elevation model for development of open-source geoinformatic systems. *Adv. Curr. Nat. Sci.* **2018**, *12*, 390–395.
44. Yousefi, M.; Carranza, E.J.M. Prediction area (P-A) plot and C-A fractal analysis toclassify and maps for mineral prospectivity modelling. *Comput. Geosci.* **2015**, *79*, 69–81. [CrossRef]
45. Shevyrev, S.L. Experimental Scripts for pyLEFA Data Analysis. Repository. Available online: https://github.com/SergeiShevyrev/pyLEFA/tree/main/prototypes (accessed on 13 December 2024).
46. Heatmap (Kernel Density Estimation). QGIS Docs. Available online: https://docs.qgis.org/3.34/en/docs/user_manual/processing_algs/qgis/interpolation.html (accessed on 19 April 2024).
47. Syakur, M.A.; Khotimah, B.K.; Rohman, E.M.; Satoto, B.D. Integration K-means clustering method and elbow method for identification of the best customer profile Cluster. *IOP Conf. Ser. Mater. Sci. Eng.* **2018**, *336*, 012017. [CrossRef]

48. Evaluation Metrics for Classification Models—How to Measure Performance of Machine Learning Models? Available online: https://www.machinelearningplus.com/machine-learning/evaluation-metrics-classification-models-r/ (accessed on 7 February 2025).
49. Sim, J.; Wright, C.C. The KappaS tatistic in Reliability Studies: Use, Interpretation, and Sample Size Requirements. *Phys. Ther.* **2005**, *85*, 257–268. [CrossRef]
50. Earth Explorer. Available online: https://earthexplorer.usgs.gov (accessed on 30 May 2024).
51. Shevyrev, S.L. pyLEFA Program's Officia lWebsite. Lineament Extraction and Fracture Analysis. Available online: http://lefa.geologov.net/download-2/pylefa/ (accessed on 18 May 2024).

Disclaimer/Publisher's Note: The statements, opinions and data contained in all publications are solely those of the individual author(s) and contributor(s) and not of MDPI and/or the editor(s). MDPI and/or the editor(s) disclaim responsibility for any injury to people or property resulting from any ideas, methods, instructions or products referred to in the content.

minerals

MDPI

Article

Timing and Evolution of Gold Mineralization in the Maljavr Occurrence (NW Russia), NE Part of the Fennoscandian Shield

Arkadii A. Kalinin *, Nickolay M. Kudryashov and Yevgeny E. Savchenko

Geological Institute, Kola Science Center, Russian Academy of Science, 184200 Apatity, Russia; n.kudryashov@ksc.ru (N.M.K.); ye.savchenko@ksc.ru (Y.E.S.)
* Correspondence: a.kalinin@ksc.ru; Tel.: +7-921-663-68-36

Abstract: Gold occurrence Maljavr is the first Archean conglomerate-hosted gold mineralization found in the Fennoscandian Shield. Gold-mineralized metasomatic rocks form a set of lenses within a 10 m thick linear zone, conformable to the bedding of host conglomerates. The lenses are up to 10 m long and up to 1 m thick and they clearly exhibit three alteration envelopes: the rock in the central part consists of garnet and quartz or garnet-only; biotite, garnet, and quartz make the intermediate biotite–garnet envelope; hornblende, hedenbergite, and quartz are the principal rock-forming minerals in the outer zone of the lenses. All metasomatic rocks contain sulfide mineralization up to 15–20 vol.% and up to 0.6 g/t Au. The main ore mineral is pyrrhotite, and the minor minerals are arsenopyrite, chalcopyrite, pentlandite, löllingite, and troilite. The age of zircon from biotite gneiss in the zone of alteration is 2664 ± 18 Ma, this is considered as the time of formation of lenses of metasomatic rocks. Biotite gneiss-conglomerate and metasomatic rocks were later intruded by tourmaline granite pegmatite 2508 ± 7 Ma. The injection of pegmatite caused re-crystallization of sulfides (mainly arsenopyrite and löllingite) and redistribution of gold. Visible gold in association with Bi minerals native bismuth, ehrigite, maldonite, bismuthinite, joseite-B, and hedleyite was found in inclusions in recrystallized arsenopyrite and löllingite. Au content in the rocks with recrystallized arsenopyrite and löllingite is >1 g/t, up to 30 g/t in hand samples. The 2508 Ma pegmatite is interpreted as synchronous with formation of gold mineralization in its present form. The linkage of gold mineralization with pegmatite and geochemical association Au-As-Se-Te-Bi in the mineralized rocks agree with characteristics of intrusion-related gold deposits worldwide. Biotite gneiss–metaconglomerate, hosting the mineralized altered rocks, was the probable primary source of arsenic and gold for mineralization.

Keywords: Archean conglomerate; greenstone belt; alteration; gold; bismuth; ehrigite; U-Pb age; zircon

1. Introduction

Paleoplacers in Precambrian conglomerates are the most important genetic type of gold deposits: half of gold ever mined on the Earth was mined from Witwatersrand Mesoarchean conglomerate basin in South Africa [1]. Conglomerates with gold are known in other Precambrian shields in the world as well—for example, Tarkwa in Ghana (Western Africa) [2], Jacobina in Brazil (South America) [3], Pardo in Canada (North America) [4,5], Purdy's Reward in Pilbara Craton (Australia) [6,7], Gorumahisani-Badampahar conglomerates in Craton Singhbhum, India (Asia) [8]. High gold grades are mainly connected with alluvial placers along river paleovalleys, but sea beach paleoplacers are also known (for example, in Australia—[6]). In the Fennoscandian shield, conglomerates with gold were found in the Lehtinskaya and Onezhskaya structures in Russian Karelia and in the Central Lapland greenstone belt in Finland, where these gold occurrences are considered as Paleoproterozoic gold paleoplacers in fluvio-deltaic fans [9–11].

The Precambrian gold-bearing conglomerates are either monomictic with quartz pebbles or polymictic with pebbles of different composition, up to ultramafic pebbles [4–7].

Gold concentrates mainly in the conglomerate matrix, not in the pebbles [1–3]. The matrix may be clayey, sandy, or up to coarse-grained sands.

Paleoplacers (and gold as a mineral) were more or less modified during late regional metamorphic and hydrothermal-metasomatic events. The paleoplacers, mentioned in the previous paragraph, are mainly metamorphosed greenschist [1–11]. If these modifying events are more intensive (amphibolite facies), then gold deposits and occurrences will display features of orogenic and/or intrusion-related deposits: structural-control of mineralized rocks, mineral associations (amphibole, pyroxene, biotite, garnet, etc.) indicating high PT-conditions of metasomatic processes in the altered rocks, geochemical association of minor elements introduced by fluids of metamorphic or magmatic origin. In this case paleoplacers play a role as interim gold concentrators.

The Maljavr gold occurrence, located in amphibolite metamorphosed rocks in the Uragubsky greenstone belt (north-eastern part of the Fennoscandian Shield) (Figure 1, inset), is an occurrence of this kind. It is the first conglomerate-hosted gold occurrence of Archean age to be found in the Fennoscandian Shield.

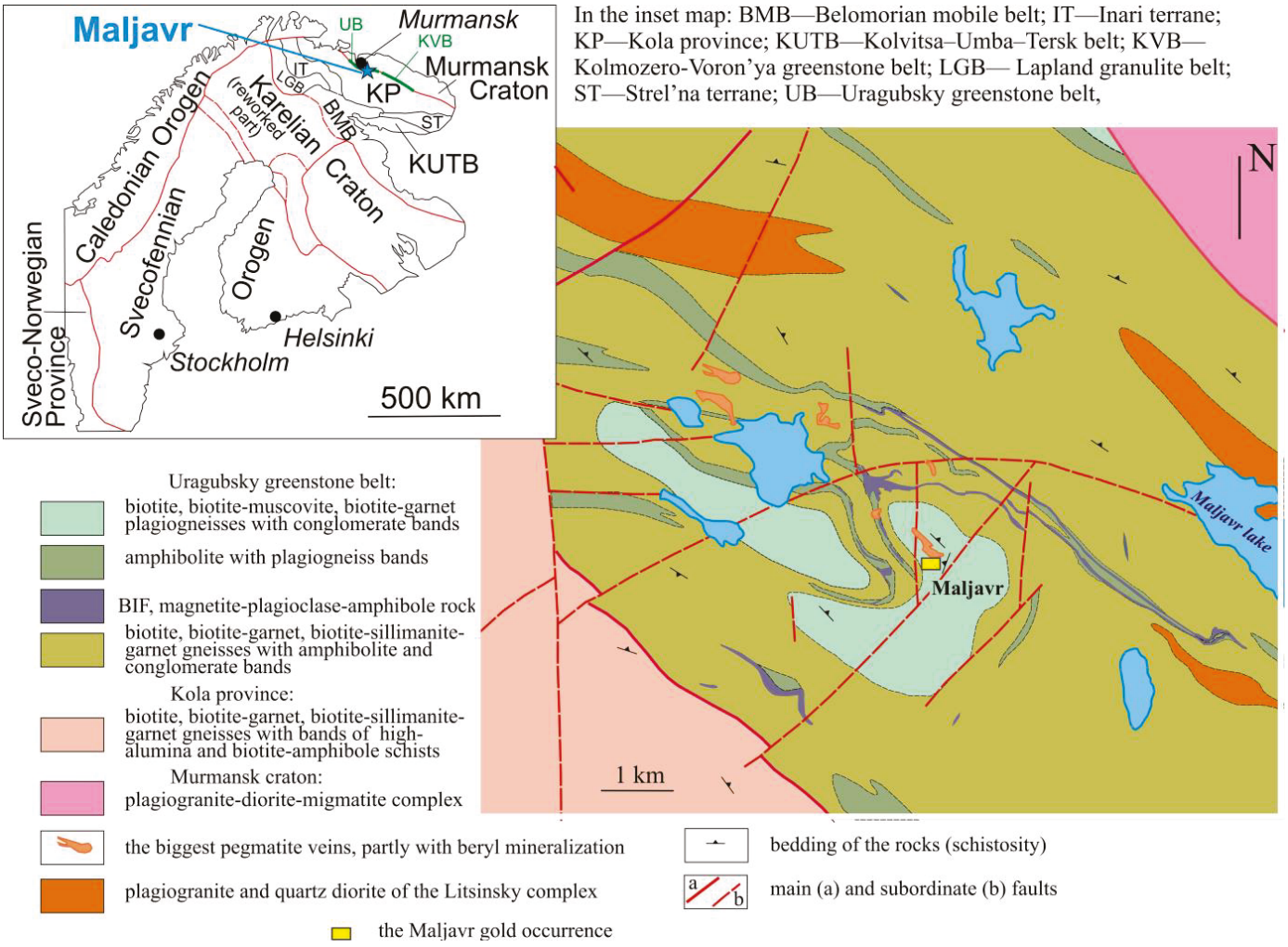


Figure 1. Schematic geological map of the Maljavr gold occurrence area, designed using data from [12], and position of the Maljavr occurrence in the tectonic map of the Fennoscandian Shield (inset).

2. Geological Overview of the Study Area

The Maljavr gold occurrence is located in the north-western part of Russian Arctic within the Uragubsky greenstone belt (Figure 1, inset). This belt, together with the larger and more extensive Kolmozero-Voron'ya belt in the south-east, makes a system of

greenstone belts, which traces the boundary between two big blocks of the Fennoscandian Shield—the Murmansk Craton and the Kola-Norwegian Province (or simply Kola Province) (Figure 1, inset).

The Uragubsky belt has an approximately 80 km strike length and a width of up to 4 km. The history of the formation of the Uragubsky and Kolmozero-Voron'ya belts, as described in [13], includes the following events: formation of an island arc at 2.87–2.83 Ga; a break of 50 million years and subsequent accretion of the island arc to the Murmansk continent; formation of an accretionary orogen (2.78–2.76 Ga); probable collapse of the orogen with formation of post-orogenic (or possibly anorogenic) granite intrusions.

The geological section of the Uragubsky belt includes the lower terrigenous sequence with basal conglomerates, the middle komatiite–basalt volcanic sequence, and the upper sedimentary-volcanic sequence [14]. The lower terrigenous sequence is composed mainly of fine and medium grained biotite and two-mica gneisses and cataclastic pebble and boulder–pebble rocks. The middle sequence is composed of mafic–ultramafic volcanics; it also contains tuff horizons, fine-grained biotite and biotite–amphibole gneiss horizons and lenses, layers of BIF and magnetite–amphibole rocks (Figure 1). The upper sedimentary-volcanic sequence consists predominantly of biotite, biotite–garnet, biotite–staurolite–sillimanite, biotite–sillimanite–garnet gneisses with subordinate thin foliated amphibolite bodies. Chemical composition of the gneisses corresponds to dacite and rhyolite; paragneisses are subordinate. The U-Pb SHRIMP II age of zircon from gneiss–metadacite is 2838 ± 23 Ma, this age is considered as the age of volcanism [15,16].

The volcanic–sedimentary rocks were metamorphosed amphibolite at a temperature of 600–620 °C, under a pressure of 4 kbar [17]. The U-Pb age of metamorphism was reported as 2786 ± 31, 2774 ± 12 Ma (SHRIMP-II, zircons of metamorphic genesis) [15], 2763 ± 8 Ma [14].

The volcanic–sedimentary sequences are cut by intrusions of plagioclase/microcline granite (2696 ± 9 Ma), aplite veins (2697 ± 10 Ma) [18], and tourmaline granite pegmatite veins.

Pebble conglomerates were mapped at the southern contact of the belt with migmatized gneisses and plagiogranites of the Kola province in the lower part of the basal terrigenous sequence [14,19,20]. Thickness of the conglomerate layer is 2–5 m, sometimes up to 10 m. The conglomerates are matrix-supported, pebble dimensions vary predominantly from 3 × 5 to 5 × 10 cm. Fine grained greywacke (biotite and muscovite–biotite gneiss) makes the conglomerate matrix.

Layers and lenses of pebble conglomerate and gritstone were also observed throughout the entire biotite gneiss sequence. Every conglomerate layer is an alternation of conglomerate, gritstone, and sandstone (Figure 2A,B) with thickness of strata 10–20 cm. The rocks preserved obvious signatures of their terrigenous origin such as graded rhythmical bedding (Figure 2A,B) and psephytic–psammitic structures. The clasts consist predominantly of plagiogranite (up to diorite) and quartz; pebbles and gravel are cemented by biotite or biotite–muscovite gneiss–metagraywacke. Plagiogranite in the pebbles contains partially sericitizated oligoclase, quartz, and minor biotite and tourmaline. Gneiss in the matrix is similar to the biotite paragneiss in the lower sequence of the volcanic–sedimentary section as it consists of quartz, plagioclase (labradorite), biotite, ±muscovite; accessory minerals are apatite, zircon, chlorite, tourmaline, allanite.

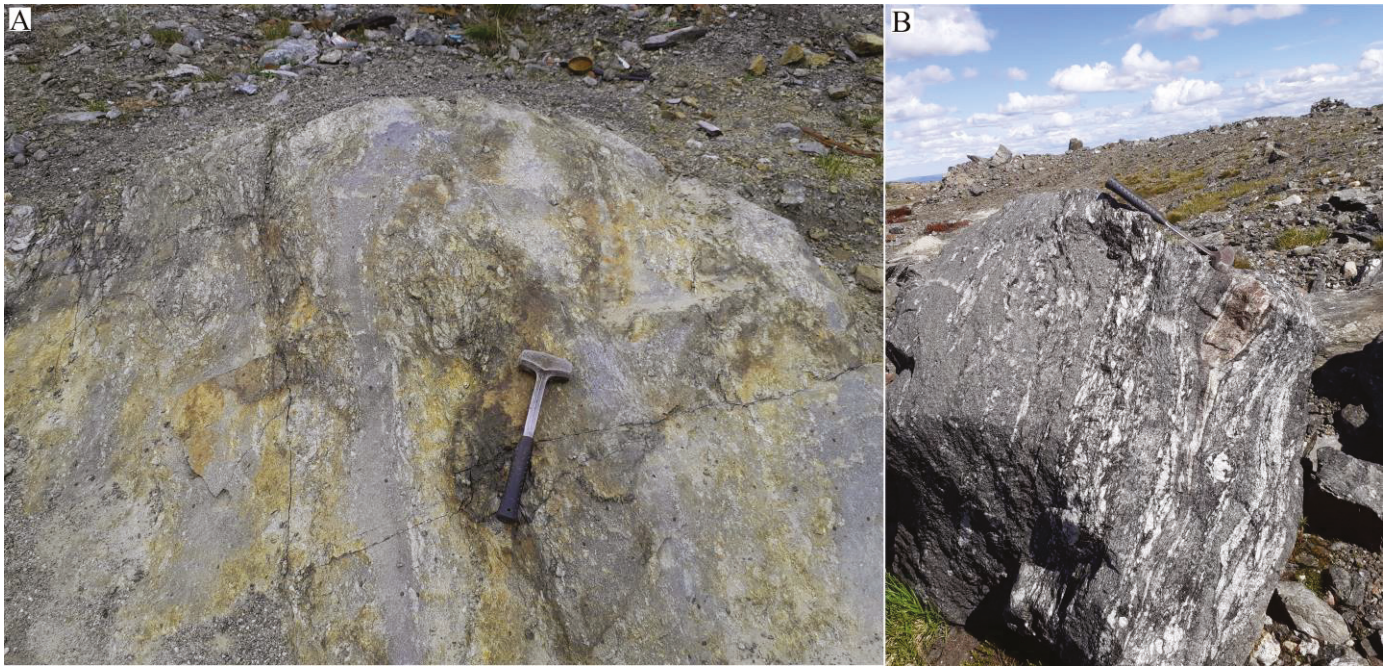


Figure 2. Graded rhythmical bedding in conglomerate in an outcrop (**A**) and in a block (**B**).

3. Materials and Methods

Investigations of wall rock alteration, metasomatic zoning, and determination of pre-ore, ore-related, and post-ore mineral assemblages in altered rocks were based on the study of rocks in the outcrops, on examination of mineral relations in thin and polished sections, as well as on the results of assaying the primary and altered rocks. More than 50 specimens and samples (1.5–10 kg), supplemented by chips for thin and polished sections, were collected by the authors in the outcrops and trenches in 2022–2023. The samples were assayed for 12 major (rock-forming) elements in the chemical laboratory of the Geological Institute, Kola Science Centre of Russian Academy of Sciences, Apatity, Russia, with flame atomic absorption spectrometry (FAAS). Data on 40 trace elements, which determined the geochemical characteristics of the rocks, were obtained by ICP-MS with nitric acid digestion in the Institute of Geology and Geochemistry of the Ural Branch of the Russian Academy of Sciences, Ekaterinburg,

Mineral composition of the ores was studied in thin and polished sections of the rocks and in epoxy-polished sections of heavy mineral concentrates, separated with the Sochnev magnet and bromoform from the crushed hand samples. Thin and polished sections were studied with the reflected light microscope Axioplan 2 Imaging (Carl Zeiss, Jena, Germany) and with the electron microscope Zeiss Evo-25 (Carl Zeiss, Jena, Germany), equipped with the energy-dispersive system (EDS) AZtec UltimMax-100 (Oxford Instruments, Oxford, UK) in the Geological Institute of the Kola Science Center. Sulfides, tellurides, and native metals were identified and photographed in the regime of back-scattered electron image (BSE). Chemical composition of mineral phases was defined with EDS AZtec UltimMax-100 (Oxford Instruments), operating at accelerating voltage 20 kV, beam current 2 nA, spectrum accumulation time 100 s. The following analytical lines and standards were used for silicates and oxides: FKα (fluorapatite), SiKα and CaKα (wollastonite), ClKα (atacamite), FeKα (hematite), LaLα (LaSe), CeLα (CeS), NdLα ($LiNd(MoO_4)_2$), TiKα and NaKα (lorenzenite), MnKα ($MnCO_3$), SKα, and SrLα, MgKα, AlKα, KKα, NiKα (metal); analytical lines (standards) for sulfides and metals were PbMα and TeLα (PbTe, in some cases HgTe for TeLα), BiMα and SeLα (Bi_2Se_3), AsKα (InAs), AgLα (metal), AuMα (metal), FeKα и SKα (pyrite) (in some cases metal for FeKα), NiKα (metal), CoKα, (metal), ZnKα (metal or sphalerite), BrKα (KBr), CdLα (metal or CdSe).

Microprobe analysis (MS-46, CAMECA, Gennevilliers Cedex, France), accelerating voltage 22 kV, beam current 30–40 nA, standards (analytical lines; detection limit, wt%): $Fe_{10}S_{11}$ (FeKα; 0.01 and SKα; 0.05), Bi_2Se_3 (BiMα; 0.1 and SeKα; 0.05), $LiNd(MoO_4)_2$ (MoLα; 0.1), PbS (PbMα; 0.1), pure metals Co (CoKα; 0.01), Ni (NiKα; 0.01), Cu (CuKα; 0.01), Pd (PdLα; 0.05), Ag (AgLα; 0.05), Te (TeLα; 0.05), Re (ReLα; 0.05), Au (AuLα; 0.05), was performed for grains larger than 20 μm (analyst Ye. Savchenko). Beam size was 2–10 nm, depending on stability of the matter under the beam current. Measurement time was 10 s for major elements, 20 s for minor elements, and 10 s for background measurements. The results of 4–5 measurements for each element were averaged.

Zircon U-Pb dating was undertaken at the Geological Institute of the Kola Science Center (Apatity, Murmansk region, Russia). Isotope dilution-thermal ionization mass spectrometry (ID-TIMS) was used. Prior to analysis, zircons were extracted using magnetic separation with the Sochnev magnet and heavy liquid separation in bromoform, with surface contamination removed using alcohol, acetone, and 1 M HNO_3.

The zircon dissolution and chemical recovery of Pb and U were performed using the technique described in [21], with U and Pb concentrations determined by isotope dilution employing a Finnigan MAT-262 (RPQ) mass spectrometer and a mixed ^{208}Pb + ^{235}U tracer, with silica gel used as an ion emitter. Blank levels had maximum values of 100 ng Pb and 10–50 ng U, and all isotope ratios were corrected for mass fractionation by analysis of the SRM-981 and SRM-982 standards (0.12 $\pm$ 0.44%). The uncertainties on the resulting U-Pb ratios are 0.5%. The raw experimental data were processed using PbDAT and ISOPLOT [22,23], with age values calculated using conventional U decay constant values [24] and common Pb corrections following [25]. All uncertainties are reported at a 2σ confidence level.

4. Results

4.1. The Maljavr Occurrence: Geological Structure, Alteration, Ore Minerals

The Maljavr gold occurrence is located at the SW flank of the belt, where biotite gneiss of the lower sequence forms an anticline fold with the upper bend dipping SE (Figure 1). Biotite gneiss (metamorphosed sandstone, gritstone, and conglomerate) is cut by a tourmaline granite pegmatite N-striking vein, about 40 m thick (Figure 3). Rock forming minerals in pegmatite are quartz, plagioclase (albite–oligoclase), microcline, muscovite, and tourmaline, and minor minerals are biotite, apatite, zircon.

The western contact of the vein is sharp, but the eastern contact is transitional, through a 10 m-wide zone of foliation (Figure 4A) and migmatization (Figure 4B). In the zone of foliation, pebbles are deformed together with the matrix (Figure 4A). The biotite gneiss is intensely tourmalinizated at both sides of the pegmatite vein (Figure 3). Deformation and tourmalinization intensity in the biotite gneiss decreases within ~20 m distance from the pegmatite contact.

Smaller lenses of pegmatite were found up to 50 m away from the main pegmatite vein and zone of migmatization. The biggest lenses are up to 20 m long, smaller lenses are less than 20–30 cm (Figure 4C,D). The pegmatite lenses cut biotite gneiss, including the pebbles in metaconglomerate (Figure 4C).

A series of lenses of metasomatic rocks is controlled by a ~10 m thick zone, striking NNE 10–15° and dipping vertically, conformably to schistosity in the biotite gneiss (Figure 3). This zone was traced for 50 m in outcrop and farther on is covered by soil. The biggest lenses of metasomatic rocks reach the length of 10 m and 1 m thickness (Figure 3), small lenses have less than 1 m strike length (Figure 5).

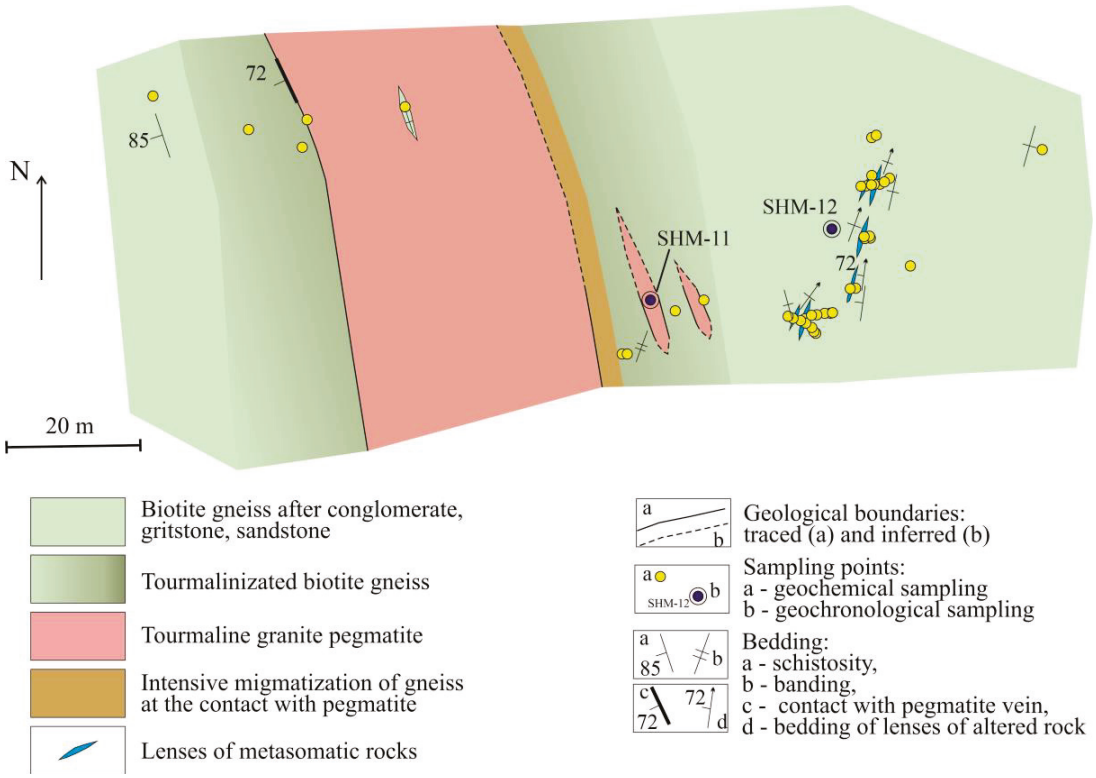


Figure 3. Schematic geological map of the Maljavr gold occurrence.



Figure 4. Photographs of outcrops in the Maljavr occurrence. (**A**) foliation in the biotite gneiss–metaconglomerate; (**B**) migmatization at the contact of biotite gneiss with pegmatite; (**C**,**D**) small pegmatite lenses, cutting schistosity in metaconglomerate.

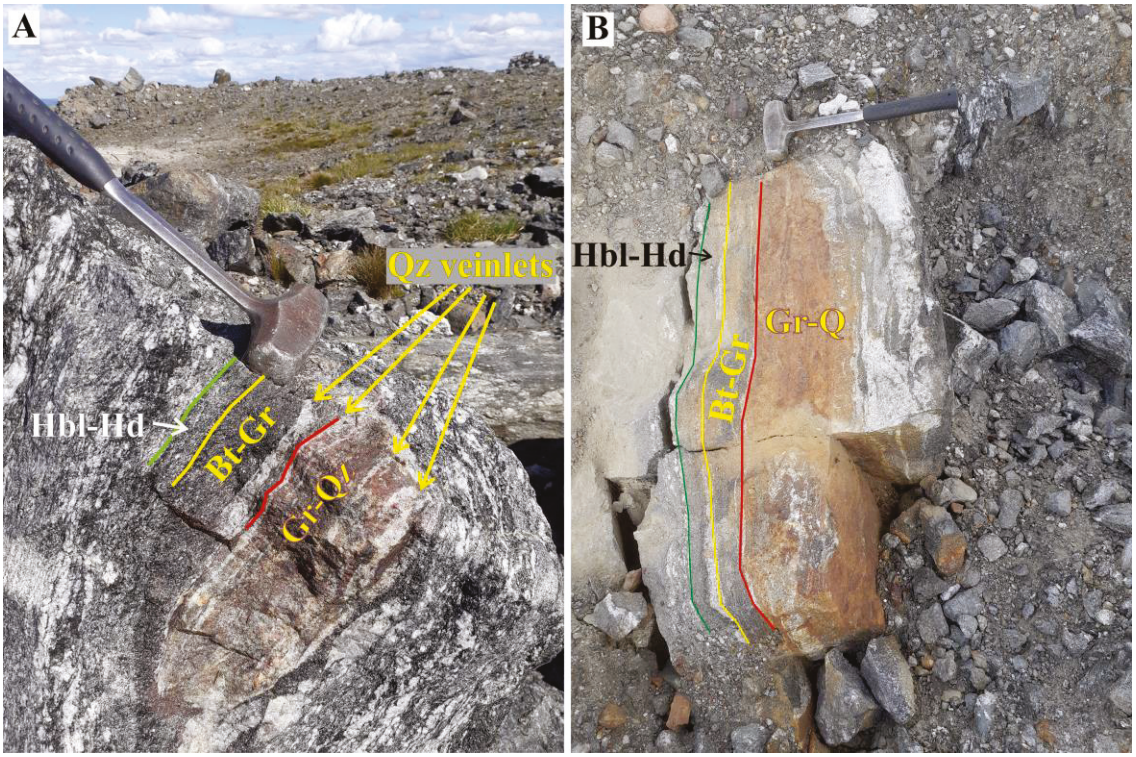


Figure 5. Lenses of altered rocks in the metaconglomerate in a block (**A**) and in an outcrop (**B**). Red, yellow and green lines show the boundaries of garnet-quartz (Gr-Q), biotite-garnet (Bt-Gr) and hornblende-hedenbergite (Hbl-Hd) metasomatic rocks, correspondingly.

The lenses of metasomatic rocks clearly exhibit three alteration envelopes (Figure 5). The central parts (the cores) of the lenses consist of garnet and quartz (Figure 6D) or garnet-only (garnetite) (Figure 5), the cores are 10–40 cm thick. Biotite, garnet, and quartz make the intermediate biotite–garnet envelope (Figure 6C). Thickness of this envelope is up to 20 cm in the biggest lenses. Hornblende, hedenbergite, and quartz are the principal rock-forming minerals in the outer zone, where minor minerals are epidote, quartz, and garnet (Figure 6B). Thickness of the outer hornblende–hedenbergite envelope is variable, not more than 20 cm; in some lenses, this zone is reduced or absent.

Metasomatic rocks are massive, medium- to coarse-grained: garnet grains reach 1 cm, other minerals are 1–3 mm in size. Biotite flakes and needle crystals of amphibole and pyroxene are differently oriented (Figure 6B,C). Quartz veinlets penetrate all zones of metasomatic rocks, the veinlets are oriented along the strike of the lenses (Figure 5).

Biotite gneiss in between the lenses is generally similar to the gneiss throughout the entire biotite gneiss sequence, but garnet appears (1–2 vol.%) and sulfide content increases from <1 to 1–2 vol.% close to the contact with metasomatic lenses.

The spidergrams (Figure 7) illustrate change in chemical composition of the rocks during alteration processes. The diagrams exhibit general loss of SiO_2 and Na_2O and gain of FeO in all metasomatic rocks: Fe content systematically increases from the outer envelope to the core of the lenses. Al_2O_3, CaO, MgO, K_2O were re-deposited during alteration and formed metasomatic zoning. Hornblende–hedenbergite rock has high CaO, low Al_2O_3, Na_2O, and K_2O. Biotite–garnet rock contains high Al_2O_3, MgO, and K_2O, but low CaO. Garnet–quartz rock in the central part of the lenses has high FeO, and lower content of other general elements (Figure 7, Table S1).

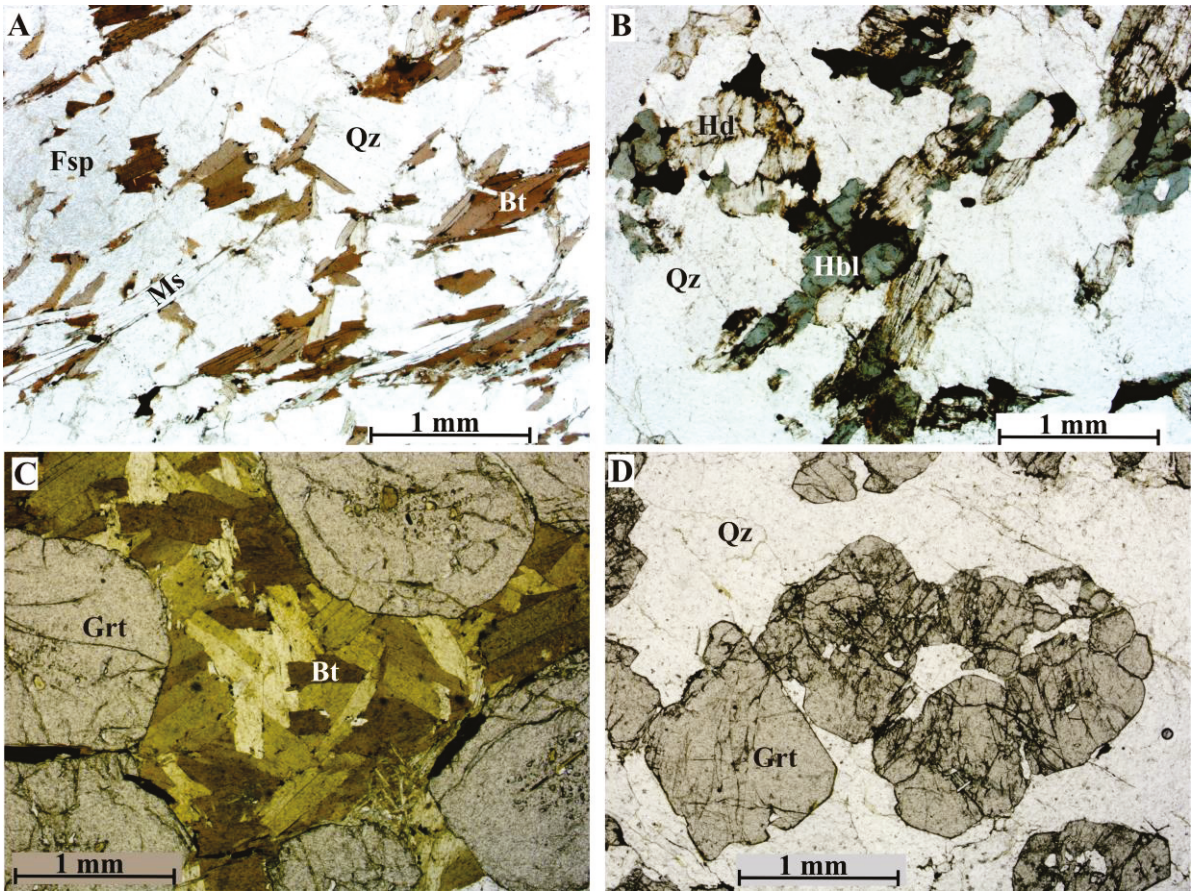


Figure 6. Thin section microscope photos of unaltered biotite gneiss (**A**), hornblende–hedenbergite (Hbl-Hd) (**B**), biotite–garnet (Bt-Gr) (**C**) and garnet–quartz (Gr-Q) (**D**) metasomatic rocks, plane polarized light. Bt—biotite, Fsp—feldspar (plagioclase), Grt—garnet, Hbl—hornblende, Hd—hedenbergite, Ms—muscovite, Qz—quartz. Here and below all mineral symbols are given according to IMA recommendations [26].

Change of mineral composition of the rocks during alteration processes is chiefly limited to severe alteration of plagioclase in the biotite gneiss, recrystallization of biotite and quartz, and formation of garnet, amphiboles, and pyroxene. Sodium, released during plagioclase alteration, was removed from the altered rocks. Calcium was re-deposited in the outer hornblende–hedenbergite envelope, where it formed hornblende, hedenbergite, and high-Ca almandine. The residual alumina from the altered plagioclase together with iron, which was added to the system, formed garnet (almandine) in biotite–garnet and garnet–quartz rocks. Potassium, concentrated in the primary biotite in gneiss, was re-deposited mainly in the garnet–biotite rock.

GER (general element ratio) diagrams [27] (Figure 8) illustrate change of both mineral and chemical composition during alteration and formation of metasomatic zoning in terms of element ratios: loss of sodium due to severe alteration of plagioclase (Figure 8A,B), redistribution of potassium, connected with recrystallization of biotite (Figure 8A,B), addition of Fe and redistribution of Ca and Al, which lead to formation of Ca-rich almandine, hornblende, and hedenbergite (Figure 8C,D).

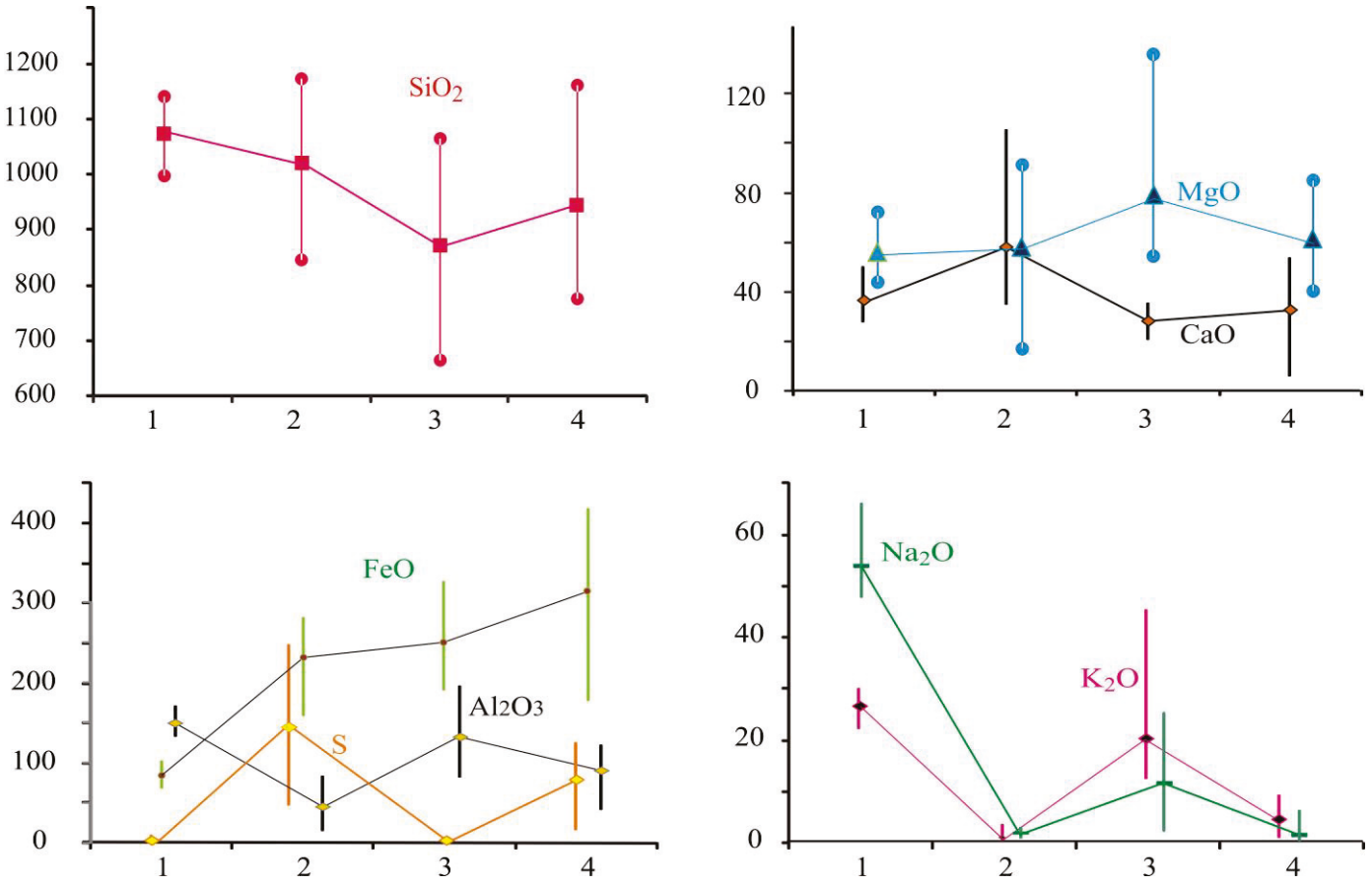


Figure 7. Variation of the main components content in altered rocks: maximum, minimum and mean values, in molar quantities. Rocks: 1—unaltered biotite plagiogneiss (8 samples), 2–4—altered rocks: 2—hornblende–hedenbergite (11), 3—garnet–biotite (5), 4—garnet–quartz and garnet-only (10 samples) (see Table S1 for assay results).

All Fe-Mg silicates in the altered rocks are Fe-rich (Table S2): pyroxene is hedenbergite, amphiboles are ferro–hornblende and grunerite, chlorite is chamosite, and mica is Fe-biotite. Garnet is almandine in the garnet–quartz and garnet–biotite rocks, and Ca-rich almandine with mole proportion of grossular 14–28% in the hornblende–hedenbergite rock (Table S2).

Altered rocks, if compared with the unaltered biotite gneiss, display loss of Rb, Cs, Sr, Ba, Zr, Nb, LREE, U, Pb, and gain of As, Ag, Te, Se, Bi, Cu (Table S3, Figure 9). It is important to note high As in the unaltered biotite gneiss; arsenic is 3–15 times higher than the average for the upper continental crust [28]. Concentration of As, Te, Se, and Bi in the gold-mineralized rocks is by 1–2 orders of magnitude more than in non-mineralized metasomatic rocks (Table S3, Figure 9).

Gold content in the unaltered biotite gneiss is 0.004 g/t (Table S1) and increases in the lenses of metasomatic rocks. Distribution of gold is very uneven: sulfide-mineralized rocks in all metasomatic envelopes contain 0.03–0.5 g/t Au, but where coarse-grained arsenopyrite appears, gold content increases to >1 g/t, and reaches 30 g/t in some hand samples [12]. Channel sampling across one of the lenses of altered rocks gave 1.78 g/t Au for 0.8 m [12].

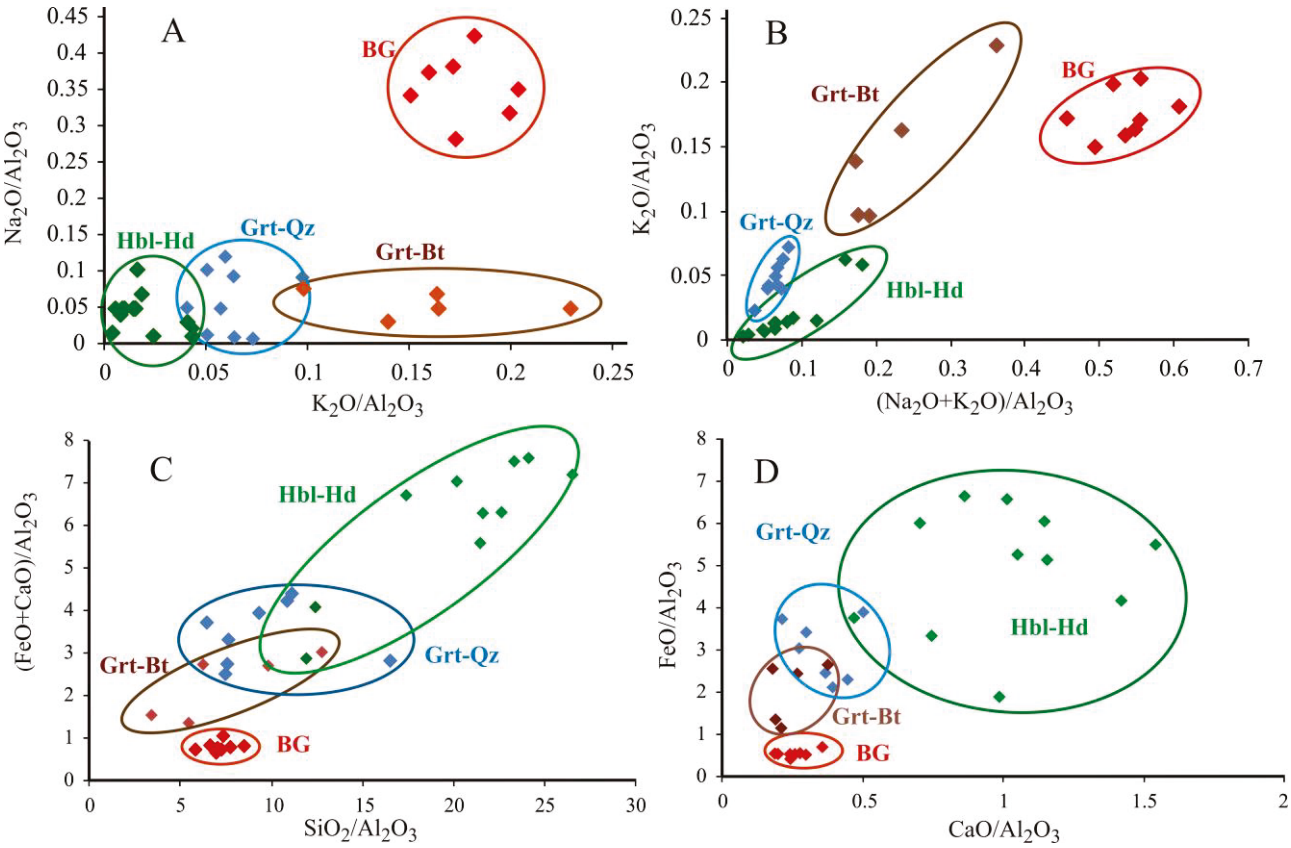


Figure 8. General element ratio diagrams [27] for altered rocks of the Maljavr occurrence in coordinates Na_2O/Al_2O_3—K_2O/Al_2O_3 (**A**), K_2O/Al_2O_3—$(Na_2O + K_2O)/Al_2O_3$ (**B**), $FeO + CaO)/Al_2O_3$—SiO_2/Al_2O_3 (**C**), and FeO/Al_2O_3—$CaO)/Al_2O_3$ (**D**). BG—unaltered biotite gneiss (red symbols); altered rocks: Gr-Qz—garnet–quartz rock (blue), Grt-Bt—garnet–biotite rock (brown), Hbl-Hd—hornblende–hedenbergite rock (green symbols).

Unaltered biotite gneiss (metaconglomerate, metagritstone, metasandstone) contains disseminated sulfide mineralization < 1 vol.%; sulfide minerals are pyrrhotite (prevails), arsenopyrite, rarely chalcopyrite, and late pyrite; oxide minerals are ilmenite and rare magnetite. No sulfide mineralization was found in the migmatizated rocks at the contact of biotite gneiss with pegmatite.

Sulfide content increases significantly to 1 to 25 vol.% in the lenses of metasomatic rocks, sulfide-rich rocks (>10 vol.%) were found in different alteration envelopes of the lenses. Texture of mineralization is disseminated, veinlet-disseminated, or nested. Mineral composition is not complicated: the main minerals are pyrrhotite and arsenopyrite, minor sulfides are chalcopyrite, löllingite, troilite, pentlandite, molybdenite. Oxide minerals are ilmenite and magnetite (the latter is more rare, but up to 10% in some samples).

Two generations of arsenopyrite were detected in the metasomatic rocks, the generations differ in grain form and size (Figures 10 and 11), and in chemical composition (Table 1). The early arsenopyrite-1 occurs as small grains up to 0.2 mm in disseminated sulfides. It contains high Co and Ni, and some grains are clearly zoned (Figure 11A) with As-, Co- and Ni-rich core (As 38.2–39.7 at.%, Co 3.12–4.11 wt%, Ni 1.62–2.89 wt%) and lower As, Co and Ni in the rim (As 34.6–35.0 at.%, Co 2.23–2.44, and Ni 0.38–0.81 wt%) (Table 1). Late re-crystallized coarse-grained (0.5–3 mm in size) arsenopyrite-2 is disseminated in the altered rocks, or it forms chains of euhedral grains (Figures 11B and 12–the detailed fragment). Zoning in arsenopyrite-2 is complicated—there are zones with lower (32.7–33.8 at.% As) and higher (34.6–35.9 at.% As) arsenic alternate in the grains (Figure 11C,D). Co and Ni impurities are below 0.5 wt%.

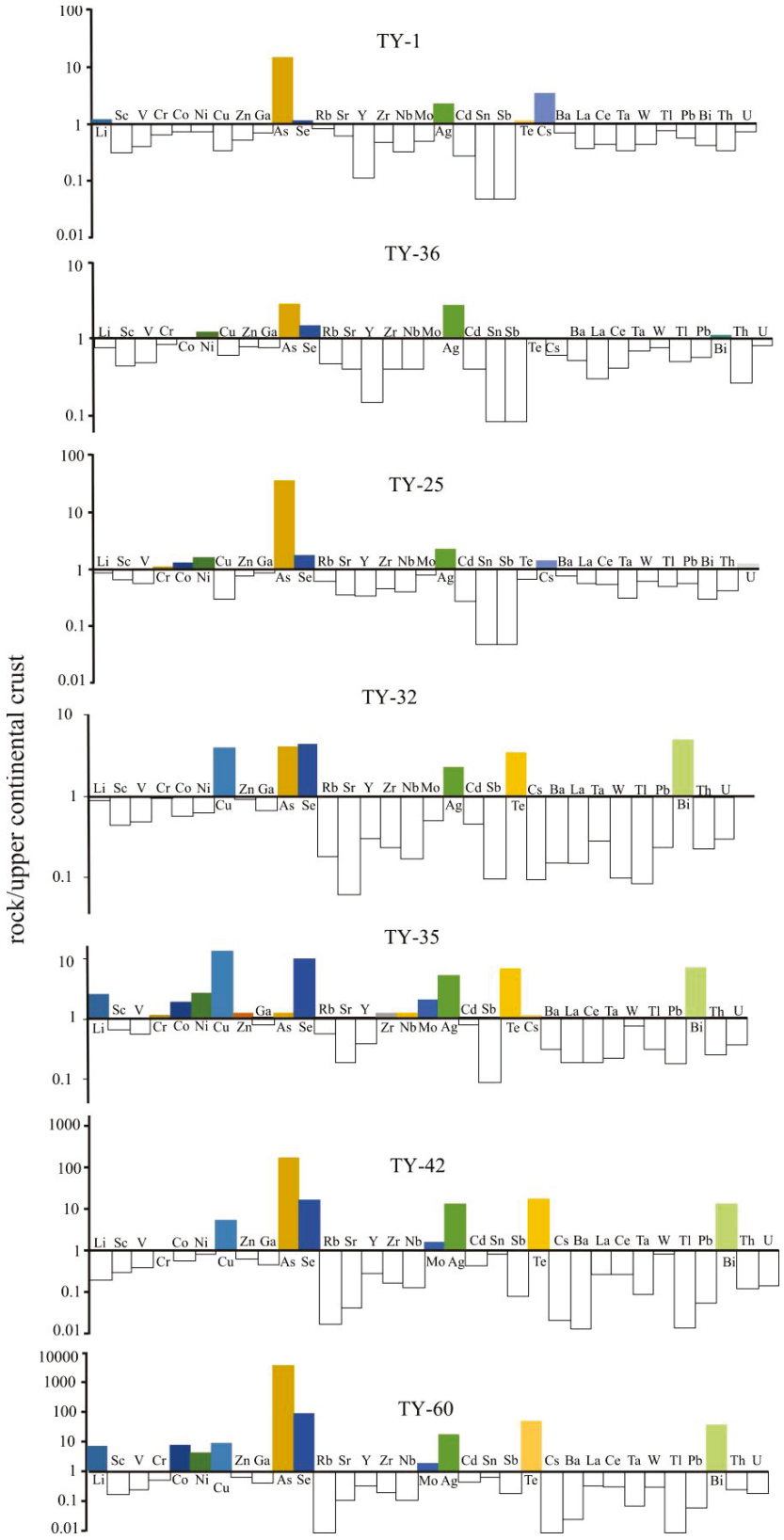


Figure 9. Geochemical spectra of unaltered biotite gneiss–metaconglomerate (TY-1, TY-36), slightly altered biotite gneiss at the contact with a lens of altered rock (TY-25), unmineralized altered rocks (samples TY-32, TY-35 with 0.04–0.05 g/t Au), and gold-mineralized altered rocks (samples TY-42, TY-60 with >1 g/t Au), normalized by the average for the upper continental crust [28].

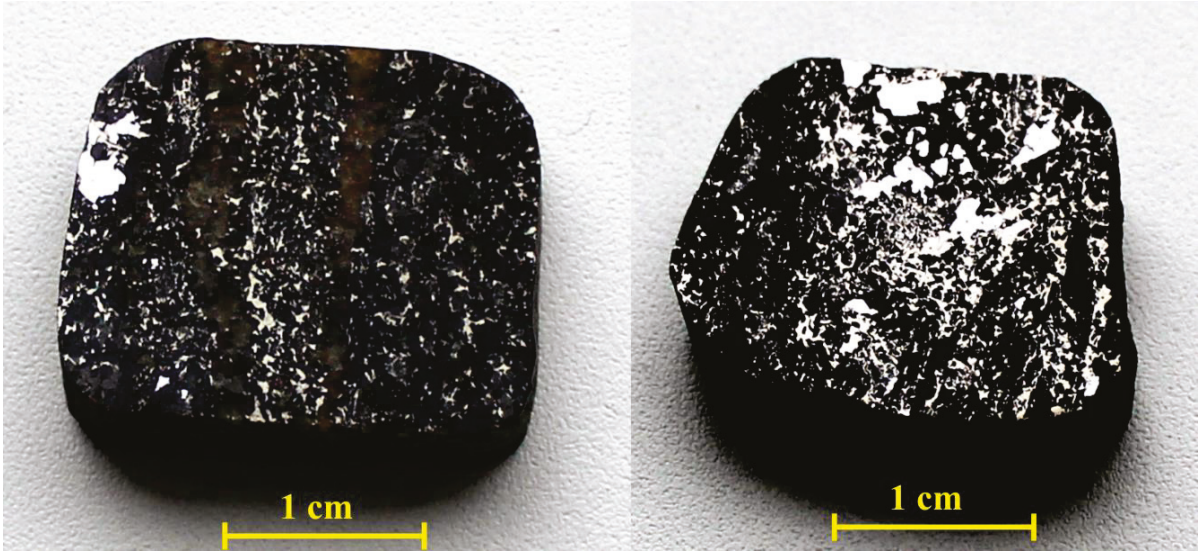


Figure 10. Recrystallized arsenopyrite (big white grains) in hornblende–hedenbergite metasomatic rocks with pyrrhotite–arsenopyrite dissemination. Photos of polished sections.

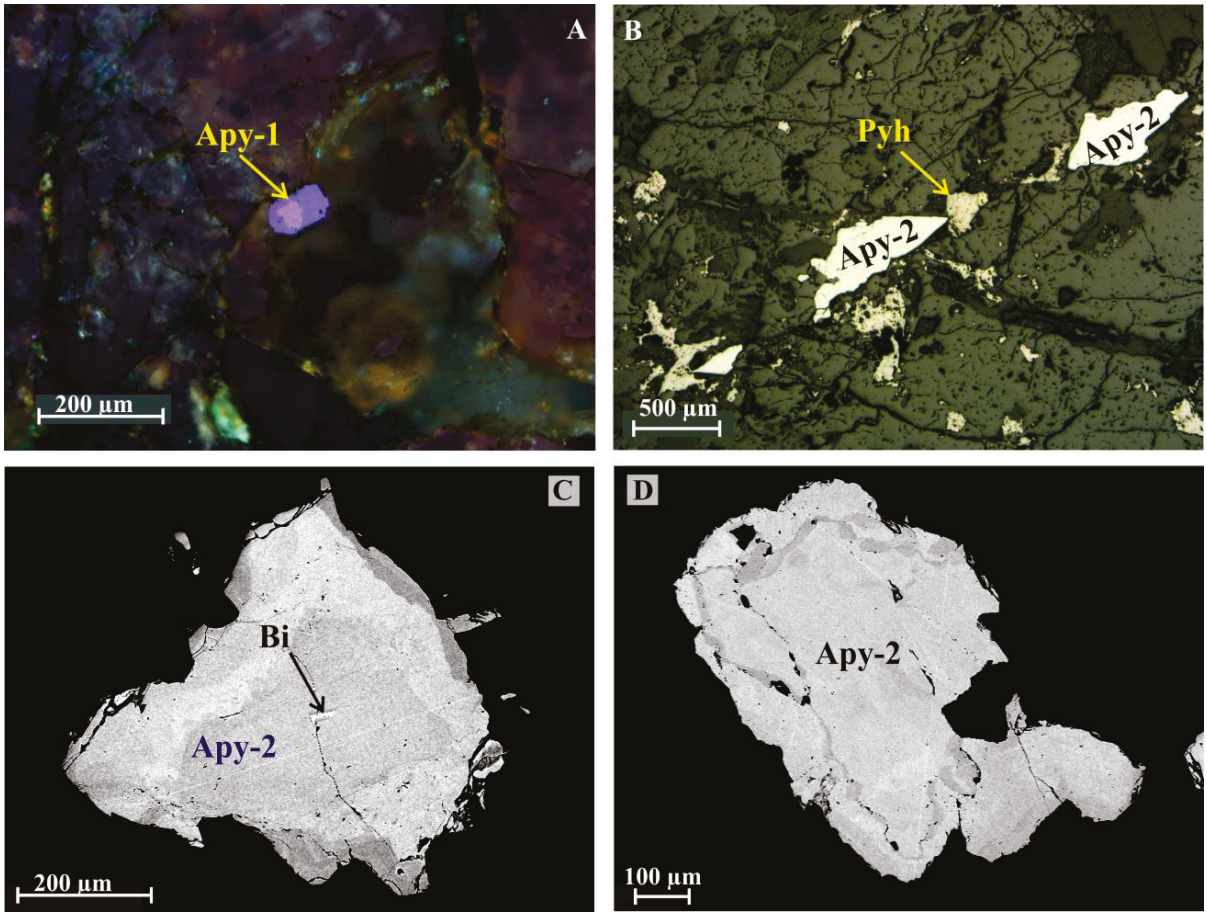


Figure 11. Arsenopyrite from the Maljavr gold occurrence. (**A**) zoning in arsenopyrite-1, polished section photo, crossed polarized light. (**B**) a chain of arsenopyrite-2 grains in hornblende–hedenbergite rock, polished section photo, plane polarized light. (**C**,**D**) complicated zoning in arsenopyrite-2—back-scattered electron (BSE) images: arsenic-rich zones are lighter than arsenic-poor. Apy—arsenopyrite, Bi—native bismuth.

Table 1. Microprobe data for arsenopyrite (Apy) and löllingite (Lo) of the Maljavr gold occurrence, wt%.

Sample No.	ТУ-25-1	ТУ-25-1	ТУ-25-2	ТУ-25-2	ТУ-31	ТУ-31	ТУ-41	ТУ-41	ТУ-45	ТУ-45	TY-41-1	TY-41-1	TY-41-2	TY-41-2	TY-29	TY-42	TY-42	TY-41	TY-41	TY-29	TY-42	TY-42
Mineral	**Apy-1-C**	**Apy-1-R**	**Apy-1-C**	**Apy-1-R**	**Apy-1-C**	**Apy-1-R**	**Apy-1-C**	**Apy-1-R**	**Apy-1-C**	**Apy-1-R**	**Apy-2-C**	**Apy-2-R**	**Apy-2-C**	**Apy-2-R**	**Apy-2**	**Apy-2**	**Apy-2**	**Lo**	**Lo**	**Lo**	**Lo**	**Lo**
S	14.94	18.32	16.08	18.94	15.49	18.36	18.16	20.03	17.93	19.28	18.66	19.30	17.77	19.28	17.37	18.06	18.21	1.40	1.98	1.84	1.83	2.04
Fe	26.46	31.4	27.92	30.56	27.73	31.49	33.15	34.61	31.89	33.65	33.25	34.54	33.43	34.36	33.78	33.62	33.63	27.66	28.23	28.03	25.11	26.31
Co	3.76	2.32	3.12	2.44	4.11	2.23	0.47	0.13	1.28	0.48	0.34	0.12	0.39	0.09	0.07	0.24	0.17	0.08	0.13	0.10	0.49	0.42
Ni	2.89	0.64	2.25	0.81	1.62	0.38	0.24	bdl	0.29	0.02	0.49	bdl	0.38	bdl	0.17	0.26	0.11	0.09	0.10	0.13	2.07	0.68
As	51.83	47.69	50.57	47.45	50.93	46.8	47.86	45.47	48.52	46.38	47.96	46.72	48.59	45.80	48.80	47.87	48.09	70.27	69.35	69.94	70.26	70.04
Total	99.88	100.37	99.93	100.2	99.88	99.26	99.88	100.25	99.91	99.81	100.70	100.67	100.55	99.53	100.19	100.05	100.21	99.51	99.79	100.04	99.76	99.49
Atoms per formula unit																						
S	0.805	0.946	0.852	0.965	0.831	0.957	0.94	1.014	0.927	0.986	0.952	0.982	0.921	0.992	0.908	0.937	0.939	0.089	0.125	0.116	0.114	0.127
Fe	0.819	0.931	0.850	0.894	0.854	0.942	0.985	1.006	0.946	0.987	0.975	1.009	0.996	1.015	1.014	1.001	0.996	1.009	1.024	1.013	0.904	0.944
Co	0.110	0.065	0.090	0.068	0.120	0.063	0.013	0.004	0.036	0.013	0.009	0.003	0.011	0.002	0.002	0.007	0.005	0.003	0.004	0.003	0.017	0.014
Ni	0.085	0.018	0.065	0.023	0.048	0.011	0.007	0.000	0.008	0.001	0.014	0.000	0.011	0.000	0.005	0.007	0.003	0.003	0.003	0.004	0.071	0.023
As	1.195	1.054	1.148	1.035	1.169	1.043	1.06	0.986	1.073	1.014	1.048	1.018	1.079	1.008	1.092	1.063	1.061	1.911	1.875	1.884	1.886	1.873
at.% As	39.7	35.0	38.2	34.7	38.7	34.6	35.3	32.7	35.9	33.8	34.9	33.8	35.7	33.4	36.1	35.2	35.3	63.4	61.8	62.4	63.0	62.8

Note: bdl = below the detection limit. Atoms per formula unit are calculated for As + S = 2. Apy-1 and Apy-2—arsenopyrite of the first and the second generations, correspondingly. C—data for the central part of the grain, R—data for the rim.

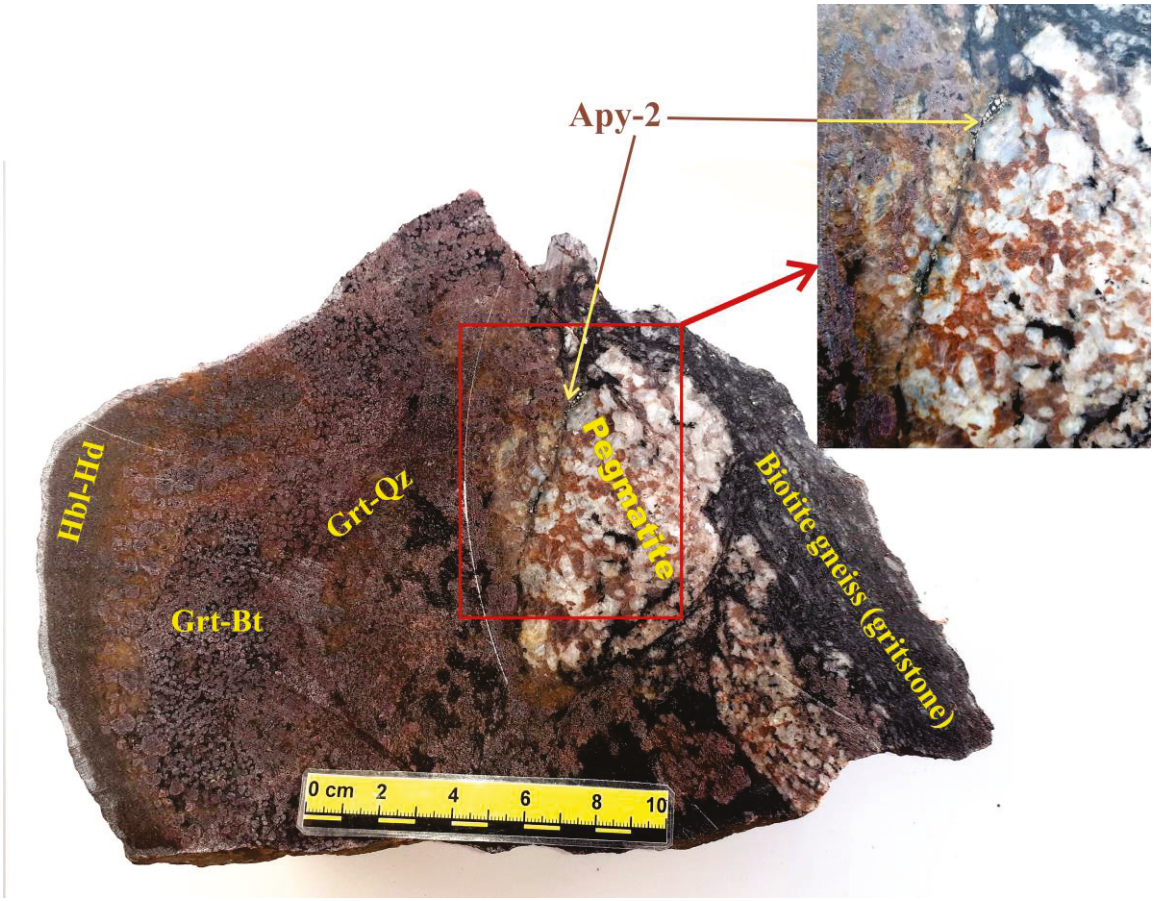


Figure 12. Pegmatite lenses, cutting biotite gneiss and metasomatic rock, a specimen photo with detail area. The arrows point at a chain of arsenopyrite-2 grains in a thin biotite veinlet between two pegmatite lenses. Apy—arsenopyrire, Bt—biotite, Grt—garnet, Hbl—hornblende, Hd—hedenbergite, Qz—quartz.

Löllingite occurs as inclusions in arsenopyrite-2 (Figure 13), rarer as separate euhedral grains up to 0.5 mm in size. Löllingite contains impurities of Ni (<2 wt%), Co (<0.5 wt%), and S (<2 wt%) (Table 1).

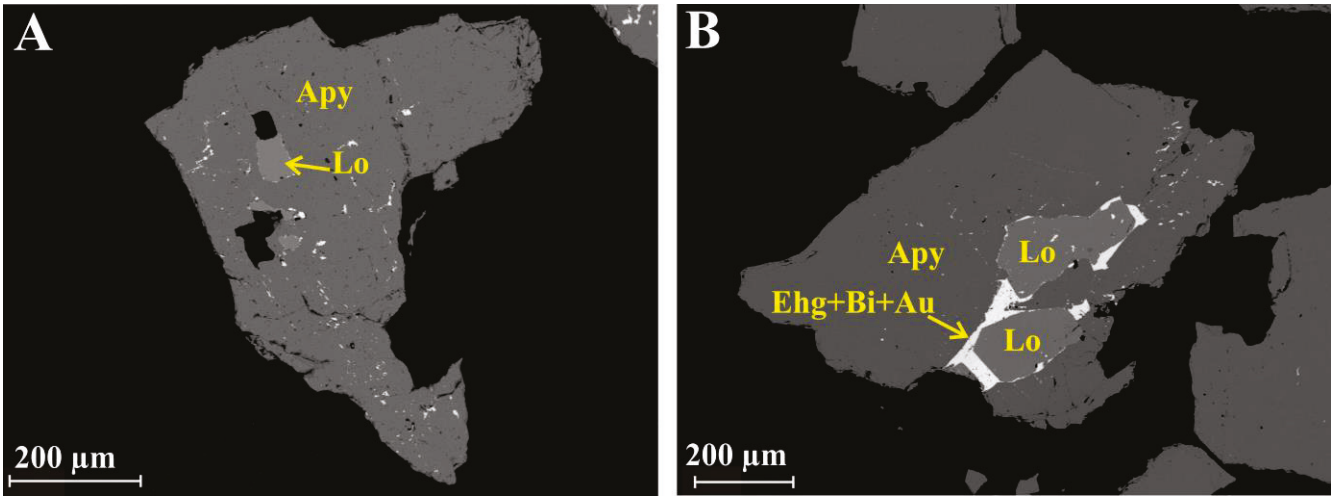


Figure 13. Inclusions of löllingite, gold, native bismuth, and ehrigite in arsenopyrite-2 (**A**), and concentration of bismuth–ehrigite–gold inclusions at the contact arsenopyrite–löllingite (**B**). BSE-images. Apy—arsenopyrite, Au—native gold, Bi—native bismuth, Ehg—ehrigite, Lo—löllingite.

Gold was found in numerous inclusions in arsenopyrite-2 and löllingite (Figure 13), except the only gold grain in quartz, reported in [12]. The inclusions are monomineral or polymineral, in the polymineral inclusions gold associates with native bismuth and bismuth telluride ehrigite Bi_8Te_3 (the second finding in the world after Good Hope gold mine [29]) (Table 2, Figures 14 and 15). Rarer mineral phases, found in the inclusions, are maldonite, bismuthinite, joseite-B, hedleyite, hessite, bismoclite, and demicheleite-Br. The inclusions are of irregular angular form, up to 0.2 mm sized (Figures 13 and 14). High concentration of bismuth–ehrigite–gold inclusions is reached at the contact arsenopyrite–löllingite, or these minerals form veinlets along arsenopyrite–löllingite boundary (Figure 13B).

Table 2. Microprobe data for ehrigite (Ehg), hedleyite (Hdl), maldonite (Mdo), and native bismuth (Bi) of the Maljavr gold occurrence, wt%.

Mineral	Ehg	Ehg	Ehg	Ehg	Ehg	Ehg	Ehg	Hdl	Hdl	Mdo	Mdo	Bi	Bi	Bi
S	bdl	bdl	bdl	bdl	bdl	bdl	bdl	bdl	bdl	bdl	bdl	0.06	bdl	bdl
Fe	0.27	bdl	bdl	0.45	0.27	0.96	1.33	bdl	bdl	bdl	2.89	0.27	0.27	1.37
As	0.08	bdl	bdl	0.00	0.03		0.10	bdl	bdl	bdl	0.12	0.13	0.05	0.14
Te	18.61	18.68	18.34	16.38	18.29	18.36	18.25	23.45	24.93	bdl	bdl	0.00	bdl	bdl
Au	bdl	bdl	bdl	bdl	bdl	bdl	bdl	bdl	bdl	63.78	62.82	bdl	bdl	bdl
Pb	bdl	0.78	bdl	bdl	bdl	0.94	bdl	4.08	bdl	bdl	bdl	bdl	bdl	bdl
Bi	81.49	80.54	80.23	82.49	80.36	79.64	79.05	72.47	75.07	36.22	33.85	99.02	99.88	98.43
Total	100.45	100.00	98.56	99.39	98.95	99.89	98.73	100.00	100.00	100.00	99.68	99.49	100.20	99.94
Atoms per formula unit														
S				0.047								0.004		
Fe	0.099			0.168	0.099	0.347	0.479				0.291	0.010	0.010	0.049
As	0.022				0.008		0.028				0.009	0.004	0.001	0.004
Te	2.962	3.006	2.998	2.646	2.956	2.896	2.879	3.340	3.523			0.000		
Au										1.954	1.791			
Pb		0.077				0.091		0.358						
Bi	7.917	7.915	8.003	8.140	7.934	7.667	7.615	6.302	6.477	1.046	0.910	0.982	0.989	0.947

Notes: bdl = below the detection limit. Atoms per formula unit are calculated for 11 atoms in ehrigite, 10 atoms in hedleyite, and 3 atoms in maldonite.

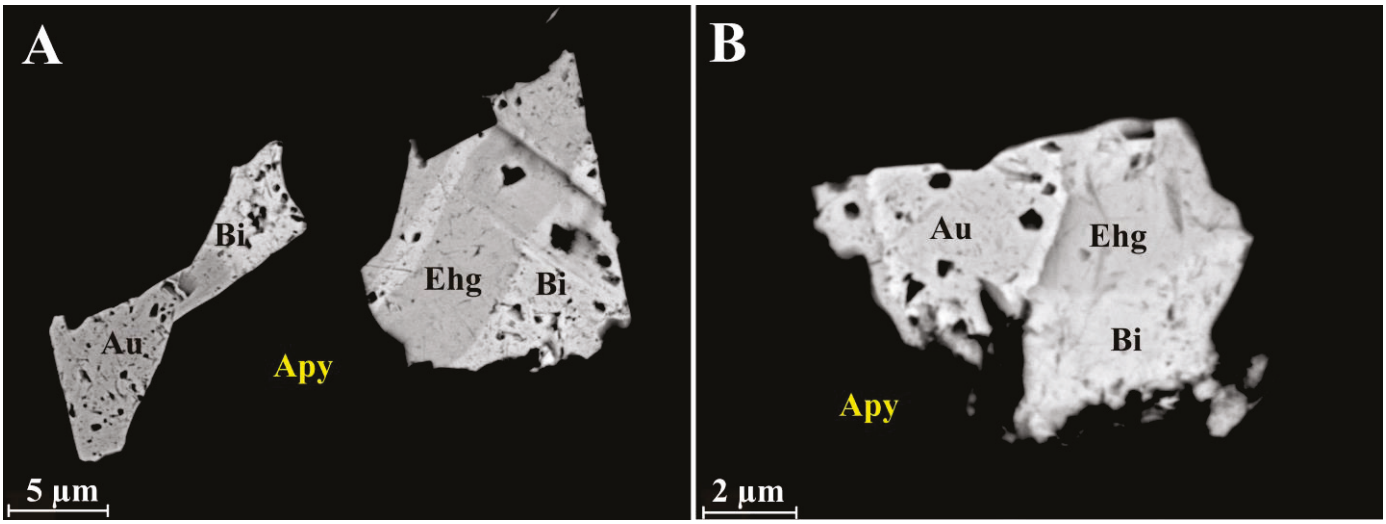


Figure 14. Inclusions of native gold and bismuth, bismuth and ehrigite (**A**), and polymineral gold–bismuth–ehrigite inclusion (**B**) in arsenopyrite-2. BSE-images. Apy—arsenopyrite, Au—native gold, Bi—native bismuth, Ehg—ehrigite.

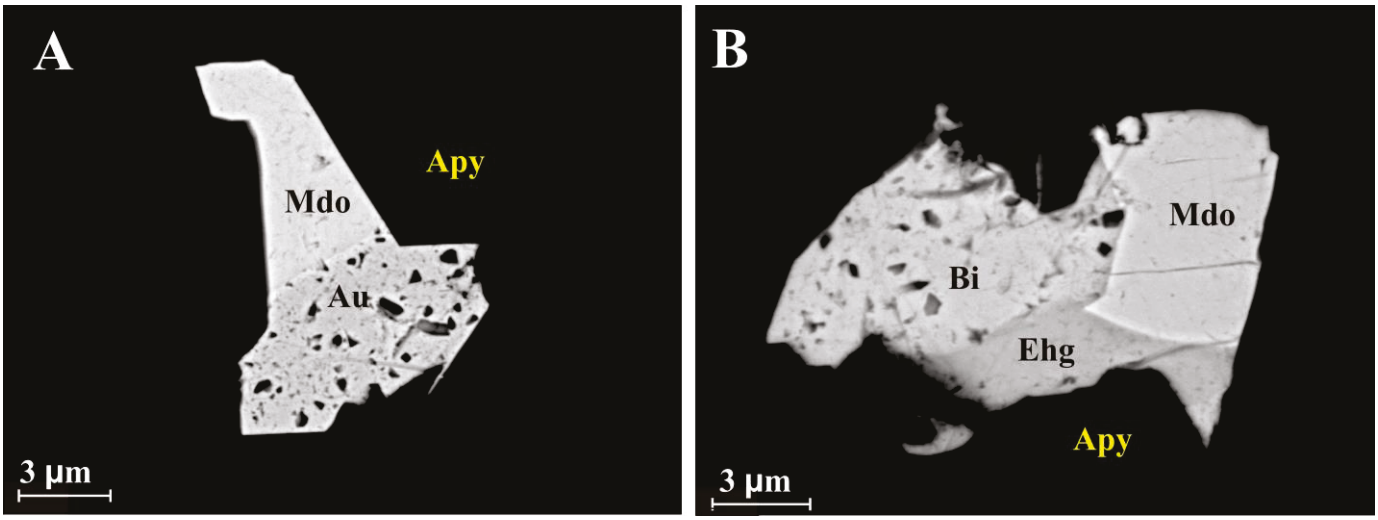


Figure 15. Maldonite with gold (**A**) and with native bismuth and ehrigite (**B**) in polymineral inclusions in arsenopyrite-2, BSE-images. Apy—arsenopyrite, Au—native gold, Bi—native bismuth, Ehg—ehrigite, Mdo—maldonite.

Gold fineness is high or medium, it contains from 53 to 99 wt% Au with two peaks at 72–82 and 88–98 wt%. The main impurities are Ag (4–30 wt%), Fe and As (<0.2 wt%) (Table 3). One more gold mineral in the deposit is maldonite Au_2Bi (Table 2), which occurs in the inclusions in arsenopyrite and löllingite together with gold, native bismuth, and ehrigite (Figure 15).

Table 3. Microprobe data for native gold of the Maljavr gold occurrence, wt%.

Fe	1.94	0.48	1.48	1.12	1.71	0.77	0.24	1.11	0.11	0.24	1.35	1.67
As	0.04	0.01	0.04	bdl	0.03	0.07	0.10	0.11	bdl	bdl	bdl	bdl
Ag	7.34	21.22	35.73	45.78	3.78	4.78	29.71	8.78	18.17	18.68	6.23	bdl
Au	88.97	77.08	61.42	53.10	94.19	92.83	69.32	89.45	77.69	78.62	91.16	99.22
Total	98.29	98.80	98.67	100.00	99.71	98.46	99.37	99.45	95.98	97.53	98.75	100.89
					Atoms per formula unit							
Fe	0.063	0.014	0.040	0.028	0.056	0.026	0.007	0.036	0.003	0.007	0.044	0.056
As	0.001	0.000	0.001		0.001	0.002	0.002	0.003				
Ag	0.123	0.330	0.494	0.594	0.064	0.084	0.435	0.146	0.298	0.300	0.106	
Au	0.814	0.656	0.465	0.378	0.879	0.889	0.556	0.816	0.698	0.692	0.850	0.944

4.2. Zircons in the Rocks of the Maljavr Occurrence and Age of Zircons

Zircon from sample SHM-12 of biotite gneiss–metaconglomerate forms euhedral transparent pale yellow fractured crystals, with plain facets and smoothed edges. Prism {110} and di-pyramid {111} facets are predominant. The crystal size is 50–150 μm, the elongation coefficient varies from 2.0 to 3.0 (Figure 16). Some grains contain inclusions of monazite and biotite (Figure 16). Coarse zoning was noted in the outer part of some zircon crystals.

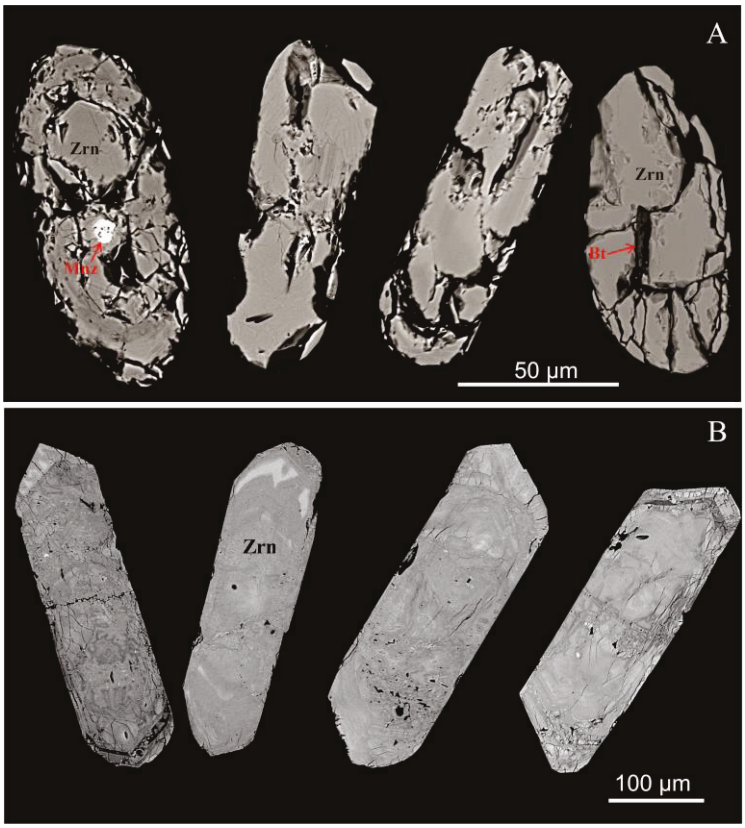


Figure 16. BSE images of zircons from the Maljavr occurrence: (**A**) zircons from biotite gneiss, (**B**) zircons from tourmaline granite pegmatite. Bt—biotite, Mnz—monazite, Zrn—zircon.

Ten samples of the least altered zircon crystals, selected from different size fractions, were assayed for U and Pb isotopes (Table 4). Analytical points of isotopic composition of ten zircon fractions lie in discordia with the age 2664 ± 18 Ma at the upper intersection with the concordia, MSWD = 9.5 (Figure 17). The lower intersection with the age 378 ± 77 Ma reflects the Paleozoic tectonic activity and formation of the Khibiny and Lovozero alkaline intrusions [30].

Zircon from sample SHM-11 of tourmaline granite pegmatite forms euhedral long-prysmatic transparent fractured crystals of brown color. Prism {110} and di-pyramid {111} facets are predominant, the crystal faces are rough, and the edges are sharp. The inner structure is nonhomogeneous, with dark and light areas of irregular form, some grains contain small inclusions of uraninite (Figure 16). The crystal size is 100–300 μm, the elongation coefficient varies from 3.0 to 4.0. Five samples of the least altered and free of inclusions zircon crystals were selected from different size fractions and assayed for U and Pb isotopes (Table 4). Analytical points of isotopic composition of five zircon fractions lie in discordia with the age 2508 ± 7 Ma at the upper intersection with the concordia, MSWD = 1.4 (Figure 18). The lower intersection with the concordia occurs at 358 ± 57 Ma.

Table 4. Results of U-Pb geochronological studies of zircons from biotite gneiss–metaconglomerate and tourmaline granite–pegmatite.

Sample No./ Fraction No.	Weight, mg/ Size, μm	Pb, ppm	U, ppm	Isotope Ratios					Rho	Age, Ma		
				$^{206}Pb/^{204}Pb$ *	$^{207}Pb/^{206}Pb$ *	$^{208}Pb/^{206}Pb$ *	$^{206}Pb/^{238}U$	$^{207}Pb/^{235}U$		$^{206}Pb/^{238}U$	$^{207}Pb/^{235}U$	$^{207}Pb/^{206}Pb$
Sample SHM-12—biotite gneiss												
SHM-12/1	0.2/<100	165	358	533	0.1999 ± 0.0001	0.1281 ± 0.0002	0.3958 ± 0.0015	9.669 ± 0.038	0.91	2150 ± 9	2404 ± 10	2627 ± 3
SHM-12/2	0.5/>100	130	341	702	0.1907 ± 0.0001	0.1246 ± 0.0002	0.3322 ± 0.0049	7.9400 ± 0.012	0.99	1849 ± 27	2224 ± 33	2590 ± 2
SHM-12/3	0.5/>100	141	337	822	0.1891 ± 0.0001	0.1291 ± 0.0002	0.3639 ± 0.0011	8.7448 ± 0.026	0.96	2000 ± 6	2312 ± 7	2599 ± 2
SHM-12/4	0.2/>50	164	363	485	0.1972 ± 0.0001	0.3042 ± 0.0001	0.3418 ± 0.0014	8.1055 ± 0.040	0.91	1896 ± 8	2243 ± 11	2577 ± 4
SHM-12/5	0.5/<100	361	803	1178	0.1845 ± 0.0001	0.2709 ± 0.0001	0.3551 ± 0.0007	8.5313 ± 0.017	0.94	1959 ± 4	2289 ± 5	2599 ± 1
SHM-12/6	0.3/<50	158	371	539	0.1909 ± 0.0001	0.2773 ± 0.0001	0.3226 ± 0.0016	7.6289 ± 0.038	0.96	1834 ± 9	2188 ± 11	2539 ± 3
SHM-12/7	0.4/<50	186	432	818	0.1829 ± 0.0001	0.2064 ± 0.0001	0.3457 ± 0.0010	8.2387 ± 0.025	0.88	1962 ± 6	2258 ± 7	2538 ± 2
SHM-12/8	0.4/<100	175	406	1242	0.1829 ± 0.0001	0.2062 ± 0.0001	0.3565 ± 0.0011	8.5121 ± 0.025	0.92	1966 ± 6	2287 ± 7	2588 ± 2
SHM-12/9	0.3/<50	255	615	574	0.1942 ± 0.0001	0.1505 ± 0.0001	0.3502 ± 0.0017	8.3507 ± 0.0011	0.96	1935 ± 9	2270 ± 11	2586 ± 3
SHM-12/10	0.5/<50	142	305	550	0.1968 ± 0.0001	0.2235 ± 0.0001	0.3723 ± 0.0016	8.9664 ± 0.0011	0.94	2040 ± 9	2335 ± 10	2603 ± 3
Sample SHM-11—tourmaline granite pegmatite												
SHM-11/1	0.3/<200	1218	2587	1426	0.1724 ± 0.0001	0.03001 ± 0.0001	0.4633 ± 0.0005	10.509 ± 0.011	0.90	2463 ± 2	2481 ± 2	2495 ± 1
SHM-11/2	0.9/<150	729	1534	1233	0.1741 ± 0.0001	0.05311 ± 0.0002	0.4449 ± 0.0007	10.068 ± 0.015	0.95	2373 ± 4	2441 ± 4	2499 ± 1
SHM-11/3	0.6/>100	793	1619	1723	0.1719 ± 0.0001	0.02737 ± 0.0001	0.4715 ± 0.0011	10.714 ± 0.026	0.99	2490 ± 6	2499 ± 6	2506 ± 1
SHM-11/4	1.7/>250	1109	2370	2347	0.1695 ± 0.0001	0.02410 ± 0.0001	0.4529 ± 0.0009	10.265 ± 0.021	0.96	2408 ± 5	2459 ± 5	2501 ± 1
SHM-11/5	1.2/>200	1140	2643	2091	0.1686 ± 0.0001	0.02238 ± 0.0001	0.4182 ± 0.0009	9.3869 ± 0.017	0.94	2252 ± 5	2377 ± 5	2485 ± 1

* Isotope ratios are corrected for the blank and common lead; Rho—the correlation coefficient of the $^{207}Pb/^{235}U$-$^{206}Pb/^{238}U$ ratios.

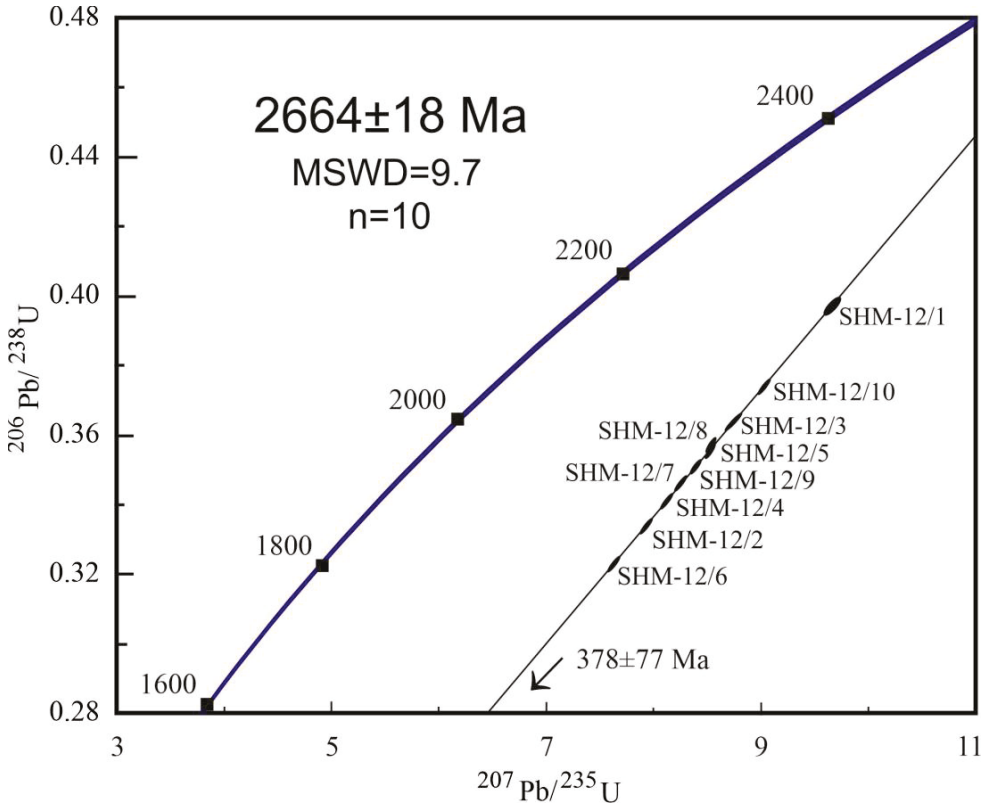


Figure 17. Diagram with concordia for biotite gneiss from the Maljavr occurrence.

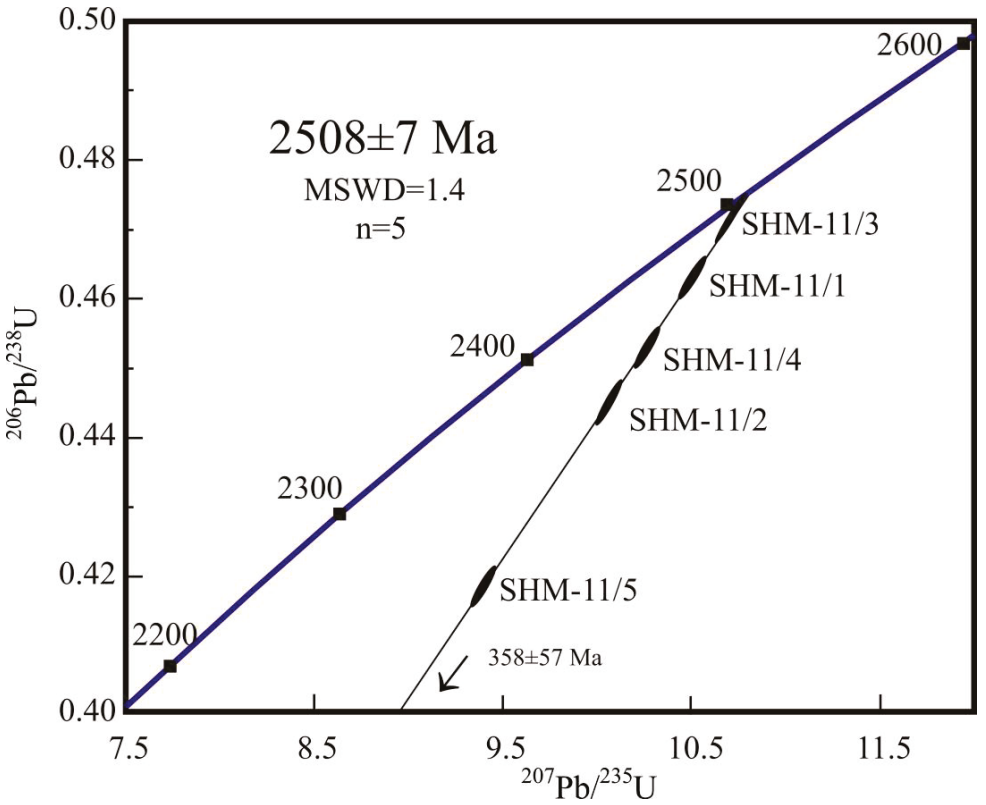


Figure 18. Diagram with concordia for tourmaline granite pegmatite from the Maljavr occurrence.

5. Discussion

The sequence of volcanic–sedimentary rocks, including the conglomerate hosting the Maljavr gold occurrence, formed during the period from 2.95 to 2.83 Ga. The lower boundary of the time interval is defined by the age of detrital zircons from the basal conglomerates 2952–2939 Ma: the zircons are primarily magmatic, the probable parental rock was TTG gneiss in the Kola province [14]. The upper time boundary of the interval is specified by the age gneiss–metadacite 2838 ± 23 Ma (zircon, U-Pb, SHRIMP II) in the upper sequence of the Uragubsky belt [16].

The volcanic sedimentary sequence was metamorphosed amphibolite at a temperature of 600–620 °C, under a pressure of 4 kbar [17] during the period from 2.87 to 2.66 Ga. It was the time of several accretion events, which lead to formation of the continent Kenorland [13]. An ancient island arc (the Kolmozero-Voron'ya and Uragubsky greenstone belts, at present) and the Kola province were successively accreted to the Murmansk block 2.78–2.76 Ga ago [13]. The peak of the Neoarchean metamorphic event in the Uragubsky greenstone belts was reached at ~2.77 Ga: the U-Pb age of metamorphism is 2786 ± 31, 2774 ± 12 Ma (SHRIMP-II, zircons of metamorphic genesis) [16,17], 2763 ± 8 Ma [15].

Age of zircon from the biotite gneiss in the zone of alteration in the Maljavr occurrence is 2664 ± 18 Ma (Figure 17, Table 4), i.e., it is younger than the age of volcanic sedimentary rocks and younger than regional metamorphism in the Uragubsky belt. Textural and structural characteristics of the metasomatic rocks in the Maljavr gold occurrence, such as massive fabrics with different orientation of biotite flakes and amphibole crystals (Figure 6B,C), indicate alteration processes after the peak of regional metamorphism under conditions of undirected pressure. Biotite–garnet [31,32] and amphibole–garnet [31] geothermometers, applied to the composition of coexisting biotite–almandine and hornblende–almandine, correspondingly (Table S2), indicate temperature of metasomatic rocks formation 600–630 °C, it is close to the temperature of regional metamorphism in the Uragubsky belt [17].

This zircon age of biotite gneiss in the zone of alteration corresponds well to the age of granulite metamorphism in the Kola-Norwegian province, adjacent to the Uragubsky belt from SW (Figure 1, inset). The rocks of the Kola-Norwegian province were metamorphosed granulite during the period 2.71–2.50 Ga [33,34]. This metamorphic event was dated with the outer zones of zircon crystals, which defined the interval 2707–2656 Ma [33], and with zircon from biotite–garnet–sillimanite gneiss 2648 ± 18 Ma [34].

The tectonic events 2.71–2.50 Ga in the Kola-Norwegian province are reflected in the neighboring Uragubsky and Kolmozero-Voron'ya greenstone belts. The volcanic–sedimentary sequences of the belts were intruded with plagioclase/microcline granites and granite aplite dykes at 2696 ± 9 Ma [18]. These tectonic events probably caused increasing intensity of hydrothermal processes in the greenstone belts: in the Kolmozero-Voron'ya belt metasomatic rocks were dated 2629 ± 64 Ma [35], and we consider the age of zircon from the Maljavr occurrence 2664 ± 18 Ma as the time of alteration of the biotite gneiss, when the lenses of metasomatic rocks with sulfide (pyrrhotite-arsenopyrite) mineralization formed. Morphological and isotope characteristics of zircons from the biotite gneiss agree with the zircons of metamorphic genesis [36,37]: zircon grains are isometric or ellipsoid, crystal zoning is weakly displayed or absent (Figure 16A). The discordancy of the analytical points (Figure 17) appears probably due to zircon fracturing, which promoted partial loss of radiogenic lead.

The more recent recognized stage of formation of the Maljavr occurrence was the injection of tourmaline pegmatite with age of 2508 ± 7 Ma. Morphological and isotope characteristics of zircons from the tourmaline granite pegmatite agree with the magmatic zircons (Figure 16B, Table 4). Thin euhedral zoning can be seen in the outer crystal zones, and zoning is blurred in the central parts of the zircon grains. Inhomogeneity of the inner structure (Figure 16B) may be explained by later fluid alteration, which did not significantly modify the crystal structure.

The pegmatite affected the biotite gneiss and metasomatic rocks and caused tourmalinization and recrystallization of sulfides (arsenopyrite and löllingite): a chain of arsenopyrite

grains, recrystallized due to pegmatite injection, can be seen in a thin veinlet of biotite gneiss between two lenses of pegmatite (Figure 12). Recrystallization of sulfides resulted in gold–bismuth mineralization in a form of numerous inclusions in arsenopyrite-2 and löllingite grains.

The temperature of formation of arsenopyrite-2 (and gold–bismuth mineralization) was determined with the arsenopyrite geothermometer [38]. The arsenopyrite geothermometer is believed to be the most reliable for sulfide systems, because arsenopyrite composition is resistant to change of PT-parameters in the surrounding medium [39]. The thermometer can be applied only to arsenopyrites with Co and Ni impurities less than 0.5 wt%: arsenopyrite-1 does not fit this requirement, but arsenopyrite-2 is acceptable (Table 1). Composition of arsenopyrite-2 and its association with pyrrhotite indicate two temperature intervals: 500–600 °C for arsenopyrite with As 34.6–35.9 at.% and 400–510 °C for arsenopyrite with As 32.7–33.8 at.%. The first interval can be related to the temperature of metasomatic rock's formation. The second temperature interval 400–510 °C corresponds well to the conditions of pegmatite crystallization: T = 415–460 °C was estimated for pegmatite in the area of the Maljavr occurrence with different mineral thermometers and study of fluid inclusions in beryl [40].

Two stages of gold mineralization evolution in the Maljavr gold occurrence are supposed: 1—the stage of formation of lenses of metasomatic rocks with sulfide pyrrhotite-arsenopyrite mineralization (0.03–0.5 g/t Au) at ~2.66–2.67 Ga; 2—gold concentration in re-crystallized arsenopyrite and löllingite at the time of pegmatite injection ~2.51 Ga. Therefore, the pegmatite age of 2508 ± 7 Ma reflects the time of formation of gold–bismuth mineralization in its present form.

As it was shown in the example of the Suurikuusikko and Iso-Kuotko deposits in the Central Lapland belt in Northern Finland [41], gold-mineralized rocks form with a series of impulses of hydrothermal activity. In the Central Lapland belt, these impulses correlate with magmatic events—the formation of different generations of minor granite intrusions and dykes. Multi-stage formation was also supposed for gold mineralization in the Rompas-Rajapalot deposits in the Perapohja belt (Northern Finland) [42].

The geological position of the Maljavr occurrence, the geochemical association Au-As-Se-Te-Bi in the mineralized rocks, and the linkage of gold mineralization with pegmatite—all these characteristics agree with the reduced intrusion related type of gold deposits [43–45], but paucity of relevant data (fluid inclusions and isotope study) does not allow constraint of the genetic type with certainty. Biotite gneiss–metaconglomerate, hosting the mineralized metasomatic rocks, could be the primary source of arsenic and, probably, gold for the mineralization, which formed during the later metasomatic event.

In Northern Fennoscandia, two stages of gold deposit formation are identified—the Neoarchean (2.7–2.6 Ga) and Paleoproterozoic (1.92–1.74 Ga) [46]. Gold occurrences of Neoarchean age are located in the north-eastern part of the region, within the Kola province and north of it, in the Kolmozero-Voron'ya belt [46]. The deposits and occurrences, located south of the Kola province, are of Paleoproterozoic age, even those hosted by the Archean greenstone belts [46].

The Neoarchean Maljavr gold occurrence (2.67–2.51 Ga) in the Uragubsky belt (north of the Kola province) fully fits this model. Close age 2.64–2.68 Ga (U-Pb, SHRIMP, outer zones of zircon) was obtained for gold-mineralized in skarnoids in the Olenegorsk BIF deposit [47] in the Kola province. Gold deposits in the Kolmozero-Voron'ya belt are older: ~2.82 Ga (Oleninskoe) and ~2.78 Ga (Nyalm-1) [46].

In the northern part of the Fennoscandian shield, two conglomerate-hosted gold occurrences (Kaarestunturi and Outapää) were found in the 1970′s in the Central Lapland greenstone belt in Finland [10,11]. The occurrences are hosted in quartzite and oligomictic conglomerate of the Kumpu Group (<1850 Ma), deposited discordantly on graywackes and carbonate metasedimentary rocks; the rocks are metamorphosed greenschist. In the Kaarestunturi occurrence, Au-bearing lenses, containing up to 5.0 ppm Au, form a set of up to 30 m long and up to 1 m (typically 30 cm) thick lenses within a 30–60 m thick

conglomerate sequence. Free gold (about 5% Ag), with grain size of 0.03–0.4 mm, occur in the matrix of the conglomerate. Other ore minerals are chalcopyrite, minor galena, pyrite, magnetite, ilmenite, and hematite at Kaarestunturi, and rare magnetite and hematite at Outapää. The gold occurrences are considered as Paleoproterozoic gold paleoplacers in fluvio-deltaic fans [10,11]. Probable sources for gold are the "mesothermal" lode-gold deposits in the greenstones stratigraphically below the metasedimentary host rocks [10,11].

The Maljavr occurrence is the first gold occurrence in the Fennoscandian Shield, hosted in Archean conglomerates. It differs from the occurrences in Paleoproterozoic conglomerates in high grade metamorphism, intensive alteration of the rocks, modification by pegmatite injection, and in more diverse composition of mineralization.

6. Conclusions

The following story of formation of the Maljavr gold occurrence is reconstructed:

1. Deposition of sedimentary rocks, including the conglomerates hosting the Maljavr gold occurrence, in the interval 2.95–2.83 Ga.
2. Regional upper amphibolite metamorphism of the volcanic–sedimentary sequence in the interval 2.77–2.79 Ga.
3. Alteration of the biotite gneiss–metaconglomerate and formation of lenses of metasomatic rocks with sulfide pyrrhotite–arsenopyrite mineralization; this event took place in a local zone of NNE strike at ~2.66–2.67 Ga. Geochemical association of the metasomatic rocks includes Au, As, Ag, Se, Te, Bi, and Cu.
4. Injection of tourmaline pegmatite veins at ~2.51 Ga caused recrystallization of sulfides and formation of gold–bismuth mineralization in its present form. Gold and bismuth minerals (native gold, maldonite, native bismuth, ehrigite, and other tellurides) occur in inclusions in recrystallized arsenopyrite (arsenopyrite-2) and löllingite.

Biotite gneiss–metaconglomerate, hosting the mineralized metasomatic rocks, was the probable primary source of arsenic and gold for mineralization, which formed later. The geological position of the Maljavr occurrence, the linkage of gold mineralization with pegmatite, the geochemical association Au-As-Se-Te-Bi in the mineralized rocks all correspond to the type of gold deposits, which are associated with intrusions. The Maljavr occurrence is the first gold occurrence in the Fennoscandian Shield, to be reported from Archean conglomerates.

Supplementary Materials: The following supporting information can be downloaded at: https://www.mdpi.com/article/10.3390/min14060535/s1, Table S1: Chemical composition of biotite gneiss–metaconglomerate and altered rocks; Table S2: Microprobe data for rock-forming minerals, Table S3: Content of minor elements in biotite gneiss–metaconglomerate and altered rocks.

Author Contributions: Conceptualization, A.A.K. and N.M.K.; methodology, A.A.K.; investigation, A.A.K., N.M.K. and Y.E.S.; writing—original draft preparation, A.A.K. and N.M.K.; writing—review and editing, A.A.K., N.M.K. and Y.E.S.; project administration, N.M.K.; funding acquisition, N.M.K. All authors have read and agreed to the published version of the manuscript.

Funding: The work was carried out under Project FMEZ-2024-0004 of the Russian Academy of Science.

Data Availability Statement: The data presented in this study are available on request from the corresponding author.

Acknowledgments: The authors thank students of the Murmansk State Technical University Alexandr Ermolin, Mariam Khachatryan, and Julia Samsonova for productive work in the field, Tatiana Zykova, Elena Galeeva, Alyona Kompanchenko, and Olga Goychuk for sample preparation and microprobe analyses of zircon.

Conflicts of Interest: The authors declare no conflicts of interest.

References

1. Tucker, R.F.; Viljoen, R.P.; Viljoen, M.J. A review of the Witwatersrand Basin. *Episodes* **2016**, *39*, 105–134. [CrossRef]
2. Smith, A.J.B.; Henry, G.; Frost-Killian, S. A review of the Birimian Supergroup- and Tarkwaian Group-hosted gold deposits of Ghana. *Episodes* **2016**, *39*, 177–198. [CrossRef]
3. Milesi, J.P.; Ledru, P.; Marcoux, E.; Mougeot, R.; Johan, V.; Lerouge, C.; Sabate, P.; Bailly, L.; Respaut, J.P.; Skipwith, P. The Jacobina Paleoproterozoic gold-bearing conglomerates, Bahia, Brazil: A "hydrothermal shear-reservoir" model. *Ore Geol. Rev.* **2002**, *19*, 95–136. [CrossRef]
4. Ulrich, T.; Long, D.G.F.; Kamber, B.S.; Whitehouse, M. In-situ trace element and sulfur isotope analysis of pyrite in a Paleoproterozoic gold placer deposit, Pardo and Clement Townships, Ontario, Canada. *Econ. Geol.* **2011**, *106*, 667–686. [CrossRef]
5. Long, D.G.F.; Ulrich, T.; Kamber, B.S. Laterally extensive modified placer gold deposits in the Paleoproterozoic Mississagi Formation, Clement and Pardo Townships, Ontario. *Can. J. Earth Sci.* **2011**, *48*, 779–792. [CrossRef]
6. Munroe, S.; Cunningham, M. The Pilbara's Conglomerate Gold. *Aust. Resour. Invest.* **2018**, *12*, 74–76.
7. Spinks, S.C.; Pearce, M.A.; Vaillant, M.L.; Fox, D.; Tyler, I.M.; Godel, B.; Stromberg, J.; Mead, E.; White, A.J.R. The Neoarchean Conglomerate-Hosted Gold of the West Pilbara Craton, Western Australia. *Econ. Geol.* **2021**, *116*, 629–650. [CrossRef]
8. Chakravarti, R.; Singh, S.; Akella, V.S. Gold Mineralisation within Quartz Pebble Conglomerates of Gorumahisani Badampahar Schist belt, Singhbhum Craton, Eastern India. *J. Geosci. Res.* **2017**, *1*, 27–34.
9. Ivashchenko, V.I.; Golubev, A.I. *Gold and Platinum in Karelia: Formational-Genetic Types of Mineralization and Prospects*; Karelian Research Centre of RAS: Petrozavodsk, Russia, 2011; p. 369. (In Russian)
10. Kaarestunturi Deposit Report. Geological Survey of Finland, 17.01.2024. Available online: https://tupa.gtk.fi/karttasovellus/mdae/raportti/382_Kaarestunturi.pdf (accessed on 10 April 2024).
11. Outapää Mineral Deposit Report. Geological Survey of Finland, 06.01.2020. Available online: https://tupa.gtk.fi/karttasovellus/mdae/raportti/403_Outap%C3%A4%C3%A4.pdf (accessed on 10 April 2024).
12. Voronyaeva, L.V.; Krupenik, Z.V. A new gold prospect in the Titovsko-Uragubskaya greenstone Late Archean structure (Kola region). *Reg. Geol. Metallog.* **2021**, *86*, 82–91. (In Russian) [CrossRef]
13. Mints, M.V.; Suleimanov, A.K.; Babayants, P.S. *Deep Structure, Evolution, and Minerals in the Early Precambrian Basement of the East European Platform: Interpretation of Materials on Referent Profile 1-EV, Profiles 4V and TATSEIS*; Geokart Geos: Moscow, Russia, 2010; ISBN 978-5-89118-531-9. (In Russian)
14. Smol'kin, V.F.; Mezhelovskaya, S.V.; Mezhelovsky, A.D. The Sources of the Clastic Material of the Terrigenous Sequences of the Neoarchean and Paleoproterozoic Paleobasins in the Eastern Part of the Fennoscandian Shield Based on Isotope Analysis Data for Detrital Zircons (SIMS, LA-ICP-MS). *Stratigr. Geol. Correl.* **2020**, *28*, 571–602. [CrossRef]
15. Myskova, T.A.; Mil'kevich, R.I.; Bogomolov, Y.S.; Guseva, V.F. New data on composition and age of the protolith of the high-alumina gneisses of the Kolskaya and Tundrovaya series. In Geology and Geodynamics of the Archean, Proceedings of the I Russian Conference on the Problems in Geology and Geodynamics of the Precambrian, Sankt-Peterburg, Russia, 27–29 September 2005; IGGP: Mendota Heights, MN, USA, 2005; pp. 272–275. (In Russian).
16. Myskova, T.A.; Glebovitsky, V.A.; Mil'kevich, R.I.; Berezhnaya, N.G.; Skublov, S.G. Improvement of composition and age of aluminum gneisses of the Uragubskaya greenstone Later Achaean structure, Kola Peninsula. *Proc. Russ. Min. Soc.* **2010**, *139*, 15–21. (In Russian)
17. Glebovitsky, V.A. (Ed.) *The Early Precambrian of the Baltic Shield*; Nauka: Sankt-Peterburg, Russia, 2005; 711p. (In Russian)
18. Vrevskii, A.B. Specifics of Neoarchean plume–lithospheric processes in the Kola–Norwegian Province of the Fennoscandian Shield: I. Composition and age of the komatiite–tholeiite association. *Petrology* **2018**, *26*, 121–144. [CrossRef]
19. Bogdanova, V.S.; Dagelayskiy, V.B. Age position of the rocks of the Tundrovaya series and conglomerates in the area of Ura river (Kola Peninsula). In *Absolute Age of the Precambrian Rocks in the USSR*; Nauka: Moscow-Leningrad, Russia, 1965; pp. 74–83. (In Russian)
20. Smol'kin, V.F.; Borisova, V.V.; Svetov, S.A.; Borisov, A.E. Late Archean komatiites of the Ura Bay–Titovka Structure, northwestern Kola region. *Petrology* **2000**, *8*, 177–199.
21. Krogh, T.E. A low-contamination method for hydrothermal decomposition of zircon and extraction of U and Pb for isotopic age determination. *Geochim. Cosmochim. Acta* **1973**, *37*, 485–494. [CrossRef]
22. Ludwig, K.R. PbDat for MS-DOS, Version 1.21. In *U.S. Geological Survey Open-File Report*; U.S. Geological Survey: Reston, VA, USA, 1991; pp. 88–542.
23. Ludwig, K.R. ISOPLOT/Ex. Version 2.06. In *A Geochronological Toolkit for Microsoft Excel*; Berkley Geochronology Center Special Publication: Berkeley, CA, USA, 1999; 49p.
24. Steiger, R.H.; Jager, E. Subcomission of geochronology: Convention of the use of decay constants in geo- and cosmochronology. *Earth Planet. Sci. Lett.* **1976**, *36*, 359–362. [CrossRef]
25. Stacey, J.S.; Kramers, I.D. Approximation of terrestrial lead isotope evolution by a two-stage model. *Earth Planet. Sci. Lett.* **1975**, *26*, 207–221. [CrossRef]
26. Warr, L.N. IMA–CNMNC approved mineral symbols. *Mineral. Mag.* **2021**, *85*, 291–320. [CrossRef]
27. Stanley, C. Molar Element Ratio Analysis of Lithogeochemical Data: A Toolbox for Use in Mineral Exploration and Mining. *Geochemistry: Exploration, Environment, Analysis* **2020**, *20*, 233–256. [CrossRef]
28. Taylor, S.R.; McLennan, S.M. *The Continental Crust: Its Composition and Evolution*; Blackwell: Oxford, UK, 1985; 312p.

29. Ciobanu, C.L.; Cook, N.J.; Yao, J.; Slattery, A.; Wade, B. Ehrigite, IMA 2023-074, in: CNMNC Newsletter 77. *Eur. J. Mineral.* **2024**, *36*, 165–172. [CrossRef]
30. Kramm, U.; Kogarko, L.N.; Kononova, V.A.; Vartiainen, H. The Kola alkaline province of the CIS and Finland: Precise Rb-Sr ages define 380-360 age range for all magmatism. *Lithos* **1993**, *30*, 33–44. [CrossRef]
31. Glebovitsky, V.A. (Ed.) *Thermo- and Barometry of Metamorphic Rocks*; Nauka: Leningrad, Russia, 1977; 207p. (In Russian)
32. Gul'bin, Y.L. Optimization of the garnet-biotite geothermometer. 1. Temperature trends. *Geol. Ore Depos.* **2011**, *53*, 528–542. [CrossRef]
33. Balashov, Y.A.; Mitrofanov, F.P.; Balagansky, V.V. New geochronological data on Archaean rocks of the Kola Peninsula. In *Correlation of Precambrian Formations of the Kola-Karelian Region and Finland*; Kola Science Centre of the Russian Academy of Sciences: Apatity, Russia, 1992; pp. 13–34. (In Russian)
34. Myskova, T.A.; Milkevich, R.I. Aluminiferous gneisses of the Kola series, Baltic Shield (geochemistry, nature and age of protolith). *Tr. Karel. Nauchn. Tsentra RAN* **2016**, *10*, 34–62. (In Russian)
35. *State Geological Map of Russian Federation. Scale 1:1000000 (the Third Generation). Series Severo-Karsko-Barentsevomorskaya. Sheet R-37, 38—Cape Svyatoy Nos, Cape Kanin Nos. Explanatory Note*; Kartograficheskaya fabrika VSEGEI: Sankt-Peterburg, Russia, 2008; 251p. (In Russian)
36. Rubatto, D. Zircon: The metamorphic mineral. *Rev. Mineral. Geochem.* **2017**, *83*, 261–295. [CrossRef]
37. Wu, Y. Metamorphic Zircon. In *Encyclopedia of Geology*, 2nd ed.; Academic Press: Cambridge, MA, USA, 2021; pp. 584–596; ISBN 9780081029091. [CrossRef]
38. Kretschmar, U.; Scott, P.D. Phase relations involving arsenopyrite in the system Fe-As-S and their application. *Can. Mineral.* **1976**, *14*, 363–386.
39. Tyukova, Y.E.; Voroshin, S.V. Arsenopyrite Mineral Composition and Parageneses in Ore Deposits and Host Rocks throughout the Upper Kolyma River Area (Interpreting the Genesis of Sulfide Mineral Assemblages). North-Eastern Integrated Research Institute of Far East department of RAS: Magadan, Russia, 2007; 108p. (In Russian)
40. Ponomareva, N.I.; Gordienko, V.V.; Shurekova, N.S. *Physicochemical Circumstances of Beryl Generation in "Bol'shoy Lapot" Deposit (Kola Peninsula)*; Series 7; Vestniks of Saint Petersburg University: Saint Petersburg, Russia, 2015; Volume 3, pp. 4–20. (In Russian)
41. Molnar, F.; Middelton, A.; Stein, H.; O'Brien, H.; Lahaye, Y.; Huhma, H.; Pakkanen, L.; Johanson, B. Repeated syn and post orogenic gold mineralization events between 1.92 and 1.76 Ga along Kiistala Shear Zone in the Central Lapland greenstone belt, northern Finland. *Ore Geol. Rev.* **2018**, *101*, 936–959. [CrossRef]
42. Molnár, F.; O'Brien, H.; Stein, H.; Cook, N.D.J. Geochronology of hydrothermal processes leading to the formation of the Au–U mineralization at the Rompas prospect, Peräpohja belt, Northern Finland: Application of paired U-Pb dating of uraninite and Re–Os dating of molybdenite to the identification of multiple hydrothermal events in a metamorphic terrane. *Minerals* **2017**, *7*, 171. [CrossRef]
43. Groves, D.I.; Santosh, M. Province-scale commonalities of some world-class gold deposits: Implications for mineral exploration. *Geosci. Front.* **2015**, *6*, 389–399. [CrossRef]
44. Hart, C.J.R. Reduced intrusion-related gold systems. In *Mineral deposits of Canada: A Synthesis of Major Deposit Types, District Metallogeny, the Evolution of Geological Provinces, and Exploration Methods*; Special Publication No. 5; Goodfellow, W.D., Ed.; Geological Association of Canada, Mineral Deposits Division, 2007; pp. 95–112. ISBN 978-1-897095-24-9.
45. Baker, T.; Lang, J.R. Fluid inclusion characteristics of intrusion related gold mineralization, Tombstone-Tungsten magmatic belt, Yukon Territory, Canada. *Mineral. Depos.* **2001**, *36*, 563–582. [CrossRef]
46. Kalinin, A.A. Stages of Gold Deposits Formation in the Precambrian of the North-Eastern Fennoscandia. *Minerals* **2022**, *12*, 537. [CrossRef]
47. Goryainov, P.M.; Ivanyuk, G.Y.; Bayanova, T.B.; Bazay, A.V.; Astaf'ev, B.Y.; Voinova, O.A. Composition, genesis, and age of rare-earth and precious metal mineralization in the rocks of banded iron formation in the Kola Peninsula. *Proc. Fersman Sci. Sess.* **2012**, *9*, 235–238. (In Russian)

Disclaimer/Publisher's Note: The statements, opinions and data contained in all publications are solely those of the individual author(s) and contributor(s) and not of MDPI and/or the editor(s). MDPI and/or the editor(s) disclaim responsibility for any injury to people or property resulting from any ideas, methods, instructions or products referred to in the content.

minerals

MDPI

Article

Mineralization Styles in the Orogenic (Quartz Vein) Gold Deposits of the Eastern Kazakhstan Gold Belt: Implications for Regional Prospecting

Dmitry L. Konopelko [1,*], Valeriia S. Zhdanova [2], Sergei Y. Stepanov [2], Ekaterina S. Sidorova [1], Sergei V. Petrov [1], Aleksandr K. Kozin [2], Emil S. Aliyev [3], Vasiliy A. Saltanov [3], Mikhail A. Kalinin [2], Andrey V. Korneev [4] and Reimar Seltmann [5]

[1] Institute of Earth Sciences, St. Petersburg State University, 7/9 University Embankment, St. Petersburg 199034, Russia; sidorovaleo@mail.ru (E.S.S.); petrov64@gmail.com (S.V.P.)
[2] South Ural Federal Scientific Center of Mineralogy and Environmental Geology, Ural Branch, Russian Academy of Sciences, Miass 456317, Russia; valeriia.zh.rock@gmail.com (V.S.Z.); stepanov-1@yandex.ru (S.Y.S.); kozin@mineralogy.ru (A.K.K.); mih7d@mail.ru (M.A.K.)
[3] LLP General Geology Group, Astana 010000, Kazakhstan; wlifter@mail.ru (E.S.A.); s@ltanov.ru (V.A.S.)
[4] LLC Ural Exploration, Ekaterinburg 620100, Russia; geol_korf@mail.ru
[5] Center for Russian and Central Eurasian Mineral Studies, Department of Earth Sciences, Natural History Museum, Cromwell Road, London SW7 5BD, UK; r.seltmann@nhm.ac.uk
* Correspondence: konopelko@inbox.ru or d.konopelko@spbu.ru

Abstract

The Eastern Kazakhstan Gold Belt is a major black-shale-hosted gold province in Central Asia where the main types of deposits comprise mineralized zones with auriferous sulfides (micro- and nano-inclusions of gold and refractory gold) and quartz veins with visible gold. The quartz vein deposits are economically less important but may potentially represent the upper parts of bigger ore systems concealed at depth. In this work, the mineralogy of the quartz vein deposits and related wall rock alteration zones was studied using microscopy and SEM-EDS analysis, and the geochemical dispersion of the ore elements in primary alteration haloes was documented utilizing spatial distribution maps and statistical treatment methods. The studied auriferous quartz veins are classified as epizonal black-shale-hosted orogenic gold deposits. The veins generally have linear shapes with an average width of ca. 1 m and length up to 150 m and contain high-grade native gold with minor amounts of sulfides. In supergene oxidation zones, the native gold is closely associated with Fe-hydroxide minerals cementing brecciated zones within the veins. The auriferous quartz veins are usually enclosed by the wall rock alteration envelopes, where two types of alteration are distinguished. Proximal phyllic alteration (sericite-albite-pyrite ± chlorite, Fe-Mg-Ca carbonates, arsenopyrite, and pyrrhotite) develops as localized alteration envelopes, and pervasive carbonation accompanied by chlorite ± sericite and albite is the dominant process in the distal alteration zones. The rocks within the alteration zones are enriched in Au and chalcophile elements, and three groups of chemical elements showing significant positive mutual correlation have been identified: (1) an early geochemical assemblage includes V, P, and Co (±Ni), which are the chemical elements characteristic for black shale formations, (2) association of Au, As, and other chalcophile elements is distinctly overprinting, and manifests the main stage of sulfide-hosted Au mineralization, and (3) association of Bi and Hg (±Sb and U) includes the chemical elements that are mobile at low temperatures, and can be explained by activity of the late-stage hydrothermal or supergene fluids. The chalcophile elements show negative slopes from proximal to distal alteration zones and form overlapping positive anomalies on spatial distribution mono-elemental maps. Thus, the geochemical methods can provide useful tools to delineate the

ore elemental associations and to outline reproducible anomalies for subsequent regional gold prospecting.

Keywords: Eastern Kazakhstan Gold Belt; West Kalba zone; orogenic gold deposits; black shale; quartz veins; primary alteration halo; gold hyper-enrichment

1. Introduction

The Eastern Kazakhstan Gold Belt is one of the biggest black-shale-hosted gold provinces in Central Asia, containing several hundred placer and lode gold deposits with total endowment ca. 500 t Au [1–4]. Similar to other major black-shale-hosted gold provinces of the region, including the world-class Muruntau and Kumtor ore districts in the Tien Shan Gold Belt, the lode gold deposits of Eastern Kazakhstan occur as structurally controlled mineralization zones in metamorphosed carbonaceous flyschoid sediments [1,3,5–8]. Two main types of deposits distinguished in the Eastern Kazakhstan Gold Belt comprise the mineralized zones with auriferous sulfides and quartz vein-type deposits with visible native gold [7,8]. The largest Au deposits of the belt, including the Bakyrchik-Bolshevik mining district (Kyzyl Gold Project), Akzhal, Vasilievskoe, and Suzdalskoe, are classified as mineralized zones and are relatively well studied [4,9–11], while numerous small and sub-economic quartz vein deposits and occurrences, potentially representing upper parts of the hidden ore systems at depth, remain insufficiently investigated [4]. In order to fill in this gap, several newly discovered and re-examined quartz vein-type deposits have been studied in the course of the ongoing exploration projects. The mineralogical composition of the ore zones and related alteration envelopes was elucidated using conventional microscopy and scanning electron microscopy/energy-dispersive X-ray spectroscopy (SEM-EDS analysis), and the geochemical dispersion of the ore elements in primary alteration haloes was documented utilizing spatial distribution maps and statistical treatment methods. The obtained results help to better understand the ore-controlling factors playing an important role in formation of gold deposits and can be used as valuable guidelines for regional prospecting.

2. Geological Setting of Eastern Kazakhstan

Geological formations exposed in Eastern Kazakhstan are part of the Central Asian Orogenic Belt, one of the largest accretionary orogens comprising Precambrian and Paleozoic microcontinents and island arcs that amalgamated during the final closure of the Paleo-Asian Ocean in the late Paleozoic [12–17]. Tectonic units of Eastern Kazakhstan include several NW–SE elongated terranes formed during the evolution of the Ob-Zaisan branch of the Paleo-Asian Ocean. The Ob-Zaisan oceanic basin separated the early Paleozoic (Caledonian) micro-continent of Paleo-Kazakhstan from Peri-Siberian continental blocks of Altai-Sayan and was closed in the course of the late Paleozoic (Hercynian) collisional events. From west to east, the tectonic units of Eastern Kazakhstan include the Chingiz-Tarbagatai block, Zharma-Saur volcanic arc, West Kalba zone, Kalba-Narym belt, Irtysh shear zone, and Rudny-Altai terrane (Figure 1).

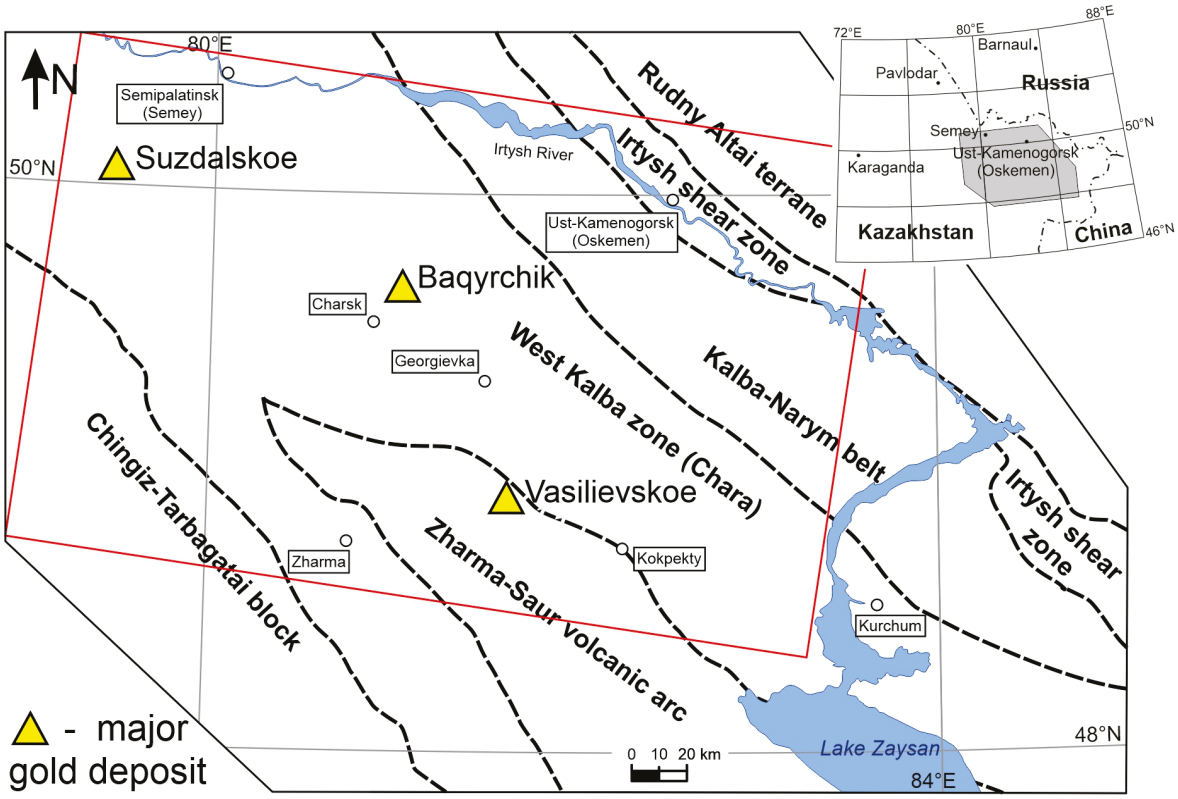


Figure 1. Major tectonic units of Eastern Kazakhstan. After [18], modified by the authors. Red box indicates the territory shown in Figure 2.

The westernmost Chingiz-Tarbagatai block is composed of deformed early Paleozoic volcanic arc formations comprising the basement of the Caledonian Paleo-Kazakhstan continent [19–21]. The early Paleozoic basement of the Chingiz-Tarbagatai is partially overlain by Devonian to early Carboniferous volcanics formed when subduction under the Paleo-Kazakhstan continent resumed in the middle–late Paleozoic [22].

The Zharma-Saur volcanic arc is a 10–15 km-wide discontinuous belt of early Carboniferous (Moscovian) volcanics stretching along the eastern margin of the Chingiz-Tarbagatai block. To the southeast, this arc can be traced in the Tarbagatai Range and further east in the Sawur Mountains of China [20,23–26].

The West Kalba, also known in the literature as the Chara zone, represents the largest (ca. 50–70 km wide) regional tectonic unit that hosts numerous Au deposits and occurrences, described as the Eastern Kazakhstan Gold Belt [8,10,27]. The West Kalba zone is interpreted as a superimposed Carboniferous sedimentary basin filled with flysch-like and turbiditic terrigenous sediments, derived from a juvenile intra-oceanic arc, which change upsection to coarse-grained clastics and limnic molasses [28]. It is suggested that the opening of this basin in the early Carboniferous (Visean) postdated the early stages of Hercynian collisional events in the area, while subsequent collisional compression and shearing resulted in strong deformation of the basin fill during the late Carboniferous–early Permian [20,27]. The deformations were accompanied by the greenschist facies metamorphism and small-scale granitoid magmatism, and can be generally characterized as top-to-the-west thrusting at the stage of collision and strong sinistral strike-slip faulting and shearing in the NW–SE direction at the post-collisional stage that occurred due to clockwise rotation of Siberia relative to the Paleo-Kazakhstan continent [27,29,30]. The thrusting produced numerous tectonic sheets of different geodynamic origin. One of them is the Char ophiolite mélange located in the central part of the West Kalba zone [31]. Late Carboniferous volcanics and

associated rocks are developed in the southwestern part of the West Kalba zone. Intrusive rocks are relatively rare and comprise Carboniferous diorites and granodiorites with ages in the range 325–305 Ma and early Permian granites that form dikes and stocks in the Carboniferous sediments [27,32].

The main volume of the early Permian post-collisional granitoids was emplaced in the Kalba-Narym zone located to the east. In this area, batholiths of S-type granites, which also marginally intrude in the West Kalba zone, occupy up to 70% of the territory on the present-day erosion surface and host significant tin and rare metal mineralization [6,24,32,33]. The basement of the Kalba-Narym zone is composed of the late Devonian–early Carboniferous clastic sediments derived from the continental margins of Peri-Siberian blocks located to the east.

Further east, the Irtysh shear zone is a 5–10 km-wide band of deformations and high-grade metamorphic rocks developed along a system of continental-scale sinistral strike-slip faults separating the Kalba-Narym zone from the Rudny-Altai terrane, a Hercynian Peri-Siberian active continental margin hosting a number of world-class massive sulfide deposits [20].

3. Types of Deposits and Metallogenic Features of the Eastern Kazakhstan Gold Belt

The Eastern Kazakhstan Gold Belt, which is also known in the literature as the West Kalba or Chara Gold Belt, stretches for more than 300 km along the NW striking West Kalba zone and contains several hundred placer and lode gold deposits with total endowment estimated at ca. 500 t Au [1,5,6,8,34].

The lode gold deposits are hosted by the Carboniferous flyschoids (black shales) developed in the central and northeastern parts of the West Kalba zone and by Devonian to Carboniferous volcanics in the southern part of the zone (Figure 2). Based on field relationships and isotopic age determinations, it is generally accepted that major ore-forming events took place during the late Carboniferous–early Permian (310–280 Ma) and were related to the main phase of deformations and greenschist facies metamorphism in the West Kalba zone [7,35,36]. The deposits are classified as typical orogenic gold deposits [34,37]; however, based on geological and mineralogical features, they can be subdivided into two major types: (1) structurally controlled mineralized zones with auriferous sulfides (pyrite and arsenopyrite) and (2) quartz veins with visible native gold [7,8]. There is also one auriferous skarn and several gold occurrences in jasperoids, demonstrating the Carlin-type deposit signatures [38].

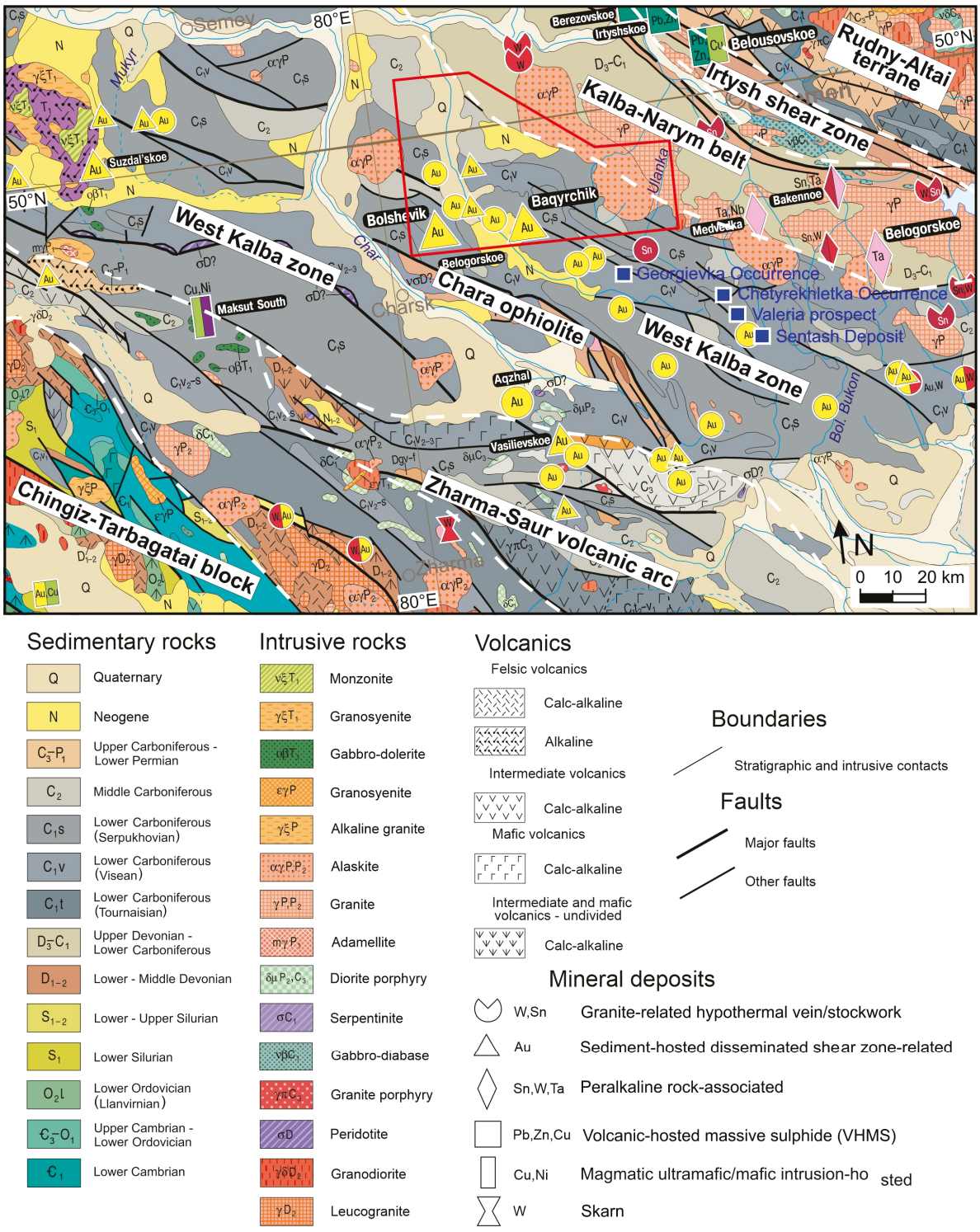


Figure 2. Part of the Mineral Deposits Map of Central Asia [39] showing Au deposits of the Eastern Kazakhstan Gold Belt and study areas shown as blue squares out of scale. Red frame indicates the territory shown in Figure 3.

Most of the major lode gold deposits, such as the largest Bakyrchik (or Baqyrchik) deposit with estimated reserves of 240 t Au, and several smaller deposits, including Bolshevik (~30 t Au), Akzhal (~14 t Au), Vasilievskoe (~18 t Au), and Suzdalskoe (~24 t Au), can be defined as tectonically controlled mineralized zones, where strongly deformed host rocks undergo potassic, propylitic, and carbonate-phyllic alteration [4,7,9–11,40]. The ore zones in these deposits comprise disseminated or veinlet sulfide mineralization with main

ore minerals represented by auriferous arsenopyrite and pyrite ± native gold with minor amounts of galena, chalcopyrite, pyrrhotite, sphalerite, and tennantite-tetrahedrite [7,9].

In contrast to mineralized zones, the ores of the quartz vein-type deposits are dominated by high-karat native gold with only minor amounts of sulfide minerals [4,10]. These deposits usually represent a series of individual quartz veins or stockwork vein systems often surrounded by alteration envelopes in the country rocks. The quartz veins can be generally classified as crack-seal-type; however, metasomatic replacement veins are also present in the areas of upper greenschist facies metamorphism [41]. The veins are generally characterized by linear or slightly bended shapes with average width 0.5–1.5 m and length up to 100–150 m. Deposits of this type are relatively small, with estimated reserves rarely exceeding 2–5 t Au; however, they often contain ultra-high-grade native gold ore-shoots, which represent attractive exploration targets for junior companies. Examples from the ongoing exploration projects conducted in the quartz vein deposits are presented herein and discussed in detail below.

Both types of deposits are structurally controlled. The regional-scale ore-controlling lineaments include the Kyzyl thrust-shear zone hosting the Bakyrchik and Bolshevik deposits and the Akzhal-Boko fault system, in which the Akzhal and Vasilievskoe deposits are located [4,6,7,10]. Character of deformations, ore-controlling faults, and spatial relationships between the two types of Au deposits are illustrated by the schematic geological map of the Bakyrchik ore field shown in Figure 3. In this map, late sublatitudinal top-to-the-south thrusts that formed in a thrust-shear deformation regime distorting the early NW trending structural pattern and controlling gold mineralization can be clearly seen. On a local scale, the emplacement of individual quartz veins and mineralized zones was controlled by transpressional structures, such as thrust planes, fold hinges, flexural folds, etc., where zones of boudinage and mylonitization and/or tectonic breccia were formed [7,42,43]. Extensional structures, as well as granitoid dikes and black shale intervals in the sedimentary section, are considered as important ore-controlling factors in the Eastern Kazakhstan Gold Belt [4,6,10].

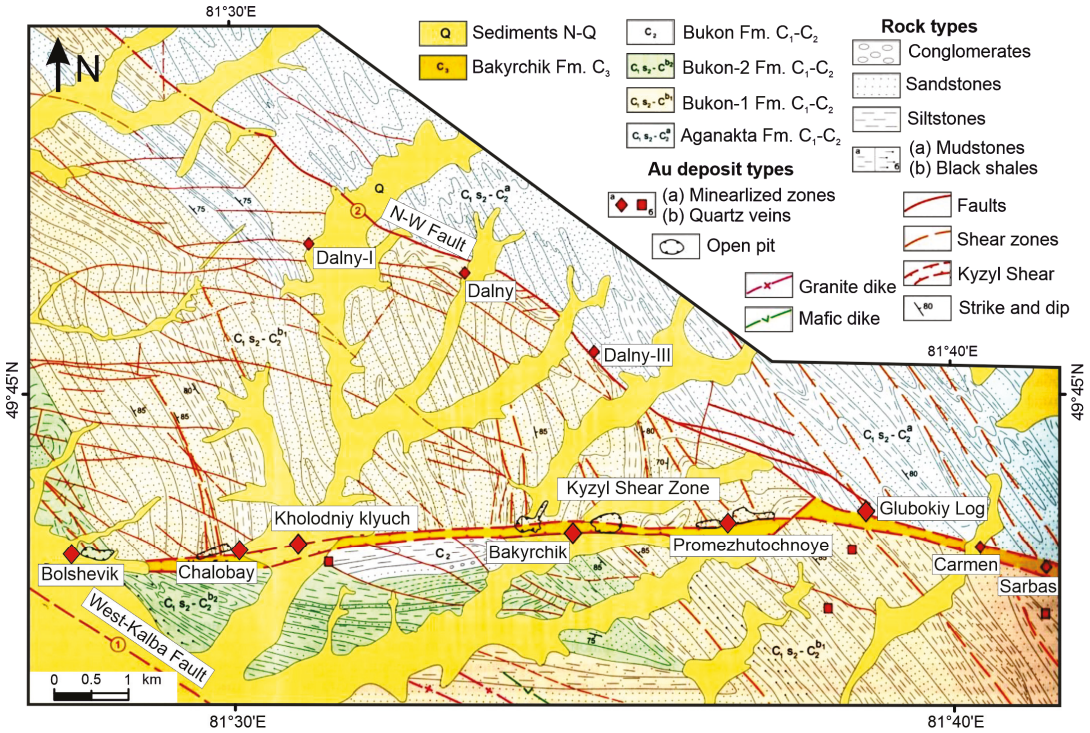


Figure 3. Schematic geological map of the Bakyrchik ore field. Modified after [44].

4. Analytical Methods

The research methods used in this study aimed to characterize the mineralogical and chemical composition of the rocks from the studied gold deposits and to elucidate geochemical processes operating in the ore-forming systems. Description and preliminary identification of the ore minerals were conducted in the Analytical Centre of Saint-Petersburg University, Russia, utilizing optical microscopy. Further identification of minerals in the ores and altered rocks and determination of their chemical composition was conducted utilizing a Hitachi S-3400N scanning electron microscope equipped with an Oxford Instruments Energy-Dispersive Spectrometer X-Max20 (SEM-EDS) (Oxford Instruments, Abingdon, UK). The spectra were processed automatically using the AzTec Energy software package (version 3.1.) using the TrueQ technique. The electron beam accelerating voltage of 20 kV and a current of 1.6 nA were used. X-ray acquisition time was 30 s in spot-mode. The energy-dispersive spectra were processed using the AzTec Energy software package. Quantification of elemental compositions was conducted using natural and synthetic standards, including pyrite, InAs, PbTe, and pure metals Zn, Cu, Bi, W, Sn, Cd, Sb, and Mn. X-ray lines measured were Ag Lα, Sb Lα, As Lα, Pb Lα, Zn Lα, Sn Lα, Fe Kα, Cu Kα, and S Kα. The analytical errors for most elements were below 0.5–0.7 wt.% (1σ). The lower detection limits for the analyzed elements were estimated at ~0.1 wt.% [45].

The composition of native gold particles was analyzed using a scanning electron microscope Tescan VEGA-3 system equipped with an Oxford EDS detector in the South Ural Federal Scientific Center of Mineralogy and Environmental Geology in Miass, RF.

Lithogeochemical and section whole-rock samples were analyzed in the LLC "Stewart Geochemical and Assay" in Moscow, RF. A total of 23 chemical elements were determined. The analytical methods included multi-channel arc atomic emission spectrometry (Arc AES) for Ag, As, B, Bi, Cd, Co, Cr, Cu, Ge, Hg, Li, Mn, Mo, Ni, P, Pb, Sb, Sn, U, V, W, and Zn, and fire assay with atomic absorption spectroscopy (FA-AAS) for Au.

The visible gold-bearing quartz vein samples were investigated utilizing a Neoscan N80 X-ray microtomograph (Neoscan, Mechelen, Belgium) in the Analytical Centre of Saint-Petersburg University, RF. The data were processed with the Neoscan 80 software, and subsequent visualization of the data was performed using the Dataviewer (version 1.5.2.4) and CTVox software (version 1.5.2) applications (Bruker Corporation, Karlsruhe, Germany).

5. Description of the Studied Gold Deposits/Occurrences and Sampling

The studied mineralization sites are located 40–60 km southeast of the Bakyrchik deposit in the area hosting the majority of the quartz vein-type deposits of the Eastern Kazakhstan Gold Belt (Figure 2). This area is composed of flyschoid sediments of the lower Carboniferous (Serpukhovian) Dalankarninskaya Formation that changes upsection to coarse molasse sediments of the middle Carboniferous (Bashkirian) Taubinskaya Formation [4,46,47]. The sediments are strongly deformed. The northwest-trending folding dominates and is usually characterized by compressed, close to isoclinal folds inclined to the northeast at an angle of 60–70° (Figure 4A). North-dipping longitudinal faults and top-to-the-south thrusts are a characteristic feature. Along with the dominant northwestern linear folding, superimposed transverse folding of northeastern orientation is locally developed [46]. Both formations contain carbonaceous mudstones and siltstones that are turned into shales in the areas of green schist facies metamorphism. Carbonaceous sediments reach up to 150 m in thickness and contain from 0.44 to 1.37 wt.% organic matter, which is typical for black shales elsewhere [46].

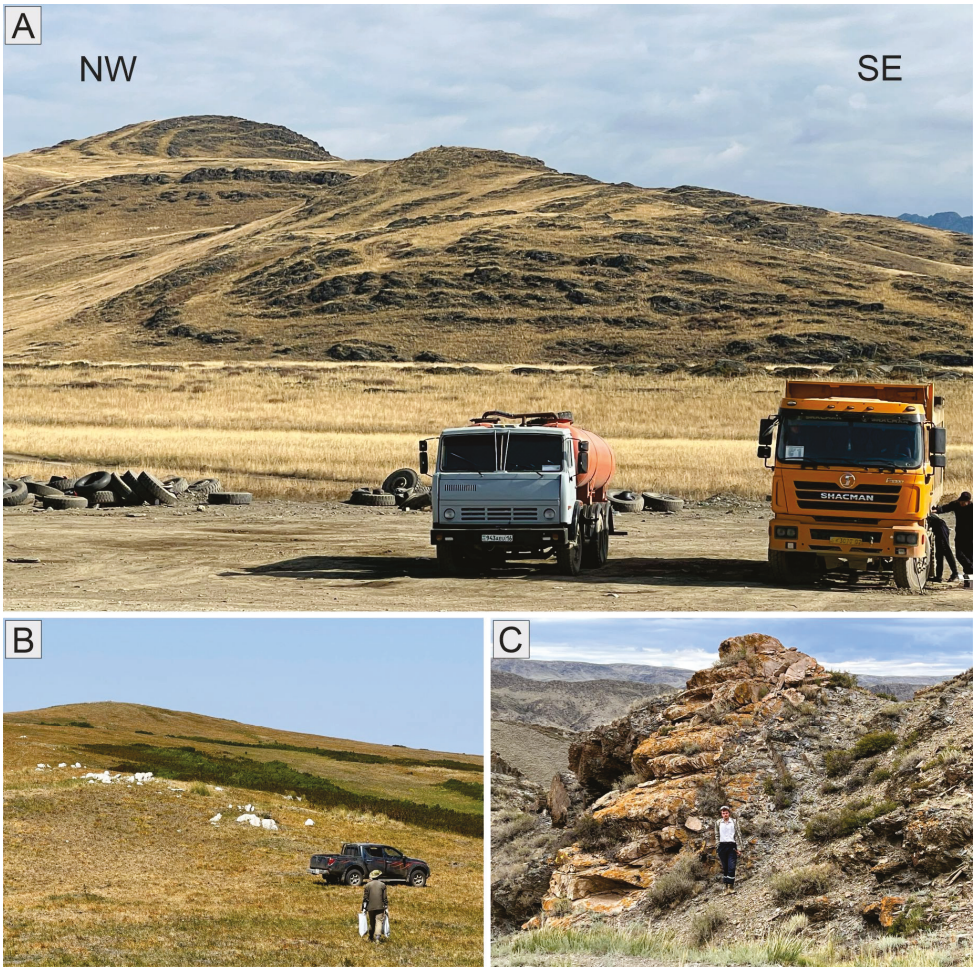


Figure 4. Typical geological features of the Sentash deposit area: (**A**) folded Carboniferous flyschoids showing the NW vergence of folding, (**B**) quartz veins in the steppe regions are preserved on the surface as large fragments of white quartz, and (**C**) dike of Carboniferous granitoid crosscutting the layering of country shales.

Intensive prolonged deformation of the sediments under greenschist facies conditions enabled mobilization of silica and formation of numerous quartz veins emplaced in extensional structures all over the area. Individual quartz veins can be up to 5 m thick and 100–300 m long and are well preserved on the surface in the steppe regions of eastern Kazakhstan as large fragments of white quartz (Figure 4B). Auriferous quartz veins are virtually indistinguishable from the barren veins, which makes exploration in this area a challenging task because, statistically, only one out of several hundred veins may contain economic gold mineralization [4,46,47].

Another characteristic feature of this area comprises dikes and stocks of the Kunush gabbro-plagiogranite suite (Figure 4C). Dike swarms of the Kunush plagiogranite porphyry were reported from many ore fields and dated at ca. 310–300 Ma [27]. The dikes are deformed and hydrothermally altered together with surrounding sediments. Based on geophysical data, the presence of bigger concealed intrusions was supposed under several mineralized quartz vein systems of the region [4,7,47].

Currently operating quartz vein-type deposits in the study area include the Sentash, Dzhumba, and Kuludzhun gold mines. Three gold occurrences in the vicinity of the Sentash deposit where exploration projects resumed in the last years were studied in this work, and their geological features are briefly described below.

5.1. Sentash Deposit

The Sentash mine, where the exploration trenches and open pits were investigated in the course of this study, was used as a reference site to characterize the alteration and mineralization styles of a typical quartz vein-type deposit. The deposit includes 60 auriferous quartz veins on the territory of ca. 100 square km. Most veins were mined in the past and are now abandoned, however, several new exploration projects were initiated at the deposit in the last years.

The quartz veins crosscut deformed flyschoid sediments of the Dalankarninskaya Formation, which undergo phyllic alteration and contain altered dikes of granodiorite porphyry [46,47]. The veins predominantly have simple linear forms. The largest Udalaya vein that produced 2.2 t Au is a short tabular body emplaced in a tectonic detachment zone formed in the core of an anticlinal fold. The Udalaya vein is 1–5 m thick with a length of about 70 m and was traced to a depth of 300 m [46]. The other ore bodies with average reserves of about 0.1–0.3 t Au are represented by 0.1–1.0 m-thick quartz veins crosscutting the layering of the country rocks and filling the fractures of northwestern strike. These types of ore bodies are exemplified by a schematic geological map of exploration site No. 49 shown in Figure 5.

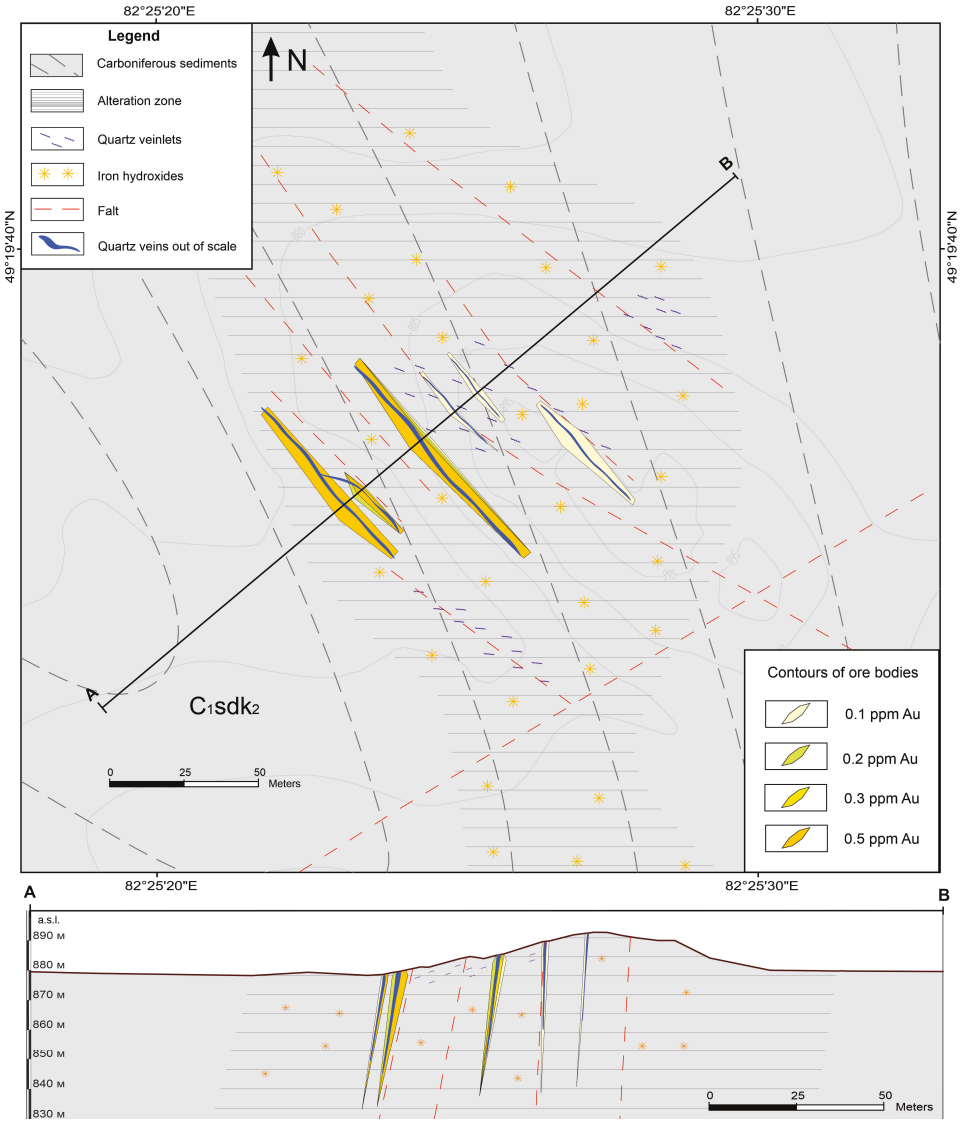


Figure 5. Schematic geological map and trans-section of exploration site No. 49, Sentash deposit.

The auriferous quartz veins are the major host of gold in the Sentash deposit. However, altered country rocks enclosing the veins may also contain economic concentrations of Au represented by native gold particles hosted in quartz veinlets and surrounding altered sediments. Typical mineralized quartz veins and veinlets in altered sandy shale are illustrated in Figure 6A. More than 95% of gold in the ore is native high-karat gold. Minor sulfides are represented mainly by pyrite, and small amounts of pyrrhotite, chalcopyrite, and arsenopyrite. The average gold grade is usually in the range of 2–5 ppm Au, however, it may vary significantly within individual veins, reaching several kg per ton in the hyper-rich ore-shoots. Photographs of native gold from hyper-rich ore-shoots from the Sentash deposit, presented in Figure 6C–F, show that free gold in supergene oxidation zones usually associates with Fe-hydroxide minerals, filling the space between quartz fragments in brecciated veins.

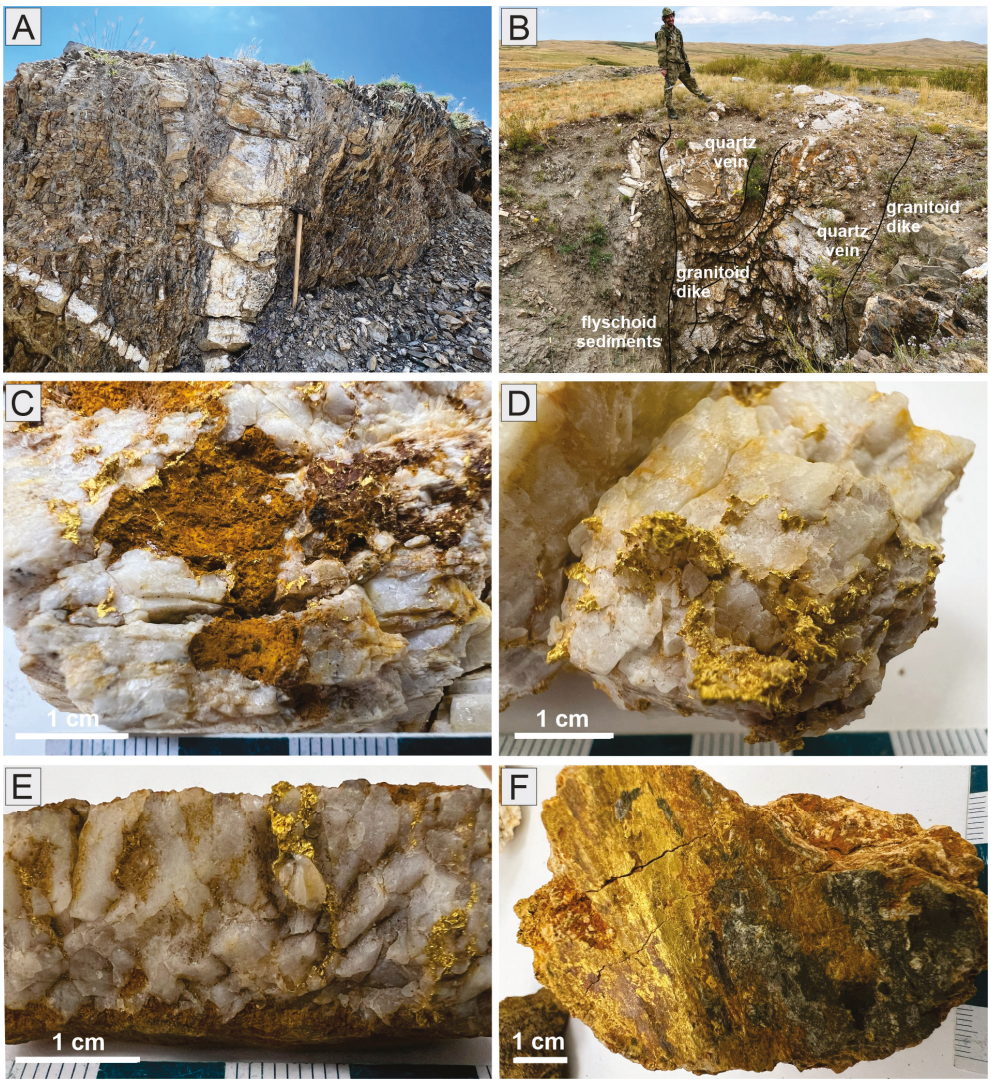


Figure 6. Auriferous quartz veins in the Sentash deposit area: (**A**) auriferous quartz veins/veinlets in altered sandy shale at Sentash deposit, (**B**) auriferous quartz veins in contacts of granitoid dike at Chetyrekhletka occurrence, and (**C**–**F**) specimens of quartz veins with native gold from hyper-rich ore-shoots from Sentash deposit. Note the association of native gold with Fe-hydroxide minerals (**C**,**F**), elongation of gold particles perpendicular to the strike of thin veins (**E**), and the slicken-side formed along the native gold veinlet in Fe-hydroxide-filled fracture (**F**). Photographs C–F were courtesy of LLC "Sentas".

Six representative rock samples collected at the Sentash deposit were used in this study to characterize the mineralogical and chemical composition of mineralized rocks. Three samples were investigated utilizing the SEM-EDS method (Supplementary Table S1). All samples were analyzed for 23 elements, and the results were included in the dataset for statistical treatment (Supplementary Table S1).

5.2. Chetyrekhletka Occurrence

The Chetyrekhletka occurrence located 16 km northeast of the Sentash deposit (Figure 2) contains one linear ore zone where the gold mineralization associates with auriferous quartz veins developed in contacts of strongly altered granitoid dike emplaced parallel to schistosity in surrounding flyschoid sediments (Figures 6A and 7). Steeply dipping ore-body with Au grade 2–5 ppm is 1.5–3 m thick and can be traced for approximately 300 m [48]. Twenty representative rock samples collected along the profile across the ore zone were used in this study to characterize the mineralogical composition of the ore and alteration of the country rocks. Eight samples were investigated utilizing the SEM-EDS method (Supplementary Table S1). Au concentrations analyzed in 75 section samples collected from trench No. 1 (Figure 7) are given in Supplementary Table S1.

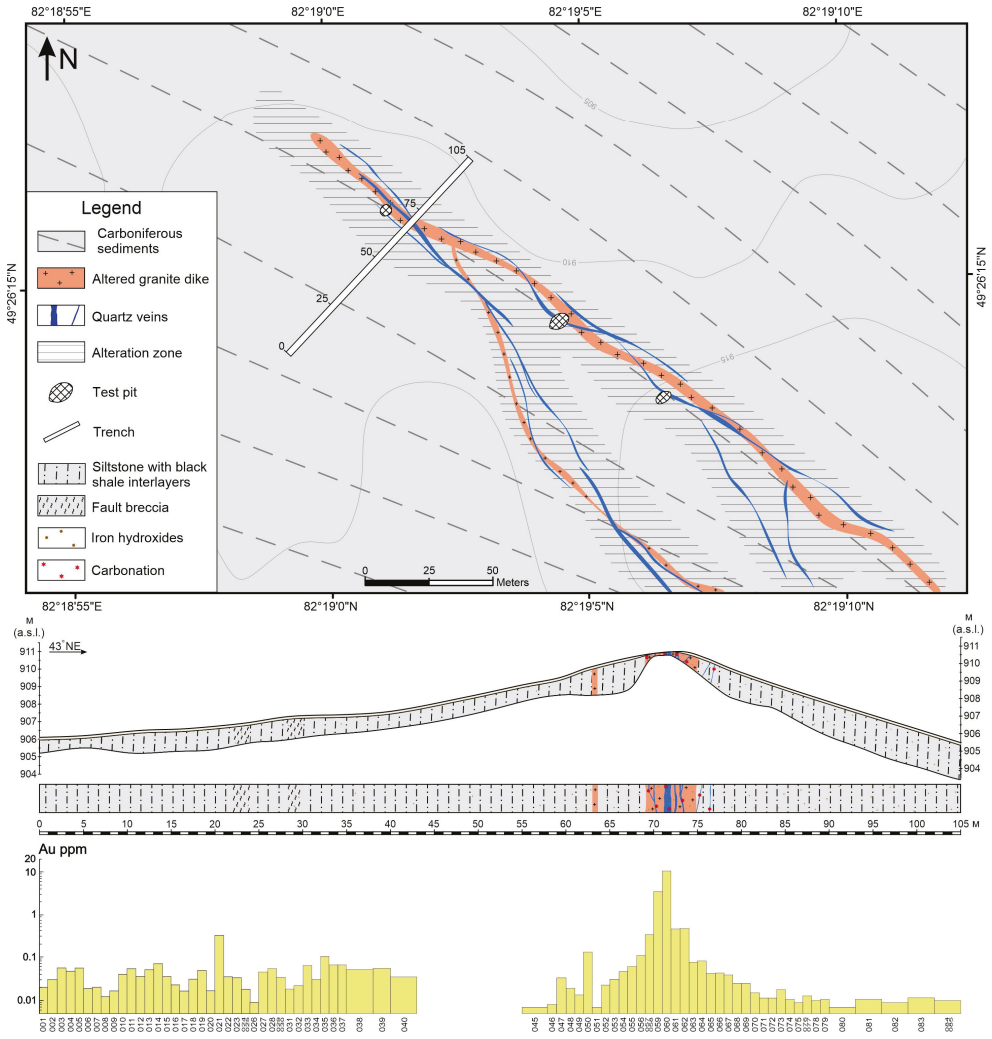


Figure 7. Schematic geological map of Chetyrekhletka occurrence and trans-section along trench No. 1 showing gold concentrations in section samples. Sample numbers as in Supplementary Table S1.

5.3. Valeria Prospect

The Valeria prospect is a 2 km × 2 km area located 7 km south of the Chetyrekhletka occurrence (Figure 2), where the positive geochemical As anomaly was detected in the course of 1:200,000 geological mapping in the 1960s [48]. Intercalating carbonaceous and sandy shales exposed in this area predominantly strike NW and enclose several 100–300 m-thick alteration zones, where the shales contain characteristic brownish porphyroblasts of carbonate minerals and abundant veinlets of quartz. Valeria prospect was re-examined within the frame of the ongoing exploration project, and lithogeochemical sampling conducted along ca. 2 km-long profiles across strike of alterations zones revealed elevated concentrations of gold in metasomatically altered shales. Eighty-eight lithogeochemical samples were analyzed for twenty-three elements, and the results were used to construct mono-element geochemical maps for main ore-forming metals and included in the dataset for statistical treatment (Supplementary Table S1). Two representative rock samples from Valeria prospect were investigated utilizing optical microscopy and SEM-EDS techniques in order to characterize the mineral composition of auriferous alteration zones (Supplementary Table S1).

5.4. Georgievka Occurrence

This mineralization site in fresh road-cut near Georgievka village (Figure 2) was recently discovered in the course of the ongoing exploration project. It represents a linear NW striking 300 m-thick alteration zone in sandy shales that contains 1–2 m-thick quartz veins with sulfide minerals and visible gold identified in polished thin sections. Three samples from the Georgievka occurrence were investigated utilizing optical microscopy and SEM-EDS techniques (Supplementary Table S1), and eleven samples analyzed for twenty-three elements were included in the dataset for statistical treatment (Supplementary Table S1). In addition, 2 quartz vein samples containing visible gold were studied using the computer tomography method.

6. Results

6.1. Petrography and Mineralogy of Alteration Zones

The mineralized alteration zones in the study area occur in the poorly sorted immature Carboniferous flyschoids that vary in composition from carbonaceous mudstones to coarse-grained graywacke sandstones [28]. The sediments are metamorphosed under lower greenschist facies conditions and characterized by a low degree of recrystallization and well-preserved sedimentary structures (Figure 8A) locally obliterated by schistosity, cleavage, and mylonitic foliations as a result of regional folding. Two types of alteration are distinguished: (1) Pervasive carbonate ± chlorite alteration is expressed in the field by the appearance of characteristic brownish porphyroblasts of iron-rich carbonate commonly replaced by Fe-hydroxide minerals (Figure 8B). This type of alteration is widely developed in the area and can be defined as distal to mineralization. (2) Proximal sericite-albite-pyrite alteration is expressed in the rocks as the light coloration zones often containing abundant porphyroblasts of pyrite, which can develop pervasively (Figure 8C) or aligned to the fractures serving as conduits for fluids (Figure 8D). Because these alteration styles are typical for all studied localities, they are described below collectively.

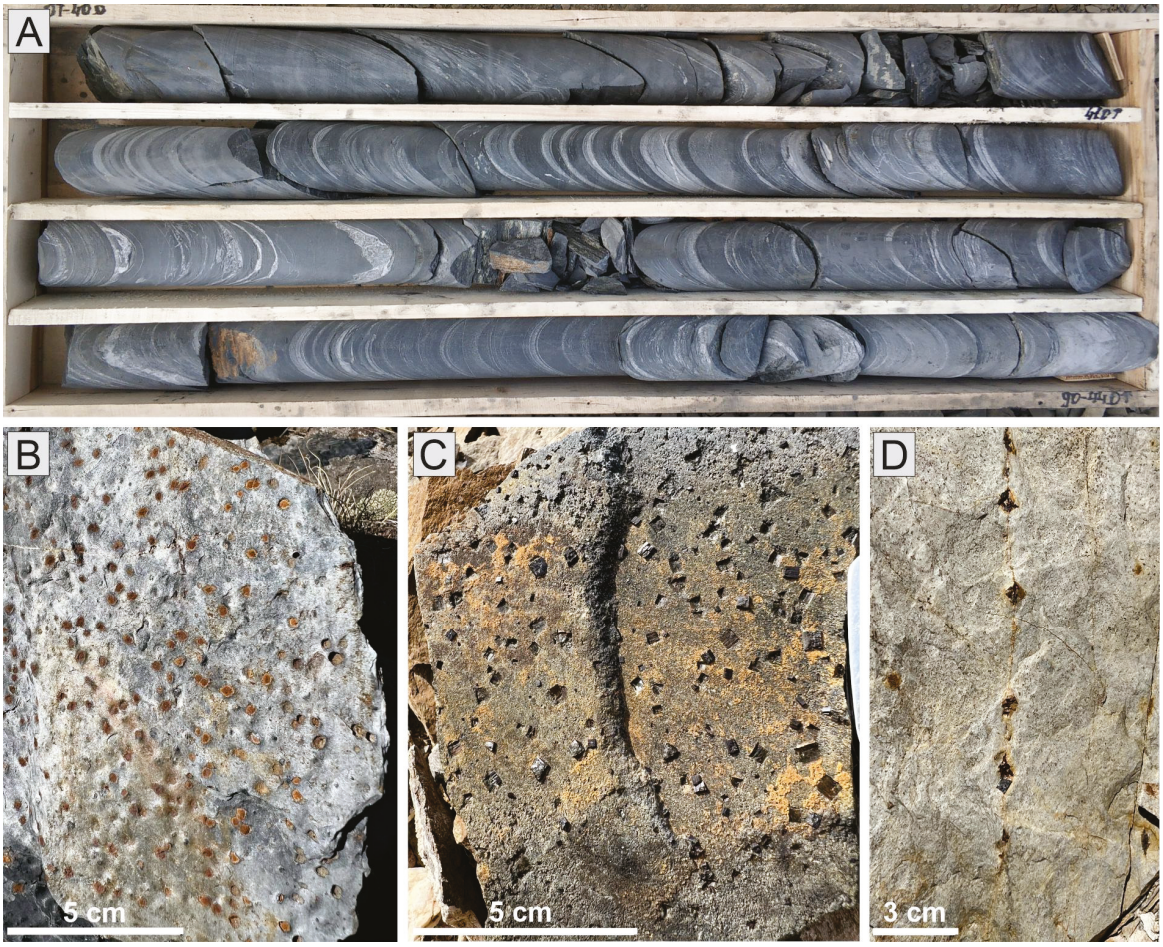


Figure 8. Characteristic alteration patterns in the study area: (**A**) Serpukhovian carbonaceous siltstone of the Dalankarninskaya Formation with rhythmical bedding in the vicinity of Chetyrekhletka occurrence, (**B**) brownish porphyroblasts of Fe-rich carbonate replaced by Fe-hydroxide minerals in sandy shale from Valeria prospect, (**C**) pervasively developed pyrite porphyroblasts in altered siltstone from Georgievka occurrence, and (**D**) pyrite porphyroblasts aligned to fracture, Georgievka occurrence.

Brownish composite porphyroblasts predominantly composed of carbonate minerals is a characteristic feature of the distal alteration zones that may be partially related to regional metamorphism [49]. The porphyroblasts, comprising up to 30–40 vol.% of the rock, vary in size from 2 to 10 mm and usually preserve the shapes of original carbonate crystals. However, most of the porphyroblasts are characterized by complex internal structures, and several compositional varieties were distinguished as a result of microscopic investigations. Porphyroblasts of iron-rich carbonate (supposedly ankerite) completely replaced by Fe-hydroxide minerals are a typical feature of the wall rock alteration at the Sentash deposit and Chetyrekhletka occurrence (Figure 9A,B). Zoned porphyroblasts with fine-grained quartz-chlorite aggregate in the cores and ferrodolomite-iron hydroxide rims, shown in Figure 9C,D, were described in distal parts of alteration zones at the Chetyrekhletka occurrence. Calcite porphyroblasts are characteristic for iron-poor rock types (Figure 9E), and chlorite-dominated porphyroblasts with sericite rims were observed in black shales at several localities (Figure 9F).

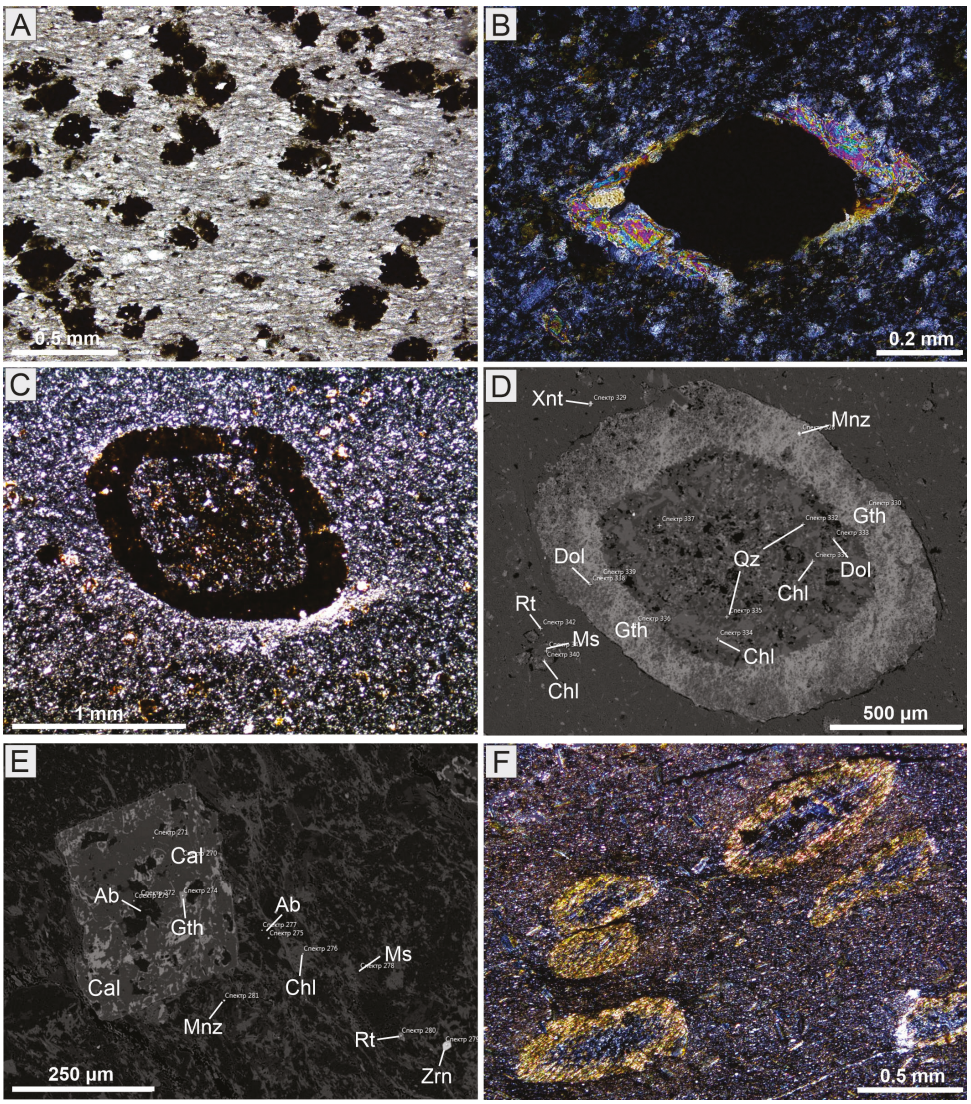


Figure 9. Mineralogy of distal alteration zones. (**A**) Microphotograph of porphyroblasts of Fe-rich carbonate replaced by Fe-hydroxide minerals in altered siltstone from Sentash deposit. Plane polarized transmitted light. (**B**) Microphotograph of Fe-rich carbonate porphyroblast replaced by Fe-hydroxide minerals with sericite-filled pressure shadows in altered sandstone from Chetyrekhletka occurrence. Transmitted light and crossed polarizers. (**C**) Microphotograph of composite porphyroblast with quartz-chlorite core and ferrodolomite-iron hydroxide rim in altered siltstone from Sentash deposit. Transmitted light and crossed polarizers. (**D**) BSE image showing mineral phases identified in composite porphyroblasts from Sentash deposit. (**E**) BSE image showing mineral phases identified in altered siltstone with calcite porphyroblasts from Sentash deposit. (**F**) Microphotograph of chlorite-dominated porphyroblasts with sericite rims in black shales from Chetyrekhletka occurrence. Transmitted light and crossed polarizers. Abbreviations: Qz—quartz, Ab—albite, Chl—chlorite, Dol—dolomite, Cal—calcite, Ms—muscovite, Gth—Fe-hydroxide minerals, Rt—rutile, Zrn—zircon, Mnz—monazite, and Xnt—xenotime.

Carbonation is also manifested in the groundmass of the rocks, where it is accompanied by the development of chlorite ± sericite and albite occurring as irregularly distributed clusters and/or branching microveinlets (Figure 9E). Monazite, rutile, and zircon occur as accessory and trace minerals (Figure 9E). SEM-EDS analysis has shown that the compositions of carbonate minerals in the groundmass correspond to those in the porphyroblasts and vary from ferrodolomite to calcite, with only one analysis plotting in the ankerite field on the classification diagram (Figure 10 and Supplementary Table S1). The composition

of carbonate minerals is probably controlled by the iron content in the host rocks and by the degree of preservation of ankerite, which is easily decomposed and replaced by Fe-hydroxide minerals and dolomite in the supergene oxidation zones [49]. Distal alteration also includes silification expressed by the quartz-carbonate veinlets/veins typical for central parts of alteration zones. Gold mineralization is interpreted as part of this alteration assemblage, with highest concentrations (up to 0.2 ppm Au) found in veinlet-rich samples.

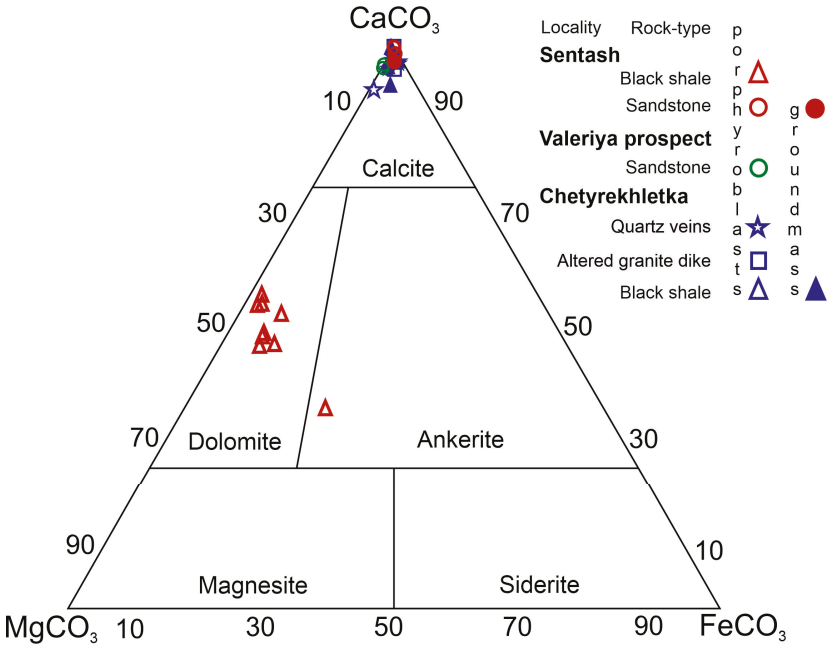


Figure 10. Compositions of carbonate minerals from auriferous alteration zones in flyschoid sediments on a classification diagram.

Proximal alteration zones usually occur as envelopes enclosing the auriferous quartz veins and comprise typical phyllic alteration assemblage, including sericite, albite, pyrite ± chlorite, Fe-Mg-Ca carbonates, arsenopyrite, and pyrrhotite. Pervasive phyllic alteration develops irrespectively of the host rock, affecting various types of sediments and granitoid dikes to the same extent (Figure 11A,B). Sericite predominantly replaces the matrix of sedimentary rocks and occurs as flakes and microveinlets comprising up to 50 vol.% of quartz-albite ± pyrite metasomatites (Figure 11C,D). Chlorite and calcite are characteristic secondary minerals in altered granitoid dikes, where the ferromagnesian phases are replaced by chlorite, and the primary feldspars are replaced by a fine-grained aggregate of quartz, albite, carbonate, and sericite with patches of Fe-hydroxide minerals (Figure 11E). Accessory minerals include apatite, ilmenite, rutile, zircon, and monazite (Figure 11C–F). Sulfide mineralization is mainly represented by pyrite, which is usually replaced by Fe-hydroxides as a result of supergene oxidation (Figure 11F). Concentrations of Au in proximal alteration zones may vary significantly, with native gold being the main host of this metal in the supergene oxidation zones.

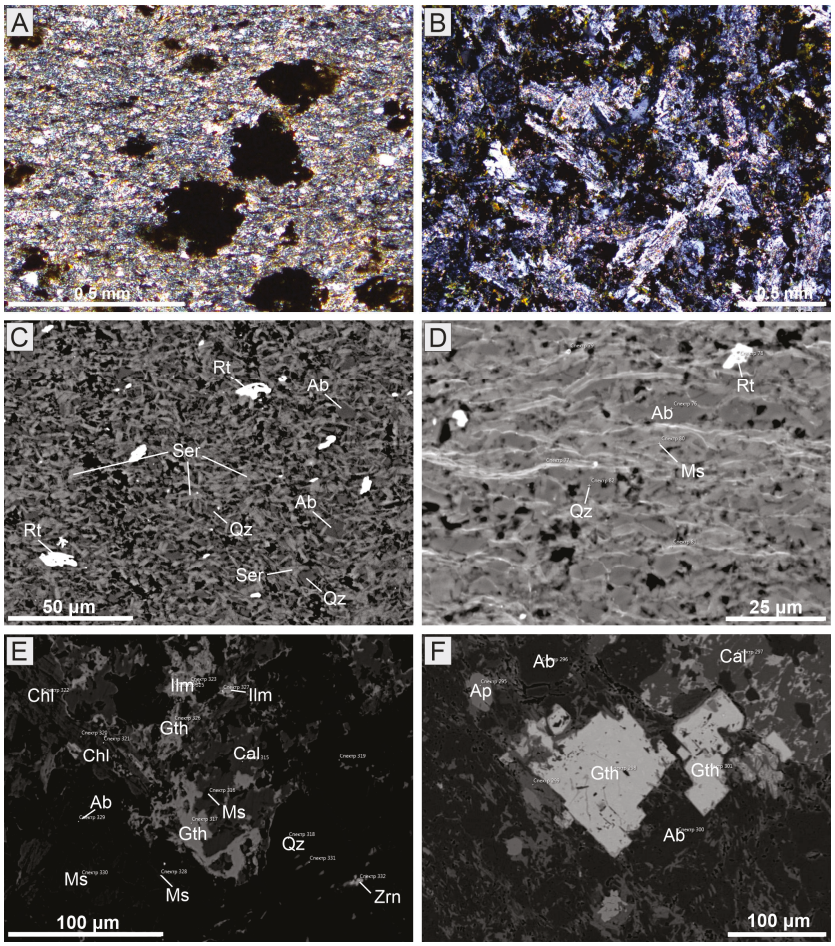


Figure 11. Mineralogy of proximal alteration zones. (**A**) Microphotograph showing pervasive sericite alteration and oxidized porphyroblasts of Fe-rich carbonate in siltstone from Sentash deposit. Transmitted light and crossed polarizers. (**B**) Microphotograph of pervasively altered granitoid dike with relics of porphyritic texture from Chetyrekhletka occurrence. Transmitted light and crossed polarizers. (**C**) BSE image showing mineral phases identified in sericite metasomatite from Sentash deposit. (**D**) BSE image showing mineral phases and internal structure of quartz-albite-sericite metasomatite from Sentash deposit. (**E**) BSE image showing mineral phases identified in altered granitoid dike from Chetyrekhletka occurrence. (**F**) BSE image of pyrite and carbonate porphyroblasts in altered siltstone from Sentash deposit. Abbreviations: Qz—quartz, Ab—albite, Chl—chlorite, Cal—calcite, Ms—muscovite, Gth—Fe-hydroxide minerals, Rt—rutile, Zrn—zircon, Ilm—ilmenite, and Ap—apatite.

6.2. Petrography and Mineralogy of Auriferous Quartz Veins

The auriferous quartz veins have sharp contacts with country rocks typical of crack-and-seal-type veins [46,47]. The main constituent of the veins is milky white quartz containing irregularly distributed patches of Fe-hydroxide minerals. Brecciation and recrystallization are common and point to multiple episodes of deformation and fluid circulation. Breccia zones usually contain coarse fragments of recrystallized quartz cemented together by a matrix composed of Fe-hydroxide minerals (up to 50 vol.%). Microscopic studies show that quartz displays multiple growth stages and a variety of textures, including sheared quartz, comb quartz, and a mosaic texture of variably recrystallized quartz (Figure 12A). All quartz veins contain variable amounts of carbonate minerals occurring as late-stage fracture-filling aggregates and some veins occasionally contain plagioclase and K-feldspar grains (Figure 12A,B). Accessory and trace minerals identified in the quartz veins include apatite, monazite, zircon, and ilmenite. Most quartz vein samples studied in this work represent su-

pergene oxidation zones, and unoxidized sulfides were found only in the quartz veins from the Georgievka occurrence. In this locality, clusters of unoxidized pyrite in milky white quartz are enclosed by the oxidized zones, where the sulfides are replaced by Fe-hydroxide minerals and reddish vuggy quartz, and the transition between the oxidized zones and the unoxidized sulfides is abrupt (Figure 12C). SEM-EDS analysis of samples from the Georgievka occurrence has shown that sulfide minerals are predominantly represented by pyrite with small inclusions of chalcopyrite, arsenopyrite, and galena (Figure 12D). Botryoidal aggregate of Fe-hydroxide minerals with colloform banding, developed in the oxidized parts of the quartz veins, contains relics of pyrrhotite and microinclusions of iodargyrite (or iodyrite, AgI) and Bi phases (Figure 12E and Supplementary Table S1). Native gold in the quartz veins usually occurs as variably sized particles in association with Fe-hydroxide minerals (Figure 6C,F and Figure 12F) and as free grains and stringers filling the fractures between the quartz grains (Figure 6D,E). Microprobe analyses of gold particles recovered from the Chetyrekhletka occurrence have shown that most of the analyzed grains were represented by high- and very-high-grade gold with fineness generally in the range 970–995‰ and Au/Ag ratios from 1:50 to 1:170 (Supplementary Table S1).

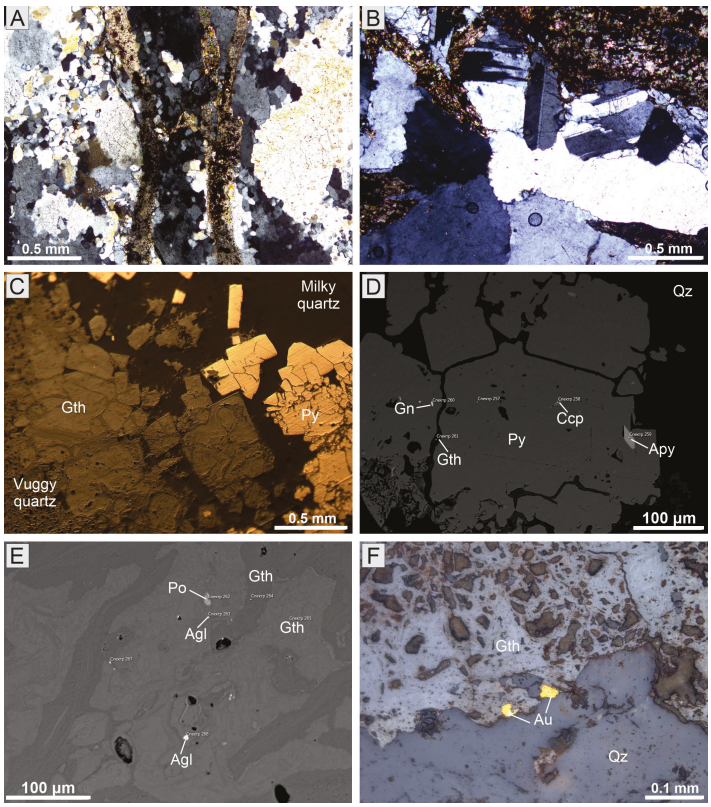


Figure 12. Mineralogy of auriferous quartz veins. (**A**) Microphotograph showing mosaic texture of variably recrystallized quartz and crosscutting carbonate veinlets in quartz veins from Chetyrekhletka occurrence. Transmitted light and crossed polarizers. (**B**) Microphotograph of plagioclase grains and late carbonate veinlets in quartz vein from Chetyrekhletka occurrence. Transmitted light and crossed polarizers. (**C**) Microphotograph showing distribution of oxidized and unoxidized pyrite in quartz vein from Georgievka occurrence. Reflected light and crossed polarizers. (**D**) BSE image of unoxidized pyrite in quartz vein from Georgievka occurrence. (**E**) BSE image showing mineral phases identified in Fe-hydroxide aggregate in quartz vein from Georgievka occurrence. (**F**) Microphotograph of native gold in quartz vein from Georgievka occurrence. Reflected light and crossed polarizers. Abbreviations: Qz—quartz, Gth—Fe-hydroxide minerals, Py—pyrite, Ccp—chalcopyrite, Apy—arsenopyrite, AgI—iodargyrite, Gn—galena, Po—pyrrhotite, and Au—native gold.

In order to further corroborate the distribution of gold particles within Fe-hydroxide aggregate, a sample of visible gold-bearing quartz vein from the Georgievka occurrence was scanned utilizing X-ray computed micro-tomography. This method generates a shadowgraph of a sample, where the differences in greyscale represent degrees of X-ray absorption that is a function of the density and atomic number of the sample materials [50,51]. Figure 13 shows two images of the gold-bearing quartz vein sample where the quartz appears dark grey, the phases with the brightest grey values are Fe-hydroxide minerals, and native gold particles appear bright yellow. In the image, shown in Figure 13A, the sample is rendered opaque to illustrate the general distribution of Fe-hydroxide minerals in quartz, and in the image shown in Figure 13B, quartz and Fe-hydroxide minerals are rendered semitransparent, allowing the distribution and size of the gold particles in the central part of the sample to be seen. Thus, the computed micro-tomography data matches well the observations made in the hand specimens (Figure 6C,F) and under the microscope (Figure 12F), showing that aggregates of Fe-hydroxide minerals are the main host of native gold in the supergene oxidation zones.

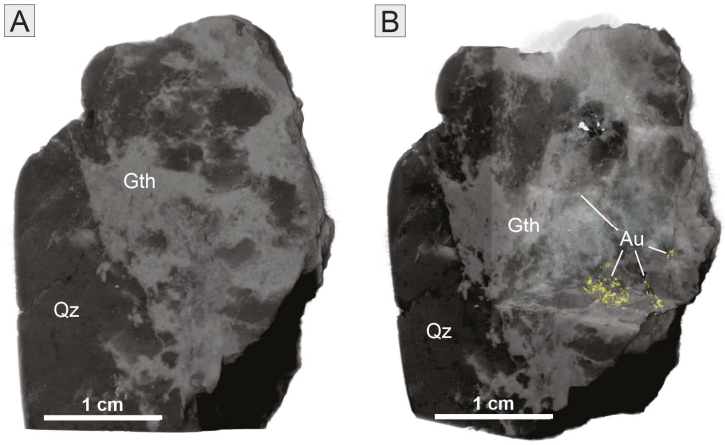


Figure 13. Three-dimensional visualizations of visible gold-bearing quartz vein sample from Georgievka occurrence generated by volume rendering of computed micro-tomography data: (**A**) sample is rendered opaque, showing distribution of Fe-hydroxide minerals in quartz, and (**B**) quartz and Fe-hydroxide minerals are rendered semitransparent, allowing the distribution and size of gold particles to be seen.

6.3. Geochemistry of Mineralized Alteration Zones

Geochemical methods are widely used to analyze, visualize, and interpret data for further mineral exploration [52–55]. Extensive lithogeochemical sampling conducted in the course of this work allowed for the recognition of general metallogenic tenors in the mineralized areas, and corresponding datasets for the studied localities are compiled in Supplementary Table S1.

The wall rock alteration envelopes surrounding the auriferous quartz veins are enriched in Au and chalcophile elements, and the concentrations of the ore metals show positive slopes from distal to proximal parts of the alteration zones (Figure 7). Thus, the alteration zones in flyshoid sediments, which may or may not contain the auriferous quartz veins exposed on the surface, can be considered as the primary dispersion haloes, and their geochemical characteristics can provide important information relevant to ore genesis. Therefore, in addition to mineralogical characterization of the alteration zones, analysis of spatial distribution of the ore elements in the alteration zones and statistical analysis of geochemical data were applied to determine the ore-forming elemental association.

6.3.1. Spatial Distribution of Ore Elements in Alteration Zones

Spatial distribution of the ore elements was studied at the Valeria prospect, where several alteration zones, described in Section 5.3, were sampled in the course of lithogeochemical exploration. The mono-elemental maps illustrating the spatial distributions of Au and other relevant ore elements were created by interpolating the lithogeochemical data. The interpolated geochemical maps for Au, As, and Pb, presented in Figure 14A–C, were constructed by classifying the measured concentration values into six groups using the ArcGIS software (version 10.8.2, Environmental Systems Research Institute, Redlands, CA, USA), with each concentration group equally covering approximately 15% of the total variation range.

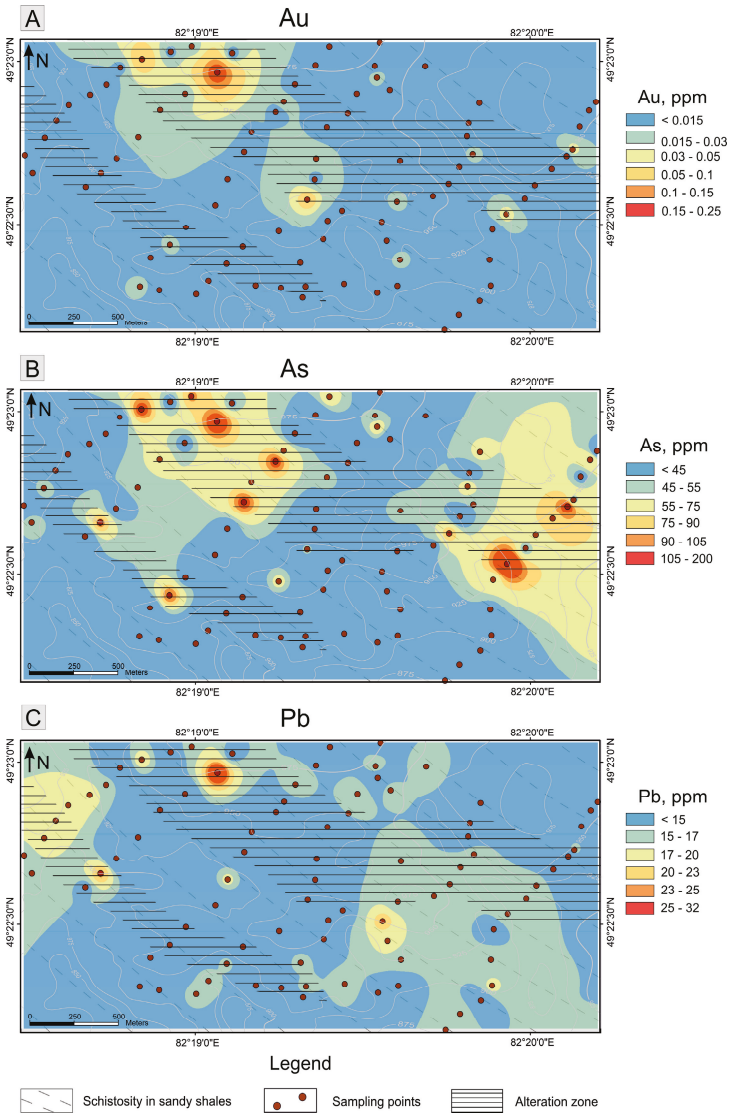


Figure 14. Mono-elemental maps illustrating spatial distribution of Au (**A**), As (**B**), and Pb (**C**) at Valeria prospect.

As seen in Figure 14A, the whole-rock gold anomalies reaching up to 0.15 ppm Au spatially overlap with the alteration zones in sandy shales that were identified and mapped during the field work. The gold anomalies mainly coincide with broad anomalies of As (up to 200 ppm; Figure 14B) and Pb (up to 25 ppm; Figure 14C). In addition, elevated concentrations of Cu (up to 300 ppm) and Zn (up to 200 ppm) were found in the same areas (Supplementary Table S1).

6.3.2. Statistical Treatment of Geochemical Data

Statistical treatment is widely used for interpretation of geochemical data and employs various statistical techniques that help to better understand the relationships between different geochemical variables and identify the ore-forming processes, e.g., [56,57]. Herein, the statistical treatment was applied to lithogeochemical datasets and included pairwise correlation coefficients and factor analysis. Before entering the statistical treatment, the data were processed following standard procedures including the log-ratio transformation and censoring the data below the detection limit and outliers [57,58], and statistical analysis was carried out utilizing the software platform IBM SPSS Statistics v30 [59,60].

Pairwise Correlation Coefficients

Correlation coefficients help to assess the degree of linear correlation between the concentrations of different chemical elements. Pairwise correlation coefficients, based on the Pearson's correlation coefficient formula, were calculated for the data from each of the studied mineralized areas and collectively. Positive correlation of Au with As and strong mutual correlations in the distribution of the chalcophile elements (Zn, Cd, Cu, Pb, Sb, Ag, Ge, and Hg) were established in all datasets and are exemplified here by the correlation matrix calculated for lithogeochemical data from the Valeria prospect (Table 1). In this dataset, where a correlation coefficient greater than the critical value indicated a significant correlation (n = 39, α = 0.05, critical value = 0.41), gold showed a statistically significant positive correlation with As (r = +0.44), Pb (r = +0.55), and Sb (r = +0.49; Figure 15). Mutual correlation between the chalcophile elements is exemplified by Zn, which had positive correlation with Cd, Cu, Pb, Ag, and Ge. Apart from gold, Sb showed a strong positive correlation with Bi, Hg, and U, comprising association of the "low-temperature" chemical elements. Ni had a predictably strong positive correlation with Co, Cu, and V, and the latter also showed a positive correlation with other chalcophile elements and P. The results of the pairwise correlation analysis point to the existence of distinct geochemical associations in the analyzed database that are further corroborated by the factor analysis.

Table 1. Pairwise correlation coefficients between concentrations of chemical elements in the lithogeochemical dataset from Valeria prospect. Correlation coefficients greater than the critical value, indicating a statistically significant correlation, are marked in bold print.

	Au	**Ag**	**As**	**B**	**Bi**	**Cd**	**Co**	**Cr**	**Cu**	**Ge**	**Hg**	**Li**	**Mn**	**Mo**	**Ni**	**P**	**Pb**	**Sb**	**U**	**V**	**W**	**Zn**
Au	1																					
Ag	0.07	1																				
As	**0.44**	0.09	1																			
B	0.08	**0.60**	0.34	1																		
Bi	0.24	−0.21	0.14	−0.28	1																	
Cd	0.09	**0.56**	0.17	**0.58**	−0.34	1																
Co	0.13	0.16	0.09	0.03	−0.36	0.13	1															
Cr	0.20	0.07	0.30	0.17	0.18	−0.04	0.08	1														
Cu	0.24	**0.43**	0.33	**0.50**	−0.39	**0.41**	**0.59**	0.21	1													
Ge	0.13	0.18	0.22	**0.46**	0.21	0.31	−0.24	0.27	0.20	1												
Hg	0.26	−0.19	0.10	−0.32	**0.96**	−0.28	−0.40	0.17	−0.42	0.23	1											
Li	-	0.18	−0.20	0.39	−0.67	**0.56**	0.22	−0.38	0.31	−0.01	−0.65	1										
Mn	0.13	−0.24	0.26	−0.09	0.13	−0.05	0.30	0.23	0.20	0.06	0.06	−0.21	1									
Mo	0.01	−0.17	−0.21	−0.25	0.29	−0.36	−0.14	−0.07	−0.19	0.08	0.31	−0.38	-	1								
Ni	0.28	0.28	0.40	0.16	0.35	0.13	0.28	**0.71**	**0.42**	0.30	0.32	−0.30	0.36	−0.01	1							
P	-	0.29	0.23	**0.56**	−0.43	**0.44**	0.12	0.22	**0.54**	0.40	−0.48	0.36	0.10	−0.14	0.16	1						
Pb	**0.55**	0.25	0.29	**0.44**	−0.45	0.40	0.37	0.22	**0.45**	0.10	−0.47	0.34	0.22	−0.25	0.14	0.50	1					
Sb	**0.49**	0.07	0.18	0.09	**0.68**	0.12	−0.27	−0.03	−0.16	**0.48**	**0.70**	−0.20	0.01	0.06	0.18	−0.18	−0.01	1				
U	0.25	−0.15	0.19	−0.26	**0.98**	−0.27	−0.36	0.21	−0.34	0.26	**0.97**	−0.63	0.09	0.24	0.39	−0.41	−0.44	0.73	1			
V	0.01	**0.50**	0.13	**0.79**	−0.51	**0.61**	0.28	0.29	**0.68**	0.36	−0.55	**0.50**	0.17	−0.21	0.27	**0.69**	**0.56**	−0.17	−0.50	1		
W	-	**0.62**	0.09	0.32	−0.20	**0.56**	0.04	0.04	0.19	0.06	−0.21	0.32	−0.17	−0.15	0.13	0.25	0.26	−0.01	−0.14	0.37	1	
Zn	0.04	**0.52**	0.17	0.72	−0.41	**0.52**	0.30	0.15	**0.71**	**0.49**	−0.44	**0.42**	0.04	−0.17	0.21	**0.80**	**0.48**	−0.09	−0.40	**0.75**	0.27	1

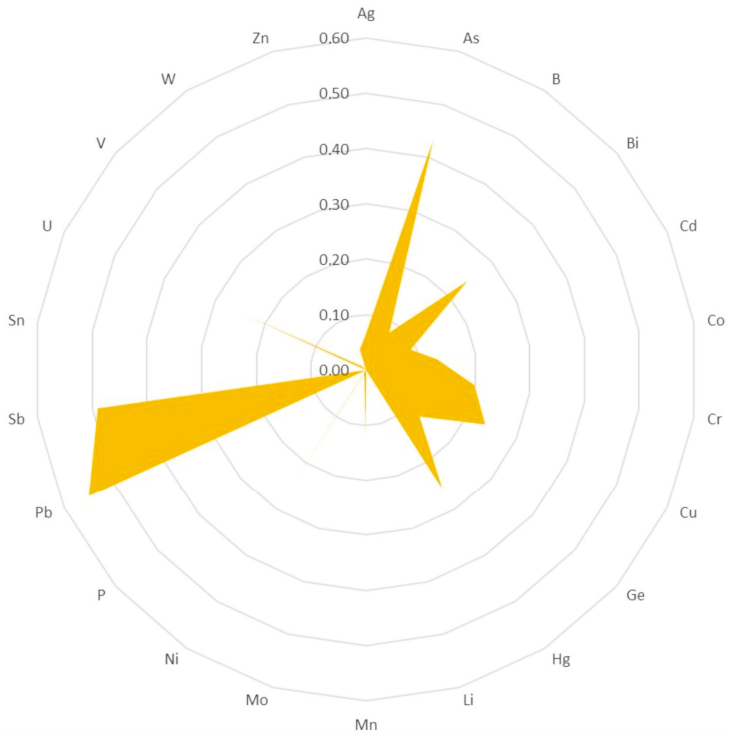


Figure 15. Circular diagram visualizing strong positive correlations of Au with As, Pb, and Sb in the lithogeochemical dataset from Valeria prospect.

Factor Analysis

Principal component analysis and factor analysis are routinely applied in processing of geochemical data to reduce the dimensionality of large datasets, by transforming a large set of variables into a smaller one that still contains most of the information in the large set [57]. The factor analysis, in particular, aims to produce a small number of factors, which can explain the observed variance in the larger number of variables [57,61]. It was shown that the factor analysis was capable of uncovering relationships between the variables that were not recognizable in the pairwise correlation and cluster analyses [62,63]. It was shown that the factor analysis was capable of uncovering hidden relationships between chemical elements, potentially indicating specific geochemical processes and/or mineralization events that were not recognizable in the pairwise correlation and cluster analyses, even with limited datasets [57,62,63].

In this study, the factor analysis was applied to a dataset containing 115 whole-rock geochemical samples analyzed for 20 chemical elements (variables). The results are summarized in Table 2, and a full report is given in Supplementary Table S1. After extraction and Varimax rotation, three distinct linear components (or factors) accounting for 55% of the total variance with the eigenvalue >1 were delineated within the dataset. It is commonly suggested that the factors with eigenvalues above 1 could be considered significant and that the proportion of the total variance explained by the extracted factors should be greater than 50% [57,64]. The results of the data processing in this study show that 55% common variance shared by 20 variables can be accounted for by 3 factors with eigenvalues greater than one. Although the first three factors account for only 55% of the total variance, it is considered as a good outcome because the identified factors are geologically meaningful and are in line with the main principle of factor analysis that lithologically controlled and regionally distributed variables are generally extracted first and then the more locally controlled variables are identified [56,57].

Table 2. Results of factor analysis from the n = 115 whole-rock geochemical data, including the 20 variables in relation to the first 3 factors accounting for 55% of the total data variance. Elements with largest positive loadings onto each factor are marked in bold print.

	Factor 1	Factor 2	Factor 3
Au	**0.83**	0.09	0.04
Ag	**0.89**	−0.01	−0.01
As	**0.74**	0.04	0.17
B	−0.09	−0.41	0.51
Bi	0.16	**0.82**	0.01
Co	0.31	0.02	**0.59**
Cr	0.06	0.11	0.41
Cu	0.31	−0.09	**0.73**
Hg	−0.20	**0.91**	−0.08
Li	−0.28	−0.59	0.23
Mn	0.49	0.36	0.31
Mo	0.56	0.04	0.13
Ni	0.11	0.43	**0.80**
P	−0.01	−0.22	**0.57**
Pb	0.49	−0.33	0.46
Sb	0.18	**0.58**	0.12
U	−0.03	**0.94**	0.07
V	0.04	−0.50	**0.63**
W	0.04	−0.23	0.31
Zn	**0.76**	−0.14	0.28
Explained variance	3.77	4.07	3.27
Cumulative variance (%)	18.84	20.34	16.35

The first factor accounting for 19% of the total variance is dominated by large positive loadings for main ore elements, including Au (0.83), Ag (0.89), As (0.74), and Zn (0.76). The second factor has explained 20% of the total variance. Variables that strongly contribute to the second factor with positive loadings are U (0.94), Hg (0.91), Bi (0.82), and Sb (0.58), representing the chemical elements that are mobile at low temperatures. Factor three, explaining 16% of the variance, is dominated by large positive loadings for Ni (0.80), Cu (0.73), V 0.63), Co (0.59), and P (0.57), which represent the chemical elements typical for the black shale formations.

The results of the factor analysis are in line with pairwise correlation coefficients and provide further details on the dispersion of chemical elements in primary haloes and internal structure of the dataset under study.

7. Discussion

7.1. Quartz Vein Deposits as Part of the Regional Ore-Forming System

Two major deposit types in the Eastern Kazakhstan Gold Belt comprise structurally controlled mineralized zones with auriferous sulfides and quartz veins with visible native gold [2,6,7,9–11,35,48]. Fluid inclusion data from the Bakyrchik mining district show that the mineralized zones with auriferous sulfides formed from aqueous-carbonic fluids at temperatures in the range 315–240 °C and pressures of ca. 1.3–1 kbar [7]. Comparable conditions with slightly lower temperatures were reported for the hydrothermal breccias and quartz veins with visible gold that were interpreted as the late manifestations of Au mineralization at the Bakyrchik ore field [7]. The stable isotope studies point to a variable (sedimentary to magma-derived) isotopic composition of sulfur and to a predominantly sedimentary to metamorphic source of carbon [7]. Similar results were reported for the Kostobe deposit in the Eastern Kazakhstan Gold Belt [65]. In general, the pressures reported for deposits of the Eastern Kazakhstan Gold Belt are slightly lower than pressure estimates for the Muruntau (~1.6 kbar) and Kumtor (~1.2–1.3 kbar) Au deposits in the Tien Shan

orogenic belt and are comparable with the pressures reported for the Olympiada Au deposit in the Yenisei Ridge [7]. Thus, available pressure estimates for Au deposits of Eastern Kazakhstan correspond to lithostatic depths of ~4–5 km, which is typical for relatively epizonal black-shale-hosted orogenic Au deposits elsewhere [7,37].

The quartz vein-type deposits in the study area do not associate with economically significant sulfide-rich mineralized zones; however, in the other areas of Eastern Kazakhstan, the two types of deposits are closely associated, allowing for the recognition of vertical and lateral zonation within the regional ore systems. In particular, the vertical zonation was studied in several major mineralized areas, including the Espe, Kulundzhun, and Kostobe deposits [4,46,65], and the Bakyrchik ore field [7,46,66]. The general features of the vertical zonation delineated in these deposits include the appearance of auriferous sulfides (Espe and Kulundzhun) and granitoid stocks (Kostobe and Bakyrchik) at the deeper levels of quartz vein-type deposits, and the vertically zoned alteration pattern with carbonate-sericite-phlogopite-quartz zone occurring at deeper levels that changes upsection to typical phyllic alteration and to argillic alteration in the supergene oxidation zones [4,7,10,48,67]. In addition, an increase in the arsenopyrite/pyrite ratio with depth was reported for several ore systems that led some authors to propose an intrusion-related model for their genesis [7,48]. Although the detailed study of the genesis of Au deposits was not the aim of this work, the abovementioned features suggest that the quartz vein Au deposits, investigated herein, may represent the upper parts of bigger concealed ore systems with significant potential for future gold exploration.

7.2. Alteration Patterns, Geochemistry, and Implications for Regional Prospecting

Mineralogical characteristics of the alteration zones in combination with new lithogeochemical data, obtained in this study, enable a better understanding of principal geochemical processes operating in the ore-forming systems. Hydrothermal alteration assemblages associated with the studied quartz vein Au deposits can be subdivided into two types: distal and proximal to mineralized quartz veins. Pervasive carbonation locally accompanied by the development of chlorite ± sericite and albite is the dominant process in the distal alteration zones. The proximal phyllic alteration (sericite-albite-pyrite ± chlorite, Fe-Mg-Ca carbonates, arsenopyrite, and pyrrhotite) develops as localized several-hundred-meter-wide alteration envelopes in the wall rocks and is often superimposed onto the mineral assemblages of distal alteration. These alteration styles are similar to those described in the other Au deposits of the Eastern Kazakhstan Gold Belt [4,7,9,35,40,48] and in the black-shale-hosted orogenic gold deposits elsewhere [7,49,68–71].

Proximal alteration zones are characterized by elevated concentrations of Au (up to 0.2 ppm), As (up to a several hundred ppm), and other chalcophile elements, such as Zn, Pb, and Cu (Supplementary Table S1). The distribution of Au and chalcophile elements generally shows negative slopes from proximal to distal alteration zones, which is well seen in the profile lines across the ore zones (Figure 7 and Supplementary Table S1). The ore-forming elemental association can be further recognized utilizing statistical treatment of lithogeochemical data and mono-elemental geochemical maps. Pairwise correlation coefficients and factor analysis of the lithogeochemical dataset revealed three groups of chemical elements showing significant positive mutual correlations: (1) Au and As (±Ag, Sb, Cu, Pb, and Zn), (2) V and P (±Co, Ni, Mo, and Cu), and (3) Bi, Hg, U, and Sb (Tables 1 and 2). The association of V and P, which are characteristic chemical elements of black shale formations, is interpreted as an early geochemical assemblage, and a positive correlation of V and P with Co (±Ni) can be explained by the presence of early authigenic pyrite enriched in these elements. The association of Au, As, and chalcophile elements is distinctly overprinting, and is explained by the development of gold-bearing sulfides

(pyrite and arsenopyrite), manifesting the main stage of the gold mineralization in the area. Finally, association of Bi and Hg (±Sb and U) includes the chemical elements that are mobile at low temperatures and can be related to the late-stage hydrothermal or supergene fluids. Similar patterns of distribution of the ore elements have also been reported for the large Bakyrchik gold deposit by Soloviev et al., 2020 [7], and for black shale-hosted orogenic gold deposits of the Yenisei Ridge by Mansurov and Tarasov, 2017 [49].

Spatial distribution maps represent another method to visualize the ore elemental association of Au, As, and chalcophile elements in the alteration zones. Positive anomalies of Au, As, and Pb on mono-elemental maps constructed for the Valeria prospect broadly coincide with each other, and with the alteration zones in the sandy shales identified in the field (Figure 14). Distribution of concentrations shows that the alteration process has led to an increase in the content of Au and chalcophile elements by several orders relative to background values. Because the alteration zones at the Valeria prospect do not associate with any known auriferous quartz veins outcropped on the surface, they can represent the primary dispersion haloes above the concealed ore bodies, which make them potentially interesting for future gold exploration. Thus, the geochemical methods can provide useful tools to delineate the ore elemental associations and to outline reproducible regional anomalies for subsequent follow-up.

7.3. Bonanza Quartz Veins and Formation of Ultra-High-Grade Ore-Shoots

The auriferous quartz veins are usually enclosed by the wall rock alteration envelopes where the degree of alteration and concentrations of gold increase toward the central parts of the zones. This is illustrated by the sampling profile from the Chetyrekhletka occurrence showing gradual increase of gold concentrations toward the central part of the alteration envelope where a series of high-grade auriferous quartz veins is located (Figure 7). Similar geochemical patterns were observed in the other studied mineralized areas (Supplementary Table S1). Although the gradual increase of gold concentrations in the alteration zones is evident, the content of gold in the altered wall rocks usually do not exceed 0.1–0.2 ppm that, compared with high and ultra-high concentrations of gold in bonanza-type quartz veins, may indicate that the process responsible for the accumulation of gold in the ultra-high-grade ore-shoots was geochemically different. This conclusion is corroborated by the spatial distribution maps of As and Au for the Valeria prospect where the localized Au anomalies only partially overlap with broad anomalies of As (Figure 14). Such distribution patterns of Au and As anomalies, also reported for the Bakyrchik mining district [48] and for other black-shale-hosted gold provinces, e.g., [70], may indicate that the quartz vein-type gold mineralization was localized and superimposed onto larger pre-existing alteration zones containing disseminated sulfides.

It is generally accepted that the ultra-high-grade gold concentrations in bonanza veins, exceeding the Au solubility expected for fluids in orogenic gold deposits, can be explained by the physical transport of gold as solid colloidal nanoparticles and their aggregates in suspension [72–75]. This mechanism matches well the thermodynamic conditions typical for the black-shale-hosted gold provinces where hydrothermal activity, associated with deformations and greenschist facies metamorphism, resulted in the mobilization of large volumes of silica [71,73]. Rapid precipitation of amorphous silica was accompanied by precipitation and accumulation of gold particles and occurred when fluids experienced rapid changes in chemical composition and/or physical state (liquid–gas phase transitions) as a result of decompression, cooling, or flash vaporization in the fault valve systems [73,76,77]. In this model, the observed association of native gold with Fe-hydroxide minerals can be explained by oxidation of ankerite and sulfides by the late-stage hydrothermal or supergene fluids, and precipitation of Fe-hydroxide minerals in the brecciated zones within the quartz

veins. This process resulted in recrystallization and further concentration of native gold and formed the low-temperature mineral assemblages, including Ag (AgI) and Bi phases typical for supergene oxidation zones [43,78].

8. Conclusions

The quartz vein deposits of the Eastern Kazakhstan Gold Belt are classified as epizonal orogenic Au deposits. The auriferous quartz veins, hosted in Carboniferous flyschoids (black shales), have linear or slightly bended shapes with average width 0.5–1.5 m and length up to 100–150 m, and contain high-karat native gold with only minor amounts of sulfide minerals. In supergene oxidation zones, the native gold is closely associated with Fe-hydroxide minerals cementing brecciated zones within the veins.

The auriferous quartz veins are usually enclosed by the wall rock alteration envelopes where two types of alteration are distinguished. Proximal phyllic alteration (sericite-albite-pyrite ± chlorite, Fe-Mg-Ca carbonates, arsenopyrite, and pyrrhotite) develops as localized alteration envelopes, and pervasive carbonation accompanied by chlorite ± sericite and albite is the dominant process in the distal alteration zones.

The rocks within the alteration zones are enriched in Au and chalcophile elements, and three groups of chemical elements showing significant positive mutual correlation have been identified: (1) an early geochemical assemblage includes V, P, and Co (±Ni)—chemical elements characteristic for black shale formations, (2) association of Au, As, and chalcophile elements is distinctly overprinting, and manifests the main stage of the sulfide-hosted Au mineralization, and (3) association of Bi and Hg (±Sb and U) includes the chemical elements mobile at low temperatures. The chalcophile elements form reproducible positive anomalies on spatial distribution maps and can be used as reliable pathfinders for regional gold prospecting.

Supplementary Materials: The following supporting information can be downloaded at: https://www.mdpi.com/article/10.3390/min15080885/s1. Supplementary Table S1: Analytical data for lithogechemical samples.

Author Contributions: Conceptualization, D.L.K., V.S.Z. and S.Y.S.; formal analysis, D.L.K., V.S.Z., E.S.S. and S.V.P.; funding acquisition, S.Y.S. and E.S.A.; investigation, D.L.K., V.S.Z., S.Y.S., S.V.P., E.S.S., A.K.K., V.A.S., M.A.K. and R.S.; methodology, D.L.K., V.S.Z. and E.S.S.; resources, D.L.K., S.V.P., E.S.S., V.S.Z., S.Y.S., A.K.K., V.A.S., A.V.K. and E.S.A.; supervision, D.L.K., S.V.P. and V.S.Z.; visualization, D.L.K., V.S.Z. and E.S.S.; writing—original draft, D.L.K., V.S.Z. and E.S.S.; writing—review and editing, D.L.K. and V.S.Z. All authors have read and agreed to the published version of the manuscript.

Funding: This work was supported by the state assignment of the South Ural Federal Scientific Center of Mineralogy and Environmental Geology, Ural Branch, Russian Academy of Sciences (state registration No. 102 403 270 0054-4-1.5.2.) to V.S.Z., S.Y.S., and A.K.K.

Data Availability Statement: The original contributions presented in this study are included in the article/Supplementary Materials. Further inquiries can be directed to the corresponding author.

Acknowledgments: We are grateful to Anatoly Glavatsky, Faiz Belyalov, Artem Kozhemonyan, Ivan Trofimov, Maxim Vigelin, Rasul Shebzukhov, and Rishat Narbinov for their help and cooperation during field work in Kazakhstan. Alexander Kul'kov is acknowledged for his assistance with X-ray computed micro-tomography, and Natalia Vlasenko for her help with SEM-EDS analyses that were performed in the "X-ray diffraction" and "Geomodel" Resource Centers of St. Petersburg State University, correspondingly. Anatoly Zaitsev is acknowledged for his assistance with interpretation of carbonate minerals. We are thankful for the detailed and valuable comments of the academic editor and three anonymous reviewers that helped to improve the original version of the manuscript. R.S. appreciates the long-standing fruitful cooperation on West Kalba gold belt.

Conflicts of Interest: The authors declare no conflicts of interest. Emil S. Aliyev and Vasiliy A. Saltanov are employees of LLP General Geology Group. Andrey V. Korneev is employee of LLC Ural Exploration. The paper reflects the views of the scientists and not the company.

References

1. Rafailovich, M.S.; Mizernaya, M.A.; Dyachkov, B.A. *Large Gold Deposits in Black Shales: Formation Conditions and Features of Similarity*; Luxe Media Group: Almaty, Kazakhstan, 2011; 272p. (In Russian)
2. Rafailovich, M.S. *Geology of Gold in Central Asia: Evolution of Mineralization, Metasomatic Formations, Explosive Breccias*; Book Print: Almaty, Kazakhstan, 2013; 423p. (In Russian)
3. Dyachkov, B.A.; Mizernaya, M.A.; Kuzmina, O.N.; Zimanovskaya, N.A.; Oitseva, T.A. *Tectonics and Metallogeny of East Kazakhstan. Tectonics: Problems of Regional Setting*; IntechOpen Limited: London, UK, 2018; pp. 67–84. [CrossRef]
4. Bespayev, K.A.; Globa, B.A.; Abishev, V.M.; Gulyaeva, H.Y. *Gold Deposits of Kazakhstan, Directory*; Qazgeoaqparat: Almaty, Kazakhstan, 2019; 298p. (In Russian)
5. Maslennikov, V.V. Black shale formations of gold ore regions (on the example of Eastern Kazakhstan). *Metallog. Miner.* **1993**, *2*, 88–98. (In Russian)
6. Dyachkov, B.A.; Mizernaya, M.A.; Khromykh, S.V.; Bissatova, A.Y.; Oitseva, T.A.; Miroshnikova, A.P.; Frolova, O.V.; Kuzmina, O.N.; Zimanovskaya, N.A.; Pyatkova, A.P. Geological History of the Great Altai: Implications for Mineral Exploration. *Minerals* **2022**, *12*, 744. [CrossRef]
7. Soloviev, S.G.; Kryazhev, S.G.; Dvurechenskaya, S.S.; Trushin, S.I. The large Bakyrchik orogenic gold deposit, eastern Kazakhstan: Geology, mineralization, fluid inclusion, and stable isotope characteristics. *Ore Geol. Rev.* **2020**, *127*, 2–52. [CrossRef]
8. Dyachkov, B.A.; Titov, D.V.; Sapargaliev, E.M. Ore belts of the Greater Altai and their ore resource potential. *Geol. Ore Depos.* **2009**, *51*, 197–211. [CrossRef]
9. Kovalev, K.R.; Kalinin, Y.A.; Naumov, E.A.; Pirajno, F.; Borisenko, A.S. Mineralogical study of the Suzdal sediment-hosted gold deposit, Eastern Kazakhstan: Implications for ore genesis. *Ore Geol. Rev.* **2009**, *35*, 186–205. [CrossRef]
10. Mizernaya, M.A.; Dyachkov, B.A.; Miroshnikova, A.P.; Mizerny, A.I.; Orazbekova, G.B. Large sulfide-quartz stockwork gold deposits of Kazakhstan-formation conditions and predicting criteria. *Visnyk Taras Shevchenko Natl. Univ. Kyiv-Geol.* **2017**, *3*, 82–88. [CrossRef]
11. Kalinin, Y.A.; Kovalev, K.R.; Serdyukov, A.N.; Gladkov, A.S.; Sukhorukov, V.P.; Naumov, E.A.; Travin, A.V.; Semenova, D.V.; Serebryakov, E.V.; Greku, E.D. Age constraints and metallogenic prediction of gold deposits in the Akzhal-Boko-Ashalin ore zone (Altai accretion-collision system). *Geodyn. Tectonophys.* **2021**, *12*, 392–408. [CrossRef]
12. Şengör, A.M.C.; Natal'in, B.A.; Burtman, V.S. Evolution of the Altaid tectonic collage and Paleozoic crust growth in Eurasia. *Nature* **1993**, *364*, 299–307. [CrossRef]
13. Windley, B.F.; Alexeiev, D.; Xiao, W.; Kröner, A.; Badarch, G. Tectonic models for accretion of the Central Asian Orogenic Belt. *J. Geol. Soc.* **2007**, *164*, 31–47. [CrossRef]
14. Burtman, V.S. Tien Shan, Pamir, and Tibet: History and geodynamics of Phanerozoic oceanic basins. *Geotectonics* **2010**, *44*, 388–404. [CrossRef]
15. Xiao, W.J.; Windley, B.F.; Allen, M.; Han, C.M. Paleozoic multiple accretionary and collisional tectonics of the Chinese Tianshan orogenic collage. *Gondwana Res.* **2013**, *23*, 1316–1341. [CrossRef]
16. Kröner, A.; Kovach, V.; Belousova, E.; Hegner, E.; Armstrong, R.; Dolgopolova, A.; Selt-mann, R.; Alexeiev, D.V.; Hoffmann, J.E.; Wong, J.; et al. Reassessment of continental growth during the accretionary history of the Central Asian Orogenic Belt. *Gondwana Res.* **2014**, *25*, 103–125. [CrossRef]
17. Biske, Y.S.; Konopelko, D.L.; Seltmann, R. Paleozoic collisional belt of the South Tien Shan: A review. *Earth-Sci. Rev.* **2024**, *248*, 104637. [CrossRef]
18. Khromykh, S.V.; Kotler, P.D.; Izokh, A.E.; Kruk, N.N. A review of Early Permian (300–270 Ma) magmatism in eastern Kazakhstan and implications for plate tectonics and plume interplay. *Geodyn. Tectonophys.* **2019**, *10*, 79–99. [CrossRef]
19. Degtyarev, K.E.; Tretyakov, A.A.; Shatagin, K.N.; Kovach, V.P. The formation processes and isotopic structure of continental crust of the Chingiz range Caledonides (Eastern Kazakhstan). *Geotectonics* **2015**, *49*, 485–514. [CrossRef]
20. Safonova, I.Y. Juvenile versus recycled crust in the Central Asian Orogenic Belt: Implications from ocean plate stratigraphy, blueschist belts and intra-oceanic arcs. *Gondwana Res.* **2017**, *47*, 6–27. [CrossRef]
21. Konopelko, D.; Seltmann, R.; Dolgopolova, A.; Safonova, I.; Glorie, S.; De Grave, J.; Sun, M. Adakite-like granitoids of Songkultau: A relic of juvenile Cambrian arc in Kyrgyz Tien Shan. *Geosci. Front.* **2021**, *12*, 147–160. [CrossRef]
22. Degtyarev, K.E. Tectonic evolution of early Paleozoic island-arc systems and continental crust formation in the Caledonides of Kazakhstan and the North Tien Shan. *Geotectonics* **2011**, *45*, 23–50. [CrossRef]
23. Khromykh, S.V.; Kotler, P.D.; Semenova, D.V. Geochemistry, age and geodynamic settings of the formation of the Saur gabbro-granitoid intrusive series (Eastern Kazakhstan). *Geospheric Res.* **2019**, *2*, 6–26. (In Russian) [CrossRef]

24. Khromykh, S.V.; Semenova, D.V.; Kotler, P.D.; Gurova, A.V.; Mikheev, E.I.; Perfilova, A.A. Orogenic volcanism in Eastern Kazakhstan: Composition, age, and geodynamic position. *Geotectonics* **2020**, *54*, 510–528. [CrossRef]
25. Xu, Y.; Li, A.; Liao, W.; Han, B.-F. Ages and tectonic attributes of late Palaeozoic stratigraphic units in the Tarbagatay, West Junggar (NW China): Revisited. *Int. Geol. Rev.* **2021**, *64*, 2766–2782. [CrossRef]
26. Vladimirov, A.G.; Kruk, N.N.; Khromykh, S.V.; Polyansky, O.P.; Chervov, V.V.; Vladimirov, V.G.; Travin, A.V.; Babin, G.A.; Kuibida, M.L.; Khomyakov, V.D. Permian magmatism and lithospheric deformation in the Altai caused by crustal and mantle thermal processes. *Russ. Geol. Geophys.* **2008**, *49*, 468–479. [CrossRef]
27. Khromykh, S.V.; Tsygankov, A.A.; Kotler, P.D.; Navozov, O.V.; Kruk, N.N.; Vladimirov, A.G.; Travin, A.V.; Yudin, D.S.; Burmakina, G.N.; Khubanov, V.B.; et al. Late Paleozoic granitoid magmatism of Eastern Kazakhstan and Western Transbaikalia: Plume model test. *Russ. Geol. Geophys.* **2016**, *57*, 773–789. [CrossRef]
28. Safonova, I.; Perfilova, A.; Obut, O.; Kotler, P.; Aoki, S.; Komiya, T.; Wang, B.; Sun, M. Traces of intra-oceanic arcs recorded in sandstones of eastern Kazakhstan: Implications from U-Pb detrital zircon ages, geochemistry, and Nd-Hf isotopes. *Int. J. Earth Sci. (Geol. Rundsch.)* **2022**, *111*, 2449–2468. [CrossRef]
29. Didenko, A.N.; Mossakovskiy, A.A.; Pecherskiy, D.M.; Ruzhentsev, S.G.; Samygin, S.G.; Kheraskova, T.N. Geodynamics of Paleozoic oceans of Central Asia. *Russ. Geol. Geophys.* **1994**, *35*, 48–62. [CrossRef]
30. Buslov, M.M. Tectonics and geodynamics of the Central Asian foldbelt: The role of late Paleozoic large-amplitude strike-slip faults. *Russ. Geol. Geophys.* **2011**, *52*, 66–90. [CrossRef]
31. Safonova, I.; Komiya, T.; Romer, R.; Simonov, V.; Seltmann, R.; Rudnev, S.; Yamamoto, S.; Sun, M. Supra-subduction igneous formations of the Char ophiolite belt, East Kazakhstan. *Gondwana Res.* **2018**, *59*, 159–179. [CrossRef]
32. Kuibida, M.L.; Dyachkov, B.A.; Vladimirov, A.G.; Kruk, N.N.; Khromykh, S.V.; Kotler, P.D.; Rudnev, S.N.; Kruk, E.A.; Kuibida, Y.V.; Oitseva, T. Contrasting granitic magmatism of the Kalba fold belt (East Kazakhstan): Evidence for late Paleozoic postorogenic events. *J. Asian Earth Sci.* **2019**, *175*, 178–198. [CrossRef]
33. Kotler, P.D.; Khromykh, S.V.; Vladimirov, A.G.; Travin, A.V.; Kruk, N.N.; Murzintsev, N.G.; Navozov, O.V.; Karavaeva, G.S. New data on the age and geodynamic interpretation of the Kalba-Narym granitic batholith, Eastern Kazakhstan. *Dokl. Earth Sci.* **2015**, *462*, 565–569. [CrossRef]
34. Yakubchuk, A.S.; Seltmann, R.; Shatov, V.V.; Cole, A. The Altaids: Tectonic evolution and metallogeny. *Soc. Econ. Geol. Newsl.* **2001**, *46*, 7–14. [CrossRef]
35. Naumov, E.; Borisenko, A.; Kovalev, K.; Kalinin, Y.; Seltmann, R. Gold deposits of Ob–Zaisan fold zone (western Siberia and eastern Kazakhstan): Types and ages of mineralization, correlation with magmatic complexes [abs.]. In Proceedings of the 34th International Geological Congress, Brisbane, Australia, 5–10 August 2012. (Abstract).
36. Kovalev, K.R.; Kalinin, Y.A.; Naumov, E.A.; Myagkaya, M.K. Relationship of antimony with gold mineralization in the ore districts of Eastern Kazakhstan. *Russ. Geol. Geophys.* **2014**, *55*, 1170–1182. [CrossRef]
37. Goldfarb, R.J. Lode Gold Deposits in Time and Space. In *Encyclopedia of Geology*, 2nd ed.; Alderton, D., Elias, S.A., Eds.; Academic Press: Cambridge, MA, USA, 2021; pp. 663–679. [CrossRef]
38. Kuz'mina, O.N.; Dyachkov, V.A.; Vladimirov, A.G.; Kirillov, M.V.; Redin, Y.O. Geology and mineralogy of East Kazakhstan gold-bearing jasperoids (by the example of the Baybura ore feld). *Russ. Geol. Geophys.* **2013**, *54*, 1471–1483. [CrossRef]
39. Seltmann, R.; Shatov, V.; Yakubchuk, A. *Mineral Deposits Database and Thematic Maps of Central Asia, Scale 1:1,500,000, ArcGIS 10.1 Package and Explanatory Notes: Centre for Russian and Central Eurasian Mineral Studies (CERCAMS)*; London, Natural History Museum: London, UK, 2014; 120p.
40. Antonov, Y.A. Structural-Lithological Regularities of Gold Ore Localization at the Bolshevik Deposit, East Kazakhstan. Ph.D. Thesis, Tomsk Polytechnical University, Tomsk, Russia, 2012; p. 22. (In Russian).
41. González-Esvertit, E.; Canals, A.; Prieto-Torrell, C.; Bons, P.D.; Llorens, M.-G.; Casas, J.M.; Aguilar, C.; Neilson, J.; Elburg, M.A.; Gomez-Rivas, E. Granitoid Metasomatism and Giant Quartz Vein Formation by Mineral Replacement: Insights from the Canigó Massif, Eastern Pyrenees. *J. Petrol.* **2025**, *66*, egaf007. [CrossRef]
42. Patalakha, E.I.; Slepikh, Y.F. *Intersecting Folding (Geometric Analysis)*; Nedra: Moscow, Russia, 1974; 120p. (In Russian)
43. Urambekova, Z.T. Gold Ore Processes and Predictive Geological Data for Deposits in Kazakhstan (Bakyrshik, Bestobe, Arkharly). Ph.D. Thesis, Satbayev Kazakh National Technical University, Almaty, Kazakhstan, 2020; 149p. (In Russian, unpublished).
44. Starova, M.M. Bakyrshik deposit. In *Metallogeny of Kazakhstan*; Nauka: Alma-Ata, Kazakhstan, 1980; pp. 52–61. (In Russian)
45. Konopelko, D.L.; Cherny, R.I.; Petrov, S.V.; Strekopytov, S.; Seltmann, R.; Vlasenko, N.S.; Strekopytov, V.V.; Mamadjanov, Y.M.; Wang, X.S.; Plotinskaya, O.Y.; et al. The Mushiston Sn deposit in Tajik Tien Shan as the type locality for stannite-cassiterite-hydrostannate mineralization: New mineral chemistry data and genetic constraints. *J. Geochem. Explor.* **2022**, *239*, 107017. [CrossRef]
46. Maslennikov, V.V. Factors of Ore Localization and Criteria for Forecasting Gold Ore Deposits in Black Shale Strata (Based on the Example of Eastern Kazakhstan). Ph.D. Thesis, Tomsk Politechnical University, Tomsk, Russia, 1998, (In Russian, unpublished).

47. Bespayev, K.A.; Mukayeva, A.E.; Grebennikov, S.I. General patterns of formation and placement and forecasting-prospecting criterias of gold ore deposits in the black shale strata of the West Kalba belt of east Kazakhstan. *News Natl. Acad. Sci. Repub. Kazakhstan Ser. Geol. Tech. Sci.* **2018**, *5*, 172–183. [CrossRef]
48. Khisamutdinov, M.G. *State Geological Map of the USSR 1:200,000*, 1st ed.; Ser. Rudno-Altayskaya; M-44-XXIII, Explanatory note; Nedra: Moscow, Russia, 1965; 100p.
49. Mansurov, R.K.; Tarasov, A.V. Features of the geological structure and gold mineralization of the ore occurrence Yuzhnoe (the Yenisei Ridge). *Vestn. SPbSU Earth Sci.* **2017**, *62*, 63–88. [CrossRef]
50. Kyle, J.R.; Ketcham, R.A. Application of high resolution X-ray computed tomography to mineral deposit origin, evaluation, and processing. *Ore Geol. Rev.* **2015**, *65*, 821–839. [CrossRef]
51. Ketcham, R.A.; Mote, A.S. Accurate measurement of small features in X-ray CT data volumes, demonstrated using gold grains. *J. Geophys. Res. Solid. Earth* **2019**, *124*, 3508–3529. [CrossRef]
52. Harris, J.R.; Wilkinson, L.; Grunsky, E.; Heather, K.; Ayer, J. Techniques for analysis and visualization of lithogeochemical data with applications to the Swayze greenstone belt, Ontario. *J. Geochem. Explor.* **1999**, *67*, 301–334. [CrossRef]
53. Hronsky, J.M.A.; Groves, D.I. Science of targeting: Definition, strategies, targeting and performance measurement. *Aust. J. Earth Sci.* **2008**, *55*, 3–12. [CrossRef]
54. De Vivo, B.; Lima, A.; Ni, P.; Cicchella, D. Introduction to the thematic issue: Mineral deposits exploration and environmental geochemistry: Case studies in Italy and in China. *Geochem. Explor. Environ. Anal.* **2018**, *18*, 277. [CrossRef]
55. Berzin, S.V.; Konopelko, D.L.; Petrov, S.V.; Proskurnin, V.F.; Berzon, E.I.; Kurapov, M.Y.; Golovina, T.A.; Chernenko, N.Y.; Chervyakovskiy, V.S.; Palamarchuk, R.S.; et al. Evaluation of Granite Fertility Utilizing Porphyry Indicator Minerals (Zircon, Apatite, and Titanite) and Geochemical Data: A Case Study from an Emerging Metallogenic Province in the Taimyr Peninsula, Siberian High Arctic. *Minerals* **2024**, *14*, 1065. [CrossRef]
56. Howarth, R.J.; Sinding-Larsen, R. Multivariate analysis. In *Statistics and Data Analysis in Geochemical Prospecting*; Howarth, R.J., Ed.; Handbook of Exploration Geochemistry; Elsevier: Amsterdam, The Netherlands, 1983; Volume 2, pp. 207–291.
57. Reimann, C.; Filzmoser, P.; Garrett, R.G. Factor analysis applied to regional geochemical data: Problems and possibilities. *Appl. Geochem.* **2002**, *17*, 185–206. [CrossRef]
58. Reimann, C.; Filzmoser, P. Normal and lognormal data distribution in geochemistry: Death of a myth. Consequences for the statistical treatment of geochemical and environmental data. *Environ. Earth Sci.* **2000**, *39*, 1001–1014. [CrossRef]
59. Afifi, A.; Clark, V.A.; May, S. *Computer-Aided Multivariate Analysis*, 4th ed.; CRC Press: New York, NY, USA, 2003.
60. Marques de Sá, J.P. *Applied Statistics Using Spss, Statistica, Matlab and R*; Springer: Berlin, Germany, 2007; 505p.
61. Filzmoser, P.; Hron, K.; Reimann, C.; Garrett, R. Robust factor analysis for compositional data. *Comput. Geosci.* **2009**, *35*, 1854–1861. [CrossRef]
62. Liu, G.; Dai, M.; Qi, J.; Zhang, J. Geochemical characteristics of primary halos and ore-search prospecting in the depth of the Zijinshan copper-gold deposit, Fujian province. *Geophys. Geochem. Explor.* **2014**, *38*, 434–440, (In Chinese with English Abstract). [CrossRef]
63. Templ, M.; Filzmoser, P.; Reimann, C. Cluster analysis applied to regional geochemical data: Problems and possibilities. *Appl. Geochem.* **2008**, *23*, 2198–2213. [CrossRef]
64. Kaiser, H.F. The application of electronic computers to factor analysis. *Educ. Psychol. Meas.* **1960**, *20*, 141–151. [CrossRef]
65. Wong, K.-H.; Zhou, M.-F.; Chen, W.T.; O'Brien, H.; Lahaye, Y.; Chan, S.-L.J. Constraints of fluid inclusions and in-situ S-Pb isotopic compositions on the origin of the North Kostobe sediment-hosted gold deposit, Eastern Kazakhstan. *Ore Geol. Rev.* **2017**, *81*, 256–269. [CrossRef]
66. Marchenko, L.G. Genesis and Mineral Associations of Gold and PGE in the "Black Shale-Type" Gold Deposits in Kazakhstan. Master's Thesis, VSEGEI, Saint Petersburg, Russia, 2012; 294p. (In Russian).
67. Novozhilov, Y.I.; Gavrilov, A.M. *Gold-Sulfde Deposits in Carbonaceous–Terrigenous Formations*; TsNIGRI: Moscow, Russia, 1999; 175p. (In Russian)
68. Zhdanova, V.S.; Stepanov, S.Y.; Kuznetsov, A.B.; Kozin, A.K.; Aliyev, E.S.; Korneev, A.V. Hydrothermal Gold in Quartz Veins of the Neoproterozoic Rocks of the Bolshoi Karatau Ridge (Tien Shan Range). *Dokl. Earth Sci.* **2025**, *521*, 3. [CrossRef]
69. Konopelko, D.; Klemd, R.; Petrov, S.V.; Apayarov, F.; Nazaraliev, B.; Vokueva, O.; Scherstén, A.; Sergeev, S. Precambrian gold mineralization at Djamgyr in the Kyrgyz Tien Shan: Tectonic and metallogenic implications. *Ore Geol. Rev.* **2017**, *86*, 537–547. [CrossRef]
70. Yudovskaya, M.A.; Distler, V.V.; Prokofiev, V.Y.; Akinfiev, N.N. Gold mineralization and orogenic metamorphism in the Lena province of Siberia as assessed from Chertovo Koryto and Sukhoi Log deposits. *Geosci. Front.* **2016**, *7*, 453–481. [CrossRef]
71. Christie, A.B.; Brathwaite, R.L. Brathwaite Hydrothermal alteration in metasedimentary rock-hosted orogenic gold deposits, Reefton goldfield, South Island, New Zealand January. *Miner. Depos.* **2003**, *38*, 87–107. [CrossRef]
72. Herrington, R.J.; Wilkinson, J.J. Colloidal gold and silica in mesothermal vein systems. *Geology* **1993**, *21*, 539–542. [CrossRef]

73. Amagai, T.; Okamoto, A.; Niibe, T.; Hirano, N.; Motomiya, K.; Noriyoshi, T. Silica nanoparticles produced by explosive flash vaporization during earthquakes. *Sci. Rep.* **2019**, *9*, 9738. [CrossRef] [PubMed]
74. Duncan, F.; McLeish, A.; Williams-Jones, E.; Vasyukova, O.V.; Warwick, S. Board Colloidal transport and flocculation are the cause of the hyperenrichment of gold in nature. *Proc. Natl. Acad. Sci. USA* **2021**, *118*, e2100689118. [CrossRef]
75. Petrella, L.; Thébaud, N.; Fougerouse, D.; Tattitch, B.; Martin, L.; Turner, S.; Suvorova, A.; Gain, S. Nanoparticle suspensions from carbon-rich fluid make high-grade gold deposits. *Nat. Commun.* **2022**, *13*, 3795. [CrossRef] [PubMed]
76. Pokrovski, G.S.; Akinfiev, N.N.; Borisova, A.Y.; Zotov, A.V.; Kouzmanov, K. Gold speciation and transport in geological fluids: Insights from experiments and physicalchemical modelling. *Geol. Soc. Lond. Spec. Publ.* **2014**, *402*, 9–70. [CrossRef]
77. Weatherley, D.; Henley, R. Flash vaporization during earthquakes evidenced by gold deposits. *Nat. Geosci.* **2013**, *6*, 294–298. [CrossRef]
78. Andreu, E.; Proenza, J.A.; Tauler, E.; Chavez, C.; Espaillat, J. Gold and iodargyrite in the Gossan of Cerro de Maimón Deposit (Central Dominican Republic). *Macla* **2010**, *13*, 41–42.

Disclaimer/Publisher's Note: The statements, opinions and data contained in all publications are solely those of the individual author(s) and contributor(s) and not of MDPI and/or the editor(s). MDPI and/or the editor(s) disclaim responsibility for any injury to people or property resulting from any ideas, methods, instructions or products referred to in the content.

MDPI AG
Grosspeteranlage 5
4052 Basel
Switzerland
Tel.: +41 61 683 77 34

Minerals Editorial Office
E-mail: minerals@mdpi.com
www.mdpi.com/journal/minerals



Disclaimer/Publisher's Note: The title and front matter of this reprint are at the discretion of the Guest Editors. The publisher is not responsible for their content or any associated concerns. The statements, opinions and data contained in all individual articles are solely those of the individual Editors and contributors and not of MDPI. MDPI disclaims responsibility for any injury to people or property resulting from any ideas, methods, instructions or products referred to in the content.





Academic Open
Access Publishing

mdpi.com

ISBN 978-3-7258-8714-9